Alfred-Wegener-Institut, Helmholtz-Zentrum für Polar- und Meeresforschung
Periglazialforschung - Fernerkundung

Ground-Based Hyperspectral and Spectro-Directional Reflectance Characterization of Arctic Tundra Vegetation Communities

- Field Spectroscopy and Field Spectro-Goniometry of Siberian and Alaskan Tundra in Preparation of the EnMAP Satellite Mission -

Dissertation
zur Erlangung des akademischen Grades
"doctor rerum naturalium"
(Dr. rer. nat.)
in der Wissenschaftsdisziplin „Geowissenschaftliche Fernerkundung“

eingereicht am
Institut für Erd- und Umweltwissenschaften
der
Mathematisch-Naturwissenschaftlichen Fakultät
der Universität Potsdam

von
M.Sc. (TUM) Dipl.-Forsting. (FH)
Marcel Buchhorn

Potsdam, den 13. November 2013

Published online at the
Institutional Repository of the University of Potsdam:
URL http://opus.kobv.de/ubp/volltexte/2014/70189/
URN urn:nbn:de:kobv:517-opus-70189
http://nbn-resolving.de/urn:nbn:de:kobv:517-opus-70189

… Nothing shocks me. I'm a scientist.

(Indiana Jones and the Temple of Doom, 1984

ABSTRACT

The Arctic tundra, covering approx. 5.5 % of the Earth's land surface, is one of the last ecosystems remaining closest to its untouched condition. Increased tundra productivity, which is thought to be mainly a response to climate warming, and anthropogenic impacts on the physical environment lead to major implications for this ecosystem. Consequently, detailed information about the status of Arctic tundra ecosystems is needed to effectively monitor human impacts and to evaluate the influence of climate change as recommended by the Kyoto Protocol from 1997. Remote sensing is able to provide information at regular time intervals and large spatial scales on the structure and function of Arctic ecosystems. Specifically, reflectance data in the optical light spectrum can be related to biophysical plant parameters which are important input parameters for models. But almost all natural surfaces reveal individual anisotropic reflectance behaviors, which can be described by the bidirectional reflectance distribution function (BRDF). This effect can cause significant changes in the measured surface reflectance depending on solar illumination and sensor viewing geometries.

The aim of this thesis is the hyperspectral and spectro-directional reflectance characterization of important Arctic tundra vegetation communities at representative Siberian and Alaskan tundra sites as basis for the extraction of vegetation parameters, and the normalization of BRDF effects in off-nadir and multi-temporal remote sensing data. Moreover, in preparation for the upcoming German EnMAP (Environmental Mapping and Analysis Program) satellite mission, the understanding of BRDF effects in Arctic tundra is essential for the retrieval of high quality, consistent and therefore comparable datasets. Because hyperspectral or multi-angle satellite and aerial data are not operationally available for tundra regions, the research in this doctoral thesis is based on field spectroscopic and field spectro-goniometric investigations of representative Siberian and Alaskan measurement grids belonging to the Greening-of-the-Arctic program.

Performing ground-based spectro-directional measurements with currently available spectro-goniometer instruments is impractical in the Arctic due to the environmental and logistical challenges. Therefore, the first objective of this thesis was the development of a lightweight, transportable, and easily managed field spectro-goniometer system which nevertheless provides reliable spectro-directional data. I developed the *Man*ual *T*ransportable *I*nstrument platform for ground-based *S*pectro-directional observations (ManTIS). The ManTIS can be equipped with various sensor systems and allows spectro-directional measurements with up to 30° viewing zenith angle by full 360° viewing azimuth angles, in unison with a high angular accuracy and fast execution of the measurements. The developed data processing chain in connection with the self-programmed software for the semi-automatic control provides a reliable method to reduce temporal effects during the measurements. Another outcome of the thesis is that the innovative design and operation mode of the ManTIS was nationally and internationally registered for patent (patent publication number: DE 10 2011 117 713.A1).

The second objective of this thesis is the hyperspectral characterization of Arctic tundra. The outcome of the field spectro-radiometrical measurements at the Low Arctic study sites along important environmental gradients (regional climate, soil pH, toposequence, and soil moisture) show that the different plant communities can be distinguished by their nadir-view reflectance spectra. For this purpose, spectral metrics, including the averaged reflectance and absorption-related metrics, were investigated with respect to "greenness", biomass, vegetation height, and soil moisture regimes. The results especially reveal separation possibilities between the different tundra vegetation communities in the visible (VIS) blue and red wavelength regions. Additionally, the near-infrared (NIR) shoulder and NIR reflectance plateau, despite their relatively low values due to the low structure of tundra vegetation, are still valuable information sources and can separate communities according to their biomass and vegetation structure. The main spectro-radiometrically-based differences among these communities are: (i) southern sites along the climate gradient have taller shrubs and greater overall vegetation biomass, which leads to higher reflectance in the NIR; (ii) vegetation height and surface wetness have opposing effects that balance each other out with respect to the NIR reflectance along the toposequence and soil moisture gradients; (iii) moist acidic tundra (MAT) sites have "greener" species, more leaf biomass, and green-colored moss species that lead to higher absorption by photosynthetic pigments compared to moist non-acidic tundra (MNT) sites. The regression analyses with biomass indicate the possibility of separating out MAT and MNT vegetation via hyperspectral vegetation indices (VI), such as the narrowband Normalized Difference Vegetation Indices (NDVI); these communities have not been previously separable in such a good way using broadband data. Nevertheless, the field spectroscopy also exhibits some universal reflectance characteristics for tundra vegetation. In general, all different tundra plant communities show: (i) low maximum NIR reflectance; (ii) a weakly or nonexistent visible green reflectance peak in the VIS spectrum; (iii) a narrow "red-edge" region between the red and NIR wavelength regions; and (iv) no distinct NIR reflectance plateau.

These common nadir-view reflectance characteristics are essential for the understanding of the variability of BRDF effects in Arctic tundra. For the third objective – the investigation of the spectro-directional reflectance characteristics of tundra vegetation communities – the spectro-goniometry was performed at solar noon in order to gain comparable datasets. None of the analyzed tundra communities showed an even closely isotropic reflectance behavior. In general, tundra vegetation communities: (i) usually show the highest BRDF effects in the solar principal plane; (ii) usually show the reflectance maximum in the backward viewing directions, and the reflectance minimum in the nadir to forward viewing directions; (iii) usually have a higher degree of reflectance anisotropy in the VIS wavelength region than in the NIR wavelength region; and (iv) show a more bowl-shaped reflectance distribution in longer wavelength bands (>700 nm). The explanation for these findings is that tundra communities form an overall more erectophile canopy, and that the dense moss and lichen mats in the understory exclude soil BRDF effects. The fourth objective of this thesis is the analysis of the influence of high sun zenith angles on the reflectance anisotropy. Therefore,

spectro-goniometry was carried out at varying sun zenith angles ranging from 46° to 68°. The results show that with increasing sun zenith angles, the reflectance anisotropy changes to azimuthally symmetrical, bowl-shaped reflectance distributions with the lowest reflectance values in the nadir view position.

The fifth objective of this thesis is the investigation of the variability in remote sensing products for Low Arctic tundra environments that is attributable to changes in the illumination-target-sensor geometry. The spectro-directional analyses show that remote sensing products such as the NDVI or relative absorption depth products are strongly influenced by BRDF effects, and that the anisotropic characteristics of the remote sensing products can significantly differ from the observed BRDF effects in the original reflectance data. The results show that in relative absorption depth products the off-nadir values can deviate with increasing sensor view zenith angle up to 25 % from the nadir value. But the results further show that the NDVI can minimize view angle effects relative to the contrary spectro-directional effects in the red and NIR bands. For the researched tundra plant communities, the overall difference of the off-nadir NDVI values compared to the nadir value increases with increasing sensor viewing angles, but on average never exceeds 10 %.

In conclusion, this study shows that changes in the illumination-target-viewing geometry directly lead to an altering of the reflectance spectra of Arctic tundra communities according to their object-specific BRDFs. Since the different tundra communities show only small, but nonetheless significant differences in the surface reflectance, it is important to include spectro-directional reflectance characteristics in the algorithm development for remote sensing products. In preparation of the upcoming EnMAP satellite mission, (i) the availability of ground-based multi-angular and hyperspectral data, (ii) the possibility of measuring with a field-adapted, resistant and light-weight spectro-goniometer such as the developed ManTIS, and (iii) the understanding of the BRDF effects in low-growing tundra biomes are crucial for the normalization of off-nadir remote sensing data as well as the potential derivation of vegetation structure parameters for tundra and permafrost landscapes.

Keywords: Arctic tundra; spectro-directional remote sensing; field spectroscopy; field spectro-goniometry; BRDF characteristics; hyperspectral analyses; EnMAP

KURZFASSUNG

Die arktische Tundra ist mit circa 5,5 % der Landoberfläche eines der letzten großen verbliebenen fast unberührten Ökosysteme unserer Erde. Der nachgewiesene Anstieg der Biomasseproduktivität ist eine vermutete Folge der globalen Erwärmung und führt zusammen mit anderen menschlichen Einflüssen in der Arktis zu großen negativen Aus-wirkungen auf dieses Ökosystem. Zur Beurteilung des Einflusses des Klimawandels auf die Tundra sowie dessen Monitoring werden detaillierte Informationen über den Zustand des arktischen Ökosystems benötigt. Diese Zustandsdaten sind auch für die Evaluierung der Maßnahmen im Rahmen des Kyoto-Protokolls von 1997 notwendig. Nur die Fernerkundung ist in der Lage, die benötigten Informationen über Struktur und Zustand des Ökosystems großräumig und in regelmäßigen Zeitabständen zur Verfügung zu stellen. Reflektanzdaten im optischen Spektrum des Lichts können in Beziehung zu biophysikalischen Pflanzenparametern gesetzt werden. Diese Parameter dienen als wichtige Eingangsparameter für Modelle. Aber fast alle natürlichen Oberflächen zeigen individuelle anisotrope Reflexionsverhaltensweisen, welche durch die bidirektionale Reflektanzverteilungsfunktion (englisch: BRDF) beschrieben werden können. Dieser Effekt kann zu erheblichen Veränderungen im gemessenen Reflexionsgrad der Oberfläche in Abhängigkeit von den solaren Beleuchtung- und Blickrichtungsgeometrien führen.

Zielstellung dieser Arbeit ist die hyperspektrale und spektro-direktionale Charakterisierung der Oberflächenreflexion wichtiger und repräsentativer arktischer Pflanzengesellschaften der Tundra in Sibirien und Alaska, als Grundlage für die Extraktion von Vegetationsparametern und die Normalisierung von BRDF-Effekten in Off-Nadir und multi-temporalen Fernerkundungsdaten. In Vorbereitung auf die bevorstehende nationale EnMAP (Environmental Mapping and Analysis Program) Satellitenmission ist ein Grundverständnis der BRDF-Effekte in der arktischen Tundra von wesentlicher Bedeutung für die Erstellung von hochqualitativen, konsistenten und damit vergleichbaren Datensätzen. Da für die Polarregionen keine operativen Luft- und Satellitendaten im hyperspektralen Bereich bzw. mit Mehrfachblickwinkel verfügbar sind, beruhen die in dieser Arbeit genutzten Daten auf geländespektroskopische und geländespektro-goniometrische Untersuchungen von repräsentativen Messflächen des Greening-of-the-Arctic Programmes in Sibirien und Alaska.

Die Durchführung von bodengestützten spektro-direktionalen Messungen mit bisher eingesetzten Instrumenten (auch als Spektro-Goniometer bezeichnet) ist durch die ökologischen und logistischen Herausforderungen in der Arktis nur eingeschränkt möglich. Die Entwicklung eines leichten, transportablen und einfach anzuwendenden Geländespektro-Goniometers, welches dennoch zuverlässig spektro-direktionale Daten liefert, war daher die erste zu lösende Aufgabe dieser Dissertation. Das von mir entwickelte Geländespektro-Goniometer mit der Bezeichnung ManTIS („*Man*ual *T*ransportable *I*nstrument platform for ground-based *S*pectro-directional observations“) stellt eine Plattform dar, die ausgestattet mit verschiedenen Sensoren, spektro-direktionale Messungen mit Betrachtungszenitwinkel bis zu 30° und voller 360° Azimutabdeckung in Verbindung mit einer hohen Winkelmessgenauigkeit sowie einer schnellen Messdurchführung ermöglicht. Die entwickelte Datenverarbeitungskette bietet in

Verbindung mit der selbst programmierten Software für die semi-automatische Steuerung des ManTIS eine zuverlässige Methode zur Reduzierung von solaren Änderungseinflüssen während der Messdurchführung. Das innovative Design des ManTIS wurde national und international zum Patent angemeldet (Patentoffenlegungsschrift: DE 10 2011 117 713.A1).

Die hyperspektrale Reflektanz-Charakterisierung der arktischen Tundra ist die zweite Aufgabenstellung dieser Arbeit. Die Ergebnisse der geländespektro-radiometrischen Messungen der Untersuchungsflächen entlang wichtiger ökologischer Gradienten (regionales Klima, pH-Wert des Bodens, Bodenfeuchte, Toposequenz) zeigen, dass die Pflanzengesellschaften sich anhand ihrer Nadir-Reflektanzen unterscheiden lassen. Zu diesem Zweck wurden spektrale Messgrößen in Beziehung zur Biomasse, der Wuchshöhe und der Bodenfeuchte untersucht. Die Ergebnisse zeigen insbesondere die Möglichkeit der Differenzierung der verschiedenen Pflanzengesellschaften der Tundra im sichtbaren (VIS) blauen und roten Wellenlängenbereich. Die Nah-Infrarot (NIR) Schulter und das NIR-Reflektanzplateau sind trotz ihrer niedrigeren Reflektanzwerte, resultierend aus der niedrigen Vegetationsstruktur, eine wertvolle Informationsquelle, die genutzt werden kann um die Pflanzengesellschaften entsprechend ihrer Biomasse und der Vegetationsstruktur voneinander zu unterscheiden. Die wichtigsten spektro-radiometrischen Unterschiede sind: (i) höhere Sträucher und eine insgesamt höhere Vegetationsbiomasse in den südlich gelegenen Untersuchungsgebieten entlang des Klimagradienten führen zu einer höherer Reflektanz im NIR-Spektrum (ii) Vegetationshöhe und Oberflächenfeuchte sind Antagonisten in Bezug auf die Oberflächenreflektanz im NIR-Spektrum und heben sich entlang der Toposequenz- und Bodenfeuchte-Gradienten gegenseitig auf; (iii) Tundravegetation im feucht-sauren Milieu (englisch: moist acidic tundra = MAT) hat „grünere“ Pflanzenarten, höhere Blattbiomasse und „grüne“ Moosarten, welches zu einer höheren Pigmentabsorption im Vergleich zur Tundravegetation im feucht-basischen Milieu (englisch: moist non-acidic tundra = MNT) führt. Die Regressionsanalysen mit Biomasse kennzeichnen die Möglichkeit der Separation von MAT und MNT Vegetation mittels hyperspektraler Vegetationsindizes (VI) wie den Normalized Difference Vegetation Indices (NDVI). Diese Differenzierung war mit Breitband-Fernerkundungsdaten bisher in dieser Qualität nicht möglich. Die Geländespektroskopie deckt aber auch gemeinsame Reflektanzeigenschaften für die Tundravegetation auf. Die verschiedenen Pflanzengesellschaften der Tundra zeigen: (i) niedrige maximale NIR-Reflektanz; (ii) ein schwaches oder nicht sichtbares lokales Reflektanzmaximum im grünen VIS-Spektrum; (iii) einen schmalen „red-edge“ Bereich zwischen dem roten und NIR-Wellenlängenbereich und (iv) kein deutliches NIR-Reflektanzplateau.

Diese gemeinsamen Nadir-Reflektanzeigenschaften sind entscheidend für das Verständnis der Variabilität der BRDF-Effekte in der arktischen Tundra. Für die dritte Aufgabe der Arbeit, die Untersuchung der spektro-direktionalen Reflektanzeigenschaften von Pflanzengesellschaften der Tundra, wurde zur Gewinnung vergleichbarer Datensätze die Geländespektro-Goniometrie zum Sonnenhöchststand durchgeführt. Keine der untersuchten Pflanzen-gesellschaften wies hierbei isotrope Reflektanzeigenschaften auf. Im Allgemeinen zeigt Tundravegetation: (i) die höchsten BRDF-Effekte in der solaren Hauptebene; (ii) die maximalen Reflexionsgrade in den rückwärts gerichteten Blickrichtungen und die minimalen Reflexionsgrade in den Nadir bis vorwärts gerichteten Blickrichtungen; (iii) höhere Grade an

Anisotropie im VIS-Spektrum als im NIR-Spektrum und (iv) schüsselförmige Reflexionsgradverteilungen in den längeren Wellenlängenbereichen (>700 nm). Erklären lassen sich diese Ergebnisse damit, dass Pflanzengesellschaften der Tundra mit ihren dichten Moos- und Flechtenmatten im Unterwuchs eine insgesamt eher erectophile Vegetationsstruktur ohne den Einfluss von Boden BRDF-Effekten bilden. Die Analyse des Einflusses von hohen Sonnenzenitwinkeln auf die Anisotropie der Rückstrahlung ist die vierte Teilaufgabe dieser Dissertation. Hierfür wurden spektro-goniometrische Untersuchungen bei variierenden Sonnenzenitwinkeln im Bereich von 46° bis 68° durchgeführt. Die Messergebnisse belegen, dass sich mit zunehmenden Sonnenzenitwinkeln die Anisotropie-Eigenschaften in azimutalsymmetrische schüsselförmige Reflexionsgradverteilungen mit den niedrigsten Reflexionsgraden in der Nadir-Position ändern.

Die Untersuchung der Variabilität in Fernerkundungsprodukten für arktische Tundravegetation aufgrund von Änderungen in der Sonnen-Objekt-Sensor-Geometrie ist die fünfte und abschließende Aufgabe dieser Arbeit. Die spektro-direktionalen Analysen ergeben, dass Fernerkundungsprodukte wie der NDVI oder die relative Absorptionstiefe stark von BRDF-Effekten beeinflusst werden. Sie zeigen auch, dass sich die anisotropen Eigenschaften der Fernerkundungsprodukte erheblich von den beobachteten BRDF-Effekten in den ursprünglichen Reflektanzdaten unterscheiden können. Die Ergebnisse dokumentieren, dass mit zunehmendem Betrachtungszenitwinkel für die relative Absorptionstiefe die Werte in den Off-Nadir Blickrichtungen bis zu 25 % vom Nadir-Wert abweichen können. Auch lässt sich aus den Ergebnissen ableiten, dass der NDVI relativ gesehen zu den gegensätzlichen spektro-direktionalen Reflektanzeigenschaften in den roten und NIR-Bändern die blickrichtungsabhängigen BRDF-Effekte minimieren kann. Für die untersuchten Pflanzengesellschaften der Tundra steigen die Off-Nadir NDVI-Werte im Vergleich zu den Nadir-Werten mit zunehmendem Betrachtungszenitwinkel an, im Durchschnitt beträgt die Abweichung aber nicht mehr als 10 %.

Im Resümee dieser Studie wird nachgewiesen, dass Änderungen in der Sonnen-Objekt-Sensor-Geometrie direkt zu Reflektanzveränderungen in den Fernerkundungsdaten von arktischen Pflanzengesellschaften der Tundra entsprechend ihrer objekt-spezifischen BRDF-Charakteristiken führen. Da die verschiedenen Arten der Tundravegetation nur kleine, aber signifikante Unterschiede in der Oberflächenreflektanz zeigen, ist es wichtig die spektro-direktionalen Reflexionseigenschaften bei der Entwicklung von Algorithmen für Fernerkundungsprodukte zu berücksichtigen. In Vorbereitung auf die bevorstehende EnMAP Satellitenmission ist (i) die Verfügbarkeit von bodenbasierten Hyperspektraldaten mit Mehrfachblickwinkeln, (ii) die Möglichkeit der Messung mit einem leichten, robusten und geländeangepassten Spektro-Goniometer wie das entwickelte ManTIS und (iii) das Grundverständnis der BRDF-Effekte in niedrig wachsenden Tundrabiomen von entscheidender Bedeutung für die Normalisierung von Off-Nadir Fernerkundungsdaten sowie der potentiellen Ableitung von Vegetationsstrukturparametern für die Tundralandschaften der Permafrostregionen.

Schlagwörter: arktische Tundra; spektro-direktionale Fernerkundung; Geländespektroskopie; Geländespektro-Goniometrie; BRDF Eigenschaften; hyperspektrale Analysen; EnMAP

TABLE OF CONTENTS

LIST OF FIGURES

LIST OF TABLES

LIST OF ABBREVIATIONS

AAM	Azimuth Angle adjustment Module
ANIF	ANIsotropy Factor
ANIX	ANIsotropy indeX
approx.	approximately
ASCII	American Standard Code for Information Interchange
ASG	Automated Spectro-Goniometer
AVHRR	Advanced Very High Resolution Radiometer
AVIRIS	Airborne Visible and InfraRed Imaging Spectrometer
AWI	Alfred Wegener Institute, Helmholtz Centre for Polar and Marine Research
BRDF	Bidirectional Reflectance Distribution Function
BRF	Bidirectional Reflectance Factor
CAVM	Circumpolar Arctic Vegetation Map
CHRIS/Proba	Compact High Resolution Imaging Spectrometer/ Project for On-Board Autonomy
CNC	Computerized Numerical Control
dd	decimal degree
DH_z	Deadhorse – zonal study site for field spectroscopy
DN	Digital Number
DOI	Digital Object Identifier
e.g.	*exempli gratia* (for example)
EAT	Eurasia Arctic Transect
ECI	Earth Cryosphere Institute
EME	ElectroMagnetic Energy
EMR	ElectroMagnetic Radiation
EMS	ElectroMagnetic Spectrum
EnMAP	Environmental Mapping and Analysis Program
EO-1/Hyperion	Earth Observing 1/ Hyperion instrument
et al.	*et alii* (and others)
FB_d	Franklin Bluffs – dry study site for field spectroscopy
FB_m/z	Franklin Bluffs – mesic/zonal study site for field spectroscopy
FB_w	Franklin Bluffs – wet study site for field spectroscopy
FBG1 - FBG4	Franklin Bluffs G1 – G4 spectro-goniometry sites in Alaska
FIGIFIGO	Finnish Geodetic Institute Field Goniospectrometer
FIGOS	Field Goniometer System
FOV	Field Of View
fPAR	fraction of Photosynthetically Active Radiation

GIFOV	Ground Instantaneous Field of View
GOA	Greening of the Arctic
GPS	Global Positioning System
GSD	Ground Sampling Distance
GUI	Graphical User Interface
HCRF	Hemispherical Conical Reflectance Factor
HDRF	Hemispherical Directional Reflectance Factor
HICO	Hyperspectral Imager for the Coastal Ocean
HIS/HJ-1A	HyperSpectral Imager on board the HJ-1a satellite
HNB	Hyperspectral NarrowBand
HTBVI	Hyperspectral Two-Band Vegetation Indices
HV_fs	Happy Valley – footslope study site for field spectroscopy
HV_hc	Happy Valley – hill crest study site for field spectroscopy
HV_ms/z	Happy Valley – midslope/zonal study site for field spectroscopy
HVG1 - HVG2	Happy Valley G1 – G2 spectro-goniometry sites in Alaska
HVI	Hyperspectral Vegetation Index
hy-ARC-VEG	Hyperspectral method development for ARCtic VEGetation biomes
hyDRaCAT	Hyperspectro-Directional Reflectance Characteristics of Arctic Tundra
IAC ETH	Institute for Atmospheric and Climate science of the ETH
IFOV	Instantaneous Field Of View
IPAR	Intercepted Photosynthetically Active Radiation
IPY	International Polar Year
LAI	Leaf Area Index
LCLUC	Land Cover/Land Use Change
ManTIS	Manual Transportable Instrument platform for ground-based Spectro-directional observations
MAT	Moist Acidic Tundra
MISR	Multiangle Imaging SpectroRadiometer
MNT	Moist Non-acidic Tundra
n	number of samples
NAAT	North American Arctic Transect
NASA	National Aeronautics and Space Administration
NDVI	Normalized Difference Vegetation Index
NIR	Near-InfraRed
PARABOLA	Portable Apparatus for Rapid Acquisition of Bidirectional Observations of Land and Atmosphere
PCA	Principal Component Analysis
PLS	Partial Least Squares
PRISMA	PRecursore IperSpettrale of the application mission

R^2	Coefficients of determination
R_{nadir}	Nadir view reflectance
RS	Remote Sensing
SpInMine	Spectral Index Data Mining Tool
SW_MAT	Sagwon Hills – zonal MAT study site for field spectroscopy
SW_MNT	Sagwon Hills – zonal MNT study site for field spectroscopy
SWI	Summer Warmth Index
SWIR	Short-Wavelength InfraRed
SZA	Sun Zenith Angle
TDR	Time Domain Reflectrometry
TIROS-1	Television and Infrared Observation Satellite-1
USA	United States of America
USB	Universal Serial Bus
VB	Visual Basic
VDG1 - VDG2	Vaskiny Dachi G1 – G2 spectro-goniometry sites in West-Siberia
VI	Vegetation Indices
VIS	VISible
VNIR	Visible-Near-InfraRed

LIST OF SYMBOLS

c_{diff}	Correction factor to reduce short-term temporal solar changes	dimensionless
c_{ref}	Correction factor of reference panel for BRDF effects	dimensionless
dE_i	Incident irradiance within a project solid angle	$[Wm^{-2}nm^{-1}]$
dL_i	Incident radiance within a project solid angle	$[Wm^{-2}nm^{-1}sr^{-1}]$
dL_r	Reflected radiance from the target of projected solid angle	$[Wm^{-2}nm^{-1}sr^{-1}]$
E_{diff}	Diffuse total irradiance	$[Wm^{-2}nm^{-1}]$
$f_r()$	Functions characterizing the reflected radiation	
L_r	Reflected radiance from the target	$[Wm^{-2}nm^{-1}sr^{-1}]$
L_{ref}	Reflected radiance from the reference panel	$[Wm^{-2}nm^{-1}sr^{-1}]$
R	Reflectance factor	dimensionless
R_{ref}	Reflectance factor of reference panel (calibration coefficient)	dimensionless
t_0	timestamp of radiance measurement of the reference panel	[sec]
t_x	timestamp of radiance measurement of the target	[sec]
θ_i, ϕ_i	Zenith and azimuth angle of the direction of illumination	[°]
θ_r, ϕ_r	Zenith and azimuth angle of the direction of reflection	[°]
λ	Wavelength	[nm]

1 INTRODUCTION

1.1 Background and Scientific Setting

The Arctic tundra is one of Earth's few remaining wilderness areas that resembles its original, untouched ecological condition [*Moore and Garratt*, 2006]. Geographically, the Arctic tundra biome is found in the northern High Latitudes (generally > 60° N) bordered by the Arctic Ocean to the north and by the northern limit of tree growth (10°C July mean isotherm) to the south [*Moore and Garratt*, 2006]. Therefore, it shows a circumpolar distribution and is underlain by continuous permafrost. Overall, the Arctic tundra covers ~75,000 km², representing 5.5 % of the Earth's land surface, and can be divided into three zones: North America, Eurasia, and Greenland & Iceland [*Moore and Garratt*, 2006].

Time series of optical satellite data from 1982 to 2011 have shown an increase in the productivity, or "greenness" of Arctic tundra [*Bhatt et al.*, 2010; *Bhatt et al.*, 2013; *Eastman et al.*, 2013; *Myneni et al.*, 1997; *Zhou et al.*, 2001]. This greening trend is thought to be mainly a response to climate warming [*Callaghan et al.*, 2011b; *Epstein et al.*, 2012; *Lawrence et al.*, 2008; *Walker*, 2006]. This warming trend in the Arctic is also confirmed by other studies [*Hinzman et al.*, 2005; *Kaufman et al.*, 2009]. Moreover, the Arctic is warming at nearly double the general planetary rate [*Blunden et al.*, 2011; *Winton*, 2006] leading to major implications for tundra ecosystems, including changes in active layer depth, permafrost and thermokarst distribution, carbon cycling, hydrology, and wildlife [IPCC, 2007; *Walker et al.*, 2012a]. In addition to the already occurring and pronounced impacts due to climate warming, rapid social-ecological changes due to rapid oil and gas development, intensive subsistence use by the local people, and increased ecotourism endanger sensitive permafrost environments, especially in the North Slope of Alaska, USA and the Yamal Peninsula, Russia [*Chapin III et al.*, 2006; *Forbes et al.*, 2009; *Walker et al.*, 2009b].

Consequently, detailed and sustained environmental monitoring is needed to develop new management approaches to help local leaders, land managers and policy makers. Intensive ground-based observations along transects that traverse the complete Arctic bioclimate gradient in northern Alaska and the Yamal region have been carried out (e.g., [*Walker et al.*, 2012b; *Walker et al.*, 2009b; *Walker et al.*, 2011b]), and have been coupled to extensive social-ecological research (e.g., [*Chapin et al.*, 2006; *Forbes et al.*, 2009; *Kumpula et al.*, 2012; National Research Council (NRC), 2003]). Due to the remoteness and large area of the tundra biome, these *in-situ* studies are mainly limited to accessible, "hotspot" regions [*Lubin and Massom*, 2006]. For the generalization and upscaling of small-scale *in-situ* results, continuous monitoring of larger geographic areas is needed. Therefore, spaceborne remote sensing (RS) provides the best available tool for land-cover mapping and change detection in the Arctic [*Callaghan et al.*, 2011a; *Lubin and Massom*, 2006]. In particular, the optical part of the electromagnetic spectrum (between 400 nm to 2,500 nm) is the most important for RS of surface features such as vegetation, soils, and rocks [*Kaufmann et al.*, 2012].

Although optical RS, thus the gathering of reflectance data of the Earth's surface from a considerable distance, is cost-effective and has already been applied for decades, most optical spaceborne missions are primarily designed for image acquisition in the tropical and middle latitudes [*Lubin and Massom*, 2006]. Further, the short growing season for tundra vegetation, the accelerated phenology, frequent cloud cover, high standing water and surface water coverage, and extreme illumination conditions (sun zenith angles in Arctic latitudes always larger than 43°) challenge optical airborne and spaceborne RS of high latitude vegetation [*Kääb*, 2008; *Stow et al.*, 2004; *Vierling et al.*, 1997].

The era of RS of polar regions started in the 1960's with the launch of the first civilian satellite called TIROS-1 (Television and Infrared Observation Satellite-1) [*Lubin and Massom*, 2006]. But the first detailed multi-spectral map of the Earth's surface and the opportunity to detect and monitor environmental changes in the Arctic emerged only in the early 1970's with the launch of the Landsat-1 satellite [*Lubin and Massom*, 2006]. Since then, several sensors mounted on spaceborne platforms have been launched which provide RS data for Arctic tundra at various spectral, spatial and temporal resolutions. These data have been used as inputs for regional and global climate models, to detect land use and land cover changes, and to extract biophysical plant parameters [*Callaghan et al.*, 2011a]. The next boost in the usage of RS data in environmental and social-ecological studies in the Arctic began with the International Polar Year (IPY) 2007-8, a large scientific campaign focusing on the polar regions which encompassed hundreds of projects in over 60 nations [International Council for Science, 2004]. A good overview of past and recent studies using RS data for vegetation analysis and modeling in Arctic tundra can be found in *Stow et al.* [2004] and *Callaghan et al.* [2011a], while *Kääb* [2008] provides an overview about RS techniques for the detection and monitoring of permafrost-related problems and hazards.

Several studies have shown the capability of multi-spectral satellite and aerial RS data to extract biophysical parameters as well as to detect land use and land cover changes in the Arctic tundra. These studies mainly used vegetation indices, a mathematical compression of the received reflectance data in the sensed wavelength regions to one value, such as the Normalized Difference Vegetation Index (NDVI) [*Epstein et al.*, 2012; *Hope et al.*, 1993; *Huemmrich et al.*, 2010; *Laidler et al.*, 2008; *Olthof and Latifovic*, 2007; *Riedel et al.*, 2005; *Stow et al.*, 2004; *Vierling et al.*, 1997; *Walker et al.*, 2003]. The NDVI is also an important input parameter for regional and global climate models, vegetation models, and land-atmosphere energy flux models. NDVI observations from spaceborne sensors such as the Advanced Very High Resolution Radiometer (AVHRR), which acquires a daily, global dataset at coarse spatial resolution (> 1 x 1 km pixel), indicate that circumpolar Arctic tundra vegetation "greenness" has increased during the 32 year satellite record [*Bhatt et al.*, 2013; *Jia et al.*, 2003; *Stow et al.*, 2004; *Verbyla*, 2008]. Additionally, land-cover classifications based on the AVHRR NDVI were used to create a circumpolar Arctic vegetation map (CAVM) [*Walker et al.*, 2005]. By integrating *in-situ* biomass sampling studies along Arctic transects [*Epstein et al.*, 2008; *Walker et al.*, 2012b] with co-incident AVHRR NDVI observations, it was possible to estimate the total biomass as well as temporal changes in

biomass of Arctic tundra biomes [*Raynolds et al.*, 2012; *Walker et al.*, 2003]. AVHRR NDVI data records and the plant functional types defined by the CAVM were recently used in a dynamic vegetation model, which predicts an increased tundra shrubification and a tree-line shift to higher latitudes due to climate warming [*Zhang et al.*, 2013]. Increases in shrub cover in the tundra biome, as well as northward and upslope expansion of trees into tundra-dominated areas, has been confirmed for the Siberian Low Arctic by comparing RS data from the 1960's and recent years [*Frost and Epstein*, 2013]. This may lead to an overall weakening of the global important Arctic tundra carbon sink [*Zhang et al.*, 2013].

In contrast to multi-spectral RS, which covers several, discrete wavelength regions, spectral sampling by imaging spectroscopy, also called hyperspectral RS, provides continuous information across the electromagnetic spectrum, thus enabling the development of new algorithms for more detailed vegetation analysis, species identification, and monitoring. Hyperspectral RS of Arctic landscapes to date is mainly limited to airborne platforms, and therefore studies using the advantages of imaging spectroscopy are limited to several small-scale research sites. To date, detailed knowledge about the reflectance characteristics of tundra vegetation over the whole optical wavelength region is mainly acquired by ground-based spectro-radiometric measurements, called field spectroscopy. For example, *Ulrich et al.* [2009] used field spectroscopy to characterize radiometric properties of tundra vegetation on different periglacial surfaces and geomorphological units in the Arctic Lena Delta, Russia. This may led to a better classification of land-cover units in satellite RS data, and therefore a better monitoring of land-cover changes.

Vegetated surfaces show significant absorption and reflection features in the visible and near-infrared wavelength region. However, satellite data from platforms with pointing capabilities or with wide imaging swaths are influenced by the bidirectional reflectance distribution function (BRDF). This effect can cause significant changes in the measured spectral surface reflectance depending on the solar illumination and sensor viewing geometry. Therefore, spectro-directional RS, analyzing not only the spectral reflectance characteristics but also the anisotropic reflectance behavior, has become more and more important in recent years for the calibration of off-nadir satellite images, the normalization of multi-temporal images with varying sun zenith angles, and the extraction of canopy parameters [*Martonchik et al.*, 2000; *Schaepman*, 2007]. Up to now, RS systems delivering spectro-directional data from Arctic tundra landscapes are few. One of the existing systems is the Multiangle Imaging Spectroradiometer (MISR) [*Diner et al.*, 2007]. An Arctic study of *Selkowitz* [2010] showed that the implementation of the directional domain can significantly increase the accuracy of fractional shrub canopy mapping, and therefore improve monitoring of shrub expansions. Large knowledge gaps remain, however, because the few existing studies about the spectro-directional reflectance characteristics of tundra vegetation communities are based on ground-based measurements at a few selected test sites [*Vierling et al.*, 1997], or alternatively, the BRDF properties are derived from ground-based measurements in comparable biomes [*Peltoniemi et al.*, 2005; *Peltoniemi et al.*, 2008; *Solheim et al.*, 2000].

1.2 Motivation and Research Questions

Condensed, detailed information about the status of Arctic tundra ecosystems is critically important for monitoring human impacts in the Arctic and to forecast the Earth's climate in the framework of the Kyoto Protocol [United Nations Framework Convention on Climate Change (UNFCCC), 1998], as well as for carbon cycle research [Global Carbon Project, 2003]. Remote sensing provides the best prospective tools for global-scale monitoring of permafrost and tundra landscapes. Specifically, hyperspectral RS data can be related to vegetation indices (VI), leaf area index (LAI) and the fraction of photosynthetically active radiation (fPAR). These biophysical parameters are important input parameters for regional and global models. However, airborne and spaceborne RS of vegetated surfaces in the visible and near-infrared wavelength region is influenced greatly by viewing geometry and solar illumination angle changes. In preparation for the upcoming German hyperspectral and multi-angle capable EnMAP (Environmental Mapping and Analysis Program) satellite mission, the understanding of BRDF effects in tundra biomes is essential for the retrieval of high quality, consistent and therefore comparable and reproducible hyperspectral Arctic datasets. Further, the knowledge of the spectral and directional reflectance characteristics is critical for the calibration of off-nadir as well as multi-temporal RS data of past and current sensors. Therefore, field spectroscopy and field spectro-goniometry are valuable tools for the acquisition of ground-based hyperspectral and spectro-directional reflectance data of tundra vegetation communities.

The aim of this thesis is the ground-based hyperspectral and spectro-directional reflectance characterization of important Arctic tundra vegetation communities using field spectroscopy and field spectro-goniometry of representative Siberian and Alaskan tundra sites in preparation of the EnMAP satellite mission. In order to achieve this aim, five specific objectives and research questions have been defined:

- BRDF effects are strongly influenced by the underlying spectral nadir reflectance variability of the measured vegetation surface. Therefore, the first objective is the hyperspectral nadir-view reflectance characterization of Low Arctic tundra along important environmental gradients in order to understand the geoecological characteristics which affect the spectral reflectance characteristics.
- The second objective of the thesis is the development of a lightweight, transportable, cheap, and easy managed field spectro-goniometer system which nevertheless provides reliable spectro-directional data. The main motivation for this is that existing spectro-goniometers are impractical to use in the Arctic due to the environmental and logistical challenges.
- The third objective is the ground-based spectro-directional reflectance characterization of representative vegetation communities in order to get an overview of the variability of BRDF effects in Arctic tundra. To maximize the comparability of the acquired data, the spectro-goniometry for this objective has been performed at solar noon. Further,

all results are presented in the spectral resolution of the EnMAP sensor by using its spectral response curves for the spectral resampling.

- Since BRDF effects as well as the nadir reflectance spectra of vegetated surfaces are sensitive to illumination zenith angle changes, the fourth objective is the investigation of the influence of high sun zenith angles on the reflectance anisotropy.
- The fifth objective is the investigation of the variability in RS products for Low Arctic tundra environments due to changes in the illumination-target-sensor geometry.

1.3 Structure of Thesis

Based on the above research objectives, this thesis is structured as follows. The introduction including the scientific setting and problem description is given in Chapter 1. Chapter 2 deals with the fundamentals of RS primarily with respect to the hyperspectral and spectro-directional RS of vegetation. This chapter also includes a short description of the German EnMAP satellite mission, as well as the current state-of-knowledge of spectro-goniometer systems for the ground-based measurement of BRDF effects.

Chapter 3 gives a brief overview of the tundra permafrost study locations and their environment, while the first part of the observations and methodology chapter (Chapter 4) explains the geoecological characteristics of the study sites in more detail. The second part of Chapter 4 describes the methodology used for the field work and data analysis. For the sake of readability, the technical description of the developed spectro-goniometer and the sensor systems, the error assessment for field spectro-goniometer measurements, the sampling strategy, the data processing chain, and the data visualization are presented in a separate, extended methodology chapter (Chapter 5).

The examination of the hyperspectral nadir-view reflectance characteristics of tundra vegetation communities along environmental gradients is combined in a stand-alone chapter (Chapter 6), and followed by the presentation of the results of the spectro-goniometer measurements (Chapter 7). The spectro-goniometry results are structured into three parts giving an overview of the spectro-directional reflectance characteristics of Low Arctic tundra vegetation, showing the influence of high sun zenith angles on the reflectance anisotropy, and analyzing the variability of multi-angular RS products. A detailed discussion of the spectro-directional characteristics in combination with the specific canopy properties and received hyperspectral nadir-view reflectance characteristics of Arctic tundra vegetation as well as the occurring high sun zenith angles is given in Chapter 8. Further, the applicability of multi-angle RS products in context of the EnMAP satellite system is discussed in this chapter.

Finally, the conclusions drawn from this thesis with respect to the posed research objectives, as well as a brief outlook with suggestions for further research close the dissertation and can be found in Chapter 9. Supplementary data, consisting of a list of existing field and laboratory spectro-goniometer systems, a print of the patent application for the developed AWI ManTIS spectro-goniometer system, and the detailed data reports of the spectro-goniometry results can be found in the Appendix.

2 FUNDAMENTALS OF HYPERSPECTRAL AND SPECTRO-DIRECTIONAL REMOTE SENSING

2.1 Hyperspectral Remote Sensing of Vegetation

Remote sensing is defined as "the science of acquiring, processing, and interpreting images, and related data, obtained from … [devices] that record the interaction between matter and electromagnetic radiation" [*Sabins*, 2007]. Electromagnetic energy (EME) propagates in the form of sine waves with specific distances between the waves [*Sabins*, 2007]. The distances are defined as wavelengths measured in nm to m. The total range of these wavelengths is called the electromagnetic spectrum (EMS). Remote sensing operates in several regions of the EMS, but the optical part, especially between 400 nm to 2,500 nm, is the most important for RS of surface materials such as vegetation, soils, and rocks [*Kaufmann et al.*, 2012]. The amount of EME detected by a RS sensor is altered by several interactions of the electromagnetic radiation (EMR) with the atmosphere and the Earth's surface which cause the EMR to be either reflected, absorbed, transmitted or scattered (Figure 2-1A). As a result of absorption by atmospheric gases and aerosols, only certain wavelength regions in the EMS, called atmospheric transmission windows, are usable for spaceborne optical RS (Figure 2-1B) [*Sabins*, 2007].

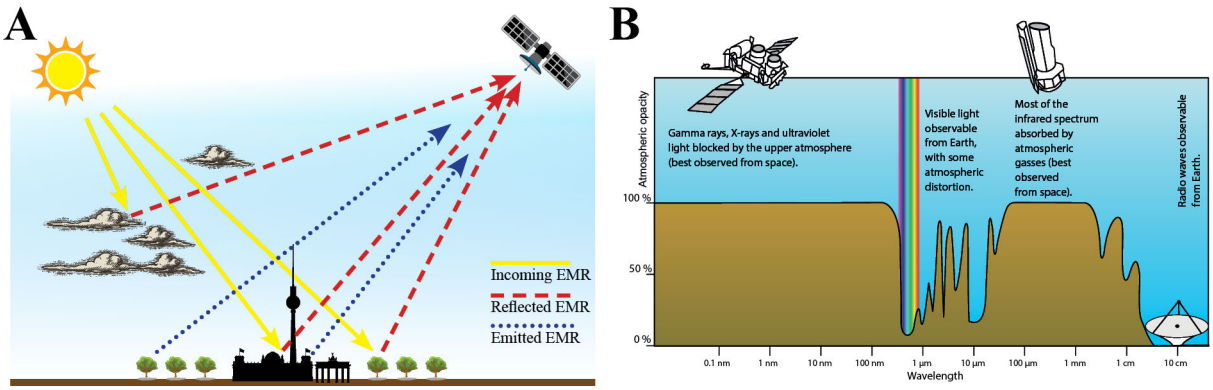

Figure 2-1: (**A**) The concept of passive remote sensing (RS) ([*Malgorzata*, 2010], modified). (**B**) The atmospheric transmission windows for optical RS (NASA, public domain, modified).

Different materials such as vegetation, soil, water, or buildings reflect the EME in different ways. Therefore, the physical and chemical properties of an object determine the spectral reflectance, a function of reflection coefficient over wavelength, of the object [*Jakomulska et al.*, 2003]. The best way to record the reflectance spectrum, often termed the spectral reflectance signature, of an object is the acquisition of simultaneous nadir-viewing images in many narrow wavelength bands (i.e., "narrowbands" with band widths <= 10 nm; band widths > 10 nm are termed "broadband"), so that a reflectance spectrum can be derived for each pixel in the image [*Schaepman*, 2007] (Figure 2-2A). The term "hyperspectral" refers to RS systems which simultaneously record the EME within more than 15 wavelength bands over the EMS, while RS systems with less than 15 bands are called "multi-spectral" (Figure 2-2B).

Since the most significant absorption and reflection features occur in the 400 – 2,500 nm wavelength region [*Kaufmann et al.*, 2012], passive RS using the sun as an illumination source can be used for the monitoring and characterization of ecosystems. Several studies have shown the capability of multi-spectral and broadband aerial and satellite RS to identify the biophysical attributes of vegetation. Multi-spectral, broadband RS data may not, however, be adequate to extract sharp reflectance changes in narrow spectral regions [*Horler et al.*, 1983] (Figure 2-2B). Recent technical developments in airborne and spaceborne sensors open the door for new methods that can use the entire spectral feature space of imaging spectroscopy [*Asner*, 1998; *Schaepman et al.*, 2009]. Therefore, imaging spectroscopy (Figure 2-2A), also called hyperspectral RS, of vegetation can be used as a tool to detect and identify ecological succession processes, plant health, phenological status, and invasive species to provide information about ecosystem conditions and composition [*Asner et al.*, 2008; *Schmidtlein and Sassin*, 2004; *Ustin et al.*, 2004].

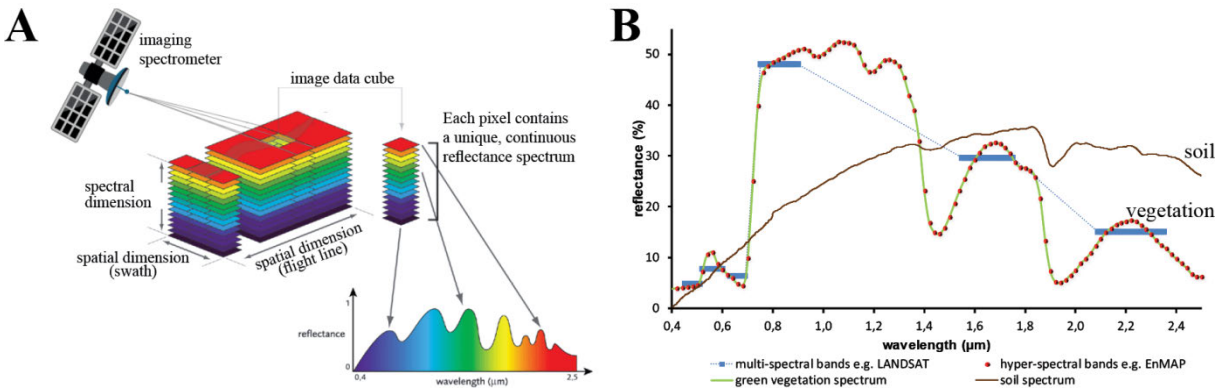

Figure 2-2: (**A**) The imaging spectroscopy concept ([VITO], modified). (**B**) Multi-spectral (blue colored bands) versus hyperspectral (red dots) RS, and exemplary reflectance signatures of vegetation (green) and soil (brown) (signatures retrieved from [*Baldridge et al.*, 2009]).

Reflectance spectra from vegetated surfaces are highly differentiated by wavelength. The visible (VIS) EMS (400 – 700 nm) is strongly influenced by the pigment absorption of the plants [*Gitelson et al.*, 2003; *Jakomulska et al.*, 2003] (Figure 2-2B). The main pigment groups are chlorophylls, carotenoids, and anthocyanins. Photosynthetic light absorption is mainly done by chlorophyll, with absorption maxima in the blue (~440 nm for chlorophyll-a; ~470 nm for chlorophyll-b) and red (~663 nm for chlorophyll-a; ~657 nm for chlorophyll-b) wavelength regions. Carotenoids have their absorption maxima in the blue and green wavelength regions, and the group of anthocyanins in the green wavelength region [*Gitelson et al.*, 2003]. The main function of carotenoids is to protect chlorophyll and cell tissue against damage by ultraviolet radiation [*Armstrong and Hearst*, 1996]. Many arctic and alpine plants that are exposed to high solar radiation maintain high concentrations of carotenoids [*Ziska et al.*, 1992]. Since the blue region of the EMS is more strongly scattered in the atmosphere than longer wavelengths, the red wavelength region is considered to be a better indicator for chlorophyll content in spaceborne RS [*Maas and Dunlap*, 1989]. The reflectance in the near-infrared (NIR) wavelength region (700 – 1,400 nm) is mainly influenced by plant cell structure and vegetation biomass (Figure 2-2B). Multiple scattering of radiation between air

spaces and cell walls in leaf tissue leads to high reflectance values in the NIR wavelength region, a phenomenon often referred to as the NIR reflectance plateau [*Gausman*, 1974]. Absorption by liquid water in plant tissue can create clearly visible absorption features at 980 nm and 1,200 nm in the NIR reflectance plateau. The short-wavelength infrared (SWIR) region (1,400 to 3,000 nm) is mainly influenced by the water content of leaf tissue [*Jakomulska et al.*, 2003] (Figure 2-2B). A unique feature of green vegetation is the so called 'red-edge' at around 700 nm (680 – 740 nm) (Figure 2-2B), a spectral transition zone between low reflectance in the red wavelength region and high reflectance in the NIR wavelength region [*Horler et al.*, 1983]. The 'red edge' can be directly used as a metric of the chlorophyll content [*Gates et al.*, 1965], with changes in the chlorophyll content resulting in a 'red edge' shift [*Horler et al.*, 1983]. Further, this reflectance difference is commonly used in RS for calculating VIs [*Richardson and Wiegand*, 1977].

Although aerial and satellite RS data can be applied to some extent without other information, the best results are obtained by linking RS measurements with ground-based spectro-radiometric measurements and biophysical parameters of the vegetation. Therefore, field spectroscopy is a valuable tool that facilitates more robust interpretation and contextualization of satellite-based observations.

2.2 Spectro-Directional Remote Sensing of Vegetation

Spectro-directional RS, also called multi-angular RS, is defined as "the simultaneous acquisition of spatially coregistered images, in many, spectrally contiguous bands, at various observation and illumination angles, in an internationally recognized system of units from a remotely operated platform" [*Schaepman*, 2007]. Therefore, spectro-directional RS adds the analysis of the directional reflectance characteristics (angular domain) to the spectral reflectance analysis of surfaces which is normally performed from nadir-viewing instruments (Figure 2-3A). Spectro-directional RS data can be acquired by using either several sensors viewing a target area from different angles, or by using a sensor platform with pointing capabilities. If we broaden the definition, then multi-angle datasets can also be created by successive passes of instruments either with nadir pointing, or with wide imaging swaths.

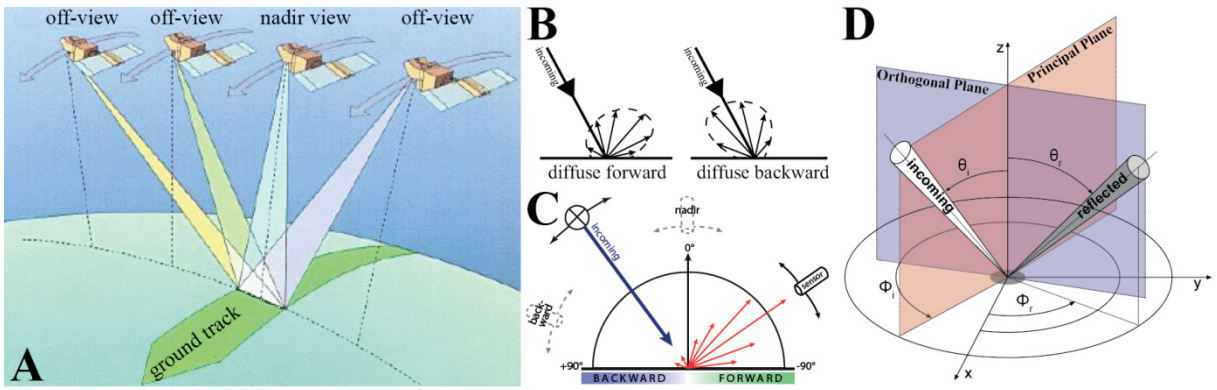

Figure 2-3: (**A**) The spectro-directional RS concept ([CRISP, 2001], modified). (**B**) Radiance scattering through interactions of incoming radiation with the surface. (**C**) Concept of observing anisotropic reflectance distributions in an azimuthal plane ([*Müller*, 2008], modified. (**D**) Concept of the bidirectional reflectance-distribution function (BRDF) ([*Küster*, 2011], modified).

Spectro-directional RS takes advantage of the fact that most of the natural and man-made surfaces do not show Lambertian reflectance behavior [*Deering et al.*, 1999; *Peltoniemi et al.*, 2005; *Pinter, JR. et al.*, 1990; *Sandmeier et al.*, 1998a; *Sandmeier et al.*, 1999; *Solheim et al.*, 2000; *Vierling et al.*, 1997]. This is because surfaces interact differently with incoming EMR depending on their physical properties. Therefore, they display anisotropic reflectance distributions, e.g. surfaces can show a preferred forward or backward reflectance scattering pattern (Figure 2-3B) when observed in a defined azimuthal plane (Figure 2-3C). Reflectance anisotropy is more strongly pronounced in the principal plane - an azimuthal plane where the illumination source, the target and the sensor are in one plane [*Sandmeier and Itten*, 1999; *Sandmeier*, 2000] - and decreases towards the orthogonal plane. Thus, these illumination-target-viewing geometries are preferred for the analysis of the angular reflectance signature, a function of reflectance over wavelength and viewing angle in a given azimuthal plane, of an object. To quantify and characterize the reflectance anisotropy of a surface, the theoretical concept of the BRDF, a mathematical function "relating the irradiance incident from one given direction to its contribution to the reflected radiance in another direction" [*Nicodemus et al.*, 1977] is used (Figure 2-3D). Direct BRDF measurements are not possible, but the BRDF can be approximately determined by measuring the hemispherical conical reflectance factor (HCRF) of an object.

The BRDF characteristics of vegetated surfaces are mainly controlled by the vegetation canopy geometry and multiple scattering effects within the vegetation canopy. The canopy geometry influences the distribution and proportion of shadowed and illuminated surfaces within the plant canopy which change under varying viewing-illumination geometries [*Hapke et al.*, 1996; *Sandmeier et al.*, 1998a]. Multiple scattering effects in the vegetation canopy regulate the intensity ("darkness") of the shadows [*Sandmeier et al.*, 1998a]. That is, because the relatively low amount of radiation in the vegetation canopy in wavelength regions with high absorption (visible blue and red chlorophyll absorption bands) reduces the multiple scattering effects, the contrast between shadowed and illuminated surfaces increases and therefore enhances the reflectance anisotropy [*Sandmeier and Itten*, 1999]. By the same token, higher multiple scattering effects in wavelength regions with higher reflection (visible green and near-infrared bands) reduce the contrast in the canopy. Therefore, the spectral reflectance characteristics of the surface create the spectral dependence of BRDF effects. Moreover, the calculation of VIs from spectro-directional data create new functions (called vegetation index distribution functions) [*Küster*, 2011]. Thus, the spectral variability of the reflectance anisotropy has impacts on VIs which may confound comparisons of different images acquired over time.

In conclusion, the anisotropic reflectance behavior of surfaces affects hyperspectral RS of vegetation in several ways. Changes in the illumination-target-viewing geometry directly lead to an altering of the spectral reflectance signature of the sensed objects according to their object-specific BRDFs. Therefore, the spectro-directional information source can be used to facilitate the production of high quality, consistent and therefore comparable and reproducible datasets, by minimizing the impact of reflectance anisotropy in RS data acquired by

instruments with pointing capabilities or wide swaths [*Schaepman*, 2007]. Moreover, numerous studies have shown that canopy architecture properties can be derived from spectro-directional RS data [*Coburn et al.*, 2010; *Deering et al.*, 1999; *Gianelle and Guastella*, 2007; *Sandmeier and Deering*, 1999; *Selkowitz*, 2010; *Walter-Shea et al.*, 1997], and that a combination of spectral and angular information sources can improve the accuracy of image classification approaches [*Barnsley et al.*, 1997; *Buchhorn and Schneider*, 2010].

2.3 The EnMAP Satellite System

Currently, spaceborne imaging spectroscopy in the optical part of the EMS is limited to the CHRIS/Proba (Compact High Resolution Imaging Spectrometer / Project for On-Board Autonomy) [*Barnsley et al.*, 2004], EO-1/Hyperion (Earth Observing 1 / Hyperion instrument) [*Pearlman et al.*, 2003], HICO (Hyperspectral Imager for the Coastal Ocean) [*Lucke et al.*, 2011] and HIS/HJ-1A (Hyperspectral Imager on board the HJ-1a satellite) [*Wang et al.*, 2010] sensors (Figure 2-4A). The Environmental Mapping and Analysis Program (EnMAP), a German hyperspectral satellite mission launching in 2017, is the next step in this line and will provide observations with a high spectral and spatial resolution.

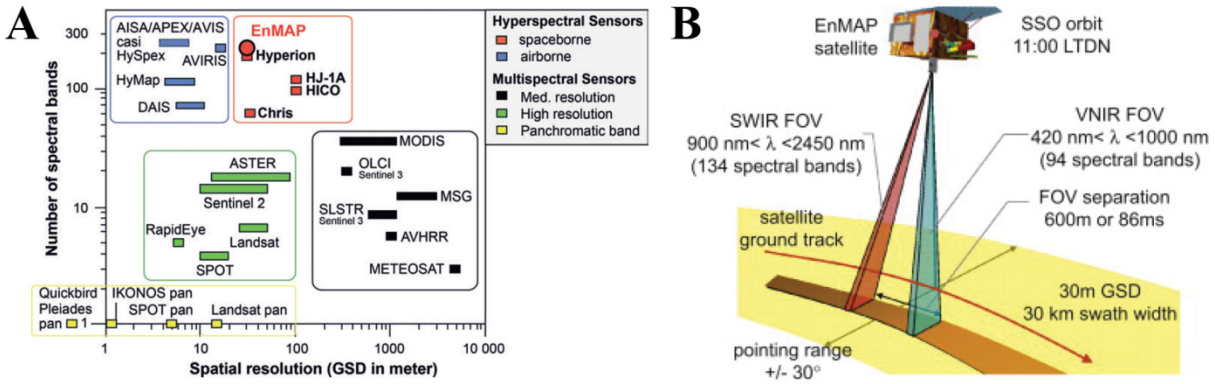

Figure 2-4: (**A**) Placing of the spectral and spatial resolution of the EnMAP sensor in the context of important airborne and spaceborne hyperspectral and multi-spectral sensors ([*Kaufmann et al.*, 2012], modified). (**B**) Specifications of the Environmental Mapping and Analysis Program (EnMAP) satellite mission ([German Aerospace Center (DLR), 2013], modified).

The ENMAP hyperspectral imager is a push broom sensor with two separate spectral detectors: one for VNIR (visible-near-infrared) ranging from 420 to 1,000 nm and one for the SWIR ranging from 900 to 2,450 nm [*Stuffler et al.*, 2007]. Therefore, the EnMAP sensors record the EMR in a wavelength range from 420 to 2,450 nm in 242 continuous and 10 – 40 nm wide bands sampled at 5 – 20 nm intervals [*Kaufmann et al.*, 2012]. The planned orbit height of about 643 km will result in a spatial ground sampling distance (GSD) of 30 x 30 m and a nominal swath width of 30 km at nadir [*Stuffler et al.*, 2007]. The satellite operates in a sun-synchronous orbit which enables EnMAP to overfly any point on the Earth's surface at the same local solar time. Moreover, the sun-synchronous orbit allows a global coverage within a 27 day repeating cycle when operating in near-nadir mode (±5°) [*Kaufmann et al.*, 2012]. A specific feature of EnMAP is the across-track pointing capability of ±30°. Therefore, the accessible target range increase to ±390 km, and the ±30° off-nadir pointing feature allows

that each point on earth can be investigated and revisited every 3 – 4 days [*Stuffler et al.*, 2009]. Overall, the daily areal coverage is at least 150,000 km² in near-nadir looking operation mode, corresponding to a total strip length of ~5,000 km per day [*Stuffler et al.*, 2009]. Figure 2-4B summarizes the main characteristics of the EnMAP satellite mission, while Figure 2-5A shows a drawing of the satellite in orbit.

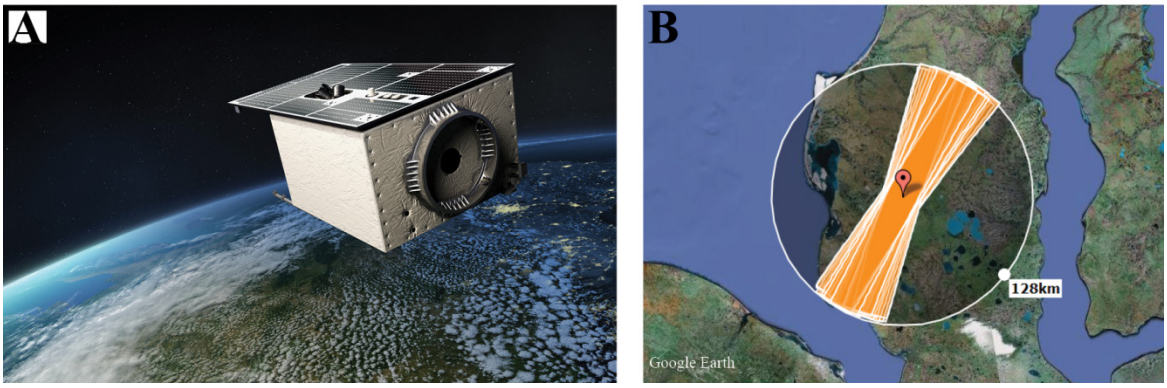

Figure 2-5: (**A**) Visualization of the EnMAP satellite [German Aerospace Center (DLR), 2013]. (**B**) Simulated overflight paths of the EnMAP satellite for the 27 day repeating cycle at Vaskiny Dachi, Russia (oral communication: [Ute Heiden, 2011]; Google Earth, 2011).

In conclusion, the EnMAP space mission will serve the increasing demand "… to derive relevant surface parameters on a global scale with an accuracy not achievable by currently available spaceborne sensors, to assimilate those parameters in physically based ecosystem models, and ultimately to provide information products reflecting the status of various terrestrial ecosystems" [*Stuffler et al.*, 2007]. Since the EnMAP sensor has pointing capabilities, both spectral and directional reflection characteristics can be measured with high spatial, spectral, and temporal resolution. Moreover, the EnMAP mission is well-suited to acquire spectro-directional RS data in the Arctic, and therefore for the monitoring and characterization of tundra landscapes: due to EnMAPs sun-synchronous orbit and the across-track pointing capability, Arctic target surfaces can be observed on a near-daily basis. For example, the simulation of EnMAP orbits for the 27 day repeating cycle at the Vaskiny Dachi study location on the Yamal Peninsula, Russia shows 24 acquisition opportunities (Figure 2-5B, Table 2-1). In comparison, only 6 to 7 acquisitions are possible in the same time span in the mid-latitudes.

Table 2-1: Off-nadir viewing angles of the simulated EnMAP satellite overflight paths for the 27 day repeating cycle at Vaskiny Dachi, Russia. (oral communication: [Ute Heiden, 2011]).

Nr	Date	Time	Off-nadir [°]		Nr	Date	Time	Off-nadir [°]
1	2011/08/01	08:38:51	29.0		13	2011/08/15	08:09:01	11.6
2	2011/08/02	07:27:38	18.4		14	2011/08/16	08:34:29	27.0
3	2011/08/04	08:18:40	17.8		15	2011/08/17	07:23:14	21.3
4	2011/08/06	07:32:55	14.8		16	2011/08/18	07:48:47	3.1
5	2011/08/07	07:58:28	4.0		17	2011/08/19	08:14:17	15.2
6	2011/08/08	08:23:57	21.1		18	2011/08/20	08:39:44	29.5
7	2011/08/09	07:12:38	28.0		19	2011/08/21	07:28:31	17.7
8	2011/08/10	07:38:13	10.9		20	2011/08/22	07:54:04	0.9
9	2011/08/11	08:03:44	7.8		21	2011/08/23	08:19:34	18.5
10	2011/08/12	08:29:13	24.1		22	2011/08/25	07:33:49	13.9
11	2011/08/13	07:17:56	24.7		23	2011/08/26	07:59:21	4.8
12	2011/08/14	07:43:30	7.0		24	2011/08/27	08:24:50	21.7

Despite the advanced capabilities of EnMAP, robust processing and calibration techniques will be needed to produce comparable and reproducible datasets, and to extract canopy properties from spectro-directional RS data of tundra landscapes acquired by EnMAP. The development of such techniques, in turn, requires detailed knowledge of the hyperspectral and spectro-directional reflectance characteristics of tundra vegetation communities.

2.4 Spectro-Goniometer Systems for the Ground-Based Measurement of BRDF Effects

Since direct BRDF measurements of natural and man-made surfaces are not possible, BRDF characteristics are approximately determined by measuring the HCRF of the surface at various illumination-viewing geometries. Various ground-based instruments, termed spectro-goniometers, have been developed in the recent years to measure HCRF in both laboratory and *in-situ* field conditions. Laboratory spectro-goniometers have the advantage that all of the potential influences on measurement can be controlled, while field spectro-goniometers measure the target reflectance under natural illumination conditions. An overview of existing spectro-goniometer systems is assembled in Appendix A.

Ground-based spectro-directional data are used for (i) the investigation of the physical mechanisms of BRDF effects; (ii) the development and validation of BRDF models; (iii) the investigation of relationships between BRDF effects and biophysical parameters; and (iv) the validation of airborne and spaceborne BRDF data [*Sandmeier*, 2000]. In principle, spectro-goniometers are mechanical devices for the spectro-radiometric measurement of surface reflectance under varying geometric attributes of sensor viewing azimuth (ϕ_r), sensor viewing zenith (θ_r), and illumination direction (ϕ_i, θ_i). This principle follows the BRDF definition (Figure 2-3D). Figure 2-6 illustrates the concept for the reproducibility of spectro-directional remote sensing data through ground-based measurements. It shows that the viewing direction of the spectro-goniometer (Figure 2-6A) can be directly correlated to the viewing direction of an airborne or spaceborne imaging spectrometers with pointing capabilities or wide swaths (Figure 2-6B).

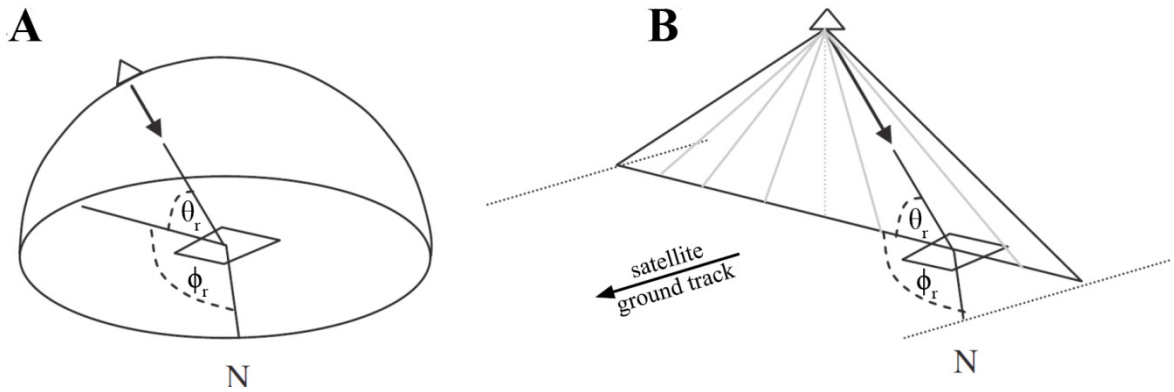

Figure 2-6: Concept for the reproducibility of spectro-directional remote sensing data through ground-based spectro-directional measurements. (**A**) Definition of the sensor azimuth and zenith viewing position (ϕ_r, θ_r) for measurements with spectro-goniometer devices. (**B**) Equivalent sensor azimuth and zenith viewing position for airborne and spaceborne imaging spectrometers with pointing capabilities or wide swaths. Source: [*Feingersh et al.*, 2010], modified.

The main components of spectro-goniometer devices consist of a platform and a spectro-radiometer. The platform is used for the positioning and orientation of the sensor. The angular accuracy of the platform and the specifications of the spectro-radiometer are essential for the quality as well as the spectral and spatial resolution of the received spectro-directional reflectance data. Two general spectro-goniometer design principles can be distinguished, one with a constant observation center (Figure 2-7A), and the other with a constant sensor position (Figure 2-7B).

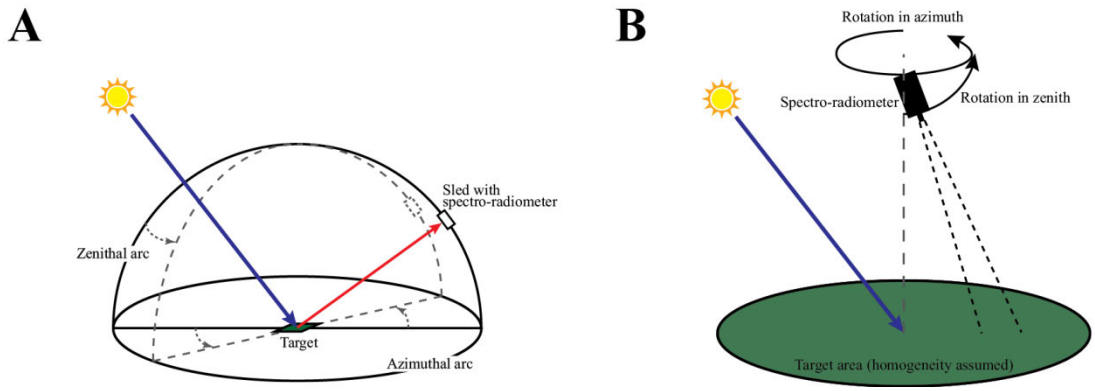

Figure 2-7: Basic concepts for the construction of spectro-goniometers. (**A**) Spectro-goniometer with a constant observation center. (**B**) Spectro-goniometer with a constant sensor position. Source: [*Schopfer*, 2008], modified.

Spectro-goniometer systems with a constant observation center are commonly designed using some type of azimuth goniometer-arc, and a zenith goniometer-arc with a mounted sled holding the spectro-radiometer [*Bourgeois et al.*, 2006b; *Painter et al.*, 2003; *Sandmeier and Itten*, 1999]. The main advantage of this design is that the observation distance remains the same for all viewing directions, because the target is kept at the center of the device while the sled is positioned in the spanned observation hemisphere (Figure 2-7A). Since the target area can be small in this construction principle, the reflectance anisotropy of small-scale homogeneous surfaces can be characterized [*Schopfer*, 2008]. Disadvantages of this design, however, are that measurements of targets are only possible up to a certain height, and that the obtained spectro-directional reflectance characteristics are not necessarily representative of larger areas [*Schopfer*, 2008].

For measurements with spectro-goniometer systems with a constant sensor position, the sensor rotates around its lateral axis in order to point in the desired viewing direction [*Schopfer*, 2008]. Therefore, for such systems, the spectro-radiometer is commonly mounted on some kind of boom or crane (Figure 2-7B) [*Bruegge et al.*, 2000; *Schneider et al.*, 2004]. The primary advantage of this design is that spectro-directional reflectance characterization is possible for tall vegetation communities such as forests. Disadvantages are that the entire sensor viewing area must be assumed to be homogeneous, and that the distances between the sensor and the observed part of the sensor viewing area change with positioning of the sensor. This can lead to scaling effects in the measured target reflectance and therefore in the derived BRDF characteristics [*Schopfer*, 2008].

3 THE TUNDRA PERMAFROST STUDY LOCATIONS AND THEIR ENVIRONMENT

The CAVM divides the Arctic into five bioclimate subzones (A-E) [*Walker et al.*, 2005] (Figure 3-1A). In the framework of the IPY Greening of the Arctic project, two Arctic transects traversing all five bioclimate subzones have been established. The transect locations were chosen to research the consequences of climate change in a continental climate setting compared to a relatively maritime setting. The continental transect covers the bioclimatic gradient from northern Canada to Alaska, USA and is known as the North American Arctic Transect (NAAT) [*Walker et al.*, 2008b], while the maritime transect also known as the Eurasia Arctic Transect (EAT) covers the bioclimatic gradient from Franz Josef Land to Yamal Peninsula, Russia [*Walker et al.*, 2009b]. The research within the scope of this dissertation was carried out in study locations within the Low Arctic part (subzone D and E) of these two transects. In detail, four study locations (Deadhorse, Franklin Bluffs, Sagwon Hills, Happy Valley) are situated in the Low Arctic part of the NAAT, and two study locations (Vaskiny Dachi, Laborovaya) are situated in the Low Arctic part of the EAT. All study locations contain one to three homogeneous study sites and were visited during the ECI-GOA-Yamal 2011 [*Heim et al.*, 2012] and EyeSight-NAAT-ALASKA 2012 expeditions [*Buchhorn and Schwieder*, 2012].

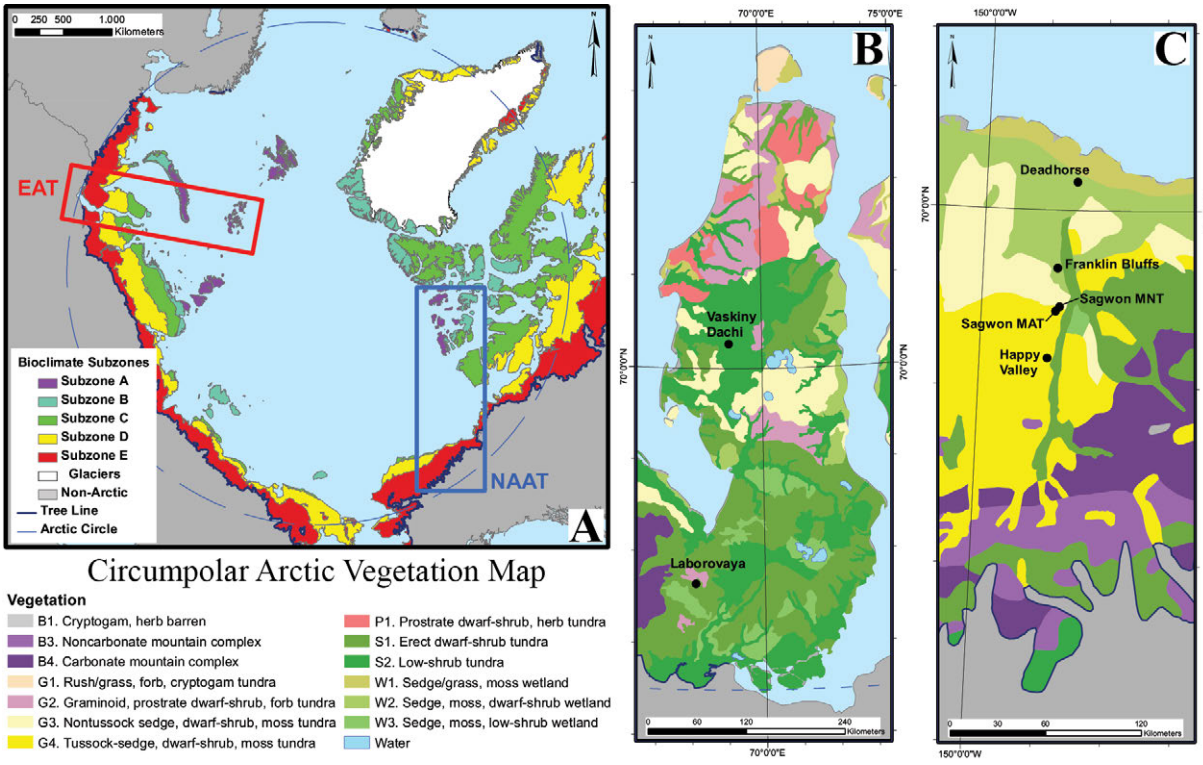

Figure 3-1: (**A**) The Arctic bioclimate subzones of the CAVM [*Walker et al.*, 2005]. The blue rectangle marks the NAAT and the red rectangle marks the EAT. (**B**) The Low Arctic part of the EAT with the study locations Laborovaya and Vaskiny Dachi. (**C**) The Low Arctic part of the NAAT with the study locations Happy Valley, Sagwon Hills, Franklin Bluffs, and Deadhorse.

3.1 The Eurasia Arctic Transect (EAT)

A detailed description of all study locations along the EAT can be found in data reports published by the Alaska Geobotany Center [*Walker et al.*, 2011a; *Walker et al.*, 2009a; *Walker et al.*, 2008a; *Walker et al.*, 2009c]. For the Low Arctic study locations a brief description will be presented in the next two sections.

3.1.1 Geological and Climatic Setting

The EAT was established in 2007 – 2010 and the Low Arctic part of this transect is located on the Yamal Peninsula, Russia (Figure 3-1B). The EAT has a more maritime climate which is strongly influenced by the North Atlantic [*Walker et al.*, 2012b]. Moreover, compared to the NAAT the EAT has nearly double the precipitation. The Yamal Peninsula is a relatively homogeneous plain which is thought to have been unglaciated during the Last Glacial Maximum [*Walker et al.*, 2012b]. The soils in the Low Arctic part are mainly acidic silt loam and clay loam [*Walker et al.*, 2009a].

The Laborovaya study location (subzone E) is situated in the foothills at the northern end of the Polar Urals in the continuous permafrost zone. The study sites are located on a flat plain with thaw lakes to the east and north. In the west and south the plain is bordered by sandstone bedrock [*Walker et al.*, 2009a]. The Vaskiny Dachi study location (subzone D) is situated southeast of the main Bovanenkova gas field in the central part of the Yamal Peninsula. The study sites are located in the watersheds of the Se-Yakha and Mordy-Ykha rivers on different alluvial-lacustrine-marine plains and terraces [*Walker et al.*, 2009a]. The surfaces are influenced by windblown basic sands.

3.1.2 Vegetation

The central part of the Yamal Peninsula shows extensive landslide events mainly caused by tabular ground ice [*Walker et al.*, 2012b]. The successional vegetation sequence following landslides that are mainly willow communities and the heavy grazing pressure due to reindeer tended by indigenous people have a big influence on the vegetation.

The dominant vegetation at Laborovaya is sedge, dwarf shrub, moss tundra (*Carex bigelowii-Betula nana-Aulaconium palustre*) [*Walker et al.*, 2009a]. Where one study site (LV1) shows a more moist sedge, dwarf shrub, moss tundra on moist clayey soils, the second study site (LV2) shows a relatively dry sedge, dwarf shrub, moss-lichen tundra on sandy soils.

The vegetation at Vaskiny Dachi is strongly influenced by grazing. Moreover, willow patches covering hill slopes and valley bottoms are widely distributed. The study site VD1 shows a heavily grazed sedge, dwarf shrub, moss tundra (*Carex bigelowii-Vaccinium vitis idaea-Hylocomium splendens*) on moist clayey soils [*Walker et al.*, 2009a]. The soils at VD2 are a mix of sand and clay, and show a dominant vegetation of dwarf shrub, graminoid, moss tundra (*Betula nana-Calamagrostis holmii-Aulacomnium turgidum*) [*Walker et al.*, 2009a]. The study site VD3 has a dwarf shrub, lichen tundra vegetation (*Carex bigelowii-Vaccinium vitis idaea-Sphaerophorus globosus*) on dry sandy soils [*Walker et al.*, 2009a].

3.2 The North American Arctic Transect (NAAT)

A detailed description of all study locations along the NAAT can be found in several publications of the Alaska Geobotany Center [*Kade et al.*, 2005; *Raynolds et al.*, 2008; *Vonlanthen et al.*, 2008; *Walker et al.*, 2008b; *Walker et al.*, 2011c]. For the Low Arctic study locations a brief description will be presented in the next two sections.

3.2.1 Geological and Climatic Setting

The NAAT has a more continental climate due to the presence of perennial sea ice in the Beaufort Sea [*Walker et al.*, 2012b]. The Low Arctic part of the NAAT, established in 2001–2006, follows the road network of the Dalton Highway (Figure 3-1C). The Happy Valley study location is situated in the foothills of Alaska's North Slope in the bioclimate subzone E. The foothills are old upland surfaces not glaciated during the Last Glacial Maximum and have acidic silt loam to silty clay loam soils [*Barreda et al.*, 2006]. The Arctic Foothills are bordered by the Brooks Range in the south and in the north by the Arctic Coastal Plain.

The Franklin Bluffs and Deadhorse study locations are situated in the coastal plain of Alaska's North Slope in the bioclimate subzone D. The coastal plain was glaciated during the Last Glacial Maximum and has circumneutral to basic soils in association with silty loess that is blown from the major rivers in the eastern part of the Arctic Coastal Plain [*Barreda et al.*, 2006]. An important soil pH boundary occurs at the Sagwon Hills study location [*Walker et al.*, 1998]. This boundary separates the predominantly moist acidic tundra (MAT) south of the boundary from the predominantly moist non-acidic tundra (MNT) to the north. The boundary is close to but not coincident with a physiographic boundary separating the Arctic Foothills to the south from the Arctic Coastal Plain to the north [*Zhang et al.*, 1996].

3.2.2 Vegetation

The dominant vegetation of bioclimate subzone E in Alaska (Happy Valley, Sagwon-MAT) is moist acidic tussock-sedge, dwarf shrub, moss tundra (*Sphagno-Eriophoretum vaginati*) [*Walker et al.*, 2005]. This plant community is also called MAT and corresponds to the zonal plant community in this subzone. The zonal study site at Happy Valley was complemented with two additional study sites following a toposequence from a hill crest to a footslope.

The zonal plant community of bioclimate subzone D in northern Alaska (Sagwon-MNT, Franklin Bluffs, Deadhorse) is moist non-acidic non-tussock sedge, dwarf shrub, moss tundra (*Dryado integrifoliae-Caricetum bigelowii*), also called MNT [*Walker et al.*, 2005]. An important component of the MNT is the abundant nonsorted circles (frost boils), which are small patterned ground features caused by soil frost heave and cover large parts of most MNT surfaces [*Walker et al.*, 2008b; *Washburn*, 1980]. In order to study the influence of soil moisture changes on MNT vegetation, two additional study sites were established at the Franklin Bluffs study location.

Please note that a more detailed vegetation description of the nine NAAT study sites can be found in Chapter 6.2.2 as well as for all NAAT and EAT study sites in Appendix C.

4 OBSERVATIONS AND METHODOLOGY

4.1 Observations Used for this Study

4.1.1 The ECI-GOA-Yamal 2011 Expedition

The ECI-GOA-Yamal 2011 expedition of the teams of the Earth Cryosphere Institute (ECI), Siberian Branch of the Russian Academy of Science, RU; the University of Virginia, US; the University of Alaska Fairbanks, US; and the Alfred Wegener Institute for Polar and Marine Research (AWI), DE, took place as part of the NASA Yamal Land Cover/Land Use Change (NASA Yamal-LCLUC) and the Greening of the Arctic (GOA) program during the period from July 11th to September 9th, 2011. The AWI expedition team, Birgit Heim and Marcel Buchhorn, carried out field work from August 1st to September 1st, 2011 on the Yamal Peninsula. A detailed schedule and description of the expedition as well as the field work that was carried out is published as a data report within the NASA Yamal-LCLUC report published by the Alaska Geobotany Center [*Heim et al.*, 2012].

The established measurements grids of the NASA Yamal-LCLUC project [*Walker et al.*, 2009a; *Walker et al.*, 2008a] have been re-visited and spectro-radiometric properties were measured at Laborovaya, with the study sites LA1 and LA2, and at Vaskiny Dachi, with the study sites VD1, VD2, and VD3. Each study site has five 50 m transects and five 5 m x 5m study plots in order to examine how the terrain and anthropogenic factors of reindeer herding and resource development combined with the climate variations on the Yamal Peninsula affect the spatial and temporal patterns of vegetation.

4.1.2 The EyeSight-NAAT-Alaska 2012 Expedition

The EyeSight-NAAT-Alaska 2012 expedition took place as part of the AWI hy-ARC-VEG (hyperspectral method development for arctic vegetation biomes) and the GOA programs. The field work was carried out along the Low Arctic part of the NAAT from June 25th to July 17th, 2012. The core expedition team consisted of Marcel Buchhorn (AWI) and Marcel Schwieder (Humboldt-Universität zu Berlin). Geobotanical scientific support was provided by the Alaska Geobotany Center of the University of Alaska Fairbanks, US. A detailed schedule and description of the expedition as well as the field work that was carried out is published in the AWI "Reports on Polar and Marine Research" [*Buchhorn and Schwieder*, 2012].

Overall nine study sites containing homogeneous 10 x 10 m (100 m²) grids representing the typical vegetation along environmental gradients (soil moisture, pH-value, toposequence, regional climate) were visited. These grids are long-term research sites established by the Alaska Geobotany Center [*Barreda et al.*, 2006]. Therefore, detailed vegetation descriptions of the study sites are available. Moreover, various publications confirm that the study sites represent the typical vegetation along environments gradients in Alaska [*Epstein et al.*, 2012; *Epstein et al.*, 2008; *Kade et al.*, 2005; *Raynolds et al.*, 2008; *Walker et al.*, 2003].

4.1.3 Data Used for Hyperspectral Characterization of Arctic Tundra

Due to the extreme severe weather conditions in August 2011 (continuous storms and rain), only limited field spectroscopy data from the Siberian tundra communities is available. Therefore, the hyperspectral characterization of EAT tundra communities is limited to the study plots used for the spectro-goniometer measurements. Consequently, for the detailed ground-based hyperspectral characterization of Low Arctic tundra along environmental gradients (soil moisture, pH-value, toposequence, regional climate) only the field spectroscopy data from the Alaskan study sites were used. Table 4-1 shows the field spectroscopy measurements used in the dissertation.

Table 4-1: The field spectroscopy measurements used for the nadir-view hyperspectral characterization of Arctic tundra vegetation along environmental gradients. ***Note:*** SZA = sun zenith angle; MAT = moist acidic tundra; MNT = moist non-acidic tundra; dd = decimal degree.

Code	Study site	Coordinates (dd, WGS 84)	Date	SZA	Samples
HV_hc	Happy Valley – hill crest site	N 69.1468 W 148.8521	2012-06-29	47°	100
HV_ms/z	Happy Valley – midslope site (zonal site of subzone E)	N 69.1468 W 148.8482	2012-06-29	47°	100
HV_fs	Happy Valley – footslope site	N 69.1470 W 148.8469	2012-06-29	47°	100
SW_MAT	Sagwon Hills – zonal site of subzone E	N 69.4255 W 148.6959	2012-07-04	48°	100
SW_MNT	Sagwon Hills – zonal site of subzone D	N 69.4335 W 148.6717	2012-07-04	48°	100
FB_w	Franklin Bluffs – wet site	N 69.6741 W 148.7171	2012-07-10	47°	100
FB_m/z	Franklin Bluffs – mesic site (zonal site of subzone D)	N 69.6745 W 148.7212	2012-07-09	47°	100
FB_d	Franklin Bluffs – dry site	N 69.6747 W 148.7209	2012-07-09	47°	100
DH_z	Deadhorse – zonal site of transition C/D	N 70.1614 W 148.4668	2012-07-11	49°	100

The vegetation change along a toposequence is represented by the three measurement grids at the Happy Valley study location. The dominant vegetation is acidic tussock, graminoid, erect dwarf shrub, moss tundra (Figure 4-1). Due to the water movement downslope, the hill crest study site (HV_hc) shows a drier and the footslope study site (HV_fs) shows a wetter environment compared to the moist midslope study site (HV_ms/z). The midslope study site also represents the zonal plant community in the Alaskan bioclimate subzone E which is MAT. The soil moisture gradient is represented by the three measurement grids at the Franklin Bluffs study location. The study site with the highest soil moisture values (FB_w) shows a non-acidic graminoid, moss and sedge dominated tundra vegetation (Figure 4-1). The dry Franklin Bluffs study site (FB_d) shows a non-acidic prostrate dwarf shrub, lichen and sedge dominated tundra vegetation, while the mesic study site (FB_m/z) shows a non-acidic graminoid, sedge, prostrate dwarf shrub tundra vegetation (Figure 4-1). Again, the mesic study site also represents the zonal plant community in Alaskan bioclimate subzone D which

is MNT. The two study sites at Sagwon Hills form the transition from the acidic (SW_MAT) to the non-acidic (SW_MNT) tundra. The vegetation in these two study sites correspond to the dominant vegetation in bioclimate subzone E (MAT) and bioclimate subzone D (MNT) (Figure 4-1). Finally, the five zonal study sites of all study locations (HV_ms/z, SW_MAT, SW_MNT, FB_m/z, DH_z) show the temperature changes from south to north, which describes the regional climate gradient. Therefore, the Deadhorse study site (DH_z) shows a moist/wet non-acidic graminoid, sedge, prostrate dwarf shrub tundra vegetation (Figure 4-1).

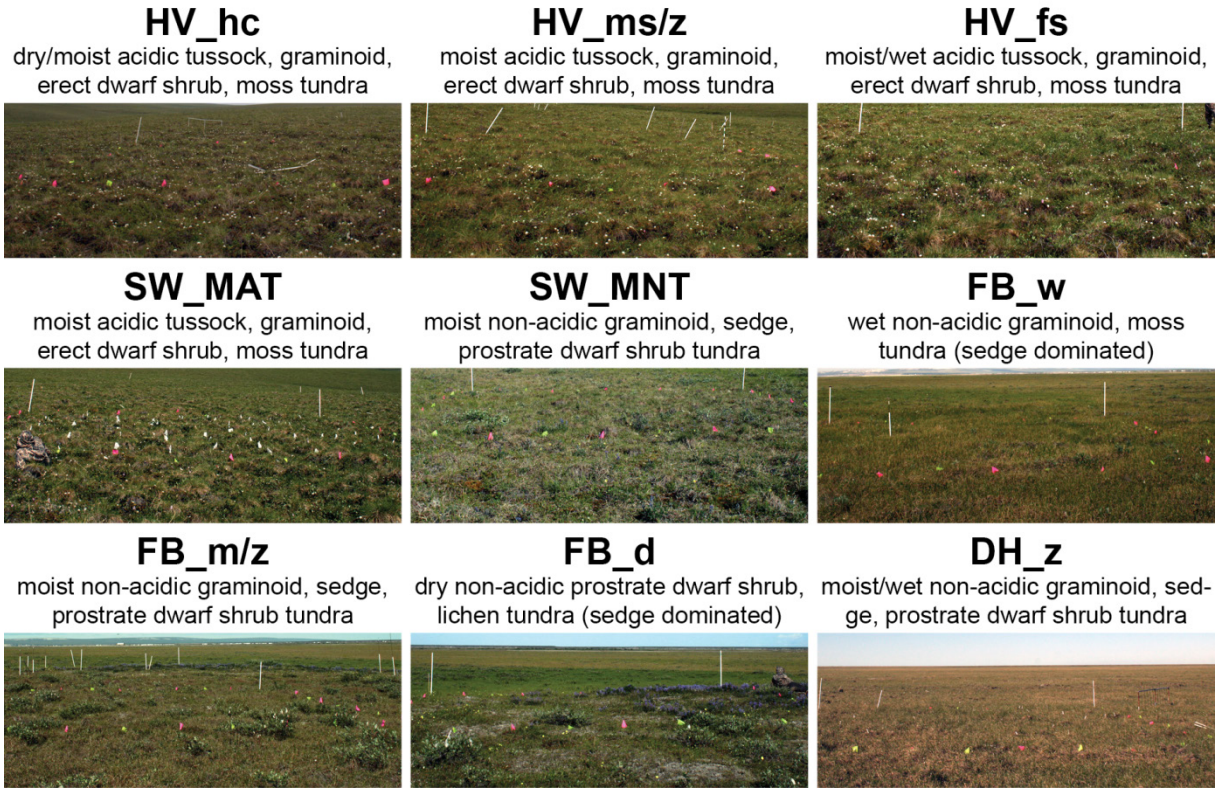

Figure 4-1: The nine study sites used for the ground-based hyperspectral characterization of Arctic tundra vegetation along environmental gradients. ***Note:*** HV = Happy Valley; SW = Sagwon Hills; FB = Franklin Bluffs; DH = Deadhorse; hc = hill crest; ms = midslope; fs = footslope; z = zonal; MAT = moist acidic tundra; MNT = moist non-acidic tundra; w = wet; m = mesic; d = dry.

A more detailed vegetation description of the study sites and their relation to the environmental gradients and zones concept can be found in Chapter 6.2.2.

4.1.4 Data Used for Spectro-Directional Characterization of Arctic Tundra

Ground-based spectro-directional reflectance measurements can only be carried out during optimal sky conditions. Due to the severe weather limitations in August 2011, only two study plots near the VD1 study site at the Vaskiny Dachi study location could be measured using the developed AWI field spectro-goniometer. However, these plots could be measured under several sun zenith angles. In contrast, six study plots at the Happy Valley and Franklin Bluffs study locations were measured with the spectro-goniometer under varying sun zenith angles during the Alaska 2012 expedition. Overall 24 full hemispheres of eight representative Low Arctic tundra vegetation communities under sun zenith angles ranging from 46° to 68° could

be acquired. Nevertheless, Table 4-2 shows the field spectro-goniometer measurements which have been selected for the spectro-directional reflectance analyses in the dissertation.

Table 4-2: The field spectro-goniometer measurements used for the spectro-directional characterization of Arctic tundra vegetation. ***Note:*** SZA = sun zenith angle; dd = decimal degree.

Code	Location	Coordinates (dd, WGS 84)	Date	Local time	SZA	Sky
VDG1_02	Vaskiny Dachi	N 70.2758 E 68.8913	2011-08-12	13:20	55°	cirrostratus
VDG2_03	Vaskiny Dachi	N 70.2757 E 68.8908	2011-08-29	12:31	61°	cirrostratus
HVG1_01	Happy Valley	N 69.1469 W 148.8518	2012-06-30	10:17	56°	cirrostratus
HVG1_02	Happy Valley	N 69.1469 W 148.8518	2012-06-30	11:35	50°	clear
HVG1_03	Happy Valley	N 69.1469 W 148.8518	2012-06-30	13:47	46°	clear
HVG2_03	Happy Valley	N 69.1469 W 148.8520	2012-07-02	13:52	46°	cirrostratus
FBG1_03	Franklin Bluffs	N 69.6744 W 148.7210	2012-07-07	13:56	47°	cirrostratus
FBG1_04	Franklin Bluffs	N 69.6744 W 148.7210	2012-07-07	15:49	50°	clear
FBG1_05	Franklin Bluffs	N 69.6744 W 148.7210	2012-07-07	18:02	59°	cirrostratus
FBG1_06	Franklin Bluffs	N 69.6744 W 148.7210	2012-07-07	19:52	68°	cirrostratus
FBG2_03	Franklin Bluffs	N 69.6744 W 148.7207	2012-07-09	13:48	47°	cirrostratus
FBG3_01	Franklin Bluffs	N 69.6745 W 148.7209	2012-07-13	13:56	48°	cirrostratus
FBG4_01	Franklin Bluffs	N 69.6744 W 148.7202	2012-07-15	14:03	48°	clear

The dominant vegetation of the two Siberian study plots at the Vaskiny Dachi study location differ only in one anthropogenic factor - the grazing pressure through reindeer herding by indigenous people. The VDG1 study plot shows a sedge, dwarf shrub, moss tundra vegetation, while the VDG2 study plot shows a heavily grazed sedge, dwarf shrub, moss tundra vegetation (Figure 4-2). The dominant vegetation of the HVG1 study plot at Happy Valley is moist acidic tussock sedge, erect dwarf shrub, moss tundra, and therefore corresponds to the zonal plant community in Alaskan bioclimate subzone E which is MAT. At the second study plot (HVG2), an erect dwarf shrub plant community with moss and lichen mats in the understory, representing the typical dwarf shrub community in bioclimate subzone E, was measured. The dominant vegetation of the FBG1 study plot at the Franklin Bluffs study location is moist non-acidic non-tussock sedge, prostrate dwarf shrub, moss tundra (Figure 4-2). Again this study plot corresponds to the zonal plant community in Alaskan bioclimate subzone D which is MNT. The FBG2 study plot is the counterpart to the HVG2 study plot. It shows a prostrate dwarf shrub plant community with moss and lichen mats in the understory representing the typical dwarf shrub community in bioclimate subzone D. In MNT, the abundant nonsorted circles are an important component. Therefore, the FBG3 study

plot shows a frost boil community (moss-lichen-liverwort mix) as dominant vegetation (Figure 4-2). The spectro-goniometer measurements at the FBG4 study plot (Franklin Bluffs) were performed over a horsetail community. Horsetail communities are not dominant vegetation in the Low Arctic, but were frequently seen in the Alaskan and Siberian study locations. A more detailed vegetation description of the study plots can be found in Appendix C.

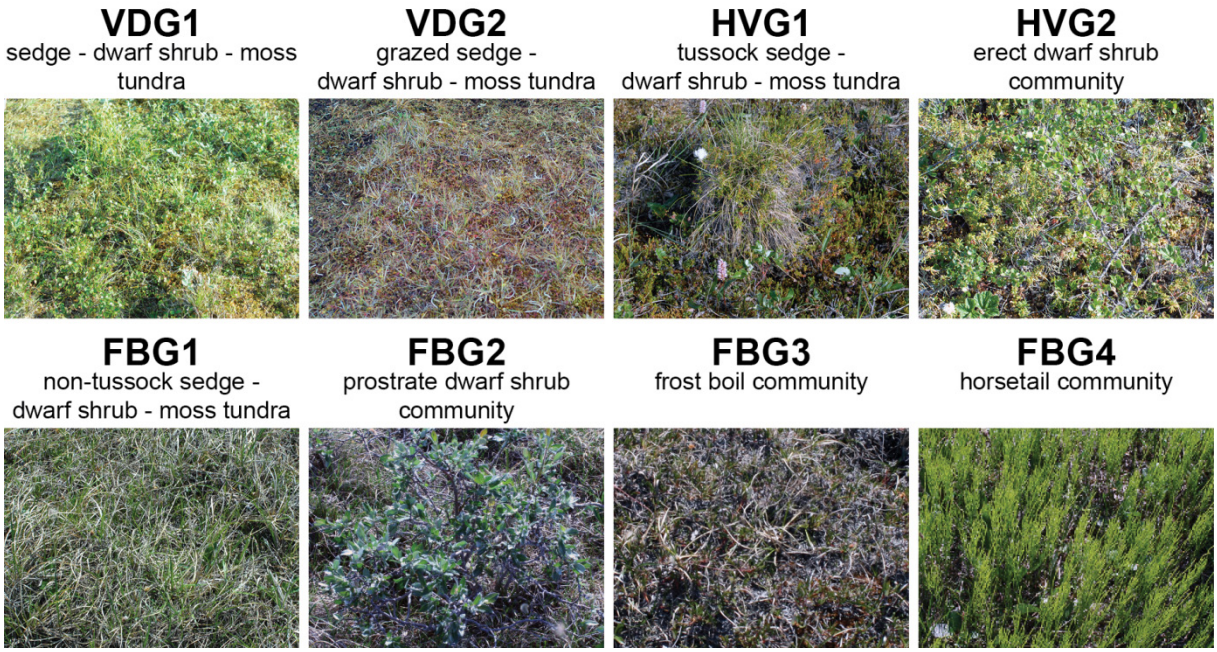

Figure 4-2: The eight study plots used for the ground-based spectro-directional characterization of Arctic tundra vegetation. ***Note:*** VD = Vaskiny Dachi; HV = Happy Valley; FB = Franklin Bluffs; G1 to G4 = number of the goniometer study plots within the study location.

4.2 Methodology Used for Field Work and Data Analysis

4.2.1 Field Spectroscopy and Hyperspectral Data Analysis

Since the ground-based hyperspectral characterization of Low Arctic tundra vegetation along environmental gradients as one objective of the dissertation was published as an research article and is inserted as stand-alone chapter (Chapter 6), more detailed methodology for the fieldwork, data processing and data analysis can be found in Chapter 6.2.3 and 6.2.4.

In summary: for the spectro-radiometric characterization of the study sites, each homogeneous vegetation grid of 100 m² was subdivided into one hundred 1 x 1 m quadrats. In each quadrat the spectral signature of the vegetation was measured with a nadir viewing GER-1500 field spectro-radiometer (350 – 1,050 nm) following the recommendations of *Milton* [1987] and *Milton et al.* [2009]. The averaged reflectance spectra of all 100 quadrats represent the spectral reflectance of the whole grid at the 10 x 10 m scale. These averaged signatures are used for all further calculations and comparisons. In order to describe the vegetation characteristics, the scalar cover estimates of the Braun-Blanquet approach used in the original description [*Dierschke*, 1994] were used. The average soil-moisture content was calculated from point measurements with a TDR (Time Domain Reflectrometry) soil moisture meter.

Since the vegetation of the study sites represent the main environmental gradients in Alaska's Low Arctic, a descriptive and quantitative analysis was carried out for comparing the average reflectance spectra of the study sites. Therefore spectral metrics were extracted, including the averaged reflectance in various important plant-related wavelength regions and absorption-related metrics such as relative absorption depths and area of continuum removal in the blue and red wavelength regions. The spectral metrics were investigated with respect to "greenness", biomass, vegetation height, and soil moisture regimes.

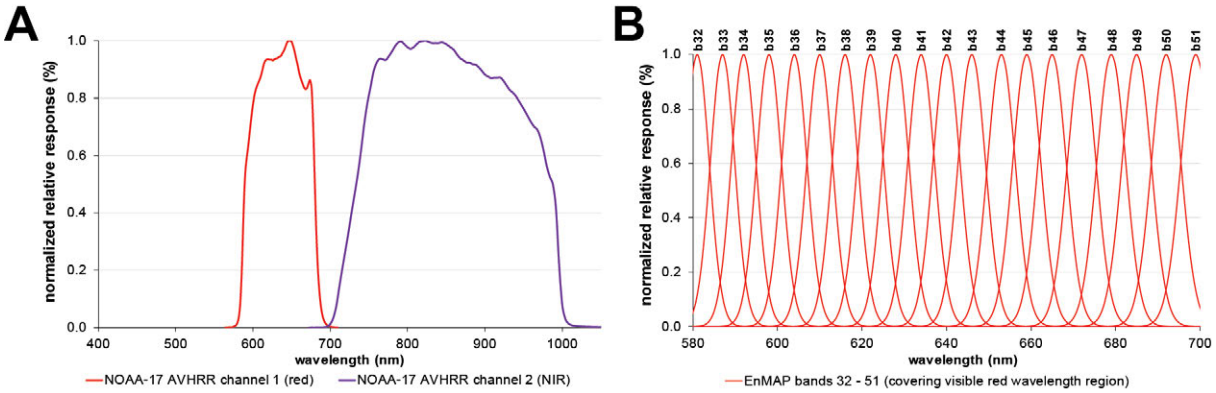

Figure 4-3: (**A**) Spectral response curves of the broadband NOAA-17 AVHRR visible red and NIR channel. (**B**) Spectral response curves of the 20 narrowband channels from the EnMAP satellite sensor which cover the visible red wavelength region. ***Note:*** For a better overview, only the visible red wavelength is shown. The EnMAP sensor covers with overall 242 continuous bands, showing band widths of 6.5 to 11 nm, the wavelength region from 420 – 2,450 nm.

Furthermore, in preparation of the EnMAP space mission, the average reflectance spectra were spectrally resampled to EnMAP bands. From these bands, three narrowband NDVIs were calculated in order to compare the performance of hyperspectral to broadband vegetation indices via regression analysis of the above-ground biomass versus NDVIs. The broadband NDVI was calculated from simulated AVHRR sensor bands using the spectral response curves of the satellite sensor (Figure 4-3A). Figure 4-3B shows the visible red wavelength section of the spectral response curves for the hyperspectral EnMAP sensor bands #32 – #51.

4.2.2 Considerations for the Field Spectro-Goniometer Measurements and the Spectro-Directional Data Analysis

Arctic environments make high demands on instruments for the ground-based spectro-directional characterization of Low Arctic tundra vegetation. To date, no suitable field spectro-goniometer system was available. Therefore, within the hy-ARC-VEG project a new light-weight and transportable field spectro-goniometer was designed and built. This instrument consists of a sensor platform called ManTIS (*Man*ual *T*ransportable *I*nstrument Platform for Ground-Based *S*pectro-Directional Observations) and an attachable hyperspectral sensor system. For the sake of readability, the technical description of the ManTIS and the sensor systems, the error assessment for field spectro-goniometer measurements with the ManTIS spectro-goniometer, the sampling strategy, the data processing chain, and the data visualization were transferred into a separate, extended methodology chapter (Chapter 5).

For the analysis, all acquired spectro-directional data of the eight study plots (Figure 4-2) were stored in a database together with the metadata of the surfaces. This metadata includes the vegetation description and spectral metrics, illumination and viewing geometries, external influence factors, and timestamps of all spectro-goniometer measurements. The eight solar noon measurements of the study sites (Table 4-2) are used to spectro-directionally characterize Low Arctic tundra surfaces at the peak of the vegetation period, while the spectro-goniometer measurements of MAT (HVG1 plot) and MNT (FBG1 plot) performed under increasing sun zenith angles are used to analyze the influence of high sun zenith angles on the reflectance anisotropy. Therefore, the data was processed following the Equations 5.3 to 5.5 described in Chapter 5.5.1. Detailed data reports can be found in Appendix C. In preparation of the EnMAP space mission, the HCRF data were spectrally resampled to EnMAP bands continuously covering the 400 to 1,050 nm wavelength region using the spectral response curves of the sensor (Figure 4-3B). A convenient side effect is that the spectral resampling reduces noise in the continuous reflectance data by an indirect smoothing.

To get a first expression of the reflectance anisotropy of tundra vegetation within the ManTIS hemisphere (up to 30° viewing zenith angle and 360° viewing azimuth angle), the HCRF data for four important wavelengths in the visible blue (EnMAP band #12, center wavelength 479 nm), green (EnMAP band #26, center wavelength 549 nm), red (EnMAP band #47, center wavelength 672 nm) as well as near-infrared spectrum (EnMAP band #73, center wavelength 864 nm) are visualized as 2D polar plots. While EnMAP band #12 and #47 show the maximum chlorophyll absorption in the blue and red wavelength region, EnMAP band #26 shows the maximum green reflectance peak. The EnMAP band #73 corresponds to the reflectance in the central NIR reflectance plateau.

With help of the anisotropy factor (ANIF = HCRF data normalized by the nadir reflectance) the spectral-directional characteristics along an azimuth plane as well as the distribution of the reflectance values over the hemisphere can be compared between different target surfaces or at changing illumination geometry. Reflectance anisotropy is more strongly pronounced in the solar principal plane [*Sandmeier and Itten*, 1999]. Furthermore, the red and NIR wavelength region normally show the strongest difference in the degree of reflectance anisotropy [*Sandmeier et al.*, 1998a]. Therefore, the ANIF data along the solar principal and orthogonal plane as well as of the full ManTIS hemisphere in the EnMAP bands #47 and #73 are analyzed and compared between the study plots and under varying sun zenith angles. For quantifying the spectral variability of the reflectance anisotropy, the anisotropy index (ANIX) [*Sandmeier and Itten*, 1999] development along the solar principal plane is analyzed.

The spectral variability of the reflectance anisotropy also has impacts on RS products [*Küster*, 2011]. The hyperspectral characterization of the Low Arctic tundra vegetation along environmental gradients (Chapter 6) showed that the relative absorption depth in the visible blue and red wavelength regions as well as narrowband NDVIs can be used to separate the vegetation communities. Therefore, the influence of BRDF effects on these RS products calculated for the EnMAP sensor is analyzed by comparing the nadir normalized products between the eight study plots and under varying sun zenith angles.

5 DEVELOPMENT AND PRECOMMISSIONING INSPECTION OF THE MANTIS FIELD SPECTRO-GONIOMETER

This extended methodology chapter has been published as original research article in the journal "*Sensors*" under the title: "A Manual Transportable Instrument Platform for Ground-Based Spectro-Directional Observations (ManTIS) and the Resultant Hyperspectral Field Goniometer System" by MDPI, Basel, Switzerland. This article is an open access article distributed under the terms and conditions of the Creative Commons Attribution license (http://creativecommons.org/licenses/by/3.0/).

The full citation is: Buchhorn, M.; Petereit, R; Heim, B. (2013), A Manual Transportable Instrument Platform for Ground-Based Spectro-Directional Observations (ManTIS) and the Resultant Hyperspectral Field Goniometer System. *Sensors*, 13(12), 16105-16128; DOI: 10.3390/s131216105.

As first author, I reviewed the relevant literature for the design, construction and patent registration of the ManTIS field spectro-goniometer. I was responsible for the concept and design, the 3D modeling, the purchase of technical equipment for the goniometer construction and sensor system, the modification of the sensor system, and the calibration of the ManTIS field spectro-goniometer. Moreover, I developed and coded the computer software for the semi-automatic control, developed the measurement scheme and processing chain for the data analysis and visualization, and was responsible for the documentation of all work steps as well as for the patent registration. The ManTIS was nationally registered for patent on 25 October 2011, and internationally registered for patent on 27 June 2012. The patent publication number is DE 10 2011 117 713 and has been published on 31 January 2013. The national patent has been granted on 27 February 2014.

For the manuscript itself, I reviewed the relevant literature, organized and contributed to the field work, analyzed and interpreted the data, and initiated, wrote, and coordinated the manuscripts. The co-authors participated in design and construction of the spectro-goniometer device, contributed data, and/or critically reviewed and discussed manuscript drafts.

Please note: A copy of the patent can be found in Appendix B.

Table 5-1: Affiliation and contributed work of the co-authors of the manuscript.

Co-Author	Affiliation	Work
Petereit, Reinhold	AWI	reviewed the design; construction of the field spectro-goniometer system; assembly drawings; contributed data
Heim, Birgit	AWI	contributed data; critically reviewed and discussed manuscript drafts

5.1 Introduction

Spectro-directional remote sensing (RS) has become more and more important in recent years [*Martonchik et al.*, 2000; *Schaepman*, 2007]. The angular information source can be used to minimize the impact of reflectance anisotropy in RS data of sensor systems with pointing capabilities or wide swaths achieving high quality, consistent and therefore comparable and reproducible datasets [*Schaepman*, 2007]. Moreover, various studies have shown that canopy architecture properties can be derived from spectro-directional RS data [*Coburn et al.*, 2010; *Deering et al.*, 1999; *Gianelle and Guastella*, 2007; *Sandmeier and Deering*, 1999; *Selkowitz*, 2010; *Walter-Shea et al.*, 1997]. The directional reflectance properties of a surface are mathematically specified by the bidirectional reflectance distribution function (BRDF) [*Nicodemus et al.*, 1977]. Direct BRDF measurements are not possible, but the anisotropic reflectance behavior of a surface can be approximately determined by measuring the hemispherical conical reflectance factor (HCRF) in the field. Therefore, various ground-based measurement instrumentation called field spectro-goniometers have been developed in the recent years [*Anderson et al.*, 2012; *Bourgeois et al.*, 2006b; *Bruegge et al.*, 2000; *Coburn and Peddle*, 2006; *Landis and Aber*, 2007; *Manakos et al.*, 2004; *Painter et al.*, 2003; *Pegrum et al.*, 2006; *Sandmeier and Itten*, 1999; *Schopfer et al.*, 2008; *Suomalainen et al.*, 2009; *Timmermans et al.*, 2009].

Field spectro-goniometers are used as a tool to provide spectro-directional characteristics of various surfaces for (i) the investigation of the physical mechanism of BRDF effects, (ii) the development and validation of BRDF models, (iii) the investigation of the relationship between BRDF effects and biophysical parameters, as well as (iv) the validation of satellite and aircraft based BRDF data [*Sandmeier*, 2000]. Up to now, most of the developed field spectro-goniometer systems due to their design are not applicable in geographical and logistical challenging regions such as the Arctic or on permafrost surfaces. Performing spectro-goniometer measurements in these challenging regions demands specific technical requirements such as (i) a lightweight construction, (ii) a low-cost production, (iii) standard parts for easy replacement, (iv) a disassembly and storage in boxes for transport by small helicopters with a helicopter sling or on sleds, and (v) a secure footing on small building areas. But at the same time the design and sensor configuration has to be robust enough to allow observations with (i) a high angular accuracy, (ii) a minimum distance of 2 m between the vegetated surface and the sensor, (iii) a constant observation center, (iv) a fast scanning in all directions reducing the impact of temporal illumination changes, and (v) a high spectral resolution [*Sandmeier*, 2000; *Schneider et al.*, 2007]. Moreover, a high level of automation of the measurement process used by field spectro-goniometers such as the dual-view FIGOS [*Schopfer et al.*, 2008], the IAC ETH goniospectrometer [*Bourgeois et al.*, 2006b], the PARABOLA III [*Bruegge et al.*, 2000], the ASG [*Painter et al.*, 2003], or the FIGIFIGO [*Suomalainen et al.*, 2009] is expensive in the development of the sensor and controlling system, and also may be susceptible to damage in geographical regions with fast changing weather conditions.

Following these requirements, a spectro-goniometer system was developed at the Alfred Wegener Institute (AWI) for the spectro-directional characterization of low-growing vegetation communities in the Arctic. This system consists of a low-cost, lightweight instrument platform for the angular positioning of the sensor within 30° view zenith and 360° view azimuth angle, and a hyperspectral sensor system including two spectro-radiometers for the radiance and irradiance measurements. The sensor system itself can be customized to the research needs. The reason for the smaller defined view zenith pointing capability is that many present and upcoming satellite sensors such as RapidEye [*Tyc et al.*, 2005], Environmental Mapping and Analysis Program (EnMAP) [*Stuffler et al.*, 2007], and PRecursore IperSpettrale of the application mission (PRISMA) [*Galeazzi et al.*, 2008] have a maximal off-nadir tilting of ±30° (RapidEye ±25°, EnMAP ±30°, PRISMA ±15°). Moreover, this pointing capability is adequate for BRDF analysis in multi-angle datasets created by successive passes of satellite sensor systems with nadir pointing, or for the BRDF normalization in RS data acquired by satellite sensors with wide swaths.

The emphasis of this article is the presentation and technical description of the *MAN*ual *T*ransportable *I*nstrument platform for ground-based *S*pectro-directional observations (called ManTIS) as well as the description of the sensor system used for the resultant hyperspectral field spectro-goniometer system. Moreover, we present the measurements strategy for HCRF acquisitions in the field in connection with an error assessment as well as the processing and visualization of the HCRF data. Finally, the HCRF measurements of an example surface are processed, presented and discussed.

5.2 Theoretical Background

Most of the natural surfaces do not show Lambertian reflectance behavior [*Deering et al.*, 1999; *Peltoniemi et al.*, 2005; *Pinter, JR. et al.*, 1990; *Sandmeier et al.*, 1998a; *Sandmeier et al.*, 1999; *Solheim et al.*, 2000; *Vierling et al.*, 1997]. Instead of that, they display anisotropic reflectance distributions which affect all remotely sensed radiation data. This reflectance anisotropy is based on the properties of the observed surface and can be physically described by a set of functions ($f_r[sr^{-1}]$) characterizing the reflected radiation as a function of the incident beam [*Schaepman-Strub et al.*, 2006]. In detail, according to *Nicodemus et al.* [1977] this so called BRDF is defined as the ratio of the radiance dL_r [$W \cdot m^{-2} \cdot nm^{-1} \cdot sr^{-1}$] reflected from the surface in one direction (θ_r, ϕ_r) to the incident irradiance dE_i [$W \cdot m^{-2} \cdot nm^{-1}$] illuminating the surface outgoing from direction (θ_i, ϕ_i). Since diffuse reflection causes the incident radiance dL_i to be reflected in all directions over the hemisphere, the BRDF uses the incident irradiance dE_i and is not dimensionless, and therefore measured in sr^{-1}. This relationship is visualized in Figure 5-1A and mathematically expressed in Equation 5.1.

$$BRDF_\lambda = f_r(\lambda;\theta_i,\phi_i;\theta_r,\phi_r) = \frac{dL_r(\lambda;\theta_i,\phi_i;\theta_r,\phi_r)}{dE_i(\lambda;\theta_i,\phi_i)}\left[sr^{-1}\right] \qquad (5.1)$$

Furthermore, the BRDF is not only dependent on the illumination and viewing directions each identified by two angles, the illumination (resp. viewing) zenith angle θ_i (resp θ_r) and the illumination (resp. viewing) azimuth angle ϕ_i (resp. ϕ_r), but also depends on the wavelength (λ) of the electromagnetic radiation.

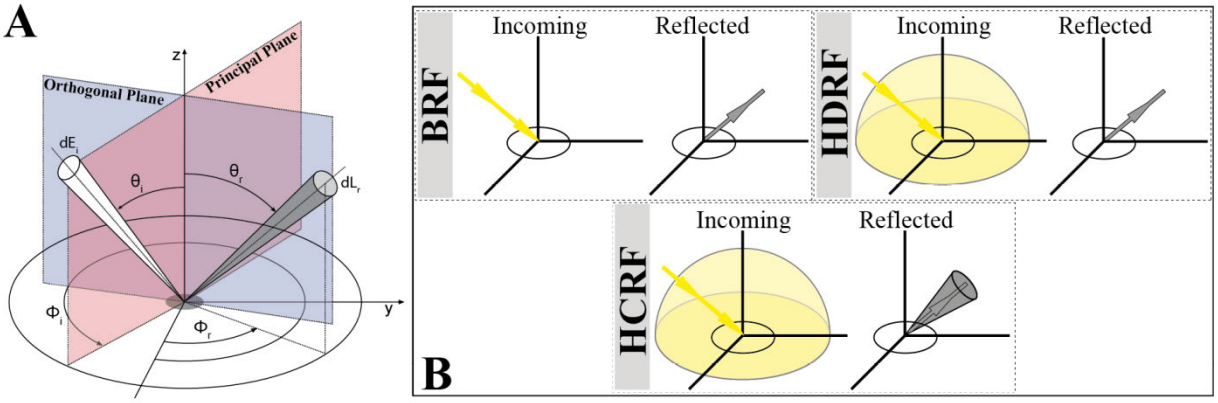

Figure 5-1: (**A**) Concept of the bidirectional reflectance distribution function (BRDF) [*Nicodemus et al.*, 1977]. (**B**) Reflectance nomenclature as a function of geometrical aspects used in this study [*Schaepman-Strub et al.*, 2006].

For practical reasons the bidirectional reflectance factor (BRF) is used to describe the reflectance anisotropy of a surface. The BRF can be estimated by the ratio of the radiance L_r reflected from the surface in a specific direction to the radiance L_{ref} reflected from a lossless reference panel with Lambertian reflectance behavior, both measured under identical illumination geometry [*Nicodemus et al.*, 1977]. Since white reference panels like Spectralon® panels do not show ideal Lambertian reflectance characteristics, the radiance L_{ref} has to be corrected by a panel calibration coefficient R_{ref}. BRF measurements like those shown in Equation 5.2 are dimensionless and interrelated to the BRDF. Under the assumption that the irradiance is isotropic and that the BRDF is constant within the illumination-sensor-geometry, the BRF divided by π approximately reproduces the BRDF of the surface [*Schaepman-Strub et al.*, 2006].

$$BRF(\lambda;\theta_i,\phi_i;\theta_r,\phi_r) = \frac{L_r(\lambda;\theta_i,\phi_i;\theta_r,\phi_r)}{L_{ref}(\lambda;\theta_i,\phi_i;\theta_r,\phi_r)} \cdot R_{ref}(\lambda;\theta_i,\phi_i;\theta_r,\phi_r) \qquad (5.2)$$

For BRF measurements under field conditions, Equation 5.2 is still not applicable. Since the illumination is hemispherical under natural illumination conditions, the best estimation for the BRF would be the measurement of the hemispherical directional reflectance factor (HDRF) [*Nicodemus et al.*, 1977; *Schaepman-Strub et al.*, 2006]. Exact HDRF measurements would require a sensor optic with infinitesimally small instantaneous field of view (IFOV) which is impossible to obtain. The best estimation of reflectance anisotropy in the field is therefore the measurement of the HCRF [*Nicodemus et al.*, 1977; *Schaepman-Strub et al.*, 2006]. Figure 5-1B shows the relation of incoming and reflected radiance terminology used to describe the three (BRF, HDRF, and HCRF) reflectance quantities [*Schaepman-Strub et al.*, 2006].

Since the spectro-radiometers considered for the ManTIS field spectro-goniometer uses foreoptics with an IFOV smaller than 10°, the observation geometry of the sensor is conical [*Manakos et al.*, 2004]. Under the assumption that the HCRF is constant over the IFOV of the sensor, we could equate our HCRF measurements with the HDRF [*Martonchik et al.*, 2000]. Different publications have shown that this is done for sensor IFOVs smaller than 3° [*Bourgeois et al.*, 2006b; *Sandmeier and Itten*, 1999; *Schopfer et al.*, 2008], but in our case it has still to be proofed. Therefore, to avoid misunderstandings, we want to clarify that the spectro-directional measurements with the ManTIS field spectro-goniometer in its current sensor configuration are HCRF measurements.

5.3 Description of the Field Spectro-Goniometer System

5.3.1 Construction Schedule

The preliminary considerations for a field spectro-goniometer platform started in October 2010 and were followed by a two month design-related period. The main focus during this design phase was on the transportability and lightweight construction of the prototype which was built from January to February 2011 by the scientific workshop of the AWI in Bremerhaven, Germany. Afterwards, the prototype ran through the first field experiments. These initial tests showed promising results, but also exposed room for improvements. In March 2011, we started with the revision of the structural design of the platform. Therefore, a computer-based 3D model was created and optimized with the help of a ray tracing simulation. The construction phase of the revised version of the prototype ran from May to June 2011. Afterwards the ManTIS was equipped with a customized sensor system, calibrated and tested at the AWI facility in Potsdam, Germany. In July 2011, the AWI ManTIS field spectro-goniometer became fully operational and was packed for its first Arctic mission on the Yamal 2011 expedition (25 July to 9 September 2011) to the Yamal Peninsula, West-Siberia, Russia [*Heim et al.*, 2012].

During the Yamal expedition, the field spectro-goniometer was extensively tested under Arctic conditions and showed excellence results. Nevertheless, the selected design showed also some challenges in the assembling of the system prior the measurements. The Arctic conditions demand an easy assembly without tools for screws and nuts as well as require adjustment wheels on setting screws which can be handled with gloves. Therefore, we decided to revise the design of the ManTIS prototype once more and additionally bring the prototype to maturity phase. All parts were built now by computerized numerical control (CNC) machines. This improvement allows a fast reproducibility of missing parts or the whole instrument platform (mass production). Moreover, plug-and-socket connections with self-locking screws and nuts allow now a faster assembly in the field and an improved stability under load on permafrost surfaces. The design phase of the improved ManTIS ran from October to December 2011, where the main construction phase ran from January to April 2012. Again, all parts were built and pre-assembled by the scientific workshop of the AWI in Bremerhaven, Germany. In May 2012, the field spectro-goniometer system was calibrated and tested for the next field season at the AWI facility in Potsdam, Germany. By

the end of May 2012 the improved ManTIS field spectro-goniometer reached its final stage of extension and became fully operational. Once more, it was packed for detailed field tests on the Alaska 2012 expedition (21 June to 22 July 2012) to the North Slope, Alaska, USA [*Strauss et al.*, 2012].

Overall, the design, construction and setup of the ManTIS field spectro-goniometer has required about 18 months with approx. 1,500 working hours and additional 135 machine hours.

5.3.2 Description of the Field Spectro-Goniometer Platform (ManTIS)

The field spectro-goniometer platform consists of five major parts: a tripod with a stabilized center post; a cantilever connected to the center post and stabilized by bracings; a rotatable and fixable suspension including the azimuth angle adjustment module (AAM) connected to the cantilever; a zenith arc with one end connected to the suspension; and a sensor sled which slides on the zenith arc (Figure 5-2A). All components are made of black anodized aluminum, reducing the overall weight to only 27 kg (without sensor system). The complete ManTIS can be disassembled and stored in a box with the dimensions of 146 x 47 x 29 cm increasing the overall weight then to 42 kg. This weight and box size permits the transport in station wagons and as normal luggage in passenger planes and trains, and therefore allows for fast and convenient access to logistically demanding study sites.

The tripod design was chosen because it keeps the center post in its vertical position and provides the best weight-to-stability ratio against downward and horizontal forces. Moreover, it can be setup and leveled in all kinds of Arctic environments. The feet of the tripod are formed as floor plates. Depending on the substrate, special shoes can be attached on the floor plates to improve stability e.g. for permafrost surfaces the shoes have a drift pin. The cantilever consists of two slightly bent tubes which can be folded up, and is fixed on the upper end of the center post. Moreover, the cantilever is laterally braced to the center post. Through adjustments of the bracings of the cantilever, the overall distance between the surface and the zenith arc can be set. The suspension is connected via a ball-and-socket join to the other end of the cantilever. This connection allows the exact leveling of the suspension in the vertical center line of the target (correspond to the nadir view position), and therefore also permits spectro-goniometer measurements in rough terrain. The other end of the suspension contains the AAM which has a fixed square joint to the end of the zenith arc (Figure 5-2C). To stabilize this connection, the other end of the zenith arc is connected to the middle part of the suspension via a bracing, which further helps to guide electrical and optical cables to the sensor sled. Important to mention is that the center post, the cantilever and the suspension are matched to each other so that the zenith arc is positioned at the distance of the arc radius (2.05 m) above the ground. All mounting and adjustment screws are made of steel but with large adjustment wheels made of cold-resistant plastic.

Since the zenith arc can be fully rotated about the center line of the AAM and the sensor sled can be positioned on the zenith arc in any off-view angle up to 30°, the spectro-radiometer

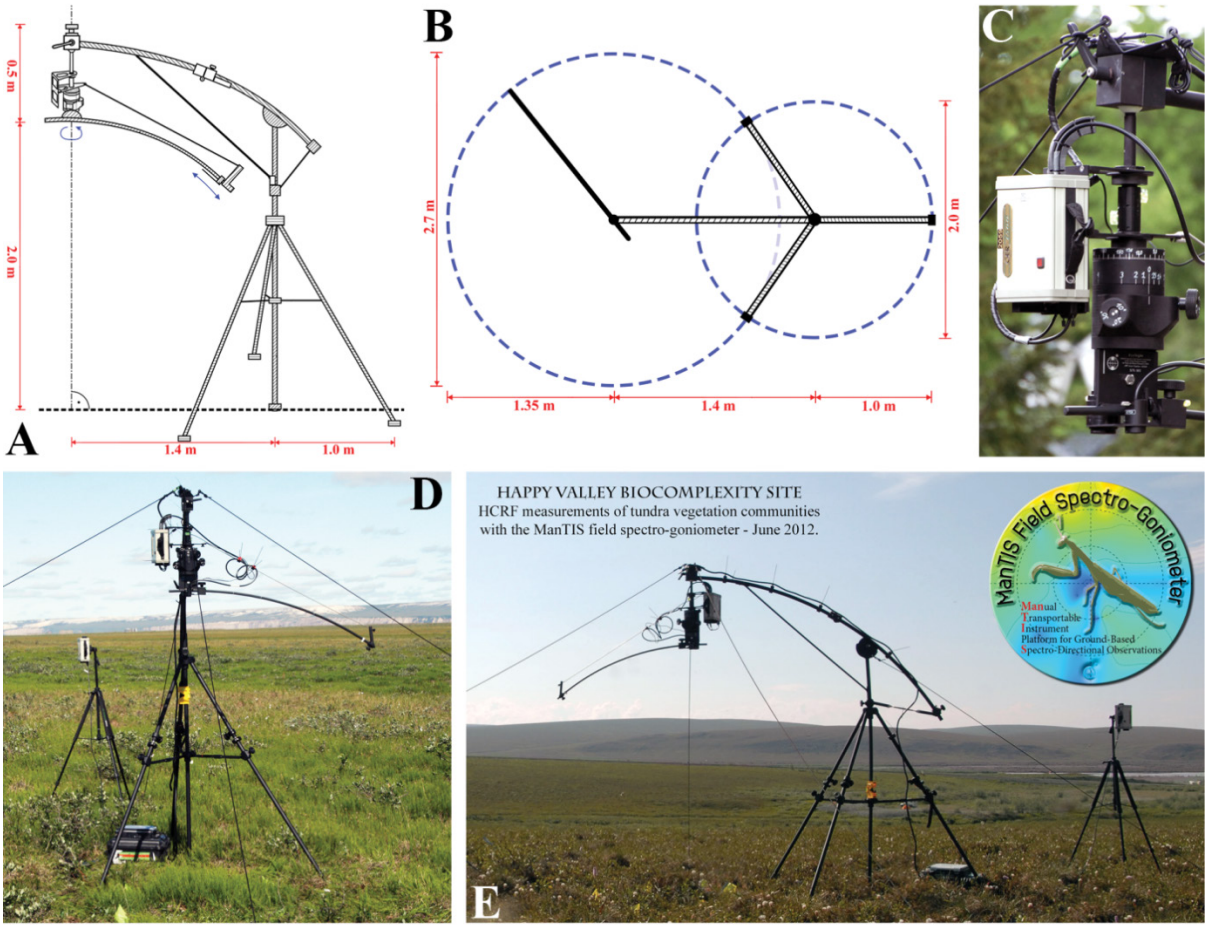

Figure 5-2: (**A**) Design and dimensions of the ManTIS (front view). (**B**) Design and dimensions of the ManTIS (top view). (**C**) The suspension including the azimuth angle adjustment module (AAM) with connected GER-1500 spectro-radiometer. (**D**) ManTIS field spectro-goniometer (lateral view). (**E**) Overview of ManTIS field spectro-goniometer assembled for a field campaign in the Alaskan Low Arctic showing both GER-1500 spectro-radiometers (front view).

connected to the sensor sled of the ManTIS can measure the target with view zenith angles from -30° to +30° and at all desired view azimuth angles. Moreover, this setting allows measurements with a constant observation center. The angular positioning of the sled is carried out manually; consequently the zenith arc has engraved labels with a resolution of 1°. To decrease the time for repositioning the view azimuth angle, the AAM has an internal quick-action locking system. In detail, preferred view azimuth angles (up to two different measurement schemes) can be engraved on a cylinder in the inner core of the AAM. Through a locking screw, the zenith arc can be fixed in an azimuth plane, preferably the solar principal plane. Outgoing from this azimuth plane, the zenith arc can then only be rotated in the azimuthally angular distances provided by the engraved measurement scheme. The measurement scheme itself can be chosen by two additional set screws. A 360° scale engraved on an additional outer ring of the AAM also allows the view azimuth angles to be freely set with respect to the solar principal plane. Also important to mention is that in order to measure in the solar principal plane, the zenith arc has been mounted eccentrically on the AAM and only the sensor sled itself moves directly in the solar principal plane. In order to help to set the zenith arc into the solar principal plane, the AAM has an additional second

outer ring with a 360° engraved scale which can be orientated to geographic north by a compass. This second outer ring is independent and does not rotate when the zenith arc is moved.

5.3.3 Sensor Configuration of the AWI ManTIS Field Spectro-Goniometer

The ManTIS was designed as a platform which can be equipped with various kinds of spectro-radiometers and other hardware in order to form field spectro-goniometer systems customized to the specific research needs. In its current configuration the platform was modified for EnMAP purposes and is equipped with two PC-controlled GER-1500 portable spectro-radiometers (Spectra Vista Corporation, Poughkeepsie, NY, USA), a Navilock NL-402U global positioning system (GPS) receiver (Tragant GmbH, Berlin, Germany), a NC-Eye camera system designed for Arctic environments (AnKoTec Anton Kothe, Postbauer-Heng, Germany), and a Spectralon® white panel (Labsphere, Inc., North Sutton, NH, USA).

The GER1500 spectro-radiometers measure radiance across the wavelength range of 350 – 1,050 nm with sampling intervals of 1.5 nm [Spectra Vista Corporation, 2009], and are connected via serial cables (nine-pin RS-232) to a field computer. One GER-1500 is mounted to the suspension of the ManTIS and measures the radiance reflected from the target surface (Figure 5-2C-E). The foreoptic of this spectro-radiometer is mounted to the sensor sled and connected via a 1.6 m long fiber optic cable. In its current configuration, the foreoptic has an IFOV of 8.5°. In order to measure the radiance reflected from a Spectralon® reference panel, a sub-arm with a mounting clip can be attached to the sensor sled allowing precise alignment of the reference panel to the vertical center line of the target surface in the nadir measurement position.

Additionally, a video camera connected via universal serial bus (USB) cable to the field computer is mounted on the sensor sled next to the foreoptic of the spectro-radiometer. The center of projection of the camera lens can be made to coincide with the center of the ground instantaneous field of view (GIFOV) of the foreoptic via adjustable mounting clamps. The USB GPS receiver is mounted on top of the cantilever in line with the center line of the suspension, providing the exact geographical position of the target surface. The second GER-1500 spectro-radiometer is equipped with a cosine diffusor foreoptic and mounted at a height of 1.80 m on a tripod for measuring the down-welling total irradiance (Figure 5-2D-E). This extra tripod is placed near the center post of the ManTIS.

All required sensor cables are combined in a cable loom which is guided from the suspension of the ManTIS over the cantilever to the center post. This reduces the risk of cable jams and facilitates quick setup during the assembling stage. Overall, the sensor system including the cable loom has a weight of approx. 7 kg and it stored in a box with the dimensions of 53 x 44 x 22 cm. Therefore, the weight of the AWI ManTIS field spectro-goniometer in its current field configuration (platform + sensor system) is approx. 34 kg. Together with the two transport boxes, the total shipping weight is approx. 54 kg.

The overall dimensions of the field spectro-goniometer can be seen in Figure 5-2A-B. The maximum height is 2.5 m, where the zenith arc is positioned at a height of 2.05 m and the sensor of the mounted spectro-radiometer is positioned at a constant distance of approx. 2 m from the target. Since the zenith arc rotates around the vertical center line of the target, a sphere of 1.35 m in radius around the target is created. Additional space around the center post (approx. 1 m in radius) is required for the assembly of the tripod. About 45 min are needed to build up the ManTIS and setup the sensor system with a team of two people. In locations with influence of wind, an additional wind brace made of distortion-free rope can be used to further stabilize the field spectro-goniometer (Figure 5-2D-E).

5.3.4 Measurement Strategy

Due to the relatively small IFOV and the short distance between the foreoptic and the target, the sampling area of the ManTIS field spectro-goniometer is small. In order to acquire representative measurements, targets should be homogeneous surfaces. On the other hand, this small sampling size has the advantage that already homogeneous plots with a size of 1 m x 1 m can be investigated.

In preparation of the spectro-goniometer measurements, the selected sampling plot is marked with small flags in the corners. Next, the center post is positioned at a distance of 1.40 m to the north of the center of the sampling plot and vertically fixed. This prevents a shadowing of the plot by the ManTIS itself. After mounting the cantilever to the center post, the suspension is connected to the cantilever and the zenith arc is locked to the AAM of the suspension. Then the sensor sled is clipped on the zenith arc, and all sensors are mounted. Afterwards, the cable loom is installed and the sensor system is connected to the field computer. Since the center post can be rotated, the assembling can be done outside the sampling plot and the cantilever is then turned towards the target and fixed. This avoids disturbance of the plot during the assembling phase. In order to bring the center line of the AAM in conformity with the vertical center line of the target (nadir view position), final adjustments have to be done at the ball-and-socket join of the suspension with the cantilever. In conclusion, the center of the foreoptic of the spectro-radiometer is now exactly vertical positioned above the center of the sampling plot. By rotating the zenith arc and displacing the sensor sled along the zenith arc, it is possible to position the foreoptic at any point on the spanned spherical shell.

The design of the measurement scheme as well as the documentation of the sampling plot and measurements follow the recommendation of *Sandmeier* [2000]. In its current configuration, the ManTIS field spectro-goniometer uses a measurement scheme with 61 viewing positions on the spanned spherical shell (Figure 5-3). Since reflectance anisotropy is more strongly pronounced in the solar principal plane [*Sandmeier and Itten*, 1999; *Sandmeier*, 2000], the measurement scheme has a higher measuring density around the solar principal plane [*Manakos et al.*, 2004]. In the beginning of each measurement scheme, the zenith arc is aligned with the solar principal plane with the help of the AAM. The first target measurement is taken in the nadir view position. Then the sensor sled is positioned at the 5° view zenith angle position on the zenith arc and target measurements with increasing view azimuth angles

are carried out by rotating the zenith arc around the AAM. Afterwards, the sensor sled is positioned to the next view zenith angle position on the zenith arc and the procedure to take target measurements is repeated. Where the target measurements with a 5° view zenith angle are taken at 12 view azimuth angle positions, target measurements with a 10°, 20°, and 30° view zenith angle are taken at 16 view azimuth angle positions (Figure 5-3).

At the beginning and end of each measurement scheme, the radiance reflected from the Spectralon® reference panel is measured in the nadir view position. Moreover, simultaneously to all target measurements, the irradiance profiles are recorded by the second spectro-radiometer with the attached cosine diffusor foreoptic. A video showing the whole measuring process is available on the internet at http://tinyurl.com/ManTISmovie (DOI: 10.1594/PANGAEA.819494). The total acquisition time for this measurements scheme (61 target, two reference panel, and 63 irradiance measurements) is approx. 18 minutes.

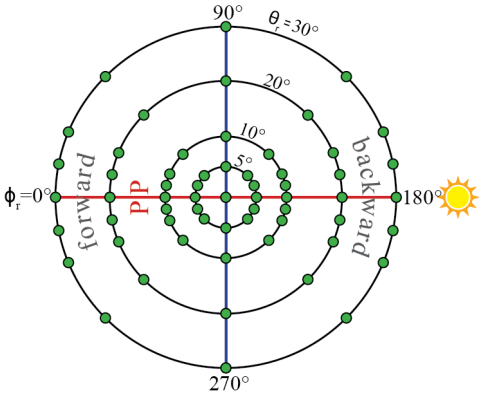

View Zenith Angle (θ_r)	View Azimuth Angle (ϕ_r) (with respect to the solar principal plane)
0°	0°
5°	**0°**,22.5°, 45°, **90°**, 135°, 157.5°, **180°**, 202.5°, 225°, **270°**, 315°, 337.5°
10°	**0°**,10°, 22.5°, 45°, **90°**, 135°, 157.5°, 170°, **180°**, 190°, 202.5°, 225°, **270°**, 315°, 337.5°, 350°
20°	**0°**,10°, 22.5°, 45°, **90°**, 135°, 157.5°, 170°, **180°**, 190°, 202.5°, 225°, **270°**, 315°, 337.5°, 350°
30°	**0°**,10°, 22.5°, 45°, **90°**, 135°, 157.5°, 170°, **180°**, 190°, 202.5°, 225°, **270°**, 315°, 337.5°, 350°

Figure 5-3: Default measurement scheme of the ManTIS field spectro-goniometer with overall 61 target measurements positions on the spanned spherical shell. The measurement scheme shows a higher measuring density around the solar principal plane (PP).

5.3.5 Software for Semi-Automatic Control

A software application for the semi-automatic control of the ManTIS field spectro-goniometer was written and coded in visual basic (VB). The graphical user interface (GUI) helps to enter and set the required advance information prior the measurements. Moreover, the software application calculates from the received GPS information the solar zenith and azimuth position prior to each target measurement as well as calculates the magnetic declination in order to determine the geographic north by the compass. Then the GUI visualizes all configurations for the AAM in order to setup the view zenith and azimuth angles for the target measurements in the selected measurement scheme (Figure 5-4).

Furthermore, the software communicates with the spectro-radiometers and secures that the radiance and irradiance measurements are taken simultaneously as well as that the received data is correctly named and stored. Additionally, the software controls the video camera system to take a photo of the sampling plot simultaneously along with each target measurement and stores it together with all other data in the database. The generated log file includes all realized software operations with a time stamp.

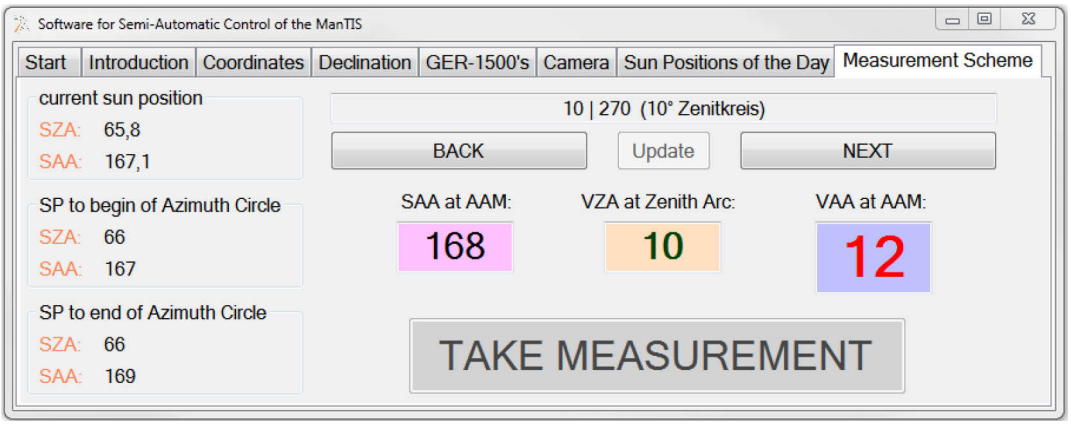

Figure 5-4: Graphical user interface (GUI) of the software application for the semi-automatic control of the ManTIS field spectro-goniometer.

5.4 Error Assessment

The errors in HCRF acquisitions with the ManTIS field spectro-goniometer can be divided into two broad categories: internal and external error sources. Internal error sources are here defined as measuring inaccuracies through problems with the platform or spectro-radiometer including radiometrical accuracy, white reference calibration, angular accuracy from both positioning and opening angle of the optics, and sensor shadowing. External errors include the variation of incident light through the measurement scheme, environmental influences, representativeness of the sample, and diurnal changes of vegetated surfaces.

5.4.1 Radiometrical Accuracy

The radiometrical accuracy of the spectro-goniometer measurements follows the same principles as any spectro-radiometer measurements, and depends on a good calibration of the devices. In its current configuration, we use two GER-1500 spectro-radiometers which have an average radiance accuracy of 1.2 x 10^{-10}W · cm^{-2} ·nm^{-1}· sr^{-1} [Spectra Vista Corporation, 2009] (last calibrated in May 2011). By transferring the wavelength dependent radiance accuracy stated in the calibration certificate to the spectro-goniometer measurements in the Arctic, the GER-1500 shows in its wavelength range from 350 – 1,050 nm a reflectance uncertainty of 0.59 % at 400 nm, of 0.20 % at 700 nm, and of 1.59 % at 900 nm. In order to increase the signal-to-noise ratio, 32 individual measurements are averaged per one target scan.

Since all HCRF values are calculated as a ratio between the radiance reflected of the surface and a Spectralon® white reference panel, errors due to the condition of the panel or a tilt of the reference panel can cause a systematical error [*Jackson et al.*, 1992]. Therefore, regular calibration of the Spectralon® panel at the factory is recommended. In order to decrease tilt errors, we use bubble levels to balance the reference panel. Moreover, *Sandmeier et al.* [1998b] showed that calibrated Spectralon® panels can even in the nadir view position have changes in the measured radiance depending on the illumination zenith angle. Under the assumption that the reflectance anisotropy is nearly invariant between different Spectralon® panels [*Bruegge et al.*, 2001], we use the correction algorithm developed by *Sandmeier et al.*

[1998b] in order to reduce systematical errors. This approach is already tested and used with other spectro-goniometers [*Bourgeois et al.*, 2006b; *Sandmeier and Itten*, 1999].

5.4.2 Pointing Accuracy

The angular accuracy of the spectro-goniometer measurements is defined by the roundness of the zenith arc, the precision in the positioning of the sensor sled on the zenith arc, and the correctness in setting the view zenith angle in the AAM. In case of the ManTIS field spectro-goniometer, an additional factor has to be considered. Since the zenith arc is freely suspended in the center of the sampling plot, care has to be taken that the center line of the AAM (on which the zenith arc is orthogonally mounted) is in conformity with the vertical center line of the target and also that the zenith arc is positioned at the distance of the arc radius above the ground. Therefore, the suspension is equipped with bubble levels for all axes, and the cantilever can be adjusted in height.

In order to investigate the pointing accuracy of the ManTIS field spectro-goniometer, the sensor sled was equipped with a laser pointer replacing the foreoptic of the spectro-radiometer. Afterwards, a full measurement scheme was carried out and the path left by the laser beam on the surface was recorded. The deviation of the laser beam representing the center of the sensor GIFOV shows values within ±6 cm (Figure 5-5A). The deviation increases with increasing view zenith angles, indicating that the zenith arc in not perfectly round or that the weight of the sensor sled slightly bends down the freely suspended zenith arc in higher view zenith angle positions.

5.4.3 Ground Instantaneous Field of View and Sensor Self-Shadowing

In its current configuration, the foreoptic of the spectro-radiometer for the target measurements has an IFOV of 8.5°. The distance of the foreoptic to the ground can be slightly adjusted between 1.98 and 2.03 m, and is set currently to 2.02 m. The GIFOV changes with increasing view zenith angle. In the current ManTIS field spectro-goniometer configuration, the maximum view zenith angle is 30°. Therefore, at nadir an almost circular footprint with 30.0 cm occurs that becomes slightly elliptical towards higher view zenith angles reaching a major half axis of 34.8 cm in the 30° view zenith angle position. Figure 5-5B visualizes the change in footprint area for the main view zenith angle positions of the default measurement scheme. Thus, the spectro-radiometer is always measuring approximately the same surface area in the center of the hemisphere. However, when also including the pointing accuracy of ±6 cm, a homogeneous sampling area of approximately 25 cm in radius around the center of the target plot is needed to acquire representative spectro-goniometer measurements.

Another big issue in spectro-goniometer measurements is abnormalities in the HCRF measurements through sensor self-shadowing which mainly occurs when the foreoptic of the spectro-radiometer is aligned with the sun [*Sandmeier and Itten*, 1999]. This position is also known as the hot spot position. Spectro-directional measurements in this region have to be replaced by simulated data. Hot spots cannot appear in ManTIS spectro-goniometer measurements in the Arctic, since the ManTIS has a maximum view zenith angle of 30° and

the illumination zenith angles are always larger than 43° in these geographical positions [*Kääb*, 2008]. Shadowing of the sampling plot by ManTIS parts (zenith arc, suspension) itself is unavoidable, but only minimal through the eccentric position of the zenith arc and the small profile of the obstruct aluminum tubes. Again, the high illumination zenith angles in the Arctic reduce the shadowing of the sampling plot, because the freely suspended zenith arc is highly mounted over the ground.

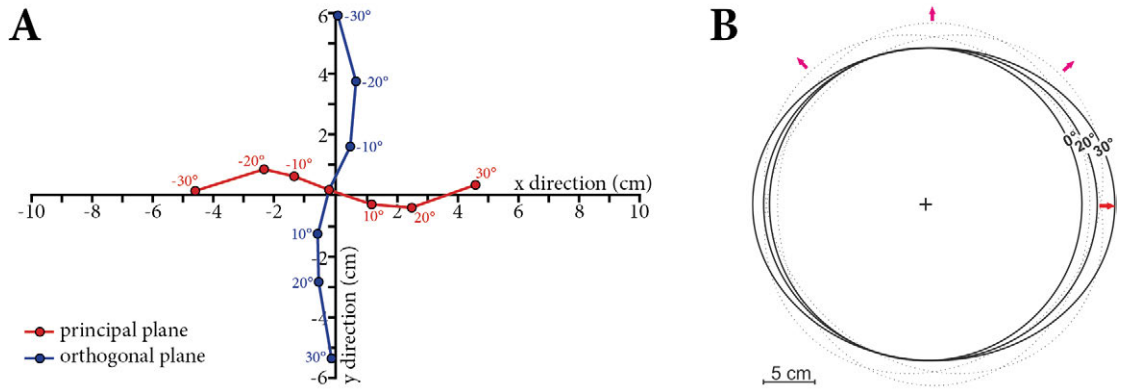

Figure 5-5: (**A**) Pointing accuracy of the ManTIS. The coordinate system center is aligned to the center of the target. (**B**) Ground instantaneous fields of view (GIFOV) for the range of view zenith angles of the ManTIS. The dotted lines show three view azimuth angles for a constant view zenith angle of 30°. The arrows indicate viewing direction of the foreoptic.

5.4.4 Temporal Illumination Changes and Environmental Influences

Field measurements have a disadvantage compared to laboratory measurements, since in the laboratory the influencing factors on the reflectance anisotropy of a surface can be controlled and narrowed to the canopy geometry, multiple scattering effects and sensor-illumination geometry. In the field, additional environmental factors can affect the measurements which cannot be measured or validated in detail at all times. The main factors are upcoming wind during the measurements, changes in the moisture and temperature regime during the day, plant stress, heliotropic leaf movements, and presence of dew on the canopy in the morning [*Jackson et al.*, 1990; *Pinter, JR. et al.*, 1990; *Sandmeier*, 2000]. Here, only carefulness in the choice of the sampling plot can reduce these measurement errors.

The 61 target measurements of the default measurement scheme should be ideally performed simultaneously, but this is not possible. To reduce short-term temporal changes in irradiation and illumination zenith angle changes between the beginning and end of a measurement scheme, we developed a cos-conical dual-beam approach where two spectro-radiometers simultaneously measure the radiance reflected from the target and the total sky irradiance. Instead of using the recorded irradiance directly, we used the irradiance spectra with the aim to interpolate the radiance measurement of the reference panel to the time of the target measurement. This can be only done under the assumption that changes in the irradiance over the time period affect the radiance measurements of the reference panel to a similar degree in the certain wavelength region [*Schopfer et al.*, 2008]. This approach has already been used by various groups, but mostly with a sunphotometer with limited spectral bands for irradiance

recording [*Schopfer et al.*, 2008; *Suomalainen et al.*, 2009]. A more detailed consideration of this approach is given in section 5.5.1. Moreover, we developed an outlier indicator system showing in which sensor positions higher illumination changes occurred, and therefore stronger interpolation of the reference panel measurement was needed. This shows at which sensor positions more caution is needed in the interpretation of the spectro-directional results.

Another technical challenge is the sun azimuth angle change over time during the beginning and end of the measurements. The measurement scheme is optimized towards the solar principal plane, and a change in the sun azimuth angle leads to a shift in the results. Therefore, the developed software application calculates for each azimuth circle (overall five) within the measurement scheme a correction factor which can be set in the AAM at the chosen view zenith angle position (0°, 5°, 10°, 20°, 30°) before the zenith arc is rotated. This regular manual correction of the solar principal plane during the measurements decreases the divergence between the projected and real principal plane to 0.5°. However, since the geographic north is determined by a compass and manually set in the AAM, the uncertainty between the projected and real principal plane increases to 1.5° to 2°.

5.5 Data Analysis

5.5.1 Data Processing

First, all acquired measurements are transferred into a database and pre-processed. Since the GER-1500 spectro-radiometers produce DN (digital number) values as output, the first pre-processing step is their conversion to radiance and irradiance values with the help of the sensor calibration files provided by the manufacturer, as well as the storage in a standard ASCII (American Standard Code for Information Interchange) format. Then automatic quality tests for detecting outliers in the measurement scheme and sensor noise are realized.

In order to derive the HCRF for each viewing positions, Equation 5.2 has to be adapted. Due to practical reasons, Spectralon® reference panel measurements are performed only from the nadir view direction. Moreover, the used reference panel has an 8° hemispherical spectral reflectance calibration, and therefore a correction factor R_{ref} which ideally corresponds to the BRF of the reference panel. Since it is known that the BRF of the reference panel also depends on the sun zenith angle (θ_i), a correction factor c_{ref} is replacing R_{ref}. This correction factor c_{ref} uses the correction algorithm developed by *Sandmeier et al.* [1998b] under the assumption that the reflectance anisotropy is nearly invariant between different Spectralon® panels [*Bruegge et al.*, 2001]. Equation 5.3 shows the modified HCRF formula:

$$HCRF(\lambda;\theta_i,\phi_i;\theta_r,\phi_r) = \frac{L_r(\lambda;\theta_i,\phi_i;\theta_r,\phi_r)}{L_{ref}(\lambda;\theta_i,\phi_i)} \cdot c_{ref}(\lambda,\theta_i) \qquad (5.3)$$

As mention in Section 5.4.4, the spectro-goniometer measurements at various sensor positions cannot be performed at the same time. Therefore, short-term temporal changes in irradiation as well as illumination zenith angle changes between the beginning and end of a

measurements scheme occur. We try to account for these effects by interpolating the reference panel measurement L_{ref} taken at time t_0 towards the timestamp t_x of the actual target measurement L_r with help of a weight factor c_{diff}. The weight factor c_{diff} is obtained using the diffuse total irradiance measurements E_{diff} of the second spectro-radiometer at the timestamp t_0 and t_x (Equation 5.4). Therefore, we assume that changes in the irradiance over the time period affect the radiance measurements of the reference panel to a similar degree in the certain wavelength region [*Schopfer et al.*, 2008].

$$c_{diff}(\lambda;\theta_i,\phi_i;t_x) = \frac{E_{diff}(\lambda;\theta_i,\phi_i;t_x)}{E_{diff}(\lambda;\theta_i,\phi_i;t_0)} \tag{5.4}$$

In order to evaluate the quality of this approach, we introduced an outlier indicator which uses the continuous irradiance readings and the L_{ref} measurements at the beginning and end of a measurement scheme. The visualization of this outlier indicator helps to interpret the HCRF measurements of the full hemisphere. Thus, the HCRF calculation from ManTIS field measurements results in the following formula introducing the relative time span between the L_{ref} measurement in the nadir view position and the L_r measurement in the actual viewing position of the measurement scheme:

$$HCRF(\lambda;\theta_i,\phi_i;\theta_r,\phi_r) = \frac{L_r(\lambda;\theta_i,\phi_i;\theta_r,\phi_r;t_x)}{L_{ref}(\lambda;\theta_i,\phi_i;t_0)\cdot c_{diff}(\lambda;\theta_i,\phi_i;t_x)} \cdot c_{ref}(\lambda,\theta_i,t_0) \tag{5.5}$$

Only under the assumption that the HCRF is constant over the IFOV of the sensor and that the measurements are taken under clear sky with predominantly direct radiation, the measured HCRF values approximate the BRF. In order to separate the BRDF effects from the underlying surface reflectance characteristics, the HCRF data of one hemisphere has to be normalized by the nadir viewing reflectance signature of the target surface [*Sandmeier et al.*, 1998a; *Sandmeier and Itten*, 1999]. This normalization creates the anisotropy factor (ANIF) (Equation 5.6) [*Sandmeier and Itten*, 1999]:

$$ANIF(\lambda;\theta_i,\phi_i;\theta_r,\phi_r) = \frac{HCRF(\lambda;\theta_i,\phi_i;\theta_r,\phi_r)}{HCRF_{nadir}(\lambda;\theta_i,\phi_i;\theta_r=0,\phi_r=0)} \tag{5.6}$$

With help of the ANIF the spectral-directional characteristics can be compared between different target surfaces or at changing illumination geometry. For an overall estimation of the reflectance anisotropy in a certain wavelength and in order to further analyze the spectral variability of the reflectance anisotropy, *Sandmeier et al.* [1999] developed the anisotropy index (ANIX) (Equation 5.7):

$$ANIX(\lambda,\theta_i) = \frac{HCRF_{\max}(\lambda,\theta_i)}{HCRF_{\min}(\lambda,\theta_i)} \tag{5.7}$$

The ANIX is the ratio of the maximum HCRF and minimum HCRF of a measured hemisphere, and is calculated for a certain wavelength region as well as a defined azimuth

plane [*Sandmeier and Itten*, 1999]. Since reflectance anisotropy is more strongly pronounced in the solar principal plane [*Sandmeier and Itten*, 1999; *Sandmeier*, 2000] and for easier comparability, the ANIX is usually presented with respect to the solar principal plane.

5.5.2 Data Visualization

The processed HCRF data together with metadata of the surface measured at a certain illumination geometry are stored in a database following the recommendations of *Sandmeier* [2000]. For a better interpretation and comparison of the spectro-directional data, the visualization as surface models in 2D and 3D plots is commonly used. Therefore, we aligned a visualization model of *Küster* [2011], coded in the programming language Python, to our measurement scheme. To avoid misinterpretation of the visualization, Figure 5-6A-B shows the polar coordinate system used for presenting the results.

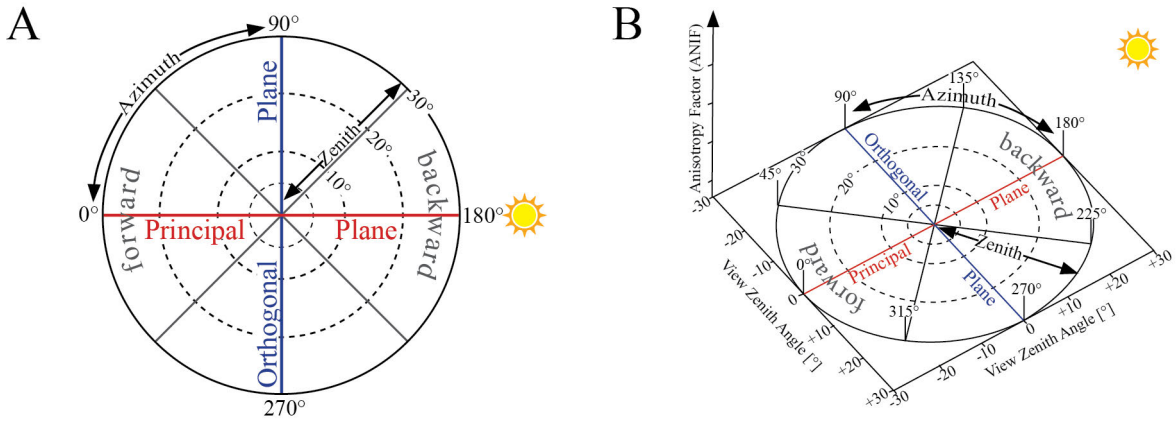

Figure 5-6: (**A**) Polar coordinate system used for presenting BRDF data in 2D plots. (**B**) Polar coordinate system used for presenting BRDF data in 3D plots.

5.6 Performance of ManTIS Field Spectro-Goniometer in the Field

5.6.1 Test Site and Experiment Setup

The ManTIS field spectro-goniometer was already field-tested on two Arctic expeditions [*Heim et al.*, 2012; *Strauss et al.*, 2012]. In order to show the quality of field HCRF retrieval and the BRDF analyzing approach, we present a spectro-directional characterization of a low growing vegetation community in a challenging geographic location for field spectro-goniometer measurements. The HCRF datasets of the sample plot at the Franklin Bluffs study location, Alaska, USA (69°40′28″N, 148°43′15″W, 122 m ASL) were measured in the summer season of 2012 (Figure 5-7A-B).

The sample plot FBG2 is located in the bioclimate subzone D of the circumpolar arctic vegetation map (CAVM) [*Walker et al.*, 2005] and is part of the North American Arctic transect (NAAT) established by *Walker et al.* [2008b]. The dominant vegetation can be described as moist non-acidic tundra (MNT) [*Raynolds et al.*, 2008]. The sample plot shows a homogenous coverage with a prostrate dwarf deciduous shrub (*Salix arctica*) community as well as sedges and forbs (Figure 5-7C). Important to mention is that there are dense and thick moss and lichen mats in the understory, therefore no open soil is exposed. The average

vegetation height of the shrub layer is 35 cm, of the sedge and forb layer 15 cm, and of the moss and lichen layer 2 cm. At the day of the measurements (2012-07-09), the vegetation was nearly at the peak of the phenological stadium. Since the sample plot FBG2 is located next to the well-established and researched Franklin Bluffs moist / zonal study site (FB_m/z), a more detailed vegetation description of the study location can be found in *Kade et al.* [2005]. Moreover, *Buchhorn et al.* [2013] presents a detailed hyperspectral characterization of the Franklin Bluffs study location and MNT vegetation (Chapter 6).

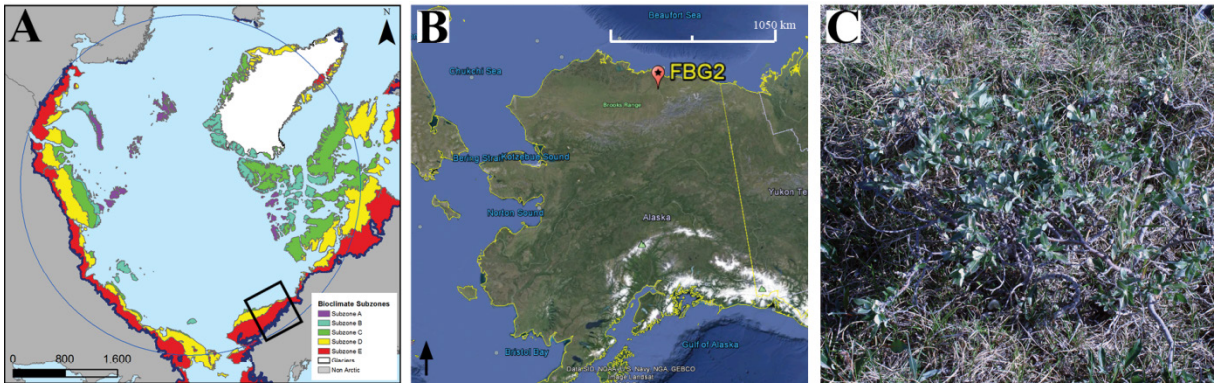

Figure 5-7: (**A**) The study location in respect to the bioclimate subzones of the circumpolar arctic vegetation map (CAVM) [*Walker et al.*, 2005]. (**B**) Location of the sample plot FBG2 in the Alaskan Low Arctic. Image Source: Google Earth, 2013. (**C**) Photo of the prostrate dwarf deciduous shrub community measured at solar noon (sun zenith angle of 47°).

For the presented case study, a complete hemispherical cycle was measured on a clear-sky day at solar noon (measurements started at 13:48 local time) and under gentle wind conditions. Therefore, the illumination direction had a sun zenith angle of 47° and a sun azimuth angle of 180°. The time needed to complete the measurement scheme with 61 sensor positions was 25 minutes and therefore not optimal. The sun zenith angle changes between the beginning and the end of the measurement scheme amount to 0.4° and the sun azimuth changes amount to 8°. The HCRF values were calculated following Equation 5.5.

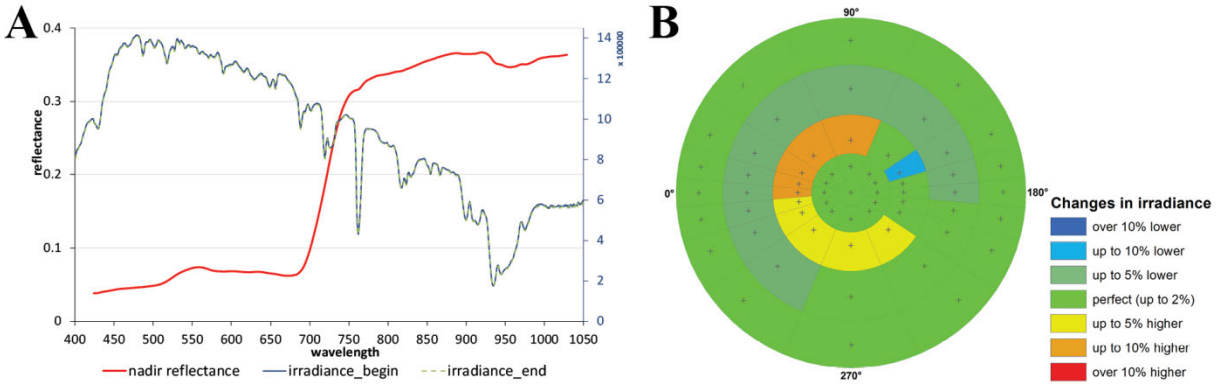

Figure 5-8: (**A**) Nadir reflectance spectrum and irradiance profiles of the prostrate dwarf shrub-nontussock sedge-moss tundra sample plot FBG2 at the beginning and end of the measurement scheme. (**B**) Polar plot of the outlier indicator showing short-term illumination changes during the measurement scheme.

Figure 5-8A shows the reflectance spectrum as well as the irradiance spectra of the nadir viewing position to the beginning and end of the measurement scheme, where Figure 5-8B presents the quality assessment of the interpolation approach used to reduce temporal errors. It is notable that in the third measurement circle (10° viewing zenith angle position) of the measurement scheme stronger atmospheric changes occurred which had to be corrected. This region of the ManTIS hemisphere needs more caution in the interpretation of the spectro-directional characteristics of the surface.

5.6.2 Results and Discussion

The spectral HCRF and ANIF data of the prostrate dwarf shrub community for the main view zenith directions in the solar principal plane are presented in Figure 5-9. Where in the HCRF data (Figure 5-9A) changes in the reflectance anisotropy are barely visible, the ANIF data (Figure 5-9B) exempted from the underlying surface reflectance characteristics show the strong spectral variability in the reflectance anisotropy. The ANIF data show that equal to higher reflectance values compared to the nadir value appear in the backward viewing directions of the solar principal plane, and that the reflectance values in the forward viewing directions are lower. This is especially well observable in Figure 5-10, where the HCRF and ANIF data for specific wavelengths are presented over the view zenith angles in the solar principal plane. The ANIF values in the solar principal plane range from 1.0 to 1.45 in the visible and 0.9 – 1.1 in the near-infrared wavelength region of the backward viewing directions, whereas in the forward viewing directions the ANIF values range from 0.7 to 0.95 in the visible to near-infrared wavelength region (Figure 5-9B). Therefore, a higher degree in reflectance anisotropy occurs in the visible (400 – 700 nm) than in the near-infrared (700 – 1,400 nm) wavelength region.

These findings have been also found in other spectro-directional studies of planophile and erectophile vegetation [*Peltoniemi et al.*, 2005; *Sandmeier et al.*, 1998a; *Sandmeier et al.*, 1999]. The reason for the specific reflectance shape along the view zenith direction is the canopy geometry, influencing the distribution and proportion of shadowed and illuminated surfaces within the plant canopy which change under varying viewing-illumination geometries [*Hapke et al.*, 1996; *Sandmeier et al.*, 1998a]. Multiple scattering effects in the vegetation canopy regulate the intensity (“darkness”) of the shadows [*Sandmeier et al.*, 1998a], and create therefore the spectral dependence of the BRDF effects.

Since in wavelength regions with high absorption (visible blue and red chlorophyll absorption bands) the relatively low amount of radiation in the vegetation canopy reduces the multiple scattering effects, the contrast between shadowed and illuminated surfaces increases and therefore enhances the reflectance anisotropy [*Sandmeier and Itten*, 1999]. Vice versa, higher multiple scattering effects in wavelength regions with higher reflection (visible green and near-infrared bands) reduce the contrast in the canopy.

Figure 5-11A-D shows the visualization of the HCRF data in 2D polar plots for four important wavelengths in the visible blue, green, and red as well as near-infrared spectrum.

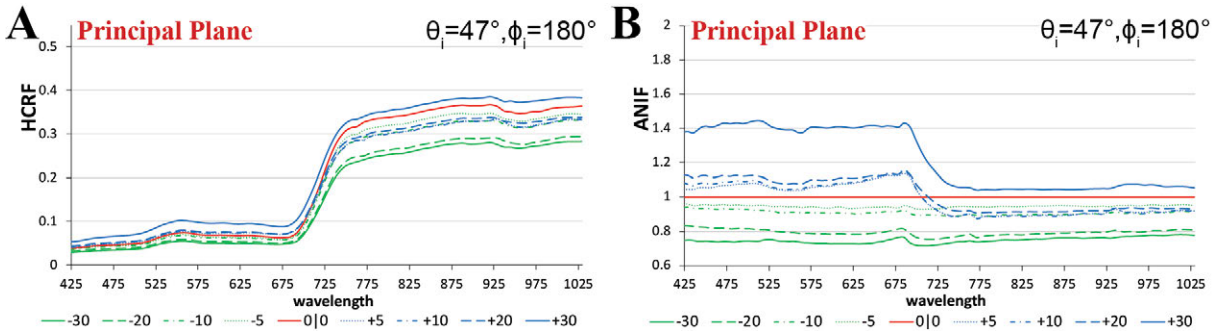

Figure 5-9: (**A**) HCRF values of the prostrate dwarf shrub community for various view zenith angles in the solar principal plane. (**B**) Anisotropy factors (ANIF) of the prostrate dwarf shrub community for various view zenith angles in the solar principal plane.

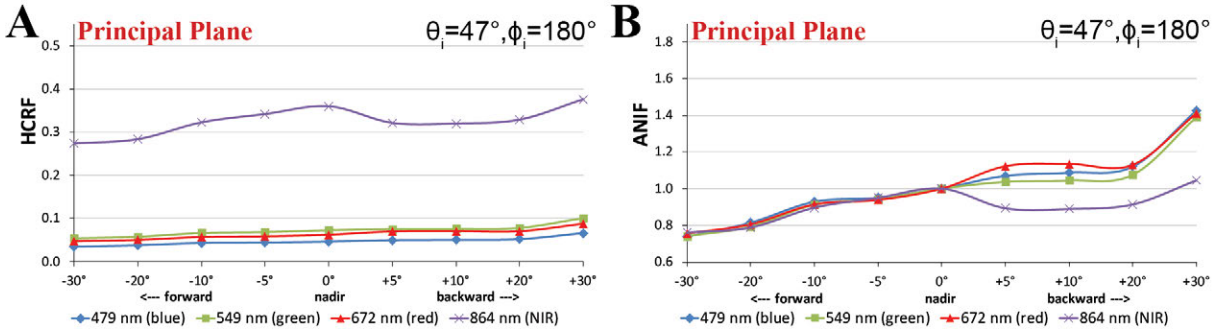

Figure 5-10: (**A**) HCRF values versus view zenith angles in the solar principal plane. (**B**) Anisotropy factors (ANIF) versus view zenith angles in the solar principal plane.

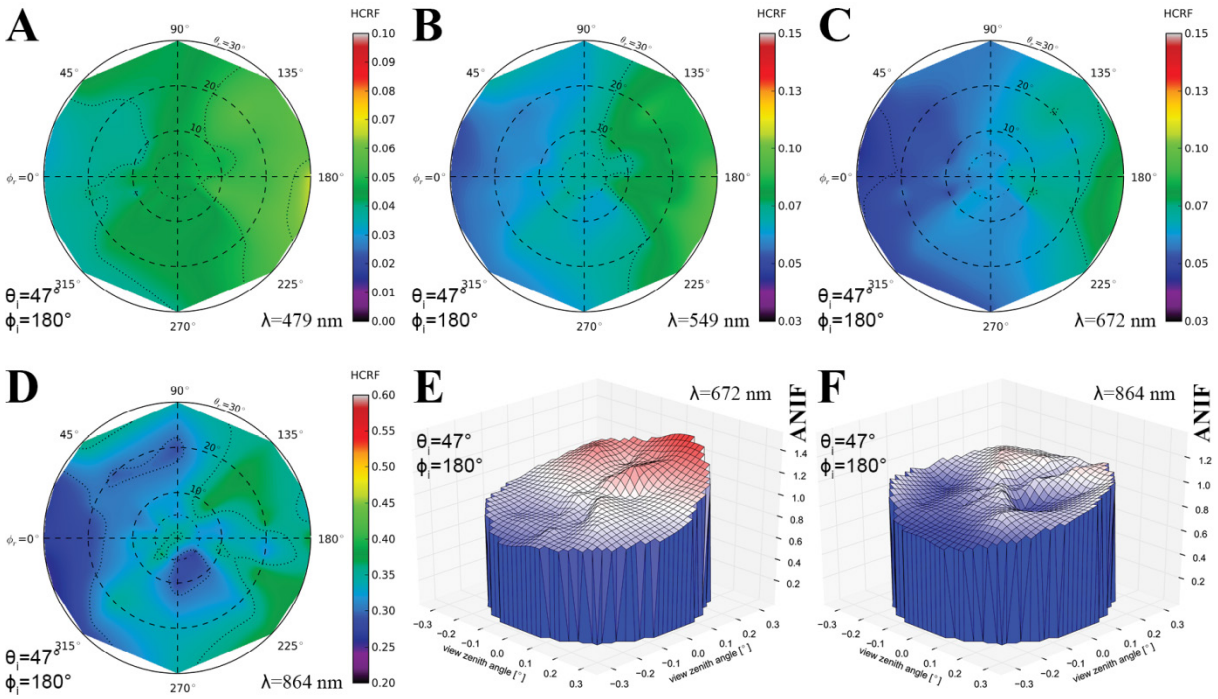

Figure 5-11: (**A–D**) Polar plots of the HCRF data for all view angles at wavelengths of (**A**) 479 nm, (**B**) 549 nm, (**C**) 672 nm, and (**D**) 864 nm. (**E–F**) 3D visualization of the ANIF data for all view angles at wavelengths of (**E**) 672 nm and (**F**) 864 nm.

It is viewable that the BRDF effects in the prostrate dwarf shrub community are strongest in the solar plane and decrease towards the solar orthogonal plane. Moreover, the distribution of the HCRF values over the hemisphere shows in some viewing positions outliers, especially in the near-infrared wavelength region (Figure 5-11D). An explanation could be that the vegetation cover of the sampling plot is not perfectly homogeneous due to the chosen prostrate dwarf shrub community or that the periodic presence of wind has influenced the vegetation canopy and thus the HCRF measurements.

Figure 5-11E-F shows the visualization of the ANIF data in 3D of the visible red and near-infrared wavelength spectrum. The differences in the degree of reflectance anisotropy between the visible and near-infrared wavelength region are well notable. A more quantitative analysis of the spectral variability of the BRDF effects of the prostrate dwarf shrub community allows the plotting of the ANIX over the spectral range for the solar principal and orthogonal plane (Figure 5-12A). It shows that BRDF effects are pronounced in the solar principal plane and low in the solar orthogonal plane. It also shows an unexpected fact; normally the ANIX graph in the solar principal plane has to show a strong dip in the visible green (500 – 550 nm) because of the increase in multiple scattering though more available radiation in the vegetation canopy, and therefore reduced reflectance anisotropy. However in this case this was not observed. A reason could be that since MNT vegetation do not have a distinct green reflectance peak [*Buchhorn et al.*, 2013], less multiple scattering appears in this wavelength region. Figure 5-12B shows the expected linkage of the degree of reflectance anisotropy and degree of reflectance by plotting ANIX against the nadir reflectances of the prostrate dwarf shrub community.

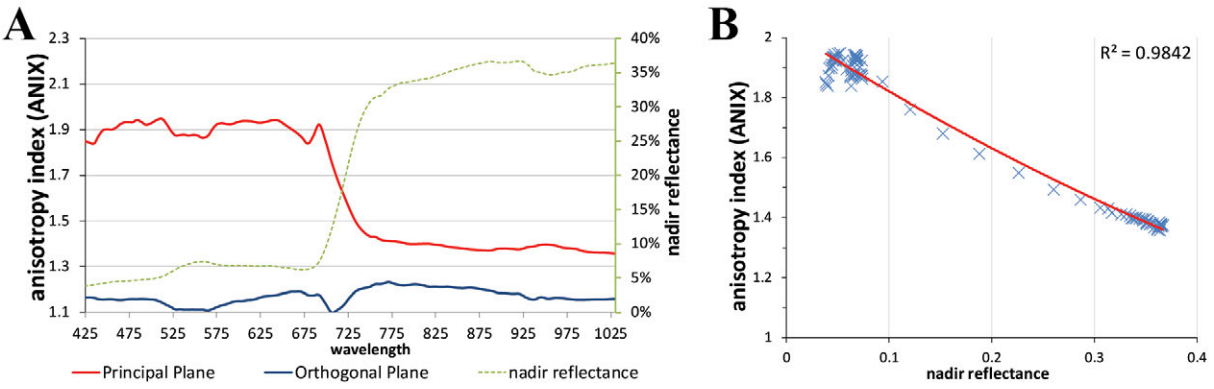

Figure 5-12: (**A**) Anisotropy index (ANIX) versus wavelength in the solar principal and orthogonal plane. (**B**) ANIX versus nadir reflectance showing strong linkage (higher degree of reflectance in nadir view position = lower degree of reflectance anisotropy).

The calculation of vegetation indices (VI) from spectro-directional data create new functions (called vegetation index distribution functions) [*Küster*, 2011]. Therefore, the spectral variability of the reflectance anisotropy has impacts on VIs such as the normalized difference vegetation index (NDVI). Especially the NDVI, calculated from two wavelength regions (visible red and near-infrared) with completely different BRDF characteristics, is affected. Several studies have already researched the influence of BRDF effects on the NDVI in the broadband and hyperspectral domain [*Jackson et al.*, 1990; *Küster*, 2011; *Verrelst et al.*,

2008; *Vierling et al.*, 1997]. In the analyzed prostrate dwarf shrub community, the NDVI values observed under viewing zenith angle up to ±30° increase towards the forward viewing directions and decrease towards the backward viewing directions in the solar principal plane (Figure 5-13A). The highest difference is notable in the +30° backward viewing direction of the solar principal plane where the off-view NDVI is 12% lower than in the nadir viewing position. Figure 5-13B shows the NDVI values of all possible viewing positions within the ManTIS hemisphere normalized to the nadir NDVI.

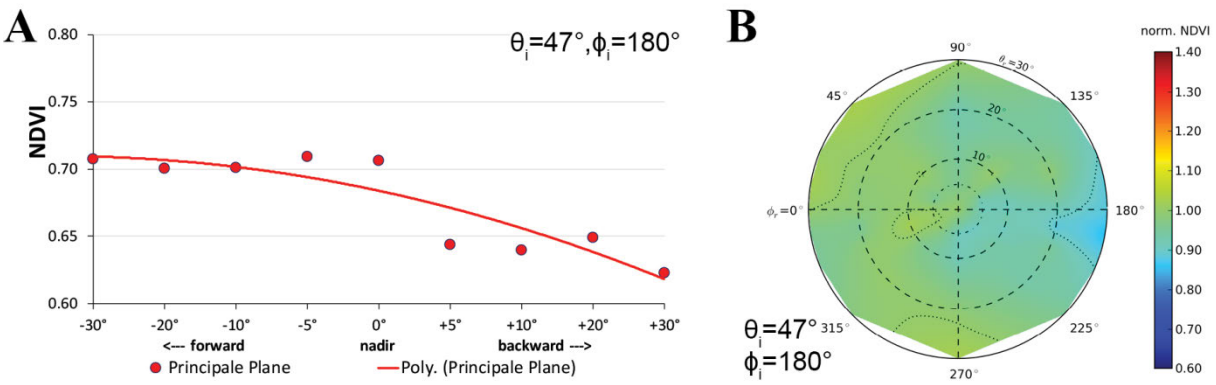

Figure 5-13: (**A**) NDVI for various view zenith angles in the solar principal plane. (**B**) Polar plot of the nadir normalized NDVI data for all view angles of the dwarf shrub community.

5.7 Conclusions and Outlook

The availability of ground-based multi-angular RS data is important for the calibration of off-nadir reflection data as well as the potential derivation of canopy structure parameters from remote sensing data. The ManTIS field spectro-goniometer was developed for this purpose, and represents a tool for ground-based multi-angular observations of low-growing vegetated surfaces (up to 1 m vegetation height) which can be used in geographical challenging environments such as the Arctic were heavy or fully automated field goniometers reach their limits.

In this paper, the development of a manual transportable instrument platform for ground-based spectro-directional observations (called ManTIS) and the resultant hyperspectral field spectro-goniometer system has been described. The ManTIS can be equipped with various sensor systems and represent a lightweight, stable, and low-cost platform for spectro-directional observations with up to 30° viewing zenith angle and 360° viewing azimuth angle. The innovative mounting of the zenith arc enables instrument setup on small assembly space. But nevertheless it offers a 2 m distance between the surface target and the sensor in unison with a high angular accuracy and fast execution of the measurements. The platform is equipped in its current configuration as AWI ManTIS field spectro-goniometer with two GER-1500 spectro-radiometers, a GPS receiver, and a video camera system.

This article has presented the sensor configuration, measurement strategy as well as the developed software application for the semi-automatic control of the ManTIS field spectro-goniometer. The current measurement scheme with 61 viewing points was optimized with respect to the solar principal plane and allows the hemispherical conical reflectance factor

(HCRF) recording of a ManTIS hemisphere within 18 minutes under optimal conditions. The pointing accuracy of the system is within ±6 cm and the current instantaneous field of view (IFOV) of the sensor is 8.5°. Therefore, a homogeneous sampling area of approx. 25 cm in radius around the center of the target plot is needed to acquire representative spectro-goniometer measurements. The developed data processing chain in connection with the used software for the semi-automatic control provides a reliable method to reduce temporal effects during the measurements.

The AWI ManTIS field spectro-goniometer was intensely field tested on two Arctic expeditions and proved its value to characterize the spectro-directional effects of vegetation surfaces. Moreover, this article presented the results of a spectro-goniometer measured Arctic vegetation surface in order to show the high quality and the visualization approaches of the received data. The results of the two expeditions form the start of the systematic spectro-directional characterization of Arctic vegetation communities in order to create a spectral BRDF library, which will be made available to the scientific community. For future measurements it is planned that the field spectro-goniometer system will be improved by a 3D camera system delivering geometric properties of the observed vegetation.

The ManTIS was nationally registered for patent on 25 October 2011, and internationally registered for patent on 27 June 2012. The patent publication number is DE 10 2011 117 713.A1 (international publication number: WO2013013652.A1) and has been published on 31 January 2013 [*Buchhorn and Petereit*, 2011, 2013]. The patent is still pending to the time of the publication of this article. More information is available under http://patentscope.wipo.int/search/en/WO2013013652. Moreover, the ManTIS instrument platform will be produced under license and sold by W. Ludolph GmbH & Co. KG in Bremerhaven, Germany (http://www.ludolph.de/) for the international market.

6 HYPERSPECTRAL REFLECTANCE CHARACTERIZATION OF LOW ARCTIC TUNDRA VEGETATION

This chapter has been published as original research article in the journal "*Remote Sensing*" under the title: "Ground-Based Hyperspectral Characterization of Alaska Tundra Vegetation along Environmental Gradients" by MDPI, Basel, Switzerland. This article is an open access article distributed under the terms and conditions of the Creative Commons Attribution license (http://creativecommons.org/licenses/by/3.0/).

The full citation is: Buchhorn, M.; Walker, D.A.; Heim, B.; Raynolds, M.K.; Epstein, H.E.; Schwieder, M. (2013), Ground-based Hyperspectral Characterization of Alaska Tundra Vegetation along Environmental Gradients. *Remote Sensing*, 5(8), 3971 – 4005; DOI: 10.3390/rs5083971.

As first author, I reviewed the relevant literature, organized and contributed to the field work, analyzed and interpreted the data, and initiated, wrote, and coordinated the manuscripts. The co-authors participated in field work, contributed data, and/or critically reviewed and discussed manuscript drafts.

Table 6-1: Affiliation and contributed work of the co-authors of the article.

Co-Author	Affiliation	Work
Walker, Donald A.	Alaska Geobotany Center, University of Alaska Fairbanks, USA.	contributed data; critically reviewed and discussed manuscript drafts
Heim, Birgit	AWI	contributed data; critically reviewed and discussed manuscript drafts
Raynolds, Martha K.	Alaska Geobotany Center, University of Alaska Fairbanks, USA.	contributed data; critically reviewed and discussed manuscript drafts
Epstein, Howard E.	Environmental Sciences Department, University of Virginia, USA.	critically reviewed and discussed manuscript drafts
Schwieder, Marcel	Geography Department, Humboldt-Universität zu Berlin, GERMANY.	participated in field work; contributed data

6.1 Introduction

Time series of satellite data from the Advanced Very High Resolution Radiometer (AVHRR) from 1982 to 2010 have shown an increase in the Normalized Difference Vegetation Index (NDVI), an index of vegetation biomass and greenness, of about 8 % for the northern hemisphere tundra [*Bhatt et al.*, 2010]. This greening trend is caused by increased tundra productivity which is thought to be mainly a response to climate warming [*Callaghan et al.*, 2011b; *Epstein et al.*, 2012; *Lawrence et al.*, 2008; *Walker*, 2006]. The Arctic is warming at nearly double the general planetary rate [*Winton*, 2006]. Extrapolation of the NDVI trend assigning biomass data from two Arctic transects indicates an average 19.8 % increase in above-ground tundra biomass during the AVHRR NDVI record (1982-2010) [*Epstein et al.*, 2012]. This has major implications for tundra ecosystems, including changes in active layer depth, permafrost and thermokarst distribution, carbon cycling, hydrology, and wildlife [*Walker et al.*, 2012a].

Monitoring of Arctic landscapes is therefore important. Due to the remoteness and large area of the tundra biome, satellite and aerial remote sensing provide the best prospective tools for land-cover mapping and change detection [*Olthof and Fraser*, 2007; *Raynolds et al.*, 2012; *Stow et al.*, 2004; *Ulrich et al.*, 2009]. However, the short vegetation growing period and therefore accelerated phenology, frequent cloud cover, high standing water and surface water coverage, and extreme illumination conditions (sun zenith angles in arctic latitudes always larger than 43°) challenges optical remote sensing of vegetation in the Arctic [*Kääb*, 2008; *Stow et al.*, 2004; *Vierling et al.*, 1997].

Several studies have shown the capability of multi-spectral satellite and aerial remote sensing data to extract biophysical plant parameters. The studies for the North American tundra biome mainly used broadband NDVI indices [*Epstein et al.*, 2012; *Hope et al.*, 1993; *Huemmrich et al.*, 2010; *Laidler et al.*, 2008; *Olthof and Latifovic*, 2007; *Riedel et al.*, 2005; *Stow et al.*, 2004; *Vierling et al.*, 1997; *Walker et al.*, 2003]. *Horler et al.* [1983] noticed that broadband based remote sensing may not be adequate to extract sharp reflectance changes in narrow spectral regions, such as the 'red-edge,' between the red and near-infrared. The technical development in airborne and satellite imaging spectroscopy sensors like AVIRIS (Airborne Visible and Infrared Imaging Spectrometer) [*Elvidge*, 1988], CHRIS/Proba (Compact High Resolution Imaging Spectrometer / Project for On-Board Autonomy) [*Barnsley et al.*, 2004], EO-1/Hyperion (Earth Observing 1 / Hyperion instrument) [*Pearlman et al.*, 2003], and the upcoming German EnMAP (Environmental Mapping and Analysis Program) satellite mission [*Stuffler et al.*, 2007] opens the door for new methods that can use the entire spectral feature space of imaging spectroscopy [*Asner*, 1998; *Schaepman et al.*, 2009].

Reflectance from vegetated surfaces is highly differentiated by wavelength. The visible (VIS) wavelengths (400 - 700 nm) are strongly influenced by the pigment absorption of the plants in different wavelength regions [*Gitelson et al.*, 2003; *Jakomulska et al.*, 2003]. The main pigment groups are chlorophylls and carotenoids. The light absorption for photosynthesis is

mainly done by chlorophylls with absorption maxima in the blue and red wavelength regions. Carotenoids have their absorption maxima in the blue and green wavelength regions and the group of anthocyanins in the green wavelength region [*Gitelson et al.*, 2003]. The reflectance in the near-infrared (NIR) wavelength region (700 – 1,400 nm) is mainly influenced by plant cell structure and vegetation biomass. Multiple scattering of radiation between air and cell wall in leaf tissue leads to high reflectance values in this region referred to as the NIR reflectance plateau [*Gausman*, 1974]. This sharp reflectance contrast between VIS and NIR is commonly used in remote sensing for calculating vegetation indices using combinations of red and NIR wavelength regions [*Richardson and Wiegand*, 1977; *Roberts et al.*, 2011; *Thenkabail et al.*, 2000].

The use of hyperspectral data can improve the prediction of biophysical variables [*Elvidge and Chen*, 1995; *Thenkabail et al.*, 2011], but there are limited imaging spectroscopy data of North American tundra landscapes available. This is a common shortcoming all over the Arctic [*Kääb*, 2008]. Field spectroscopy is a valuable tool to gain ground-based hyperspectral data.

The objective of this paper is to characterize and distinguish Low Arctic Alaskan tundra vegetation communities along important environmental gradients via field spectroscopy. To provide an overview on the spectral characteristics assists the classification and analyses of tundra vegetation using satellite hyperspectral imagery. The North American Arctic Transect (NAAT) sites provide representative measurement grids covering gradients of zonal climate, soil moisture, and soil pH. The gradients along the Low-Arctic part of the NAAT show therefore changes in vegetation biomass, height of vegetation, leaf mass and surface moisture. We investigated if spectral characteristics are linked to geoecological characteristics of the Low Arctic tundra vegetation and their change along the gradients.

6.2 Material & Methods

6.2.1 Study Area

The circumpolar Arctic vegetation map (CAVM) divides the Arctic tundra into five bioclimate subzones (A-E) based on a combination of summer temperatures and vegetation [*Walker et al.*, 2005] (Figure 6-1A). Subzones D and E compose the Low Arctic. The North American Arctic Transect (NAAT), established in 2002–2006, follows the Dalton Highway, crossing Alaska's North Slope, and extends into the western Canadian High Arctic islands [*Walker et al.*, 2008b]. It includes study locations in all five bioclimate subzones. Along the 250 km Low Arctic part of this transect four NAAT study locations were established - Deadhorse (transition subzone C/D), Franklin Bluffs (subzone D), Sagwon Hills (transition subzone D/E), and Happy Valley (subzone E) (Figure 6-1B). All study locations contain at least one 100 m² mapped grid with homogeneous vegetation including a good representation of the zonal vegetation in subzones D and E and transition types. Nine study sites were investigated in summer 2012, during the EyeSight-NAAT-ALASKA expedition [*Buchhorn*

and Schwieder, 2012]. We carried out field spectroscopy measurements in addition to updating the vegetation descriptions and soil moisture measurements at each site.

A detailed description of plant communities and geology of the Low Arctic portion of the NAAT can be found in *Kade et al.* [2005], and *Vonlanthen et al.* [2008] provide this analysis for the High Arctic part of the NAAT. A synthesis of NAAT publications is in *Walker et al.* [2008c; 2011c], and considerable other information is available in on-line data reports [Alaska Geobotany Center, 2013].

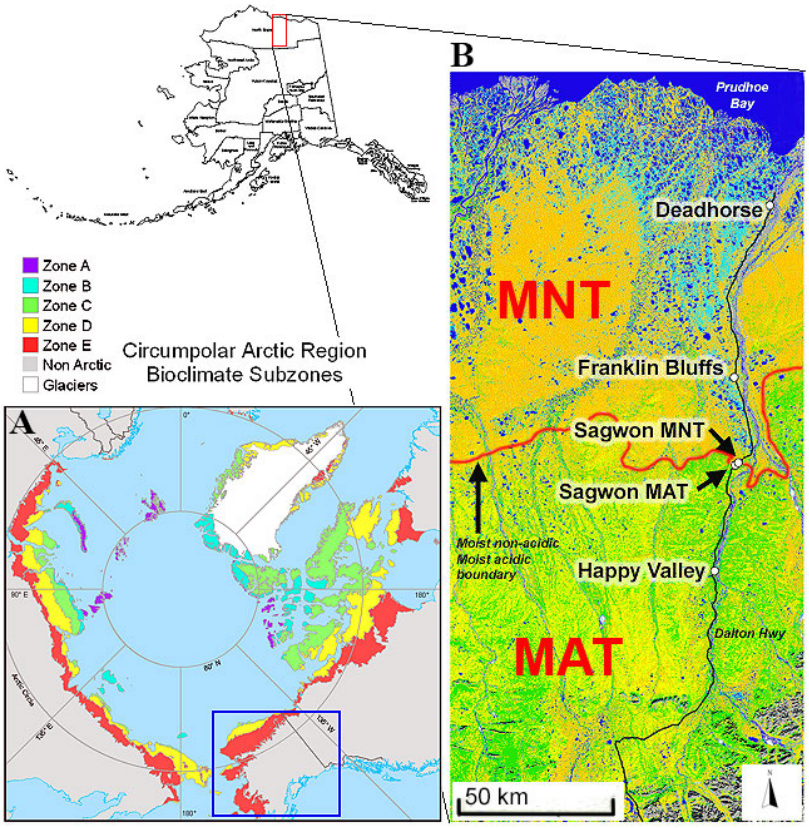

Figure 6-1: (**A**) The Arctic bioclimate subzones of the Circumpolar Arctic Vegetation Map [*Walker et al.*, 2005]. ***Note:*** The blue rectangle marks Alaska. (**B**) Low Arctic part of the NAAT with the study locations Happy Valley, Sagwon, Franklin Bluffs, and Deadhorse. The map is based on the Kuparuk River Basin Vegetation map [Alaska Geobotany Center, 2010] which is derived from a Landsat mosaic.

6.2.2 Environmental Gradients/Zones and Vegetation Description

The nine study sites represent arctic tundra vegetation communities along four arctic environmental gradients and zones: summer temperature, soil pH, soil moisture, and topography. The latitudinal climate gradient (bioclimate subzones) influences vegetation along the whole Low Arctic transect, the soil pH zoning reflects a substrate division between acidic and non-acidic soils (Figure 6-1B). The toposequence (hillslope) gradient is most relevant at landscape scales influencing lateral water fluxes, and the soil moisture gradient is influential at the site scale as well as being apparent at all scales [*Walker*, 2000]. These gradients are, however, not orthogonal. There is the general temperature gradient and pH zonation from north to south with further variations related to moisture and topography. In

order to assign a study site to a conceptual gradient, the main influencing factor was used. Figure 6-2 shows the nine study sites in relationship to the four conceptual environmental gradients and zones. Figure 6-3 outlines the main geoecological characteristics of the nine test sites.

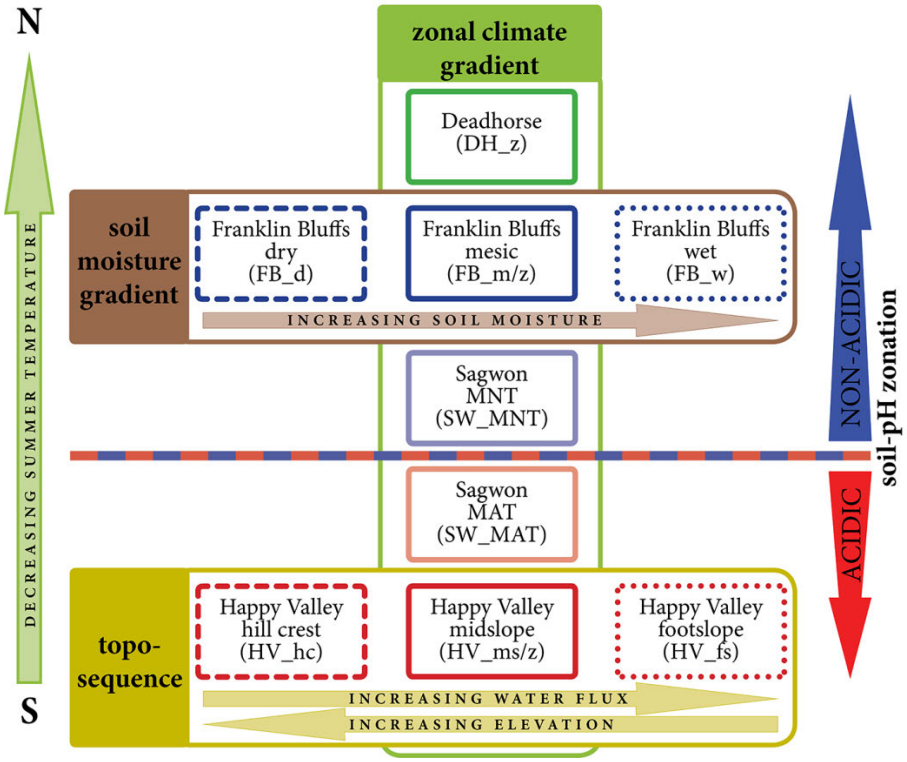

Figure 6-2: The nine study sites in relation to environmental gradients and zones concept (zonal climate, soil pH, soil moisture, and toposequence/hillslope) along the Low Arctic part of the NAAT. ***Note:*** Border color and texture are specific for each study site and will be used in all figures in order to distinguish between the sites.

The regional climate gradient with differences in the summer warmth index (SWI) is well represented by the five zonal sites of this study (Deadhorse, Franklin Bluffs-mesic, Sagwon-MNT, Sagwon-MAT, and Happy Valley-midslope) (Figure 6-2, Figure 6-3). The SWI is the sum of mean monthly temperatures greater than 0 °C [*Walker et al.*, 2003]. The term 'zonal' refers to vegetation under the influence of the regional climate, without the influences of extremes of snow, soil properties, moisture or disturbances [*Razzhivin*, 1999]. *Walker et al.* [2005] describe the zonal vegetation in bioclimate subzones D and E for the circumpolar Arctic in detail. The main influence of the regional climate is the increase in phytomass towards the south.

An important soil pH boundary occurs at Sagwon [*Walker et al.*, 1998]. Two test sites (Sagwon-MNT and Sagwon-MAT) were established at the Sagwon Hills study location to capture this variation in the patterning between Subzones D and E (Figure 6-2, Figure 6-3). This boundary separates the predominantly moist acidic tundra (MAT) south of the boundary from the predominantly moist non-acidic tundra (MNT) to the north. The boundary is close to but not coincident with a physiographic boundary separating the Arctic Foothills to the south from the Arctic Coastal Plain to the north [*Zhang et al.*, 1996]. The MAT plant community is

Sphagno-Eriophoretum vaginati [*Walker et al.*, 1994] (also called 'acidic tussock tundra' or 'tussock-sedge, dwarf shrub, moss tundra' [*Walker et al.*, 2005]) and corresponds to the zonal plant community of bioclimate subzone E in northern Alaska. It occurs widely across the foothills of northern Alaska on old upland surfaces not glaciated during the Last Glacial Maximum. The vegetation is composed of a mixture of tussock sedges, deciduous dwarf shrubs, evergreen dwarf shrubs, a few forbs, mosses and lichens. The MNT plant community is *Dryado integrifoliae-Caricetum bigelowii* [*Walker et al.*, 2005] (also called 'nontussock sedge, dwarf shrub, moss tundra' [*Walker et al.*, 2005]) and corresponds to the zonal plant community of bioclimate subzone D in northern Alaska. It occurs on circumneutral to basic soils in association with silty loess that is blown from the major rivers in the eastern part of the Arctic Coastal Plain. The dominant plants in MNT are sedges, prostrate and hemi-prostrate evergreen dwarf shrubs, prostrate dwarf deciduous shrubs, scattered erect dwarf deciduous shrubs, several forbs, mosses, and lichens. An important component of the MNT is the abundant nonsorted circles (frost boils), which are small patterned ground features caused by soil frost heave and covering large parts of most MNT surfaces [*Walker et al.*, 2008b; *Washburn*, 1980].

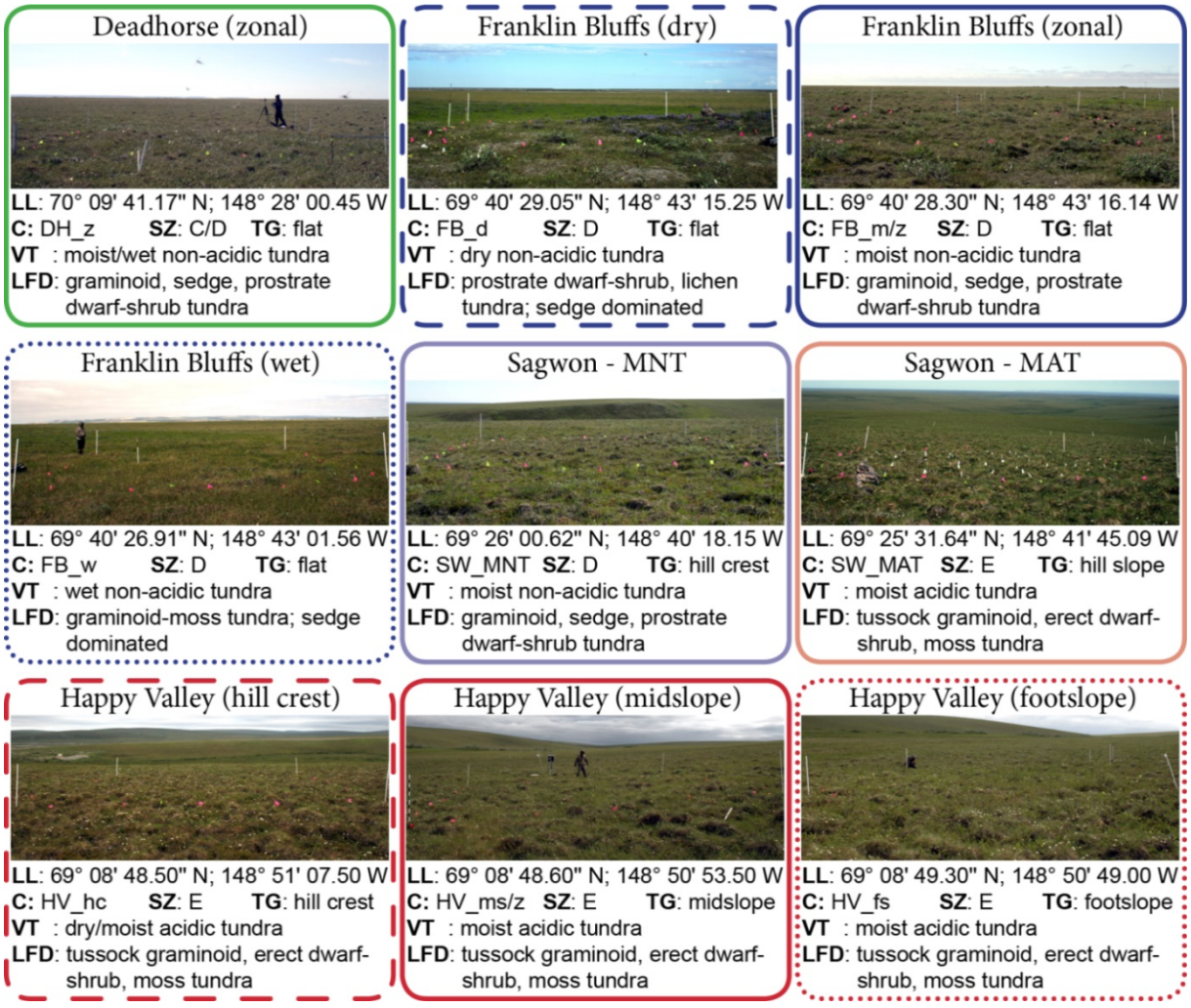

Figure 6-3: Study sites along the NAAT and the main site characteristics [*Raynolds et al.*, 2008; *Walker et al.*, 2012b]. ***Legend:*** LL: geographic coordinate (Latitude/ Longitude); C: code for test site; SZ: bioclimatic subzone; TG: topography; VT: vegetation type; LFD: life form description.

In order to analyze the vegetation changes along a toposequence, the zonal test site in Happy Valley (Happy Valley-midslope) was extended by two additional sites in this study area (Happy Valley-hill crest and Happy Valley-footslope) (Figure 6-2, Figure 6-3). Analysis of variation along short hillslope gradients is a primary tool for describing how water movement downslope over long periods of time affects soil development and ecological properties [*Billings*, 1973; *Molenaar*, 1987]. Such 'toposequences' are part of the underlying conceptual framework for describing Arctic vegetation at the landscape scale for the circumpolar Arctic [*Walker et al.*, 2005]. The vegetation, soils, patterned ground features and biomass of the small east-facing hill slope were previously characterized and mapped during several studies at this location [*Epstein et al.*, 2008; *Kade et al.*, 2005; *Raynolds et al.*, 2008; *Walker et al.*, 1997]. The grids are positioned on the hill crest at 325 m, the midslope at 310 m (representing also the zonal Happy Valley site) and the footslope at 300 m. The main difference between the hillcrest and the zonal midslope community is that the hill crest is somewhat drier with more nonsorted circles that have the plant community *Cladino-Vaccinietum vitis-idaeae* [*Kade et al.*, 2005], which has similar species composition to *Sphagno-Eriophoretum vaginati*, but with no *Sphagnum* and higher cover of grass, nontussock sedges, prostrate evergreen dwarf shrubs, the moss *Racomitrium lanuginosum* and lichens. The footslope has a greater abundance of (and taller) erect dwarf shrubs.

The fourth environmental gradient is the change in soil moisture and was investigated at the Franklin Bluffs study area (Figure 6-2, Figure 6-3). This area in the northern part of the Alaska portion of the NAAT transect is on the central Arctic Coastal Plain, a land of thaw-lakes, ice-wedge polygons, and braided river systems. Micro-topographic variations of a few centimeters to a few meters control the vegetation patterns associated with patterned-ground features, thaw lake margins and ancient river terraces. The three Franklin Bluffs study sites can be characterized as wet, mesic (zonal) and dry. They were used in previous studies to characterize the vegetation, soils, and patterned ground associated with differences in soil moisture [*Kade et al.*, 2005; *Raynolds et al.*, 2008]. The wet site is on an old floodplain of the Sagavanirktok River that is situated about 1 m below a small river terrace. It has a marshy *Scorpidium scorpioides-Carex aquatilis* plant community [*Kade et al.*, 2005] with large more-or-less barren nonsorted circles. The dominant plants of the wet site are sedges, a few forbs including horsetails, and mosses and considerable cover of water during most summers. The mesic site is composed of a mix of the zonal *Dryado integrifoliae-Caricetum bigelowii* community [*Kade et al.*, 2005] and a frost-boil subassociation, *Junco biglumis-Dryadetum integrifoliae pedicularetosum* [*Kade et al.*, 2005], which is drier with more bare soil, lichens and forbs. The dry site is on better drained soils near the edge of the terrace, where the main plant community is dominated by prostrate dwarf shrubs, cushion and mat forbs, and a large component of bare soils and lichens.

6.2.3 Data Acquisition and Pre-Processing

Field data were collected at all nine study sites from 23 June to 22 July 2012 [*Buchhorn and Schwieder*, 2012]. Since we revisited already existing, marked, and well described plots with

a size of 10 x 10 m, the sampling design for the vegetation and surface properties update was predetermined [*Raynolds et al.*, 2008]. We estimated the percentage cover of the individual dominant plant species and grouped the species into height strata in order to calculate mean percentage cover of the strata. We used the scalar cover estimates of the Braun-Blanquet approach used in the original description [*Dierschke*, 1994]. The vertical structure was analyzed by measuring the average height of the strata. The vegetation at all sites can be divided into three strata: the photosynthetic part of the moss layer (L1) with a height up to 2 cm; the mainly vascular herbaceous plant and dwarf shrub layer (L2) with a height up to 15 to 30 cm; and the top layer (L3) composed of taller shrubs with up to 50 cm height. We needed to define a new type of cover measurement for the three vegetation strata (L1, L2, and L3) that simulates the percentage cover of what the nadir-measuring field spectrometer would 'see.' This simulated percentage nadir-cover is calculated from the true areal cover by leaving the full percentage cover of the highest plant canopy layer (L3) which is the first layer that a nadir-viewing sensor measures. Then, we estimated the percentage cover of the second highest plant canopy layer (L2). Finally, subtracting the top two strata (L3, L2) from the overall percentage cover of vegetated (non-lichen) leaves the remaining percentage nadir-cover for the lowest vegetation layer (L1). This conversion does not change the percentage cover contributions of L2 and L3 as measured in the field. However, the moss layer (L1) has a much lower percentage nadir-cover value than the common 90 to 100 % true cover, but represents the contribution of this layer that is measured by field spectroscopy. For pixel-related remote sensing applications, the fractional vegetation cover summing up to 100% is the useful parameter for many environmental and climate-related applications. In order to describe the vegetation color, we used Munsell Plant Tissue Color Charts. The Munsell color notation system ranks colors based on three color dimensions: hue, value (lightness), and chroma (purity) [*Kuehni*, 2002]. The average soil moisture content was calculated from 30 randomly distributed point measurements throughout the grid using a TDR (Time Domain Reflectrometry) soil moisture meter (Campbell) with 15 cm rod length.

For the field spectroscopy each 100 m² study grid was divided into quadrats of 1 x 1 m. The averaged reflectance of all quadrats represents the spectral reflectance at the scale of the whole grid at the 10 x 10 m scale. For the surface radiometric measurements two GER1500 portable field spectroradiometers (Spectra Vista Corporation, Poughkeepsie, NY, USA) were used. The GER1500 measures radiance across the wavelength range of 350 – 1,050 nm, with sampling intervals of 1.5 nm and a radiance accuracy of $1.2 \times 10^{-10} W \cdot cm^{-2} \ nm^{-1} \cdot sr^{-1}$ (calibrated in May 2011) [Spectra Vista Corporation, 2009]. In order to increase the signal-to-noise ratio, 32 individual measurements were averaged per one target scan. To minimize variations in the target reflectance due to sun zenith angle changes, all measurements within one study location have been performed under the same sun zenith angle (Happy Valley = 47°, Sagwon = 48°, Franklin Bluffs = 47°, Deadhorse = 49°) and during clear-sky conditions. To ensure that all measurements are comparable, the sun zenith angle change between the four study locations was 2°. All measurements were taken between 29 June and 11 July 2012,

ensuring that the vegetation at all sites was in the same phenological state near peak growing season [*Stow et al.*, 2004].

A Spectralon® white panel (Labsphere, Inc.) was used for white reference normalization using the recommendation of *Milton* [1987]. Target reflectance measurements were taken by measuring the radiance of the target and the white reference panel within a short timespan (less than 10 minutes under clear-sky conditions). To reduce the short-term temporal changes in irradiation (sky- and atmospheric effects) we developed a cos-conical dual-beam approach, where two GER-1500 spectroradiometers simultaneously measured the radiance of the target and the sky irradiance. One spectrometer with a cosine diffusor foreoptic mounted at a height of 1.80 m was placed near the site pointing vertically upwards to measure the downwelling total sky irradiance. Care was taken to ensure that the sensor was not masked or shadowed. The second spectrometer was used to measure the target radiance. This spectrometer used a 4˚ field of view (FOV) foreoptic at a distance of 1.40 m to the middle of each 1 x 1 m quadrat, resulting in a measurement area with approximately 10 cm diameter. To operate two spectrometers in a dual-beam modus requires careful intercalibration of the instruments [*Milton*, 1987; *Milton et al.*, 2009]. Instead of using the recorded irradiance directly, we used the irradiance spectra with the aim to interpolate the radiance measurement of the reference panel to the time of the target measurement. It is assumed that changes in the irradiance over the time period affect the radiance measurements of the reference panel to a similar degree [*Schopfer et al.*, 2008]. This approach has already been used by various groups but mostly with a sunphotometer with limited spectral bands for irradiance recording [*Schopfer et al.*, 2008; *Suomalainen et al.*, 2009].

6.2.4 Data Analysis

The reflectance spectra of the field spectroscopy were stored in a database. One averaged reflectance spectrum with standard deviations was calculated for each site using the footprint measurements of the one hundred quadrats. The results for the nine tundra study sites are nine averaged reflectances (n = 9) representing the sites at a 10 x 10 m scale. We used the following analysis techniques to extract spectral metrics from the average reflectance spectra for comparison between the study sites: i) we calculated the averaged reflectance values for two broad wavelength bands, VIS band (400 – 700 nm) and NIR band (700 – 1,050 nm), in order to compare the variations along the environmental gradients. ii) we analyzed the NIR plateau with the maximum reflectance at 750 nm and 1,020 nm as well as the difference between the two (delta). For the analysis of the VIS part of the reflectance spectra we used iii) the ‘relative absorption depth’ approach [*Crowley et al.*, 1989] in the blue and red wavelength regions and iv) the continuum removal normalization technique [*Clark and Roush*, 1984] using a common baseline for the blue and red wavelength absorption regions in order to compare the differences in pigment absorption. The continuum removal technique was developed for geological applications, but can also be used for estimating biochemical concentrations [*Kokaly and Clark*, 1999; *Mutanga et al.*, 2004] or vegetation differentiation [*Schmidt and Skidmore*, 2003]. A detailed description of this technique can be found in

Kokaly and Clark [1999]. From the continuum removed spectra we calculated the maximum band depth and the area of the absorption feature in the blue (400 – 550 nm) and red (550 – 750 nm) wavelength regions. All calculated spectral features were then investigated in comparison to the biophysical vegetation parameters. The vegetation parameters are average vegetation height, average top height, overall above-ground biomass, and Munsell color. The term 'average top height' is the average height of the top layer in the canopy, which is mostly formed by shrubs. We investigated if the hue and value codes of the Munsell color information of a plant community are linked to its dominant color [*Romney and Fulton*, 2006].

Another method to link biophysical vegetation parameters to the reflectance spectra is the usage of vegetation indices (VI). Vegetation indices can be conceptually simple but effective (e.g. band ratios) or complex, using methods such as support vector machines [*Braun et al.*, 2010], which incorporate more data from the spectral feature space. Most of the VIs for the analysis of structural vegetation properties have been developed for broadband sensor systems but have hyperspectral equivalents [*Roberts et al.*, 2011]. Hyperspectral vegetation indices (HVIs) use narrowband features which can only be captured by hyperspectral instruments [*Roberts et al.*, 2011]. Research by *Thenkabail et al.* [2013; 2011] has shown that, due to data redundancy in the hyperspectral signal, a small number of specific hyperspectral narrowbands (HNBs) have enough information to determine structural vegetation characteristics. Therefore, hyperspectral two-band vegetation indices (HTBVI) based on normalized difference between the bands are used as a data mining tool in this study.

In preparation for the EnMAP hyperspectral space mission we resampled the field spectroscopy data to EnMAP sensor bands using the spectral response curves of the sensor. In order to assess all possible EnMAP band combinations, we calculated the HTBVI according to Equation 6.1 [*Buddenbaum et al.*, 2012; *Thenkabail et al.*, 2000; *Thenkabail et al.*, 2011]

$$HTBVI_{i,j} = \frac{(R_{band\ j} - R_{band\ i})}{(R_{band\ j} + R_{band\ i})} \tag{6.1}$$

where R is the reflectance of the EnMAP bands, and correlated the HTBVI values with biomass. This approach is already well known and used by various research groups [*Buddenbaum et al.*, 2012; *Schlerf et al.*, 2005; *Thenkabail et al.*, 2000]. We used the tool SpInMine (Spectral Index Data Mining Tool) [*Buddenbaum and Püschel*, 2012] which is implemented in the EnMAP-Box software [*Held et al.*, 2012]. Biomass (kg / 100 m²) for all nine study sites was obtained from *Raynolds et al.* [2008].

The results of the 4,560 unique HTBVIs from the 96 EnMAP bands (424 – 1,074 nm) are shown in Figure 6-4. Hotspots of correlation between the HTBVIs and biomass are located with one band in the VIS region and one band in the NIR region. Band combinations with one band in the blue region and one band in the green to red region also show high correlations. Due to the small sample size of n = 9, the optimal HNBs cannot be further constrained. Additionally, other methods to reduce the data redundancy, such as partial least squares (PLS) or principal component analysis (PCA), are not possible with such a small sample size.

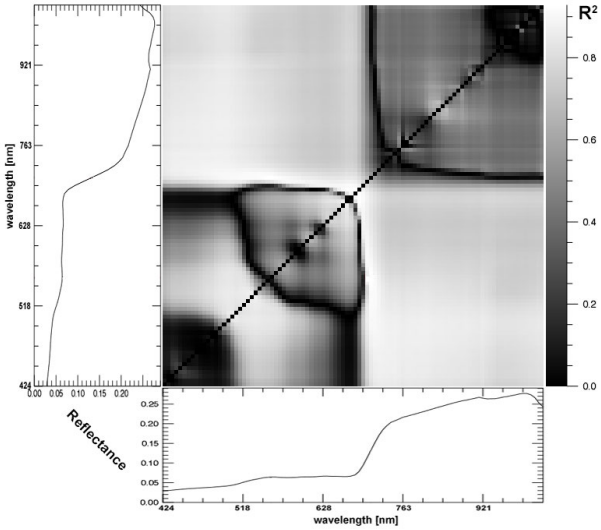

Figure 6-4: Map of R^2 values of hyperspectral two-band vegetation indices (HTBVI) of all possible simulated EnMAP band combinations correlated with biomass. ***Note:*** The graphs below and left of the 2D-correlogram contain the mean reflectance of all nine NAAT sites.

Therefore, we decided to try an alternative approach. One of the most robust and commonly used VI is the NIR and red wavelength based NDVI, which is also a normalized difference index [*Roberts et al.*, 2011; *Rouse et al.*, 1973; *Thenkabail et al.*, 2000; *Tucker*, 1979] and is calculated according to Equation 6.2.

$$NDVI = \frac{(R_{NiR} - R_{red})}{(R_{NiR} + R_{red})} \tag{6.2}$$

The NDVI based on broadband wavelengths bands has successfully been used in numerous studies along the NAAT in order to show vegetation changes and as a surrogate for various biophysical properties of vegetation, such as biomass, leaf-area index (LAI) and intercepted photosynthetically active radiation (IPAR) [*Epstein et al.*, 2012; *Hope et al.*, 1993; *Stow et al.*, 1993; *Vierling et al.*, 1997; *Walker et al.*, 2003]. To be comparable to the studies, which used mostly broadband NDVI based on AVHRR, we resampled the field spectroscopy data to AVHRR sensor bands using the response curves of the sensor (Table 6-2). Then we compared this broadband NDVI with three narrowband NDVIs compiled from simulated EnMAP data (Table 6-2). To analyze the performance of the HVIs we linked the NDVI values to the above-ground biomass via regression analysis. Also the probability distributions of the broadband and narrowband NDVIs for each site were investigated in order to assess differences between MAT and MNT. The HNBs in the red and NIR wavelength regions for the three narrowband NDVIs have been chosen by assessment of the spectral metrics, based on research in optimal HNBs for vegetation analysis by *Thenkabail et al.* [2013; 2011].

Where the central wavelength of the EnMAP red band (EnMAP band #47, center wavelength 672 nm) shows the maximum chlorophyll absorption, the NIR HNBs use the EnMAP NIR bands of the beginning of the NIR reflectance plateau (EnMAP band #59, center wavelength 756 nm), the central NIR reflectance plateau (EnMAP band #73, center wavelength 864 nm) and the maximum NIR reflectance (EnMAP band #101, center wavelength 1,020 nm). EnMAP band #59 at the beginning of the NIR reflectance plateau may be specifically

sensitive to vegetation structure. The center wavelength of EnMAP band #73 equals the center wavelength of the AVHRR NIR band (865 nm). EnMAP band #101 is around the maximal NIR reflectance at the second NIR reflectance peak that is located behind the first NIR reflectance peak around 900 to 920 nm [*Thenkabail et al.*, 2002] and the water absorption band.

Table 6-2: Center wavelengths and band width of the broadband and narrowband NDVIs used in this study, based on the spectral response curves of the AVHRR and EnMAP sensors.

NDVI	Sensor	Sensor band	Center wavelength (nm)	band width (nm)
$NDVI_{AVHRR}$ [broadband]	AVHRR/3	red: band 1 NIR: band 2	630 865	100 275
$NDVI_{47\_59}$ [narrowband]	EnMAP	red: band 47 NIR: band 59	672 756	6.5 6.5
$NDVI_{47\_73}$ [narrowband]	EnMAP	red: band 47 NIR: band 73	672 864	6.5 8
$NDVI_{47\_101}$ [narrowband]	EnMAP	red: band 47 NIR: band 101	672 1,018	6.5 11

6.3 Results

The results were compiled following the environmental gradients concept (Figure 6-2). Figure 6-5 displays the averaged reflectance spectra of each site showing the general spectral characteristics of Alaskan Low Arctic tundra communities along the NAAT. The geoecological characteristics are shown in Table 6-3, while Table 6-4 show the metrics of the spectral data analysis. Figure 6-6 displays the range of reflectance spectra of each site.

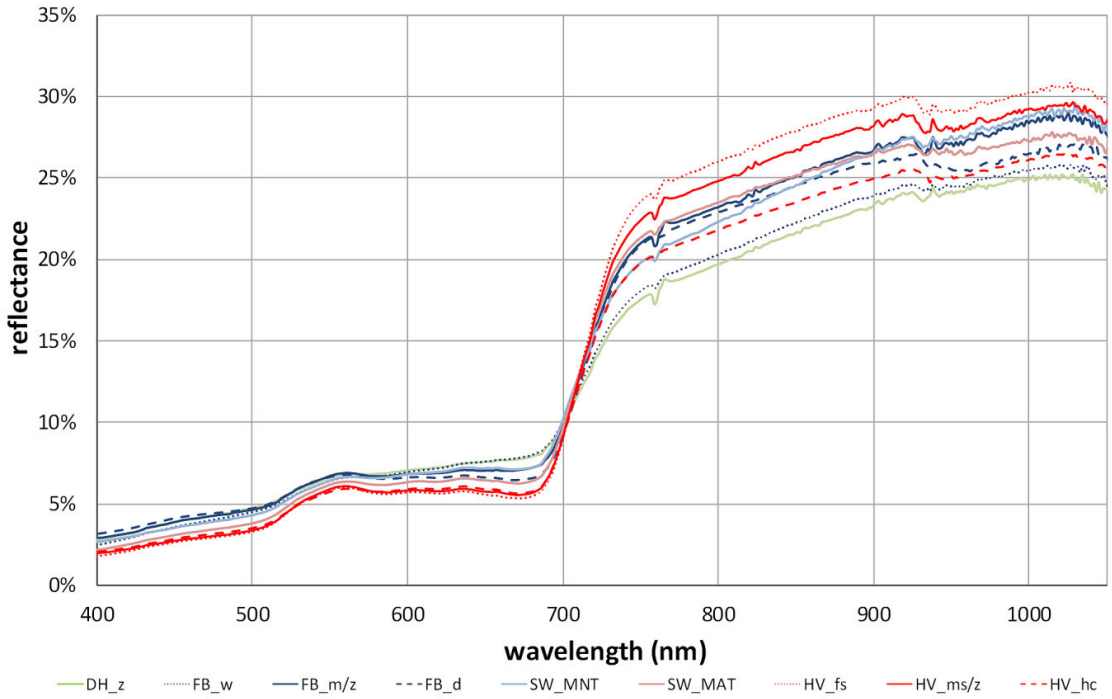

Figure 6-5: Diagnostic mean reflectance spectra of all nine study sites showing the general spectral characteristics of Alaskan Low Arctic tundra communities along the NAAT. ***Note:*** Naming and coloring of the reflectance spectra follow the concept shown in Figure 6-2.

Table 6-3: Geoecological characteristics of the nine study sites. All parameters were collected during the EyeSight-NAAT-Alaska expedition 2012, except the values for SWI, soil pH and biomass which were obtained from *Raynolds et al.* [2008]. ***Note:*** The percentage cover of the vegetation height strata (L1, L2, and L3) are calculated as nadir-cover. Therefore, for example, the percentage cover of L1 does not equal the true coverage of the moss layer.

	site code	SWI (°C)	soil parameters		vegetation parameters			Munsell color information+			
			pH-value	moisture (Vol %)	average height (cm)*	average top height (cm)Δ	biomass [kg/100 m²]	overall	L1	L2	L3
regional climate	DH_z	17.3	7.9	70	23	25	33.17	10Y (5/4)	5Y (6/8)	5GY (5/4)	
	FB_m/z	24.2	8.0	48	15	35	43.40	2.5GY (6/4)	5Y (6/8)	5GY (6/4)	5GY (5/6)
	SW_MNT	26.5	7.7	39	8	45	56.30	7.5Y (7/8)	5Y (8/10)	5GY (6/6)	5GY (5/6)
	SW_MAT	26.5	5.4	35	12	30	75.10	2.5GY (7/8)	2.5GY (8/10)	5GY (5/6)	5GY (5/4)
	HV_ms/z	29.5	5.1	38	14	45	72.08	2.5GY (6/6)	2.5GY (8/10)	5GY (5/4)	5GY (5/4)
Soil-pH (Sagwon)	SW_MNT	26.5	7.7	39	8	45	56.30	7.5Y (7/8)	5Y (8/10)	5GY (6/6)	5GY (5/6)
	SW_MAT	26.5	5.4	35	12	30	75.10	2.5GY (7/8)	2.5GY (8/10)	5GY (5/6)	5GY (5/4)
topo-sequence	HV_hc	29.5	5.1	27	12	40	73.54	2.5GY (6/8)	2.5GY (8/10)	5GY (5/6)	5GY (5/6)
	HV_ms/z	29.5	5.1	38	14	45	72.08	2.5GY (6/6)	2.5GY (8/10)	5GY (5/4)	5GY (5/4)
	HV_fs	29.5	5.1	45	25	55	73.44	5GY (6/6)	2.5GY (8/10)	5GY (6/4)	5GY (5/4)
soil-moisture	FB_d	24.2	8.1	36	14	30	48.96	2.5GY (5/6)	5Y (6/8)	5GY (5/4)	5GY (5/6)
	FB_m/z	24.2	8.0	48	15	35	43.40	2.5GY (6/4)	5Y (6/8)	5GY (6/4)	5GY (5/6)
	FB_w	24.2	7.8	74	30	35	40.39	2.5GY (6/4)	5Y (6/8)	5GY (6/4)	

	site code	soil crust (%) □	detailed vegetation parameters (nadir cover)									
			L1 cover (%)	L1 height (cm)	L1 description	L2 cover (%)	L2 height (cm)	L2 description	L3 cover (%)	L3 height (cm)	L3 description
regional climate	DH_z	10	20	< 2	moss	70	2 - 30	sedge & shrub	0	-	-
	FB_m/z	5	8	< 2	moss	82	2 - 15	sedge & shrub	5	15 - 40	shrub
	SW_MNT	3	64	< 2	moss	30	2 - 15	sedge & shrub	3	15 - 50	shrub
	SW_MAT	2	57	< 2	moss	40	2 - 25	tussock & shrub	1	25 - 35	shrub
	HV_ms/z	4	43	< 2	moss	48	2 - 20	tussock & shrub	5	20 - 50	shrub
Soil-pH (Sagwon)	SW_MNT	3	64	< 2	moss	30	2 - 15	sedge & shrub	3	15 - 50	shrub
	SW_MAT	2	57	< 2	moss	40	2 - 25	tussock & shrub	1	25 - 35	shrub
topo-sequence	HV_hc	10	43	< 2	moss	45	2 - 20	tussock & shrub	2	20 - 45	shrub
	HV_ms/z	4	43	< 2	moss	48	2 - 20	tussock & shrub	5	20 - 50	shrub
	HV_fs	2	28	< 2	moss	50	2 - 25	tussock & shrub	20	25 - 60	shrub
soil-moisture	FB_d	10	30	< 2	moss	40	2 - 15	sedge & shrub	20	15 - 35	shrub
	FB_m/z	5	8	< 2	moss	82	2 - 15	sedge & shrub	5	15 - 40	shrub
	FB_w	10	10	< 2	moss	80	2 - 40	sedge & shrub	0	-	-

Note: * of the whole test site; Δmostly shrubs which form the top layer in the canopy; +derived from Munsell Plant Tissue Color Charts
□ areas which are vegetated by lichen (no barren soil) - in close relation to the appearance or remnants of nonsorted circles

Table 6-4: Metrics of the spectral data analysis. ***Note:*** Naming of the study sites follow the concept shown in Figure 6-2.

	site code	avg. R with SD		max. R in NiR*			relative absorption		continuum removed			NDVIs with SE			
		VIS (%) (400-700)	NiR (%) (700-1050)	750 (%)	1020 (%)	delta R (1020-750)	400 - 550 (blue)	550 - 750 (red)	area 400-550	area 550-750	max. blue band depth	max. red band depth	broad $NDVI_{AVHRR}$	narrow 1 $NDVI_{47\ 59}$	narrow 2 $NDVI_{47\ 73}$	narrow 3 $NDVI_{47\ 101}$
regional climate	DH_z	5.9 (±1.4)	21.4 (±4.7)	17.8	25.2	7.4	0.40	0.68	8.7	48.4	0.11	0.43	0.48 (±0.01)	0.39 (±0.01)	0.48 (±0.01)	0.53 (±0.01)
	FB_m/z	5.8 (±1.6)	24.6 (±6.2)	21.3	28.9	7.6	0.41	0.98	11.9	64.5	0.15	0.55	0.55 (±0.01)	0.49 (±0.02)	0.56 (±0.01)	0.60 (±0.01)
	SW_MNT	5.6 (±1.8)	24.4 (±6.6)	20.2	28.9	8.7	0.44	0.92	14.2	58.3	0.17	0.52	0.55 (±0.01)	0.48 (±0.01)	0.56 (±0.01)	0.61 (±0.01)
	SW_MAT	5.1 (±1.9)	24.4 (±7.3)	21.7	27.5	5.8	0.53	1.17	17.6	68.9	0.21	0.60	0.59 (±0.01)	0.55 (±0.01)	0.61 (±0.01)	0.64 (±0.01)
	HV_ms/z	4.7 (±1.4)	25.8 (±6.4)	22.8	29.5	6.7	0.58	1.43	23.0	77.5	0.27	0.66	0.64 (±0.01)	0.60 (±0.01)	0.66 (±0.01)	0.68 (±0.01)
Soil-pH (all)	non acidic	5.8 (±1.7)	23.2 (±6.0)	19.8	27.1	7.3	0.41	0.86	10.8	57.8	0.14	0.50	0.53 (±0.01)	0.46 (±0.01)	0.53 (±0.01)	0.58 (±0.01)
	acidic	4.6 (±1.7)	25.0 (±7.2)	22.2	28.5	6.3	0.56	1.34	20.6	74.2	0.24	0.64	0.62 (±0.01)	0.59 (±0.01)	0.65 (±0.01)	0.67 (±0.01)
Soil-pH (Sagwon)	SW_MNT	5.6 (±1.8)	24.4 (±6.6)	20.2	28.9	8.7	0.44	0.92	14.2	58.3	0.17	0.52	0.55 (±0.01)	0.48 (±0.01)	0.56 (±0.01)	0.61 (±0.01)
	SW_MAT	5.1 (±1.9)	24.4 (±7.3)	21.7	27.5	5.8	0.53	1.17	17.6	68.9	0.21	0.60	0.59 (±0.01)	0.55 (±0.01)	0.61 (±0.01)	0.64 (±0.01)
topo-sequence	HV_hc	4.7 (±1.9)	23.0 (±7.0)	20.1	26.4	6.3	0.52	1.21	19.1	68.7	0.22	0.61	0.60 (±0.01)	0.57 (±0.01)	0.63 (±0.01)	0.66 (±0.01)
	HV_ms/z	4.7 (±1.4)	25.8 (±6.4)	22.8	29.5	6.7	0.58	1.43	23.0	77.5	0.27	0.66	0.64 (±0.01)	0.60 (±0.01)	0.66 (±0.01)	0.68 (±0.01)
	HV_fs	4.5 (±1.7)	26.9 (±8.2)	24.0	30.5	6.5	0.62	1.60	22.5	81.8	0.27	0.69	0.67 (±0.01)	0.64 (±0.01)	0.69 (±0.01)	0.71 (±0.01)
soil-moisture	FB_d	5.7 (±2.2)	23.7 (±6.3)	21.3	26.9	5.6	0.37	1.07	9.9	68.2	0.14	0.59	0.56 (±0.02)	0.52 (±0.02)	0.58 (±0.02)	0.61 (±0.02)
	FB_m/z	5.8 (±1.6)	24.6 (±6.2)	21.3	28.9	7.6	0.41	0.98	11.9	64.5	0.15	0.55	0.55 (±0.01)	0.49 (±0.02)	0.56 (±0.01)	0.60 (±0.01)
	FB_w	5.8 (±1.7)	21.9 (±6.0)	18.4	25.7	7.3	0.44	0.72	9.2	49.4	0.12	0.43	0.49 (±0.01)	0.40 (±0.01)	0.49 (±0.01)	0.53 (±0.01)

Note: R = reflectance; SD = standard deviation; VI = vegetation indices; SE = standard error; * of the average reflectance graph; numbers in table header are wavelengths in nm

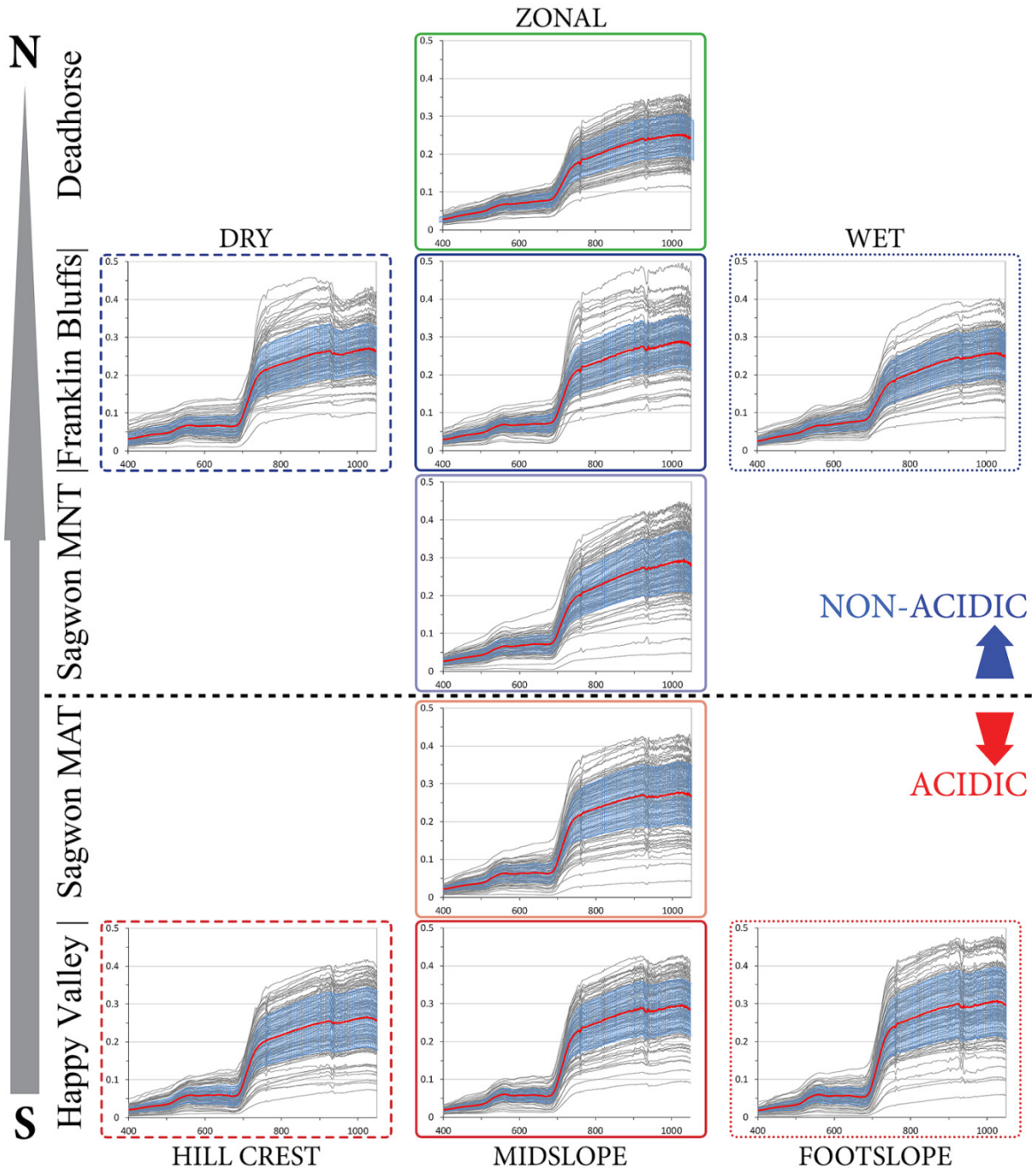

Figure 6-6: Hyperspectral reflectance spectra of the study sites (grey lines: reflectance spectra of each quadrat; red line: averaged reflectance spectra representing the arctic tundra vegetation community of the study site; blue area: standard deviation of spectral signature). ***Note:*** The x-axis of the diagrams shows the wavelength in nm, and the y-axis shows the reflectance.

6.3.1 The Zonal Climate Gradient

The zonal climate gradient is defined by the SWI, which decreases from 29.5 °C at Happy Valley, 26.5 °C at Sagwon, 24.2 °C at Franklin Bluffs to 17.3 °C at Deadhorse (Table 6-3). This temperature (climate) gradient follows the latitude of the study locations from south to north. The mean vegetation heights of the zonal sites range from 14 cm at Happy Valley

(HV_ms/z), 8 to 12 cm at Sagwon (SW_MNT, SW_MAT), 15 cm at Franklin Bluffs (FB_m/z), and 23 cm at Deadhorse (DH_z). The average top height follows a different height trend, the heights increase towards the south. The top height at HV_ms/z, Sagwon (both sites) and FB_m/z are composed of shrubs, whereas the top height at DH_z is composed by fast growing sedges. This also explains the higher mean value for vegetation height for DH_z, the most northern site, compared to the southern sites. However, the biomass including the moss layer considerably decreases towards the north, from 75.10 to 33.17 kg/100 m² (Table 6-3). The overall vegetation coverage (non-lichen) decreases from 98 % in the south to 90 % in the north. The non-vegetated areas in all test sites are never barren soil but are covered by soil crusts (lichen and bryophytes) which generally appear in the center of nonsorted circles.

The reflectance spectra of all five zonal sites are, in general, similar in shape but with an offset of up to one percentage point in the VIS. The offset in the VIS in reflectance increases towards the north. Therefore, the sites clearly differ by their VIS spectra. Both subzone E sites have the green reflectance peak as the local reflectance maxima, whereas the more northern sites have the reflectance maxima in the red wavelength region and a hardly noticeable green reflectance peak (Figure 6-7A).

The reflectance values of the 300 nm wide VIS band (Table 6-4) increase from 4.7 % at HV_ms/z, 5.1 % at SW_MAT, 5.6 % at SW_MNT, 5.8 % at FB_m/z to 5.9 % at DH_z. The relative absorption depths of the zonal site inversely follow this latitudinal trend. The further south the site, the greater the absorption depth of the blue (400 – 550 nm) and red (550 – 750 nm) absorption features. The blue relative absorption depth increases from 0.40 at DH_z to 0.58 at HV_ms/z, and the absorption depth of the red feature increases from 0.68 at DH_z to 1.43 at HV_ms/z.

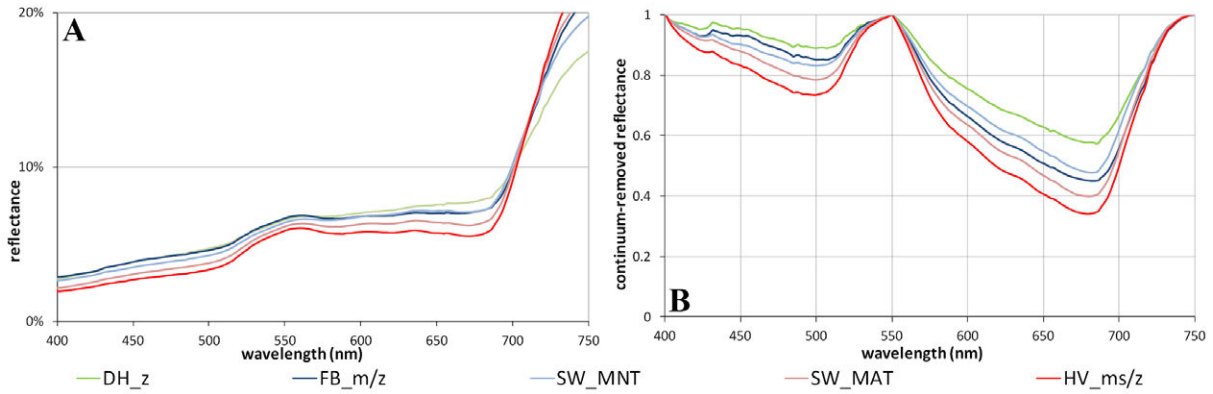

Figure 6-7: Spectral characteristics along the zonal climate gradient of the NAAT. Comparison of (**A**) the averaged reflectance spectra in the visible (400 – 700 nm), and (**B**) the continuum-removed absorption features in the blue (400 nm – 550 nm) and red (550 nm – 750 nm) wavelength regions. ***Note:*** Naming and coloring of the reflectance spectra follow the concept shown in Figure 6-2.

The spectral metrics derived from the continuum removal analysis also exhibit the same trend of increasing absorption in the blue and red wavelength regions along the climate gradient towards the south (Figure 6-7B). The area of the blue absorption feature increases from 8.7 at DH_z to 23.0 at HV_ms/z, and the maximum band depth at around 500 nm increases from

0.11 at DH_z to 0.27 at HV_ms/z. For the red absorption feature the area increases from 48.4 at DH_z to 77.5 at HV_ms/z, and the maximum band depth at around 680 nm increases from 0.43 at DH_z to 0.66 at HV_ms/z.

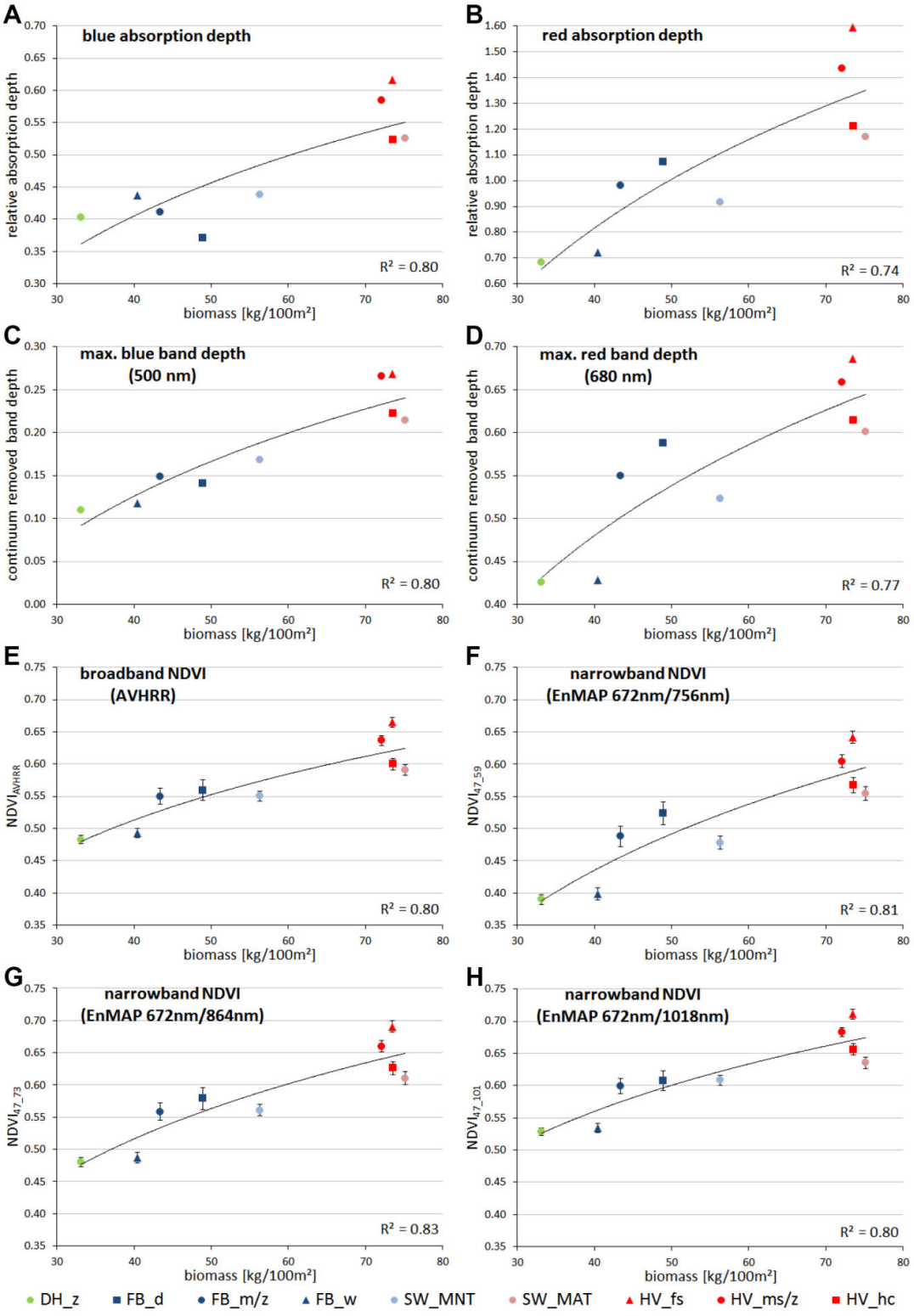

Figure 6-8: Spectral metrics of the study sites as a function of biomass. (**A**) Relative blue absorption depth vs. biomass; (**B**) Relative red absorption depth vs. biomass; (**C**) Continuum removed maximum blue band depth vs. biomass; (**D**) Continuum removed maximum red band depth vs. biomass. Correlation between (**E**) broadband NDVI with biomass compared with three (**F-H**) narrowband NDVIs with biomass.

Each reflectance spectrum along the temperature gradient shows a similar shape with a steady NIR increase, and the further south the geographic location of the site, the higher is the NIR reflectance (Figure 6-5). None of the reflectance spectra has a well-developed NIR reflectance plateau. This trend is also noticeable in the 350 nm wide NIR band reflectance and the maximum reflectance at 750 nm and 1,020 nm (Table 6-4). The reflectance of the 350 nm wide NIR band increase from 21.4 % at DH_z to 25.8 % at HV_ms/z, and the maximum reflectance at 1,020 nm increases from 25.2 % at DH_z to 29.5 % at HV_ms/z.

Broadband and narrowband NDVI values also show the latitudinal trend (Table 6-4). The broadband $NDVI_{AVHRR}$ values increase from 0.48 at DH_z in the north to 0.64 at HV_ms/z in the south. Likewise, the three narrowband NDVI values increase from north to south, but with different intervals between the minima at DH_z and the maxima at HV_ms/z. The best separation of the sites occurs with $NDVI_{47\_101}$, which uses the narrowband at 1018 nm in the NIR (the NIR maximum) (Table 6-4). $NDVI_{47\_59}$, using the narrowband at 756 nm in the NIR, shows the largest span between minimum and maximum (0.39 at DH_z and 0.60 at HV_ms/z). $NDVI_{47\_73}$ captures the separation between the sites similarly to the broadband NDVI.

The regression analyses of the spectral metrics as well as NDVI values and biomass show strong correlations with high coefficients of determination (R^2) in all cases (Figure 6-8). The correlation of the relative absorption depths in the blue and red wavelength regions with biomass (Figure 6-8A-B) illustrates the good separation of the five zonal sites in the blue ($R^2 = 0.80$) and red ($R^2 = 0.74$) reflectances according to their geographical location. These high R^2 values occur also in the regression analyses of the continuum removed maximum band depths with biomass (Figure 6-8C-D). The comparison of broadband and narrowband NDVIs (Figure 6-8E-H) indicates that the narrowband NDVIs have similar to slightly higher correlations with biomass ($NDVI_{47\_59} = 0.81$; $NDVI_{47\_73} = 0.83$; $NDVI_{47\_101} = 0.80$) compared to the broadband $NDVI_{AVHRR}$ ($R^2 = 0.80$).

6.3.2 Acidic Versus Non-Acidic Tundra (Soil pH Zones)

Whereas all four acidic sites have soil pH values between 5.1 and 5.4, the five non-acidic sites have soil pH values between 7.7 and 8.1 (Table 6-3). The vegetation composition is mainly MAT at the acidic sites and MNT at the non-acidic sites. All non-acidic sites have overall vegetation coverage from 90 to 97 %, whereas the range at the acidic sites is 90 to 98 %.

All sites with acidic tundra (three sites at Happy Valley and Sagwon-MAT) have the green reflectance peak at 550 nm as the local reflectance maximum and a distinctive chlorophyll absorption dip at 680 nm in the VIS wavelength region. In contrast, the non-acidic sites (Sagwon-MNT, all sites at Franklin Bluffs, and Deadhorse) have the local reflectance maximum in the red wavelength region and have a hardly notable green reflectance peak (Figure 6-9A).

In the VIS wavelength range, the reflectance spectra of the non-acidic sites are clearly distinguishable from the acidic sites. This differentiation can also be seen directly at the soil

pH boundary at Sagwon. The average reflectance value of the 300 nm wide VIS band of all acidic sites is 4.8 % and of all non-acidic sites 5.8 %. Directly at the soil pH boundary, the acidic Sagwon-MAT (SW_MAT) site has a reflectance of 5.1 % versus 5.6 % at the non-acidic Sagwon-MNT (SW_MNT) site. Acidic tundra has an average relative absorption depth in the blue wavelength region of 0.56 (0.53 at SW_MAT), and non-acidic tundra has a depth of 0.41 (0.44 at SW_MNT). This difference increases for the relative absorption depth of the red wavelength region. On average the acidic sites have a relative absorption depth of 1.34 (1.17 at SW_MAT), and the non-acidic sites have depths of 0.86 (0.92 at SW_MNT).

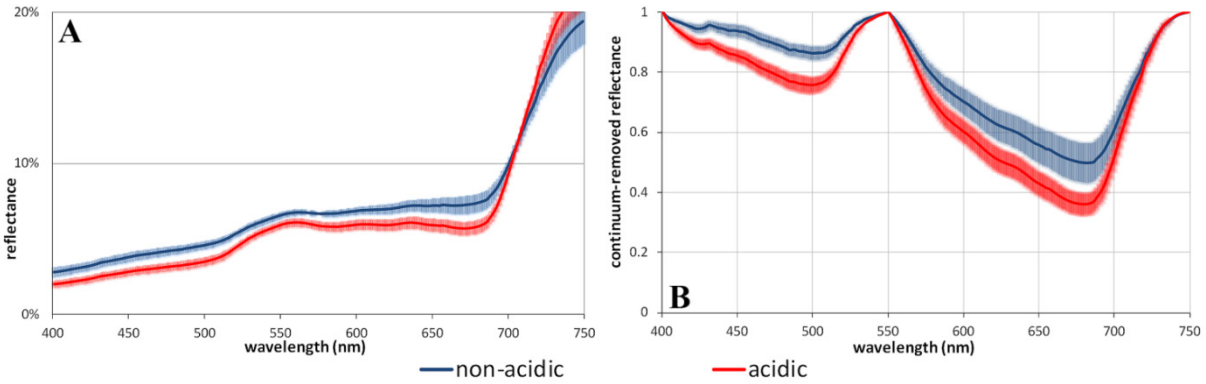

Figure 6-9: Spectral characteristics of the plant communities on acidic and non-acidic soils (soil pH zones). Comparison of (**A**) the averaged reflectance spectra in the visible (400 – 700 nm), and (**B**) the continuum-removed absorption features in the blue (400 nm – 550 nm) and red (550 nm – 750 nm) wavelength regions. ***Note:*** All spectra of the sites belonging to acidic or non-acidic soils have been averaged and are shown with ± 1 standard derivation.

The continuum removal analysis also shows a clear separation of the study sites on acidic and non-acidic soils within the chlorophyll absorption maximum around 680 nm and chlorophyll/carotenoid absorption at 500 nm (Figure 6-9B). In both absorption features the acidic sites have deeper absorption than the non-acidic sites (Table 6-4). The area of the blue absorption feature of the acidic tundra is 20.6 (17.6 at SW_MAT) and of the non-acidic 10.8 (14.2 at SW_MNT), and the maximum band depth at around 500 nm of the acidic sites is 0.24 (0.21 at SW_MAT) and 0.14 (0.17 at SW_MNT) for the non-acidic sites. Additionally, the areas of the continuum removed red absorption features decrease from 74.2 for acidic tundra (68.9 for SW_MAT) to 57.8 for non-acidic (58.3 for SW_MNT). The maximum band depth in the continuum removal is 0.64 for acidic sites (0.60 for SW_MAT) and 0.50 for non-acidic (0.52 for SW_MNT).

Such a clear separation does not occur in the NIR reflectance. Here the reflectance spectra of the acidic and non-acidic sites show some overlap (Figure 6-5), especially of the sites close to the soil pH boundary at Sagwon. The reflectance values of the 350 nm wide NIR band are on average 25.0 % for acidic soil sites (24.4 % at SW_MAT) and 23.2 % for non-acidic (24.4 % at SW_MNT).

The results of the broadband and narrowband NDVI analysis (Table 6-4) show a clear separation of acidic and non-acidic tundra. Where acidic tundra has an average broadband $NDVI_{AVHRR}$ of 0.62, non-acidic tundra has an average of 0.53. This partition is also detectable

right at the soil pH boundary at Sagwon. The acidic SW_MAT site has a broadband $NDVI_{AVHRR}$ of 0.59 and the non-acidic SW_MNT site a broadband $NDVI_{AVHRR}$ of 0.55. All three narrowband NDVIs also show this separation between acidic and non-acidic tundra (Table 6-4). A broadband and narrowband NDVI histogram analysis indicates in all cases that the distributions of acidic and non-acidic sites are distinct, with acidic sites strongly skewed to the higher NDVI values (Figure 6-10A). In a direct comparison, $NDVI_{47\_59}$ shows the clearest separation between MAT and MNT in the probability distribution relative to the broadband $NDVI_{AVHRR}$. The average broadband $NDVI_{AVHRR}$ of the acidic sites ranges from 0.59 to 0.67, whereas the broadband $NDVI_{AVHRR}$ of the non-acidic sites ranges from 0.48 to 0.56 (Figure 6-10B). The separation value between acidic and non-acidic tundra in the broadband $NDVI_{AVHRR}$ is 0.58. The narrowband $NDVI_{47\_59}$ has a separation value of 0.54, where the average $NDVI_{47\_59}$ values of MAT range from 0.55 to 0.64 and of MNT from 0.40 to 0.52.

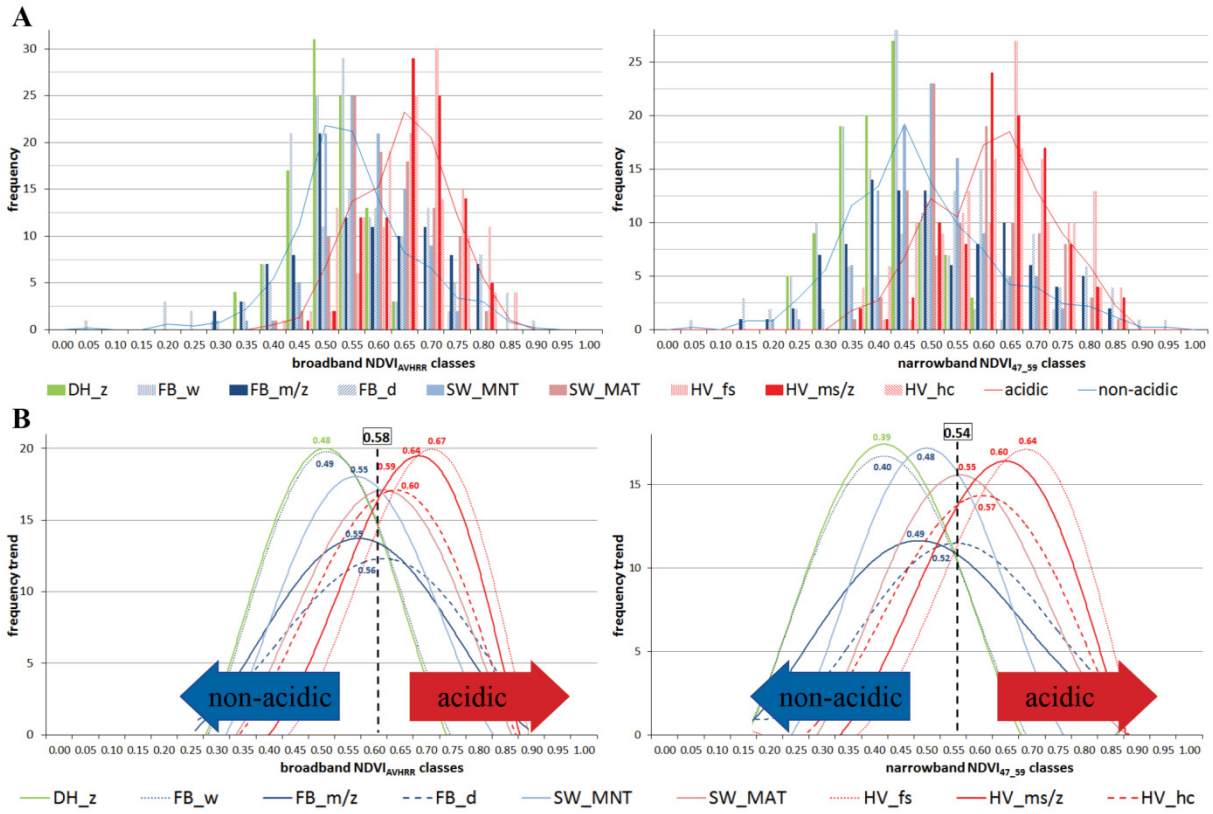

Figure 6-10: (**A**) Histogram of the probability distribution of the broadband $NDVI_{AVHRR}$ (left) and narrowband $NDVI_{47\_59}$ (right) values of each quadrat, and (**B**) polynomial trends of the broadband $NDVI_{AVHRR}$ (left) and narrowband $NDVI_{47\_59}$ (right) distributions with a separation value (black dotted line) for acidic and non-acidic tundra. ***Note:*** Naming and coloring of the data follow the concept shown in Figure 6-2.

6.3.3 The Toposequence at Happy Valley (Subzone E)

At the Happy Valley study location all three sites forming the toposequence have an identical soil pH of 5.1 and nearly the same biomass values in the range of 72 – 74 kg/100 m². The mean volumetric soil moisture increases from 27 Vol% at the hill crest site (HV_hc), over

38 Vol% at the midslope (HV_ms/z), to 45 Vol% on the footslope (HV_fs) (Table 6-3). The species composition is similar for all three sites (MAT), but the average vegetation height and average top height increase from 12 cm (40 cm respectively) at the hill crest, 14 cm (45 cm) at the midslope, to 25 cm (55 cm) on the footslope. This height increase is mainly due to an increase in the percentage nadir-cover (from 2 % at the hill crest to 20 % on the footslope) and the height (from 45 cm at the hill crest to 60 cm on the footslope) of the third stratum of the vertical vegetation structure, which is formed by shrubs. In contrast, the percentage nadir-cover and height of the second stratum formed by tussock sedge and shrubs in all three sites are nearly identical (45 – 50 % percentage cover with a height of 20 – 25 cm), and the percentage nadir-cover of the moss stratum decreases from 43 % at the hill crest to 28 % on the footslope.

The three toposequence sites show a weak separation in the reflectance spectra for the VIS wavelength region. All reflectance spectra show a similar green reflectance maximum at 550 nm and a decrease to the chlorophyll absorption maximum at 680 nm (Figure 6-11A). In the 300 nm wide VIS band the reflectance values are nearly identical, with 4.7 % for HV_hc and HV_ms/z and 4.5 % for HV_fs. A better separation can be seen in the relative absorption depth in the blue and red wavelength regions. The blue and red relative absorption depths increase from 0.52 for the blue at the hill crest (1.21 in the red), 0.58 at the midslope (1.43 in the red), to 0.62 on the footslope (1.60 in the red).

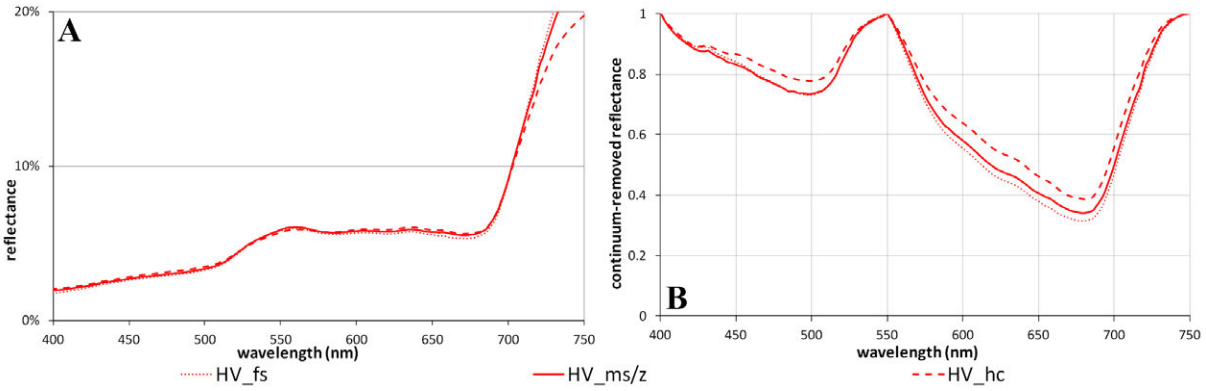

Figure 6-11: Spectral characteristics of the toposequence gradient at the Happy Valley study location. Comparison of (**A**) the averaged reflectance spectra in the visible (400 – 700 nm), and (**B**) the continuum-removed absorption features in the blue (400 nm – 550 nm) and red (550 nm – 750 nm) wavelength regions. ***Note:*** Naming and coloring of the reflectance spectra follow the concept shown in Figure 6-2.

This trend can be only partly seen in the continuum removal analysis (Figure 6-11B). The further downslope the location of the site, the greater the area and height of maximum band depth of the absorption features in the red wavelength region (Table 6-4). The area of the red absorption feature increases from 68.7 at HV_hc, 77.5 at HV_ms/z, to 81.8 at HV_fs, and the maximum band depth increases from 0.61 at the hill crest to 0.69 on the footslope. But the downslope trend does not appear in the blue wavelength region. Here the midslope and footslope sites have nearly identical values for the area (22.5 and 23.0) and identical values for the maximum continuum removed band depth (0.27).

The most distinct separation of the three sites is in the NIR wavelength region (Figure 6-5), where the hill crest site has the lowest reflectance values (maximum 26.4 % at 1,020 nm), and the footslope sites the highest (maximum 30.5 % at 1,020 nm). The maximum reflectance of the midslope site is in-between (29.5 %). This downslope trend occurs also in the 350 nm wide NIR band. There the reflectance increases from 23.0 % for the hill crest reflectance spectra, 25.8 % for the midslope, to 26.9 % for the footslope.

6.3.4 The Soil Moisture Gradient at Franklin Bluffs (Subzone D)

The three Franklin Bluffs study sites are separated into dry (36 Vol% soil moisture), mesic (zonal) (48 Vol%) and wet (74 Vol%) moisture regimes. This local soil moisture gradient is also noticeable in the averaged vegetation heights (Table 6-3). Whereas the dry site (FB_d) has a mean vegetation height of 14 cm, this increases to 15 cm at the mesic site (FB_m/z) and to 30 cm at the wet site (FB_w). The overall percentage cover of vegetation (non-lichen) ranges from 90 to 95 % across the sites due to the effect of nonsorted circles, which have centers that are mainly covered by soil crusts. There is also a change in the vegetation composition and structure. At the wet site, sedges forming the second height stratum become more dominant and cover 80 % of the whole area with a maximum height of 40 cm. The mesic site has a percentage cover of the second stratum of 82 %, and the dry site of 40 %. At both sites sedges and shrubs are the main species in this stratum. Shrubs form the third vertical stratum at the mesic site with 5 % cover and a maximum height of 40 cm, whereas at the dry site the cover increases to 20 %, but the height decreases to 35 cm. An increase of standing dead material can be seen from the dry to the wet site.

In the VIS wavelength region, the dry site has a green reflectance peak and a distinctive reflectance minimum in the red around 680 nm (Figure 6-12A). The reflectance spectrum of the mesic site has a distinctive green reflectance peak, but the local reflectance maximum is in the red wavelength region of chlorophyll absorption. The spectrum of the wet site has a steady reflectance increase up to 680 nm with even lower chlorophyll absorption and has a hardly noticeable green reflectance peak.

All three sites have nearly the same reflectance values in the 300 nm wide VIS band (5.7 to 5.8 %) (Table 6-4). The results of the relative absorption depth analysis show a minor separation of the sites along the soil moisture gradient in the blue region and a more distinct separation in the red region. The relative absorption depth in the blue spectrum increases from 0.37 at FB_d, 0.41 at FB_m/z, to 0.44 at FB_w. In the red wavelength region this trend is reversed, so the absorption depth decreases from 1.07 at FB_d, 0.98 at FB_m/z, to 0.72 at FB_w. Also the continuum removal technique shows no clear site separation along the gradient in the blue (400 – 550 nm) region (Figure 6-12B). The area of the blue continuum removed absorption feature is 9.9 at FB_d, 11.9 at FB_m/z and 9.2 at FB_w, and the maximum band depth at 500 nm is 0.14 for the dry, 0.15 for the mesic and 0.12 for the wet site. A better separation along the gradient appears for the red absorption feature from 550 – 750 nm. The area of the absorption feature increases from 49.4 at FB_w, 64.5 at FB_m/z to

68.2 at FB_d. Likewise, the maximum continuum removed band depths at 680 nm increase from 0.43 for the wet site, 0.55 for the mesic, to 0.59 for the dry site.

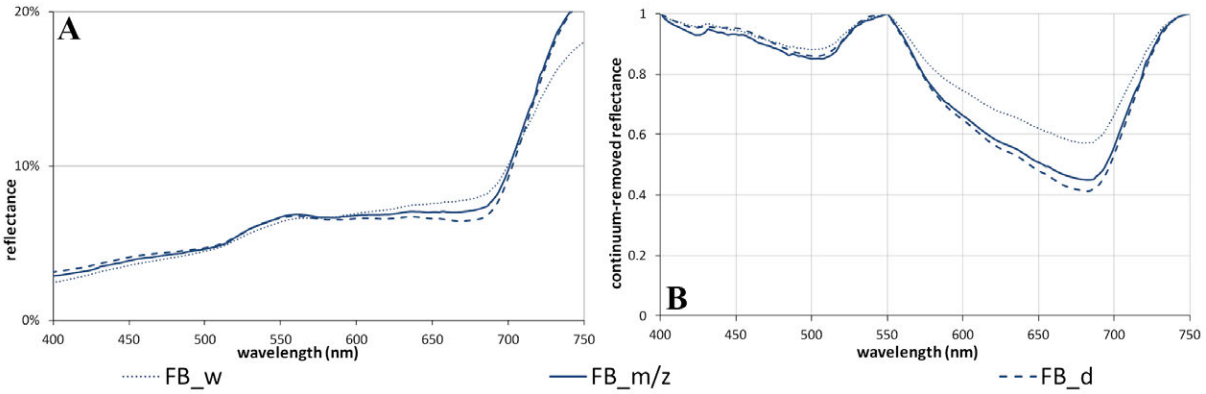

Figure 6-12: Spectral characteristics of the soil moisture gradient at the Franklin Bluffs study location. Comparison of (**A**) the averaged reflectance spectra in the visible (400 – 700 nm), and (**B**) the continuum-removed absorption features in the blue (400 nm – 550 nm) and red (550 nm – 750 nm) wavelength regions. ***Note:*** Naming and coloring of the reflectance spectra follow the concept shown in Figure 6-2.

In the NIR wavelength region the wet site has reduced reflectance values compared with the zonal and dry sites (Figure 6-5). In the 350 nm wide NIR band comparison, the wet site has an average reflectance of 21.9 %, the dry site of 23.7 %, and the mesic site of 24.6 %. This sequence also appears in the comparison of the maximum reflectance at 1,020 nm. The wet site has a maximum reflectance of 25.7 %, which increases to 26.9 % for the dry site and to 28.9 % for the mesic site.

6.4 Discussion

6.4.1 *Overview of Field Characterization and Spectral Properties along the Gradients*

The average reflectance spectra of the nine Low Arctic sites as a group are distinctly different from spectra of dominant vegetation in other higher and denser growing biomes. All the tundra spectra have generally low reflectance values, probably due to a combination of low plant canopy heights (vegetation height 8 – 30 cm, maximum shrub heights up to 55 cm) and low cover of vascular plants, relatively high cover of moss and lichen species, high surface moisture conditions, high sun zenith angles causing extreme shadowing by the plants themselves, and the large amounts of standing dead plant material. The averaged NIR reflectance for the tundra sites never exceeded 31 %. It is well known that the presence of water reduces the overall reflectance, where the vegetation cover is more open [*Weidong et al.*, 2002]. Therefore, at Deadhorse (DH_z with 70 Vol% moisture) and the Franklin Bluffs wet site (FB_w with 74 Vol% moisture), despite the relative high averaged height of the vegetation structure, the high surface moisture absorbs in the NIR, and the NIR reflectance is thereby reduced. The high sun zenith angles (always larger than 43°) in the tundra cause extreme shadowing even with low vegetation stature and micro-topography heights [*McGuffie*

and Henderson-Sellers, 1986]. Shadows decrease the reflectance in the red and NIR wavelength regions [*Ranson and T. Daughtry*, 1987]. This effect can be especially important in tussock tundra (subzone E). High percentage nadir-cover of moss and lichen in the understory (8 – 64 % in this study) reduces the reflectance in the NIR wavelength region (Figure 6-13). Lichens also reduce the reflectance in the green wavelength region (Figure 6-13). Standing dead material, commonly dead sedge leaves in tundra, leads to an increase in the reflectance in the red wavelength region due to reduced chlorophyll absorption [*Asner*, 1998; *Tucker*, 1977].

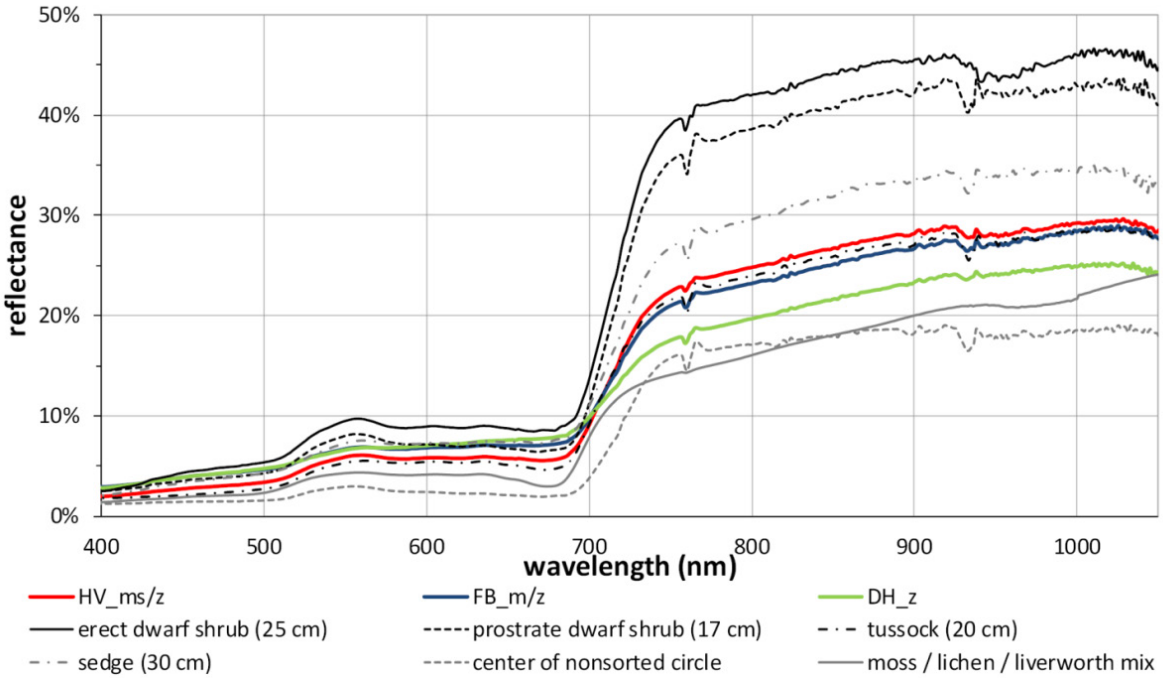

Figure 6-13: Reflectance spectra of the main plant functional types forming the plant communities of the Low Arctic portion of the NAAT. ***Note:*** For comparative purposes the mean reflectance spectra (plant community representation) of the zonal sites at Happy Valley, Franklin Bluffs and Deadhorse have been included. The reflectance spectrum of the 'moss/lichen/liverwort mix' is retrieved from *Clark et al.* [2007].

Figure 6-13 shows reflectance targets of tundra vegetation communities and of endmember targets (plant functional types) related to Arctic vegetation of subzones D and E. Two reflectance spectra have been measured over biological soil crusts: a reflectance spectrum of 'moss/lichen/liverwort mix' from *Clark et al.* [2007] and from nonsorted circles. Both reflectance spectra show considerable absorption in orange to red wavelengths with the development of a red-edge in contrast to reflectance spectra of barren soil surfaces without the development of a red-edge structure. Reflectance spectra of shrubs show high NIR backscatter with a planar NIR reflectance plateau with only minor or no slope between the beginning and end of the NIR reflectance plateau. This can be seen in the reflectance spectra of erect dwarf shrubs of 25 cm height and prostrate dwarf shrubs of 17 cm height (Figure 6-13). Both reflectance targets are characterized by dense and planophil leave structures. In contrast, reflectance spectra from sedges (30 cm) and tussock (20 cm) show NIR reflectance plateaus with stronger slopes between the beginning and end of the NIR reflectance plateau that also

characterizes all the reflectance spectra of the tundra sites (Table 6-4, delta value between 1,020 nm and 750 nm). Reflectance targets with sedges and tussock show erectophile vegetation structure as well as dead plant material. They are therefore producing less multiple backscattering in the NIR. The structural dependence on planophil and erectophil vegetation structures on the NIR reflectance has been described by *Thenkabail et al.* [2002] for crops.

The climate, soils, geomorphology, and hydrology of a site influence the vegetation characteristics, resulting in differences in leaf area and pigment composition, vegetation biomass and height, cover of plant functional types and total vegetation cover. These influence the VIS and NIR wavelength regions of the reflectance spectra. Thus, although the reflectance spectra of the main plant functional types (e.g. erect dwarf shrub, prostrate dwarf shrub, sedge) show certain diagnostic reflectance and absorption features, in combination as a plant community representing an area at larger scale (average reflectance of the site) it is challenging to distinguish the sites by their spectral signatures (Figure 6-13). The spectra of the nine tundra vegetation communities examined are superficially similar in many respects, when examined in detail, they show distinct diagnostic features mainly in the pigment absorbing wavelength bands and the height of the NIR reflectance.

The main changes in the VIS and NIR region of the spectra along the zonal climate gradient are likely due to differences in biomass, average and maximum vegetation height, and species composition. Since all contributors are physically overlapping, more research would be needed to partition the contributors causally. However, vegetation height, shrub-cover, and biomass increase toward the south [*Raynolds et al.*, 2008; *Walker et al.*, 2011c], causing higher pigment absorption in the blue and red bands and higher reflectance in the NIR bands. Site locations further north have greater cover of sedges, and are characterized by less leaf mass and fewer chlorophyll-rich shrubs. Together with higher cover of standing dead material (mostly sedges), this leads to an increase in the reflectance in the red and blue wavelength regions with no development of a green reflectance peak due to reduced leaf pigment absorption. The 5 % difference in the NIR reflectance between the northernmost (Deadhorse) and southernmost (Happy Valley) zonal study site (Table 6-4) is most likely related to canopy structure changes along the climate gradient (taller more dense vegetation in the warmer summer climates to the south). This leads to greater multiple scattering and to higher reflectance values in the NIR. The very low NIR reflectance at Deadhorse is also due to the high surface moisture conditions (up to 70 Vol% soil moisture).

Mesic acidic and non-acidic tundra are at first sight physiognomically similar in that sedges and dwarf shrubs dominate both types, but the species composition and the relative ratios of the different plant functional types are quite distinct. The very different species composition of the acidic and non-acidic tundra is likely responsible for important spectral differences. For example, MAT has a much larger component of chlorophyll-rich deciduous shrubs and generally taller and more horizontally continuous cover of green vegetation; whereas MNT is generally less green, with more standing dead sedge leaves, much less cover of erect deciduous shrubs, and greater cover of soil crust and lichen-covered soil associated with abundant nonsorted circles. The prostrate evergreen dwarf shrub *Dryas integrifolia*, an

abundant MNT plant, often has a large non-green component composed of dead leaves and stems. In addition, the most common mosses in MAT are acidic *Sphagnum* mosses, while the non-acidic moss *Tomentypnum nitens* is most common in MNT. Effects of changes in the dominant moss species on reflectance spectra have not yet been evaluated. However, the moss layer (L1) of MNT sites are characterized by non-greenish hues (5Y) of pure chroma (=10) in contrast to greenish hues (2.5GY) of pure chroma (=10) at MAT sites.

The results of the field spectroscopy support the separation of acidic and non-acidic tundra in the VIS reflectance spectrum. MAT sites have deeper chlorophyll absorption in the blue and red wavelength regions than the non-acidic sites. Moreover, the MNT sites have a greater percentage of nonsorted circles and lichen vegetated areas the further north they are [*Hope et al.*, 1993], resulting in decreases in the absorption of blue and red radiation. A separation of MAT vs. MNT in the NIR wavelength region is possible, but the averaged reflectance spectra overlap at some study sites. In this study, the hill crest site at Happy Valley shows a relatively low NIR reflectance in comparison to the other two acidic Happy Valley sites. This somewhat drier site has a higher vegetation nadir-coverage of moss and lichen and a lower nadir-coverage of taller vegetation, which can reduce the reflectance in the NIR region and produce an NIR reflectance similar to the signature of a dry non-acidic site. However, the erect deciduous dwarf shrubs, which are taller and denser than the prostrate evergreen dwarf shrubs at the non-acidic sites, have a greater multiple scattering effect, and this leads to higher reflectance values in the NIR of MAT.

Differences in the lateral water fluxes and moisture regimes along the sites also have spectral impacts. The differences in the reflectance spectra along the toposequence gradient at Happy Valley can be mainly explained by the changes in cover and height of the dwarf shrub layer, which is linked to lateral water flux from the hill crest to the footslope. There is also an increase in the cover of tussock sedges down the topographic gradient, matching findings from *Stow et al.* [1993] and *Walker and Lederer* [1987] along a toposequence at Imnavait Creek. The shrub cover in the third vertical stratum (L3) increases by 18 % from the hill crest to the footslope, and the average vegetation height increases by 13 cm. This leads to a downslope increase of green leaf area and biomass, and therefore to higher NIR reflectance values. A clear separation in the NIR region of the three reflectance spectra is therefore possible. In the VIS region the reflectance spectra of all three sites overlap. Only in the spectral metrics of absorption depth and continuum removal analysis of the red wavelength region is a separation of all three sites possible. At 680 nm, the footslope site shows the deepest chlorophyll absorption, and the hill crest site shows the least absorption. The difference can be best seen in the area of the red absorption feature from 550 – 750 nm. The hill crest site is exposed to greater stress. Due to drier soil conditions, the percentage nadir-cover of moss and lichen vegetated areas is greater, and the nadir-coverage by green leaf area is less than the other sites, which can explain the reduced chlorophyll absorption in the VIS spectra.

The three sites along the soil moisture gradient at Franklin Bluffs show an even higher contrast of the spectral contribution by water (dry site 36 Vol% soil moisture and wet site

74 Vol%). The main difference along this gradient is the percentage cover of sedge and standing dead vegetation as well as changes in surface moisture. The high percentage cover of standing dead material at the wet site increases the reflectance in the red wavelengths bands, whereas the moist and dry sites are greener and show deeper chlorophyll absorption. This can be best seen in the spectral metrics of the continuum removal analysis of the red wavelength region, as there are only minor differences in the blue absorption band depths between the sites. The spectral behavior in the NIR region is mainly influenced by the soil moisture and mean vegetation height. The reduced NIR reflectance at the wet site results from the increased surface moisture content. The mesic and dry sites have nearly similar reflectance spectra at the shorter wavelengths of the NIR, but at the dry site there is a higher nadir-coverage of moss and lichen and lower contribution from taller vegetation layers, which reduces the NIR reflectance above 900 nm. For remote sensing applications the contribution from ponds and lakes will have an influence on the reflectance of tundra landscapes and on the NDVI [*Muster et al.*, 2013].

6.4.2 Performance of Spectral Metrics and Vegetation Indices

Since the continuum removal technique normalizes the absolute differences of local reflectance peaks in the green and NIR regions, it enhances the differences in absorption strength in the blue and red wavelength regions. The absorption-related metrics confirm the reduction in pigment absorption within the red and the blue wavelength regions along the climate gradient from south to north and from MAT to MNT. This can also be well seen in the regression analyses of the relative absorption depth and continuum removed maximum band depth in the blue and red wavelength regions with biomass (Figure 6-8).

Visually, MAT is much greener in mid-summer than MNT. Both have a dull brown appearance in early June, but by July the erect dwarf shrubs and tussock sedges of MAT are fully leafed-out and mask the dead sedge leaves from the previous winter. The green-up in the MNT is less striking, because there are fewer deciduous shrubs, and the new sedge leaves do not fully mask the standing dead leaves. Furthermore, there is much greater cover of soil crust and lichens on nonsorted circles, which are usually abundant in non-acidic tundra. The very distinct assignment of the dominant non-greenish hue (5Y) of pure chroma (=10) of the MNT sites in contrast to the dominant greenish hue (2.5GY) of pure chroma (=10) of the moss layer (L1) further supports the characterization that MAT sites are ‘greener.’

The partitioning of MAT and MNT using broadband and narrowband NDVIs in this study shows promising results. A broadband $NDVI_{AVHRR}$ value of 0.58 and a narrowband $NDVI_{47\_59}$ value of 0.54 are the thresholds for separating these tundra systems in our study. The lower average NDVI values of MNT compared to MAT are mainly due to the lower quantities of shrub phytomass in MNT [*Riedel et al.*, 2005]. In non-acidic systems the phytomass is mainly composed of moss, which has a reduced NIR reflectance as well as less leaf mass with therefore reduced pigment absorption. The separation of acidic and non-acidic tundra via VIs and metrics of pigment absorption is important for remote sensing of Alaskan tundra, as this MAT/MNT threshold value can be extracted from the satellite image statistics.

That narrowband NDVIs may perform better than their broadband equivalent by setting one or both HNBs in the red and NIR to specific positions is already well known [*Elvidge and Chen*, 1995; *Roberts et al.*, 2011; *Thenkabail et al.*, 2002; *Thenkabail et al.*, 2011]. The main challenge is to find the right HNBs for an application within the large number of redundant bands provided by hyperspectral instruments [*Thenkabail et al.*, 2013]. Up to now, hyperspectral satellite and airborne data for arctic regions were limited. Therefore, ground-based hyperspectral measurements are a good alternative to determine HNBs for tundra applications. The three tested narrowband NDVIs showed similar good results in the regression analyses with biomass compared to the broadband NDVI. We assume that the performance of the broadband and narrowband NDVIs might not be fully linked to vegetation structure (i.e. NIR reflectance) due to low canopy height. The photosynthetic capacities of the tundra plant communities therefore seem to control the NDVI performance. This is illustrated by the regression relationships of biomass vs. NDVIs and biomass vs. absorption depths, respectively (Figure 6-8). The analyses indicate that the tundra sites characterized by sedges show less intense chlorophyll absorption due to more non-photosynthetically active biomass. The correlation of carotenoid absorption in the blue wavelengths with biomass (Figure 6-8A,C) therefore shows a better performance than the correlation of chlorophyll absorption with biomass (Figure 6-8B,D). This differential and its influence on the NDVI facilitate the separation of MAT and MNT. Narrowband NDVIs, specifically the $NDVI_{47\_59}$ with the EnMAP NIR band #59 at 756 nm close to the red-edge, yield better separations of the two tundra vegetation types than the broadband NDVI. Imaging spectroscopy by new satellite systems such as EnMAP can be used to apply hyperspectral algorithms based on the narrow wavelength regions that show high separation potential between tundra communities. Narrowband methods using the spectral bands of pigment absorption around 500 nm for carotenoids and around 680 nm for chlorophyll show high potential.

6.5 Conclusions

This paper provides a ground-based hyperspectral characterization of the most important plant communities in the Alaskan Low Arctic tundra (subzones D and E) along important environmental gradients. As a group, the averaged reflectance spectra of all nine sites exhibit similar characteristic profiles that are typical for Low Arctic tundra (Figure 6-5). They show: (i) low maximum near-infrared (NIR) reflectance (maximum of 31 % at 1,020 nm); (ii) weakly visible green reflectance peak or no local reflectance maximum in the visible spectrum; (iii) narrow ‘red-edge’ region between the red and NIR wavelength regions (maximum 18 % difference between red absorption minimum and NIR reflectance plateau); and (iv) no distinct NIR reflectance plateau (i.e. the ‘red-edge’ bend does not finish in a plateau, instead the reflectance values steadily increase up to the maximum reflectance at around 1,020 nm). The explanation for these findings is that a generally low reflectance in the NIR as well as the green wavelength range and a low chlorophyll absorption in the red wavelength range occur due to a low vegetation height structure and low green leaf area of the vegetation. Moreover, nadir-coverage of standing dead sedges and woody plant material

(dwarf shrubs) is generally high. These typical patterns make the reflectance spectra of low-growing tundra specific and distinguishable from other biomes, for example wetlands or local areas occupied by taller and denser growing shrubs.

This research also shows that spectral metrics follow the geoecological gradients. The reflectances of the NIR shoulder and NIR reflectance plateau are valuable information sources that separate the communities according to their biomass and vegetation structure. The spectral metrics of absorption depths and continuum removal technique reveal separation possibilities in the blue and red wavelength regions. The main spectro-radiometric findings are: (i) for the zonal gradient - there is more vegetation biomass, denser shrub cover and taller shrubs with denser leaf cover the further south along the North American Arctic Transect (NAAT). This leads to higher reflectance in the NIR wavelength region. (ii) Lower positions along toposequences and wetter sites along the soil moisture gradient show greater vegetation biomass due to higher moisture availability. But this does not always lead to higher reflectance values in the NIR wavelength region. Vegetation height and surface wetness are two antagonists that may balance each other out with respect to the NIR reflectance. (iii) Moist acidic tundra (MAT) sites, when compared to moist non-acidic tundra (MNT) sites, have 'greener' species (chlorophyll-rich deciduous shrubs and green-colored mosses), more continuous cover of green vegetation, and more leaf mass, which cause higher pigment absorption in the blue and red wavelength regions. (iv) MNT sites show relatively high reflectance in the red wavelength region, low absorption in the blue and red wavelength regions, and no distinct 'green' reflectance. The contributing factors to low greenness are the abundance of standing dead sedge leaves, evergreen shrubs with larger non-green dead components (mainly *Dryas integrifolia*), higher percentage cover of soils covered by biological soil crusts, and abundance of brown-colored mosses (e.g., *Tomentypnum nitens*).

The hyperspectral field spectrometer analysis indicate the possibility of separating out MAT and MNT vegetation communities, which have not been previously separable in such a good way using broadband data. Moreover, hyperspectral data can potentially be used for color differentiation as well as investigation of differences in the shape and slope of the 'red-edge' of MAT and MNT. Our investigation shows that additional types of field data to link to spectral metrics are needed. Future investigations should include evaluation of the amount of dead material per site as well as a more detailed assessment of the Munsell color of plant species and communities. Also time-series hyperspectral studies are needed through the growing season in combination with simultaneous studies of plant pigment concentrations in order to analyze the seasonal vegetation and color changes of tundra communities. Field spectroscopy is a useful method for obtaining hyperspectral ground data. This well-characterized spectral database of Low Arctic NAAT vegetation communities covers a wide range of geoecological parameters and serves as the basis for further investigation of spectral properties of arctic vegetation communities.

7 RESULTS OF THE SPECTRO-DIRECTIONAL REFLECTANCE INVESTIGATIONS

The results obtained from the field spectro-goniometer measurements under varying sun zenith angles (SZA) at Vaskiny Dachi (bioclimate subzone D – West-Siberia), Happy Valley (bioclimate subzone E – Alaska), and Franklin Bluffs (bioclimate subzone D – Alaska) are presented in this chapter. The first section gives an overview of the hyperspectral spectro-directional reflectance characteristics of different Low Arctic plant communities measured at solar noon. The second section analyzes the influence of high SZAs on the BRDF characteristics of the MAT and MNT plant communities. And the last section presents the influence of BRDF effects on remote sensing products of MAT and MNT plant communities.

7.1 Overview of the Spectro-Directional Reflectance Characteristics of Low Arctic Tundra Vegetation

7.1.1 Representativeness of the Study Plots Representing Tundra Vegetation

The comparison of the nadir view reflectance (R_{nadir}) spectra from the two spectro-goniometer measurements at the Vaskiny Dachi study location (VDG1_02 and VDG2_03) performed at solar noon with the reflectance spectrum of the zonal plant community of West-Siberian bioclimate subzone D [*Heim et al.*, 2012] shows that neither of the two analyzed plant communities correspond to the zonal plant community (Figure 7-1A). The VDG1_02 measurements were carried out over a dwarf shrub-moss tundra plot and the VDG2_03 measurements were carried out over a grazed dwarf shrub-moss tundra plot. Figure 7-1B shows that the R_{nadir} spectrum of the spectro-goniometer measurement HVG1_03 (tussock sedge tundra) at the Happy Valley study location corresponds to the reflectance spectrum of the zonal plant community for Alaskan bioclimate subzone E which is MAT (Figure 6-5). The R_{nadir} spectrum of HVG2_03 (Figure 7-1B) fits the reflectance spectrum of an erect dwarf shrub community (Figure 6-13). At the Franklin Bluffs study location (Figure 7-1C), the R_{nadir} spectrum of spectro-goniometer measurement FBG1_03 (non-tussock sedge) equals the reflectance spectrum of the zonal plant community for Alaskan bioclimate subzone D which is MNT (Figure 6-5). The R_{nadir} spectrum of FBG2_03 (Figure 7-1C) fits the reflectance spectrum of a prostrate dwarf shrub community (Figure 6-13), while the R_{nadir} spectrum of the FBG3_01 measurement corresponds to the reflectance spectrum of the plant community in the center of nonsorted circles (frost boils) that mainly consist of a moss-lichen-liverwort mix (Figure 6-13). Spectro-goniometer measurement FBG4_01 at Franklin Bluffs was performed over a horsetail patch at solar noon and shows an unusual R_{nadir} spectrum compared to all the others (Figure 7-1C).

Figure 7-1D shows the irradiance spectra of all eight full ManTIS hemisphere spectro-goniometer measurements performed at solar noon. Although the two study plots at the

Vaskiny Dachi study location have nearly identical irradiance spectra, the measurements were performed under different SZA (55° for VDG1_02 and 61° for VDG2_03). The two spectro-goniometer study plots at the Happy Valley study location were performed under the same SZA (46°) and thereby show nearly identical irradiance spectra (Figure 7-1D). Spectro-goniometer measurements FBG1_03 and FBG2_03 at the Franklin Bluffs study location were performed under a SZA of 47°, whereas the measurements FBG3_01 and FBG4_01 were performed under a SZA of 48°. This is also notable in the irradiance spectra (Figure 7-1D).

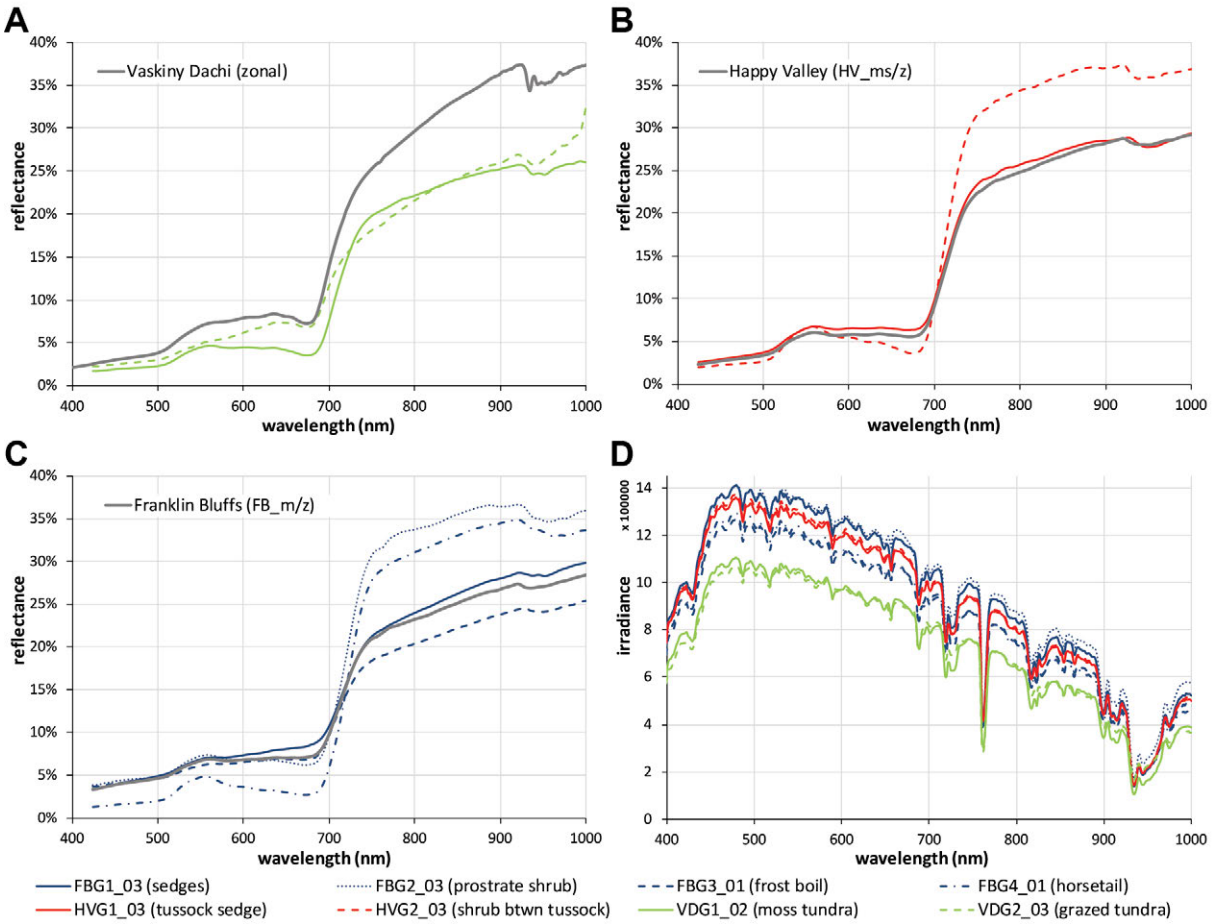

Figure 7-1: Comparison of the nadir view reflectance spectra of the eight spectro-goniometer measurements performed at solar noon. (**A**) Comparison of the two nadir view reflectance spectra at Vaskiny Dachi with the zonal plant community. (**B**) Comparison of the two nadir view reflectance spectra at Happy Valley with the zonal plant community. (**C**) Comparison of the four nadir view reflectance spectra at Franklin Bluffs with the zonal plant community. (**D**) Comparison of the irradiance profiles of the eight spectro-goniometer measurements performed at solar noon.

Please note that detailed data reports of the spectro-goniometer measurements at all study locations can be found in Appendix C.

7.1.2 Vaskiny Dachi – Bioclimate Subzone D

The spectro-directional reflectances characteristics of dwarf shrub-moss tundra (VDG1_02) and grazed dwarf shrub- moss tundra (VDG2_03) measured at the Vaskiny Dachi study location at solar noon are visualized in Figure 7-3. The HCRF data of the blue EnMAP band #12 (6.5 nm wide; center 479 nm) and the green EnMAP band #26 (6.5 nm wide; center

549 nm) are shown in Figure 7-3A. Figure 7-3B shows the HCRF data of the red EnMAP band #47 (6.5 nm wide; center 672 nm) and the NIR EnMAP band #73 (8.0 nm wide; center 864 nm) of both plant communities. The outlier indicators were used to estimate the quality of the interpolation approach in order to reduce short time atmospheric and solar changes (graphic legend, Figure 7-2). The outlier indicator of the spectro-goniometer measurements for grazed dwarf shrub-moss tundra shows that higher atmospheric and solar changes occurred during this measurement and thus required correction (Figure 7-3).

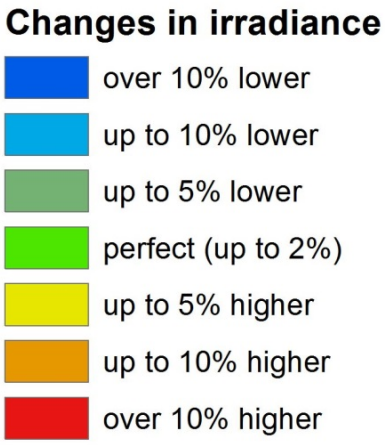

Figure 7-2: Legend of the outlier indicator graphics used in the HCRF and ANIF visualizations in order to estimate the quality of the interpolation approach for reducing short time atmospheric and solar changes.

ANIF: A more detailed spectro-directional reflectance data analysis reveals the ANIF data of the red (672 nm) and NIR (864 nm) EnMAP bands in Figure 7-4. The dwarf shrub-moss tundra plot (VDG1_02) shows the highest reflectance variation in the solar principal plane (Figure 7-4A, Figure 7-4B). The ANIF values in the solar principal plane range from 0.8 to 1.35 in the VIS and 0.7 to 1.1 in the NIR wavelength regions. Moreover, the spectro-goniometer measurement of the moss tundra plot shows a clear ANIF hotspot in the -5° to -10° forward viewing directions of the solar principal plane (Figure 7-4A). This hotspot shows together with the +30° backward viewing direction (Figure 7-4B) ANIF values over 1.0 in the VIS and NIR wavelength regions. All other viewing directions in the solar principal plane show ANIF values below 1.0. The ANIF values within the solar orthogonal plane show a bowl shape distribution with the highest ANIF values in the nadir viewing position, and decreasing ANIF values with increasing forward and backward viewing zenith angles.

The ANIF data of the grazed dwarf shrub-moss tundra plot (VDG2_03) show higher reflectance values in the backward viewing directions and also equal to higher reflectance values in the forward viewing directions compared to the nadir viewing position (Figure 7-4A). The highest reflectance variation is viewable in the EnMAP bands along the solar principal plane (Figure 7-4B). The ANIF values reach up to 1.5 in the VIS and 1.3 in the NIR wavelength regions of the backward viewing directions in the solar principal plane, whereas the ANIF values increase with backward viewing zenith angle. The ANIF values of all forward viewing directions are clumped and show ANIF values of 0.95 to 1.0 in the VIS

and ANIF values up to 1.1 in the NIR wavelength regions. The reflectance variation within the solar orthogonal plane reaches up to 35 %, and the ANIF values in all viewing directions are higher than 1.0.

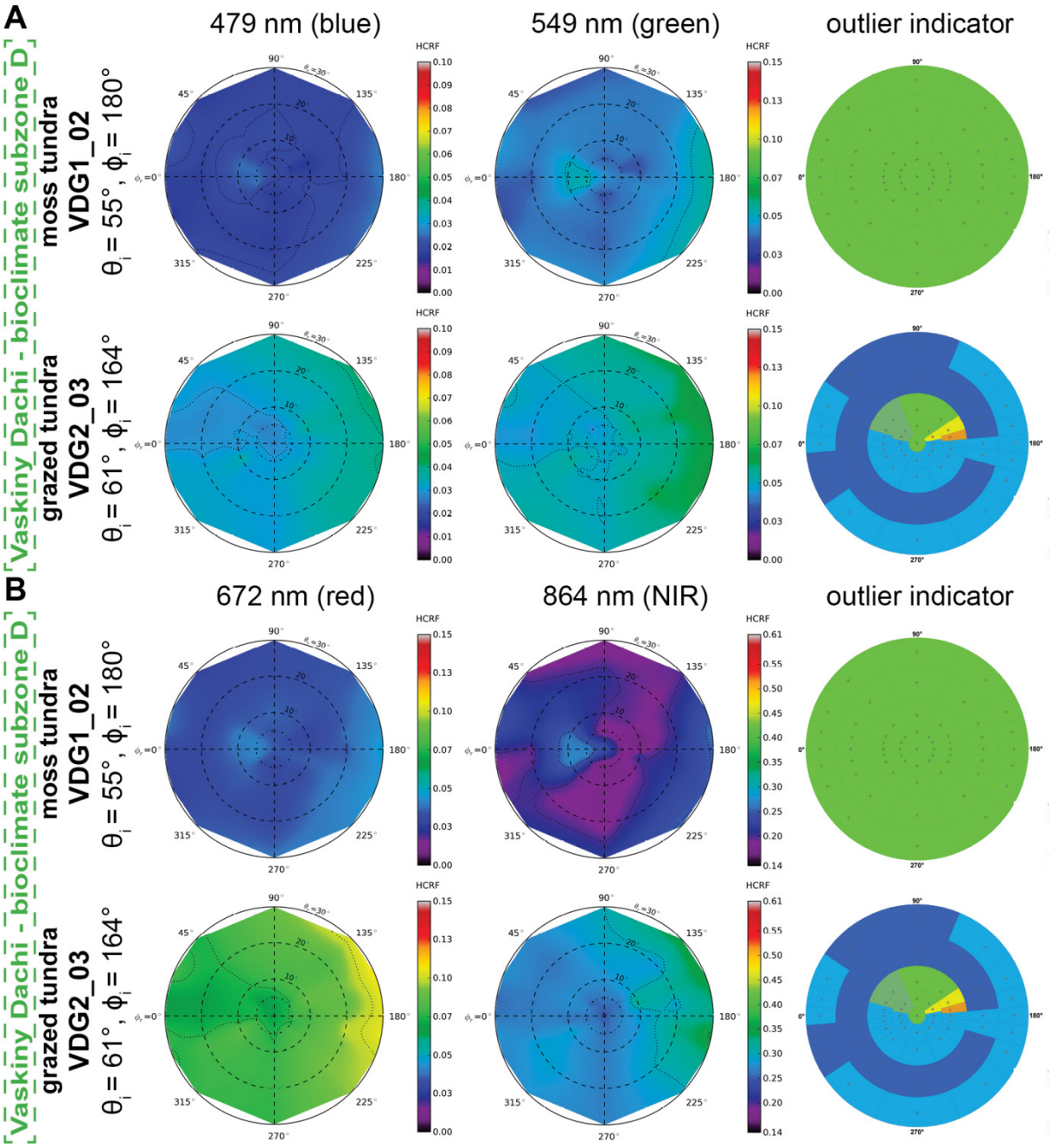

Figure 7-3: HCRF visualization of the Vaskiny Dachi spectro-goniometer measurements performed at solar noon. (**A**) HCRF visualization of the blue (479 nm) and green (549 nm) EnMAP bands. (**B**) HCRF visualization of the red (672 nm) and NIR (864 nm) EnMAP bands. ***Note:*** See Figure 7-2 for legend of the outlier indicator graphics.

ANIX: The comparison of the R_{nadir} spectrum with the ANIX development in the solar principal and orthogonal plane is shown in Figure 7-5. For dwarf shrub-moss tundra (VDG1_02) the ANIX values in the solar principal plane increase from 1.5 to 1.67 in the VIS wavelength region and stay at 1.65 to 1.7 in the NIR wavelength region. In the solar orthogonal plane the ANIX values in the VIS wavelength region are 1.32 to 1.37 and jump to

1.53 – 1.58 in the NIR wavelength region. This shows that dwarf shrub-moss tundra has a slightly higher degree of reflectance anisotropy in the NIR than in the VIS wavelength region.

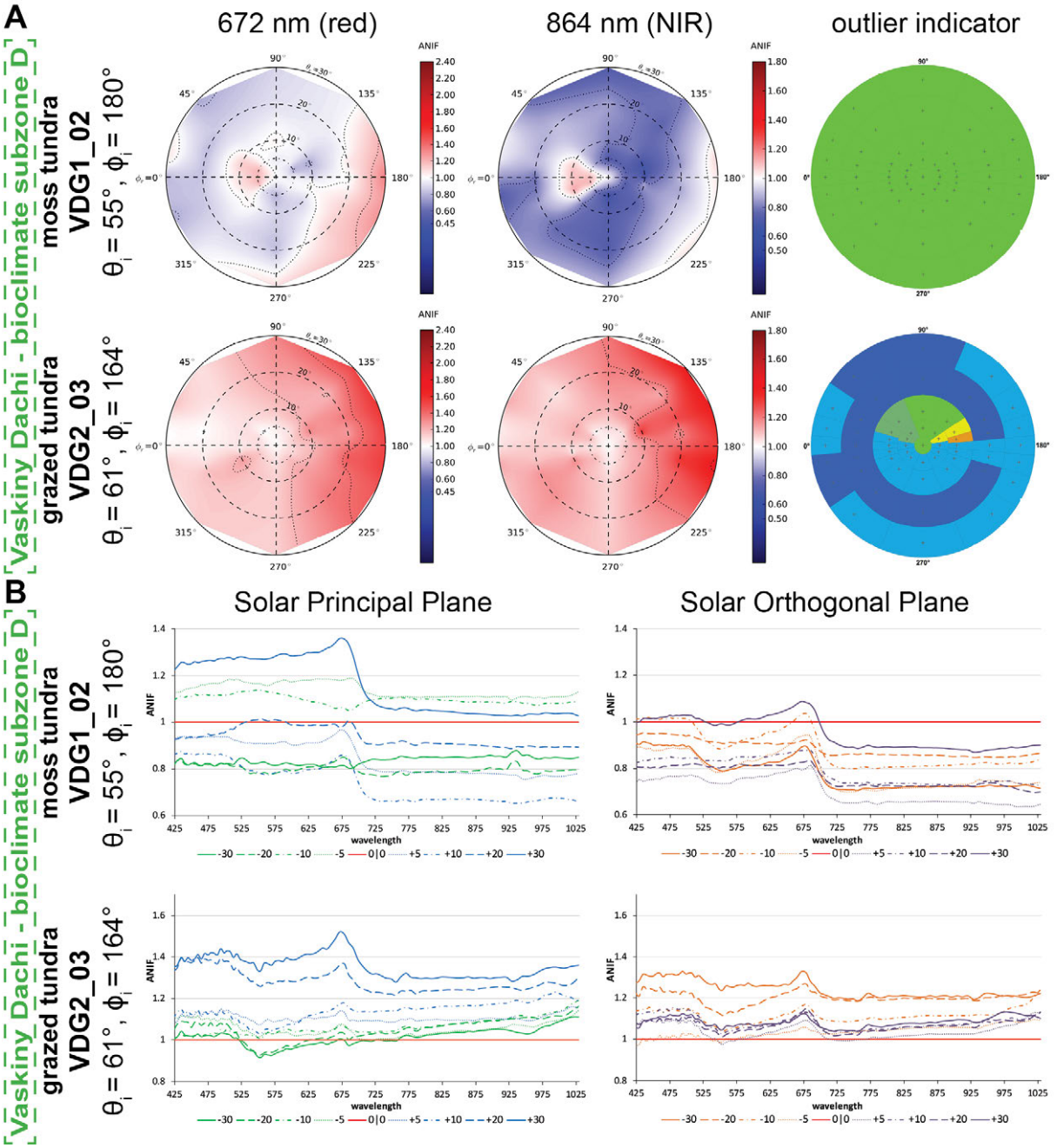

Figure 7-4: ANIF visualization of the Vaskiny Dachi spectro-goniometer measurements performed at solar noon. (**A**) ANIF visualization of the red (672 nm) and NIR (864 nm) EnMAP bands. (**B**) ANIF development in the solar principal and orthogonal plane of the EnMAP bands. ***Note:*** See Figure 7-2 for legend of the outlier indicator graphics.

The ANIX values in the solar principal and orthogonal plane of grazed dwarf shrub-moss tundra (VDG2_03) behave inversely. In the solar principal plane the ANIX values increase from 1.37 to 1.52 in the VIS and drop to 1.3 – 1.37 in the NIR wavelength region, where in the solar orthogonal plane the ANIX values stay at 1.28 to 1.32 in the VIS and drop to 1.20 – 1.23 in the NIR wavelength region. Therefore, grazed dwarf shrub-moss tundra shows a higher degree of reflectance anisotropy in the VIS than in the NIR wavelength region.

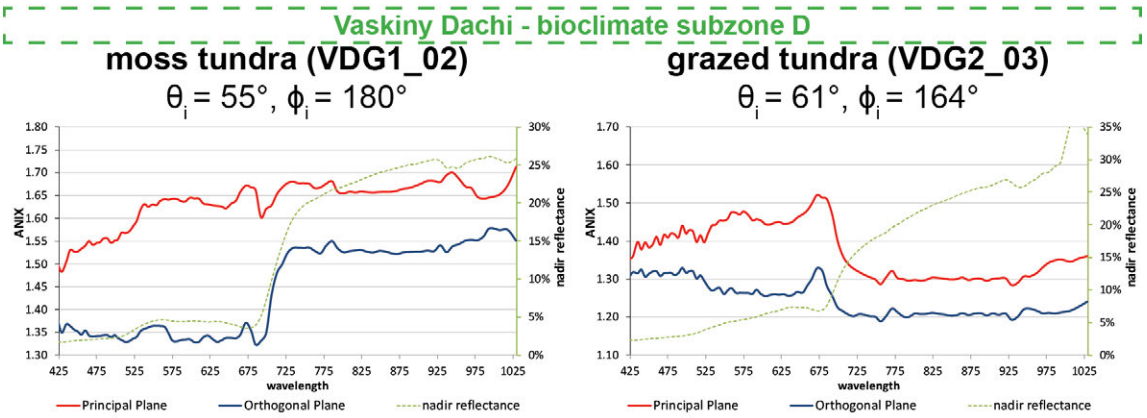

Figure 7-5: ANIX visualization in the solar principal and orthogonal plane of the Vaskiny Dachi spectro-goniometer measurements performed at solar noon in comparison to the nadir view reflectance spectra.

7.1.3 Happy Valley – Bioclimate Subzone E

At the Happy Valley study location, the spectro-directional reflectances characteristics of tussock sedge tundra (HVG1_03) and an erect dwarf shrub community between tussock sedges (HVG2_03) measured at solar noon are visualized in Figure 7-6. The HCRF data of the blue EnMAP band #12 (6.5 nm wide; center 479 nm) and the green EnMAP band #26 (6.5 nm wide; center 549 nm) are shown in Figure 7-6A. Figure 7-6B shows the HCRF data of the red EnMAP band #47 (6.5 nm wide; center 672 nm) and the NIR EnMAP band #73 (8.0 nm wide; center 864 nm) of both plant communities. The outlier indicator of the spectro-goniometer measurements of tussock sedge tundra show that only small atmospheric and solar changes occurred during these measurements (Figure 7-6). The outlier indicator of the HVG2_03 measurements shows that stronger atmospheric and solar changes occurred that had to be corrected.

ANIF: The ANIF data of tussock sedge tundra (HVG1_03) show in the solar principal and orthogonal plane an indistinct sequence (Figure 7-7A, Figure 7-7B). The ANIF values in the solar principal plane reach from 0.50 to 1.40 in the VIS and 0.45 to 1.42 in the NIR wavelength region. Only the ANIF values in the +20° and +30° backward viewing directions have ANIF values above 1.0 in the VIS and NIR wavelength regions. All other viewing directions show ANIF values between 0.45 and 0.9. The highest reflectance variation occurs in the solar orthogonal plane (Figure 7-7B). While in the VIS wavelength region (mainly in the blue wavelength region) an ANIF hotspot with ANIF values up to 1.6 in the backward viewing directions occurs, the NIR wavelength region shows ANIF values below 1.0 in all viewing directions. Moreover, all ANIF values in the solar orthogonal plane of the forward viewing directions are lower than in the nadir viewing position.

The ANIF data of the erect dwarf shrub community between tussock sedges (HVG2_03) show only in the VIS wavelength region higher reflectance values in the backward viewing directions and lower to equal reflectance values in the forward viewing directions compared to the nadir viewing position (Figure 7-7A, Figure 7-7B). In the NIR wavelength region all reflectance values are lower to equal to the reflectance values in the nadir viewing position.

Therefore, the highest reflectance variation is viewable in the red EnMAP band along the solar principal plane (Figure 7-7B). The ANIF values in the solar principal plane range from 0.9 to 1.55 in the VIS wavelength region and 0.8 to 1.05 in the NIR wavelength region of the backward viewing directions, whereas in the forward viewing directions the ANIF values range from 0.65 to 1.2 in the VIS and 0.7 – 0.85 in the NIR wavelength region. The reflectance variation within the solar orthogonal plane behave like the reflectance variability within the solar principal plane but with ANIF values ranging from 0.7 to 1.3 in the VIS and 0.8 – 0.95 in the NIR wavelength region.

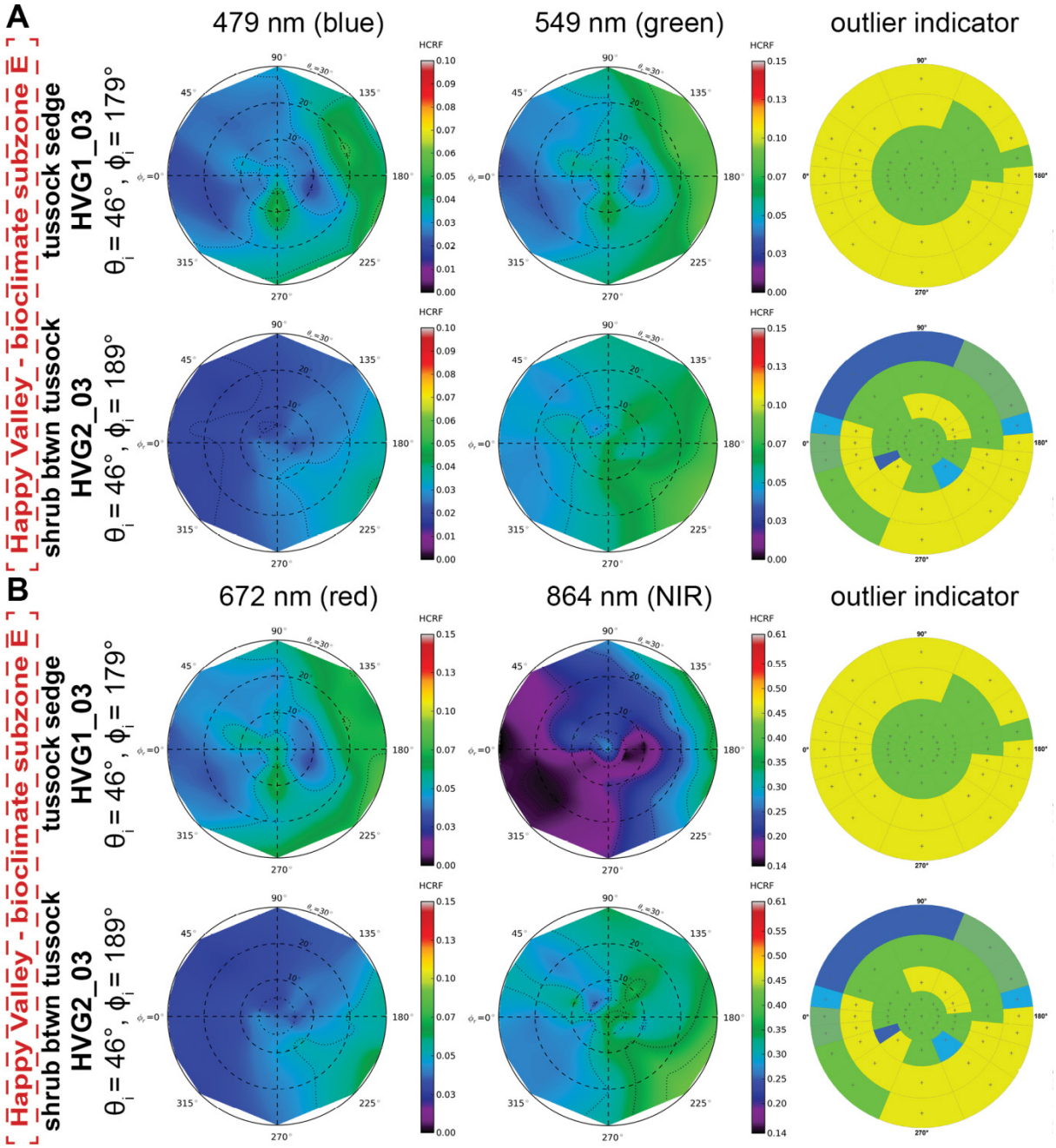

Figure 7-6: HCRF visualization of the Happy Valley spectro-goniometer measurements performed at solar noon. (**A**) HCRF visualization of the blue (479 nm) and green (549 nm) EnMAP bands. (**B**) HCRF visualization of the red (672 nm) and NIR (864 nm) EnMAP bands. ***Note:*** See Figure 7-2 for legend of the outlier indicator graphics.

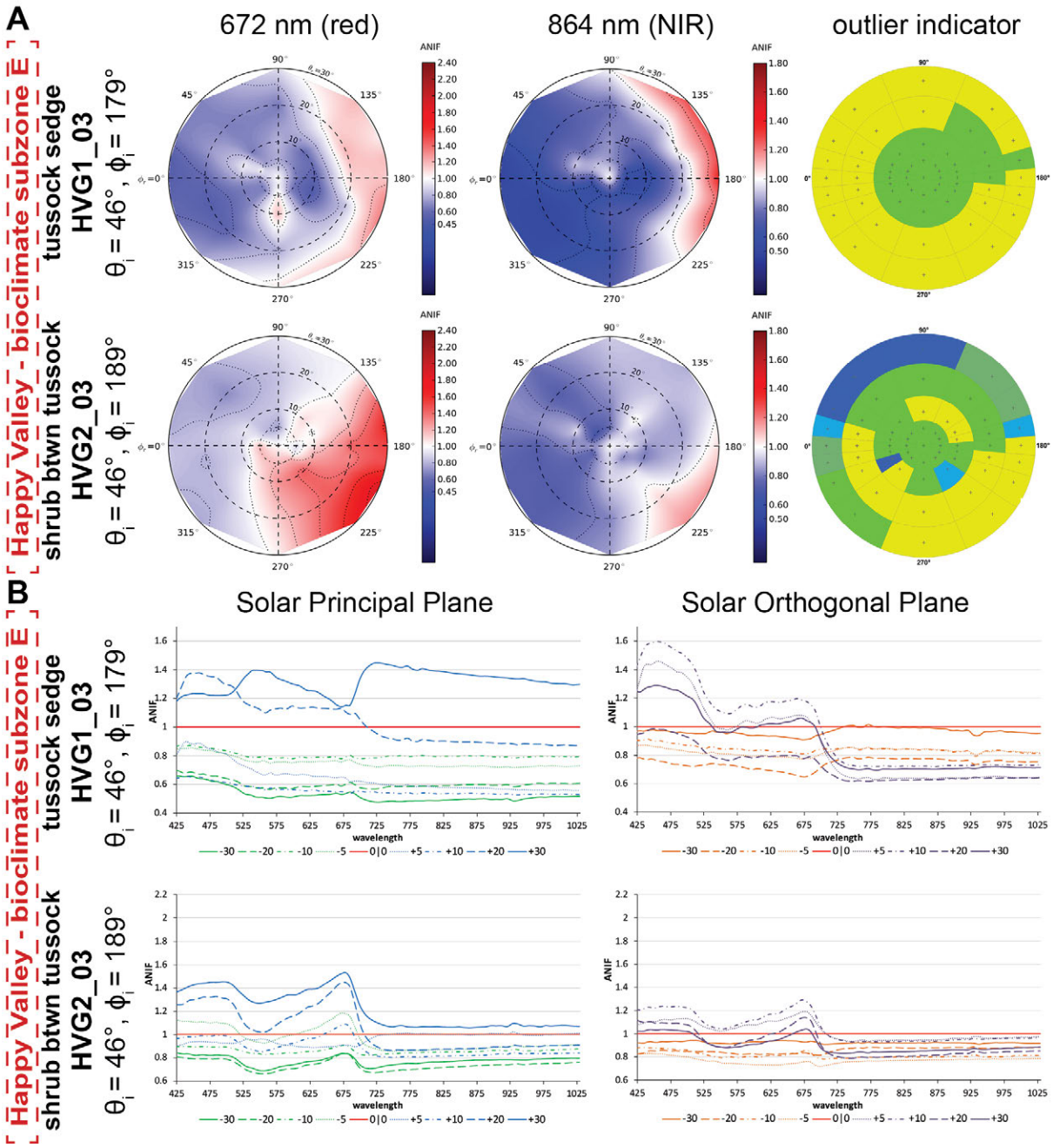

Figure 7-7: ANIF visualization of the Happy Valley spectro-goniometer measurements performed at solar noon. (**A**) ANIF visualization of the red (672 nm) and NIR (864 nm) EnMAP bands. (**B**) ANIF development in the solar principal and orthogonal plane of the EnMAP bands. ***Note:*** See Figure 7-2 for legend of the outlier indicator graphics.

ANIX: The spectral dependence of the ANIX values along the solar principal plane of tussock sedge tundra (HVG1_03) is unexpected (Figure 7-8). The ANIX values in the blue (425 – 500 nm) and the red maximum absorption depth (~ 670 nm) range between 2.1 and 2.2, where the ANIX values in the green to orange wavelength region are between 2.3 and 2.7. In the NIR wavelength region the ANIX values start at 3.0 and slowly decrease to 2.5 with higher wavelengths. In the solar orthogonal plane the ANIX values are between 1.45 and 2.05. This shows that tussock sedge tundra has a higher degree of reflectance anisotropy in the NIR than in the VIS wavelength region.

For the HVG2_03 measurements (erect dwarf shrub between tussock sedges) the ANIX values show a higher degree of reflectance anisotropy in the VIS than in the NIR wavelength region. In the solar principal plane the ANIX values stay between 1.7 and 1.9 in the VIS and drop to 1.4 – 1.5 in the NIR wavelength region, where in the solar orthogonal plane the ANIX values range between 1.4 and 1.7 in the VIS and drop to 1.20 in the NIR.

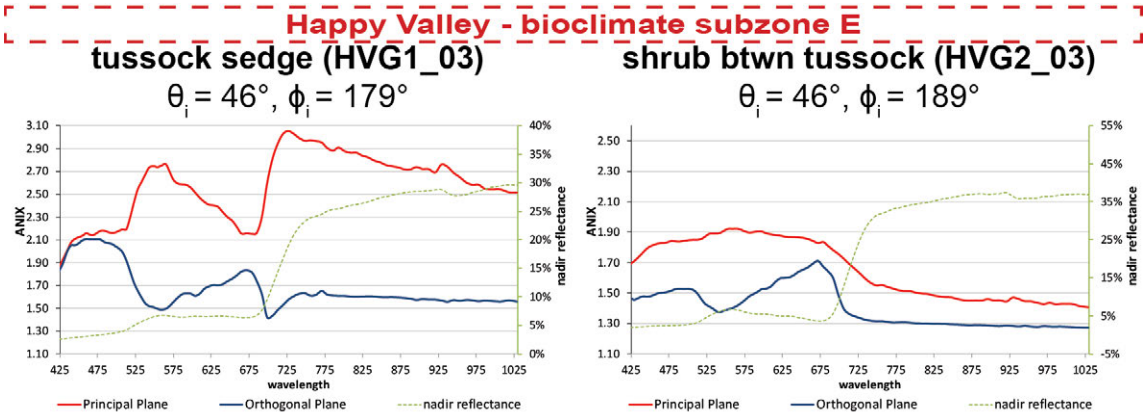

Figure 7-8: ANIX visualization in the solar principal and orthogonal plane of the Happy Valley spectro-goniometer measurements performed at solar noon in comparison to the nadir view reflectance spectra.

7.1.4 Franklin Bluffs – Bioclimate Subzone D

The spectro-directional reflectances characteristics of non-tussock sedge tundra (FBG1_03), a prostrate dwarf shrub community (FBG2_03), a plant community in the center of nonsorted circles (FBG3_01), and a horsetail community (FBG4_01) measured at Franklin Bluffs at solar noon are visualized in Figure 7-9. The HCRF data of the blue (#12; 479 nm) and green (#26; 549 nm) EnMAP bands are shown in Figure 7-9A, where Figure 7-9B shows the HCRF data of the red (#47; 672 nm) and NIR (#73; 864 nm) EnMAP bands.

The outlier indicator of the spectro-goniometer measurements of non-tussock sedge tundra shows that higher atmospheric and solar changes occurred during these measurements and had to be corrected (Figure 7-9). In contrast, the outlier indicators of the spectro-goniometer measurements of the prostrate dwarf shrub community and the plant community in the center of nonsorted circles show that only small atmospheric and solar changes occurred during these measurements. The atmospheric and solar conditions during the spectro-goniometer measurements of the horsetail community were optimal.

ANIF: The ANIF data of non-tussock sedge tundra (FBG1_03) show in the solar principal and orthogonal plane a sequence in the reflectance values from the forward to the backward viewing directions (Figure 7-10A, Figure 7-10B). The ANIF data show higher reflectance values in the backward viewing directions and lower reflectance values in the forward viewing directions compared to the nadir viewing position (Figure 7-10A). The highest reflectance variation is visible in the solar principal plane (Figure 7-10B). The ANIF values in the solar principal plane range from 1.1 to 1.55 in the VIS and NIR wavelength regions of the backward viewing directions, whereas in the forward viewing directions the ANIF values

range from 0.85 to 0.95 in the VIS and NIR wavelength regions. The reflectance variation within the solar orthogonal plane behaves like the reflectance variability within the solar principal plane but with ANIF values ranging from 1.05 to 1.2 in the VIS and NIR wavelength regions of the backward viewing directions, and 0.8 – 0.95 in the VIS and NIR wavelength regions of the forward viewing directions.

The prostrate dwarf shrub community (FBG3_03) shows ANIF data of equal to higher reflectance values in the backward viewing directions and lower reflectance values in the forward viewing directions compared to the nadir viewing position (Figure 7-10A, Figure 7-10B). The ANIF values in the solar principal plane range from 1.0 to 1.45 in the VIS and 0.9 – 1.1 in the NIR wavelength regions of the backward viewing directions, whereas in

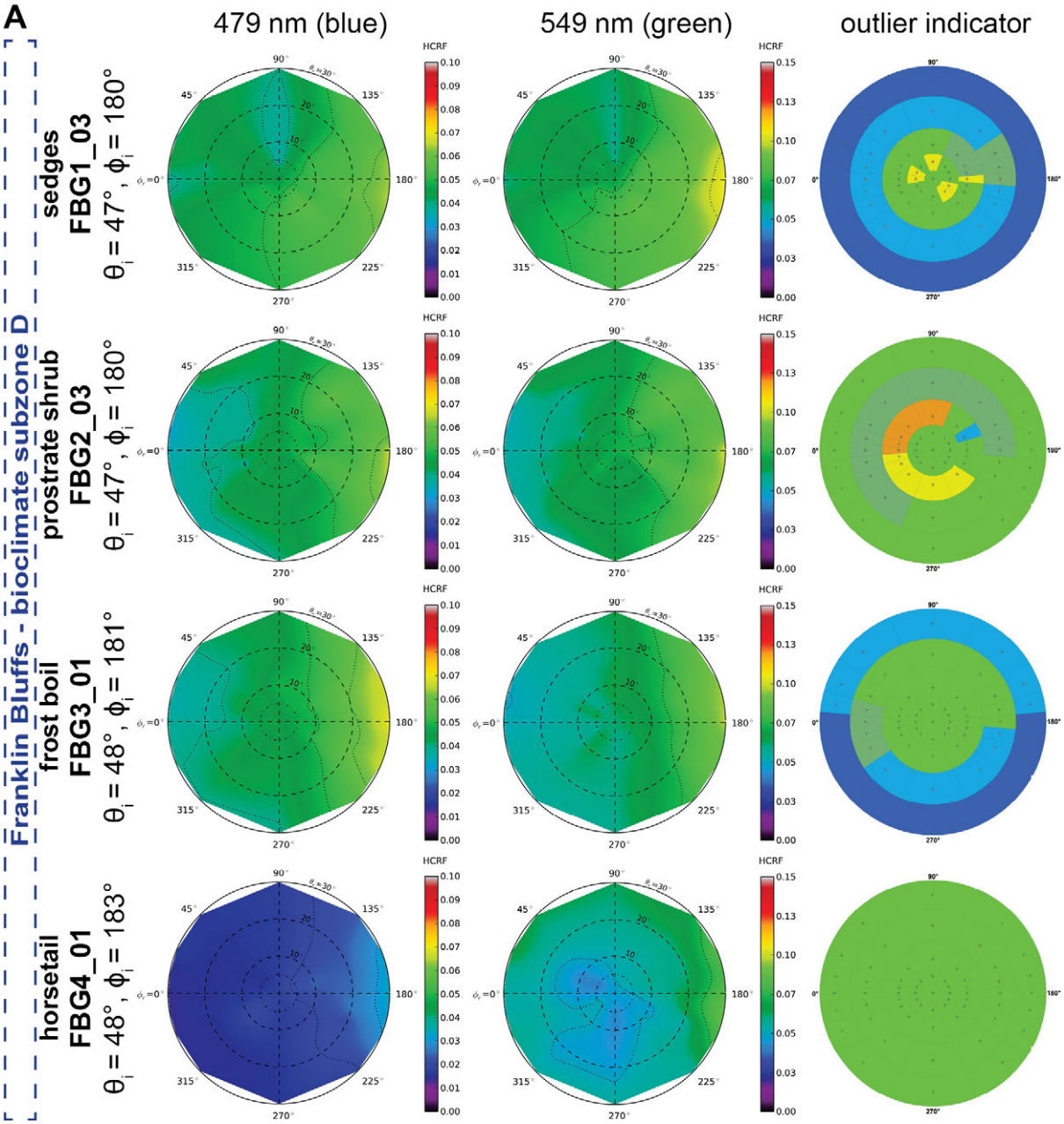

Figure 7-9: HCRF visualization of the Franklin Bluffs spectro-goniometer measurements performed at solar noon. (**A**) HCRF visualization of the blue (479 nm) and green (549 nm) EnMAP bands. ***Note:*** See Figure 7-2 for legend of the outlier indicator graphics.

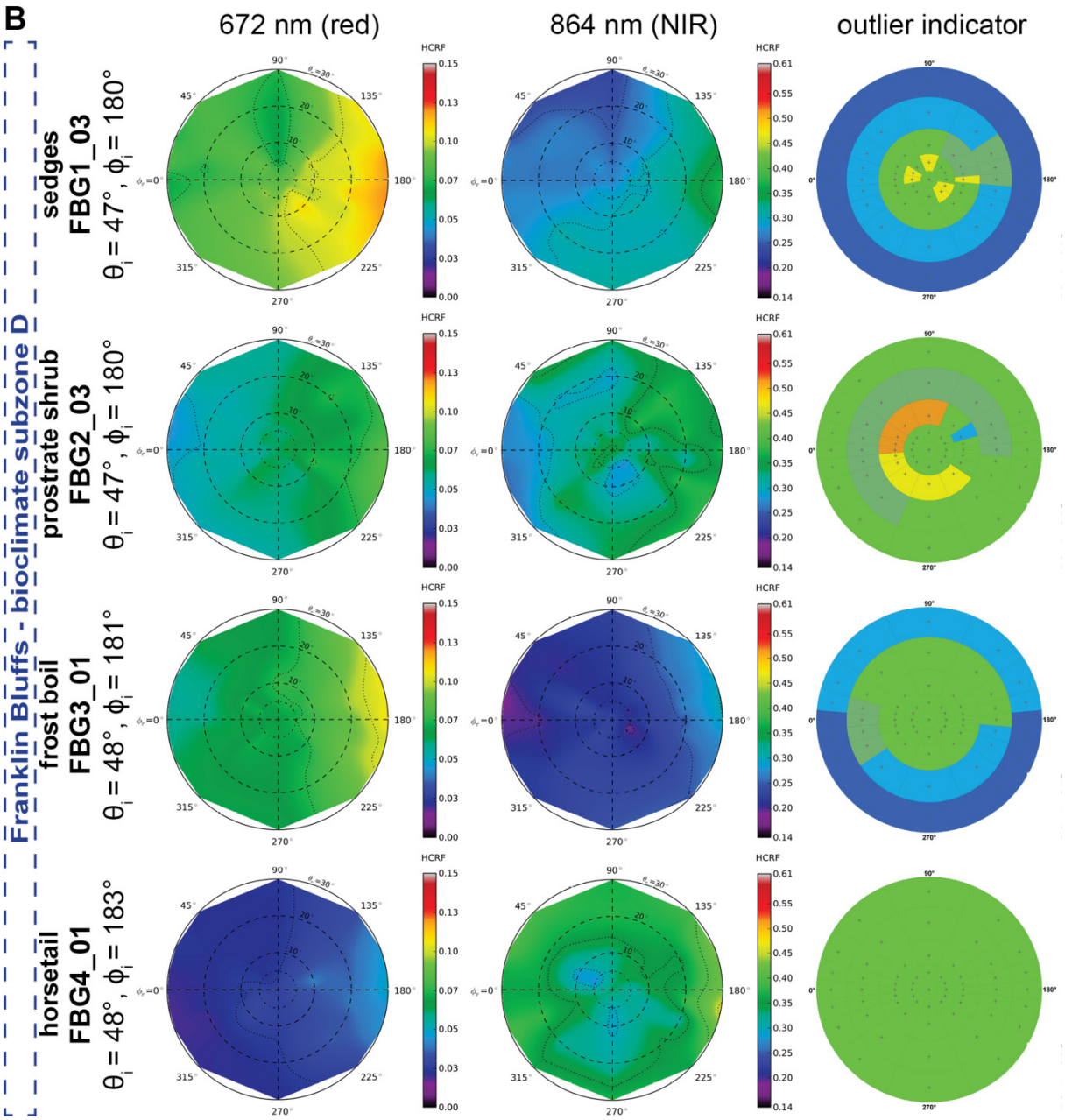

Figure 7–9 ***(cont.)*****:** HCRF visualization of the Franklin Bluffs spectro-goniometer measurements performed at solar noon. (**B**) HCRF visualization of the red (672 nm) and NIR (864 nm) EnMAP bands. ***Note:*** See Figure 7-2 for legend of the outlier indicator graphics.

the forward viewing directions the ANIF values range from 0.7 to 0.95 in the VIS and NIR wavelength regions. In the solar orthogonal plane all ANIF values in the VIS and NIR wavelength regions of the prostrate dwarf shrub community are lower than in the nadir viewing position, and therefore show a bowl shape distribution.

In the solar principal plane, the ANIF data of the nonsorted circles plant community (FBG3_01) perform nearly identical to the ANIF data of the prostrate dwarf shrub community (FBG3_03) (Figure 7-10A, Figure 7-10B). The highest reflectance variation is viewable in the solar principal plane. The ANIF values in the backward viewing directions of the solar principal plane range from 1.1 to 1.6 in the VIS and 0.95 – 1.35 in the NIR wavelength region, whereas the ANIF values range from 0.85 to 1.0 in the VIS and NIR wavelength

regions of the forward viewing directions. In the solar orthogonal plane the ANIF values are clumped around an ANIF value of 1.0, and show a reflectance variation from up to 20 % in the red and NIR wavelength regions.

The ANIF values of the horsetail community (FBG4_01) show higher reflectance values in the backward viewing directions compared to the nadir viewing position, whereas in the forward viewing directions the ANIF values are clumped around an ANIF value of 1.0 in the VIS and NIR wavelength regions (Figure 7-10A, Figure 7-10B). In the backward viewing directions the ANIF values range from 1.05 to 1.95 in the VIS and 1.0 – 1.3 in the NIR wavelength region. Like in the FBG3_01 spectro-goniometer measurement, the ANIF values in the solar orthogonal plane are clumped around an ANIF value of 1.0,

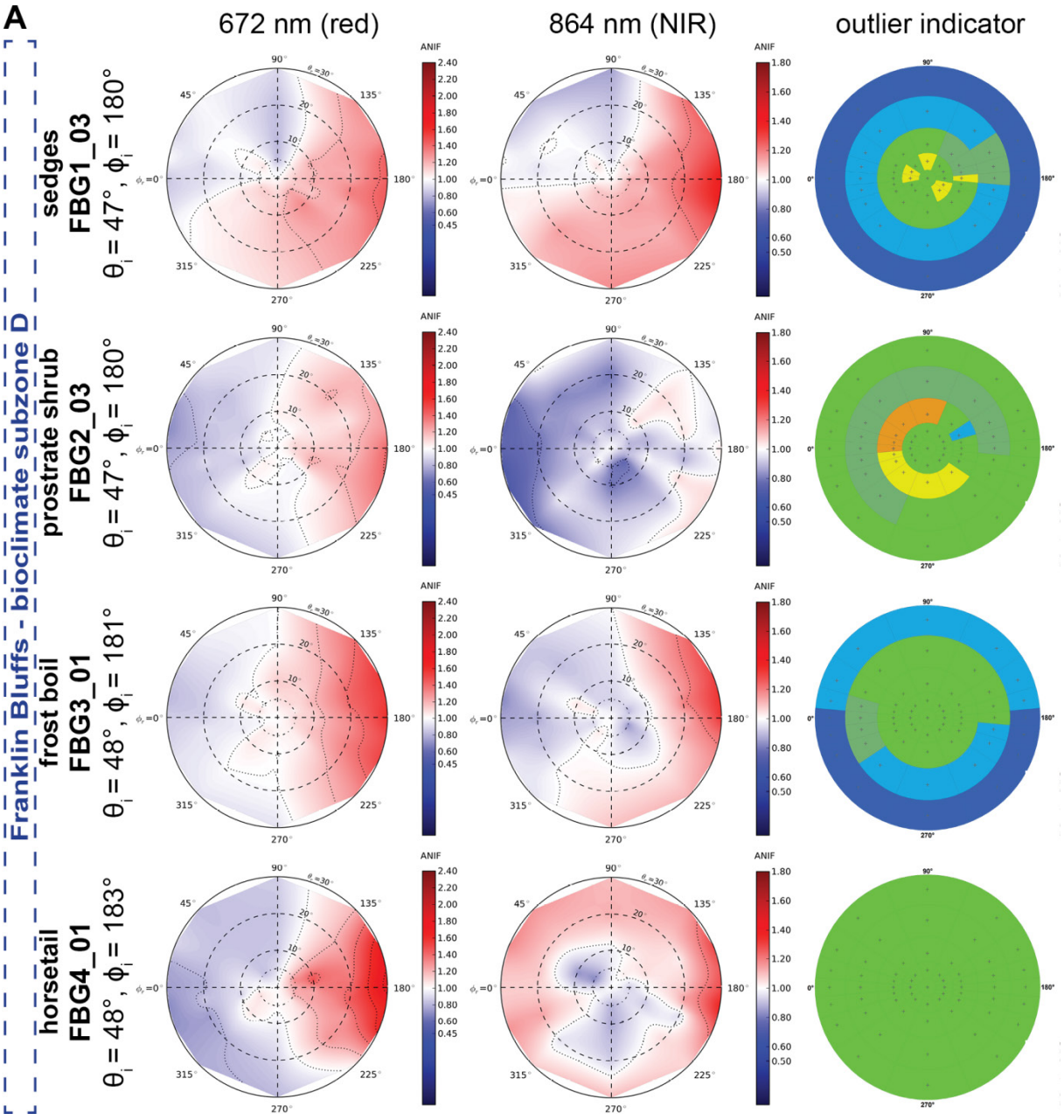

Figure 7-10: ANIF visualization of the Franklin Bluffs spectro-goniometer measurements performed at solar noon. (**A**) ANIF visualization of the red (672 nm) and NIR (864 nm) EnMAP bands. ***Note:*** See Figure 7-2 for legend of the outlier indicator graphics.

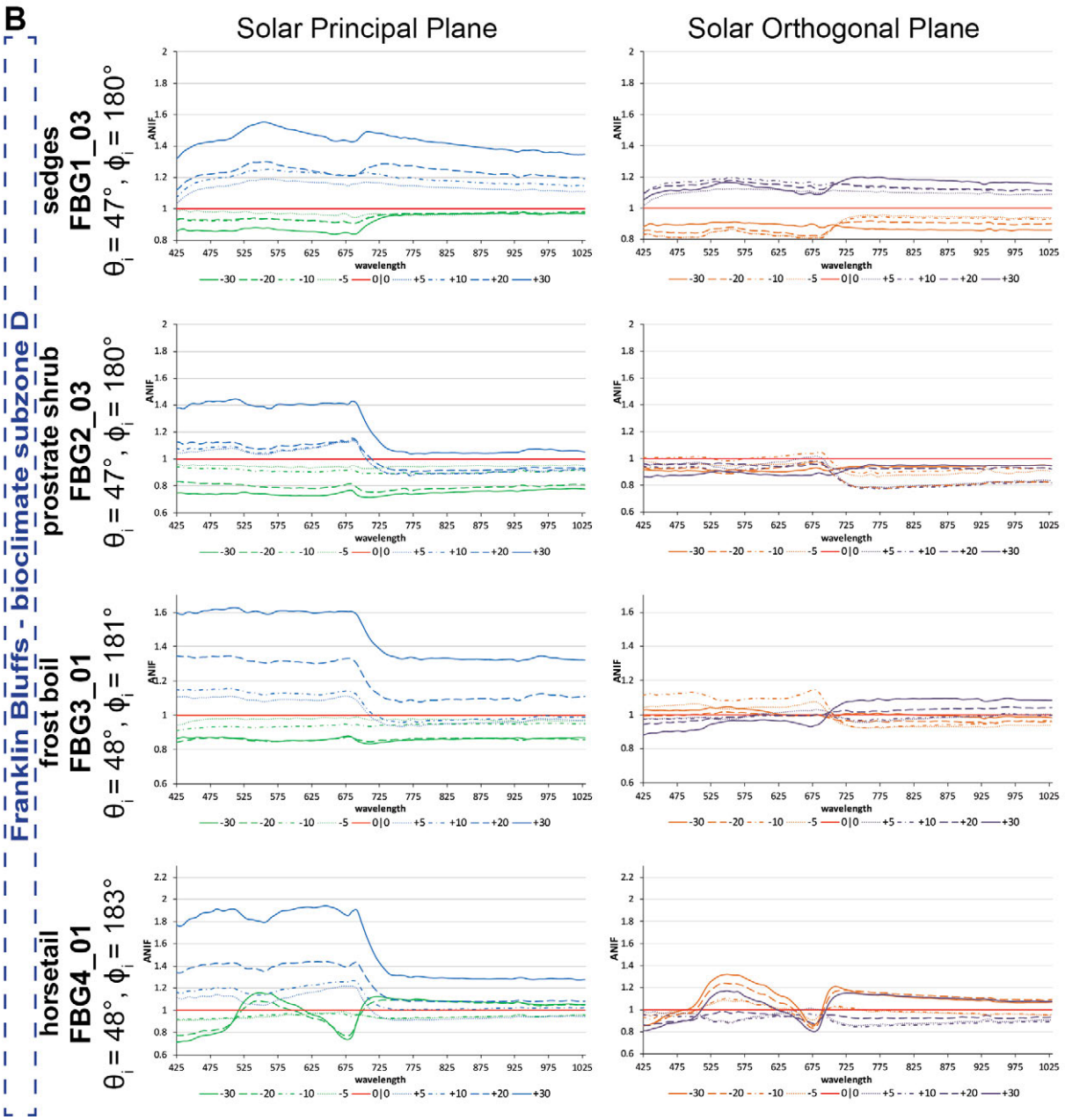

Figure 7–10 ***(cont.)*****:** ANIF visualization of the Franklin Bluffs spectro-goniometer measurements performed at solar noon. (**B**) ANIF development in the solar principal and orthogonal plane of the EnMAP bands.

and show a reflectance variability of up to 30 %.

ANIX: In the ANIX development along the solar principal plane of all four Franklin Bluffs spectro-goniometer measurements is notable in that there is higher degree of reflectance anisotropy in the VIS wavelength region than in the NIR wavelength region (Figure 7-11). In contrast, the degree of reflectance anisotropy within the orthogonal plane of all four study sites equals in the VIS and NIR wavelength regions. The ANIX values in the solar principal plane of the non-tussock sedge tundra (FBG1_03) are within the range of 1.5 to 1.75 in the VIS and drop to 1.4 – 1.5 in the NIR wavelength region. For the prostrate dwarf shrub community (FBG2_03) and the nonsorted circles plant community (FBG3_01) the ANIX values in the solar principal plane of the VIS wavelength region are around 1.9 and drop to

1.4 – 1.55 in the NIR. The ANIX values of the horsetail community (FBG4_01) show a maximum of 2.5 in the blue (425 – 500 nm) and red (around 670 nm) wavelength regions, where the ANIX values in the NIR wavelength region drop to 1.4.

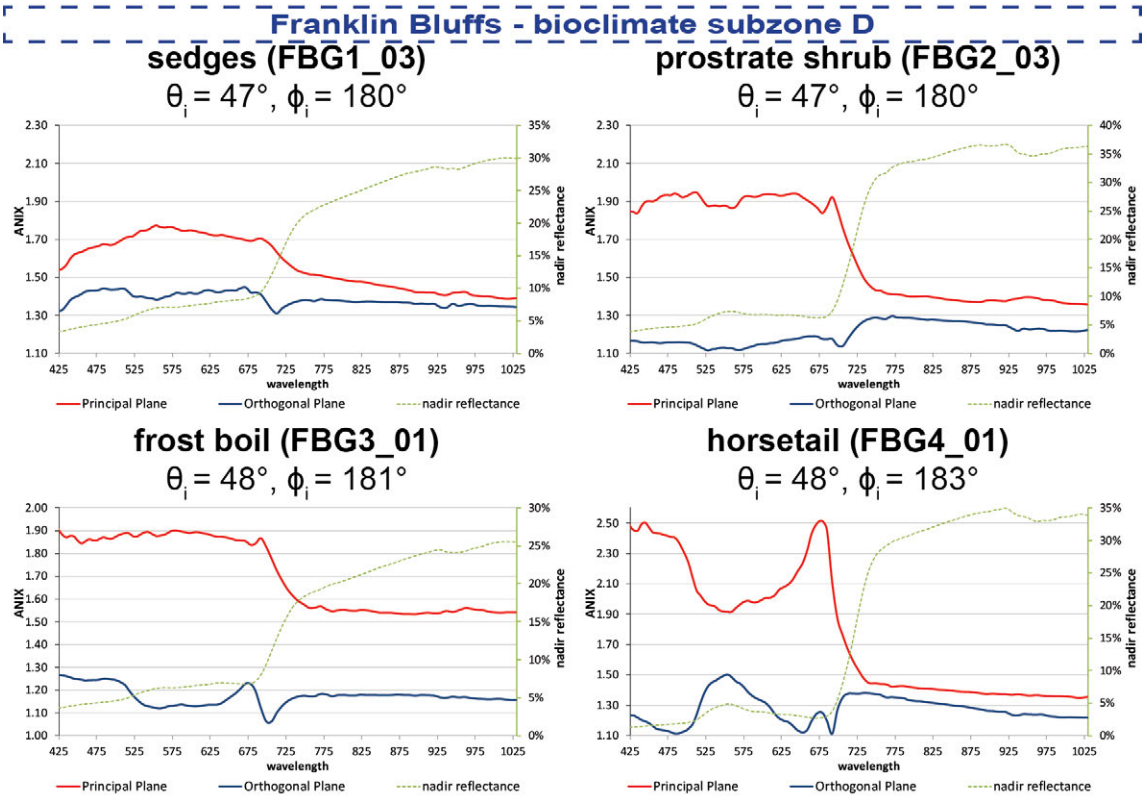

Figure 7-11: ANIX visualization in the solar principal and orthogonal plane of the Franklin Bluffs spectro-goniometer measurements performed at solar noon in comparison to the nadir view reflectance spectra.

7.2 Influence of High Sun Zenith Angles on the Reflectance Anisotropy

The change in illumination zenith angle is an important influence factor on BRDF effects. In order to investigate the influence of high SZAs (in arctic latitudes always greater than 43° [*Kääb*, 2008]) on the spectro-directional reflectance characteristics of Low Arctic vegetation, the main zonal plant communities of Alaskan bioclimate subzone D and E were spectro-goniometer measured under varying SZAs. Since the zonal plant community of subzone E is MAT, the tussock sedge (HVG1) site were measured at SZAs of 46° (HVG1_03), 50° (HVG1_02), and 56° (HVG1_01). Figure 7-12A shows the R_{nadir} spectra of the three MAT spectro-goniometer measurements at the Happy Valley study location. Where the R_{nadir} spectrum of the measurement at solar noon (SZA = 46°) fits to the reflectance spectra of MAT (Figure 6-5), the measurements at the SZAs of 50° and 56° show the same reflectance shape but with an offset (Figure 7-12A). The visualization of the irradiance spectra (Figure 7-12C) of the MAT measurements point out that this offset in the reflectance is inversely connected to the irradiance spectra. Where the irradiance is decreasing with increasing SZAs, the offset in the reflectance spectra is increasing with increasing SZAs.

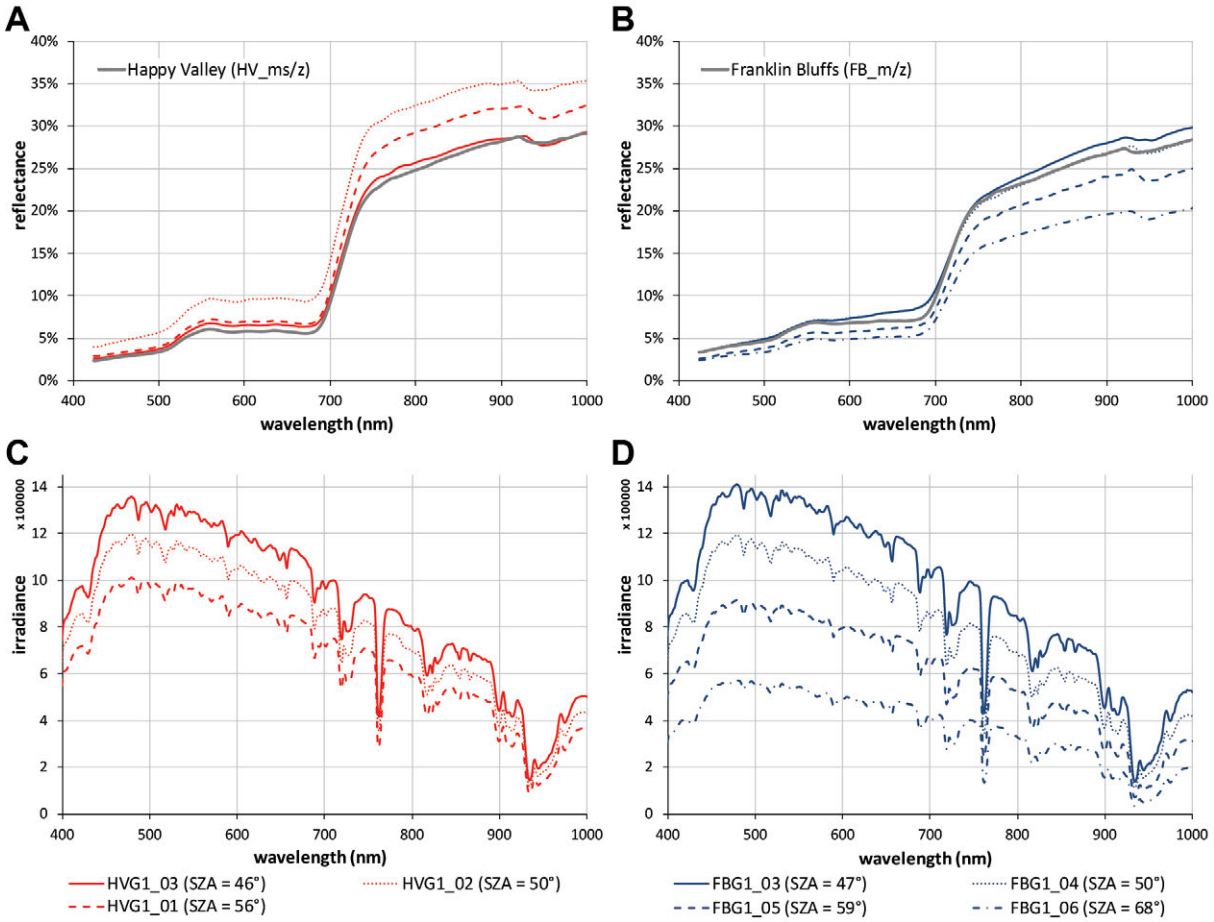

Figure 7-12: Comparison of the nadir view reflectance spectra of the MAT and MNT spectro-goniometer measurements under varying sun zenith angles. (**A**) Comparison of the three nadir view reflectance spectra of MAT under varying sun zenith angles with the zonal plant community. (**B**) Comparison of the four nadir view reflectance spectra of MNT under varying sun zenith angles with the zonal plant community. (**C**) Comparison of the irradiance profiles of the MAT spectro-goniometer measurements under varying sun zenith angles. (**D**) Comparison of the irradiance profiles of the MNT spectro-goniometer measurements under varying sun zenith angles.

The influence of changing SZAs on the spectro-directional reflectance of MNT, the zonal plant community of subzone D, was investigated at the Franklin Bluffs study location. The non-tussock sedge site (FBG1) was measured at SZAs of 47° (FBG1_03), 50° (FBG1_04), 59° (FBG1_05), and 68° (FBG1_06). The R_{nadir} spectra of the four MNT spectro-goniometer measurements are visualized in Figure 7-12B. Where the R_{nadir} spectra of the measurements at solar noon (SZA = 47°) and 50° fits to the reflectance spectra of MNT (Figure 6-5), the measurements at SZAs of 59° and 68° show the same reflectance shape but with an offset (Figure 7-12B). In contrast to the MAT measurements, this offset in the reflectance is positively connected to the irradiance spectra of the MNT measurements (Figure 7-12D). Therefore, when the irradiance is decreasing with increasing SZAs, the offset in the reflectance spectra is also decreasing with increasing SZAs.

7.2.1 MAT (Happy Valley)

The visualization of the MAT spectro-directional reflectance data (HCRF data) under varying SZAs of the blue (479 nm), green (549 nm), red (672 nm) and NIR (864 nm) EnMAP bands

can be found in Appendix C.5. Figure 7-13 shows the visualization of the MAT ANIF data under varying SZAs of the red (672 nm) and NIR (864 nm) EnMAP bands as 2D polar plots. The outlier indicator of the spectro-goniometer measurements shows that only small atmospheric and solar changes occurred during the measurements with SZAs of 46° and 50°. In contrast, during the HVG1_01 (SZA = 56°) spectro-goniometer measurements stronger atmospheric and solar changes occurred that had to be corrected (Figure 7-13). The ANIF development in the solar principal and orthogonal plane of MAT for the three SZAs for all EnMAP bands is shown in Figure 7-14.

ANIF: The HCRF and ANIF characteristics of the tussock sedge (MAT) plot measured at solar noon (HVG1_03 with SZA = 46°) have already been described in Chapter 7.1.3. Therefore in condensed form, the ANIF values in the solar principal plane at a SZA of 46° range from 0.50 to 1.40 in the VIS and 0.45 to 1.42 in the NIR wavelength region (Figure 7-14). Only the ANIF values in the +20° and +30° backward viewing directions have ANIF values above 1.0 in the VIS and NIR wavelength regions. All other viewing directions show ANIF values between 0.45 and 0.9. In the VIS wavelength region (mainly in the blue wavelength region) of the solar orthogonal plane the ANIF values in the backward

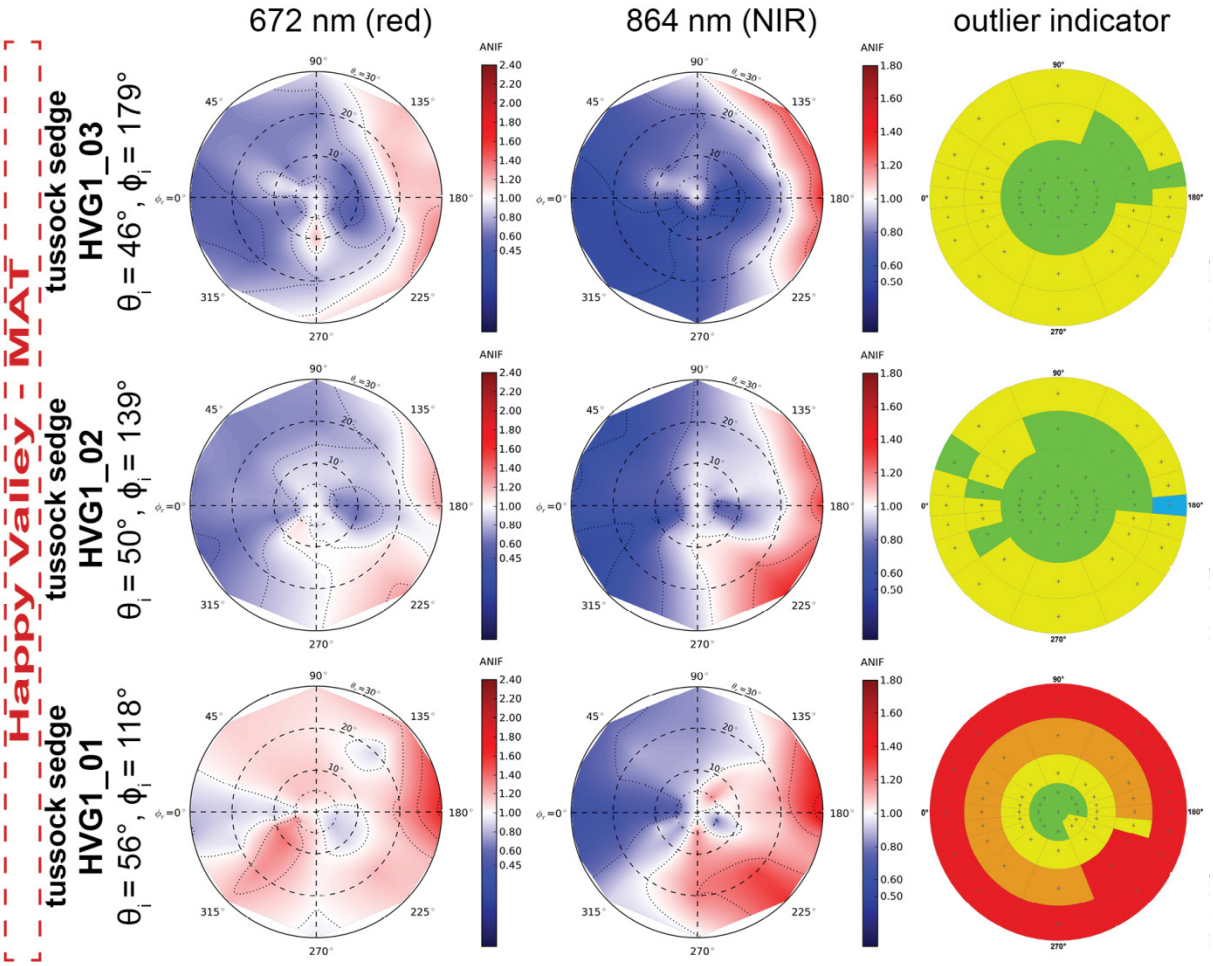

Figure 7-13: ANIF visualization of the red (672 nm) and NIR (864 nm) EnMAP bands of the MAT spectro-goniometer measurements under varying sun zenith angles. ***Note:*** See Figure 7-2 for legend of the outlier indicator graphics.

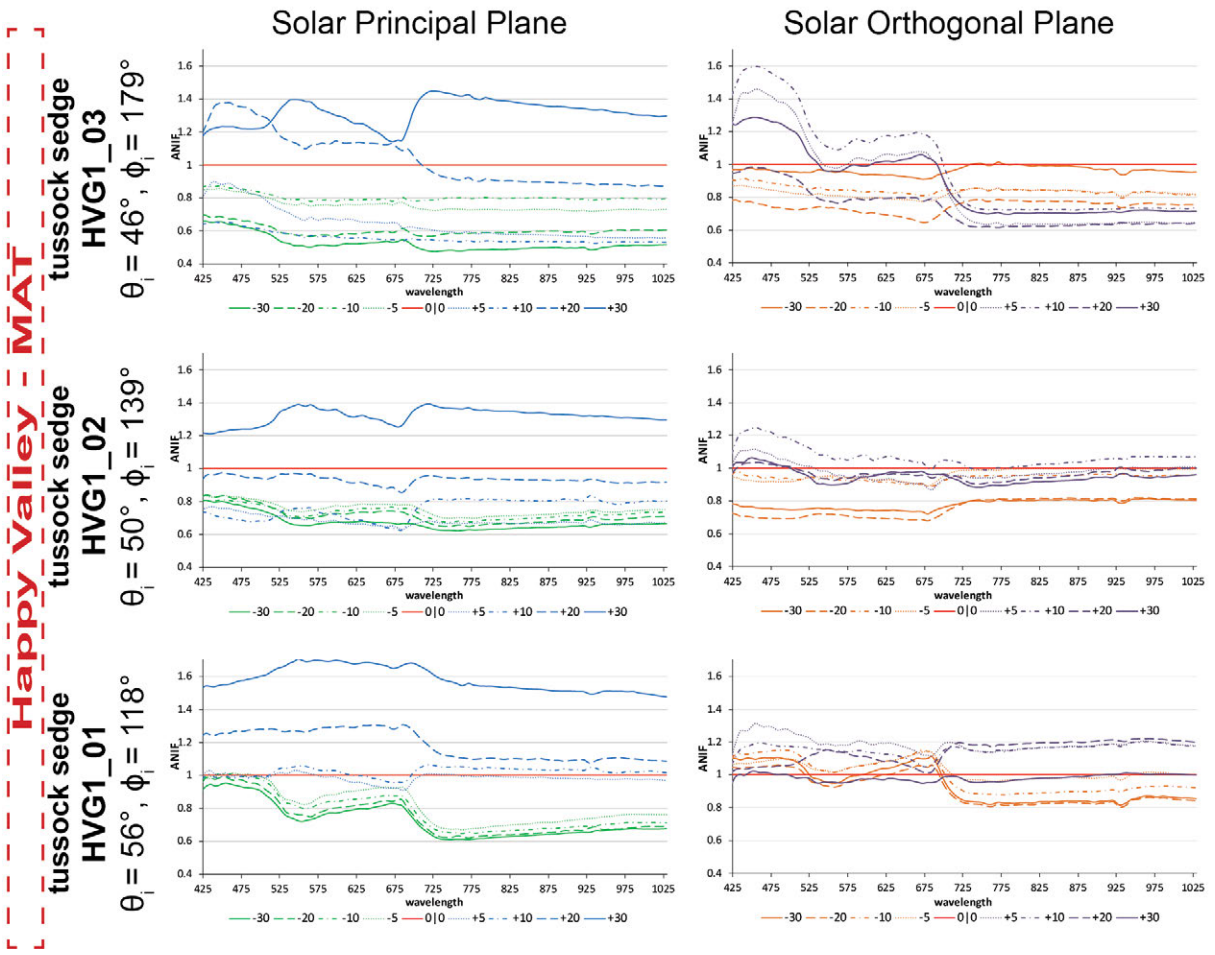

Figure 7-14: ANIF development in the solar principal and orthogonal plane of the MAT spectro-goniometer measurements under varying sun zenith angles for all EnMAP bands.

viewing directions increase up to 1.6, where in the NIR wavelength region the ANIF values are below 1.0. Moreover, all ANIF values in the solar orthogonal plane of the forward viewing directions are lower than in the nadir viewing position.

At a SZA of 50° (HVG1_02) the ANIF values in the solar principal plane in all viewing directions, expect in the +30° backward viewing direction, range from 0.6 to 1.0 in the VIS and NIR wavelength regions. The ANIF values of the +30° backward viewing direction are between 1.2 and 1.4 in the VIS and NIR wavelength regions. In the solar orthogonal plane the ANIF values in the VIS and NIR wavelength regions at a SZA of 50° vary from 0.95 to 1.3 in the backward viewing directions, and range from 0.7 to 1.0 in the forward viewing directions.

The ANIF values in the backward viewing directions in the solar principal plane at a SZA of 56° (HVG1_01) range from 0.95 to 1.7 in the VIS and 1.0 – 1.5 in the NIR wavelength regions, whereas the ANIF values in the forward viewing directions vary from 0.7 to 1.0 in the VIS and 0.6 – 1.0 in the NIR wavelength regions. In the solar orthogonal plane the ANIF values are clumped around the nadir viewing position with an ANIF value of 1.0, and show a reflectance variation of up to 25 %.

ANIX: The spectral dependence of the ANIX values along the solar principal plane of MAT at a SZA of 46° (Figure 7-15A) is unexpected. The ANIX values in the blue (425 – 500 nm)

and the red maximum absorption depth (~ 670 nm) range between 2.1 and 2.2, where the ANIX values in the green to orange wavelength region are between 2.3 and 2.7. In the NIR wavelength region the ANIX values start at 3.0 and slowly decrease to 2.5 with higher wavelengths. The ANIX graphs at the SZAs of 50° and 56° follow this trend with an offset to lower ANIX values. In the solar orthogonal plane (Figure 7-15B) the ANIX values at a SZA of 46° are between 1.45 and 2.05, where at a SZA of 50° the ANIX values range from 1.3 to 1.8. At a SZA of 56° the ANIX values in the solar orthogonal plane vary between 1.2 to 1.3 in the VIS and drop to 1.4 – 1.5 in the NIR wavelength regions. In summary, at all three SZAs of MAT vegetation it is observable that the degree of reflectance anisotropy is higher in the NIR than in the VIS wavelength region.

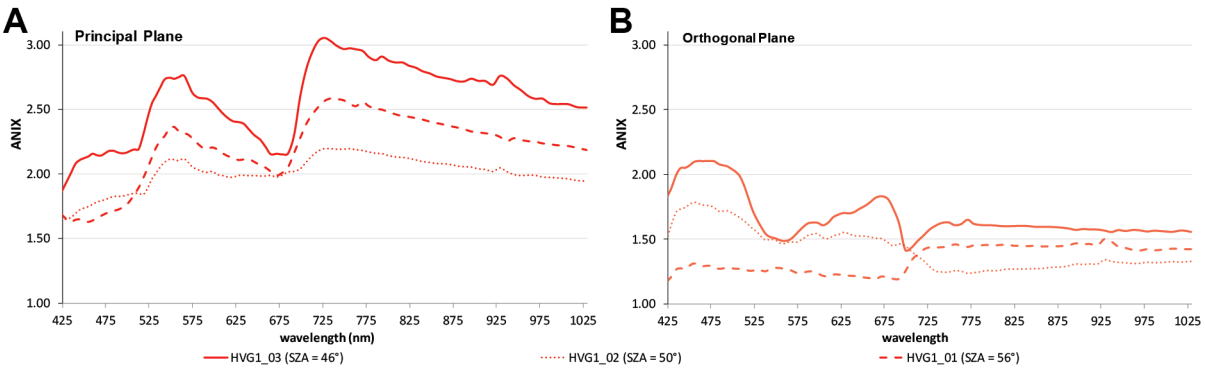

Figure 7-15: ANIX visualization in the solar principal (**A**) and orthogonal (**B**) plane of the MAT spectro-goniometer measurements under varying sun zenith angles for all EnMAP bands.

7.2.2 MNT (Franklin Bluffs)

The HCRF data visualization under varying SZAs of the MNT plant community for the blue (479 nm), green (549 nm), red (672 nm) and NIR (864 nm) EnMAP bands can be found in Appendix C.1. The ANIF data visualization of MNT at the four SZAs of the red (672 nm) and NIR (864 nm) EnMAP bands as 2D plots are shown in Figure 7-16. The outlier indicator of the spectro-goniometer measurements of MNT vegetation at a SZA of 47° (FBG1_03) and a SZA of 68° (FBG1_06) show that higher atmospheric and solar changes occurred during these measurements and had to be corrected. In contrast, during the measurements at a SZA of 50° (FBG1_04) and 59° (FBG1_05) only small atmospheric and solar changes occurred. The ANIF development in the solar principal and orthogonal plane of MNT for the four SZAs for all EnMAP bands is shown in Figure 7-17.

ANIF: Again, the HCRF and ANIF characteristics of the non-tussock sedge (MNT) plot measured at solar noon (FBG1_03 with SZA = 47°) have already been described in Chapter 7.1.4. The main findings in condensed form are that the ANIF data in the solar principal and orthogonal plane show a sequence in the reflectance values from the forward to the backward viewing directions (Figure 7-16, Figure 7-17). The ANIF data show higher reflectance values in the backward viewing directions (1.1 to 1.55 in the VIS and NIR wavelength regions) and lower reflectance values in the forward viewing directions (0.85 to 0.95 in the VIS and NIR wavelength regions) compared to the nadir viewing position. The reflectance variation within

the solar orthogonal plane behaves like the reflectance variability within the solar principal plane but with ANIF values ranging from 1.05 to 1.2 in the backward viewing directions, and 0.8 – 0.95 in the forward viewing directions.

At a SZA of 50° (FBG1_04) the range of the ANIF values in the solar principal plane in the VIS and NIR wavelength regions behave like the ANIF values at 47°. The main difference is that the graphs of the backward viewing directions show clearer separation in the VIS wavelength region. In the solar orthogonal plane the ANIF values in the VIS and NIR wavelength regions at a SZA of 50° start to agglomerate. While the ANIF values in the backward viewing directions vary from 1.0 to 1.3 in the VIS and NIR wavelength regions, the ANIF values in the forward viewing directions vary from 0.85 to 1.15. The ANIF values

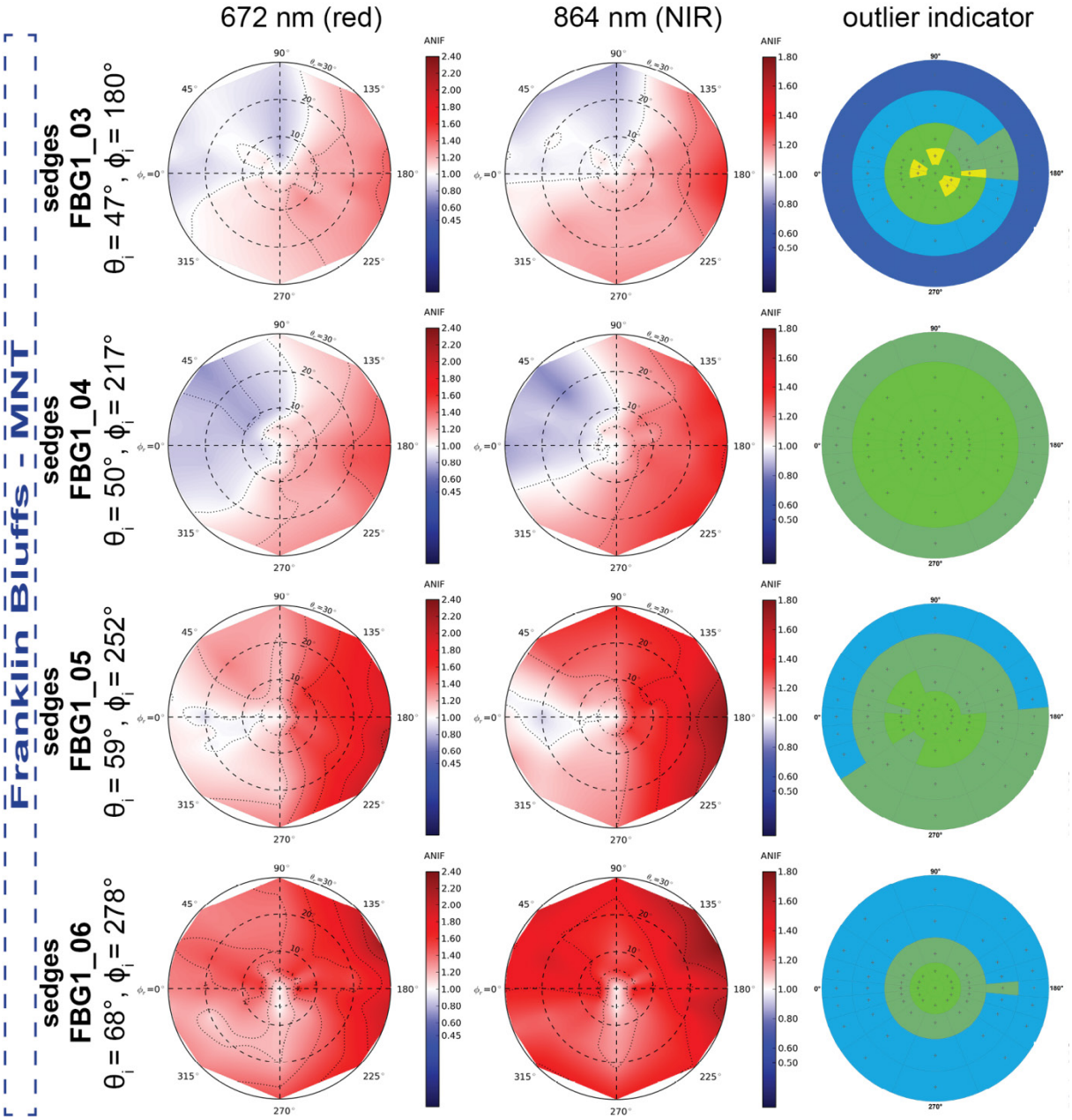

Figure 7-16: ANIF visualization of the red (672 nm) and NIR (864 nm) EnMAP bands of the MNT spectro-goniometer measurements under varying sun zenith angles. ***Note:*** See Figure 7-2 for legend of the outlier indicator graphics.

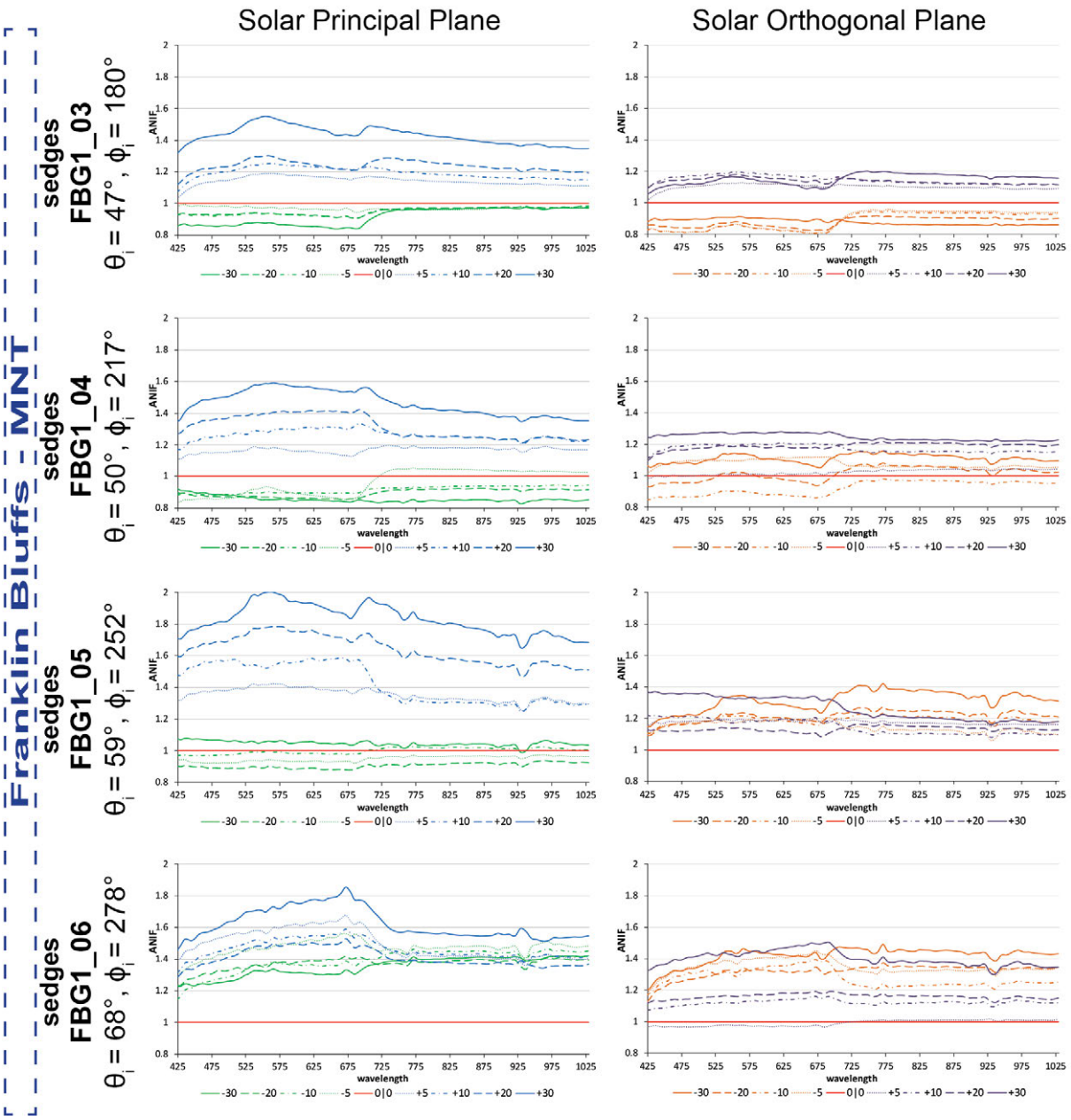

Figure 7-17: ANIF development in the solar principal and orthogonal plane of the MNT spectro-goniometer measurements under varying sun zenith angles for all EnMAP bands.

within the solar orthogonal plane start to display a bowl shape distribution with the lowest ANIF values in the nadir viewing position, and increasing ANIF values with increasing forward and backward viewing zenith angles (Figure 7-17).

At a SZA of 59° (FBG1_05) the ANIF values in the solar principal plane also start to develop a bowl shape distribution with the lowest ANIF values in the nadir viewing position and increasing ANIF values with increasing forward and backward viewing zenith angles (Figure 7-17), whereas in the solar orthogonal plane the bowl shape in the ANIF data is fully developed. In the solar principal plane the ANIF values in the backward viewing directions range from 1.3 to 2.0 in the VIS and NIR wavelength regions, while the forward viewing directions show ANIF values between 0.9 and 1.1. In the solar orthogonal plane the ANIF values are clumped around an ANIF value of 1.2 with a reflectance variation of up to 15 %.

The ANIF values of MNT vegetation at a SZA of 58° (FBG1_06) show in the solar principal and orthogonal plane a fully developed bowl shape distribution with increasing ANIF values with increasing forward and backward viewing zenith angles (Figure 7-17). In the solar principal plane the ANIF values range from 1.2 to 1.85 in the VIS and NIR wavelength regions, where in the solar orthogonal plane the ANIF values vary from 1.0 to 1.5 in the VIS and NIR wavelength regions.

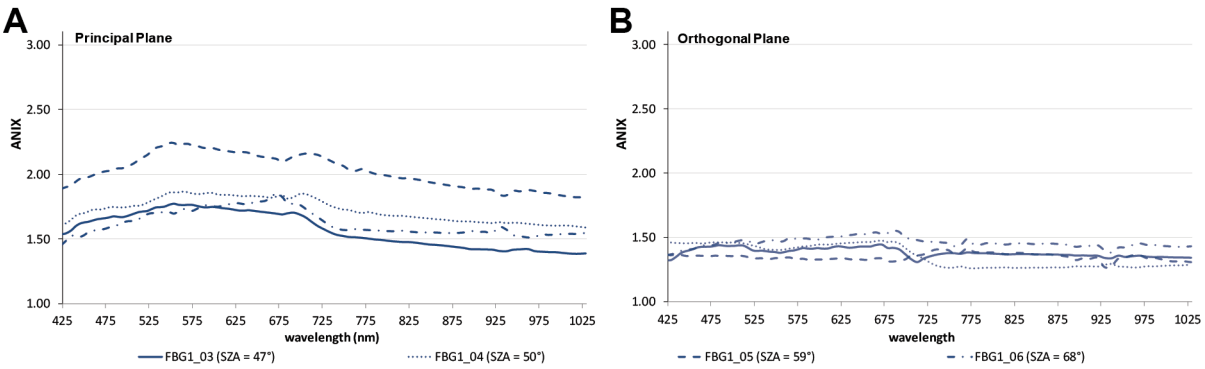

Figure 7-18: ANIX visualization in the solar principal (**A**) and orthogonal (**B**) plane of the MNT spectro-goniometer measurements under varying sun zenith angles for all EnMAP bands.

ANIX: The ANIX development along the solar principal plane of MNT vegetation at all four SZAs shows that there is a slightly higher degree of reflectance anisotropy in the VIS wavelength region than in the NIR wavelength region (Figure 7-18A). In contrast, the reflectance anisotropy within the orthogonal plane (Figure 7-18B) at all four SZAs is similar in the VIS and NIR wavelength regions and is clumped around an ANIX value of 1.4 with a variation of up to 10 %. The ANIX values in the solar principal plane at a SZA of 47° are in the range from 1.5 to 1.75 in the VIS and jump to 1.4 – 1.5 in the NIR wavelength region. The ANIX graphs at the SZAs of 50°, 59°, and 68° follow this trend with an offset, where measurements with higher SZA show a higher degree of reflectance anisotropy.

7.3 Variability in Multi-Angular Remote Sensing Products of Low Arctic Tundra Environments

One of the main questions regarding the application of multi-angle remote sensing in Arctic environments is the extent of the influence of BRDF effects on vegetation remote sensing products. Since vegetation remote sensing products, such as the relative pigment absorption depth and NDVI, are calculated from different wavelength regions which are differently influenced by BRDF effects, the spectro-directional characteristics of the products can deviate significantly from the spectro-directional characteristics of the reflectance data of the surface [*Küster*, 2011]. The results of the spectro-directional analysis of the relative absorption depths in the blue (400 – 550 nm) and red (550 – 750 nm) wavelength regions as well as of the EnMAP NDVI for all eight examined tundra vegetation communities measured at solar noon are presented in Table 7-1 and Figure 7-19, while the results of the spectro-directional analysis of MAT and MNT vegetation under varying SZAs are presented in Table 7-2 and Figure 7-20.

7.3.1 Spectro-Directional Variability of Different Low Arctic Plant Communities

The spectro-directional analysis of the nadir normalized relative absorption depths in the blue and red wavelength regions indicates that the BRDF characteristics of the relative absorption depth products of all study sites behave similarly within their study locations (Table 7-1). At the Vaskiny Dachi study location, the dwarf shrub-moss and grazed dwarf shrub-moss tundra vegetation show in the nadir normalized blue relative absorption depth values between 0.73 and 1.14 over all viewing geometries, while the red relative absorption depth values range from 0.69 and 1.14. The tussock sedge and erect dwarf shrub plots at the Happy Valley study location have nadir normalized values between 0.59 and 1.28 for the blue relative absorption depth and between 0.47 and 1.28 for the red relative absorption depth within the ManTIS hemisphere. The non-tussock sedge, prostrate dwarf shrub and frost boil (nonsorted circles) vegetation communities at the Franklin Bluffs study location have nadir normalized values between 0.82 and 1.22 for the blue and values between 0.56 and 1.22 for the red relative absorption depth. The only exception is the horsetail community at the Franklin Bluffs study location which shows in the nadir normalized blue relative absorption depth values between 0.82 and 1.68 over all viewing geometries, while the values in the red relative absorption depth range from 0.65 to 1.68. The BRDF effects on the relative absorption depths in the blue and red wavelength regions are visualized in Figure 7-19A and in Figure 7-19B.

Table 7-1: Minima and maxima of the nadir normalized remote sensing products (relative blue absorption depth, relative red absorption depth, EnMAP NDVI) over all viewing geometries for the main plant communities at the Vaskiny Dachi, Happy Valley, and Franklin Bluffs study sites.

Site	SZA	Relative Blue Absorption Depth		Relative Red Absorption Depth		$NDVI_{EnMAP}$	
		min	max	min	max	min	max
moss tundra	55°	0.79	1.14	0.69	1.14	0.90	1.03
grazed moss tundra	61°	0.73	1.07	0.82	1.07	0.90	1.04
tussock sedge	46°	0.59	1.28	0.47	1.28	0.70	1.09
erect shrub btwn tussock	46°	0.66	1.12	0.56	1.12	0.88	1.02
non-tussock sedge	47°	0.87	1.22	0.85	1.22	0.90	1.10
prostrate shrub	47°	0.87	1.10	0.63	1.10	0.85	1.03
frost boil	48°	0.82	1.22	0.64	1.22	0.81	1.10
horsetail	48°	0.82	1.68	0.65	1.68	0.92	1.06

The influence of BRDF effects on narrowband NDVIs calculated from the EnMAP bands #47 (center 672 nm) and #73 (center 864 nm) for all tundra communities (n = 8) is lower over than on the relative absorption depth products (Table 7-1, Figure 7-19). At the Vaskiny Dachi study location, the dwarf shrub- moss tundra community show nadir normalized NDVI values between 0.90 and 1.03 over all viewing geometries, where the grazed dwarf shrub-moss tundra community has values between 0.90 and 1.04. Therefore, the maximum variation in the

EnMAP NDVI data is 10 % within the 30° forward and backward viewing directions. The tussock sedge (MAT) plant community at Happy Valley shows a maximum NDVI variation of up to 30 % within the ManTIS hemisphere. The nadir normalized NDVI values range from 0.70 to 1.09. The erect dwarf shrub community shows with nadir normalized NDVI values between 0.88 and 1.02 over all viewing geometries a slightly lower maximum NDVI variability. The maximum variation in the NDVI data for the four Franklin Bluffs spectro-goniometer measurements ranges from 8 % to 19 % within the ManTIS hemisphere. The non-tussock sedge plant community has nadir normalized NDVI values between 0.90 and 1.10 over all viewing geometries; the prostrate shrub community shows values from 0.85 to 1.03,

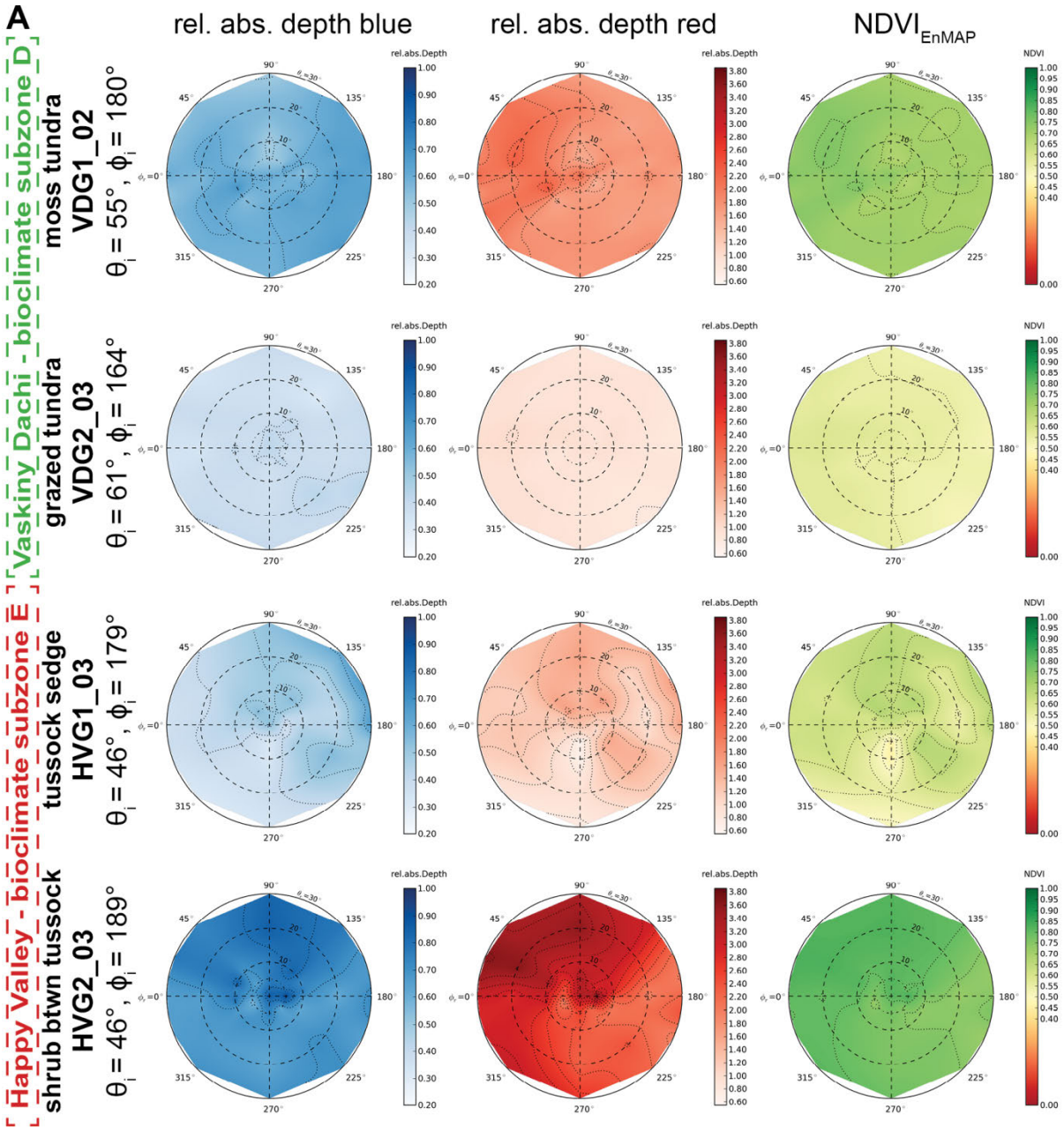

Figure 7-19: Influence of BRDF effects on remote sensing products. (**A**) BRDF Effects in the relative absorption depth of the blue and red wavelength regions, and EnMAP NDVI of the main plant communities at the Vaskiny Dachi and Happy Valley study sites.

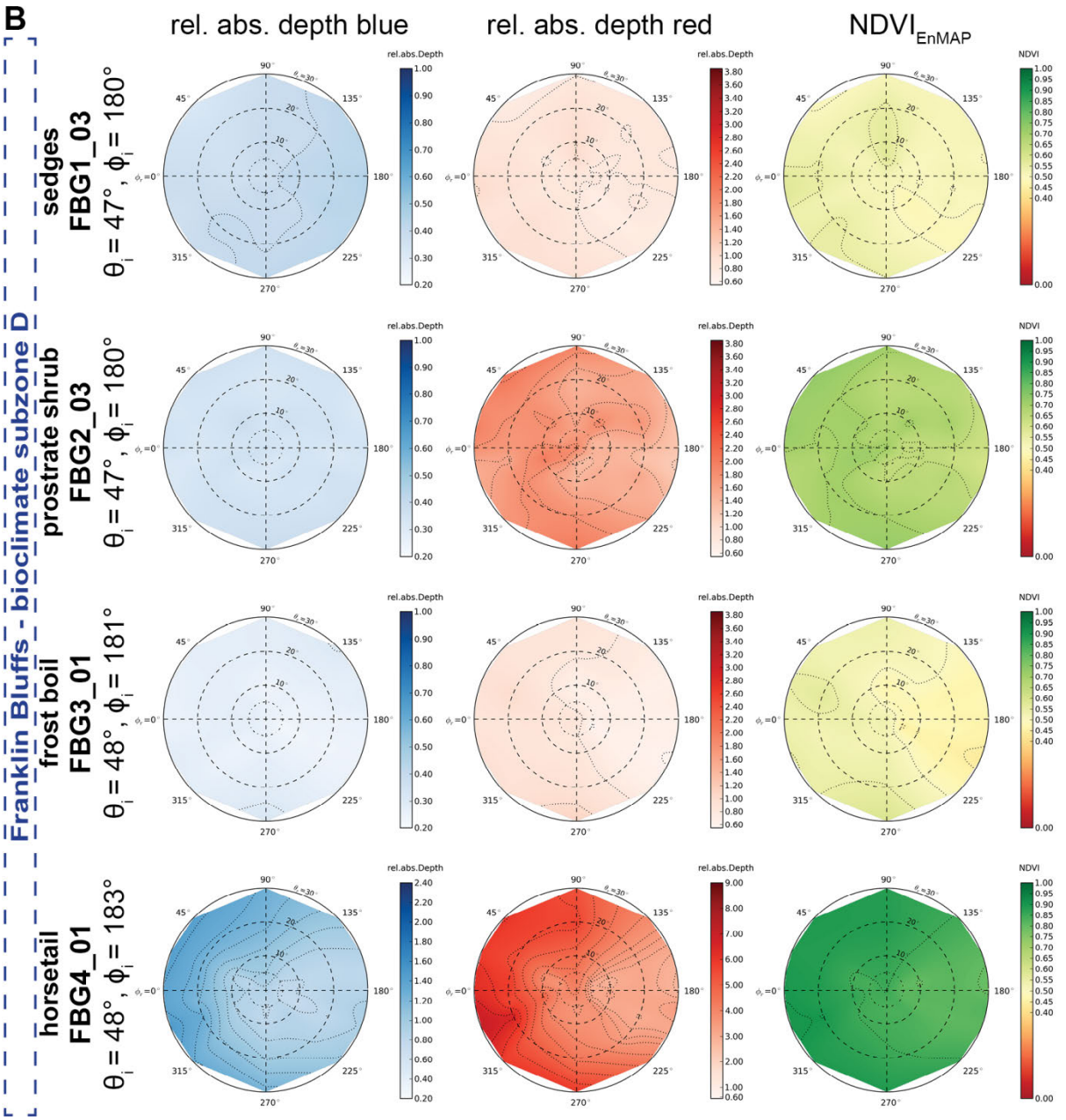

Figure 7–19 ***(cont.)*****:** Influence of BRDF effects on remote sensing products. (**B**) BRDF Effects in the relative absorption depth of the blue and red wavelength regions, and EnMAP NDVI of the main plant communities at the Franklin Bluffs study sites. ***Note:*** All spectro-goniometer measurements were performed at solar noon.

the frost boil community has values between 0.81 and 1.10, and the nadir normalized NDVI values of the horsetail community range from 0.92 to 1.06 within the 30° forward and backward viewing directions.

7.3.2 Spectro-Directional Variability under Varying Sun Zenith Angles

The influence of changing SZAs on the spectro-directional characteristics of the relative absorption depth in the blue and red wavelength regions of MAT vegetation is slightly higher than of MNT vegetation (Table 7-2). At a SZA of 46° (solar noon), MAT vegetation shows nadir normalized values between 0.59 and 1.28 for the blue relative absorption depth and

between 0.47 and 1.28 for the red relative absorption depth over all viewing geometries. With increasing SZAs these MAT relative absorption depth values shift to higher minima and maxima. At a SZA of 50° the nadir normalized relative absorption depth values in the blue wavelength region range from 0.68 to 1.40 and from 0.62 to 1.40 in the red wavelength region within the ManTIS hemisphere, where at a SZA of 56° the values range from 0.62 to 1.20 for the blue and 0.50 to 1.20 for the red relative absorption depths. In contrast, MNT vegetation shows at all analyzed SZAs a lower variation in the spectro-directional data of the blue and red relative absorption depths. At solar noon (SZA = 47°), MNT vegetation has nadir normalized blue relative absorption depth values between 0.87 and 1.22 over all viewing geometries, where the values in the red relative absorption depth range from 0.65 to 1.68 for all viewing geometries. MNT vegetation at a SZA of 50° shows nadir normalized values between 0.89 and 1.29 for the blue relative absorption depth and between 0.80 and 1.29 for the red relative absorption depth within the ManTIS hemisphere. A further increase in the illumination zenith angle to a SZA of 59° shifts the range of the nadir normalized relative absorption depth values in the blue wavelength region to 0.84 – 1.16 and to 0.79 – 1.16 in the red wavelength region, where at a SZA of 68° the values range from 1.00 to 1.22 for the blue and 0.79 to 1.22 for the red relative absorption depths over all viewing geometries.

Table 7-2: Minima and maxima for all viewing geometries of the nadir normalized remote sensing products (relative blue absorption depth, relative red absorption depth, EnMAP NDVI) for MAT and MNT vegetation under varying sun zenith angles.

Site		SZA	Relative Blue Absorption Depth		Relative Red Absorption Depth		$NDVI_{EnMAP}$	
			min	max	min	max	min	max
MAT (tussock sedge)	HVG1_03	46°	0.59	1.28	0.47	1.28	0.70	1.09
	HVG1_02	50°	0.68	1.40	0.62	1.40	0.80	1.15
	HVG1_01	56°	0.62	1.20	0.50	1.20	0.77	1.07
MNT (non-tussock sedge)	FBG1_03	47°	0.87	1.22	0.85	1.22	0.90	1.10
	FBG1_04	50°	0.89	1.29	0.80	1.29	0.87	1.14
	FBG1_05	59°	0.84	1.16	0.79	1.16	0.87	1.05
	FBG1_06	68°	1.00	1.22	0.79	1.22	0.86	1.08

The influence of BRDF effects on narrowband NDVIs of MAT and MNT vegetation under varying SZAs is relatively stable over all analyzed SZAs (Table 7-2, Figure 7-20). MAT vegetation shows at a SZA of 46° nadir normalized NDVI values between 0.70 and 1.09, at a SZA of 50° values between 0.80 and 1.15, and at a SZA of 56° values between 0.77 and 1.07 over all viewing geometries. The variation in the NDVI data of MNT vegetation is smaller; at a SZA of 47° the nadir normalized NDVI values range from 0.90 to 1.10, where at an illumination angle increase to a SZA of 50° the values range from 0.87 to 1.14 within the ManTIS hemisphere. A further increase to a SZA of 59° or 68° does not show strong effects, since the nadir normalized NDVI values under these SZAs vary from between 0.87 – 1.05 and 0.86 – 1.08 respectively over all viewing geometries.

Therefore, the maximum variability in the EnMAP NDVI data of MAT vegetation at the three analyzed SZAs is 30 % within the 30° forward and backward viewing directions, while the maximum NDVI variability of MNT vegetation at the four analyzed SZAs is only 14 % within the ManTIS hemisphere. These spectro-directional effects on the simulated narrowband EnMAP NDVI of MAT and MNT vegetation under varying SZAs are visualized in Figure 7-20.

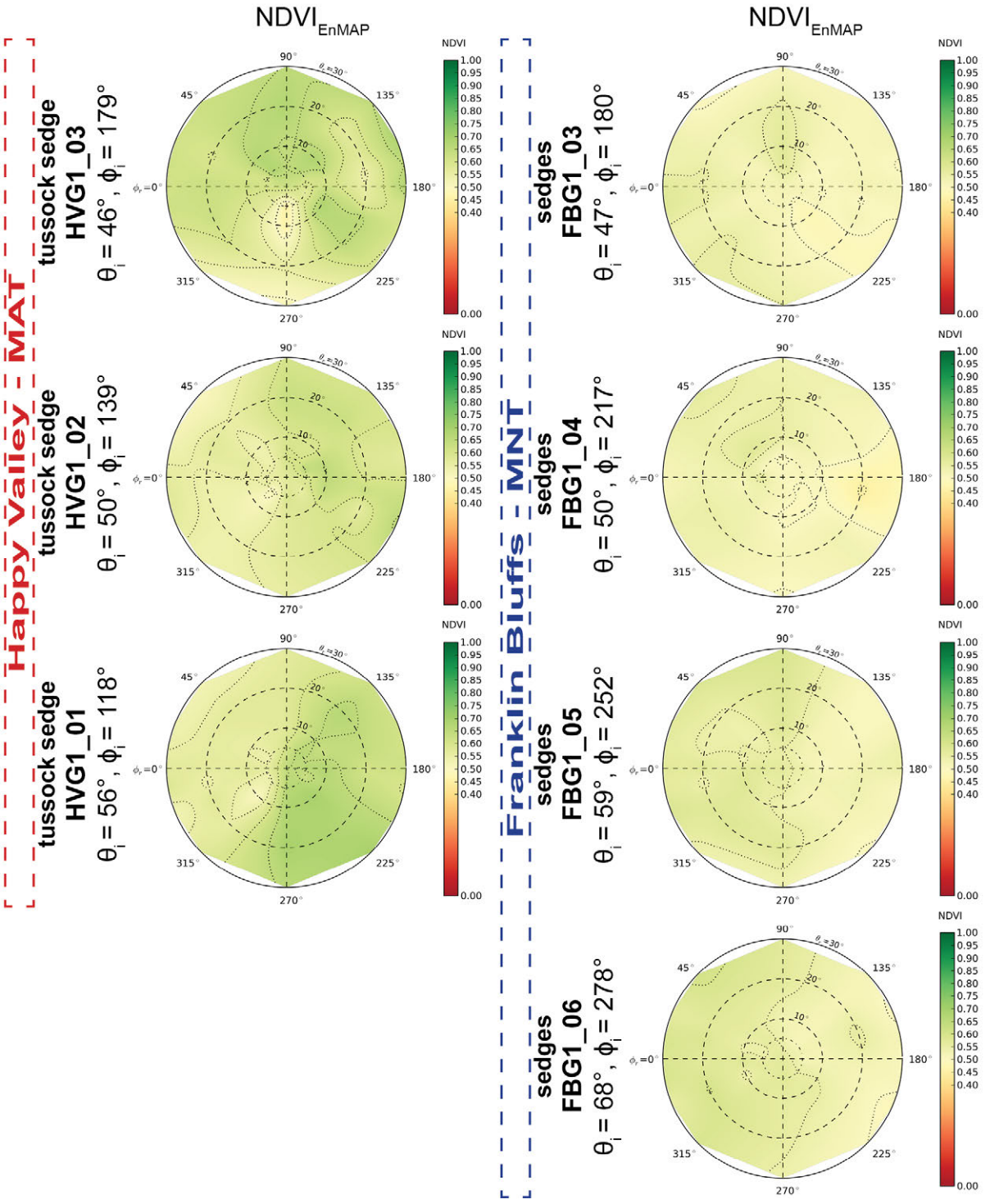

Figure 7-20: Influence of BRDF effects on remote sensing products (EnMAP NDVI) of MAT and MNT under varying sun zenith angles.

8 DISCUSSION

8.1 The Hyperspectral Reflectance Characteristics of Tundra Vegetation in Context of the Spectro-Goniometer Measurements

To understand the BRDF effects of tundra vegetation communities it is important to comprehend the hyperspectral characteristics of the underlying target reflectance signatures and the geoecological plant characteristics which affect the spectral characteristics. Spectro-directional data is strongly influenced by the spectral reflectance variability of the measured vegetation surface, specifically BRDF effects are related to the reflectance intensity in the continuous nadir reflectance spectrum [*Sandmeier et al.*, 1998a; *Sandmeier and Deering*, 1999; *Sandmeier et al.*, 1999]. In Chapter 6, the nadir hyperspectral characteristics of Alaskan tundra communities have been analyzed and discussed in detail, and it was shown which geoecological drivers existed for the respective communities.

In brief, although the reflectance spectra of the main plant functional types (e.g. erect dwarf shrub, prostrate dwarf shrub, sedge, tussock sedge) show certain diagnostic reflectance and absorption features, in combination as a plant community representing an area at larger scales it is challenging to distinguish the sites by their spectral signatures. The tundra communities in the Alaskan Low Arctic generally show low reflectance values compared to vegetation in other taller and denser growing biomes. Additional typical reflectance characteristics are: (i) weakly visible green reflectance peak or no local reflectance maximum in the visible spectrum; (ii) narrow 'red-edge' region between the red and NIR wavelength regions; (iii) low maximum NIR reflectance (maximum of 31 % at 1,020 nm); and (iv) no distinct NIR reflectance plateau. The explanation for these findings is probably a combination of low plant canopy heights and low cover of vascular plants (causing low reflectance in the NIR as well as the green wavelength region); relatively high cover of moss and lichen species (causing reflectance reduction in the green and NIR wavelength regions); high surface moisture conditions (causing higher reflectance absorption in the NIR wavelength region [*Weidong et al.*, 2002]); high SZAs causing extreme shadowing by the plants themselves (decreasing the reflectance in the red and NIR wavelength regions [*Ranson and T. Daughtry*, 1987]); and the large amounts of standing dead plant material (leads to an increase in the reflectance in the red wavelength region due to reduced chlorophyll absorption [*Asner*, 1998; *Tucker*, 1977]). These general reflectance characteristics are also valid for the dwarf shrub-moss tundra in the West-Siberian study location (Vaskiny Dachi). Therefore, it is to be assumed that the reflectance anisotropy in Low Arctic tundra is reduced in the NIR wavelength region as well as slightly raised in the VIS wavelength region compared to taller growing biomes.

The spectral metrics analysis of absorption depths and continuum removal technique reveal separation possibilities between the different tundra vegetation communities in the blue and red wavelength regions. Also the reflectances of the NIR shoulder and NIR reflectance

plateau are valuable information sources that separate the communities according to their biomass and vegetation structure. The hyperspectral field spectrometer analysis indicates the possibility of separating out MAT and MNT vegetation communities, which have not been previously well distinguished using broadband data. The absorption-related metrics confirm the reduction in pigment absorption within the red and the blue wavelength regions along the climate gradient from south to north and from MAT to MNT. The partitioning of MAT and MNT using broadband and narrowband NDVIs in this study shows promising results. Therefore, the main important questions are: if MAT and MNT can be clearly separated under varying view and illumination geometries, as well as how high is the BRDF influence on narrowband NDVIs calculated from EnMAP sensor data.

8.2 Applicability of the ManTIS Field Spectro-Goniometer System

The development of the ManTIS (Manual Transportable Instrument Platform for Ground-Based Spectro-Directional Observations) field spectro-goniometer system has been described in detail in Chapter 5, as well as the processing chain in order to analyze and visualize collected spectro-directional data. Spectro-goniometer measurements were carried out on two arctic expeditions. While on the expedition to Yamal Peninsula the weather conditions restricted the measurements, on the second expedition to the Alaska's Low Arctic the ManTIS system proved its value. The lightweight, transportable instrument provided reliable spectro-directional data of the main Alaskan and West-Siberian Low Arctic plant communities.

The analysis of the ManTIS measurements showed that the pointing accuracy and off-view viewing range (±30° view zenith angle change) is lower than that of already established field spectro-goniometer systems like the FIGOS [*Sandmeier and Itten*, 1999; *Schopfer et al.*, 2008] or the FIGIFIGO [*Suomalainen et al.*, 2009]. Nevertheless, the ManTIS field spectro-goniometer still shows good spectro-directional reflectance measurement results with an average pointing accuracy of 6 cm. Since the homogeneous vegetation plots are measured by a sensor with a FOV of 8.5° and a distance of 2 m to the target, the measurement errors due to the pointing error can be neglected. More important is that the lightness of the ManTIS (approx. 34 kg in field configuration and 54 kg with transport cases), compared for example with the FIGOS (approx. 230 kg) [*Sandmeier et al.*, 1995] or other spectro-goniometers based on the construction principle of FIGOS, allows for operation in nearly all geographical locations. The ManTIS field spectro-goniometer has been already transported as normal luggage in passenger planes or trains, in small helicopters or in station wagons to logistically demanding locations. Moreover, the ManTIS off-view capability is adequate for spectro-directional data comparison with many satellite systems with pointing capabilities (RapidEye ±25°, EnMAP ±30°, PRISMA ±15°, SENTINEL-2 ±21°) or systems with wide swaths.

The developed semi-automatic control for the spectro-goniometer measurements has reduced the recoding time for a full measurement scheme to 18 minutes, and the automated processing and visualization scripts allow pre-analysis immediately after the end of the measurements. Overall, 24 full spectro-goniometer measurements of eight main Alaskan and West-Siberian tundra communities under varying SZAs could be carried out on the expeditions.

8.3 The Spectro-Directional Reflectance Characteristics of Tundra Vegetation

The ground-based spectro-directional reflectance measurements of the Low Arctic tundra vegetation communities (n = 8) measured at solar noon reveal that there occurs significant reflectance anisotropy in all measured samples. None of the analyzed vegetation communities show an even closely isotropic reflectance characteristic.

The spectral-directional reflectance characteristics of the eight vegetation communities differ from each other, but also show common characteristics when measured at equivalent SZAs which range from 43° to 50° at solar noon in the short Low Arctic growing season (please note: SZA changes are not considered in this list). In general:

- Low Arctic tundra communities usually show the reflectance maximum in the backward viewing directions, and the reflectance minimum in the nadir to forward viewing directions.
- The degree of reflectances anisotropy is usually the highest in the solar principal plane, and the lowest close to the solar orthogonal plane.
- The reflectance anisotropy is usually the highest in wavelength regions with high absorption, and the lowest in wavelength regions with high reflection (spectral variability in reflectance anisotropy).
- The overall difference in the degree of reflectance anisotropy between the VIS (on average 40 %, in particular cases up to 80 %) and NIR (on average 20 %, in particular cases up to 40 %) wavelength regions is not very distinct.
- Due to the high SZA in the Arctic, no hot-spot effects can appear in multi-angular data of sensors with up to ±30° pointing capability.

The main influence factors on the reflectance anisotropy in vegetated surfaces are canopy architecture and multiple scattering effects inside the canopy [*Kimes*, 1983; *Sandmeier et al.*, 1998a]. The canopy geometry factors influence the distribution and proportion of shadowed and illuminated surfaces within the plant canopy which change under varying viewing-illumination geometries [*Hapke et al.*, 1996; *Sandmeier et al.*, 1998a]. Whereas multiple scattering effects controlled by the canopy optical properties regulate the intensity ("darkness") of the shadows [*Sandmeier et al.*, 1998a]. These two mechanisms (canopy geometry and multiple scattering) have been described in detail by *Kimes* [1983] for broadband multispectral data of erectophile and planophile vegetation, and have been applied and extended by *Sandmeier et al.* [1998a] for hyperspectral data. The unique vegetation structure of Low Arctic vegetation communities is responsible for the shared spectral-directional reflectance characteristics of the eight analyzed surfaces.

In detail, Low Arctic tundra is characterized by low growing vegetation communities which form a dense surface observed from nadir. The vascular plants have, depending on their latitudinal location, maximum top heights of 25 – 45 cm and in their understory dense moss and lichen mats, showing high light absorption, that together exclude the contribution of soil

surfaces in the reflectance characteristics. The normally planophile dwarf shrubs do not usually have a dense leaf coverage in the Low Arctic. Together with the erectophile sedges, the Low Arctic plant communities form an overall more erectophile canopy (Figure 8-1D, Figure 8-2D). The orientation of the leaves in an erectophile canopy allows the view to lower canopy levels (called gap effect) [*Kimes*, 1983]. With increasing viewing zenith angles and constant SZA the sensor measures only the reflectance of the well-illuminated top layers of the canopy which leads to higher reflectance values in the forward and backward viewing directions than in the nadir position [*Sandmeier et al.*, 1998a]. A second effect, the backshadow effect, influences the reflectance mainly in the forward viewing direction at the same time. The backshadow effect defined by *Kimes* [1983] appears because with viewing azimuth angles pointing towards the illumination direction, the sensor measures more surfaces with unilluminated, shadowed leaves and canopy components which are not exposed to direct sunlight. Up to a view zenith angle of 30° the backshadow effect is dominant [*Kimes*, 1983], and the reflectance values of the measured surfaces in the forward viewing directions are lower than in the nadir or backward viewing directions.

Where the distribution of shadowed and illuminated areas within a canopy is given by the canopy geometry and change with the viewing direction, the second influence factor (multiple scattering) is wavelength dependent [*Sandmeier et al.*, 1998a]. In more detail, BRDF effects are inversely related to the reflectance intensity in the continuous nadir reflectance spectrum [*Sandmeier et al.*, 1998a; *Sandmeier and Deering*, 1999; *Sandmeier et al.*, 1999] (Figure 5-12B). Multiple scattering (also called volume scattering) appears when leaves reflect or transmit radiance and produce a diffuse radiation which is brightening the shadowed areas. Therefore, the contrast between the shadowed and illuminated surfaces decreases and the reflectance anisotropy is reduced [*Sandmeier et al.*, 1998a]. In wavelength regions with low absorption (green and NIR wavelength region), more light is available within the canopy for scattering and the reflectances in these wavelength regions start to become more isotropic in all view azimuth angles [*Sandmeier et al.*, 1998a]. In reverse, in wavelength regions with high absorption (blue and red chlorophyll absorption bands) not enough radiation is reflected to decrease the contrast between shadowed and illuminated surfaces, thus these bands show a higher degree of reflectance anisotropy.

Therefore, multiple scattering effects mainly control the degree of reflectance anisotropy and dominate in wavelength regions with high nadir reflectance values. Together with the combination of the gap and backshadow effects, these three effects explain (i) why Low Arctic tundra communities usually show the reflectance maximum in the backward viewing directions, and the reflectance minimum in the nadir to forward viewing directions; (ii) why the degree of reflectance anisotropy is higher in the VIS wavelength region; and (iii) why the reflectance distribution in longer wavelength bands become more bowl-shaped. Moreover, *Solheim et al.* [2000] and *Peltoniemi et al.* [2005] have shown that moss and lichen mats in the understory show a depression in the reflectance in the forward viewing directions and higher reflectances in the backward viewing directions. This spectro-directional reflectance behavior of the understory is present in all measurements.

Additionally, the extreme illumination conditions in the Low Arctic also influence the gap, backshadow and multiple scattering effects. Since already low surface features produce long shadows at high SZAs, the contrast between shadowed and illuminated surfaces is reduced. This explains the low overall difference in the degree of reflectance anisotropy between the VIS and NIR wavelength regions.

Another important fact is that due to the high SZAs (larger than 43°) in the Arctic, no hotspot effects can occur in multi-angular data of sensors with up to ±30° pointing capability. The hotspot is an area in the backscattering direction where the sensor zenith angle equals the illumination zenith angle. At this special angle, the shadows are partly visible because the radiation scatters hide their own shadows [*Hapke et al.*, 1996]. Thus, the reflectance of the surface becomes maximal over all wavelengths.

Furthermore, it is important to mention that the field spectro-goniometer measurements have an additional challenge compared to laboratory measurements. In the laboratory the influence factors on the anisotropy of a surface can be controlled and narrowed to the canopy geometry, multiple scattering effects and sensor-illumination geometry. In the field additional external factors can affect the measurements which cannot be measured or validated in detail at all times. The main factors are upcoming wind during the measurement, short time atmospheric changes, changes in the moisture and temperature regime during the day, plant stress, heliotropic leaf movements, presence of dew on the canopy in the morning, as well as short term problems in the accuracy of the spectro-goniometer during one measurement [*Jackson et al.*, 1990; *Pinter, JR. et al.*, 1990; *Sandmeier*, 2000]. Therefore, a direct comparison of the spectro-directional reflectance measurements is difficult even if the measurements have been conducted at the same SZA.

In order to compare the spectro-directional reflectance characteristics of the eight analyzed tundra vegetation communities, it is important to separate the BRDF effects from the underlying surface reflectance characteristics [*Sandmeier et al.*, 1998a]. Therefore the HCRF data was normalized by the nadir viewing reflectance signature of the particular spectro-goniometer measurement. Together with the ANIX data, characterizing the spectral variability in reflectance anisotropy within the solar principal plane at a certain wavelength, the ANIF data comparison in the solar principal plane reveals the difference between the eight tundra vegetation communities. Figure 8-1 and Figure 8-2 point out the main characteristics in the red and NIR wavelength regions which were described in detail in Chapter 7.1.

At the Vaskiny Dachi study location, the dwarf shrub-moss tundra plot has a low average vegetation height (up to 10 cm) and moss mat coverage dominates [*Heim et al.*, 2012]. The canopy shows in the VIS wavelength region a strong anisotropy with a slope in the forward viewing direction and a reflectance maximum in the backward viewing direction caused by a dominating backshadow effect in this erectophile canopy (Figure 8-1A). The spectro-directional characteristics are almost symmetrical about the principal plane. But in the NIR wavelength region the spectro-directional characteristics are odd and show a reversed bowl shape distribution with the highest reflectance values in the nadir and lower values in the

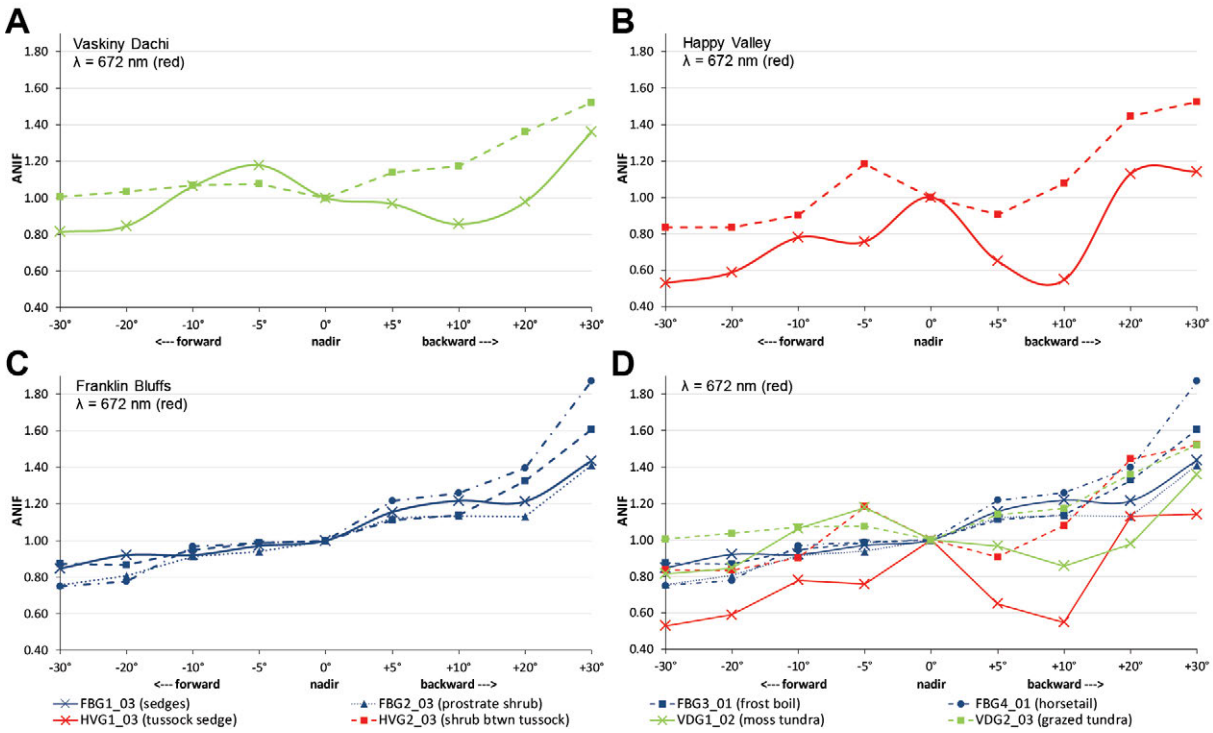

Figure 8-1: ANIF development in the solar principal plane of the eight tundra vegetation communities in the red (672 nm) ENMAP band measured at solar noon. (**A**) ANIF comparison of the two Vaskiny Dachi sites. (**B**) ANIF comparison of the two Happy Valley sites. (**C**) ANIF comparison of the four Franklin Bluffs sites. (**D**) ANIF comparison of all study sites.

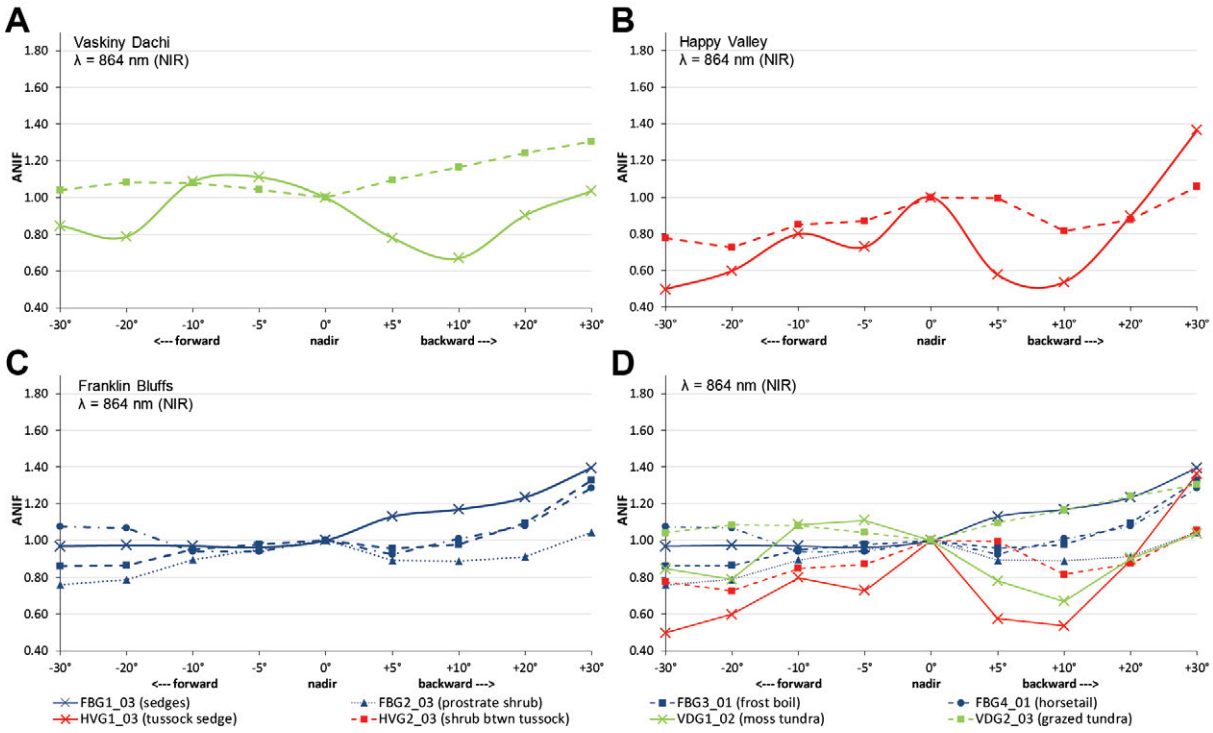

Figure 8-2: ANIF development in the solar principal plane of the eight tundra vegetation communities in the NIR (864 nm) ENMAP band measured at solar noon. (**A**) ANIF comparison of the two Vaskiny Dachi sites. (**B**) ANIF comparison of the two Happy Valley sites. (**C**) ANIF comparison of the four Franklin Bluffs sites. (**D**) ANIF comparison of all study sites.

higher view zenith angles (Figure 8-2A). Normally, the multiple scattering within the canopy has to create a more isotropic reflectance behavior. The ANIX data show that the degree of reflectance anisotropy in the VIS and NIR wavelength regions are nearly identical, and that in the solar orthogonal plane the NIR wavelength region has an even higher reflectance anisotropy than in the VIS. Possible reasons could be that the vegetation is situated already at the end of the phenological stadium or that the moss and lichen mats in the understory more strongly influence the reflectances in the longer wavelength regions and higher view zenith angles. To further analyze this, more precise information on the canopy optical and biophysical properties is needed.

The grazed dwarf shrub-moss tundra plot at the Vaskiny Dachi study location shows in contrast a typical spectro-directional reflectance behavior of an erectophile canopy. The backshadow effects dominate the gap effect, therefore the reflectances are reduced in the forward viewing directions and reach their maxima in the backward viewing directions (Figure 8-1A, Figure 8-2A). Moreover, the multiple scattering effects reduce the reflectance anisotropy in the NIR wavelength region. This spectro-directional reflectance behavior is already well known for grass targets [*Sandmeier et al.*, 1998a; *Sandmeier et al.*, 1999].

At the Happy Valley study location, the plot with the erect dwarf shrub community which is located between tussock sedges shows also a typical spectro-directional reflectance behavior of an erectophile canopy. That is surprising since shrubs normally have more planophile leave structures. The reflectance minima are located in the forward viewing directions and the maxima in the backward viewing directions, which prove the domination of the backshadow effect over the gap effect. The vegetation height (up to 45 cm) and cover density of the erect dwarf shrub community is enough to produce strong multiple scattering which reduces the reflectance anisotropy and creates a nearly isotropic reflectance behavior in the NIR wavelength region (Figure 8-2B). This anisotropic behavior is already known from taller tree communities described by *Deering et al.* [1999]. The main difference is that in the Low Arctic the overall reflectance values are lower and that the moss-lichen understory influences the spectro-directional characteristics. Maybe the moss-lichen understory is responsible for the erectophile spectro-directional reflectance behavior in this community. Again, further research is needed to clarify this connection.

The tussock sedge tundra plot at the Happy Valley study location, which also represents the zonal vegetation community of Alaskan bioclimate subzone E (MAT), shows a unique spectro-directional reflectance behavior. The reflectance maxima are located in the backward viewing directions and the reflectance values decrease towards the forward viewing directions (domination of the backshadow effect), but the nadir position also shows a reflectance maxima with reflectance values equally to slightly lower than in the +30° backward viewing direction. Moreover, the ANIX data reveals that the wavelength regions with the lowest absorption (green and NIR) have the highest reflectance anisotropy. Therefore, the multiple scattering within the canopy does not reduce the reflectance anisotropy in the green and NIR wavelength regions. This is viewable in Figure 8-1B and Figure 8-2B, since both bands (EnMAP red and NIR band) show nearly the same ANIF values in the red and NIR

wavelength regions at all view zenith angles. Reasons for this unique spectro-directional reflectance behavior could be the complex vegetation structure of tussock sedges and the fact that between tussock sedges holes can appear. The structure of tussock sedges promotes the creation of long shadows and complex canopy geometries depending on the viewing-illumination geometry. Therefore, the contrast of illuminated and shadowed areas within the structure can rapidly change from one viewing zenith angle to the next. To further analyze these anomalies, more precise information on the canopy optical and biophysical properties of tussock sedge communities is needed.

At the Franklin Bluffs study location, the non-tussock sedge tundra plot represents the zonal vegetation community of Alaskan bioclimate subzone D (MNT). This plant community shows a nearly perfect spectro-directional reflectance behavior of an erectophile canopy with the sole exception that the reflectance is not perfectly symmetrical about the solar principal plane. One reason for this could be the influence of wind [*Kimes*, 1983] which has moved the sedge stems. Nevertheless, the reflectances are reduced in the forward viewing directions and reach their maxima in the backward viewing directions which point out that the backshadow effect is dominating in this canopy (Figure 8-1C, Figure 8-2C). Although the average vegetation height of the non-tussock sedge is low (up to 15 cm), in the dense canopy strong multiple scattering appears and reduces the reflectance anisotropy in the NIR wavelength region.

The prostrate dwarf shrub community at the Franklin Bluffs study location shows a nearly identical anisotropic behavior like the erect dwarf shrub community at the Happy Valley study location (compare Figure 8-1B and Figure 8-2B with Figure 8-1C and Figure 8-2C). Although the prostrate dwarf shrub community has a slightly lower vegetation height (up to 35 cm) than the erect dwarf shrub community (up to 45 cm), the ANIX values are nearly identical. Therefore, it can be assumed that the vegetation height difference (10 cm) between prostrate and erect dwarf shrubs does not have a high influence on the multiple scattering effects within the canopy and thus the reflectance anisotropy reduction in the NIR wavelength region is nearly identical for both communities. Moreover, it can be assumed that in prostrate dwarf shrub communities the moss-lichen understory has a higher influences on the spectro-directional characteristics. Further spectro-goniometer measurements of erect and prostrate dwarf shrub communities are needed in order to clearly identify the relations.

The frost boil community (plant community in the center of nonsorted circles) is mainly composed of moss and lichen mats. Therefore, multiple scattering effects appear on a limited scale, therefore the reflectance anisotropy is only slightly reduced in the NIR wavelength region. Consequently, the ANIF values in the NIR wavelength region are only minimally lower than in the VIS wavelength region. Overall, the frost boil community shows a depression in the reflectance in the forward viewing directions and higher reflectances in the backward viewing directions (Figure 8-1C, Figure 8-2C). This reflectance anisotropy behavior like mentioned above is well-known from studies of *Solheim et al.* [2000] and *Peltoniemi et al.* [2005] for such vegetation surfaces.

The horsetail community is again a special case. In the VIS wavelength regions the spectro-directional characteristics show a depression in the reflectance values of the forward viewing directions and a reflectance increase towards the backward viewing directions (the backshadow effect is dominating) (Figure 8-1C). Whereas in the longer wavelength regions a slightly azimuthally symmetric bowl shape distribution is recognizable with the lowest reflectance values in the nadir position and increasing reflectance values towards higher view zenith angles (Figure 8-2C). An explanation could be that since horsetail has a more horizontal orientation of the leaves, the spectro-directional reflectance characteristics are in-between an erectophile and planophile canopy. With initiation of the multiple scattering in wavelengths with higher reflection the canopy of horsetail produces at higher view zenith angles a stronger scattering in all directions. Again, to further analyze these anomalies, more precise information on the canopy properties is needed.

8.4 Variability in Reflectance Anisotropy at High Sun Zenith Angles

The previous section dealt with the spectro-directional characteristics of Low Arctic tundra vegetation communities without the influence of illumination angle changes. It is well-known that SZA changes have an important influence on the nadir view reflectance of surfaces [*Middleton*, 1991] as well on the spectro-directional reflectance characteristics [*Bourgeois et al.*, 2006a; *Jackson et al.*, 1990; *Kimes*, 1983; *Sandmeier et al.*, 1998a; *Sandmeier et al.*, 1999]. In dense erectophile vegetation canopies without the influence of soil, the backshadow effect which is shifting the minimum reflectance towards the forward viewing directions is only dominant up to SZA smaller than 55° [*Kimes*, 1983]. Therefore, at high SZAs the gap effect which creates azimuthally symmetrical bowl shape reflectances distributions with the lowest reflectance values in the nadir position suppress more and more the backshadow effect. The SZAs at solar noon in the Low Arctic (~65° N – ~70° N) during the vegetation period (June – August) range from 43° to 50° depending on the geographical position. In most existing spectro-directional studies these SZAs are already described as extreme illumination conditions which significantly affect the distribution of shadowed and illuminated surfaces within a canopy and the multiple scattering between the leaves within the canopy. With further increasing SZA the total irradiance is decreasing up to a point where no optimal radiometric measurements are possible. Moreover, at high SZAs the direct irradiance decreases and the diffuse irradiance increases. In this part of the study we discuss the influence of high SZAs (50° – 68°) on the spectro-directional characteristics of the zonal plant communities of Alaskan bioclimate subzone E and D (MAT and MNT) and compare the results to the spectro-goniometer measurements performed at solar noon.

MAT vegetation is mainly composed of tussock sedges which have a unique spectro-directional reflectacne behavior already at solar noon (SZA = 46°). This behavior is described in detail in the previous section 8.3. Briefly, tussock sedge tundra shows reflectance maxima in the backward viewing directions and the reflectance values decrease towards the forward viewing directions (backshadow effects dominate), but show also a strong depression at the backward +10° viewing zenith angle. At a SZA of 50° the depression in the backward +10°

viewing direction decreases and at the same time the ANIF values in the higher forward viewing directions start to increase. This is notable in the red as well as NIR wavelength region (Figure 8-3A,C). At a SZA of 56° the depression in the backward +10° viewing direction nearly vanishes, and the ANIF values in the higher forward and backward viewing directions significantly increase (Figure 8-3A,C). This proves that the gap effect start to become more dominant in MAT vegetation at higher SZAs. At higher SZAs and with increasing viewing zenith angles only the well-illuminated top layers of the tussock sedge (MAT) canopy are measured by the sensor, which creates a more and more azimuthally symmetric bowl shape. Nevertheless, the backshadow effect is still viewable at a SZA of 56°. Surprising is that with increasing SZAs the reflectance values (HCRF) in all wavelength regions and viewing directions increase. Normally it is to be assumed that with decreasing SZA and thus deceasing total irradiance the HCRF values decrease. An explanation could be that with increasing SZA, the diffuse irradiance increase and therefore the overall reflectances in all wavelengths increase because the contrast between illuminated and shadowed areas is reduced over all wavelengths. Mainly responsible for this situation is the complex vegetation structure of tussock sedges. A detailed analysis of the canopy architecture is needed for a more precise explanation of this spectro-directional reflectance behavior. Moreover, the analysis of the ANIX data shows that at SZA over 50° the degree of reflectance anisotropy decrease in the VIS as well as the NIR wavelength region to similar level.

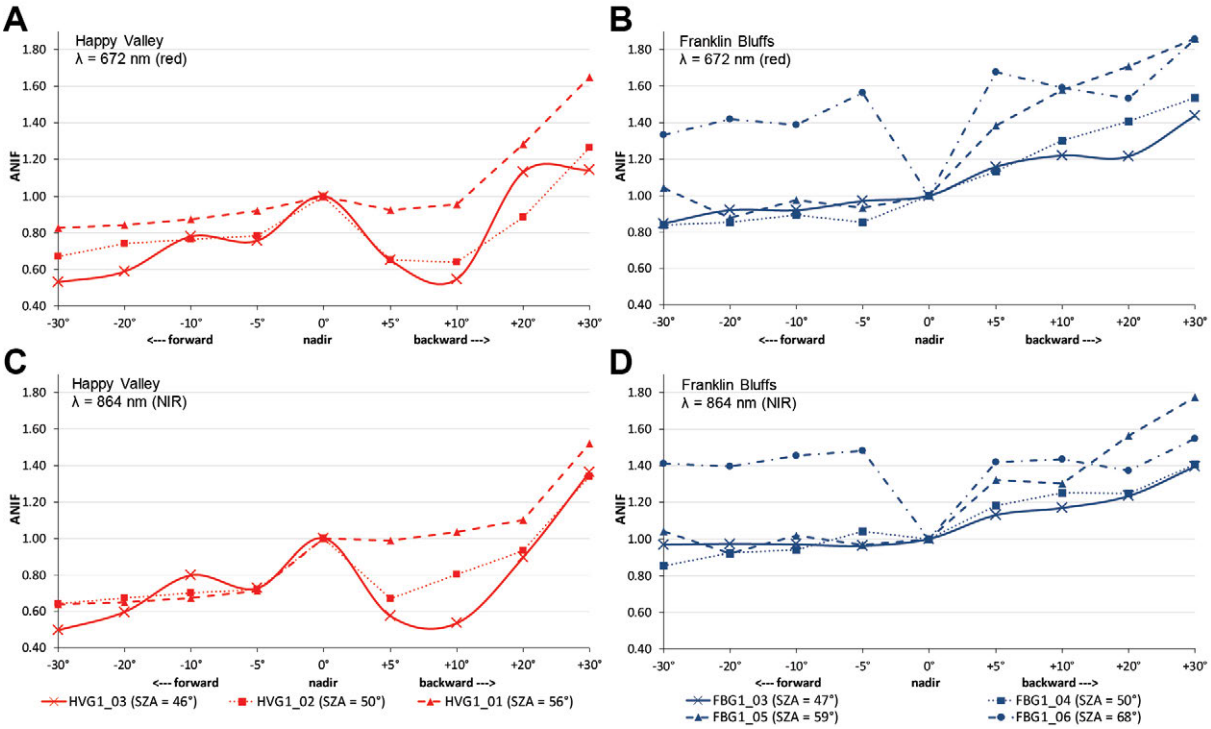

Figure 8-3: ANIF development in the solar principal plane of MAT and MNT under varying sun zenith angles. (**A**) ANIF comparison of MAT in the red (672 nm) EnMAP band. (**B**) ANIF comparison of MNT in the red (672 nm) EnMAP band. (**C**) ANIF comparison of MAT in the NIR (864 nm) EnMAP band. (**D**) ANIF comparison of MNT in the NIR (864 nm) EnMAP band.

At a SZA of 47° (solar noon measurement) the MNT vegetation show a nearly perfect spectro-directional reflectance behavior of an erectophile canopy as described by *Sandmeier*

et al. [1998a] and *Kimes* [1983]. Briefly, the reflectances are reduced in the forward viewing directions and reach their maxima in the backward viewing directions which point out that the backshadow effect is dominating the gap effect. Moreover, the reflectance anisotropy is higher in wavelength regions with high absorption due to the multiple scattering effects which reduce the reflectance anisotropy in wavelength regions with high reflectance. Like in the MAT vegetation, it is notable that the gap effect starts to become more dominant at higher SZAs. Where the spectro-directional characteristics at a SZA of 50° are nearly similar to the characteristics at a SZA of 47°, increases in the ANIF values in the red and NIR wavelength regions with higher view zenith angles occur at a SZA of 59° (Figure 8-3B,D). At a SZA of 68° the gap effect completely dominates the backshadow effect in this erectophile canopy, thereby the ANIF values in all viewing azimuth and zenith angles are higher than in the nadir position and form an azimuthal symmetric bowl shape distribution. Due to the low vegetation height, the multiple scattering in the wavelength regions with low absorption is unincisive, thus the reflectance anisotropy is only minimally reduced in the NIR wavelength region.

8.5 Applicability of Multi-Angular Remote Sensing Products for Arctic Tundra Environments

The calculation of vegetation indices (VI) from spectro-directional data create new functions (called vegetation index distribution functions) which are mainly characterized by the mode of calculation of the VI [*Küster*, 2011]. Since BRDF effects are spectral variable, the more complex and the more wavelength regions with disparate spectro-directional reflectance characteristics are included in the formula, the higher is the possibility that the anisotropic characteristics of the VI differ from that of the original reflectance data source. Therefore, the knowledge of the anisotropic characteristics of VIs is important for the comparability of remote sensing products from multi-angular data sources or different sensor systems.

The relative absorption depths in the blue (400 – 550 nm) and red (550 – 750 nm) wavelength regions and the NDVI calculated from the EnMAP narrowbands #47 (center wavelength 672 nm) and #73 (center wavelength 864 nm) showed promising results for the classification and differentiation of Low Arctic tundra communities in the hyperspectral analysis of this study (Chapter 6). The results of the spectro-directional characterization of the relative absorption depth products of the eight tundra communities show that the relative absorption depth products behave in their BRDF characteristics like the HCRF data in the same wavelength region. This is notable for the spectro-goniometer measurements at solar noon and under varying SZAs. This result is justified because for example the blue relative absorption depth is calculated from three narrow wavelength bands in the blue region (400 – 550 nm) which have all nearly the same degree of reflectance anisotropy in the same viewing positions over the hemisphere.

More complex is the anisotropic behavior of the narrowband NDVI, since the NDVI is calculated from two wavelength regions (red and NIR) which show different amounts of reflectance anisotropy. Generally, NDVI values of Low Arctic tundra communities observed under viewing zenith angles up to ±30° increase towards the forward viewing directions and

decrease towards the backward viewing directions (Figure 8-4D). Thus, in the nadir position the NDVI values usually do not show any extreme values (Figure 8-4A-C). The highest variation in the NDVI data is viewable in the solar principle plane and creates there various kinds of asymmetric bowl shape distributions. This behavior is already known from other multi-angular NDVI analysis or modeling for other biomes [*Jackson et al.*, 1990; *Küster*, 2011; *Verrelst et al.*, 2008; *Vierling et al.*, 1997]. One exception is the anisotropic behavior of tussock sedge tundra (MAT). Here the NDVI values increase towards the backward viewing direction and the NDVI values in the forward viewing directions equal the nadir value (Figure 8-4B). When normalized to the nadir value, the tussock sedge tundra NDVI values show an S-shape along the viewing directions (Figure 8-4D). *Vierling et al.* [1997] showed that the anisotropic NDVI behavior in tussock tundra also depends on the shrub coverage. Therefore, tussock tundra without shrubs show at comparable SZAs symmetrical bowl shape distributions with the highest NDVI values in the nadir position, where tussock tundra with shrubs show the above described general NDVI behavior (higher NDVI values in the forward and lower NDVI values in the backward viewing directions). Since the tussock sedge plot in this study had some coverage with *Ledum palustre*, a certain amount of woody material is measured during the spectro-goniometer measurements. Whether the influence of *Ledum palustre* modifies the shape of the NDVI behavior at changing view zenith angles needs to be furthered analyzed. Therefore, more precise information on the canopy properties of tussock sedge tundra is needed.

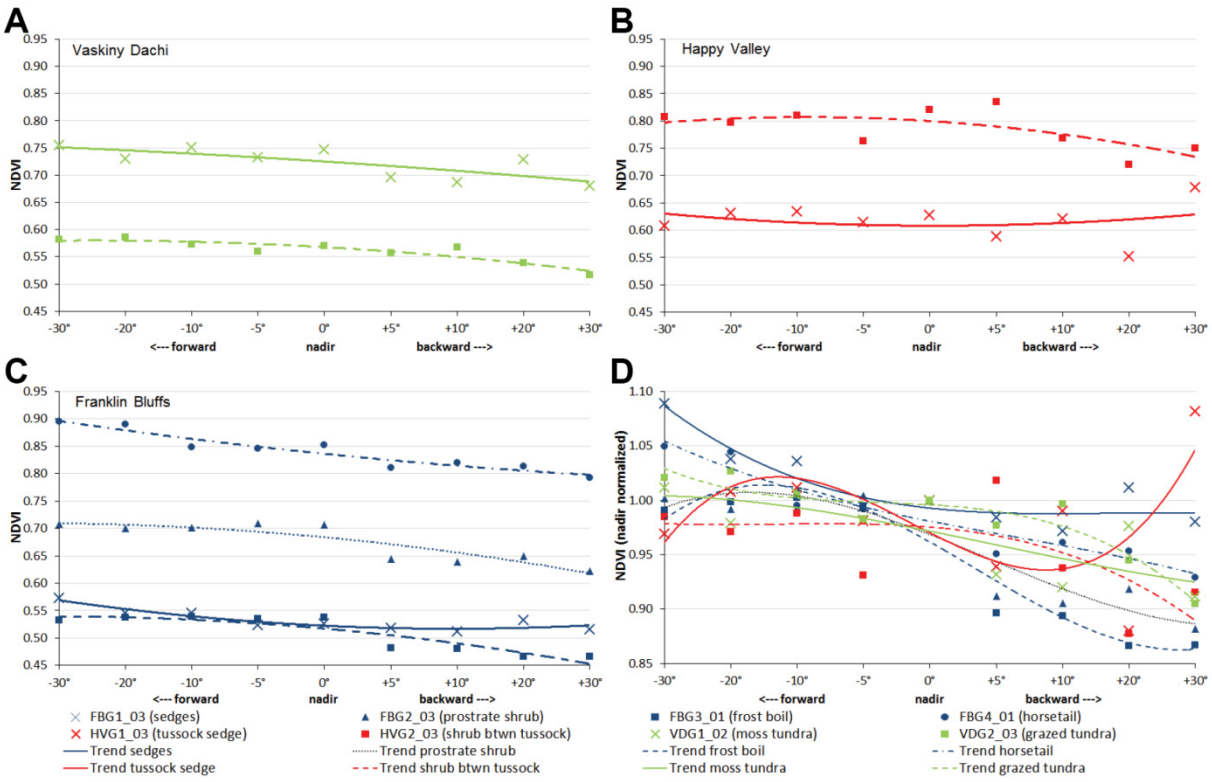

Figure 8-4: NDVI development in the solar principal plane of the eight tundra vegetation communities measured at solar noon. (**A**) NDVI development of the two Vaskiny Dachi sites. (**B**) NDVI development of the two Happy Valley sites. (**C**) NDVI development of the four Franklin Bluffs sites. (**D**) NDVI comparison of all study sites – all NDVI values are normalized to the nadir position.

If we look on the overall influence of BRDF effects on the NDVI of the EnMAP sensor in the solar principle plane within its ±30° pointing capability, than the average overall difference from the nadir value never exceed 10 %. A separation into forward and backward viewing directions is neglected in this consideration and only the solar noon measurements (SZAs of 43° to 50°) are included. If we only look on the quasi nadir (±5°) EnMAP measurements, than the deviation from the nadir NDVI is 6 %. This deviation of 6 % can be also seen at view zenith angles of ±10°, and increase to a difference from the nadir NDVI value of 8 % at view zenith angles of ±20° as well as of 10 % at view zenith angles of ±30 °.

The variability in the NDVI data of the eight analyzed Low Arctic tundra communities does not behave all the time in such a linear correlation. The sites can be sorted into 3 groups (Table 8-1). The first group shows an increase in the deviation from the nadir NDVI value with increasing view zenith angle (grazed dwarf shrub-moss tundra, non-tussock sedge tundra or MNT, and the horsetail community). The second group shows also an increase in the deviation from the nadir NDVI value with increasing view zenith angles, but shows in addition a dip / rise in the ±20° view zenith angle and the deviation at the ±5° view zenith angle is already over 6 % (dwarf shrub-moss tundra, erect dwarf shrub community in-between tussock sedges, prostrate dwarf shrub community, and the frost boil community). Moreover, the frost boil community shows the highest difference from the nadir NDVI with 10 – 13 % in all view zenith angles. The third group shows an indifferent correlation of viewing zenith angle with the NDVI data variability. The tussock sedge tundra belongs in this group with its S-shape anisotropic behavior.

Table 8-1: Variability in EnMAP simulated NDVI data within the solar principal plane of all eight analyzed Low Arctic tundra communities measured at solar noon. ***Note:*** The communities are grouped according to their variability behavior with increasing view zenith angles.

Site	SZA	View Zenith Angle			
		± 5°	± 10°	± 20°	± 30°
grazed dwarf shrub-moss tundra (VD)	61°	2%	1%	6%	10%
non-tussock sedge tundra – MNT (FB)	47°	2%	4%	4%	9%
horsetail community (FB)	48°	5%	4%	5%	7%
dwarf shrub-moss tundra (VD)	55°	7%	8%	2%	9%
erect dwarf shrub btwn tussock (HV)	46°	7%	6%	12%	8%
prostrate dwarf shrub community(FB)	47°	9%	9%	8%	12%
frost boil community(FB)	48°	10%	11%	13%	13%
tussock sedge tundra - MAT (HV)	46°	6%	1%	12%	8%

A change in the illumination zenith angle has an important influence on the dimension of the NDVI. *Middleton* [1991] showed that there is a statistically significant dependence of VIs on SZA in erectophile vegetation already in nadir acquired data. Various other studies confirm that this SZA influence on the NDVI values appears in all viewing directions of broadband data [*Huete et al.*, 1992; *Jackson et al.*, 1990; *Vierling et al.*, 1997]. Especially *Vierling et al.* [1997] showed this dependence in tussock tundra. Therefore, the broadband NDVI values

increased in the nadir position with increasing SZA for MAT vegetation. This study can confirm this trend also for narrowband NDVI values in MAT and MNT vegetation (Figure 8-5). *Middleton* [1991] explained this effect as a result of linearly increasing or constant reflectance in the NIR wavelength region in combination with nonlinear decreasing or constant reflectance in the red wavelength region.

Looking at the off-view angles, it is notable that with increasing SZAs in MAT vegetation the changes in the spectro-directional reflectance characteristics to an asymmetric bowl shape distribution affect the BRDF characteristic of the NDVI. But this time it leads to lower NDVI values in the forward viewing directions and equal to higher NDVI values in the backward viewing directions than in the nadir position (Figure 8-5A). Moreover, the anisotropic NDVI behavior of the tussock sedge tundra plot at a SZA of 56° correspond to the results of *Vierling et al.* [1997] for "nonwoody" tussock tundra at a SZA of 60°.

In contrast, MNT vegetation shows a much more typical anisotropic NDVI behavior with increasing SZAs known from grass targets. The NDVI values in the nadir position increase with increasing SZA, but also the NDVI values in all other viewing directions increase (Figure 8-5B). Moreover, MNT vegetation shows at all measured SZAs higher NDVI values in the forward and lower NDVI values in the backward viewing directions. At higher SZAs, the slightly asymmetric bowl shape distribution in the NDVI data start to turn into a linear shape from the forward to the backward viewing directions.

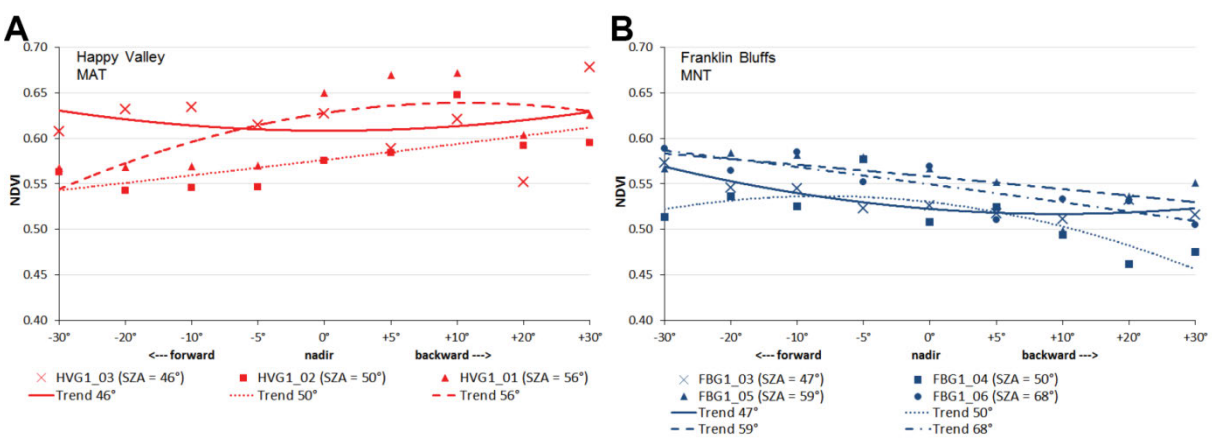

Figure 8-5: NDVI development in the solar principal plane of MAT and MNT under varying sun zenith angles. (**A**) NDVI development of MAT. (**B**) NDVI development of MNT.

Overall, this study confirms for Low Arctic tundra that the NDVI calculated from narrowband data minimizes view angle effects relative to the spectro-directional effects in the red and NIR band of the HCRF data. This effect was already validated for broadband sensor data in other biomes [*Holben and Fraser*, 1984; *Holben et al.*, 1986; *Huete et al.*, 1992; *Verrelst et al.*, 2008].

9 CONCLUSIONS & OUTLOOK

The main objective of this thesis is to characterize the hyperspectral and spectro-directional reflectance properties of the main plant communities of West-Siberian and Alaskan Low Arctic tundra. Since both the bidirectional reflectance distribution function (BRDF) effects and the nadir reflectance spectra of vegetated surfaces are sensitive to changes in illumination zenith angle, a further objective of this thesis is the investigation of the influence of high solar zenith angles on the reflectance anisotropy of tundra vegetation. Due to the lack of satellite and aerial hyperspectral and spectro-directional data, ground-based investigations via field spectroscopy and field spectro-goniometry were carried out. Performing ground-based spectro-directional measurements with existing spectro-goniometers was impractical due to the environmental and logistical challenges in the Arctic. Therefore, another objective of the thesis was the development of a lightweight, transportable, cheap, and easily managed field spectro-goniometer system which nevertheless provides reliable spectro-directional data.

The final product of the field spectro-goniometer development effort is the *Man*ual *T*ransportable *I*nstrument platform for ground-based *S*pectro-directional observations (ManTIS). The ManTIS can be equipped with various sensor systems and represent a platform for spectro-directional measurements with viewing zenith angles up to 30° and 360° viewing azimuth angles. The innovative mounting of the zenith arc allows the entire suite of instruments to be setup on a small assembly space. ManTIS nonetheless offers a 2 m distance between the target surface and the sensor, along with a high angular accuracy and fast execution of measurements. The AWI ManTIS field spectro-goniometer is currently equipped with two GER-1500 spectro-radiometers, a GPS receiver, and a video camera system. The current measurement scheme, with 61 viewing positions in the spanned hemisphere, is optimized with respect to the solar principal plane, and allows the hemispherical conical reflectance factor (HCRF) recording of a ManTIS hemisphere within 18 minutes under optimal conditions. The pointing accuracy of the system is within ±6 cm and the current instantaneous field of view (IFOV) of the sensor is 8.5°. Therefore, a homogeneous sampling area of ~25 cm radius is needed to acquire representative spectro-goniometer measurements. The custom-developed data processing chain, in conjunction with the self-developed software for the semi-automatic control of the ManTIS, provides a reliable method to reduce temporal atmospheric effects during the measurements. Field testing on two Arctic expeditions proved the value of the ManTIS field spectro-goniometer system. For the first time it was possible to carry out spectro-goniometry of Arctic vegetation above 70° north latitude. Another outcome of this thesis is that the ManTIS was nationally registered for patent on 25 October 2011, and internationally registered for patent on 27 June 2012. The patent publication number is DE 10 2011 117 713.A1 (international publication number: WO2013013652.A1) and has been published on 31 January 2013. Further, the ManTIS instrument platform will go into serial production under license by W. Ludolph GmbH & Co. KG in Bremerhaven, Germany.

The outcome of the field spectroscopy carried out along important environmental gradients (regional climate, soil pH, soil moisture, and topography) in the Alaskan Low Arctic tundra (subzones D and E) shows that the plant communities can be distinguished by their nadir-view reflectance spectra. The spectral metric analyses of absorption depths and continuum removal techniques reveal separation possibilities between the different tundra vegetation communities in the visible (VIS) blue and red wavelength regions. In addition, the near-infrared (NIR) shoulder and NIR reflectance plateau, despite their relatively low reflectance values due to the low structure of tundra vegetation, are still valuable information sources and can be used to separate the communities according to their biomass and vegetation structure. The main spectro-radiometric findings are:

(i) Along the north-south climate gradient, there is more vegetation biomass, denser shrub cover, and taller shrubs with denser leaf cover in warmer, southerly tundra, leading to higher reflectance in the NIR wavelength region;
(ii) Lower, wetter sites along gradients of topography and soil moisture support higher vegetation biomass. This is often not evident, however, in the NIR reflectance values, because increases in vegetation height and surface wetness have opposite effects on observed NIR reflectance;
(iii) Compared to moist non-acidic tundra (MNT) sites, moist acidic tundra (MAT) sites have 'greener' species (chlorophyll-rich deciduous shrubs and green-colored mosses), a more continuous cover of green vegetation, and higher aboveground biomass, which cause higher pigment absorption in the blue and red wavelength regions;
(iv) MNT sites show relatively high reflectance at red wavelengths, low absorption at blue and red wavelengths, and no distinct reflectance peak at green wavelengths.

Nevertheless, the field spectroscopy also exhibit universal reflectance characteristics for tundra vegetation. In general, all different tundra plant communities show:

(i) Low maximum NIR reflectance;
(ii) A weakly detectable green reflectance peak or no local reflectance maximum in the VIS spectrum;
(iii) A relatively narrow 'red-edge' region between the red and NIR wavelength regions;
(iv) No distinct NIR reflectance plateau (i.e., the 'red-edge' bend does not finish in a plateau, instead the reflectance values steadily increase up to the maximum reflectance at around 1,020 nm).

These common nadir-view reflectance characteristics are essential for understanding the BRDF effects in Arctic tundra, since BRDF effects are related to the reflectance intensity in the continuous nadir reflectance spectrum. None of the Low Arctic tundra vegetation communities investigated in this thesis show an even closely isotropic reflectance behavior within the analyzed hemisphere of up to 30° viewing zenith angle and 360° viewing azimuth angle. Examined at solar noon, with sun zenith angles (SZA) ranging from 43° to 50° depending on the geographical position in the Low Arctic (~65° – 70° N) during the

vegetation period (June – August), tundra vegetation communities show common spectro-directional reflectance characteristics. Tundra communities usually show:

(i) The highest BRDF effects in the solar principal plane, decreasing towards the solar orthogonal plane;
(ii) The reflectance maximum in the backward viewing directions, and the reflectance minimum in the nadir to forward viewing directions;
(iii) A higher degree of reflectance anisotropy in the VIS wavelength region than in the NIR wavelength region;
(iv) A more bowl-shaped distribution of the reflectance values over the hemisphere in longer wavelength bands (> 700 nm).

The explanation for these findings is that Arctic tundra communities have dense lichen and moss mats in the understory, which show a high light absorption and have a high impact on the BRDF effects. Moreover, these dense mats nearly cover the whole understory and therefore exclude the influence of soil BRDF effects. Overall, the erectophile moss and lichen mats together with erectophile sedges suppress the planophile dwarf shrubs. Therefore, the Low Arctic plant communities form an overall more erectophile vegetation canopy. Consequently, up to a sensor view zenith angle of 30°, the backshadow effect dominants the gap effect, which leads to lower reflectance values in the forward viewing directions compared to the nadir or backward viewing directions. In wavelength regions with low absorption (mainly the NIR wavelength region), more light is available within the canopy for scattering, and the reflectances in these wavelength regions start to become more isotropic in all sensor view azimuth angles. In addition, there is little overall difference in the degree of reflectance anisotropy between the VIS and NIR wavelength regions within the observed hemisphere of 30° view zenith angle. The explanation is that a generally low reflectance in the NIR and green wavelength region combined with a low chlorophyll absorption in the red wavelength region occur due to the low vegetation height structure and low green leaf area of tundra vegetation. These physical properties influence the multiple scattering effects which mainly control the degree of reflectance anisotropy. Moreover, it can be assumed that the difference in canopy height between prostrate and erect dwarf shrubs is generally not sufficient to have much influence on the multiple scattering effects within the canopy, and thus the reflectance anisotropy reduction in the NIR wavelength region is nearly identical for both communities. Additionally, the extreme illumination conditions in the Low Arctic also influence the gap, backshadow and multiple scattering effects. Since even low-growing plant canopies can produce long shadows at high SZAs, the contrast between shadowed and illuminated surfaces is reduced. Therefore, the BRDF effects in the VIS wavelength region are reduced, and the difference in the degree of reflectance anisotropy between the VIS and NIR wavelength region is low.

With increasing SZA, the reflectance anisotropy changes to an azimuthally symmetrical, bowl-shaped distribution of reflectances values with the lowest reflectance values in the nadir position. At a SZA of 55° to 60°, the gap effect starts to become dominant in the overall more erectophile tundra canopy, and therefore with increasing viewing zenith angles only the well-

illuminated top layers of the canopy are measured by the sensor. At a SZA beyond 68°, the gap effect completely dominates the backshadow effect. Further, the analyses show that at SZA over 50° the degree of reflectance anisotropy diminishes to similar values in the VIS and NIR wavelength regions.

The knowledge of the spectro-directional reflectance characteristics of tundra vegetation is essential for the retrieval of high quality, consistent and therefore comparable and reproducible temporal datasets from airborne and spaceborne sensors, as well as the derivation of vegetation parameters from these datasets. This need motivated a further objective of this thesis, the investigation of the variability in remote sensing (RS) products for Low Arctic tundra environments that can be attributed to viewing geometry and solar illumination angle changes. The quantitative analyses of the nadir-view reflectance spectra of tundra vegetation along environmental gradients presented here have shown that spectral metrics tend to vary predictably along the geoecological gradients (e.g., regional climate, soil pH, soil moisture, and topography). In particular, the regression analyses with biomass indicate the possibility of separating MAT and MNT vegetation via hyperspectral vegetation indices (VI), such as the narrowband Normalized Difference Vegetation Indices (NDVI) or the relative absorption depths in the blue (400 – 550 nm) and red (550 – 750 nm) wavelength regions, that have not been previously separable in such a good way using broadband data. The spectro-directional analyses confirm these separating possibilities, but also show that RS products are strongly influenced by BRDF effects. However, the anisotropic characteristics of the RS products can significantly differ from the observed BRDF effects in the original reflectance data source. This challenges the BRDF normalization of RS products.

The results of the spectro-directional characterization of relative absorption depth products show that within a given wavelength region, they behave in their BRDF characteristics like the HCRF data. Therefore, observed under viewing zenith angles up to 30°, the relative absorption depth products in the blue and red wavelength region can deviate up to 25 % from the values observed at the nadir viewing position. The deviation increases with increasing viewing zenith angle and SZA. The analysis of the influence of BRDF effects on the NDVI of tundra vegetation communities confirms that the NDVI minimizes view angle effects relative to the contrary spectro-directional effects in the red and NIR bands. The highest variation in the NDVI data is evident in the solar principle plane and creates there various kinds of asymmetric bowl shape distributions. Generally, the NDVI values observed under viewing zenith angles up to 30° increase towards the forward viewing direction and decrease towards the backward viewing direction. Thus, in the nadir position the NDVI values usually do not show any maximal values. On average for the researched tundra communities, the overall difference between NDVI values recorded under off-nadir viewing conditions and the nadir NDVI value never exceeds 10 %. Quasi-nadir (±5°) measurements can deviate from nadir NDVI up to 6 %, and increase linearly towards the higher off-nadir view positions. With increasing SZA, NDVI values increase in all viewing directions, but still show the sequence with higher NDVI values in the forward viewing directions and lower NDVI values in the backward viewing directions. Further, the decrease and equalization in the degree of

reflectance anisotropy in the VIS and NIR wavelength regions with higher SZA lead to a reduction of BRDF effects in the NDVI data.

In summary, RS provides the best prospective tools for monitoring circumpolar permafrost and tundra landscapes. Specifically, hyperspectral RS data can be used to derive important ecosystem parameters through the calculation of VIs, leaf area indices (LAI), or the fraction of photosynthetically active radiation (fPAR). The NDVI is an especially important input parameter for regional and global climate models. For RS data and derived RS products, changes in the illumination-target-viewing geometry directly alter the spectral reflectance signature of surface objects according to their object-specific BRDFs. The results of this thesis show in detail the influence of BRDF effects on NDVI by changing illumination-viewing geometries. Since the different types of tundra show only small but significant differences in the surface reflectance and derived RS products, the results of the thesis highlight the importance of including spectro-directional reflectance characteristics in the algorithm development for Arctic RS products. In preparation of the upcoming German hyperspectral EnMAP satellite mission, (i) the availability of ground-based multi-angular RS data, (ii) the possibility of measuring with a field-adapted, resitant and light-weight spectro-goniometer such as the ManTIS, and (iii) the understanding of the BRDF effects in low-growing tundra biomes are crucial for the calibration of off-nadir RS data as well as the potential derivation of canopy structure parameters in tundra and permafrost landscapes. Algorithm development in the Arctic is somewhat simplified by the fact that due to the high SZA, no hot-spot effects can appear in the EnMAP multi-angular data.

This dissertation established a spectral and directional reflectance database of Low Arctic vegetation communities in the bioclimatic subzones D and E covering a wide range of geoecological parameters, which can serve as a basis for further detailed investigation of the spectro-directional properties of Arctic vegetation communities. Thus, the well-characterized hyDRaCAT (*hy*perspectro-*D*irectional *R*eflectance *C*haracteristics of *A*rctic *T*undra) database will be made available to the scientific community. For further research, an improved 3D camera system is planned for the AWI ManTIS field spectro-goniometer system. This will help to get a better understanding of the geometric properties of the observed vegetation, and therefore the BRDF effects. A further challenge will be the upscaling of ground-based spectro-directional reflectance characteristics to airborne and spaceborne measurements. Although surface homogeneity can increase with lower spatial resolution, the evaluation of BRDF upscaling techniques is still necessary for tundra landscapes. In addition, incorporation of the gathered spectro-directional reflectance characteristics of tundra vegetation into BRDF models is planned.

ACKNOWLEDGMENTS

This thesis as well as my work at the Alfred Wegener Institute, Helmholtz Centre for Polar and Marine Research (AWI) during the last years could not have been realized without the support of many people from my scientific and private life. My research is part of the AWI "hy-ARC-VEG" (hyperspectral method development for ARCtic VEGetation biomes) project sponsored by the German Research Center for Aeronautics and Space (DLR) and funded by the German Federal Ministry of Economics and Technology [support code: 50 EE 1013] in preparation of the German EnMAP space mission.

First, I want to thank Hans-Wolfgang Hubberten and Birgit Heim for supervising this thesis and extending the opportunity to conduct this work at the AWI Potsdam. I am also grateful for the unique chance of doing field work at marvelous places in Siberia and Alaska. I will never forget these amazing impressions of Arctic tundra.

I also want to thank the members of my dissertation committee, Thomas Schneider, Kurt Günther, Sebastian van der Linden, Hans-Wolfgang Hubberten, and Birgit Heim, for continuously reviewing my work and providing their scientific input.

The development of the spectro-goniometer platform and resultant ManTIS field spectro-goniometer as well as the patent registration would not have been possible without the know-how, private engagement, and financial support of various people and institutions. Especially, I want to thank Reinhold Petereit for his know-how and dedication during the ManTIS construction phase. Moreover, I want to thank the scientific workshop of the AWI in Bremerhaven for their generous technical support, and the GFZ German Research Centre for Geosciences for their financial and scientific support. I am also indebted to Doppler H. Würflingsdobler GmbH, Germany, the Spectra Vista Corporation, USA, the AnKoTec Anton Kothe company, Germany, and the OVA Oberflächenveredelung in Adlershof GmbH, Germany, for providing free building materials or invoicing at cost price. I want to also acknowledge Theres Küster for her help during the development of the Python scripts for the visualization of the HCRF measurements. Moreover, thanks to Sabine Chabrillat and Karl Segl for the fruitful discussions about reflectance characteristics and the EnMAP sensor configurations.

The field teams of my two Arctic expeditions, in particular Birgit Heim, Patrick Gerlach, Marina Leibman, Yuri Dvornikov, Kseniya "Ksusha" Ermokhina, Alexei Gerasimov, Maria "Masha" Andreeva , Roman Ivanov, Evgeny Elantcev, Artem Khomutov, and Marcel Schwieder – Thank you all for your engagement during the field work in Siberia and Alaska.

Special thanks go to Donald A. "Skip" Walker, Howard E. Epstein, Gerald V. "J.J." Frost, Martha K. Raynolds, Amy Breen, and Edie Barbour for the great time during my research stay at the Alaska Geobotany Center (AGC), University of Alaska Fairbanks (UAF) in Fairbanks, Alaska, USA. Especially Skip Walker has become a good friend and highly

respected colleague. The research stay in Alaska would not have been possible without the funding of the Helmholtz Graduate School for Polar and Marine Research (POLMAR) and Potsdam Graduate School (PoGS) – thanks for that.

All co-authors of the peer-reviewed articles, conference abstracts, and posters produced during my time at the AWI – I really appreciate your contributions, ideas and valuable comments. The publications and this thesis highly benefited by English proof-reading from Elizabeth “Liz” Miller, Gerald V. “J.J.” Frost, Howard E. Epstein, and Donald A. “Skip” Walker. Thank you.

Many thanks for the wonderful times which I had at the AWI go to all AWI colleagues - in particular Anne Morgenstern, Thomas Opel, Frank Günther, Hugues Lantuit, Jens Strauss, Boris Biskaborn, Thomas Seiffert, Patrick Gerlach, Sina Muster, Uwe Gerlach, Gerald Müller, and all other AWI geo- and bio- PhD students and seniors. Thank you very much for the creative scientific and non-scientific discussions, the friendship, and lots of fun.

Special and heartfelt thanks go to my family and closest friends for their belief in my work. Without your support it would not have been possible to come to this point in my life.

Finally, but most important: Roswitha – thanks for your love, your patience, support and encouragement during the past years as well as your understanding that I have spent so much time with my computer and away.

REFERENCES

Alaska Geobotany Center (2010), *Kuparuk River Basin Vegetation. Vegetation classification for the Kuparuk River Basin Vegetation Mapping project*, Alaska Geobotany Center, Fairbanks, USA.

Alaska Geobotany Center (2013), *North American Arctic Transect. Data Reports*, available at http://www.geobotany.uaf.edu/naat/data, accessed February 6, 2013.

Anderson, K., H. Croft, E. J. Milton, and N. J. Kuhn (2012), A simple spectro-goniometer for collection of multiple view angle reflectance factors, *Remote Sensing Letters, 3*(2), 131–140.

Armstrong, G. A., and J. E. Hearst (1996), Carotenoids 2: Genetics and molecular biology of carotenoid pigment biosynthesis, *FASEB J, 10*(2), 228–237.

Asner, G. P. (1998), Biophysical and Biochemical Sources of Variability in Canopy Reflectance, *Remote Sensing of Environment, 64*(3), 234–253.

Asner, G. P., D. E. Knapp, T. Kennedy-Bowdoin, M. O. Jones, R. E. Martin, J. Boardman, and R. F. Hughes (2008), Invasive species detection in Hawaiian rainforests using airborne imaging spectroscopy and LiDAR, *Remote Sensing of Environment, 112*(5), 1942–1955.

Baldridge, A., S. Hook, C. Grove, and G. Rivera (2009), The ASTER spectral library version 2.0, *Remote Sensing of Environment, 113*(4), 711–715.

Barnsley, M., J. Settle, M. Cutter, D. Lobb, and F. Teston (2004), The PROBA/CHRIS mission: a low-cost smallsat for hyperspectral multiangle observations of the Earth surface and atmosphere, *IEEE Trans. Geosci. Remote Sensing, 42*(7), 1512–1520.

Barnsley, M. J., D. Allison, and P. Lewis (1997), On the information content of multiple view angle (MVA) images, *International Journal of Remote Sensing, 18*(9), 1937–1960.

Barreda, J. E., J. Knudson, D. A. Walker, M. K. Raynolds, A. Kade, and C. Munger (2006), *Biocomplexity of Patterned Ground Data Report Dalton Highway, 2001-2005*, Fairbanks.

Bhatt, U., D. Walker, M. Raynolds, P. Bieniek, H. Epstein, J. Comiso, J. Pinzon, C. Tucker, and I. Polyakov (2013), Recent Declines in Warming and Vegetation Greening Trends over Pan-Arctic Tundra, *Remote Sensing, 5*(9), 4229–4254.

Bhatt, U. S., D. A. Walker, M. K. Raynolds, J. C. Comiso, H. E. Epstein, G. Jia, R. Gens, J. E. Pinzon, C. J. Tucker, C. E. Tweedie et al. (2010), Circumpolar Arctic Tundra Vegetation Change Is Linked to Sea Ice Decline, *Earth Interact, 14*(8), 1–20.

Billings, W. D. (1973), Arctic and Alpine Vegetations: Similarities, Differences, and Susceptibility to Disturbance, *BioScience, 23*(12), 697–704.

Blunden, J., D. S. Arndt, and M. O. Baringer (2011), State of the Climate in 2010, *Bull. Amer. Meteor. Soc., 92*(6), S1.

Bourgeois, C. S., P. Calanca, and A. Ohmura (2006a), A field study of the hemispherical directional reflectance factor and spectral albedo of dry snow, *J. Geophys. Res, 111*(D20108).

Bourgeois, C. S., A. Ohmura, K. Schroff, H.-J. Frei, and P. Calanca (2006b), IAC ETH Goniospectrometer: A Tool for Hyperspectral HDRF Measurements, *J. Atmos. Oceanic Technol, 23*(4), 573–584.

Braun, A. C., U. Weidner, and S. Hinz (2010), Support Vector Machines for Vegetation Classification - A Revision, *Photogrammetrie - Fernerkundung - Geoinformation, 2010*(4), 273–281, http://dx.doi.org/10.1127/1432-8364/2010/0055.

Bruegge, C., N. Chrien, and D. Haner (2001), A Spectralon BRF data base for MISR calibration applications, *Remote Sensing of Environment, 77*(3), 354–366.

Bruegge, C. J., M. C. Helmlinger, J. E. Conel, B. J. Gaitley, and W. A. Abdou (2000), PARABOLA III: A sphere-scanning radiometer for field determination of surface anisotropic reflectance functions, *Remote Sensing Reviews, 19*(1), 75–94.

Buchhorn, M., and R. Petereit (2011), Transportables Goniospektrometer mit konstantem Observationszentrum, G01N 21/55 (2011.01)(DE102011117713.A1), 22pp.

Buchhorn, M., and R. Petereit (2013), Transportables Goniospektrometer mit konstantem Observationszentrum, in *Patentblatt. Veröffentlichungen auf Grund des Patentgesetzes*, edited by Deutsches Patent- und Markenamt (DPMA), p. 3568. München.

Buchhorn, M., and T. Schneider (2010), Synergistic Use of Spectral and Angular Signatures from Proba/CHRIS Hyper-spectral Images in a Temporal Context, in *Imagin(e,g) Europe. Proceedings of the 29th symposium of the European Association of Remote Sensing Laboratories [EARSeL], Chania, Greece ; [15th - 18th June, 2009]*, edited by I. Manakos, and C. Kalaitzidis, IOS Press. Amsterdam.

Buchhorn, M., and M. Schwieder (2012), Expedition "EyeSight-NAAT-Alaska" 2012, in Expeditions to permafrost 2012 : "Alaskan North Slope/Itkillik", "Thermokarst in Central Yakutia", "EyeSight-NAAT-Alaska", Berichte zur Polar- und Meeresforschung = Reports on polar and marine research, pp. 41–65, Alfred-Wegener-Inst. für Polar- und Meeresforschung. Bremerhaven.

Buchhorn, M., D. A. Walker, B. Heim, M. K. Raynolds, H. E. Epstein, and M. Schwieder (2013), Ground-Based Hyperspectral Characterization of Alaska Tundra Vegetation along Environmental Gradients, *Remote Sensing, 5*(8), 3971–4005.

Buddenbaum, H., and P. Püschel (2012), SpInMine (Spectral Index Data Mining Tool). Manual for Application: SpInMine (1.0), Trier, Germany.

Buddenbaum, H., O. Stern, M. Stellmes, J. Stoffels, P. Pueschel, J. Hill, and W. Werner (2012), Field Imaging Spectroscopy of Beech Seedlings under Dryness Stress, *Remote Sensing, 4*(12), 3721–3740.

Callaghan, T. V., C. E. Tweedie, J. Åkerman, C. Andrews, J. Bergstedt, M. G. Butler, T. R. Christensen, D. Cooley, U. Dahlberg, R. K. Danby et al. (2011a), Multi-Decadal Changes in Tundra Environments and Ecosystems: Synthesis of the International Polar Year-Back to the Future Project (IPY-BTF), *AMBIO, 40*(6), 705–716.

Callaghan, T. V., C. E. Tweedie, and P. J. Webber (2011b), Multi-decadal Changes in Tundra Environments and Ecosystems: The International Polar Year-Back to the Future Project (IPY-BTF), *AMBIO, 40*(6), 555–557.

Chapin, F. S., A. L. Lovecraft, E. S. Zavaleta, J. Nelson, M. D. Robards, G. P. Kofinas, S. F. Trainor, G. D. Peterson, H. P. Huntington, and R. L. Naylor (2006), Inaugural Article: Policy strategies to address sustainability of Alaskan boreal forests in response to a directionally changing climate, *Proceedings of the National Academy of Sciences, 103*(45), 16637–16643.

Chapin III, F. S., M. D. Robards, H. P. Huntington, J. F. Johnstone, S. F. Trainor, G. P. Kofinas, R. W. Ruess, N. Fresco, D. C. Natcher, and R. L. Naylor (2006), Directional Changes in Ecological Communities and Social-Ecological Systems: A Framework for Prediction Based on Alaskan Examples, *Am Nat, 168*(s6), S36.

Clark, R. N., and T. L. Roush (1984), Reflectance Spectroscopy: Quantitative Analysis Techniques for Remote Sensing Applications, *J. Geophys. Res, 89*(B7), 6329–6340.

Clark, R. N., G. A. Swayze, R. Wise, E. Livo, T. Hoefen, R. Kokaly, and S. J. Sutley (2007), *USGS digital spectral library splib06a: U.S. Geological Survey*, available at http://speclab.cr.usgs.gov/spectral.lib06, accessed February 6, 2013.

Coburn, C. A., and D. R. Peddle (2006), A low-cost field and laboratory goniometer system for estimating hyperspectral bidirectional reflectance, *Canadian Journal of Remote Sensing, 32*(3), 244–253, http://article.pubs.nrc-cnrc.gc.ca/RPAS/RPViewDoc?_handler_=HandleInitialGet&calyLang=eng&journal=cjrs&volume=32&articleFile=m06-021.pdf.

Coburn, C. A., E. van Gaalen, D. R. Peddle, and L. B. Flanagan (2010), Anisotropic reflectance effects on spectral indices for estimating ecophysiological parameters using a portable goniometer system, *Canadian Journal of Remote Sensing, 36*(Suppl. S2), S355-S364.

CRISP (2001), SPOT1,2,4. in section: "Spaceborne Remote Sensing Platforms and Sensors" from the remote sensing tutorial "Principles of Remote Sensing" contained in the CD-ROM "Space Views of Asia" 2nd. Edition, produced by CRISP., Singapore.

Crowley, J. K., D. W. Brickey, and L. C. Rowan (1989), Airborne imaging spectrometer data of the Ruby Mountains, Montana: Mineral discrimination using relative absorption band-depth images, *Remote Sensing of Environment, 29*(2), 121–134.

Deering, D. W., T. F. Eck, and B. Banerjee (1999), Characterization of the Reflectance Anisotropy of Three Boreal Forest Canopies in Spring-Summer, *Remote Sensing of Environment, 67*(2), 205–229, http://dx.doi.org/10.1016/S0034-4257(98)00087-X.

Dierschke, H. (1994), Pflanzensoziologie. Grundlagen und Methoden : 55 Tabellen, 683 S., Ulmer, Stuttgart.

Diner, D. J., L. Di Girolamo, and A. Nolin (2007), Preface to the MISR Special Issue, *Remote Sensing of Environment, 107*(1-2), 1.

Eastman, J., F. Sangermano, E. Machado, J. Rogan, and A. Anyamba (2013), Global Trends in Seasonality of Normalized Difference Vegetation Index (NDVI), 1982–2011, *Remote Sensing, 5*(10), 4799–4818.

Elvidge, C. D. (1988), Vegetation reflectance features in AVIRIS data, in Proceedings of the Sixth Thematic Conference on Remote Sensing for Exploration Geology: applications, technology, economics. May 16-19, 1988, Houston, Texas, edited by ERIM, pp. 169–182, Environmental Research Institute of Michigan. Houston, Texas.

Elvidge, C. D., and Z. Chen (1995), Comparison of broad-band and narrow-band red and near-infrared vegetation indices, *Remote Sensing of Environment, 54*(1), 38–48.

Epstein, H. E., M. K. Raynolds, D. A. Walker, U. S. Bhatt, C. J. Tucker, and J. E. Pinzon (2012), Dynamics of aboveground phytomass of the circumpolar Arctic tundra during the past three decades, *Environ. Res. Lett, 7*(1), 15506.

Epstein, H. E., D. A. Walker, M. K. Raynolds, G. J. Jia, and A. M. Kelley (2008), Phytomass patterns across a temperature gradient of the North American arctic tundra, *J. Geophys. Res, 113*(G03S02).

Feingersh, T., E. Ben-Dor, and S. Filin (2010), Correction of reflectance anisotropy: a multi-sensor approach, *International Journal of Remote Sensing, 31*(1), 49–74.

Forbes, B. C., F. Stammler, T. Kumpula, N. Meschtyb, A. Pajunen, and E. Kaarlejarvi (2009), High resilience in the Yamal-Nenets social-ecological system, West Siberian Arctic, Russia, *Proceedings of the National Academy of Sciences, 106*(52), 22041–22048.

Frost, G. V., and H. E. Epstein (2013), Tall shrub and tree expansion in Siberian tundra ecotones since the 1960s, *Glob Change Biol*, n/a, http://dx.doi.org/10.1111/gcb.12406.

Galeazzi, C., A. Sacchetti, A. Cisbani, and G. Babini (2008), The PRISMA Program, in *Proc. IEEE International Geoscience and Remote Sensing Symposium 2008*, vol. 4, pp. IV - 105 – IV - 108.

Gates, D. M., H. J. Keegan, J. C. Schleter, and V. R. Weidner (1965), Spectral Properties of Plants, *Appl. Opt, 4*(1), 11.

Gausman, H. W. (1974), Leaf Reflectance of Near-Infrared, *Photogrammetric Engineering and Remote Sensing, 40*(2), 183–191.

German Aerospace Center (DLR) (2013), *EnMAP System Parameters*, available at http://www.enmap.org/sensor, accessed October 10, 2013.

Gianelle, D., and F. Guastella (2007), Nadir and off-nadir hyperspectral field data: strengths and limitations in estimating grassland biophysical characteristics, *International Journal of Remote Sensing, 28*(7), 1547–1560.

Gitelson, A. A., Y. Gritz, and M. N. Merzlyak (2003), Relationships between leaf chlorophyll content and spectral reflectance and algorithms for non-destructive chlorophyll assessment in higher plant leaves, *Journal of Plant Physiology, 160*(3), 271–282, http://dx.doi.org/10.1078/0176-1617-00887.

Global Carbon Project (2003), *Science framework and Implementation. Edited by J.G Canadell, R Dickson, K Hibbard, M Raupach, O Young*, Earth System Science Partnership (IGBP, IHDP, WCRP, DIVERSITAS) Report No. 1; Global Carbon Project Report No. 1, Canberra.

Hapke, B., D. DiMucci, R. Nelson, and W. Smythe (1996), The cause of the hot spot in vegetation canopies and soils: Shadow-hiding versus coherent backscatter, *Remote Sensing of Environment, 58*(1), 63–68.

Heim, B., M. Buchhorn, and H.-W. Hubberten (2012), YAMAL2011 Expedition from 11th July to 9th September, 2011 - Part: AWI Data Report, Fairbanks, Alaska.

Held, M., B. Jakimow, A. Rabe, S. van der Linden, F. Wirth, and P. Hostert (2012), *EnMAP-Box Manual. Version 1.4*, Germany.

Hinzman, L. D., N. D. Bettez, W. R. Bolton, F. S. Chapin, M. B. Dyurgerov, C. L. Fastie, B. Griffith, R. D. Hollister, A. Hope, H. P. Huntington et al. (2005), Evidence and Implications of Recent Climate Change in Northern Alaska and Other Arctic Regions, *Climatic Change, 72*(3), 251–298.

Holben, B., and R. S. Fraser (1984), Red and near-infrared sensor response to off-nadiir viewing, *International Journal of Remote Sensing, 5*(1), 145–160.

Holben, B., D. Kimes, and R. S. Fraser (1986), Directional reflectance response in AVHRR red and near-IR bands for three cover types and varying atmospheric conditions, *Remote Sensing of Environment, 19*(3), 213–236.

Hope, A., J. S. Kimball, and D. A. Stow (1993), The relationship between tussock tundra spectral reflectance properties and biomass and vegetation composition, *International Journal of Remote Sensing, 14*(10), 1861–1874, http://dx.doi.org/10.1080/01431169308954008.

Horler, D. N. H., M. Dockray, and J. Barber (1983), The red edge of plant leaf reflectance, *International Journal of Remote Sensing, 4*(2), 273–288, http://dx.doi.org/10.1080/01431168308948546.

Huemmrich, F., J. A. Gamon, C. Tweedie, S. F. Oberbauer, G. Kinoshita, S. Houston, A. Kuchy, R. D. Hollister, H. Kwon, M. Mano et al. (2010), Remote sensing of tundra gross ecosystem productivity and light use efficiency under varying temperature and moisture conditions, *Remote Sensing of Environment, 114*(3), 481–489, http://dx.doi.org/10.1016/j.rse.2009.10.003.

Huete, A. R., G. Hua, J. Qi, A. Chehbouni, and W. J. D. van Leeuwen (1992), Normalization of multidirectional red and NIR reflectances with the SAVI, *Remote Sensing of Environment, 41*(2-3), 143–154, http://dx.doi.org/10.1016/0034-4257(92)90074-T.

International Council for Science (2004), A Framework for the International Polar Year 2007-2008, Paris.

IPCC (2007), Climate Change 2007: Synthesis Report. Contribution of Working Groups I, II and III to the Fourth Assessment Report of the Intergovernmental Panel on Climate Change. [Core Writing Team, Pachauri, R.K and Reisinger, A. (eds.)], IPCC, Geneva, Switzerland.

Jackson, R. D., T. R. Clarke, and M. Susan Moran (1992), Bidirectional calibration results for 11 spectralon and 16 BaSO4 reference reflectance panels, *Remote Sensing of Environment, 40*(3), 231–239, http://dx.doi.org/10.1016/0034-4257(92)90005-5.

Jackson, R. D., P. M. Teillet, P. N. Slater, G. Fedosejevs, M. F. Jasinski, J. K. Aase, and M. S. Moran (1990), Bidirectional measurements of surface reflectance for view angle corrections of oblique imagery. Concident Satellite, Aircraft, and Field Measurements at the Maricopa Agricultural Center (MAC), *Remote Sensing of Environment, 32*(2-3), 189–202, http://dx.doi.org/10.1016/0034-4257(90)90017-G.

Jakomulska, A., B. Zagajewski, and M. Sobczak (2003), Field Remote Sensing Techniques for Mountains Vegetation Investigation, in *Proceedings of the 3rd EARSeL workshop on Imaging Spectroscopy. Herrsching, Germany, May 13th to 16th 2003*, edited by European Association of Remote Sensing Laboratories, pp. 580–596. Herrsching.

Jia, G. J., H. E. Epstein, and D. A. Walker (2003), Greening of arctic Alaska, 1981–2001, *Geophys. Res. Lett, 30*(20).

Kääb, A. (2008), Remote sensing of permafrost-related problems and hazards, *Permafrost and Periglacial Processes, 19*(2), 107–136, http://dx.doi.org/10.1002/ppp.619.

Kade, A., D. A. Walker, and M. K. Raynolds (2005), Plant communities and soils in cryoturbated tundra along a bioclimate gradient in the Low Arctic, Alaska, *Phytocoenologia, 35*(4), 761–820.

Kaufman, D. S., D. P. Schneider, N. P. McKay, C. M. Ammann, R. S. Bradley, K. R. Briffa, G. H. Miller, B. L. Otto-Bliesner, J. T. Overpeck, B. M. Vinther et al. (2009), Recent Warming Reverses Long-Term Arctic Cooling, *Science, 325*(5945), 1236–1239.

Kaufmann, H., S. Förster, H. Wulf, K. Segl, L. Guanter, M. Bochow, U. Heiden, A. Müller, W. Heldens, T. Schneiderhan et al. (2012), *Science Plan of the Environmental Mapping and Analysis Program (EnMAP)*, Scientific Technical Report, Potsdam.

Kimes, D. S. (1983), Dynamics of directional reflectance factor distributions for vegetation canopies, *Appl. Opt., 22*(9), 1364.

Kokaly, R. F., and R. N. Clark (1999), Spectroscopic Determination of Leaf Biochemistry Using Band-Depth Analysis of Absorption Features and Stepwise Multiple Linear Regression, *Remote Sensing of Environment, 67*(3), 267–287.

Kuehni, R. G. (2002), The early development of the Munsell system, *Color Res. Appl, 27*(1), 20–27.

Kumpula, T., B. C. Forbes, F. Stammler, and N. Meschtyb (2012), Dynamics of a Coupled System: Multi-Resolution Remote Sensing in Assessing Social-Ecological Responses during 25 Years of Gas Field Development in Arctic Russia, *Remote Sensing, 4*(12), 1046–1068.

Küster, T. (2011), Modellierung von Getreidebestandsspektren zur Korrektur BRDF-bedingter Einflüsse auf Vegetationsindizes im Rahmen der EnMAP-Mission, *Dissertation*, Humboldt-Universität zu Berlin, Berlin.

Laidler, G., P. Treitz, and D. Atkinson (2008), Remote sensing of Arctic vegetation : relations between the NDVI, spatial resolution and vegetation cover on Boothia Peninsula, Nunavut, *Arctic, 61*(1), 1–13, http://pubs.aina.ucalgary.ca/arctic/Arctic61-1-1.pdf.

Landis, B., and J. S. Aber (2007), Low-cost field goniometer for multiangular reflectance measurements, *Emporia State Research Studies, 44*(1), 1–6, http://www.emporia.edu/esrs/vol44/landis.pdf.

Lawrence, D. M., A. G. Slater, R. A. Tomas, M. M. Holland, and C. Deser (2008), Accelerated Arctic land warming and permafrost degradation during rapid sea ice loss, *Geophys. Res. Lett, 35*(11).

Lubin, D., and R. Massom (2006), *Polar Remote Sensing. Volume I: Atmosphere and Oceans*, Springer Praxis Books, 756pp., Praxis Publishing Ltd Chichester UK, Berlin, Heidelberg.

Lucke, R. L., M. Corson, N. R. McGlothlin, S. D. Butcher, D. L. Wood, D. R. Korwan, R. R. Li, W. A. Snyder, C. O. Davis, and D. T. Chen (2011), Hyperspectral Imager for the Coastal Ocean: instrument description and first images, *Appl. Opt., 50*(11), 1501.

Maas, S. J., and J. R. Dunlap (1989), Reflectance, Transmittance, and Absorptance of Light by Normal, Etiolated, and Albino Corn Leaves, *Agronomy Journal, 81*(1), 105.

Malgorzata, V. W. (2010), *Remote Sensing. Data acquisition and integration*, available at http://www.tankonyvtar.hu/hu/tartalom/tamop425/0027_DAI6/ch01s02.html.

Manakos, I., T. Schneider, and M. P. Bekakos (2004), A mobile unit for field spectroradiometric measurements, *Neural, Parallel & Scientific Computations, 12*, 525–544.

Martonchik, J. V., C. J. Bruegge, and A. H. Strahler (2000), A review of reflectance nomenclature used in remote sensing, *Remote Sensing Reviews, 19*(1), 9–20, http://dx.doi.org/10.1080/02757250009532407.

McGuffie, K., and A. Henderson-Sellers (1986), Technical note. Illustration of the influence of shadowing on high latitude information derived from satellite imagery, *International Journal of Remote Sensing, 7*(10), 1359–1365.

Middleton, E. M. (1991), Solar zenith angle effects on vegetation indices in tallgrass prairie☆, *Remote Sensing of Environment, 38*(1), 45–62.

Milton, E. J. (1987), Review Article Principles of field spectroscopy, *International Journal of Remote Sensing, 8*(12), 1807–1827, http://dx.doi.org/10.1080/01431168708954818.

Milton, E. J., M. E. Schaepman, K. Anderson, M. Kneubühler, and N. Fox (2009), Progress in field spectroscopy. Imaging Spectroscopy Special Issue, *Remote Sensing of Environment, 113*(Supplement 1), S92-S109, http://dx.doi.org/10.1016/j.rse.2007.08.001.

Molenaar, J. G. de (1987), An Ecohydrological Approach to Floral and Vegetational Patterns in Arctic Landscape Ecology, *Arctic and Alpine Research, 19*(4), 414–424, http://www.jstor.org/stable/1551406.

Moore, P. D., and R. Garratt (2006), *Tundra*, Biomes of the Earth, xx, 220, Chelsea House, New York.

Müller, S. (2008), Vorlesungsmaterial: Computervisualistik - Integration. Institut für Computervisualistik, AG Computergraphik, Koblenz.

Muster, S., B. Heim, A. Abnizova, and J. Boike (2013), Water Body Distributions Across Scales: A Remote Sensing Based Comparison of Three Arctic TundraWetlands, *Remote Sensing, 5*(4), 1498–1523.

Mutanga, O., A. Skidmore, and H. Prins (2004), Predicting in situ pasture quality in the Kruger National Park, South Africa, using continuum-removed absorption features, *Remote Sensing of Environment, 89*(3), 393–408.

Myneni, R. B., C. D. Keeling, C. J. Tucker, G. Asrar, and R. R. Nemani (1997), Increased plant growth in the northern high latitudes from 1981 to 1991, *Nature, 386*(6626), 698–702.

National Research Council (NRC) (2003), *Cumulative Environmental Effects of Oil and Gas Activities on Alaska's North Slope,* 304pp., The National Academies Press, Washington, D.C.

Nicodemus, F. E., J. C. Richmond, J. J. Hsia, I. W. Ginsberg, and T. Limperis (1977), *Geometrical Considerations and Nomenclature for Reflectance*, NBS monograph, 52pp., U.S. Dept. of Commerce, National Bureau of Standards, Washington, D.C.

Olthof, I., and R. Fraser (2007), Mapping northern land cover fractions using Landsat ETM+, *Remote Sensing of Environment, 107*(3), 496–509.

Olthof, I., and R. Latifovic (2007), Short-term response of arctic vegetation NDVI to temperature anomalies, *International Journal of Remote Sensing, 28*(21), 4823–4840.

Painter, T. H., B. Paden, and J. Dozier (2003), Automated spectro-goniometer: A spherical robot for the field measurement of the directional reflectance of snow, *Review of Scientific Instruments, 74*(12), 5179–5188.

Pearlman, J., P. Barry, C. Segal, J. Shepanski, D. Beiso, and S. Carman (2003), Hyperion, a space-based imaging spectrometer, *IEEE Trans. Geosci. Remote Sensing, 41*(6), 1160–1173.

Pegrum, H., N. Fox, M. Chapman, and E. Milton (2006), Design and Testing a New Instrument to Measure the Angular Reflectance of Terrestrial Surfaces, in *International Geoscience and Remote Sensing Symposium, 2006. IGARSS 2006 Proceedings*, pp. 1119–1122, IEEE. [Piscataway, NJ].

Peltoniemi, J. I., S. Kaasalainen, J. Näränen, M. Rautiainen, P. Stenberg, H. Smolander, S. Smolander, and P. Voipio (2005), BRDF measurement of understory vegetation in pine forests: dwarf shrubs, lichen, and moss, *Remote Sensing of Environment, 94*(3), 343–354, http://dx.doi.org/10.1016/j.rse.2004.10.009.

Peltoniemi, J. I., J. Suomalainen, E. Puttonen, J. Näränen, and M. Rautiainen (2008), Reflectance properties of selected arctic-boreal land cover types: field measurements and their application in remote sensing, *Biogeosciences Discuss., 5*(2), 1069–1095, http://dx.doi.org/doi:10.5194/bgd-5-1069-2008.

Pinter, P. J., JR., R. D. Jackson, and M. Susan Moran (1990), Bidirectional reflectance factors of agricultural targets: A comparison of ground-, aircraft-, and satellite-based observations. Concident Satellite, Aircraft, and Field Measurements at the Maricopa Agricultural Center (MAC), *Remote Sensing of Environment, 32*(2-3), 215–228, http://dx.doi.org/10.1016/0034-4257(90)90019-I.

Ranson, K., and C. T. Daughtry (1987), Scene Shadow Effects on Multispectral Response, *IEEE Trans. Geosci. Remote Sensing, GE-25*(4), 502–509.

Raynolds, M. K., D. A. Walker, H. E. Epstein, J. E. Pinzon, and C. J. Tucker (2012), A new estimate of tundra-biome phytomass from trans-Arctic field data and AVHRR NDVI, *Remote Sensing Letters, 3*(5), 403–411.

Raynolds, M. K., D. A. Walker, C. A. Munger, C. M. Vonlanthen, and A. N. Kade (2008), A map analysis of patterned-ground along a North American Arctic Transect, *J. Geophys. Res, 113*(G03S03), http://dx.doi.org/10.1029/2007JG000512.

Razzhivin, V. Y. (1999), Zonation of vegetation in the Russian Arctic, in *The species concept in the high north: A panarctic flora initiative*, edited by I. Nordal, and V. Y. Razzhivin, pp. 113–130, Norwegian Academy of Science and Letters. Oslo, NO.

Richardson, A. J., and C. L. Wiegand (1977), Distinguishing vegetation from soil background information. A gray mapping technique allows delineation of any Landsat scene into vegetative cover stages, degrees of soil brightness, and water., *Photogrammetric Engineering and Remote Sensing, 43*(12), 1541–1552.

Riedel, S. M., H. E. Epstein, and D. A. Walker (2005), Biotic controls over spectral reflectance of arctic tundra vegetation, *International Journal of Remote Sensing, 26*(11), 2391–2405.

Roberts, D., K. Roth, and R. Perroy (2011), Hyperspectral Vegetation Indices, in *Hyperspectral Remote Sensing of Vegetation*, edited by P. S. Thenkabail, J. G. Lyon, and A. Huete, pp. 309-328, CRC Press/Taylor and Francis Group. Boca Raton, London, New York.

Romney, A. K., and J. T. Fulton (2006), Transforming reflectance spectra into Munsell color space by using prime colors, *Proceedings of the National Academy of Sciences, 103*(42), 15698–15703.

Rouse, J. W., R. H. Haas, J. A. Schell, and D. W. Deering (1973), Monitoring vegetation systems in the Great Plains with ERTS, in *Proceedings of the Third ERTS Symposium*, pp. 309–317. Washington DC.

Sabins, F. F. (2007), *Remote sensing. Principles and interpretation*, 3rd ed., xii, 494, Waveland Press, Long Grove, Ill.

Sandmeier, S., and D. Deering (1999), Structure Analysis and Classification of Boreal Forests Using Airborne Hyperspectral BRDF Data from ASAS, *Remote Sensing of Environment, 69*(3), 281–295.

Sandmeier, S., and K. Itten (1999), A field goniometer system (FIGOS) for acquisition of hyperspectral BRDF data, *IEEE Trans. Geosci. Remote Sensing, 37*(2), 978–986.

Sandmeier, S., C. Müller, B. Hosgood, and G. Andreoli (1998a), Physical Mechanisms in Hyperspectral BRDF Data of Grass and Watercress, *Remote Sensing of Environment, 66*(2), 222–233.

Sandmeier, S., C. Müller, B. Hosgood, and G. Andreoli (1998b), Sensitivity Analysis and Quality Assessment of Laboratory BRDF Data, *Remote Sensing of Environment, 64*(2), 176–191, http://dx.doi.org/10.1016/S0034-4257(97)00178-8.

Sandmeier, S., W. Sandmeier, K. I. Itten, M. E. Schaepman, and T. W. Kellenberger (1995), Swiss field-goniometer system (FIGOS), in *International Geoscience and Remote Sensing Symposium (IGARSS)*, pp. 2078–2080.

Sandmeier, S. R. (2000), Acquisition of Bidirectional Reflectance Factor Data with Field Goniometers, *Remote Sensing of Environment, 73*(3), 257–269, http://dx.doi.org/10.1016/S0034-4257(00)00102-4.

Sandmeier, S. R., E. M. Middleton, D. W. Deering, and W. Qin (1999), The potential of hyperspectral bidirectional reflectance distribution function data for grass canopy characterization, *J. Geophys. Res., 104*(D8), 9547.

Schaepman, M. (2007), Spectrodirectional remote sensing: From pixels to processes, *International Journal of Applied Earth Observation and Geoinformation, 9*(2), 204–223.

Schaepman, M. E., S. L. Ustin, A. J. Plaza, T. H. Painter, J. Verrelst, and S. Liang (2009), Earth system science related imaging spectroscopy—An assessment, *Remote Sensing of Environment, 113*, S123.

Schaepman-Strub, G., M. E. Schaepman, T. H. Painter, S. Dangel, and J. Martonchik (2006), Reflectance quantities in optical remote sensing--definitions and case studies, *Remote Sensing of Environment, 103*(1), 27–42, http://dx.doi.org/10.1016/j.rse.2006.03.002.

Schlerf, M., C. Atzberger, and J. Hill (2005), Remote sensing of forest biophysical variables using HyMap imaging spectrometer data, *Remote Sensing of Environment, 95*(2), 177–194.

Schmidt, K. S., and A. Skidmore (2003), Spectral discrimination of vegetation types in a coastal wetland, *Remote Sensing of Environment, 85*(1), 92–108, http://dx.doi.org/10.1016/S0034-4257(02)00196-7.

Schmidtlein, S., and J. Sassin (2004), Mapping of continuous floristic gradients in grasslands using hyperspectral imagery, *Remote Sensing of Environment, 92*(1), 126–138.

Schneider, T., J. Schopfer, N. Oppelt, W. Dorigo, W. Vreeling, and P. Gege (2007), GonioExp06 - A field goniometer intercomparison campaign, in support of physical model inversion and upscaling methods for hyperspectral, multidirectional RS data, in *European Space Agency, (Special Publication) ESA SP*.

Schneider, T., S. Zimmermann, and I. Manakos (2004), Field Goniometer System for Accompanying Directional Measurements, in *Proceedings of the Second CHRIS/Proba Workshop. 28 - 30 April 2004, ESA/ESRIN, Frascati, Italy, ESA SP*, vol. 578, edited by H. Lacoste-Francis, ESA Publications Div. Noordwijk, The Netherlands.

Schopfer, J., S. Dangel, M. Kneubühler, and K. I. Itten (2008), The Improved Dual-view Field Goniometer System FIGOS, *Sensors, 8*(8), 5120–5140.

Schopfer, J. T. (2008), Spectrodirectional Ground-Based Remote Sensing Using Dual-View Goniometry. Field BRF Retrieval and Assessment of the Diffuse Irradiance Distribution in Spectrodirectional Field Measurements, *Dissertation*, Universität Zürich, Zürich.

Selkowitz, D. J. (2010), A comparison of multi-spectral, multi-angular, and multi-temporal remote sensing datasets for fractional shrub canopy mapping in Arctic Alaska, *Remote Sensing of Environment, 114*(7), 1338–1352.

Solheim, I., O. Engelsen, B. Hosgood, and G. Andreoli (2000), Measurement and Modeling of the Spectral and Directional Reflection Properties of Lichen and Moss Canopies, *Remote Sensing of Environment, 72*(1), 78–94, http://dx.doi.org/10.1016/S0034-4257(99)00093-0.

Spectra Vista Corporation (2009), *GER 1500 - user manual. Revision 3.8*, Poughkeepsie, New York, USA.

Stow, D. A., B. H. Burns, and A. Hope (1993), Spectral, spatial and temporal characteristics of Arctic tundra reflectance, *International Journal of Remote Sensing, 14*(13), 2445–2462, http://dx.doi.org/10.1080/01431169308904285.

Stow, D. A., A. Hope, D. McGuire, D. Verbyla, J. Gamon, F. Huemmrich, S. Houston, C. Racine, M. Sturm, K. Tape et al. (2004), Remote sensing of vegetation and land-cover change in Arctic Tundra Ecosystems, *Remote Sensing of Environment, 89*(3), 281–308, http://dx.doi.org/10.1016/j.rse.2003.10.018.

Strauss, J., M. Ulrich, and M. Buchhorn (2012), *Expeditions to permafrost 2012 : "Alaskan North Slope/Itkillik", "Thermokarst in Central Yakutia", "EyeSight-NAAT-Alaska"*, Berichte zur Polar- und Meeresforschung = Reports on polar and marine research, 65pp., Alfred-Wegener-Inst. für Polar- und Meeresforschung, Bremerhaven.

Stuffler, T., K. Förster, S. Hofer, M. Leipold, B. Sang, H. Kaufmann, B. Penné, A. Mueller, and C. Chlebek (2009), Hyperspectral imaging—An advanced instrument concept for the EnMAP mission (Environmental Mapping and Analysis Programme), *Acta Astronautica, 65*(7-8), 1107–1112.

Stuffler, T., C. Kaufmann, S. Hofer, K. P. Förster, G. Schreier, A. Mueller, A. Eckardt, H. Bach, B. Penné, U. Benz et al. (2007), The EnMAP hyperspectral imager--An advanced optical payload for future applications in Earth observation programmes. Bringing Space Closer to People, Selected Proceedings of the 57th IAF Congress, Valencia, Spain, 2-6 October, 2006, *Acta Astronautica, 61*(1-6), 115–120, http://dx.doi.org/10.1016/j.actaastro.2007.01.033.

Suomalainen, J., T. Hakala, J. Peltoniemi, and E. Puttonen (2009), Polarised Multiangular Reflectance Measurements Using the Finnish Geodetic Institute Field Goniospectrometer, *Sensors, 9*(5), 3891–3907.

Thenkabail, P., J. Lyon, and A. Huete (2011), Advances in Hyperspectral Remote Sensing of Vegetation and Agricultural Croplands, in *Hyperspectral Remote Sensing of Vegetation*, edited by P. S. Thenkabail, J. G. Lyon, and A. Huete, pp. 3–36, CRC Press/Taylor and Francis Group. Boca Raton, London, New York.

Thenkabail, P. S., I. Mariotto, M. K. Gumma, E. M. Middleton, D. R. Landis, and K. F. Huemmrich (2013), Selection of Hyperspectral Narrowbands (HNBs) and Composition of Hyperspectral Twoband Vegetation Indices (HVIs) for Biophysical Characterization and Discrimination of Crop Types Using Field Reflectance and Hyperion/EO-1 Data, *IEEE J. Sel. Top. Appl. Earth Observations Remote Sensing, 6*(2), 427–439.

Thenkabail, P. S., R. B. Smith, and E. de Pauw (2000), Hyperspectral Vegetation Indices and Their Relationships with Agricultural Crop Characteristics, *Remote Sensing of Environment, 71*(2), 158–182.

Thenkabail, P. S., R. B. Smith, and E. de Pauw (2002), Evaluation of narrowband and broadband vegetation indices for determining optimal hyperspectral wavebands for agricultural crop characterization, *Photogrammetric Engineering and Remote Sensing, 68*(6), 607–621.

Timmermans, J., A. Ambro Gieske, C. van der Tol, W. Verhoef, and Z. Su (2009), Automated Directional Measurement System for the Acquisition of Thermal Radiative Measurements of Vegetative Canopies, *Sensors, 9*(3), 1409–1422.

Tucker, C. J. (1977), Spectral estimation of grass canopy variables, *Remote Sensing of Environment, 6*(1), 11–26.

Tucker, C. J. (1979), Red and photographic infrared linear combinations for monitoring vegetation, *Remote Sensing of Environment, 8*(2), 127–150, http://dx.doi.org/10.1016/0034-4257(79)90013-0.

Tyc, G., J. Tulip, D. Schulten, M. Krischke, and M. Oxfort (2005), The RapidEye mission design, *Acta Astronautica, 56*(1-2), 213–219.

Ulrich, M., G. Grosse, S. Chabrillat, and L. Schirrmeister (2009), Spectral characterization of periglacial surfaces and geomorphological units in the Arctic Lena Delta using field spectrometry and remote sensing, *Remote Sensing of Environment, 113*(6), 1220–1235, http://dx.doi.org/10.1016/j.rse.2009.02.009.

United Nations Framework Convention on Climate Change (UNFCCC) (1998), Report of the Conference of the Parties on its third Session, Held at Kyoto from 1 to 11 December 1997, FCCC/CP/1997/7/Add.1.

Ustin, S. L., D. A. Roberts, J. A. Gamon, G. P. Asner, and R. O. Green (2004), Using Imaging Spectroscopy to Study Ecosystem Processes and Properties, *BioScience, 54*(6), 523.

Ute Heiden (2011), Simulation of EnMAP orbits for a 27 day cycle at the Vaskiny Dachi study location, Yamal Peninsula, Russia, Oberpfaffenhofen and Potsdam, Germany.

Verbyla, D. (2008), The greening and browning of Alaska based on 1982–2003 satellite data, *Global Ecol Biogeography, 17*(4), 547–555.

Verrelst, J., M. E. Schaepman, B. Koetz, and M. Kneubühler (2008), Angular sensitivity analysis of vegetation indices derived from CHRIS/PROBA data. Earth Observations for Terrestrial Biodiversity and Ecosystems Special Issue, *Remote Sensing of Environment, 112*(5), 2341–2353, http://dx.doi.org/10.1016/j.rse.2007.11.001.

Vierling, L. A., D. W. Deering, and T. F. Eck (1997), Differences in arctic tundra vegetation type and phenology as seen using bidirectional radiometry in the early growing season, *Remote Sensing of Environment, 60*(1), 71–82, http://dx.doi.org/10.1016/S0034-4257(96)00139-3.

VITO, *Imaging Spectroscopy*, available at http://www.apex-esa.org/content/imaging-spectroscopy, accessed October 9, 2013.

Vonlanthen, C. M., D. A. Walker, M. K. Raynolds, A. Kade, P. Kuss, F. J. A. Daniëls, and N. V. Matveyeva (2008), Patterned-Ground Plant Communities along a bioclimate gradient in the High Arctic, Canada, *Phytocoenologia, 38*(1), 23–63.

Walker, D. A. (2000), Hierarchical subdivision of Arctic tundra based on vegetation response to climate, parent material and topography, *Global Change Biology, 6*(S1), 19–34.

Walker, D. A., N. A. Auerbach, J. G. Bockheim, F. S. Chapin, W. Eugster, J. Y. King, J. P. McFadden, G. J. Michaelson, F. E. Nelson, W. C. Oechel et al. (1998), Energy and trace-gas fluxes across a soil pH boundary in the Arctic, *Nature, 394*(6692), 469–472.

Walker, D. A., N. A. Auerbach, T. K. Nettleton, A. Gallant, and S. M. Murphy (1997), *Happy Valley Permanent Vegetation Plots*, Arctic System Science Flux Study Data Report, Boulder, CO 80309.

Walker, D. A., U. S. Bhatt, H. E. Epstein, P. Bieniek, J. Comiso, G. V. Frost, J. Pinzon, M. K. Raynolds, and C. J. Tucker (2012a), [The Arctic] Changing Arctic Tundra Vegetation Biomass and Greenness [in "State of the Climate in 2011"], *Bull. Amer. Meteor. Soc, 93*(7), S138-139.

Walker, D. A., S. Carlson, G. V. Frost, G. V. Matyshak, M. O. Leibman, P. Orechov, A. V. Khomutov, O. V. Khitun, M. P. Zhurbenko, O. M. Afonina et al. (2011a), *2010 Expedition to Krenkel Station, Hayes Island, Franz Josef Land Russia*, AGC Data Report, Fairbanks, Alaska, USA.

Walker, D. A., H. E. Epstein, G. J. Jia, A. Balser, C. Copass, W. J. Edwards, W. A. Gould, J. Hollingsworth, J. Knudson, H. A. Maier et al. (2003), Phytomass, LAI, and NDVI in northern Alaska: Relationships to summer warmth, soil pH, plant functional types, and extrapolation to the circumpolar Arctic, *J. Geophys. Res, 108*(D2).

Walker, D. A., H. E. Epstein, M. O. Leibman, N. G. Moskalenko, J. P. Kuss, G. V. Matyshak, E. Kaarlejärvi, and E. M. Barbour (2009a), *Data Report of the 2007 and 2008 Yamal Expeditions: Nadym, Laborovaya, Vaskiny Dachi, and Kharasavey*, AGC Data Report, Fairbanks, Alaska, USA.

Walker, D. A., H. E. Epstein, M. O. Leibman, N. G. Moskalenko, J. P. Kuss, G. V. Matyshak, E. Kaarlejärvi, and Forbes, B. C., Barbour, E. M. (2008a), *Data Report of the 2007 Yamal Expedition to Nadym, Laborovaya, and Vaskiny Dachi, Yamal Peninsula Region, Russia*, AGC Data Report, Fairbanks, Alaska, USA.

Walker, D. A., H. E. Epstein, M. K. Raynolds, P. Kuss, M. A. Kopecky, G. V. Frost, F. J. A. Daniëls, M. O. Leibman, N. G. Moskalenko, G. V. Matyshak et al. (2012b), Environment, vegetation and greenness (NDVI) along the North America and Eurasia Arctic transects, *Environ. Res. Lett, 7*(1), 15504.

Walker, D. A., H. E. Epstein, V. E. Romanovsky, C. L. Ping, G. J. Michaelson, R. P. Daanen, Y. Shur, R. A. Peterson, W. B. Krantz, M. K. Raynolds et al. (2008b), Arctic patterned-ground ecosystems: A synthesis of field studies and models along a North American Arctic Transect, *J. Geophys. Res, 113*(G3).

Walker, D. A., H. E. Epstein, and J. M. Welker (2008c), Introduction to special section on Biocomplexity of Arctic Tundra Ecosystems, *J. Geophys. Res, 113*(G3).

Walker, D. A., B. C. Forbes, M. O. Leibman, H. E. Epstein, U. S. Bhatt, J. C. Comiso, D. S. Drozdov, A. A. Gubarkov, G. J. Jia, E. Kaarlejärvi et al. (2011b), Cumulative Effects of Rapid Land-Cover and Land-Use Changes on the Yamal Peninsula, Russia, in *Eurasian Arctic Land Cover and Land Use in a Changing Climate*, edited by G. Gutman, and A. Reissell, pp. 207–236, Springer Netherlands; Springer Science+Business Media B.V. Dordrecht.

Walker, D. A., P. Kuss, H. E. Epstein, A. N. Kade, C. M. Vonlanthen, M. K. Raynolds, and F. J. Daniëls (2011c), Vegetation of zonal patterned-ground ecosystems along the North America Arctic bioclimate gradient, *Applied Vegetation Science, 14*(4), 440–463.

Walker, D. A., and N. D. Lederer (1987), Toposequence study: Site factors, soil physical and chemical properties and plant species cover. Department of Energy R4D Program Report, Colorado, Boulder, CO.

Walker, D. A., M. O. Leibman, H. E. Epstein, B. C. Forbes, U. S. Bhatt, M. K. Raynolds, J. C. Comiso, A. A. Gubarkov, A. V. Khomutov, G. J. Jia et al. (2009b), Spatial and temporal patterns of greenness on the Yamal Peninsula, Russia: interactions of ecological and social factors affecting the Arctic normalized difference vegetation index, *Environ. Res. Lett., 4*(4), 45004.

Walker, D. A., P. Orekhov, G. V. Frost, G. Matyshak, H. E. Epstein, M. O. Leibman, O. V. Khitun, A. V. Khomutov, R. P. Daanen, K. Gobroski et al. (2009c), *The 2009 Yamal Expedition to Ostrov Belyy and Kharp, Yamal Region, Russia*, AGC Data Report, Fairbanks, Alaska, USA.

Walker, D. A., M. K. Raynolds, F. J. A. Daniëls, E. Einarsson, A. Elvebakk, W. A. Gould, A. E. Katenin, S. S. Kholod, C. J. Markon, E. S. Melnikov et al. (2005), The Circumpolar Arctic vegetation map, *Journal of Vegetation Science, 16*(3), 267–282, http://dx.doi.org/10.1111/j.1654-1103.2005.tb02365.x.

Walker, M. D. (2006), From The Cover: Plant community responses to experimental warming across the tundra biome, *Proceedings of the National Academy of Sciences, 103*(5), 1342–1346.

Walker, M. D., D. A. Walker, and N. A. Auerbach (1994), Plant Communities of a Tussock Tundra Landscape in the Brooks Range Foothills, Alaska, *Journal of Vegetation Science, 5*(6), 843–866, http://www.jstor.org/stable/3236198.

Walter-Shea, E. A., J. L. Privette, D. Cornell, M. A. Mesarch, and C. J. Hays (1997), Relations between directional spectral vegetation indices and leaf area and absorbed radiation in Alfalfa, *Remote Sensing of Environment, 61*(1), 162–177, http://dx.doi.org/10.1016/S0034-4257(96)00250-7.

Wang, Q., C. Wu, Q. Li, and J. Li (2010), Chinese HJ-1A/B satellites and data characteristics, *Sci. China Earth Sci., 53*(S1), 51–57.

Washburn, A. L. (1980), Geocryology. A survey of periglacial processes and environments, 406pp., Wiley, New York.

Weidong, L., F. Baret, G. Xingfa, T. Qingxi, Z. Lanfen, and Z. Bing (2002), Relating soil surface moisture to reflectance, *Remote Sensing of Environment, 81*(2-3), 238–246, http://dx.doi.org/10.1016/S0034-4257(01)00347-9.

Winton, M. (2006), Amplified Arctic climate change: What does surface albedo feedback have to do with it?, *Geophys. Res. Lett, 33*(3).

Zhang, T., T. E. Osterkamp, and K. Stamnes (1996), Some Characteristics of the Climate in Northern Alaska, U.S.A, *Arctic and Alpine Research, 28*(4), 509–518, http://www.jstor.org/stable/1551862.

Zhang, W., P. A. Miller, B. Smith, R. Wania, T. Koenigk, and R. Döscher (2013), Tundra shrubification and tree-line advance amplify arctic climate warming: results from an individual-based dynamic vegetation model, *Environ. Res. Lett., 8*(3), 34023.

Zhou, L., C. J. Tucker, R. K. Kaufmann, D. Slayback, N. V. Shabanov, and R. B. Myneni (2001), Variations in northern vegetation activity inferred from satellite data of vegetation index during 1981 to 1999, *J. Geophys. Res., 106*(D17), 20069.

Ziska, L. H., A. H. Teramura, and J. H. Sullivan (1992), Physiological Sensitivity of Plants Along an Elevational Gradient to UV-B Radiation, *American Journal of Botany, 79*(8), 863–871, http://www.jstor.org/stable/2444995.

APPENDIX

The Appendix includes three separate parts: Appendix A - a list of existing field and laboratory spectro-goniometer systems; Appendix B - a print of the patent application for the developed AWI ManTIS spectro-goniometer system; and Appendix C - the detailed data reports of the spectro-goniometry results.

Table of Contents of the Appendix

APPENDIX A: CATALOG OF WELL-KNOWN LABORATORY AND FIELD SPECTRO-GONIOMETER

The following catalog provides an overview of existing field and laboratory spectro-goniometer systems which are still actively used in spectro-directional research, or are milestones in the development of spectro-goniometer systems. For each device the main characteristics and respective reference for further reading is stated. Over the years, numerous spectro-directional measurements have been performed with non-permanent spectro-goniometer setups. These systems are not stated in the list.

Please note: This catalog is a updated and extended version of those by *Schaepman-Strub* [2004] and *Schopfer* [2008]. Due to the increasing development of new spectro-goniometer devices, this list is not exhaustive.

Scope	Name	Explanation	Year	Location	Design principle	Characteristics	Reference
Field	**PARABOLA I**	Portable Apparatus for Rapid Acquisition of Bidirectional Observations of the Land and Atmosphere	1986	NASA / Goddard Space Flight Center, Greenbelt, Maryland, USA	Constant sensor position	Sky and ground sphere coverage; IFOV = 15°; three bands (660 nm; 830 nm; 1,650 nm)	[*Deering and Leone*, 1986]
Field	**Bausch's Goniometer**		1988	USDA-ARS Irrigation and Drainage Research, Ft. Collins, USA	Constant sensor position	Simultaneously sky and ground sphere coverage; FOV = 15°; four bands	[*Bausch et al.*, 1989]
Field	**Walter-Shea's Goniometer**	Goniometer System for Calibrating Field Reference-Reflectance Panels	1992	University of Nebraska, Lincoln, USA	Constant observation center	Ground sphere coverage; FOV = 15°; seven bands (485 nm; 560 nm; 660 nm; 830 nm; 1,225 nm; 1,650 nm; 2,215 nm)	[*Walter-Shea et al.*, 1993]
Laboratory	**ABRAMS**	Automated Bidirectional Reflectance Acquisition Measurement System	1993	University of Texas at Arlington, Arlington, USA	Constant observation center	Ground sphere coverage; FOV = 4°; one band - linearly-polarized laser light (633 nm)	[*Gibbs et al.*, 1993]
Laboratory	**EGO**	European Goniometric facility	1994	Joint Research Centre, Ispra, Italy	Constant observation center	Ground sphere coverage; FOV and spectral resolution depends on the chosen spectro-radiometer	[*Koechler et al.*, 1994]
Field	**PARABOLA II**	Portable Apparatus for Rapid Acquisition of Bidirectional Observations of the Land and Atmosphere	1994	NASA / Goddard Space Flight Center, Greenbelt, Maryland, USA	Constant sensor position	Sky and ground sphere coverage; IFOV = 5°; seven bands (443 nm; 553 nm; 673 nm; 860 nm; 1,655 nm; 550 nm; 11 µm)	[*Stockton et al.*, 1994]

Scope	*Name*	*Explanation*	*Year*	*Location*	*Design principle*	*Characteristics*	*Reference*
Laboratory	**GOSI**	Goniometric Optical Scatter Instrument	1994	National Institute of Standards and Technology, USA	Constant observation center	Ground sphere coverage, one band (633 nm)	[*Asmail et al.*, 1994]
Field	**FIGOS**	Field Goniometer System	1994	Remote Sensing Laboratories, University of Zurich, Switzerland	Constant observation center	Ground sphere coverage; FOV = 3°; hyperspectral (400 – 2,500 nm)	[*Sandmeier et al.*, 1995]
Field	**Leroux's Goniometer**	Photopolarimeter developed by the "Laboratoire d'Optique Atmospherique" in Lille, Franc	1995	Centre National de la Recherche Scientifique, Université Joseph Fourier, France	Constant observation center	Ground sphere coverage; FOV = 6°; four bands (450 nm; 650 nm; 850 nm; 1,650 nm)	[*Leroux et al.*, 1998]
Laboratory	**FEBO**		1995	Photometric Laboratory of the University of Florence, Firenze, Italy	Constant observation center	Ground sphere coverage; FOV = 0.1°; hyperspectral (250 – 900 nm)	[*Mazzinghi et al.*, 1995]
Field and Laboratory	**SIBRE**	Spectral Infrared Bidirectional Reflectance and Emissivity instrument	1996	University of California Santa Barbara, Santa Barbara, USA	Constant observation center	Ground sphere coverage, two bands (2.5-6 µm; 7-15µm)	[*Snyder and Wan*, 1996]
Field	**WAAC Goniometer**	Wide Angle Airborne Camera Goniometer	1997	Institute of Space Sensor Technology and Planetary Exploration, German Aerospace Center (DLR), Germany	Constant sensor position	Sky and ground sphere coverage; FOV = 0.015°; three bands (760 – 840 nm)	[*Demircan et al.*, 2000]

Scope	Name	Explanation	Year	Location	Design principle	Characteristics	Reference
Field and Laboratory	**ONERA/DOTA Goniometer**	Office National d'Etudes et Recherches Aérospatiales / Department Optique théorique et appliquée	1998	ONERA/DOTA/DTO, Toulouse, France	Constant observation center	Ground sphere coverage; hyperspectral (420 – 950 nm)	[*Serrot et al.*, 1998]
Field	**SFG**	Sandmeier Field Goniometer	1999	NASA / Stennis Space Center, Moffett Field, USA	Constant observation center	Ground sphere coverage; FOV = 3°; hyperspectral (400 – 2,500 nm)	[*Turner and Brown*, 2000]
Field	**MUFSPEM**	Mobile Unit for Field Spectroradiometric Measurements	1999	Technische Universität München, Freising, Germany	Constant sensor position	Ground sphere coverage; FOV = 10°; hyperspectral (400 – 2,500 nm)	[*Schneider et al.*, 2004]
Field	**Li's Goniometer**	automatic field experimental setup for multidirectional thermal infrared radiance measurement	1999	Institute of Geography Science and Natural Resource Research, Beijing, China	Constant observation center	Ground sphere coverage; one thermal band (8 – 13 µm)	[*Li et al.*, 2004]
Field	**PARABOLA III**	Portable Apparatus for Rapid Acquisition of Bidirectional Observations of the Land and Atmosphere	2000	NASA / Jet Propulsion Laboratory, California, Institute of Technology, Pasadena USA	Constant sensor position	Sky and ground sphere coverage; IFOV = 5°; eight bands (444 nm; 551 nm; 581 nm; 650 nm; 860 nm; 944 nm; 1,028 nm; 1,650 nm)	[*Bruegge et al.*, 2000]
Laboratory	**CHARISMA**	Coblentz Hemisphere based Angular Resolved and Integral Scattering Measurement Apparatus	2000	Laser-Laboratorium Göttingen, Göttingen, Germany	Constant sensor position	UV laser; three bands (157 nm; 193 nm; 633 nm)	[*Apel et al.*, 2001]

Scope	Name	Explanation	Year	Location	Design principle	Characteristics	Reference
Field	**ASG**	Automated Spectro-Goniometer	2001	Institute for Computational Earth System Science, University of California, Santa Barbara, USA	Constant observation center	Ground sphere coverage; FOV = 1°; hyperspectral (350 – 2,500 nm)	[*Painter et al.*, 2003]
Field	**FGI's Goniometer Model 2**	Finnish Geodetic Institute Goniometer Model 2	2001	Finnish Geodetic Institute, Masala, Finland	Constant observation center	Ground sphere coverage; hyperspectral (390 – 1,070 nm)	[*Peltoniemi et al.*, 2005]
Field	**RSG's Goniometer**	Optical sensor package for multi-angle measurements of the Remote Sensing Group	2002	Remote Sensing Group, University of Arizona, USA	Constant sensor position	Ground sphere coverage; FOV = 0.2°; four bands (470 nm; 575 nm; 660 nm; 835 nm)	[*Czapla-Myers et al.*, 2002]
Field	**CEReS's Goniometer**	Center for Environmental Remote Sensing (CEReS) Goniometer	2002	Center for Environmental Remote Sensing, University of Chiba, Japan	Constant sensor position	Ground sphere coverage; FOV = 21°; hyperspectral	[*Susaki et al.*, 2004]
Laboratory	**LAGOS**	Laboratory Goniometer System	2003	Remote Sensing Laboratories, University of Zurich, Switzerland	Constant observation center	Ground sphere coverage; FOV = 3°; hyperspectral (400 – 2,500 nm)	[*Dangel et al.*, 2003]
Laboratory	**CLabSpeG**	Compact Laboratory Spectro-Goniometer system	2003	Department of Land Management, Katholieke Universiteit Leuven, Belgium	Constant observation center	Ground sphere coverage; hyperspectral (350 – 2,500 nm)	[*Biliouris et al.*, 2003]

Scope	Name	Explanation	Year	Location	Design principle	Characteristics	Reference
Field	**MGS**	Mobile Goniometric System	2003	Technische Universität München, Freising, Germany	Constant observation center	Ground sphere coverage; hyperspectral (400 – 2,500 nm) and broadband thermal (8 - 12.5 µm)	[*Schneider et al.*, 2004]
Laboratory	**BUG**	Bloomsburg University Goniometer	2004	Department of Geography and Geosciences, Bloomsburg University, Bloomsburg,USA	Constant observation center	Ground sphere coverage; four bands(450 nm; 550 nm; 700 nm; 930 nm))	[*Johnson et al.*, 2004]
Field	**FGI's Goniometer Model 3**	Finnish Geodetic Institute Goniometer Model 3	2004	Finnish Geodetic Institute, Masala, Finland	Constant observation center	Ground sphere coverage; FOV = 3°; hyperspectral (350 – 2,400 nm)	[*Peltoniemi et al.*, 2005]
Field	**IAC ETH Gonio-spectrometer**	Institute for Atmospheric and Climate Science (IAC) of the Swiss Federal Institute of Technology (ETH) Goniospectrometer	2004	Institute for Atmospheric and Climate Science, ETH Zürich, Switzerland	Constant observation center	Sky and ground sphere coverage; FOV = 3°; hyperspectral (350 – 1,050 nm)	[*Bourgeois et al.*, 2006]
Field	**ULGS**	University of Lethbridge Goniometer System	2004	University of Lethbridge, Lethbridge, Canada	Constant observation center	Ground sphere coverage; hyperspectral (350 – 2,500 nm)	[*Coburn and Peddle*, 2006]
Laboratory	**IGF**	Israeli Goniometric Facility	2005	University of Tel-Aviv, Department of Geography, Tel-Aviv, Israel	Constant observation center	Ground sphere coverage; FOV = 8°; hyperspectral (350 – 2,500 nm)	[*Feingersh et al.*, 2005]

Scope	Name	Explanation	Year	Location	Design principle	Characteristics	Reference
Laboratory	**Hahlweg's Goniometer**	Full-hemispherical angle resolved spectro-radiometer based on a catadioptric system	2005	Helmut Schmidt Universität, Hamburg, Germany	Constant sensor position	Ground sphere coverage	[*Hahlweg et al.*, 2005]
Field and Laboratory	**GRASS**	Gonio RAdiometric Spectrometer System	2006	National Physical Laboratory, Teddington, UK	Constant observation center	Sky and ground sphere coverage; hyperspectral	[*Pegrum et al.*, 2006]
Field and Laboratory	**FIGIFIGO**	Finnish Geodetic Institute Field Goniospectrometer	2006	Finnish Geodetic Institute, Masala, Finland	Constant observation center	Ground sphere coverage; hyperspectral (350 – 2,500 nm)	[*Suomalainen et al.*, 2009]
Field	**Dual-View FIGOS**	Dual-View Field Goniometer System	2006	Remote Sensing Laboratories, University of Zurich, Switzerland	Constant observation center	Simultaneously sky and ground sphere coverage; FOV = 3°; hyperspectral (350 – 2,500 nm)	[*Schopfer et al.*, 2008]
Laboratory	**Padova**	Goniometer of the University of Padova	2006	University of Padova, Padova, Italy	Constant observation center	Ground sphere coverage	[*Fiorentin and Scroccaro*, 2008]
Laboratory	**SGP**	SpectroGonio-Photometer	2007	INRA, Unité d'Ecophysiologie des Plantes Fourragères, Lusignan, France	Constant sensor position	Hyperspectral (500 – 880 nm)	[*Combes et al.*, 2007]
Field	**Emporia's Goniometer**	Low-Cost field Goniometer of the Emporia State University	2007	Earth Science Department, Emporia State University, Emporia, USA	Constant observation center	Ground sphere coverage; hyperspectral	[*Landis and Aber*, 2007]

Scope	Name	Explanation	Year	Location	Design principle	Characteristics	Reference
Laboratory	**Baribeau's Goniometer**	NRC robot-based gonioreflectometer for spectral BRDF measurement	2008	National Research Council Canada, Canada			[*Baribeau et al.*, 2008]
Field	**ITC Goniometer**	Goniometer of the International Institute for Geo-Information Sciences and Earth Observation	2009	ITC, Enschede, The Netherlands	Constant observation center	Ground sphere coverage; eleven thermal bands	[*Timmermans et al.*, 2009]
Field	**Flying goniometer**	Acquisition of BRF dataset using a micro unmanned aerial vehicle	2010	Finnish Geodetic Institute, Masala, Finland	Constant observation center	Ground sphere coverage; three bands	[*Hakala et al.*, 2010]
Field	**AWI ManTIS**	Manual Transportable Instrument platform for ground-based Spectro-directional observations	2011	Alfred Wegener Institute for Polar and Marine Research, Potsdam, Germany	Constant observation center	Sky and ground sphere coverage; FOV = 8°; hyperspectral (350 – 1,050 nm)	[*Buchhorn and Petereit*, 2011]
Field	**A-Frame**	A-Frame for Multiple View Angle Measurements	2012	Department of Geography, University of Exeter, Penryn, UK	Constant observation center	Ground sphere coverage; FOV = 8°; hyperspectral (400 – 1,000 nm)	[*Anderson et al.*, 2012]
Laboratory	**University Wageningen's Goniometer**	Goniometer system based on a Kawasaki industrial robot	2012	Laboratory of Geo-Information Science and Remote Sensing, Wageningen University, The Netherlands	Constant observation center	Ground sphere coverage; hyperspectral (350 – 2,500 nm) and one thermal band (8 – 14 µm)	[*Roosjen et al.*, 2012]

Scope	Name	Explanation	Year	Location	Design principle	Characteristics	Reference
Field	**MAOS**	portable Multi-Angle Observation System	2012	Beijing Normal University, Beijing, China	Constant sensor position	Ground sphere coverage; FOV = 25°; hyperspectral (350 – 2,500 nm) and one thermal band (8 – 14 µm)	[*Yan et al.*, 2012]

APPENDIX B: PUBLISHED PATENT APPLICATION NO. DE102011117713.A1 (WO/2013/013652)

Pub. No.:	WO/2013/013652	**International App. No.:**	PCT/DE2012/000681
Publication Date:	31.01.2013	**National Patent No.:**	DE 10 2011 117 713 A1
		International Filing Date:	27.06.2012

IPC: ***G01J 3/02*** (2006.01), ***G01J 1/02*** (2006.01)

Applicants: **STIFTUNG ALFRED-WEGENER-INSTITUT FÜR POLAR- UND MEERESFORSCHUNG** [DE/EC];
BUCHHORN, Marcel [DE/DE]; (DE) *(For US Only)*.
PETEREIT, Reinhold [DE/DE]; (DE) *(For US Only)*

Inventors: **BUCHHORN, Marcel**; (DE). **PETEREIT, Reinhold**; (DE)

Priority Data: 10 2011 109 167.3 28.07.2011 DE
10 2011 117 713.6 25.10.2011 DE

Title

(DE) TRANSPORTABLES GONIOSPEKTROMETER MIT KONSTANTEM OBSERVATIONSZENTRUM
(EN) PORTABLE GONIOSPECTROMETER WITH CONSTANT OBSERVATION CENTRE

Abstract:

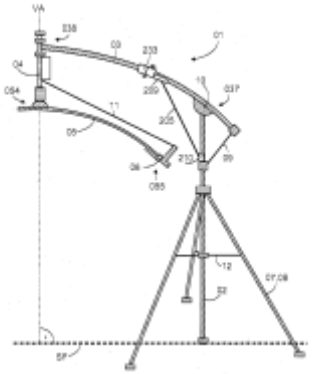

(EN) Known goniospectrometers for the radiometric measurement of the reflexion behaviour, more particularly the anisotropic radiance, of a natural surface under insolation are relatively complicated to transport and adjust. The goniospectrometer (01) according to the invention comprises on a cantilever (03) a rotatable and fixable suspension (04), which is connected to a fixed arc end (054), the other arc end being embodied as a free arc end (055). The suspension positions the arc (05) at the distance of the arc radius (BR) thereof above the natural surface (SF). A displaceable and fixable slide (06) carrying an optical unit (131) is arranged along the arc (05). By rotating the arc (05) about the suspension (04) and displacing the slide (06) along the arc (05), it is possible to position the optical unit (131) at any point on the spherical shell spanned. Measurements can be performed at arbitrary viewing angles and correlated with the measurements of a satellite (EnMAP) that can be pivoted in terms of the observation direction thereof. The correct anisotropic radiance of natural surfaces can thus be determined and used for the evaluation of ground properties, for example biomass that occurs or mineral resources that occur.

(19) Deutsches Patent- und Markenamt

(10) **DE 10 2011 117 713 B4** 2014.02.27

(12) # Patentschrift

(21) Aktenzeichen: **10 2011 117 713.6**
(22) Anmeldetag: **25.10.2011**
(43) Offenlegungstag: **31.01.2013**
(45) Veröffentlichungstag der Patenterteilung: **27.02.2014**

(51) Int Cl.: ***G01N 21/55*** (2006.01)
G01J 3/02 (2006.01)

Innerhalb von neun Monaten nach Veröffentlichung der Patenterteilung kann nach § 59 Patentgesetz gegen das Patent Einspruch erhoben werden. Der Einspruch ist schriftlich zu erklären und zu begründen. Innerhalb der Einspruchsfrist ist eine Einspruchsgebühr in Höhe von 200 Euro zu entrichten (§ 6 Patentkostengesetz in Verbindung mit der Anlage zu § 2 Abs. 1 Patentkostengesetz).

(66) Innere Priorität:
10 2011 109 167.3 28.07.2011

(73) Patentinhaber:
Alfred-Wegener-Institut Helmholtz-Zentrum für Polar- und Meeresforschung, 27570, Bremerhaven, DE

(72) Erfinder:
Petereit, Reinhold, 27711, Osterholz-Scharmbeck, DE; Buchhorn, Marcel, 14532, Stahnsdorf, DE

(56) Ermittelter Stand der Technik:
siehe Folgeseiten

(54) Bezeichnung: **Transportables Goniospektrometer mit konstantem Observationszentrum**

(57) Hauptanspruch: Transportables Goniospektrometer (01) mit konstantem Observationszentrum (BC), geeignet für die radiometrische Messung des Reflexionsverhaltens einer Oberfläche (SF), mit einer Hauptsäule (02), die eine Abstützung (08) gegenüber der Oberfläche (SF) aufweist und an ihrem oberen Säulenende (030) über eine Verschraubung (10) mit dem festgelegten Auslegerende (037) eines Auslegers (03), dessen anderes Auslegerende als freies Auslegerende (038) ausgebildet ist, verbunden ist, und mit einem Spektrometer (13) mit einem Sensor (131) und einer Auswerteeinheit (132), wobei der Sensor (131) über eine optische Faser (133) mit der Auswerteeinheit (132) verbunden ist, dadurch gekennzeichnet, dass der Ausleger (03) an seinem freien Auslegerende (038) eine um eine lotrecht zur Oberfläche (SF) ausgerichtete Vertikalachse (VA) dreh- und fixierbare Aufhängung (04) aufweist, die mit der Auswerteeinheit (132) des Spektrometers (13) und mit einem festgelegten Bogenende (054) eines Bogens (05) verbunden ist, wobei das andere Bogenende des Bogens (05) als freies Bogenende (055) ausgebildet ist, und dass die Aufhängung (04) den Bogen (05) im Abstand seines Bogenradiusses (BR) oberhalb der Oberfläche (SF) positioniert, und dass an dem Bogen (05) ein entlang des Bogens (05) verschieb- und fixierbarer Schlitten (06) angeordnet ist, der den Sensor (131) in einer Ausrichtung auf das Oberservationszentrum (BC) trägt.

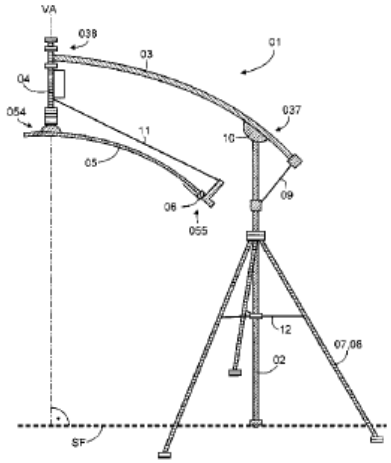

(19) Deutsches Patent- und Markenamt

(10) **DE 10 2011 117 713 B4** 2014.02.27

(56) Ermittelter Stand der Technik:

DE	26 43 647	A1
EP	1 470 413	B1
WO	2006/ 056 647	A1

C. SASKIA BOURGEOIS etal.: IAC ETH Goniospectrometer: A Tool for Hyperspectral HDRF Measurements. In: JOURNAL OF ATMOSPHERIC AND OCEANIC TECHNOLOGY, 23, APRIL 2006, 573-584.

C.A. Coburn and D.R. Peddle: A low-cost field and laboratory goniometer system for estimating hyperspectral bidirectional reflectance. In: Can. J. Remote Sensing, 32, 2006, 244-253.

E.J. Milton et al.: Progress in field spectroscopy. In: Remote Sensing of Environment, 2007, 1-18. [doi: 10. 1016/ j.rse.2007.08.001]

J. Schopfer et al.: The Improved Dual-view Field Goniometer System FIGOS. In: Sensors, 8, 2008, 5120-5140.

J. Suomnatainen et al.: Polarised Multiangular Reflectance Measurements Using the Finish Geodetic Institute Field Goniospectrometer. In: Sensors, 9, 2009, 3891-3907.

Thomas H. Painter et al.: Automated spectro-goniometer: A spherical robot for the field measurement of the directional reflectance of snow. In: Rev. Sci. Instrum., 74, DECEMBER 2003, 12, 6179-5177.

DE 10 2011 117 713 B4 2014.02.27

Beschreibung

[0001] Die Erfindung bezieht sich auf ein transportables Goniospektrometer mit konstantem Observationszentrum, geeignet für die radiometrische Messung des Reflexionsverhaltens einer natürlichen Oberfläche, mit einer Hauptsäule, die eine Abstützung gegenüber der natürlichen Oberfläche aufweist und an ihrem oberen Säulenende über eine Verschraubung mit dem festgelegten Auslegerende eines Auslegers, dessen anderes Auslegerende als freies Auslegerende ausgebildet ist, verbunden ist, und mit einem Spektrometer mit einer Optik und einem Sensor, wobei die Optik über eine optische Faser mit dem Sensor verbunden ist.

[0002] Ein Goniospektrometer (auch Spektrogoniometer, Gonioreflektometer, Reflexionsgoniometer, Reflektanzgoniometer oder auch kurz nur Goniometer, wobei ein Goniometer grundsätzlich ein Gerät zur Winkelbestimmung ist) ist ein Gerät zur Messung des Reflexionsverhaltens einer natürlichen Oberfläche, beispielsweise eines gewachsenen Untergrunds. In der Regel wird die bidirektionale Reflektanzverteilungsfunktion (BRDF) bei gegebener Lichteinfalls- und Betrachtungsrichtung ermittelt, d. h. es wird der Reflexionsfaktor in Abhängigkeit vom Sonnenstand und von der Optikposition ermittelt. Dabei werden der Azimutwinkel (Winkelrichtung der Sonne, gemessen von einer Himmelsrichtung (i. a. Norden) an (0°) im Uhrzeigersinn bis 360°) und der Zenitwinkel (Winkelstand der Sonne über dem Horizont, gemessen vom Horizont (0°) bis 90° über dem Objekt) als Parameter in der Beobachtungsgeometrie berücksichtigt. Die BRDF ist eine fundamentale optische Eigenschaft des reflektierenden Materials. Wegen der großen Variabilität der BRDF können sich praktische Anwendungen nicht auf einzelne Messungen stützen. Es werden Modelle benötigt, die die charakteristischen Eigenschaften beschreiben. Die satellitenbasierte Erdbeobachtung (seit Ende 1970) führte zu einer verstärkten Untersuchung der gerichteten Reflexionseigenschaften der Materie und damit zur Entwicklung von Modellen zur Beschreibung der gerichteten Reflexion. Beispielsweise zeigt die Vegetation in einem Permafrostgebiet, z. B. die sibirische Tundra, ein starkes anisotropes Verhalten, d. h. ein richtungsabhängiges Rückstrahlungsverhalten des Sonnenlichts. Die Stärke der Anisotropie ist dabei von der Bodenfeuchte, Sonnenzenitwinkel und Zenitwinkel der Optik des Goniospektrometers abhängig. Anisotropes Reflexionsverhalten (auch anisotrope Reflektanz oder differentielle spektroskopische Reflektanz) beeinflusst also in starkem Maße die BRDF.

[0003] Hintergrund für Feldmessungen ist die Tatsache, dass sich klimabedingte Änderungen beispielsweise in einem Permafrostgebiet in der Änderung des Oberflächentemperaturregimes und des Feuchteregimes zeigen. Sekundär wird damit die Vegetationsbedeckung und die Vegetationsentwicklung beeinflusst. Permafrostgebiete nehmen fast ein Viertel der Landoberfläche nördlich des Äquators ein und sind damit global bedeutend, dabei aber schwer zugänglich und wissenschaftlich bislang nur gering erkundet. Die hyperspektrale Fernerkundung mit Satellitenmissionen bietet hier ein großes Potenzial, um Modelle zur Kohlenstoffbilanzierung und zur Berechnung von Energie- und Treibhausgasflüssen und zur Exploration von Rohstoffen, deren Vorkommen die natürliche Oberfläche in charakteristischer Weise beeinflussen, und zur Erkundung von geeigneten Anbaugebieten, beispielsweise für Getreide oder Ölpflanzen, zu speisen. Neue Satelliten sind in der Lage, durch Verschwenkung auch Schrägaufnahmen von der Erdoberfläche zu erstellen, was zu einer Vervielfachung der Messpunkte gegenüber den einfachen Vertikalaufnahmen führt. In diesen Schrägaufnahmen ist der Einfluss der Anisotropie bislang nicht oder nicht ausreichend berücksichtigt. Um zu ermitteln, ob eine Korrektur von Schrägaufnahmen nötig ist, müssen in-situ Messungen unter realen Aufnahmebedingungen im Gelände durchgeführt werden. Hierfür werden seit Jahren Goniospektrometer genutzt. Ein transportables Goniospektrometer (auch Feld- oder Gelände-Goniospektrometer) ist für den Feldeinsatz besonders geeignet (ein Laboreinsatz ist aber auch ohne weiteres möglich). Dabei hat es sich aber gezeigt, dass bekannte Geländegoniometer für die speziellen Anforderungen, insbesondere Logistik und hohe Luftfeuchtigkeit, in Permafrost- und Arktisgebieten nur bedingt geeignet sind. Grundsätzlich kann unterschieden werden zwischen Goniospektrometern mit konstantem Observationszentrum (Messort) und Goniospektrometern mit konstanter Optikposition. Goniospektrometer mit konstantem Observationszentrum bestehen meist aus einem Azimutring (entspricht Himmelsrichtung-Horizont), auf welchem ein Zenitring (entspricht Sonnentageslauf) befestigt ist, der sich unter Führung durch den Azimutring bewegen lässt. Am Zenitring ist ein verschiebbarer Schlitten befestigt, der die Optik zur radiometrischen Messung trägt und ihn frei unter einem Zenitwinkel fixieren kann. Goniospektrometer mit einer konstanten Optikposition bestehen meist aus einem Arm, an dem eine Optik befestigt ist, welche in verschiedenen Winkeln zum Objekt eingestellt werden kann.

[0004] Das „Environmental Mapping and Analysis Program" (EnMAP) ist die erste deutsche hyperspektrale Satellitenmission. Ziel ist es, qualitativ hochwertige hyperspektrale Daten zum zeitlich hochaufgelösten Monitoring von geo- und biosphärischen Parametern der Erdoberfläche bereitzustellen. Der Start von EnMAP ist für 2015 vorgesehen. EnMAP zeichnet die Erdoberfläche auf einer sonnensynchronen Umlaufbahn aus einer Höhe von 643 km mit einer Bodenauflösung von 30 Metern auf. Die Abtastbreite beträgt 30 Kilometer, wobei der Satellit eine Streifenlänge von bis zu 5000 km pro Tag verarbeiten kann. Die Möglichkeit der Schwen-

kung des Satelliten um bis zu +/–30° erlaubt Vergleichsbeobachtungen desselben Ortes innerhalb von vier Tagen. Der ca. 766 kg schwere Satellit besitzt 218 Kanäle im reflexiven Spektralbereich zwischen 420 und 2.450 Nanometern. Aus der Analyse der spektralen Signaturen lassen sich quantitative Informationen über Vegetation, Boden und Umweltbeschaffenheit ableiten. Im Rahmen des EnMAP wird vom Alfred-Wegener-Institut das Forschungsprojekt „hy-ARK-VEG" (Hyperspektrale Methodenentwicklung für Arktische Vegetationsbiome) betrieben, das sich mit der Algorithmenentwicklung für Schmal- und Mehrband-Vegetations-Indizes für Permafrost- und Tundralandschaften beschäftigt. Ziel ist es, die entwickelten Algorithmen für Vegetations-Indizes (VI) und Leaf-Area-Indizes (LAI) mit weiter veredelten, quantitativen biophysikalischen Parametern (empirische Ableitungen zu Vegetationsbedeckung und Vegetationsbiomasse) in die EnMAP-Toolbox einzubinden. Darüber hinaus werden innovative Anisotropie-Untersuchungen mittels Geländegoniometermessungen in der arktischen Tundra und Tundra-äquivalenten Biomen in mitteldeutschen Bergbaufolgelandschaften durchgeführt, um EnMAP Aufnahmegeometrien zu simulieren und Normalisierungsmethoden für Schrägaufnahmen zu implementieren.

Stand der Technik

[0005] Der der Erfindung nächstliegende Stand der Technik wird in der Veröffentlichung I „Polarised Multiangular Reflectance Measurements Using the Finish Geodetic Institute Field Goniospectrometer" von J. Suomalainen et al. (in Sensors 2009, 9, 3891–3907) beschrieben. Das offenbarte transportable Goniometer (Akronym FIGIFIGO) wird für die radiometrische Messung des Reflexionsverhaltens von natürlichen Untergründen, gezeigt werden Messungen im Schnee, eingesetzt. Das FIGIFIGO gehört zur Gattung der Goniospektrometer mit konstantem Observationszentrum und besteht aus einer zentralen Hauptsäule, die eine Abstützung in Form einer Box gegenüber der zu vermessenden natürlichen Oberfläche, hier eine Schneedecke als natürlicher Untergrund, aufweist. Die Hauptsäule ist an einer Längsseite der Box seitlich schwenkbar angeordnet. An ihrem oberen Säulenende ist die Hauptsäule über eine Verschraubung mit dem festgelegten Auslegerende eines Auslegers verbunden. Weiterhin weist das bekannte Goniometer ein Spektrometer mit einer Optik und einem Sensor auf, wobei die Optik über eine optische Faser mit dem Sensor verbunden ist. Die Optik ist am Ort der Verschraubung angeordnet, am Ende des Auslegers befindet sich ein drehbarer Spiegel, über den die Reflexionen der Schneedecke in die Optik umgeleitet werden. Damit wird das konstante Observationszentrum nur durch den Spiegel und nicht durch die Optik erreicht. Die Verschraubung besteht aus einer Art offener Schelle, die das runde Gehäuse umfasst und durch eine Schraubverbindung festklemmt. Der Sensor ist zusammen mit einer Auswerteeinheit in der Box am unteren Säulenende der Hauptsäule untergebracht. In einer Position der Box auf der Schneedecke kann mit dem Gerät eine Messreihe in einer Ebene parallel zur Vorderkante der Box unter verschiedenen Betrachtungswinkeln (Kippen der Hauptsäule entlang der Vorderkante der Box) in einem Messort (Sichtfeld) durchgeführt werden. Um Messungen im Messort in verschiedenen Ebenen durchzuführen zu können, muss die ganze Box gedreht werden.

[0006] Das klassische Feld-Goniospektrometer mit konstantem Oberservationszentrum mit dem oben beschriebenen Aufbau aus Azimut- und Zenitring wird in der Veröffentlichung IA: „The improved Dual-view Field-Goniometer System FIGOS" von J. Schopfer et al. (in Sensors 2008, 8, pp. 5120–5140) beschrieben und hier der Vollständigkeit des Überblicks halber erwähnt. Deutlich zu erkennen ist der konstruktiv stabile, aber auch raumeinnehmende Aufbau. Nach dem Vorbild des FIGOS wurden viele weitere Gelände- und Labor-Goniospektrometer entwickelt.

[0007] Aus der Veröffentlichung II: „A low-cost field and laboratory goniometer system for estimating hyperspectral bidirectional reflectance" von C. A. Coburn et al. (in Can. J. Remote Sensing, Vol. 32, No. 3, pp. 244–253, 2006) ist der Grundtyp des Goniospektrometers mit konstantem Oberservationszentrum bekannt. Er besteht aus einem geschlossenen Azimutring, auf dem diametral ein halber Zenitring drehbar angeordnet ist. Auf dem halben Zenitring läuft ein Schlitten mit der Optik, die an jeden Punkt auf der Halbkugelschale gefahren werden kann. Ein vollständig automatisiertes Goniospektrometer mit konstantem Oberservationszentrum ist aus der Veröffentlichung III: „Automated spectro-goniometer: A spherical robot for the field measurement of the directional reflectance of snow" von T. Painter et al. (in Rev. Sci. Instrum., Vol. 74, No. 12. Dec. 2003, pp. 6179–5177) bekannt. Hier ist über einem Azimutbogen nur ein Viertel Zenitbogen vorgesehen, der an seinem Ende zwei weitere Bogenabschnitte trägt, die jeweils drehbar gelagert sind. Am Ende des zweiten Bogenabschnitts ist die Optik angeordnet. Gemessen wird die HRDF (Hemispherical directional reflectance function), die im Gegensatz zur BRDF noch die diffuse Reflexion der natürlichen Oberfläche berücksichtigt. Ein guter Überblick über die verschiedenen Entwicklungen auf dem Gebiet der Feldspektros-kopie bis 2007 wird in der Veröffentlichung IV: „Progress in field spectroscopy" von E. J. Milton et al. (in Remote Sensing of Environment (2007), doi: 10.1016/j.rse.2007.08001) gegeben. Gut zu erkennen sind die unterschiedlichen Bemühungen der Anwender, die Goniospektrometer möglichst leicht und einfach transportabel zu machen.

[0008] Aus der WO 2006/056647 A1 ist ein tragbares Goniometer zur Charakterisierung von künstlichen Oberflächen bekannt, dessen Hauptsäule mit drei Stempeln als Stützen gelagert ist. Entlang dieser Stützen ist die Hauptsäule vertikal und horizontale verfahrbar. Am unteren Säulenende ist die Hauptsäule mit dem festgelegten Auslegerende eines relativ kurzen Auslegers fest verbunden. Dessen freies Auslegerende ist fest mit der Mitte eines Bogens verbunden. Der Bogen trägt in fester Position eine Röntgenquelle und einer Optik. Durch Drehung des Auslegers um dessen Längsachse können Einstrahl- und Beobachtungswinkel relativ zum Messort in einem Winkelbereich verändert und im Labor gemessen werden.

[0009] Aus der DE 26 43 647 A1 ist eine Einrichtung zur Simulierung von Sonneneinstrahlung im Labor bekannt, bei dem an einem um die Horizontalachse des Einstrahlobjekts schwenkbarer Bogen vorgesehen ist, der einen weiteren Bogen mit orthogonaler Ausrichtung zum ersten Bogen trägt. Der weitere Bogen kann entlang des ersten Bogens verschoben werden. Am weiteren Bogen ist ein verschiebbarer Schlitten mit einer Beleuchtungsquelle angeordnet. Das Einstrahlobjekt ist auf einem Drehtisch angeordnet, sodass durch das Zusammenspiel der einzelnen Drehungen, Schwenkungen und Verschiebungen alle gerichteten Sonneneinstrahlungen auf jeden Ort des Einstrahlobjekts simuliert werden können.

[0010] Aus der EP 1 470 413 B1 ist ein transportables Diffraktometer zur Labormessung mit einer Hauptsäule bekannt, das auf einem fahrbaren Gestell angeordnet ist. An der Hauptsäule ist ein vertikaler Ausleger befestigt, der über eine drehbare Aufhängung fest mit einem Bogen verbunden ist. Auf dem Bogen ist neben einer Röntgenstrahlquelle auch ein Detektor befestigt, der auf dem Bogen verschoben werden kann. Weiterhin kann der Bogen noch um die Ebene entlang des vertikalen Auslegers verkippt werden, sodass mit dem Detektor beliebige Winkeleinstellungen auf einem Vollkreis um das Messobjekt herum eingenommen werden können.

Aufgabenstellung

[0011] Ausgehend von dem eingangs beschriebenen, gattungsbildenden transportablen Goniospektrometer mit konstantem Observationszentrum und einem Ausleger gemäß dem nächstliegenden Stand der Technik ist die Aufgabe für die vorliegende Erfindung darin zu sehen, dieses so weiterzubilden, dass eine radiometrische Messung der bidirektionalen Reflektanzverteilungsfunktion (BRDF) einer natürlichen Oberfläche, insbesondere mit anisotropem Reflektanzverhalten, unter frei wählbarem Azimut- und Zenitwinkel der Optik bei einer gegebenen Strahlungsquelle mit beliebigem Einfallswinkel, insbesondere Sonneneinstrahlung, durchführbar ist. Dabei soll das erfindungsgemäße Goniospektrometer aber besonders leicht und damit gut transportabel, robust und kostengünstig sowie besonders wetterfest sein, um auch unter erschwerten Einsatzbedingungen optimal im Gelände arbeiten zu können. Die erfindungsgemäße Lösung für diese Aufgabe ist dem Hauptanspruch zu entnehmen, vorteilhafte Weiterbildungen der Erfindung werden in den Unteransprüchen aufgezeigt und im Folgenden im Zusammenhang mit der Erfindung näher erläutert.

[0012] Das weitergebildete gattungsgemäße Goniospektrometer ist erfindungsgemäß einerseits dadurch gekennzeichnet, dass der Ausleger an seinem freien Auslegerende eine Aufhängung aufweist, die mit dem Sensor des Spektrometers und mit einem festgelegten Bogenende eines Bogens verbunden ist. Dabei ist die Aufhängung um eine vertikal zur natürlichen Oberfläche ausgerichtete Vertikalachse dreh- und fixierbar. Das andere Bogenende des Bogens ist als freies Bogenende ausgebildet. Durch die Aufhängung wird der Bogen im Abstand seines Radius oberhalb der natürlichen Oberfläche positioniert. Weiterhin ist erfindungsgemäß vorgesehen, dass an dem Bogen ein Schlitten angeordnet ist, der die Optik in einer radiometrischen Ausrichtung auf das Oberservationszentrum trägt. Dabei kann der Schlitten entlang des Bogens verschoben und an jeder Stelle fixiert werden. Bei dem erfindungsgemäßen Goniospektrometer ist also ein Bogen mit definierter Länge an seinem einen Ende an einer drehbaren Aufhängung befestigt, die ihrerseits wiederum am Ende des Auslegers befestigt ist. Es entsteht ein leichtgewichtiges Gebilde nach Art eines Mobiles, das eine einfache und leichte Ausrichtung des Bogens durch Drehung der Aufhängung ermöglicht. Dabei ist der Bogen im Abstand seines Bogenradius zur zu vermessenden natürlichen Oberfläche, auf der das Observationszentrum liegt, aufgehängt. Dadurch ist gewährleistet, dass die Optik bei der Drehung des Bogens um die Aufhängung und beim Verschieben des Schlittens entlang des Bogens immer auf das Observationszentrum ausgerichtet ist. Bei einer maximalen Bogenlänge von π und einer maximalen Bogendrehung von 2π kann damit die Optik des Sensors auf jede Azimut- und Zenitposition auf einer Halbkugelschale mit dem Observationszentrum im Mittelpunkt der Kugel eingestellt werden. Dadurch kann bei gegebenem Einfallswinkel einer Strahlungsquelle, insbesondere des Sonnenlichts, an jeder beliebigen Position auf der Halbkugelschale der BRF (bidirektionaler Reflektanzfaktor) gemessen werden, welcher dann in den BRDF-Wert umgerechnet werden kann.

[0013] Das Goniospektrometer nach der Erfindung wurde für das o. g. Forschungsprojekt des AWI entwickelt und zeichnet sich durch ein geringes Gewicht, eine hohe Transportierbarkeit und eine geringe Anfälligkeit ge-

genüber Witterungseinflüssen aus. Besonders vorteilhaft ist auch die schnelle Datenaufnahme, da immer nur ein Zenitwinkel am Bogen eingestellt wird und dann ohne weitere Umbauten alle Azimutwinkel zu diesem Zenitwinkel gemessen werden können. Bei einem Betrieb unter EnMAP-Spezifikationen (–30° bis +30° Blickzenitwinkel) und einer Zenitwinkelauflösung von 10° sind nur vier Umbauten erforderlich, um alle Zenit- und Azimutpositionen aufnehmen zu können. Das Goniospektrometer nach der Erfindung kann alle EnMAP-Aufnahmegeometrien simulieren und somit unter realen Bedingungen den Einfluss der Anisotropie auf die spektrale Signatur in arktischen Gebieten zeigen. Es verbindet die Vorteile der Vorrichtungen mit konstantem Observationszentrum (höhere Winkelgenauigkeit in der Positionseinstellung) mit denen der Vorrichtungen mit einer konstanten Optikposition (leichter, transportabler, schnell aufzubauen).

[0014] Bei einer ersten Ausgestaltung des erfindungsgemäßen Goniospektrometers ist der Ausleger bogenförmig ausgebildet. Dies führt zu einem stabilen Halt des Auslegers in einer definierten Höhe über der natürlichen Oberfläche mit dem Oberservationszentrum. Dabei ist der Ausleger aber trotzdem leicht, transportabel und robust. Einen optisch besonders ästhetischen Gesamteindruck ergibt sich, wenn der Ausleger entsprechend seines Abstands zum Bogen einen solchen Krümmungsradius aufweist, dass der Bogen und der Ausleger konzentrisch zueinander angeordnet sind. Bei einer weiteren Ausgestaltung ist vorgesehen, dass der Bogen eine solche Bogenlänge aufweist, dass der Schlitten beginnend bei der Vertikalachse um einen Bogenwinkel von 30° auf dem Bogen verschiebbar ist. Grundsätzlich kann der Bogen jede Länge bis zum Viertelkreis aufweisen. Darüber hinaus ist eine einfache Ausrichtung der Optik auf das Oberservationszentrum nicht mehr möglich. Um eine freie Verdrehbarkeit des Bogens in einem Vollkreis mit einer Drehrichtung zu ermöglichen, ist ein entsprechender Abstand zum Ausleger bzw. zur Hauptsäule einzuhalten. Dabei hängt es von der Höhe der Säule, von der Länge der Aufhängung und vom Neigungswinkel des Auslegers ab, ob das freie Bogenende bei entsprechender Bogenlänge gegen den Ausleger oder gegen die Hauptsäule stoßen könnte. Ansonsten kann der Bogen auch aus beiden Drehrichtungen bis an der Hauptsäule bzw. an den Ausleger gedreht werden. Bei einer Einbindung des Goniospektrometers in ein Programm mit einem verschwenkbaren Satelliten hängen die Einblickswinkel der Optik in das Oberservationszentrum entsprechend von den Schwenkwinkeln des Satelliten ab. Bei EnMAP kann dieser um ±30° verschwenkt werden. Folglich muss auch die Optik einen Einblickswinkel von 30° einnehmen können. Damit der Schlitten in eine entsprechende Position auf dem Bogen verfahren werden kann, ist es also nur erforderlich, dass der Bogen eine Bogenlänge von etwas über π/6 aufweist. Dadurch kann der Ausleger entsprechend kurz und stabil gehalten und immer noch gewährleistet werden, dass der Bogen frei darunter hindurchdrehen kann.

[0015] Um die Optik an jedem Oft der Kugelschale platzieren zu können, ohne dabei das gesamte Goniometer drehen zu müssen, ist es weiterhin vorteilhaft, wenn die Aufhängung in einem Vollkreis drehbar ausgebildet ist. Bei einem begrenzten Drehwinkelbereich wäre entsprechend die gesamte Apparatur zu drehen. Bei einer Positionierbedingung der Optik nur auf der einen Hälfte der Kugelschale (bei einer Symmetrie der Anisotropie der Reflexion) kann aber ein begrenzter Drehwinkelbereich ausreichend sein. Die Aufhängung kann dann entsprechend einfach konzipiert sein. Wenn gemäß einer weiteren Erfindungsausgestaltung die Aufhängung manuell verdrehbar und der Schlitten manuell verschiebbar ausgebildet ist, ist eine weitere Vereinfachung möglich. Vorteilhaft ist auch das Entfallen von elektrischen Antrieben, die unter Witterungseinflüssen, insbesondere unter Feuchtigkeit leiden können. Somit kann das Goniospektrometer nach der Erfindung auch in Regionen mit höherer Feuchte (z. B. Tundra) betrieben werden. Außerdem verringert sich durch das Wegfallen von Elektronik und ggfs. Batterien das Gesamtgewicht des Goniospektrometers.

[0016] Insbesondere das manuelle Verdrehen der Aufhängung zur Einstellung des Azimutwinkels der Optik und das manuelle Verschieben des Schlittens zur Einstellung des Zenitwinkels der Optik wird erleichtert, wenn auf dem Bogen und auf der Aufhängung eine Gradeinteilung, beispielsweise mit einer 1°-Schrittweite, vorgesehen ist. Ansonsten sind die Gradeinteilungen auch bei einer motorischen Verstellung von Vorteil, um die aktuelle Winkelposition ablesen zu können.

[0017] Zur Ermittlung zuverlässiger Messwerte muss der Abstand des Bogens über dem Observationszentrum im Bogenradius konstant sein. Dies wird zum einen bei der Erfindung durch eine ausreichende Stabilität der Materialien und Verbindungen erreicht. Eine weitere Verbesserung kann aber erreicht werden, wenn bevorzugt vorteilhaft das festgelegte Auslegerende des Auslegers über die Verschraubung hinausgeht und hinter der Verschraubung mittels einer längenverstellbaren Auslegerverstrebung mit der Hauptsäule verbunden ist. Eine an der Aufhängung und damit am freien Auslegerende angreifende Zugkraft kann dadurch nicht mehr zu einer Absenkung des Auslegers führen. Ähnliches gilt für den Bogen, der analog zum Ausleger über ein festgelegtes und ein freies Ende verfügt. Die Stabilität des Bogens kann verbessert und ein Absenken verhindert werden, wenn bevorzugt und vorteilhaft der Bogen mittels einer an seinem freien Bogenende angeordneten

längenverstellbaren Bogenverstrebung mit der drehbaren Aufhängung verbunden ist. Verstrebung und Bogen werden somit gemeinsam gedreht, sodass ein Verdrehen verhindert ist.

[0018] Ein weiterer Punkt für die Handhabbarkeit und Genauigkeit des Goniospektrometers bei der Arbeit im Feld betrifft die Abstützung der Hauptsäule gegenüber der natürlichen Oberfläche. Bekannt sind geschlossene Azimutkreise und kompakte Boxen, die aber insbesondere auf unebenen Oberflächen (Untergründen) verkippen können. Vorteilhaft ist bei der Erfindung deshalb die Abstützung der Hauptsäule gegenüber der natürlichen Oberfläche als Dreibeingestell ausgebildet, das über eine Ständerhülse mit der Hauptsäule verbunden ist, wobei jedes Bein mit seinem oberen Beinende mit der Ständerhülse und mit einer Dreibeinverstrebung mit der Hauptsäule verbunden ist und aus zumindest zwei Beinelementen besteht, die längenverstellbar miteinander verbunden sind. Ein Dreibeingestell ermöglicht eine optimale Abstützung und Unabhängigkeit von möglichen Bodenunebenheiten. Über die Standerhülse wird das Dreibeingestell in einfacher Weise mit der Hauptsäule verbunden, wobei dies in unterschiedlicher Höhe erfolgen kann, was lediglich einen unterschiedlichen Anstellwinkel der einzelnen Beine zur Folge hat. Dabei kann das Dreibeingestell noch zusätzlich in seiner Standfestigkeit gesichert werden, wenn die Hauptsäule an ihrem unteren Säulenende und die Beine des Dreibeingestells an ihren unteren Beinenden Bodenplatten aufweisen, die über Bodendorne zum Einstecken in die natürliche Oberfläche und Befestigungsplatten auf der natürlichen Oberfläche fixiert sind.

[0019] Andere wichtige Aspekte bei dem Goniospektrometer nach der Erfindung sind seine Anpassbarkeit an den und seine Transportierbarkeit zum Messort. Vorteilhaft bestehen dafür die Hauptsäule aus zumindest zwei Säulenelementen und der Ausleger aus zumindest zwei Auslegerelementen, die jeweils längenverstellbar und lösbar miteinander verbunden sind. Dabei weisen die Säulenelemente und Auslegerelemente solche Abmaße auf, dass sie in einer kompakten Transportkiste mit Griff und Rädern oder Kufen unterbringbar sind. Analoges gilt auch für das Dreibeingestell. Die Hauptsäule kann durch die längenverstellbare Mehrteiligkeit einfach in ihrer Länge eingestellt werden, um den Bogen im Radiusabstand über dem Oberservationszentrum zu positionieren. Durch die Längenverstellbarkeit können alle Komponenten optimal an den Messort und auch aufeinander abgestimmt werden. Durch die Mehrteiligkeit können sie einfach demontiert und transportiert werden. Dies kann beispielsweise in einer Box mit den Maßen 150 × 30 × 50 cm erfolgen. Zum Transport auf festem Boden kann die Box Gummireifen oder Ballonreifen aufweisen. Zum Transport auf Schnee kann sie alternativ Kufen aufweisen oder es können Kufen über die Reifen geschoben werden.

[0020] Die Verschraubung dient der Verbindung und der Einhaltung eine vorgegebenen Winkels zwischen Hauptsäule und Ausleger. Dabei muss die Verschraubung so fest sein, dass der Ausleger unter der angehängten Last nicht absinkt. Dafür kann in einer nächsten Modifikation der Erfindung bevorzugt und vorteilhaft vorgesehen sein, dass die Verschraubung zwischen Hauptsäule und Ausleger aus einer Säulenplatte an der Hauptsäule und einer Auslegerplatte am Ausleger mit einer Zentralverschraubung und einer Reihe von Fixierverschraubungen zur Einstellung eines Winkels zwischen Säulenplatte und Auslegerplatte aufgebaut ist. Die Zentralverschraubung sorgt für die feste Verbindung zwischen den Platten die Fixierschrauben für die feste Winkeleinstellung. Ein weiteres wesentliches Element bei dem Goniospektrometer nach der Erfindung ist die drehbare Aufhängung des Bogens am Ausleger. Vorteilhaft kann diese dadurch gekennzeichnet sein, dass sie aus einer Zentralstange mit einer oberen Aufnahmeplatte für den Sensor des Spektrometers und einem Drehstativkopf mit einer unteren Aufnahmeplatte zur Befestigung des festgelegten Bogenendes des Bogens aufgebaut ist. Die Aufhängung des Bogens mit der Aufnahmeplatte für den Sensor kann zusammen mit dem Bogen gedreht werden, sodass sich keine Kabelverschlingungen ergeben. Der Drehstativkopf ist insbesondere aus der Fotografie bekannt, beispielsweise kann es von der Firma Manfrotto hergestellt werden. Er erlaubt eine präzise Einhaltung der Winkelgenauigkeit und ist um 360° drehbar.

[0021] Weiterhin kann mit dem Schlitten vorteilhaft auch zusätzlich eine Videokamera zur Beobachtung des Oberservationszentrums während der Messung und zeitweilig eine Spektralonplatte mit einem Reflexionsgrad 1 zur Kalibrierung der Optik des Spektrometers verbunden sein. Weiterhin kann vorteilhaft ein satellitengestützter Ortsdetektor zur Feststellung der globalen Position des Goniospektrometers während des Messens an der Aufhängung befestigt sein. Schließlich können noch vorteilhaft Wasserwaagen zur lotrechten Ausrichtung der Hauptsäule und der Optik und/oder ein zweites Spektrometer zur Messung der Irradianz (Strahlungsflussdichte, die das Beobachtungszentrum durchquert) und der diffusen Reflexion der natürlichen Oberfläche vorgesehen sein. Die Wasserwaagen werden bevorzugt an der Hauptsäule und an der Aufhängung befestigt. Das zweite Spektrometer kann zusammen mit einem Diffusor am oberen Ende der Hauptsäule befestigt sein und dient der Bestimmung der HRDF. Alternativ zu einer direkten Befestigung am Goniospektrometer nach der Erfindung kann es auch als eigenständiges Gerät in unmittelbarer Nähr zum Goniospektrometer nach der Erfindung positioniert sein. Weitere Details zur Erfindung sind dem nachfolgenden speziellen Beschreibungsteil zu entnehmen.

Ausführungsbeispiele

[0022] Ausbildungsformen des Goniospektrometers nach der Erfindung mit konstantem Observationszentrum, insbesondere geeignet für die radiometrische Messung des anisotropen Reflexionsverhaltens einer natürlichen Oberfläche, werden nachfolgend zum weiteren Verständnis der Erfindung anhand der schematischen Figuren, die in unterschiedlichen Maßstäben dargestellt sind, näher erläutert. Dabei zeigt:

[0023] **Fig.** 1 die Beobachtungsgeometrie (Stand der Technik),

[0024] **Fig.** 2 den prinzipiellen konstruktiven Aufbau,

[0025] **Fig.** 3 im Detail die Hauptsäule,

[0026] **Fig.** 4 im Detail die Auslegerverstrebung,

[0027] **Fig.** 5 im Detail ein Dreibein als Abstützung,

[0028] **Fig.** 6 im Detail den Ausleger,

[0029] **Fig.** 7 im Detail die Verschraubung,

[0030] **Fig.** 8 im Detail die Aufhängung,

[0031] **Fig.** 9 im Detail den Bogen,

[0032] **Fig.** 10 ein Schema für den gesamten Messaufbau und

[0033] **Fig.** 11 Messschemen für Objekte ohne und mit Symmetrieachse.

[0034] Die **Fig.** 1 zeigt aus dem Stand der Technik die Beobachtungsgeometrie für anisotrope Reflektanzmessungen, oben in der Schrägsicht, unten in der Nadir-Aufsicht (Nadir = dem Zenit auf der natürlichen Oberfläche SF gegenüberliegender Lotfußpunkt; Zenit = der senkrecht über dem Beobachter liegende Scheitelpunkt des Himmelsgewölbes). In der Schrägsicht oben ist in der Projektion die Sonnenbahn (Himmelsrichtungen) mit verschiedenen Azimutwinkeln ψ_n über der Sonnenbahn (Tageslauf) mit verschiedenen Zenitwinkeln Θ_n, dargestellt. Gezeigt ist in der Mitte der Projektion ein konstantes Beobachtungszentrum BC auf einer natürlichen Oberfläche SF, in das Sonnenstrahlung SN einfällt und das von einem Satelliten ST beobachtet wird (Messung der reflektierten Strahlung). In der Nadir-Aufsicht unten ist die Grundebene PP dargestellt, die durch die Sonne (Hot Spot) verläuft und die dazu orthogonal verlaufene Querebene CP. Die Außenlinie stellt den Horizont HZ dar.

[0035] In der **Fig.** 2 ist der Aufbau des transportablen Goniospektrometers **01** nach der Erfindung in einem Prinzipschema dargestellt. Gezeigt ist eine ungekrümmte, gerade Hauptsäule **02** mit einem Ausleger **03**, einer dreh- und fixierbaren Aufhängung **04** (lotrechte Ausrichtung entlang einer Vertikalachse VA) und einem Bogen **05**, auf dem ein Schlitten **06** verschieb- und fixierbar angeordnet ist. Gezeigt ist weiterhin eine Abstützung **08** der Hauptsäule **02** in Form eines Dreibeingestells **07** sowie eine Auslegerverstrebung **09** und eine Verschraubung **10** der Hauptsäule **02** gegenüber dem Ausleger **03**. Weiterhin sind eine Bogenverstrebung **11** und eine Dreibeinverstrebung **12** dargestellt. Im Nachfolgenden werden die einzelnen Komponenten näher erläutert.

[0036] Die **Fig.** 3 zeigt die Hauptsäule **02** im Detail. Dargestellt sind zwei (erstes, zweites) Säulenelemente **021**, **022**, die über ein Verbindungsstück **023** miteinander verbunden sind. Die Hauptsäule **02** besteht im gewählten Ausführungsbeispiel aus 30 mm Aluminiumrohr mit einer Gesamtlänge von ca. 2 m. Bei dem Verbindungsstück **023** handelt es sich im gewählten Ausführungsbeispiel um eine einfache Einschiebhülse **024** mit einem Mittensteg **025**. Die Hauptsäule **02** trägt am unteren Säulenende **029** eine Bodenplatte **026** zur Aufstellung auf ebenem Gelände. Ein Bodendorn **027** dient zum Einstecken in die natürliche Oberfläche SF des weichen Erdbodens. Die Bodenplatte **026** dient dabei als Anschlag. Eine Befestigungsplatte **028** wird über das untere Säulenelement **022** geschoben und mit dem Bodendorn **027** im Boden fixiert. Am oberen Säulenelement **021** ist am oberen Säulenende **030** eine Säulenplatte **101** angeordnet, die Teil der Verschraubung **10** ist. Zur erkennen sind weiterhin eine Zentralbohrung **102** und eine Reihe von Fixierbohrungen **103**.

[0037] Die **Fig.** 4 zeigt die Auslegerverstrebung **09**, die am festgelegten Auslegerende **037** (vergleiche **Fig.** 6) des Auslegers **03** angeordnet ist. Im gezeigten Ausführungsbeispiel besteht die Auslegerverstrebung **09** aus zwei Hülsen **091**, **092**, die über die Hauptsäule **02** und über das Ende des Auslegers **03** geschoben und mit einer Rändelschraube **093** arretiert sind. Zwischen zwei Laschen **094**, **095** ist eine Verstellhülse **096** angeordnet, über die die Länge der Auslegerverstrebung **09** einstellbar ist. Alle genannten Elemente sind über Gelenke **097** miteinander verbunden.

[0038] In der **Fig.** 2 ist als Abstützung **08** ein Dreibeingestell **07** dargestellt. Die **Fig.** 5 zeigt im Detail ein Dreibein **071**, das aus zwei Beinelementen **072**, **073** besteht, die mittels einer einsteckbaren Verschraubung **074** (eingestecktes Gegengewinde) längenverstellbar miteinander verbunden sind. Jedes Dreibein **071** besteht im gewählten Ausführungsbeispiel aus einem 30 mm Aluminiumrohr mit einer Gesamtlänge von ca. 1,75 m. Am unteren Beinende **082** des unteren Beinelements **073** ist wiederum eine Bodenplatte **075** angeordnet. Mit Hilfe eines Bodendorns **076** zum Einstecken in den Boden und einer Befestigungsplatte **028** wird die Bodenplatte **075** fixiert. Über ein Verschraubungsblech **077** an seinem oberen Dreibeinende **081** ist das Dreibein **071** gelenkig mit einer Ständerhülse **078** verbunden, die über die Hauptsäule **02** geschoben und mit einer Rändelschraube **079** fixiert wird. Die Ständerhülse **078** trägt drei Verschraubungslaschen **080** (am Umfang unter 120° gleichmäßig verteilt), an die die drei Dreibeine **071** montiert werden. Weiterhin ist an jedem Dreibein **071** eine Dreibeinverstrebung **12** angeordnet, die aus einer verschieb- und fixierbaren Verstrebungshülse **121** und einem Verstrebungsarm **122** aufgebaut ist. Der Verstrebungsarm **122** ist mit einer Säulenhülse **123** verbunden, die auf der Hauptsäule **02** läuft und über eine Feststellschraube **124** höhenfixierbar ist. Je nach Höhe der Anordnung der Dreibeinverstrebung **12** an der Hauptsäule **02** und am Dreibein **071** und je nach Länge des Verstrebungsarms **122** ergibt sich ein Öffnungswinkel des Dreibeingestells **07**, der bevorzugt bei ca. 65° liegt.

[0039] Auch der Ausleger **03** kann aus einem 30 mm (Durchmesser) Aluminiumrohr mit einer Länge von ca. 2 m bestehen. Vorteilhaft kann daher für die Hauptsäule **02**, das Dreibeingestell **07** und den Ausleger **03** dann identisches Halbzeug verwendet werden. In der **Fig.** 6 sind weitere Details zum Ausleger **03** und zur Verschraubung **10** aufgezeigt. Der Ausleger **03** weist ein festgelegtes Auslegerende **037** und ein freies Auslegerende **038** auf. Dabei bedeutet „frei" nicht eingespannt, d. h. offen, und frei drehbar und „festgelegt" eingespannt, gelagert und nicht frei drehbar. Der Ausleger **03** ist ebenfalls zweiteilig und besteht aus zwei Auslegerelementen **031**, **032**, die über angearbeitete Flansche **033** und zwei Fixierschrauben **034** miteinander verbunden sind. Eine Längenverstellbarkeit ist für den Ausleger **03** nicht erforderlich. An seinem einem freien Auslegerende **038** weist der Ausleger **03** einen angearbeiteten Ring **035** zur Aufnahme der Aufhängung **04** mit einem Feststellknebel **036** zur Fixierung der Aufhängung **04** auf. Vor dem festgelegten Auslegerende **039** ist eine Auslegerplatte **104** mit einer Zentralbohrung **105** und einer Reihe von Fixierbohrungen **106** als Teil der Verschraubung **10** mit der Hauptsäule **02** angeordnet.

[0040] In der **Fig.** 7 ist die Verschraubung **10** dargestellt. Die Säulenplatte **101** ist mit der Auslegerplatte **104** mittels einer Knebelschraube **107** durch die Zentralbohrungen **102**, **105** fest verbunden. Die Winkelstellung des Auslegers **03** zur Hauptsäule **02** ergibt sich durch Einstecken eines Fixierstifts **108** in entsprechend übereinander liegende Fixierbohrungen **103**, **106**.

[0041] Die **Fig.** 8 zeigt Details zur Aufhängung **04**. Eine Zentralstange **041** trägt an ihrem oberen Ende ein Gewinde **042**, auf das der Ring **035** des Auslegers **03** aufgeschoben und zwischen zwei Gewindemuttern **043** aus einem frostfesten Kunststoff fixiert ist. Durch die auf dem Gewinde **042** drehbaren Gewindemutttern **043** kann eine Höhenfixierung der Aufhängung **04** in Relation zur natürlichen Oberfläche SF vorgenommen werden. Am unteren Ende weist die Zentralstange **041** ein Drehstativkopf **045** mit einem Vollkreisdrehbereich (beispielsweise Manfrotto nord Art. 300 N, der Fa. Manfrotto™) auf. Zur Einstellung des Drehstativkopfs **045** ist eine Gradeinteilung **050** vorgesehen. An seinem unteren Ende weist der Drehstativkopf **045** eine untere Aufnahmeplatte **046** zur höhen- und winkelverstellbaren Befestigung des Bogens **05** auf. Die Fixierung erfolgt mittels einer Knebelschraube **047**, die in eine Bohrung **048** eingeschraubt wird. Zwischen dem Drehstativkopf **045** und dem Ausleger **03** ist eine obere Aufnahmeplatte **040** zur Befestigung eines Sensors eines Spektrometers (nicht gezeigt) mittels zweier gelochter Laschen **049** über die Zentralstange **041** geschoben. Die obere Aufnahmeplatte **040** ist mit einer Fixiermutter **044** festgelegt. Die Aufhängung **04** ist insgesamt frei drehbar um den Ring **035** des Auslegers **03** gelagert.

[0042] Die **Fig.** 9 zeigt den Bogen **05**, der einteilig mit einer Länge von 1,4 m aufgebaut ist und im gewählten Ausführungsbeispiel aus einem 20 mm Aluminiumrohr besteht. An seinem festgelegten Bogenende **054** weist der Bogen **05** eine Befestigungsplatte **051** mit einem Langloch **052** auf, durch die die Knebelschraube **047** zur Befestigung an der unteren Aufnahmeplatte **046** des Drehstativkopfs **045** gesteckt ist. An freien Bogenende **055** des Bogens **05** ist ein Strebenstück **111** angeordnet, das die Bogenverstrebung **11** trägt. Über eine Län-

genverstellung **112** ist die Bogenverstrebung **11** mit der Aufhängung **04** bzw. der frei drehbaren oberen Aufnahmeplatte **040** verbunden und damit zusammen mit dem Bogen **05** ebenfalls frei drehbar. Auf dem Bogen **05** ist der Schlitten **06** frei verschiebbar angeordnet. Zur Positionierung ist auf dem Bogen **05** eine Gradeinteilung **053** vorgesehen. Die Verschiebung erfolgt über einen Läufer **061**, der mittels einer Fixierschraube **062** an jedem Ort entlang des Bogens **05** feststellbar ist. Am Läufer **061** ist eine Läuferplatte **063** befestigt, die mehrere Bohrungen **064** zur Aufnahme der Optik **131** des Spektrometers **13** und ggfs. weiterer Komponenten aufweist (vergleiche **Fig.** 10).

[0043] Die **Fig.** 10 zeigt zusammenfassend ein Schema für den gesamten Messaufbau mit dem tragbaren Goniospektrometer **01** nach der Erfindung. Schematisch dargestellt ist ein Spektrometer **13** zur Messung der Reflektanz bzw. Radianz (beispielsweise GER 1500 der Fa. SVC, Spectra Vista Corporation) mit der Optik **131** und dem Sensor **132**, die mit einer optischen Faser **133** miteinander verbunden sind. Neben der Optik **131** ist eine Videokamera **14** (beispielsweise Webcam CM-3010 AF der Firma Hama®) an der Läuferplatte **063** angeordnet, deren Zuleitung **141** ebenfalls zum Spektrometer **13** geleitet wird. Vom Spektrometer **13** verläuft ein Verbindungskabel **142** entlang des Auslegers **03** und der Hauptsäule **02** zu einem Auswerteeinheit **134** zur Datenspeicherung und -verarbeitung als Zubehör des Spektrometers **13**. Optische Faser **133** und Zuleitung **141** werden je nach Flexibilität lose mit Führungsringen **134** versehen, um die flexible Nachführung zum Schlitten **06** zu ermöglichen. Um eine Verdrehung der optischen Faser **133** und der Zuleitung **141** um die Aufhängung **04** zu vermeiden, wird der Bogen **05** nur maximal einmal im Vollkreis in eine Richtung und dann wieder zurück gedreht. Weiterhin ist ein zweites Spektrometer **15** mit einem Diffusor **151** zur Messung der Irradianz auf der Hauptsäule **02** im Bereich der Verschraubung **10** angeordnet und mit einem weiteren Verbindungskabel **152** mit der Auswerteeinheit **134** verbunden. Zur Ortsdetektion ist ein satellitengestützter Ortsdetektor **16** (beispielsweise NL-402U USB Empfänger der Fa. Navilock®) am oberen Ende des Aufhängung **04** vorgesehen, der ebenfalls mit der Auswerteeinheit **134** verbunden ist (nicht dargestellt). An der Hauptsäule **02** und an der Aufhängung **04** sind zu deren lotrechter Ausrichtung mehrere Wasserwaagen **17** angeordnet. Gezeigt ist auch eine Spektralonplatte **18** an einer Spektralonhalterungsplatte **181** zur Kalibrierung der Optik **131**.

[0044] In der Darstellung hat der Bogen **05** eine solche Länge, dass ein maximaler Beobachtungswinkel von 30° vom Lot (Vertikalachse VA) durch die Aufhängung **04** aus in das Oberservationszentrum BC durch Verschieben des Schlittens **06** erreicht werden kann. Durch Drehen des Bogens **05** um die Aufhängung **04** im Vollkreis ergibt sich damit ein Beobachtungskegel von 60°. Dies entspricht dem Beobachtungskegel durch einen Satelliten ST mit einem Schwenkwinkel von 30°. Auf der zugehörigen Kugelschale dieses Beobachtungskegels kann der Schlitten **06** (und damit die Optik **131**) an jeder Position fixiert werden. Bei einem vorgegebenen Erfassungswinkel der Optik **131** kann in der Position des Schlittens **06** lotrecht unterhalb der Aufhängung **04** ein Oberservationszentrum BC mit einer Kantenlänge von 300 mm und bei einer Position des Schlittens **06** am freien Ende des Bogens **05** (Verschiebung um π/6 bzw. um einen Bogenwinkel BW von 30°) mit einer Kantenlänge von ca. 350 mm erfasst werden.

[0045] Mit dem tragbaren Goniospektrometer **01** nach der Erfindung wird ein leichtes, stabiles, aber robustes und gut transportables Messgerät zur Verfügung gestellt, das größtenteils aus Normteilen besteht und damit relativ preisgünstig in der Herstellung ist. Die Betätigung der verschieb- und drehbaren Elemente erfolgt nicht motorisch, sondern manuell. Dadurch wird feuchteempfindliche Elektronik vermieden. Durch eine Optikhöhe BR von ca. 2 m über der natürlichen Oberfläche SF ergibt sich nur ein geringer Schattwurf durch das Gerät an sich. Die Gerätespezifikationen entsprechen den Aufnahme-Spezifikationen für EnMAP. Folgende Eckdaten zeigt das Datenblatt für das tragbare Goniospektrometer nach der Erfindung:

Gesamthöhe	2,50 m
Gewicht (ohne Spektrometer)	21,5 kg
Material	Aluminium
Höhe der Optik über Objekt	2,02 m
Grundprobenbreite GSD (nadir)	30 cm
Grundprobenbreite GSD (30°)	34,8 cm
Aufnahmemöglichkeit im Azimut	Vollkreis (360°)
Einstellgenauigkeit im Azimut	2,5°

Aufnahmemöglichkeit im Zenit	–30° bis +30°
Einstellgenauigkeit im Zenit	1°
Zeit für Durchführung einer Messreihe	ca. 20 min (Vollkreis)

[0046] Die **Fig.** 11 zeigt ein mögliches Messschema zur Positionierung der Optik **131** für Objekte ohne Symmetrieachse (links, 61 Messpunkte) und mit Symmetrieachse (rechts, 35 Messpunkte). Durch die Verringerung der Messpunkte kann die Durchführung eines Messzyklusses noch erheblich beschleunigt werden.

Bezugszeichenliste

01	Goniospektrometer
02	Hauptsäule
021	oberes Säulenelement
022	unteres Säulenelement
023	Verbindungsstück
024	Einschiebhülse
025	Mittensteg
026	Bodenplatte
027	Bodendorn
028	Befestigungsplatte
029	unteres Säulenende
030	oberes Säulenende
03	Ausleger
031	erstes Auslegerelement
032	zweites Auslegerelement
033	Flansch
034	Fixierschraube
035	Ring
036	Feststellknebel
037	festgelegtes Auslegerende
038	freies Auslegerende
04	Aufhängung
040	obere Aufnahmeplatte
041	Zentralstange
042	Gewinde
043	Gewindemutter
044	Fixiermutter
045	Drehstativkopf
046	untere Aufnahmeplatte
047	Knebelschraube
048	Bohrung
049	Lasche
050	Gradeinteilung
05	Bogen
051	Befestigungsplatte
052	Langloch
053	Gradeinteilung
054	festgelegtes Bogenende
055	freies Bogenende
06	Schlitten
061	Läufer
062	Fixierschraube
063	Läuferplatte
064	Bohrung
07	Dreibeingestell
071	Dreibein
072	oberes Beinelement
073	unteres Beinelement
074	Verschraubung

075	Bodenplatte
076	Bodendorn
077	Verschraubungsblech
078	Ständerhülse
079	Rändelschraube
080	Verschraubungslasche
081	oberes Dreibeinende
082	unteres Dreibeinende
08	Abstützung
09	Auslegerverstrebung
091	Hülse
092	Hülse
093	Rändelschraube
094	Lasche
095	Lasche
096	Verstellhülse
097	Gelenk
10	Verschraubung
101	Säulenplatte
102	Zentralbohrung
103	Fixierbohrung
104	Auslegerplatte
105	Zentralbohrung
106	Fixierbohrung
107	Knebelschraube
108	Fixierstift
11	Bogenverstrebung
111	Strebenstück
112	Längenverstellung
12	Dreibeinverstrebung
121	Verstrebungshülse
122	Verstrebungsarm
123	Säulenhülse
124	Feststellschraube
13	Spektrometer (Radianz)
131	Optik
132	Sensor
133	optische Faser
134	Auswerteeinheit
14	Videokamera
141	Zuleitung
142	Verbindungskabel
15	Spektrometer (Irradianz)
151	Diffusor
152	weiteres Verbindungskabel
16	Ortsdetektor
17	Wasserwaage
18	Spektralonplatte
181	Spektralonhalterungsplatte
BC	Beobachtungszentrum
BL	Bogenlänge
BR	Bogenradius
BW	Bogenwinkel
CP	Querebene
HZ	Horizont
PP	Grundebene
SF	natürliche Oberfläche
SN	Sonnenstrahlung

ST Satellit
VA Vertikalachse
ψ_n Azimutwinkel
Θ_n Zenitwinkel

Patentansprüche

1. Transportables Goniospektrometer (**01**) mit konstantem Observationszentrum (BC), geeignet für die radiometrische Messung des Reflexionsverhaltens einer Oberfläche (SF), mit einer Hauptsäule (**02**), die eine Abstützung (**08**) gegenüber der Oberfläche (SF) aufweist und an ihrem oberen Säulenende (**030**) über eine Verschraubung (**10**) mit dem festgelegten Auslegerende (**037**) eines Auslegers (**03**), dessen anderes Auslegerende als freies Auslegerende (**038**) ausgebildet ist, verbunden ist, und mit einem Spektrometer (**13**) mit einem Sensor (**131**) und einer Auswerteeinheit (**132**), wobei der Sensor (**131**) über eine optische Faser (**133**) mit der Auswerteeinheit (**132**) verbunden ist, **dadurch gekennzeichnet,** dass der Ausleger (**03**) an seinem freien Auslegerende (**038**) eine um eine lotrecht zur Oberfläche (SF) ausgerichtete Vertikalachse (VA) dreh- und fixierbare Aufhängung (**04**) aufweist, die mit der Auswerteeinheit (**132**) des Spektrometers (**13**) und mit einem festgelegten Bogenende (**054**) eines Bogens (**05**) verbunden ist, wobei das andere Bogenende des Bogens (**05**) als freies Bogenende (**055**) ausgebildet ist, und dass die Aufhängung (**04**) den Bogen (**05**) im Abstand seines Bogenradiusses (BR) oberhalb der Oberfläche (SF) positioniert, und dass an dem Bogen (**05**) ein entlang des Bogens (**05**) verschieb- und fixierbarer Schlitten (**06**) angeordnet ist, der den Sensor (**131**) in einer Ausrichtung auf das Oberservationszentrum (BC) trägt.

2. Tansportables Goniospektrometer (**01**) nach Anspruch 1, **dadurch gekennzeichnet,** dass der Ausleger (**03**) bogenförmig ausgebildet ist.

3. Tansportables Goniospektrometer (**01**) nach Anspruch 1 oder 2, **dadurch gekennzeichnet,** dass der Bogen (**05**) eine solche Bogenlänge (BL) aufweist, dass der Schlitten (**06**) beginnend bei der Vertikalachse (VA) um einen Bogenwinkel (BW) von 30° auf dem Bogen (**05**) verschiebbar ist.

4. Tansportables Goniospektrometer (**01**) nach einem der vorangehenden Ansprüche, **dadurch gekennzeichnet,** dass die Aufhängung (**04**) in einem Vollkreis drehbar ausgebildet ist.

5. Tansportables Goniospektrometer (**01**) nach einem der vorangehenden Ansprüche, **dadurch gekennzeichnet,** dass die Aufhängung (**04**) manuell verdrehbar und der Schlitten (**06**) manuell verschiebbar ausgebildet ist.

6. Tansportables Goniospektrometer (**01**) nach einem der vorangehenden Ansprüche, **dadurch gekennzeichnet,** dass auf dem Bogen (**05**) und auf der Aufhängung (**04**) eine Gradeinteilung (**053**, **050**) vorgesehen ist.

7. Tansportables Goniospektrometer (**01**) nach einem der vorangehenden Ansprüche, **dadurch gekennzeichnet,** dass das festgelegte Auslegerende (**037**) des Auslegers (**03**) über die Verschraubung (**10**) hinausgeht und hinter der Verschraubung (**10**) mittels einer längenverstellbaren Auslegerverstrebung (**09**) mit der Hauptsäule (**02**) verbunden ist.

8. Tansportables Goniospektrometer (**01**) nach einem der vorangehenden Ansprüche, **dadurch gekennzeichnet,** dass der Bogen (**05**) mittels einer an seinem freien Bogenende (**055**) angeordneten längenverstellbaren Bogenverstrebung (**11**) mit der drehbaren Aufhängung (**04**) verbunden ist.

9. Tansportables Goniospektrometer (**01**) nach einem der vorangehenden Ansprüche, **dadurch gekennzeichnet,** dass die Abstützung (**08**) der Hauptsäule (**02**) gegenüber der Oberfläche (SF) als Dreibeingestell (**07**) ausgebildet ist, das über eine Ständerhülse (**078**) mit der Hauptsäule (**02**) verbunden ist, wobei jedes Dreibein (**071**) mit seinem oberen Beinende (**081**) mit der Ständerhülse (**078**) und über eine Dreibeinverstrebung (**12**) mit der Hauptsäule (**02**) verbunden ist und aus zumindest zwei Beinelementen (**072**, **073**) besteht, die längenverstellbar miteinander verbunden sind.

10. Tansportables Goniospektrometer (**01**) nach Anspruch 9, **dadurch gekennzeichnet,** dass die Hauptsäule (**02**) an ihrem unteren Säulenende (**029**) und die Dreibeine (**071**) des Dreibeingestells (**07**) an ihren unteren Beinenden (**082**) Bodenplatten (**026**) aufweisen, die über Bodendorne (**027**, **076**) zum Einstecken in die Oberfläche (SF) und Befestigungsplatten (**028**) auf der Oberfläche (SF) fixiert sind.

11. Tansportables Goniospektrometer (**01**) nach einem der vorangehenden Ansprüche, **dadurch gekennzeichnet,** dass die Hauptsäule (**02**) aus zumindest zwei Säulenelementen (**021**, **022**) und der Ausleger (**03**) aus zumindest zwei Auslegerelementen (**031**, **032**) besteht, die jeweils längenverstellbar und lösbar miteinander verbunden sind, wobei die Säulenelemente (**021**, **022**) und die Auslegerelemente (**031**, **032**) solche Abmaße aufweisen, dass sie in einer kompakten Transportkiste unterbringbar sind.

12. Tansportables Goniospektrometer (**01**) nach einem der vorangehenden Ansprüche, **dadurch gekennzeichnet,** dass die Verschraubung (**10**) zwischen Hauptsäule (**02**) und Ausleger (**03**) aus einer Säulenplatte (**101**) an der Hauptsäule (**02**) und einer Auslegerplatte (**104**) am Ausleger (**03**) mit einer Zentralbohrung (**102**, **105**), in die eine Knebelschraube (**107**) eingreift, und einer Reihe von Fixierbohrungen (**106**), in die ein Fixierstift (**108**) eingreift, zur Einstellung eines Winkels zwischen Säulenplatte (**101**) und Auslegerplatte (**104**) aufgebaut ist.

13. Tansportables Goniospektrometer (**01**) nach einem der vorangehenden Ansprüche, **dadurch gekennzeichnet,** dass die drehbare Aufhängung (**04**) des Bogens (**05**) am Ausleger (**03**) aus einer drehbaren Zentralstange (**041**) mit einer oberen Aufnahmeplatte (**040**) für die Auswerteeinheit (**132**) des Spektrometers (**13**) und einem Drehstativkopf (**045**) mit einer unteren Aufnahmeplatte (**046**) zur Befestigung des festgelegten Bogenendes des Bogens (**05**) aufgebaut ist.

14. Tansportables Goniospektrometer (**01**) nach einem der vorangehenden Ansprüche, **dadurch gekennzeichnet,** dass mit dem Schlitten (**06**) zusätzlich eine Videokamera (**14**) und zeitweilig eine Spektralonplatte (**18**) für die Kalibrierung verbunden sind.

15. Tansportables Goniospektrometer (**01**) nach einem der vorangehenden Ansprüche, **dadurch gekennzeichnet,** dass mehrere Wasserwaagen (**17**) zur lotrechten Ausrichtung der Hauptsäule (**02**) und des Sensors (**131**) gegenüber der Oberfläche (SF) und/oder ein satellitengestützter Ortsdetektor (**16**) vorgesehen sind.

Es folgen 7 Seiten Zeichnungen

Anhängende Zeichnungen

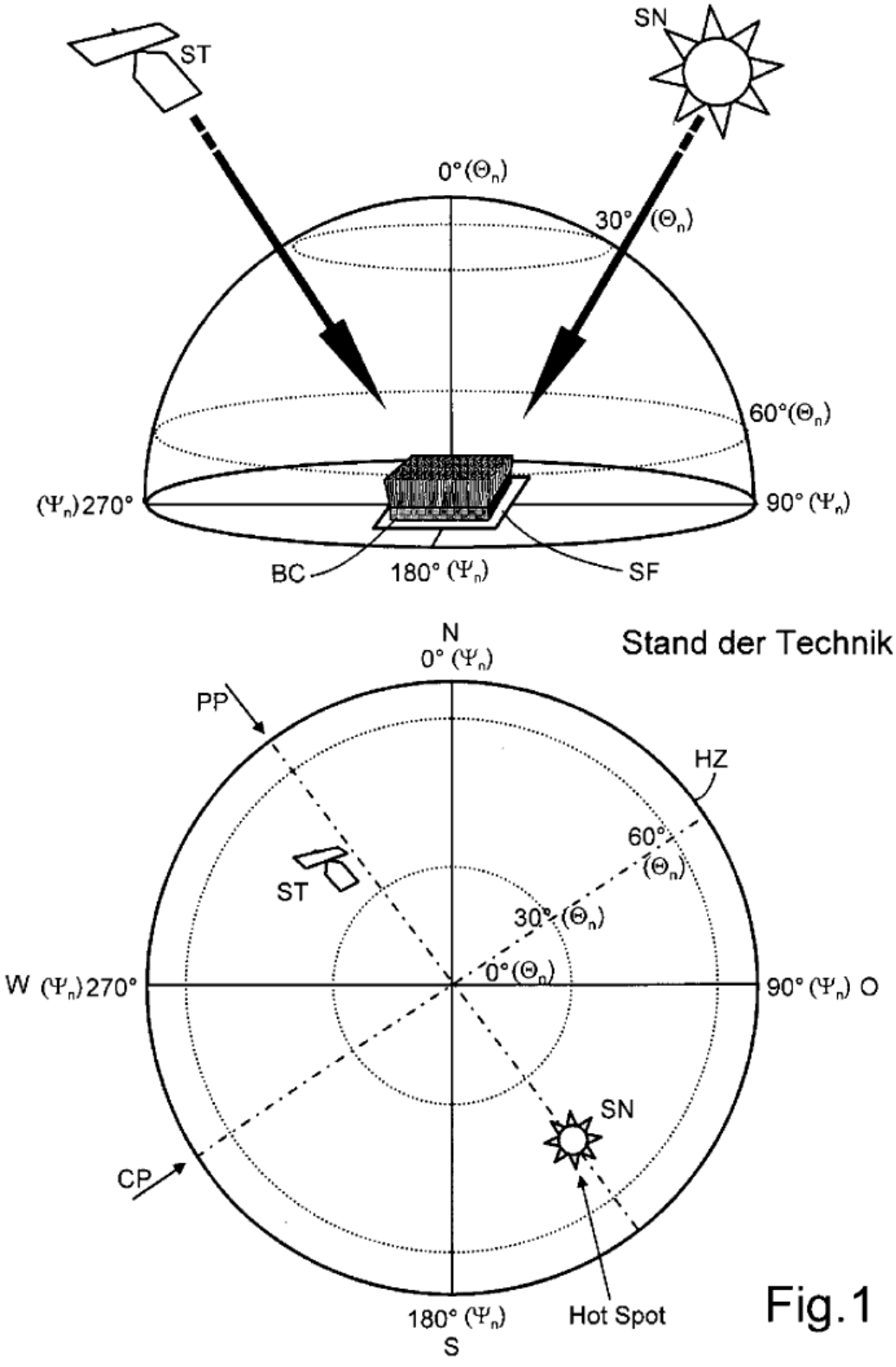

Stand der Technik

Fig.1

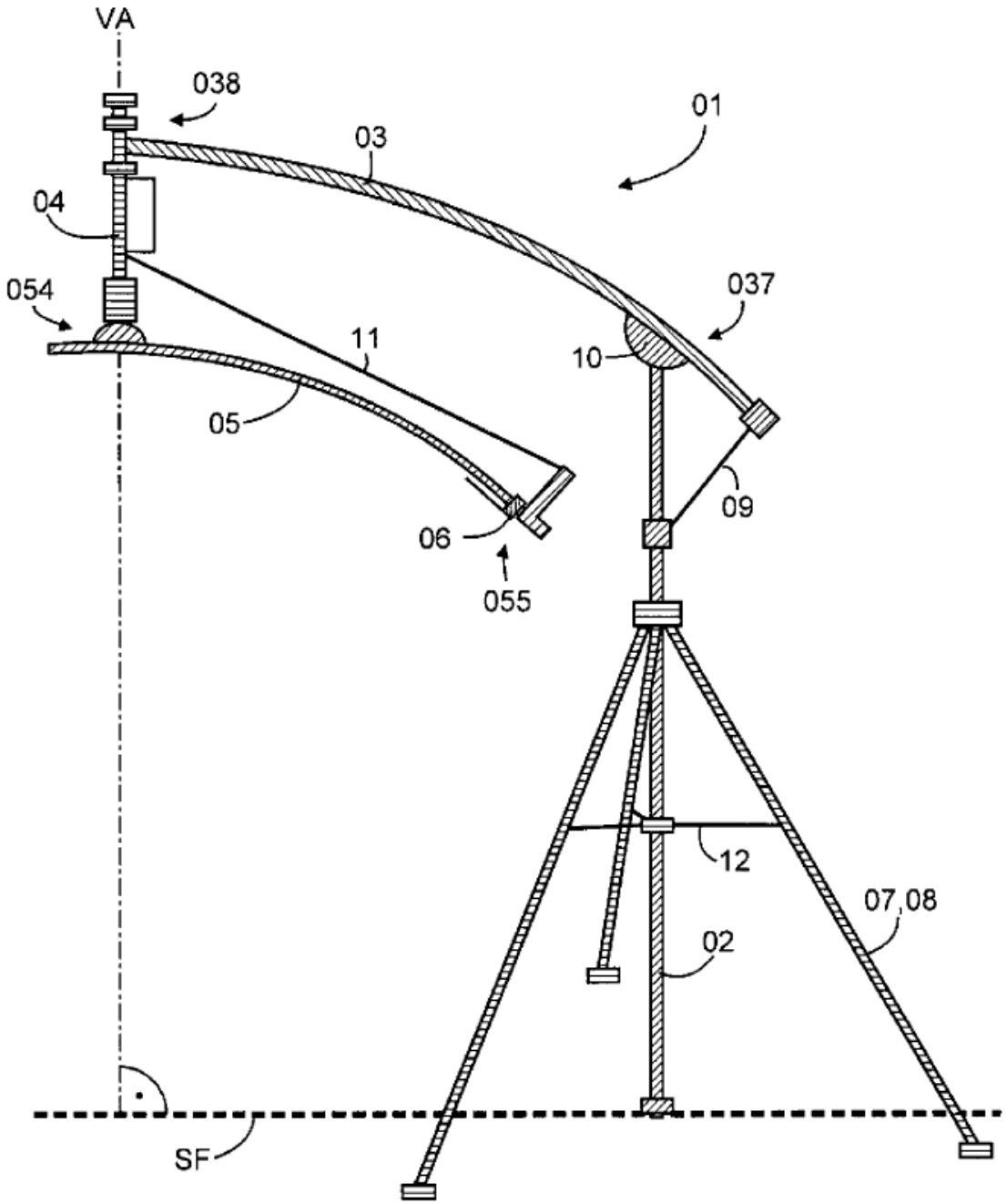

Fig.2

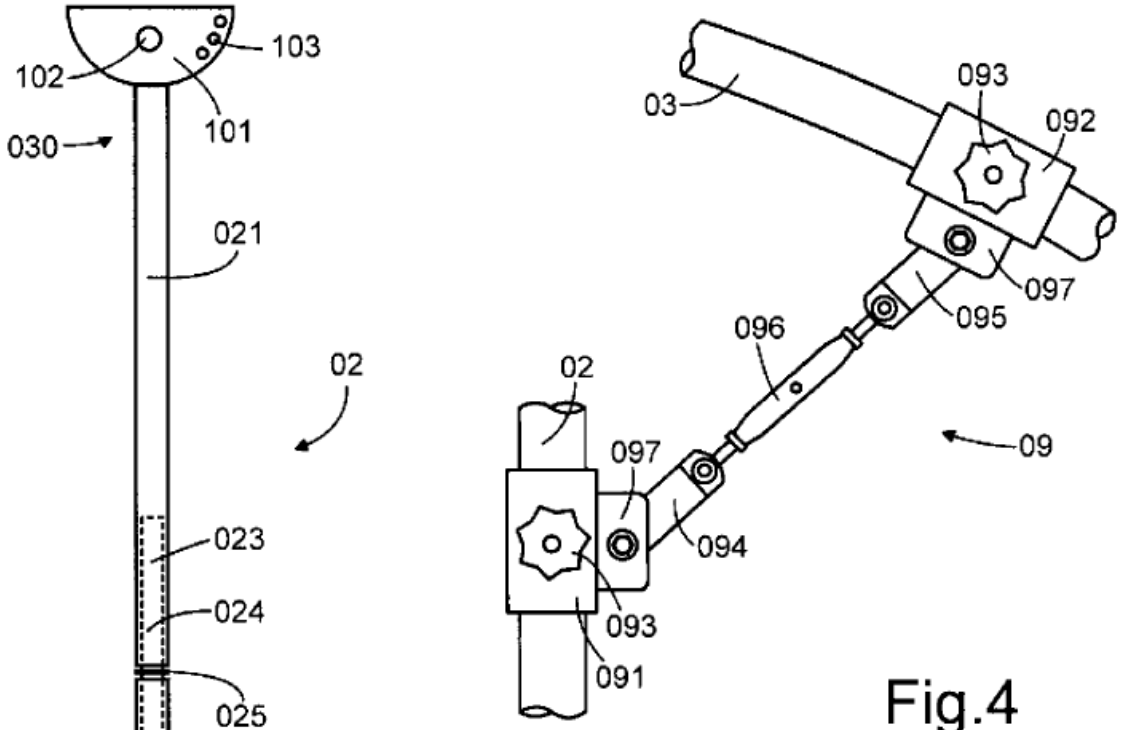
03
093
092
097
095
096
02
09
097
094
093
091

Fig.4

102
103
101
030
021
02
023
024
025
022
027
029
026
028
SF

Fig.3

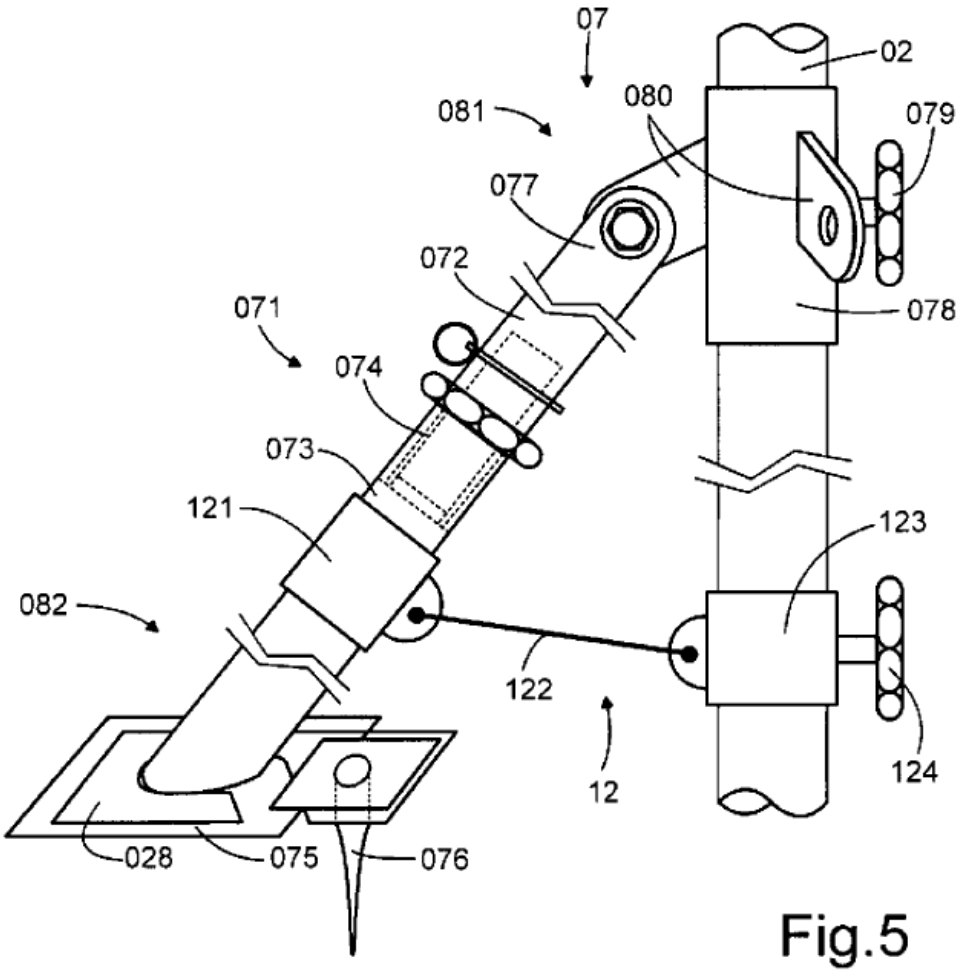
07
02
081
080
079
077
072
078
071
074
073
121
123
082
122
12
124
028
075
076

Fig.5

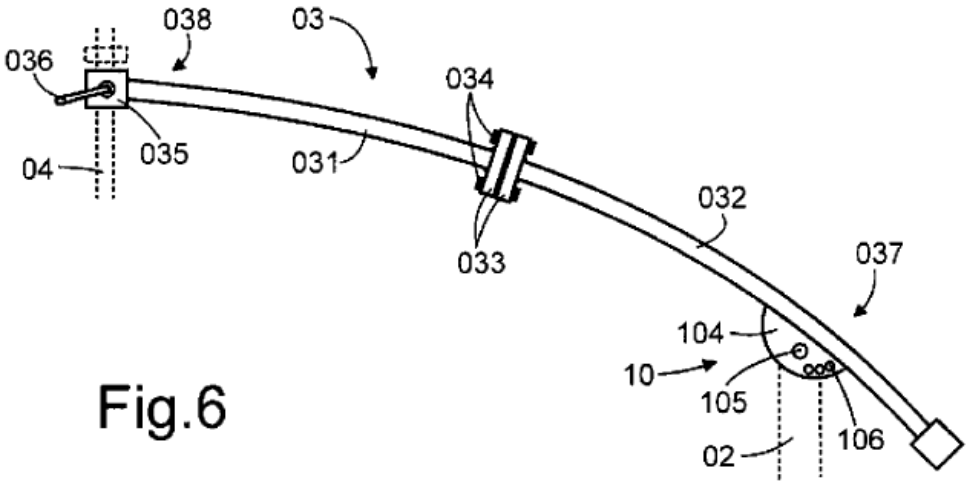
038
03
036
034
035
04
031
032
033
037
104
10
105
106
02

Fig.6

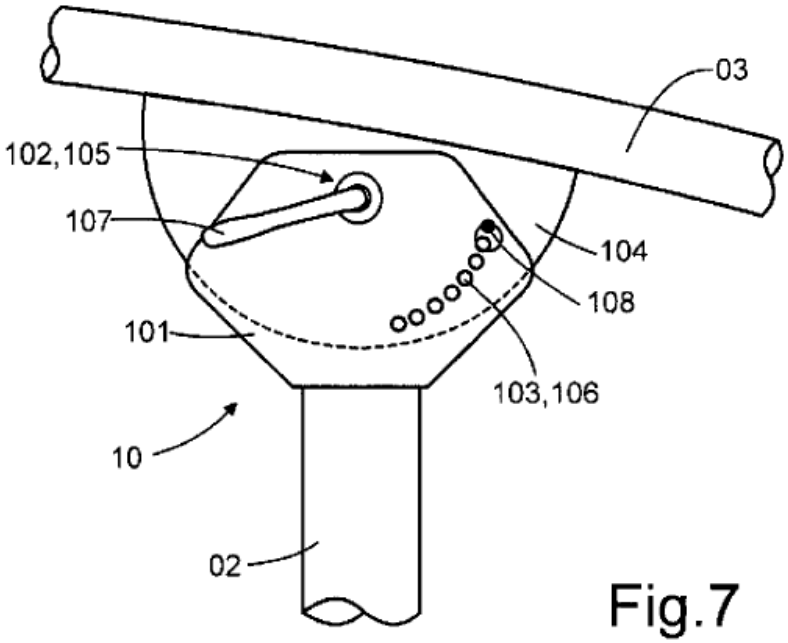
03
102,105
107
104
108
101
103,106
10
02

Fig.7

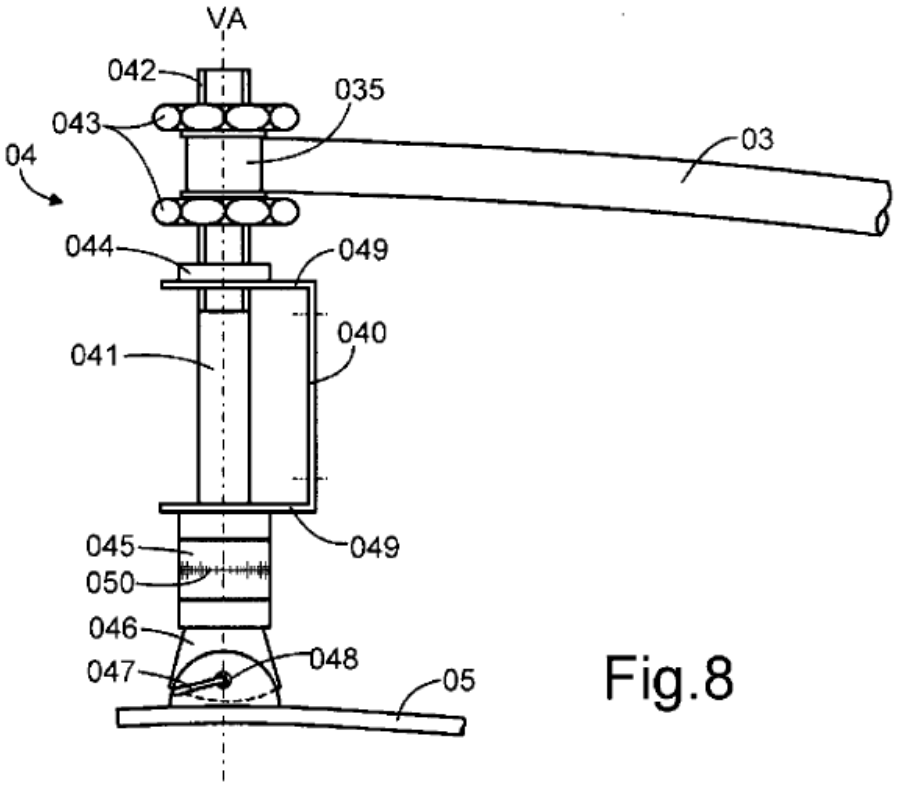
VA
042
035
043
03
04
044
049
040
041
045
049
050
046
048
047
05

Fig.8

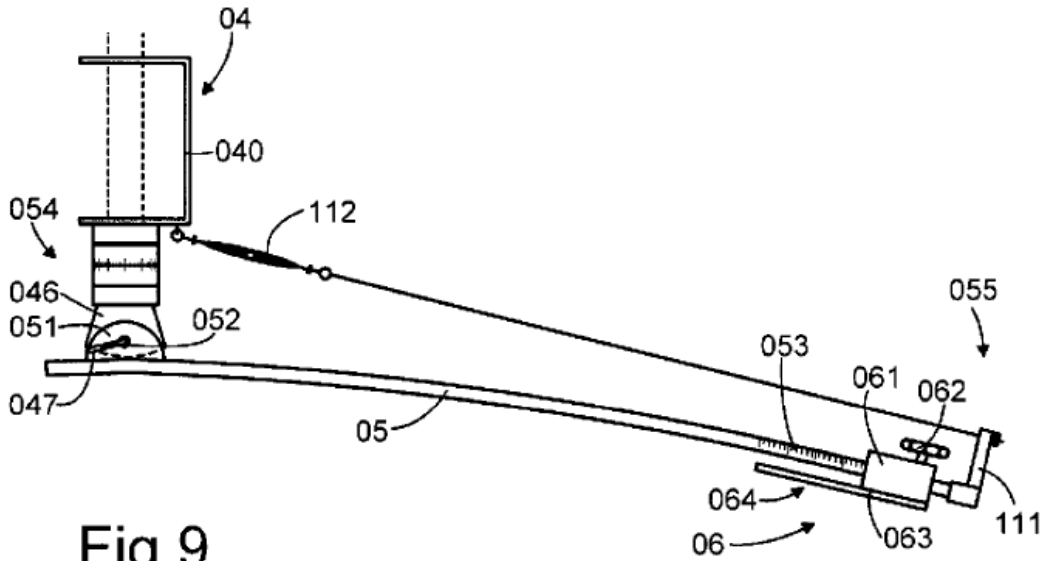
04
040
054
112
046
051
052
055
053
061
062
047
05
064
063
111
06

Fig.9

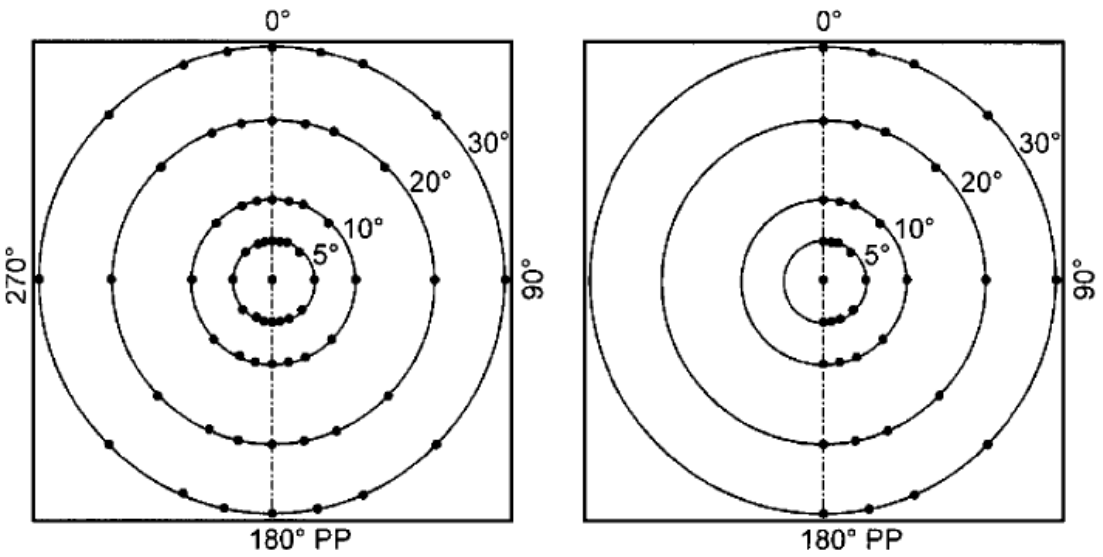
0°
30°
20°
10°
5°
270°
90°
180° PP
0°
30°
20°
10°
5°
90°
180° PP

Fig.11

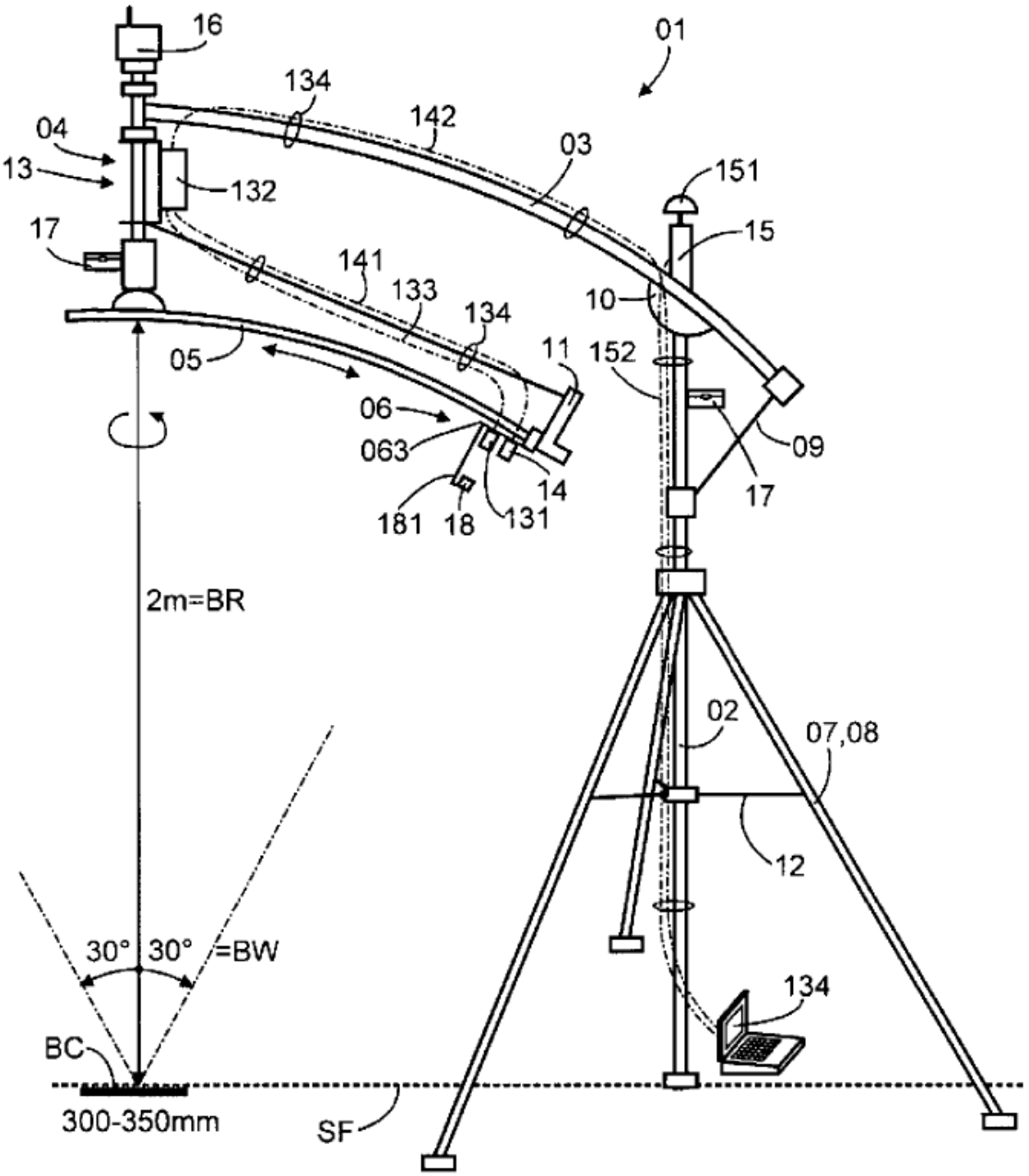
16
01
134
142
04
03
13
132
151
17
15
141
133
134
10
05
11
152
06
063
09
14
17
181
18
131
2m=BR
02
07,08
12
30°
30°
=BW
134
BC
300-350mm
SF

Fig.10

APPENDIX C: DATA REPORTS OF THE SPECTRO-DIRECTIONAL MEASUREMENTS

C.1 Study Site FBG1 (non-tussock sedge, dwarf shrub, moss tundra)

I *Location*

Name	Location	Latitude	Longitude	Altitude
FBG1	Franklin Bluffs, Arctic North Slope, Alaska, United States of America	69.674377°	-148,720972°	125 m

At an average elevation of 90 m, Franklin Bluffs is located in Subzone D about 1 km west of the Dalton Highway across from the pipeline access road APL/AMS 130 near green mile marker 375. This access road provides parking at the site. Three 10 x 10 m grids, designated dry, mesic, and wet, have been established at this location in 2002. The goniometer measurements have been carried out next to the moist / zonal site (FB_m/z). [*Barreda et al.*, 2006]

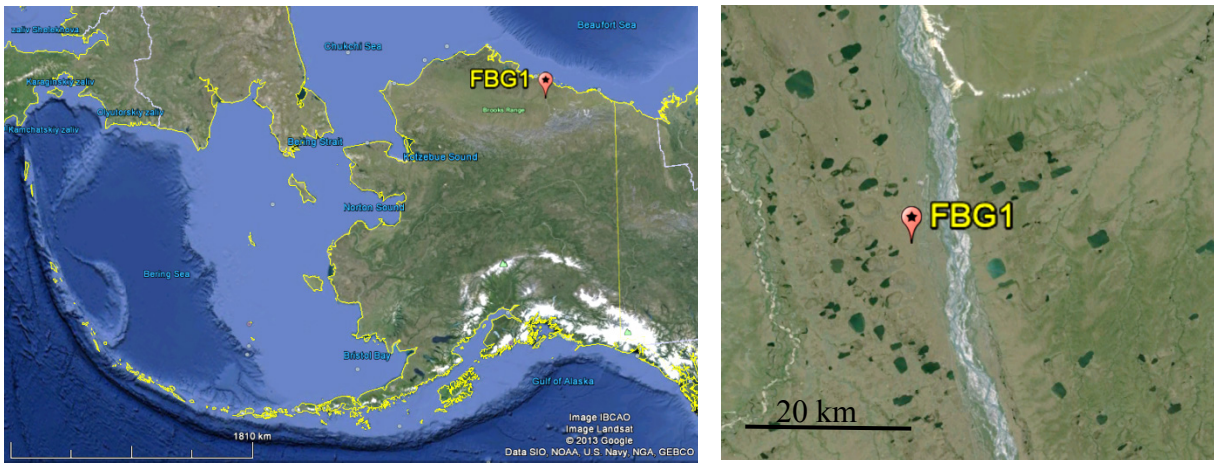

Figure C.1-1: Location of study site FBG1 in Alaska, USA. *Source:* Google Earth, 2013

Figure C.1-2: Aerial photo of a 10 x 10 m zonal grid at the Franklin Bluffs study location near the FBG1 site. *Source:* [*Barreda et al.*, 2006]

II *Main Vegetation Description*

The vegetation at the mesic Franklin Bluffs study location corresponds to the zonal vegetation in subzone D. The zonal plant community of bioclimate subzone D in northern Alaska is *Dryado integrifoliae-Caricetum bigelowii* [*Walker et al.*, 2005], also called moist non-acidic tundra (MNT), or 'nontussock sedge, dwarf-shrub, moss tundra' [*Walker et al.*, 2005]. It occurs on circumneutral to basic soils in association with silty loess that is blown from the major rivers in the eastern part of the Arctic Coastal Plain. The average soil pH of this plant community at Franklin Bluffs is 7.9; the average volumetric soil moisture of the top mineral horizon is 45 %, and average depth of thaw by late summer is 40 cm [*Kade et al.*, 2005]. The dominant plants in MNT are sedges (*Carex bigelowii, Eriophorum angustifolium* ssp. *triste, C. membranacea, C. scirpoidea, E. vaginatum*), prostrate and hemi-prostrate evergreen dwarf shrubs (*Dryas integrifolia, Cassiope tetragona*), prostrate dwarf deciduous shrubs (*Salix arctica, S. reticulata, Arctous rubra*), scattered erect dwarf deciduous shrubs (*Salix lanata, S. glauca*), several forbs (*Papaver macounii, Pedicularis lanata, Saussurea angustifolia, Senecio atropurpureus, Pedicularis capitata, Polygonum viviparum, Cardamine hyperborea, Astragalus umbellatus*), mosses *(Tomentypnum nitens, Hylocomium splendens, Aulacomnium turgidum, Rhytidium rugosum, Hypnum bambergeri, Distichium capillaceum, Ditrichum flexicaule*), and lichens (*Thamnolia subuliformis*, *Cetraria* spp.).

An important component of the MNT is the abundant nonsorted circles, also called frost boils, which are small patterned ground features caused by soil frost heave [*Walker et al.*, 2008; *Washburn*, 1980]. These features cover large parts of most MNT surfaces. The 10 x 10 m zonal grid at Franklin Bluffs has about 30 % cover of nonsorted circles. These features have drier plant communities than the mesic zonal plant communities between the circles, with high cover of lichens and bare soil.

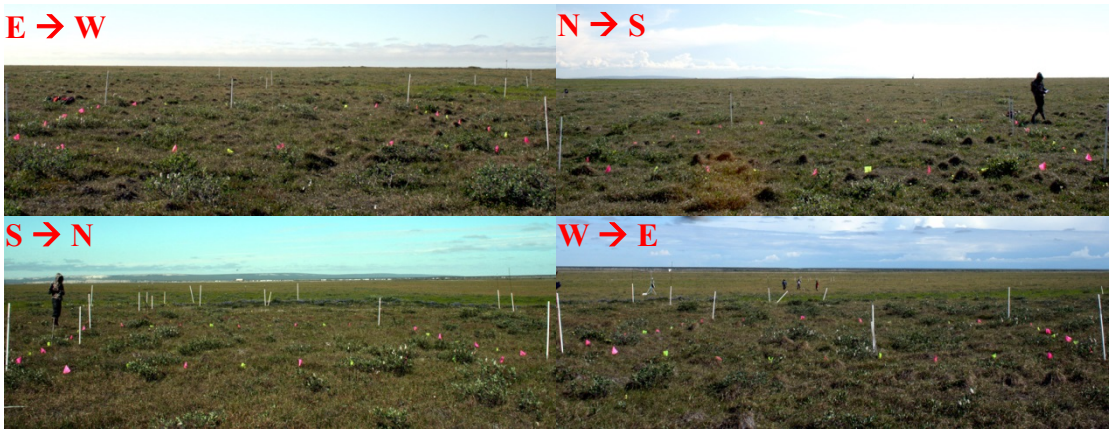

Figure C.1-3: Overview images of MNT tundra at the mesic Franklin Bluffs study location near the FBG1 site. *Source:* [*Buchhorn and Schwieder*, 2012]

III *Vegetation Description of the FBG1 Site*

The focus of the measurements at this goniometer site has been non-tussock sedges – dwarf shrub – moss tundra. The 1 x 1 m plot is homogeneously covered mainly with grass and sedges, but with forbs, mosses and lichens in the understory. Moreover, this plot correspond with the zonal plant community of Alaskan bioclimate subzone D (MNT vegetation).

Figure C.1-4: Overview images of the FBG1 vegetation from cardinal directions.

Figure C.1-5: Nadir image of the FBG1 vegetation (mainly grass and sedges).

IV *Overview of the Spectro-Goniometer Measurements*

Table C.1-1: Overview of the spectro-goniometer measurements at the FBG1 study site.

Name	Day	Starting Time	Duration	SAA	SZA	Sky
FBG1_01	2012-07-07	09:53:01	25 min	112°	59°	cirrostratus
FBG1_02	2012-07-07	11:47:17	21 min	143°	50°	cirrostratus
FBG1_03	2012-07-07	13:56:55	27 min	180°	47°	cirrostratus
FBG1_04	2012-07-07	15:49:41	19 min	217°	50°	clear
FBG1_05	2012-07-07	18:02:23	18 min	252°	59°	cirrostratus
FBG1_06	2012-07-07	19:52:40	19 min	278°	68°	cirrostratus

Table C.1-2: Spectro-directional data of the FBG1_01 spectro-goniometer measurement.

FBG1_01 (SZA = 59°; SAA = 112°)	Viewing Geometry (Viewing Zenith Angle | Viewing Azimuth Angle)																							
	0|0	5|180	5|202.5	5|225	5|270	5|315	5|337.5	5|0	5|22.5	5|45	5|90	5|135	5|157.5	10|180	10|190	10|202.5	10|225	10|270	10|315	10|337.5	10|350
HCRF EnMAP blue (479 nm)	0.0484	0.0481	0.0557	0.0453	0.0441	0.0441	0.0460	0.0426	0.0455	0.0442	0.0513	0.0476	0.0439	0.0511	0.0533	0.0543	0.0529	0.0463	0.0469	0.0438	0.0423
HCRF EnMAP green (549 nm)	0.0761	0.0781	0.0870	0.0715	0.0682	0.0693	0.0726	0.0694	0.0683	0.0675	0.0798	0.0768	0.0690	0.0793	0.0832	0.0852	0.0840	0.0732	0.0740	0.0706	0.0665
HCRF EnMAP rot (672 nm)	0.0906	0.0882	0.1052	0.0859	0.0807	0.0842	0.0865	0.0807	0.0855	0.0832	0.0968	0.0926	0.0807	0.0969	0.1018	0.1041	0.0995	0.0851	0.0874	0.0800	0.0779
HCRF EnMAP NIR (864 nm)	0.3023	0.3138	0.3093	0.2741	0.2681	0.2720	0.2913	0.2958	0.2637	0.2724	0.3086	0.3090	0.2737	0.3101	0.3277	0.3227	0.3114	0.2806	0.2834	0.2854	0.2734
ANIF EnMAP rot (672 nm)	1.0000	0.9738	1.1610	0.9487	0.8913	0.9295	0.9546	0.8907	0.9433	0.9188	1.0683	1.0226	0.8903	1.0692	1.1235	1.1495	1.0986	0.9399	0.9647	0.8836	0.8594
ANIF EnMAP NIR (864 nm)	1.0000	1.0382	1.0232	0.9068	0.8871	0.8999	0.9638	0.9787	0.8726	0.9012	1.0210	1.0225	0.9055	1.0260	1.0843	1.0676	1.0304	0.9284	0.9376	0.9444	0.9046
Rel. Blue Absorption Depth	0.3825	0.4207	0.4056	0.4074	0.3997	0.4078	0.4125	0.4225	0.3682	0.3814	0.3705	0.4084	0.3880	0.3763	0.3871	0.3935	0.4191	0.4182	0.4112	0.4175	0.3936
Rel. Red Absorption Depth	0.8805	0.9669	0.7656	0.8476	0.8748	0.8658	0.9082	0.9983	0.7982	0.8782	0.8364	0.9112	0.9151	0.8568	0.8660	0.8253	0.8393	0.8607	0.8640	0.9746	0.9468
NDVI (EnMAP)	0.5388	0.5611	0.4924	0.5226	0.5371	0.5272	0.5422	0.5714	0.5106	0.5319	0.5225	0.5387	0.5448	0.5240	0.5260	0.5120	0.5156	0.5344	0.5286	0.5620	0.5567
Nadir Norm. NDVI (AVHRR)	1.0000	1.0266	0.9208	0.9792	0.9956	0.9882	1.0071	1.0600	0.9580	0.9978	0.9723	1.0043	1.0095	0.9776	0.9811	0.9618	0.9590	0.9832	0.9851	1.0384	1.0331
Nadir Norm. NDVI (MODIS)	1.0000	1.0278	0.9215	0.9795	0.9969	0.9888	1.0095	1.0615	0.9577	0.9975	0.9730	1.0052	1.0109	0.9782	0.9807	0.9616	0.9624	0.9846	0.9872	1.0418	1.0359
Nadir Norm. NDVI (EnMAP)	1.0000	1.0414	0.9140	0.9699	0.9969	0.9785	1.0063	1.0605	0.9476	0.9872	0.9698	0.9999	1.0111	0.9725	0.9764	0.9504	0.9570	0.9919	0.9811	1.0430	1.0333

(cont.)

FBG1_01 (SZA = 59°; SAA = 112°)	Viewing Geometry (Viewing Zenith Angle | Viewing Azimuth Angle)																							
	10|0	10|10	10|22.5	10|45	10|90	10|135	10|157.5	10|170	20|180	20|190	20|202.5	20|225	20|270	20|315	20|337.5	20|350	20|0	20|10	20|22.5	20|45	20|90
HCRF EnMAP blue (479 nm)	0.0462	0.0456	0.0419	0.0446	0.0469	0.0480	0.0463	0.0495	0.0618	0.0583	0.0575	0.0488	0.0471	0.0459	0.0380	0.0458	0.0462	0.0485	0.0470	0.0442	0.0552
HCRF EnMAP green (549 nm)	0.0697	0.0698	0.0658	0.0684	0.0726	0.0764	0.0764	0.0786	0.0954	0.0941	0.0902	0.0798	0.0748	0.0717	0.0612	0.0711	0.0713	0.0767	0.0734	0.0687	0.0858
HCRF EnMAP rot (672 nm)	0.0872	0.0874	0.0781	0.0831	0.0888	0.0900	0.0870	0.0942	0.1213	0.1099	0.1105	0.0927	0.0854	0.0855	0.0673	0.0825	0.0873	0.0911	0.0879	0.0818	0.1031
HCRF EnMAP NIR (864 nm)	0.2747	0.2783	0.2771	0.2769	0.2908	0.3106	0.3138	0.3076	0.3355	0.3466	0.3182	0.3195	0.2948	0.2797	0.2717	0.2913	0.2881	0.3134	0.3053	0.2836	0.3257
ANIF EnMAP rot (672 nm)	0.9625	0.9648	0.8618	0.9171	0.9797	0.9935	0.9607	1.0394	1.3386	1.2126	1.2196	1.0227	0.9431	0.9443	0.7428	0.9107	0.9634	1.0061	0.9706	0.9028	1.1378
ANIF EnMAP NIR (864 nm)	0.9089	0.9208	0.9167	0.9162	0.9620	1.0274	1.0383	1.0178	1.1101	1.1467	1.0528	1.0572	0.9754	0.9255	0.8988	0.9636	0.9530	1.0369	1.0100	0.9381	1.0774
Rel. Blue Absorption Depth	0.3735	0.3912	0.4104	0.3782	0.3721	0.3850	0.4179	0.3929	0.3823	0.4105	0.4029	0.4385	0.4217	0.3959	0.4110	0.3877	0.3927	0.4100	0.4045	0.3820	0.3763
Rel. Red Absorption Depth	0.8238	0.8367	0.9694	0.8978	0.8658	0.9328	0.9953	0.8793	0.7101	0.8432	0.7449	0.9516	0.9269	0.8623	1.1172	0.9523	0.8738	0.9324	0.9407	0.9408	0.8285
NDVI (EnMAP)	0.5182	0.5220	0.5603	0.5385	0.5323	0.5506	0.5658	0.5313	0.4690	0.5187	0.4845	0.5504	0.5506	0.5316	0.6029	0.5585	0.5349	0.5494	0.5527	0.5523	0.5191
Nadir Norm. NDVI (AVHRR)	0.9707	0.9809	1.0452	1.0099	0.9950	1.0269	1.0449	0.9912	0.8834	0.9604	0.9078	1.0187	1.0157	0.9914	1.1069	1.0315	0.9947	1.0189	1.0263	1.0266	0.9616
Nadir Norm. NDVI (MODIS)	0.9705	0.9808	1.0466	1.0102	0.9945	1.0263	1.0466	0.9919	0.8826	0.9627	0.9089	1.0219	1.0179	0.9935	1.1103	1.0339	0.9969	1.0217	1.0286	1.0285	0.9627
Nadir Norm. NDVI (EnMAP)	0.9617	0.9688	1.0400	0.9994	0.9879	1.0219	1.0501	0.9861	0.8706	0.9626	0.8993	1.0216	1.0220	0.9867	1.1191	1.0387	0.9929	1.0197	1.0259	1.0250	0.9636

(cont.)

FBG1_01 (SZA = 59°; SAA = 112°)	Viewing Geometry (Viewing Zenith Angle | Viewing Azimuth Angle)																							
	20|135	20|157.5	20|170	30|180	30|190	30|202.5	30|225	30|270	30|315	30|337.5	30|350	30|0	30|10	30|122.5	30|45	30|90	30|135	30|157.5	30|170			
HCRF EnMAP blue (479 nm)	0.0516	0.0486	0.0570	0.0705	0.0662	0.0588	0.0523	0.0514	0.0389	0.0398	0.0390	0.0426	0.0482	0.0442	0.0456	0.0569	0.0539	0.0555	0.0616					
HCRF EnMAP green (549 nm)	0.0848	0.0804	0.0897	0.1121	0.1096	0.0968	0.0877	0.0808	0.0650	0.0652	0.0634	0.0672	0.0738	0.0706	0.0706	0.0877	0.0857	0.0944	0.0995					
HCRF EnMAP rot (672 nm)	0.0986	0.0918	0.1102	0.1367	0.1236	0.1122	0.0986	0.0946	0.0701	0.0724	0.0717	0.0782	0.0887	0.0825	0.0827	0.1053	0.1028	0.1061	0.1201					
HCRF EnMAP NIR (864 nm)	0.3404	0.3211	0.3296	0.3906	0.3935	0.3551	0.3337	0.2946	0.2818	0.2808	0.2789	0.2799	0.2920	0.3071	0.2875	0.3341	0.3128	0.3573	0.3481					
ANIF EnMAP rot (672 nm)	1.0886	1.0131	1.2166	1.5087	1.3641	1.2385	1.0881	1.0443	0.7733	0.7989	0.7919	0.8636	0.9786	0.9107	0.9127	1.1620	1.1343	1.1708	1.3253					
ANIF EnMAP NIR (864 nm)	1.1261	1.0623	1.0906	1.2922	1.3019	1.1747	1.1041	0.9746	0.9324	0.9290	0.9228	0.9262	0.9662	1.0161	0.9513	1.1054	1.0348	1.1821	1.1518					
Rel. Blue Absorption Depth	0.4191	0.4234	0.3890	0.4091	0.4419	0.4383	0.4565	0.4150	0.4460	0.4275	0.4271	0.3986	0.3785	0.4063	0.3739	0.3662	0.4013	0.4433	0.4106					
Rel. Red Absorption Depth	0.9517	0.9626	0.7867	0.7498	0.8676	0.8531	0.9351	0.8144	1.1320	1.0875	1.0820	0.9779	0.8809	1.0288	0.9374	0.8338	0.7899	0.9242	0.7523					
NDVI (EnMAP)	0.5507	0.5554	0.4988	0.4815	0.5220	0.5198	0.5439	0.5138	0.6018	0.5902	0.5908	0.5631	0.5343	0.5765	0.5533	0.5208	0.5054	0.5422	0.4871					
Nadir Norm. NDVI (AVHRR)	1.0183	1.0255	0.9307	0.8980	0.9596	0.9636	1.0017	0.9501	1.1019	1.0877	1.0840	1.0443	0.9958	1.0676	1.0236	0.9642	0.9384	0.9984	0.9081					
Nadir Norm. NDVI (MODIS)	1.0213	1.0274	0.9314	0.8990	0.9631	0.9653	1.0056	0.9547	1.1067	1.0926	1.0876	1.0469	0.9982	1.0710	1.0260	0.9658	0.9392	1.0015	0.9082					
Nadir Norm. NDVI (EnMAP)	1.0221	1.0309	0.9259	0.8938	0.9689	0.9647	1.0096	0.9537	1.1170	1.0953	1.0966	1.0452	0.9916	1.0701	1.0269	0.9667	0.9380	1.0063	0.9041					

Table C.1-3: Spectro-directional data of the FBG1_02 spectro-goniometer measurement.

FBG1_02 (SZA = 50°; SAA = 143°)	Viewing Geometry (Viewing Zenith Angle | Viewing Azimuth Angle)																							
	0|0	5|180	5|202.5	5|225	5|270	5|315	5|337.5	5|0	5|22.5	5|45	5|90	5|135	5|157.5	10|180	10|202.5	10|225	10|270	10|315	10|337.5	10|350
HCRF EnMAP blue (479 nm)	0.0412	0.0552	0.0511	0.0498	0.0556	0.0482	0.0492	0.0463	0.0468	0.0421	0.0454	0.0425	0.0489	0.0533	0.0538	0.0541	0.0502	0.0501	0.0505	0.0499
HCRF EnMAP green (549 nm)	0.0644	0.0839	0.0802	0.0780	0.0849	0.0772	0.0776	0.0726	0.0724	0.0664	0.0718	0.0709	0.0754	0.0833	0.0850	0.0838	0.0791	0.0767	0.0778	0.0768
HCRF EnMAP rot (672 nm)	0.0764	0.1045	0.0956	0.0920	0.1052	0.0887	0.0920	0.0862	0.0875	0.0780	0.0856	0.0790	0.0926	0.0997	0.1015	0.1026	0.1011	0.0931	0.0943	0.0948	0.0911
HCRF EnMAP NIR (864 nm)	0.2674	0.3071	0.3023	0.2889	0.2939	0.3067	0.3068	0.2901	0.2848	0.2747	0.2837	0.2908	0.2900	0.3152	0.3076	0.3098	0.3097	0.2882	0.2882	0.3019	0.2984
ANIF EnMAP rot (672 nm)	1.0000	1.3674	1.2514	1.2047	1.3769	1.1604	1.2039	1.1280	1.1449	1.0214	1.1202	1.0344	1.2122	1.3051	1.3280	1.3424	1.3237	1.2188	1.2339	1.2407	1.1930
ANIF EnMAP NIR (864 nm)	1.0000	1.1486	1.1305	1.0805	1.0992	1.1472	1.1472	1.0850	1.0652	1.0273	1.0608	1.0874	1.0844	1.1789	1.1502	1.1586	1.1582	1.0779	1.0777	1.1289	1.1160
Rel. Blue Absorption Depth	0.3748	0.3685	0.4022	0.4123	0.3906	0.4100	0.4143	0.4073	0.3797	0.3865	0.3881	0.4240	0.3762	0.3857	0.4039	0.4107	0.3995	0.4109	0.3770	0.3945	0.3875
Rel. Red Absorption Depth	0.9235	0.7587	0.8470	0.8147	0.7096	0.9303	0.8952	0.9046	0.8635	0.9334	0.8664	1.0051	0.8177	0.8299	0.8069	0.7912	0.8116	0.8062	0.7965	0.8440	0.8657
NDVI (EnMAP)	0.5556	0.4924	0.5194	0.5168	0.4729	0.5516	0.5387	0.5419	0.5301	0.5576	0.5364	0.5726	0.5158	0.5194	0.5039	0.5026	0.5077	0.5117	0.5070	0.5221	0.5321
Nadir Norm. NDVI (AVHRR)	1.0000	0.8972	0.9375	0.9271	0.8624	0.9873	0.9640	0.9776	0.9593	0.9972	0.9627	1.0176	0.9341	0.9350	0.9150	0.9089	0.9187	0.9197	0.9204	0.9440	0.9578
Nadir Norm. NDVI (MODIS)	1.0000	0.8961	0.9390	0.9273	0.8628	0.9891	0.9649	0.9784	0.9598	0.9979	0.9626	1.0201	0.9339	0.9352	0.9147	0.9104	0.9195	0.9216	0.9207	0.9440	0.9592
Nadir Norm. NDVI (EnMAP)	1.0000	0.8863	0.9350	0.9303	0.8512	0.9928	0.9696	0.9755	0.9542	1.0036	0.9656	1.0306	0.9285	0.9349	0.9070	0.9047	0.9139	0.9210	0.9126	0.9397	0.9577

(cont.)

FBG1_02 (SZA = 50°; SAA = 143°)	Viewing Geometry (Viewing Zenith Angle | Viewing Azimuth Angle)																							
	10|0	10|10	10|22.5	10|45	10|90	10|135	10|157.5	10|170	20|180	20|190	20|202.5	20|225	20|270	20|315	20|337.5	20|350	20|0	20|10	20|22.5	20|45	20|90
HCRF EnMAP blue (479 nm)	0.0461	0.0460	0.0428	0.0477	0.0502	0.0465	0.0530	0.0560	0.0574	0.0572	0.0579	0.0551	0.0572	0.0450	0.0522	0.0466	0.0444	0.0462	0.0441	0.0430	0.0514
HCRF EnMAP green (549 nm)	0.0721	0.0717	0.0653	0.0727	0.0771	0.0767	0.0819	0.0875	0.0942	0.0931	0.0937	0.0892	0.0869	0.0707	0.0793	0.0742	0.0694	0.0726	0.0675	0.0673	0.0781
HCRF EnMAP rot (672 nm)	0.0851	0.0852	0.0789	0.0893	0.0935	0.0869	0.1013	0.1064	0.1080	0.1107	0.1108	0.1007	0.1089	0.0826	0.0981	0.0854	0.0827	0.0852	0.0805	0.0785	0.0962
HCRF EnMAP NIR (864 nm)	0.2928	0.2855	0.2574	0.2835	0.2965	0.3058	0.2978	0.3141	0.3518	0.3454	0.3342	0.3295	0.2967	0.2877	0.3002	0.3109	0.2868	0.2872	0.2724	0.2784	0.2891
ANIF EnMAP rot (672 nm)	1.1142	1.1150	1.0327	1.1693	1.2242	1.1374	1.3257	1.3929	1.4138	1.4488	1.4508	1.3175	1.4249	1.0806	1.2835	1.1179	1.0828	1.1152	1.0542	1.0269	1.2588
ANIF EnMAP NIR (864 nm)	1.0949	1.0677	0.9625	1.0604	1.1087	1.1436	1.1136	1.1745	1.3155	1.2918	1.2497	1.2323	1.1094	1.0760	1.1227	1.1628	1.0727	1.0740	1.0188	1.0411	1.0811
Rel. Blue Absorption Depth	0.4058	0.3935	0.3667	0.3633	0.3614	0.4161	0.3751	0.3935	0.4321	0.4287	0.4300	0.4361	0.3993	0.3938	0.3778	0.4117	0.3923	0.3924	0.3642	0.3792	0.3480
Rel. Red Absorption Depth	0.9314	0.8925	0.8591	0.8251	0.8216	0.9577	0.7533	0.7600	0.8794	0.8409	0.7962	0.8746	0.6850	0.9267	0.7992	0.9997	0.9345	0.9038	0.8992	0.9567	0.7671
NDVI (EnMAP)	0.5495	0.5404	0.5307	0.5208	0.5204	0.5574	0.4924	0.4938	0.5302	0.5146	0.5019	0.5320	0.4631	0.5541	0.5076	0.5690	0.5523	0.5424	0.5436	0.5603	0.5007
Nadir Norm. NDVI (AVHRR)	0.9898	0.9743	0.9600	0.9437	0.9401	0.9962	0.8925	0.8920	0.9474	0.9304	0.9039	0.9462	0.8437	0.9940	0.9200	1.0200	0.9946	0.9750	0.9779	1.0042	0.9062
Nadir Norm. NDVI (MODIS)	0.9912	0.9742	0.9598	0.9431	0.9403	0.9985	0.8919	0.8913	0.9485	0.9322	0.9051	0.9485	0.8439	0.9953	0.9196	1.0222	0.9956	0.9765	0.9787	1.0056	0.9058
Nadir Norm. NDVI (EnMAP)	0.9891	0.9727	0.9553	0.9375	0.9367	1.0034	0.8863	0.8889	0.9543	0.9264	0.9034	0.9576	0.8336	0.9973	0.9136	1.0242	0.9941	0.9763	0.9786	1.0085	0.9013

(cont.)

FBG1_02 (SZA = 50°; SAA = 143°)	Viewing Geometry (Viewing Zenith Angle | Viewing Azimuth Angle)																							
	20|135	20|157.5	20|170	30|180	30|190	30|202.5	30|225	30|270	30|315	30|337.5	30|350	30|0	30|10	30|122.5	30|45	30|90	30|135	30|157.5	30|170			
HCRF EnMAP blue (479 nm)	0.0525	0.0617	0.0581	0.0641	0.0657	0.0663	0.0582	0.0520	0.0457	0.0458	0.0505	0.0433	0.0428	0.0464	0.0419	0.0507	0.0558	0.0652	0.0673					
HCRF EnMAP green (549 nm)	0.0856	0.0953	0.0946	0.1051	0.1079	0.1068	0.0983	0.0850	0.0734	0.0722	0.0772	0.0691	0.0660	0.0724	0.0667	0.0773	0.0912	0.1037	0.1114					
HCRF EnMAP rot (672 nm)	0.0978	0.1189	0.1082	0.1193	0.1234	0.1272	0.1053	0.0986	0.0850	0.0855	0.0920	0.0793	0.0757	0.0833	0.0772	0.0953	0.1059	0.1263	0.1254					
HCRF EnMAP NIR (864 nm)	0.3246	0.3277	0.3458	0.3808	0.3780	0.3665	0.3672	0.3249	0.3022	0.2923	0.3016	0.2944	0.2571	0.2880	0.2782	0.2901	0.3287	0.3422	0.3729					
ANIF EnMAP rot (672 nm)	1.2795	1.5564	1.4169	1.5615	1.6149	1.6649	1.3777	1.2902	1.1131	1.1197	1.2037	1.0382	0.9907	1.0904	1.0104	1.2468	1.3863	1.6533	1.6408					
ANIF EnMAP NIR (864 nm)	1.2140	1.2255	1.2934	1.4242	1.4136	1.3706	1.3732	1.2152	1.1301	1.0931	1.1280	1.1011	0.9614	1.0770	1.0402	1.0851	1.2291	1.2796	1.3945					
Rel. Blue Absorption Depth	0.4121	0.3828	0.4224	0.4344	0.4267	0.4296	0.4671	0.4454	0.4161	0.3965	0.3662	0.4015	0.3705	0.3790	0.3925	0.3543	0.4125	0.4056	0.4351					
Rel. Red Absorption Depth	0.8973	0.7002	0.8660	0.8647	0.8122	0.7563	0.9513	0.8883	0.9672	0.9106	0.8668	1.0018	0.9096	0.9378	0.9760	0.7886	0.8252	0.6955	0.7854					
NDVI (EnMAP)	0.5371	0.4675	0.5232	0.5229	0.5079	0.4847	0.5544	0.5345	0.5607	0.5472	0.5327	0.5756	0.5451	0.5513	0.5655	0.5057	0.5126	0.4608	0.4968					
Nadir Norm. NDVI (AVHRR)	0.9585	0.8491	0.9353	0.9326	0.9060	0.8727	0.9769	0.9602	1.0036	0.9837	0.9583	1.0273	0.9723	0.9879	1.0121	0.9158	0.9166	0.8391	0.8846					
Nadir Norm. NDVI (MODIS)	0.9611	0.8484	0.9383	0.9342	0.9088	0.8744	0.9825	0.9646	1.0076	0.9857	0.9605	1.0302	0.9756	0.9898	1.0141	0.9159	0.9187	0.8395	0.8870					
Nadir Norm. NDVI (EnMAP)	0.9668	0.8415	0.9418	0.9413	0.9141	0.8725	0.9980	0.9621	1.0093	0.9849	0.9589	1.0360	0.9812	0.9923	1.0179	0.9102	0.9226	0.8294	0.8943					

Table C.1-4: Spectro-directional data of the FBG1_03 spectro-goniometer measurement.

FBG1_03 (SZA = 47°; SAA = 180°)	Viewing Geometry (Viewing Zenith Angle | Viewing Azimuth Angle)																							
	0|0	5|180	5|202.5	5|225	5|270	5|315	5|337.5	5|0	5|22.5	5|45	5|90	5|135	5|157.5	10|180	10|190	10|202.5	10|225	10|270	10|315	10|337.5	10|350
HCRF EnMAP blue (479 nm)	0.0448	0.0510	0.0503	0.0536	0.0492	0.0501	0.0489	0.0439	0.0454	0.0468	0.0364	0.0468	0.0483	0.0533	0.0541	0.0508	0.0577	0.0522	0.0477	0.0486	0.0464
HCRF EnMAP green (549 nm)	0.0684	0.0812	0.0794	0.0821	0.0769	0.0770	0.0744	0.0664	0.0694	0.0724	0.0590	0.0731	0.0749	0.0853	0.0834	0.0809	0.0880	0.0816	0.0731	0.0738	0.0699
HCRF EnMAP rot (672 nm)	0.0832	0.0962	0.0949	0.1030	0.0924	0.0953	0.0917	0.0808	0.0858	0.0896	0.0675	0.0862	0.0918	0.1014	0.1016	0.0948	0.1103	0.0972	0.0885	0.0902	0.0851
HCRF EnMAP NIR (864 nm)	0.2681	0.3028	0.2988	0.2977	0.2939	0.2932	0.2837	0.2580	0.2725	0.2809	0.2536	0.2849	0.2749	0.3135	0.2950	0.2986	0.3078	0.3002	0.2883	0.2780	0.2702
ANIF EnMAP rot (672 nm)	1.0000	1.1559	1.1400	1.2379	1.1103	1.1452	1.1015	0.9704	1.0309	1.0761	0.8108	1.0356	1.1026	1.2182	1.2205	1.1392	1.3256	1.1684	1.0635	1.0837	1.0223
ANIF EnMAP NIR (864 nm)	1.0000	1.1293	1.1144	1.1102	1.0962	1.0936	1.0580	0.9621	1.0162	1.0475	0.9459	1.0626	1.0253	1.1691	1.1003	1.1135	1.1478	1.1197	1.0753	1.0366	1.0075
Rel. Blue Absorption Depth	0.3616	0.4208	0.4091	0.3922	0.4012	0.3925	0.3743	0.3542	0.3663	0.3775	0.3953	0.3825	0.3971	0.4261	0.3950	0.4198	0.3854	0.3975	0.3862	0.3680	0.3554
Rel. Red Absorption Depth	0.8331	0.8249	0.8188	0.7342	0.8335	0.8047	0.8038	0.8271	0.8135	0.8121	1.0201	0.8813	0.7689	0.8127	0.7321	0.8146	0.7045	0.8056	0.8563	0.7946	0.8273
NDVI (EnMAP)	0.5263	0.5178	0.5180	0.4858	0.5216	0.5094	0.5116	0.5232	0.5211	0.5165	0.5797	0.5355	0.4995	0.5112	0.4878	0.5180	0.4722	0.5107	0.5302	0.5100	0.5210
Nadir Norm. NDVI (AVHRR)	1.0000	0.9798	0.9809	0.9292	0.9906	0.9760	0.9768	1.0011	0.9947	0.9834	1.0915	1.0142	0.9518	0.9703	0.9299	0.9770	0.9083	0.9726	1.0124	0.9737	0.9956
Nadir Norm. NDVI (MODIS)	1.0000	0.9805	0.9814	0.9275	0.9912	0.9764	0.9764	1.0008	0.9930	0.9836	1.0930	1.0152	0.9516	0.9709	0.9298	0.9785	0.9066	0.9734	1.0130	0.9742	0.9961
Nadir Norm. NDVI (EnMAP)	1.0000	0.9839	0.9843	0.9231	0.9912	0.9679	0.9721	0.9941	0.9901	0.9814	1.1016	1.0176	0.9491	0.9714	0.9269	0.9843	0.8973	0.9704	1.0075	0.9691	0.9900

(cont.)

FBG1_03 (SZA = 47°; SAA = 180°)	Viewing Geometry (Viewing Zenith Angle | Viewing Azimuth Angle)																							
	10|0	10|10	10|22.5	10|45	10|90	10|135	10|157.5	10|170	20|180	20|190	20|202.5	20|225	20|270	20|315	20|337.5	20|350	20|0	20|10	20|22.5	20|45	20|90
HCRF EnMAP blue (479 nm)	0.0412	0.0440	0.0450	0.0444	0.0364	0.0480	0.0534	0.0512	0.0549	0.0597	0.0540	0.0546	0.0513	0.0471	0.0463	0.0423	0.0415	0.0405	0.0454	0.0446	0.0377
HCRF EnMAP green (549 nm)	0.0638	0.0668	0.0677	0.0682	0.0588	0.0744	0.0856	0.0800	0.0887	0.0935	0.0885	0.0855	0.0805	0.0750	0.0714	0.0658	0.0641	0.0622	0.0691	0.0677	0.0599
HCRF EnMAP rot (672 nm)	0.0766	0.0808	0.0849	0.0833	0.0672	0.0893	0.1032	0.0976	0.1010	0.1131	0.1008	0.1038	0.0951	0.0872	0.0864	0.0778	0.0766	0.0735	0.0826	0.0816	0.0687
HCRF EnMAP NIR (864 nm)	0.2599	0.2683	0.2595	0.2684	0.2508	0.2786	0.3113	0.2964	0.3310	0.3345	0.3202	0.2992	0.3013	0.3078	0.2781	0.2741	0.2608	0.2570	0.2716	0.2664	0.2431
ANIF EnMAP rot (672 nm)	0.9200	0.9711	1.0197	1.0010	0.8078	1.0733	1.2395	1.1728	1.2140	1.3594	1.2114	1.2466	1.1430	1.0479	1.0383	0.9344	0.9200	0.8828	0.9924	0.9807	0.8252
ANIF EnMAP NIR (864 nm)	0.9694	1.0004	0.9676	1.0008	0.9353	1.0390	1.1609	1.1055	1.2345	1.2476	1.1941	1.1160	1.1236	1.1478	1.0373	1.0222	0.9725	0.9585	1.0129	0.9933	0.9064
Rel. Blue Absorption Depth	0.3672	0.3555	0.3544	0.3624	0.3955	0.3775	0.4210	0.4008	0.4303	0.4132	0.4397	0.4063	0.3961	0.4116	0.3790	0.3828	0.3669	0.3662	0.3553	0.3516	0.3843
Rel. Red Absorption Depth	0.8963	0.8666	0.7726	0.8320	1.0086	0.8159	0.7912	0.7933	0.8759	0.7646	0.8278	0.7329	0.8330	0.9512	0.8441	0.9392	0.8965	0.9205	0.8513	0.8462	0.9400
NDVI (EnMAP)	0.5449	0.5369	0.5071	0.5262	0.5772	0.5144	0.5022	0.5046	0.5323	0.4946	0.5210	0.4851	0.5200	0.5584	0.5259	0.5580	0.5460	0.5554	0.5336	0.5309	0.5594
Nadir Norm. NDVI (AVHRR)	1.0361	1.0197	0.9693	0.9984	1.0870	0.9783	0.9562	0.9619	1.0017	0.9411	0.9785	0.9260	0.9892	1.0573	1.0009	1.0561	1.0359	1.0500	1.0076	1.0060	1.0515
Nadir Norm. NDVI (MODIS)	1.0365	1.0203	0.9674	0.9999	1.0888	0.9785	0.9576	0.9624	1.0050	0.9420	0.9808	0.9270	0.9904	1.0598	1.0023	1.0575	1.0369	1.0527	1.0085	1.0085	1.0544
Nadir Norm. NDVI (EnMAP)	1.0354	1.0203	0.9635	0.9999	1.0968	0.9775	0.9542	0.9588	1.0114	0.9398	0.9901	0.9218	0.9882	1.0610	0.9993	1.0603	1.0376	1.0553	1.0139	1.0087	1.0629

(cont.)

FBG1_03 (SZA = 47°; SAA = 180°)	Viewing Geometry (Viewing Zenith Angle | Viewing Azimuth Angle)																							
	20|135	20|157.5	20|170	30|180	30|190	30|202.5	30|225	30|270	30|315	30|337.5	30|350	30|0	30|10	30|22.5	30|45	30|90	30|135	30|157.5	30|170			
HCRF EnMAP blue (479 nm)	0.0493	0.0544	0.0543	0.0640	0.0646	0.0618	0.0557	0.0499	0.0457	0.0448	0.0410	0.0384	0.0447	0.0412	0.0443	0.0400	0.0564	0.0568	0.0639					
HCRF EnMAP green (549 nm)	0.0775	0.0874	0.0874	0.1059	0.1055	0.0991	0.0888	0.0797	0.0711	0.0679	0.0643	0.0600	0.0679	0.0621	0.0638	0.0621	0.0920	0.0937	0.1031					
HCRF EnMAP rot (672 nm)	0.0938	0.1044	0.1036	0.1196	0.1210	0.1168	0.1059	0.0914	0.0845	0.0810	0.0734	0.0705	0.0826	0.0748	0.0818	0.0746	0.1076	0.1062	0.1202					
HCRF EnMAP NIR (864 nm)	0.2867	0.3209	0.3214	0.3742	0.3736	0.3395	0.3098	0.3157	0.2930	0.2700	0.2766	0.2596	0.2709	0.2478	0.2395	0.2306	0.3311	0.3336	0.3547					
ANIF EnMAP rot (672 nm)	1.1266	1.2538	1.2446	1.4367	1.4537	1.4035	1.2721	1.0984	1.0158	0.9737	0.8825	0.8468	0.9927	0.8991	0.9834	0.8969	1.2922	1.2762	1.4443					
ANIF EnMAP NIR (864 nm)	1.0693	1.1968	1.1986	1.3955	1.3933	1.2663	1.1553	1.1774	1.0926	1.0070	1.0314	0.9682	1.0103	0.9242	0.8930	0.8600	1.2347	1.2443	1.3228					
Rel. Blue Absorption Depth	0.3967	0.4158	0.4254	0.4445	0.4408	0.4254	0.4283	0.4110	0.3847	0.3545	0.3771	0.3778	0.3591	0.3503	0.3137	0.3772	0.4185	0.4319	0.4212					
Rel. Red Absorption Depth	0.7953	0.8034	0.8139	0.8255	0.8113	0.7471	0.7456	0.9312	0.9165	0.8728	1.0205	0.9828	0.8621	0.8589	0.7332	0.7935	0.8166	0.8268	0.7629					
NDVI (EnMAP)	0.5071	0.5093	0.5125	0.5157	0.5108	0.4881	0.4906	0.5509	0.5521	0.5383	0.5803	0.5730	0.5326	0.5362	0.4906	0.5109	0.5096	0.5171	0.4938					
Nadir Norm. NDVI (AVHRR)	0.9637	0.9661	0.9712	0.9710	0.9613	0.9284	0.9331	1.0377	1.0459	1.0238	1.0910	1.0832	1.0160	1.0192	0.9460	0.9756	0.9642	0.9717	0.9335					
Nadir Norm. NDVI (MODIS)	0.9648	0.9671	0.9730	0.9755	0.9661	0.9318	0.9364	1.0422	1.0491	1.0262	1.0950	1.0859	1.0188	1.0224	0.9467	0.9780	0.9677	0.9765	0.9373					
Nadir Norm. NDVI (EnMAP)	0.9636	0.9677	0.9739	0.9799	0.9705	0.9274	0.9322	1.0468	1.0491	1.0229	1.1027	1.0887	1.0120	1.0188	0.9321	0.9708	0.9683	0.9825	0.9383					

Table C.1-5: Spectro-directional data of the FBG1_04 spectro-goniometer measurement.

FBG1_04 (SZA = 50°; SAA = 217°)	Viewing Geometry (Viewing Zenith Angle | Viewing Azimuth Angle)																							
	0|0	5|180	5|202.5	5|225	5|270	5|315	5|337.5	5|0	5|22.5	5|45	5|90	5|135	5|157.5	10|180	10|202.5	10|225	10|270	10|315	10|337.5	10|350
HCRF EnMAP blue (479 nm)	0.0455	0.0522	0.0572	0.0525	0.0454	0.0426	0.0410	0.0389	0.0441	0.0488	0.0497	0.0519	0.0504	0.0570	0.0562	0.0563	0.0542	0.0441	0.0420	0.0415
HCRF EnMAP green (549 nm)	0.0690	0.0814	0.0852	0.0814	0.0695	0.0658	0.0631	0.0640	0.0662	0.0743	0.0754	0.0827	0.0789	0.0887	0.0888	0.0869	0.0819	0.0675	0.0645	0.0634
HCRF EnMAP rot (672 nm)	0.0834	0.0944	0.1039	0.0988	0.0850	0.0784	0.0752	0.0712	0.0814	0.0880	0.0933	0.0960	0.0953	0.1084	0.1055	0.1058	0.1006	0.0809	0.0757	0.0762
HCRF EnMAP NIR (864 nm)	0.2557	0.3022	0.3028	0.2944	0.2657	0.2542	0.2510	0.2658	0.2437	0.2742	0.2708	0.2986	0.2927	0.3198	0.3245	0.3126	0.2955	0.2659	0.2450	0.2396
ANIF EnMAP rot (672 nm)	1.0000	1.1313	1.2462	1.1846	1.0192	0.9402	0.9017	0.8541	0.9759	1.0555	1.1184	1.1509	1.1430	1.2991	1.2991	1.2648	1.2059	0.9694	0.9072	0.9133
ANIF EnMAP NIR (864 nm)	1.0000	1.1819	1.1843	1.1514	1.0389	0.9942	0.9817	1.0393	0.9531	1.0725	1.0592	1.1677	1.1447	1.2506	1.2189	1.2691	1.2225	1.1557	1.0399	0.9581	0.9369
Rel. Blue Absorption Depth	0.3624	0.3913	0.3591	0.3945	0.3725	0.3726	0.3752	0.4287	0.3574	0.3667	0.3837	0.4115	0.4077	0.4005	0.3879	0.4069	0.3935	0.3799	0.3728	0.3651	0.3655
Rel. Red Absorption Depth	0.7948	0.8442	0.7506	0.7692	0.8189	0.8510	0.8926	1.0258	0.7538	0.8046	0.7405	0.8201	0.7998	0.7634	0.7999	0.8142	0.7640	0.7526	0.8608	0.8389	0.8214
NDVI (EnMAP)	0.5081	0.5241	0.4889	0.4974	0.5151	0.5285	0.5389	0.5772	0.4993	0.5140	0.4876	0.5134	0.5086	0.4938	0.5049	0.5093	0.4943	0.4921	0.5337	0.5280	0.5175
Nadir Norm. NDVI (AVHRR)	1.0000	1.0192	0.9630	0.9813	1.0174	1.0356	1.0585	1.1184	0.9845	1.0014	0.9621	0.9974	0.9974	0.9665	0.9931	1.0010	0.9756	0.9696	1.0487	1.0319	1.0175
Nadir Norm. NDVI (MODIS)	1.0000	1.0217	0.9623	0.9816	1.0177	1.0375	1.0598	1.1216	0.9848	1.0026	0.9630	0.9998	0.9979	0.9673	0.9944	1.0023	0.9764	0.9700	1.0499	1.0346	1.0186
Nadir Norm. NDVI (EnMAP)	1.0000	1.0316	0.9623	0.9791	1.0139	1.0402	1.0607	1.1361	0.9827	1.0116	0.9598	1.0105	1.0011	0.9719	0.9938	1.0025	0.9728	0.9686	1.0503	1.0393	1.0185

(cont.)

FBG1_04 (SZA = 50°; SAA = 217°)	Viewing Geometry (Viewing Zenith Angle | Viewing Azimuth Angle)																							
	10|0	10|10	10|22.5	10|45	10|90	10|135	10|157.5	10|170	20|180	20|190	20|202.5	20|225	20|270	20|315	20|337.5	20|350	20|0	20|10	20|22.5	20|45	20|90
HCRF EnMAP blue (479 nm)	0.0401	0.0368	0.0359	0.0352	0.0393	0.0519	0.0507	0.0548	0.0619	0.0648	0.0599	0.0547	0.0529	0.0428	0.0415	0.0387	0.0397	0.0379	0.0380	0.0351	0.0434
HCRF EnMAP green (549 nm)	0.0618	0.0573	0.0574	0.0559	0.0622	0.0846	0.0800	0.0836	0.0962	0.0979	0.0934	0.0876	0.0817	0.0659	0.0633	0.0587	0.0599	0.0571	0.0591	0.0533	0.0703
HCRF EnMAP rot (672 nm)	0.0746	0.0679	0.0665	0.0632	0.0717	0.0968	0.0944	0.1025	0.1174	0.1236	0.1161	0.1002	0.0986	0.0778	0.0737	0.0693	0.0713	0.0690	0.0705	0.0628	0.0781
HCRF EnMAP NIR (864 nm)	0.2399	0.2310	0.2416	0.2366	0.2478	0.3161	0.2972	0.2919	0.3189	0.3179	0.3267	0.3282	0.3090	0.2633	0.2528	0.2314	0.2361	0.2247	0.2415	0.2072	0.2695
ANIF EnMAP rot (672 nm)	0.8943	0.8142	0.7972	0.7581	0.8600	1.1610	1.1322	1.2286	1.4070	1.4819	1.3916	1.2016	1.1819	0.9329	0.8832	0.8305	0.8545	0.8275	0.8453	0.7524	0.9369
ANIF EnMAP NIR (864 nm)	0.9382	0.9034	0.9449	0.9254	0.9692	1.2360	1.1624	1.1415	1.2470	1.2431	1.2777	1.2834	1.2086	1.0297	0.9886	0.9048	0.9235	0.8789	0.9443	0.8102	1.0542
Rel. Blue Absorption Depth	0.3730	0.3740	0.3978	0.3845	0.3975	0.4406	0.4094	0.3875	0.3997	0.3898	0.4025	0.4107	0.3917	0.3660	0.3585	0.3559	0.3510	0.3491	0.3763	0.3580	0.4165
Rel. Red Absorption Depth	0.8394	0.8985	0.9864	1.0114	0.9249	0.8719	0.8242	0.7182	0.6787	0.6319	0.7171	0.8732	0.8295	0.9035	0.9065	0.8690	0.8690	0.8440	0.9153	0.8516	0.9265
NDVI (EnMAP)	0.5256	0.5456	0.5684	0.5783	0.5511	0.5309	0.5178	0.4803	0.4619	0.4401	0.4757	0.5321	0.5163	0.5438	0.5487	0.5392	0.5363	0.5301	0.5480	0.5350	0.5505
Nadir Norm. NDVI (AVHRR)	1.0326	1.0687	1.1074	1.1187	1.0697	1.0316	1.0094	0.9438	0.9091	0.8749	0.9414	1.0339	1.0143	1.0582	1.0657	1.0504	1.0475	1.0364	1.0711	1.0395	1.0567
Nadir Norm. NDVI (MODIS)	1.0336	1.0694	1.1100	1.1216	1.0733	1.0353	1.0107	0.9442	0.9102	0.8754	0.9420	1.0364	1.0166	1.0608	1.0688	1.0533	1.0507	1.0375	1.0731	1.0416	1.0623
Nadir Norm. NDVI (EnMAP)	1.0346	1.0739	1.1187	1.1381	1.0847	1.0450	1.0191	0.9454	0.9092	0.8661	0.9363	1.0473	1.0162	1.0702	1.0799	1.0612	1.0556	1.0433	1.0785	1.0530	1.0835

(cont.)

FBG1_04 (SZA = 50°; SAA = 217°)	Viewing Geometry (Viewing Zenith Angle | Viewing Azimuth Angle)																							
	20|135	20|157.5	20|170	30|180	30|190	30|202.5	30|225	30|270	30|315	30|337.5	30|350	30|0	30|10	30|122.5	30|45	30|90	30|135	30|157.5	30|170			
HCRF EnMAP blue (479 nm)	0.0519	0.0568	0.0615	0.0679	0.0662	0.0637	0.0586	0.0575	0.0494	0.0418	0.0407	0.0403	0.0417	0.0401	0.0338	0.0491	0.0555	0.0640	0.0654					
HCRF EnMAP green (549 nm)	0.0824	0.0931	0.0983	0.1091	0.1071	0.1015	0.0960	0.0874	0.0749	0.0643	0.0598	0.0587	0.0622	0.0604	0.0523	0.0786	0.0925	0.1043	0.1042					
HCRF EnMAP rot (672 nm)	0.0954	0.1037	0.1136	0.1279	0.1272	0.1201	0.1096	0.1060	0.0871	0.0747	0.0711	0.0700	0.0736	0.0693	0.0589	0.0881	0.1019	0.1209	0.1221					
HCRF EnMAP NIR (864 nm)	0.2977	0.3291	0.3319	0.3597	0.3634	0.3466	0.3567	0.3141	0.2841	0.2528	0.2256	0.2179	0.2366	0.2330	0.2119	0.2885	0.3333	0.3584	0.3415					
ANIF EnMAP rot (672 nm)	1.1440	1.2431	1.3625	1.5335	1.5255	1.4404	1.3143	1.2703	1.0449	0.8957	0.8523	0.8390	0.8828	0.8306	0.7057	1.0564	1.2219	1.4490	1.4643					
ANIF EnMAP NIR (864 nm)	1.1644	1.2869	1.2980	1.4067	1.4213	1.3556	1.3949	1.2285	1.1110	0.9887	0.8821	0.8522	0.9255	0.9113	0.8288	1.1282	1.3034	1.4015	1.3357					
Rel. Blue Absorption Depth	0.4143	0.4440	0.4218	0.4344	0.4402	0.4185	0.4297	0.3673	0.3601	0.3672	0.3293	0.3228	0.3398	0.3431	0.3720	0.4069	0.4482	0.4326	0.4211					
Rel. Red Absorption Depth	0.8138	0.8303	0.7404	0.7184	0.7401	0.7481	0.8796	0.7589	0.8730	0.9010	0.8105	0.7954	0.8350	0.8861	0.9585	0.8741	0.8787	0.7790	0.7046					
NDVI (EnMAP)	0.5146	0.5208	0.4899	0.4754	0.4814	0.4852	0.5298	0.4956	0.5305	0.5438	0.5207	0.5139	0.5254	0.5417	0.5653	0.5321	0.5316	0.4956	0.4732					
Nadir Norm. NDVI (AVHRR)	0.9930	0.9996	0.9491	0.9264	0.9445	0.9488	1.0266	0.9734	1.0330	1.0613	1.0166	1.0005	1.0215	1.0483	1.0907	1.0234	1.0261	0.9655	0.9211					
Nadir Norm. NDVI (MODIS)	0.9974	1.0048	0.9525	0.9312	0.9477	0.9509	1.0304	0.9736	1.0365	1.0650	1.0201	1.0041	1.0253	1.0530	1.0957	1.0288	1.0321	0.9694	0.9246					
Nadir Norm. NDVI (EnMAP)	1.0128	1.0251	0.9642	0.9357	0.9474	0.9550	1.0428	0.9754	1.0441	1.0703	1.0249	1.0114	1.0341	1.0661	1.1126	1.0472	1.0464	0.9755	0.9313					

Table C.1-6: Spectro-directional data of the FBG1_05 spectro-goniometer measurement.

FBG1_05 (SZA = 59°; SAA = 252°)	Viewing Geometry (Viewing Zenith Angle | Viewing Azimuth Angle)																							
	0|0	5|180	5|202.5	5|225	5|270	5|315	5|337.5	5|0	5|22.5	5|45	5|90	5|135	5|157.5	10|180	10|190	10|202.5	10|225	10|270	10|315	10|337.5	10|350
HCRF EnMAP blue (479 nm)	0.0351	0.0483	0.0486	0.0503	0.0414	0.0384	0.0363	0.0323	0.0385	0.0413	0.0411	0.0482	0.0521	0.0549	0.0502	0.0486	0.0514	0.0425	0.0384	0.0329	0.0342
HCRF EnMAP green (549 nm)	0.0552	0.0783	0.0776	0.0806	0.0656	0.0604	0.0571	0.0516	0.0599	0.0647	0.0648	0.0763	0.0813	0.0845	0.0798	0.0775	0.0794	0.0648	0.0609	0.0528	0.0548
HCRF EnMAP rot (672 nm)	0.0631	0.0872	0.0906	0.0941	0.0756	0.0684	0.0671	0.0588	0.0692	0.0730	0.0747	0.0920	0.0967	0.0996	0.0932	0.0922	0.0955	0.0761	0.0691	0.0598	0.0616
HCRF EnMAP NIR (864 nm)	0.2284	0.3017	0.2992	0.3090	0.2667	0.2393	0.2356	0.2207	0.2401	0.2538	0.2574	0.3024	0.3039	0.2976	0.3004	0.2992	0.3010	0.2515	0.2463	0.2295	0.2263
ANIF EnMAP rot (672 nm)	1.0000	1.3820	1.4355	1.4909	1.1984	1.0843	1.0643	0.9314	1.0967	1.1575	1.1835	1.4577	1.5331	1.5795	1.4774	1.4622	1.5131	1.2058	1.0946	0.9484	0.9766
ANIF EnMAP NIR (864 nm)	1.0000	1.3210	1.3097	1.3528	1.1677	1.0478	1.0313	0.9663	1.0512	1.1111	1.1270	1.3240	1.3305	1.3031	1.3152	1.3100	1.3177	1.1013	1.0783	1.0048	0.9905
Rel. Blue Absorption Depth	0.3876	0.4210	0.4229	0.4122	0.3987	0.3829	0.3809	0.3918	0.3718	0.3885	0.4071	0.4203	0.3929	0.3893	0.4108	0.4107	0.3859	0.3620	0.3967	0.4026	0.4095
Rel. Red Absorption Depth	0.9795	0.9494	0.8980	0.8856	0.9790	0.9510	0.9524	1.0274	0.9350	0.9272	0.9322	0.8855	0.8441	0.7726	0.8689	0.8780	0.8497	0.8959	0.9803	1.0582	1.0024
NDVI (EnMAP)	0.5672	0.5517	0.5353	0.5333	0.5583	0.5554	0.5564	0.5795	0.5526	0.5531	0.5503	0.5336	0.5172	0.4984	0.5284	0.5287	0.5184	0.5356	0.5621	0.5864	0.5719
Nadir Norm. NDVI (AVHRR)	1.0000	0.9692	0.9486	0.9471	0.9904	0.9795	0.9845	1.0214	0.9720	0.9622	0.9636	0.9485	0.9191	0.8813	0.9340	0.9387	0.9241	0.9517	0.9882	1.0312	1.0021
Nadir Norm. NDVI (MODIS)	1.0000	0.9720	0.9493	0.9470	0.9908	0.9806	0.9835	1.0222	0.9722	0.9644	0.9657	0.9486	0.9191	0.8817	0.9345	0.9386	0.9231	0.9512	0.9898	1.0329	1.0048
Nadir Norm. NDVI (EnMAP)	1.0000	0.9727	0.9437	0.9403	0.9844	0.9793	0.9810	1.0218	0.9744	0.9753	0.9703	0.9409	0.9118	0.8787	0.9282	0.9322	0.9141	0.9444	0.9910	1.0340	1.0084

(cont.)

FBG1_05 (SZA = 59°; SAA = 252°)	Viewing Geometry (Viewing Zenith Angle | Viewing Azimuth Angle)																							
	10|0	10|10	10|22.5	10|45	10|90	10|135	10|157.5	10|170	20|180	20|190	20|202.5	20|225	20|270	20|315	20|337.5	20|350	20|0	20|10	20|22.5	20|45	20|90
HCRF EnMAP blue (479 nm)	0.0340	0.0396	0.0415	0.0435	0.0409	0.0538	0.0543	0.0523	0.0591	0.0584	0.0542	0.0550	0.0394	0.0372	0.0337	0.0368	0.0312	0.0368	0.0406	0.0462	0.0408
HCRF EnMAP green (549 nm)	0.0547	0.0603	0.0645	0.0678	0.0670	0.0863	0.0860	0.0808	0.0983	0.0958	0.0871	0.0871	0.0629	0.0598	0.0531	0.0556	0.0491	0.0558	0.0619	0.0743	0.0677
HCRF EnMAP rot (672 nm)	0.0616	0.0715	0.0737	0.0803	0.0731	0.1025	0.1004	0.0957	0.1077	0.1087	0.1024	0.1046	0.0698	0.0667	0.0613	0.0670	0.0554	0.0669	0.0721	0.0848	0.0745
HCRF EnMAP NIR (864 nm)	0.2328	0.2346	0.2631	0.2611	0.2760	0.3248	0.3258	0.2879	0.3569	0.3575	0.3352	0.3317	0.2619	0.2536	0.2259	0.2210	0.2106	0.2281	0.2426	0.2881	0.2841
ANIF EnMAP rot (672 nm)	0.9759	1.1331	1.1688	1.2726	1.1593	1.6245	1.5922	1.5172	1.7075	1.7227	1.6227	1.6575	1.1071	1.0565	0.9723	1.0614	0.8775	1.0612	1.1431	1.3435	1.1811
ANIF EnMAP NIR (864 nm)	1.0194	1.0272	1.1518	1.1431	1.2085	1.4218	1.4263	1.2604	1.5624	1.5650	1.4676	1.4520	1.1465	1.1104	0.9890	0.9677	0.9222	0.9987	1.0623	1.2615	1.2437
Rel. Blue Absorption Depth	0.4022	0.3661	0.3788	0.3932	0.4341	0.4291	0.4037	0.3833	0.4437	0.4329	0.4116	0.4102	0.3959	0.4054	0.3932	0.3606	0.3836	0.3514	0.3587	0.4168	0.4454
Rel. Red Absorption Depth	1.0331	0.8571	0.9604	0.8635	1.0397	0.8508	0.8766	0.7846	0.9068	0.9072	0.8966	0.8586	1.0551	1.0592	1.0031	0.8613	1.0239	0.8931	0.8797	0.9168	1.0670
NDVI (EnMAP)	0.5818	0.5330	0.5622	0.5296	0.5811	0.5202	0.5287	0.5010	0.5363	0.5337	0.5321	0.5206	0.5789	0.5838	0.5729	0.5350	0.5838	0.5462	0.5418	0.5454	0.5844
Nadir Norm. NDVI (AVHRR)	1.0209	0.9398	0.9810	0.9347	1.0122	0.9174	0.9347	0.8902	0.9368	0.9414	0.9423	0.9267	1.0171	1.0225	1.0138	0.9506	1.0231	0.9618	0.9488	0.9565	1.0207
Nadir Norm. NDVI (MODIS)	1.0223	0.9403	0.9829	0.9363	1.0154	0.9190	0.9353	0.8905	0.9397	0.9436	0.9429	0.9269	1.0188	1.0251	1.0158	0.9511	1.0250	0.9624	0.9501	0.9598	1.0239
Nadir Norm. NDVI (EnMAP)	1.0257	0.9397	0.9912	0.9339	1.0246	0.9173	0.9321	0.8833	0.9456	0.9411	0.9382	0.9179	1.0207	1.0293	1.0102	0.9433	1.0293	0.9631	0.9552	0.9616	1.0304

(cont.)

FBG1_05 (SZA = 59°; SAA = 252°)	Viewing Geometry (Viewing Zenith Angle | Viewing Azimuth Angle)																							
	20|135	20|157.5	20|170	30|180	30|190	30|202.5	30|225	30|270	30|315	30|337.5	30|350	30|0	30|10	30|22.5	30|45	30|90	30|135	30|157.5	30|170			
HCRF EnMAP blue (479 nm)	0.0541	0.0565	0.0581	0.0633	0.0700	0.0652	0.0651	0.0477	0.0436	0.0386	0.0373	0.0374	0.0343	0.0375	0.0436	0.0427	0.0566	0.0624	0.0617					
HCRF EnMAP green (549 nm)	0.0860	0.0907	0.0957	0.1101	0.1131	0.1037	0.1026	0.0734	0.0641	0.0612	0.0573	0.0582	0.0528	0.0579	0.0724	0.0741	0.0914	0.1028	0.1074					
HCRF EnMAP rot (672 nm)	0.1017	0.1080	0.1110	0.1173	0.1322	0.1239	0.1233	0.0844	0.0746	0.0672	0.0668	0.0659	0.0625	0.0664	0.0777	0.0794	0.1074	0.1185	0.1167					
HCRF EnMAP NIR (864 nm)	0.3145	0.3260	0.3485	0.4050	0.3960	0.3818	0.3650	0.2735	0.2451	0.2618	0.2411	0.2381	0.2225	0.2414	0.2979	0.3129	0.3252	0.3632	0.3913					
ANIF EnMAP rot (672 nm)	1.6127	1.7114	1.7588	1.8594	2.0960	1.9637	1.9546	1.3384	1.1820	1.0646	1.0589	1.0441	0.9908	1.0519	1.2320	1.2581	1.7022	1.8791	1.8491					
ANIF EnMAP NIR (864 nm)	1.3768	1.4274	1.5256	1.7730	1.7336	1.6714	1.5982	1.1975	1.0730	1.1461	1.0556	1.0426	0.9741	1.0567	1.3041	1.3698	1.4239	1.5899	1.7132					
Rel. Blue Absorption Depth	0.4241	0.4209	0.4417	0.4772	0.4233	0.4136	0.3979	0.3697	0.3255	0.3873	0.3668	0.3776	0.3618	0.3628	0.4338	0.4786	0.4392	0.4459	0.4800					
Rel. Red Absorption Depth	0.8235	0.7958	0.8473	0.9731	0.8040	0.8266	0.7931	0.8749	0.8646	1.0875	0.9756	0.9726	0.9463	0.9627	1.0585	1.1346	0.8071	0.8208	0.9260					
NDVI (EnMAP)	0.5111	0.5024	0.5170	0.5508	0.4993	0.5100	0.4950	0.5282	0.5334	0.5917	0.5661	0.5667	0.5614	0.5687	0.5862	0.5953	0.5036	0.5078	0.5407					
Nadir Norm. NDVI (AVHRR)	0.9058	0.8903	0.9148	0.9580	0.8852	0.9045	0.8844	0.9345	0.9355	1.0326	0.9982	0.9932	0.9894	0.9971	1.0170	1.0383	0.8883	0.8934	0.9421					
Nadir Norm. NDVI (MODIS)	0.9074	0.8910	0.9154	0.9619	0.8867	0.9040	0.8842	0.9365	0.9379	1.0364	1.0010	0.9969	0.9900	0.9991	1.0222	1.0431	0.8917	0.8953	0.9451					
Nadir Norm. NDVI (EnMAP)	0.9012	0.8859	0.9115	0.9711	0.8804	0.8992	0.8728	0.9314	0.9405	1.0432	0.9981	0.9991	0.9898	1.0027	1.0335	1.0497	0.8879	0.8953	0.9534					

Table C.1-7: Spectro-directional data of the FBG1_06 spectro-goniometer measurement.

FBG1_06 (SZA = 68°; SAA = 278°)	Viewing Geometry (Viewing Zenith Angle | Viewing Azimuth Angle)																							
	0|0	5|180	5|202.5	5|225	5|270	5|315	5|337.5	5|0	5|22.5	5|45	5|90	5|135	5|157.5	10|180	10|202.5	10|225	10|270	10|315	10|337.5	10|350
HCRF EnMAP blue (479 nm)	0.0313	0.0477	0.0419	0.0368	0.0303	0.0370	0.0396	0.0442	0.0425	0.0363	0.0416	0.0459	0.0381	0.0451	0.0425	0.0407	0.0367	0.0345	0.0374	0.0410	0.0388
HCRF EnMAP green (549 nm)	0.0475	0.0749	0.0660	0.0571	0.0465	0.0586	0.0644	0.0697	0.0662	0.0570	0.0657	0.0698	0.0587	0.0720	0.0666	0.0651	0.0580	0.0532	0.0600	0.0627	0.0612
HCRF EnMAP rot (672 nm)	0.0518	0.0870	0.0751	0.0657	0.0507	0.0665	0.0723	0.0810	0.0797	0.0652	0.0753	0.0838	0.0662	0.0824	0.0773	0.0719	0.0642	0.0602	0.0664	0.0741	0.0695
HCRF EnMAP NIR (864 nm)	0.1888	0.2684	0.2546	0.2258	0.1911	0.2334	0.2675	0.2802	0.2614	0.2361	0.2514	0.2568	0.2184	0.2709	0.2477	0.2442	0.2294	0.2128	0.2446	0.2436	0.2595
ANIF EnMAP rot (672 nm)	1.0000	1.6772	1.4490	1.2671	0.9782	1.2818	1.3944	1.5619	1.5379	1.2573	1.4519	1.6162	1.2776	1.5901	1.4902	1.3872	1.2382	1.1604	1.2807	1.4291	1.3400
ANIF EnMAP NIR (864 nm)	1.0000	1.4215	1.3484	1.1955	1.0118	1.2361	1.4163	1.4839	1.3844	1.2501	1.3310	1.3601	1.1564	1.4345	1.3115	1.2932	1.2149	1.1267	1.2952	1.2899	1.3744
Rel. Blue Absorption Depth	0.3527	0.4026	0.3879	0.3738	0.3596	0.3999	0.4164	0.3985	0.3922	0.3990	0.4114	0.3673	0.3870	0.4134	0.3921	0.4047	0.3897	0.3702	0.4070	0.3675	0.3934
Rel. Red Absorption Depth	0.9947	0.8309	0.9507	0.9522	1.0411	0.9414	1.0237	0.9414	0.8693	0.9915	0.8921	0.8202	0.8804	0.9013	0.8831	0.9326	0.9892	0.9636	1.0107	0.8677	1.0152
NDVI (EnMAP)	0.5692	0.5106	0.5444	0.5492	0.5805	0.5568	0.5744	0.5516	0.5326	0.5672	0.5391	0.5080	0.5346	0.5334	0.5244	0.5450	0.5627	0.5591	0.5730	0.5335	0.5777
Nadir Norm. NDVI (AVHRR)	1.0000	0.9091	0.9711	0.9795	1.0231	0.9810	1.0138	0.9777	0.9519	1.0025	0.9560	0.9132	0.9422	0.9472	0.9402	0.9689	0.9974	0.9867	1.0095	0.9483	1.0219
Nadir Norm. NDVI (MODIS)	1.0000	0.9110	0.9706	0.9796	1.0232	0.9835	1.0153	0.9790	0.9528	1.0049	0.9585	0.9139	0.9451	0.9491	0.9399	0.9699	0.9981	0.9884	1.0124	0.9490	1.0230
Nadir Norm. NDVI (EnMAP)	1.0000	0.8972	0.9564	0.9649	1.0199	0.9782	1.0092	0.9691	0.9357	0.9966	0.9471	0.8926	0.9392	0.9371	0.9214	0.9575	0.9887	0.9824	1.0066	0.9374	1.0149

(cont.)

FBG1_06 (SZA = 68°; SAA = 278°)	Viewing Geometry (Viewing Zenith Angle | Viewing Azimuth Angle)																							
	10|0	10|10	10|22.5	10|45	10|90	10|135	10|157.5	10|170	20|180	20|190	20|202.5	20|225	20|270	20|315	20|337.5	20|350	20|0	20|10	20|22.5	20|45	20|90
HCRF EnMAP blue (479 nm)	0.0396	0.0442	0.0420	0.0416	0.0405	0.0462	0.0419	0.0457	0.0433	0.0504	0.0461	0.0438	0.0357	0.0345	0.0324	0.0381	0.0411	0.0385	0.0427	0.0391	0.0394
HCRF EnMAP green (549 nm)	0.0648	0.0703	0.0663	0.0670	0.0619	0.0720	0.0660	0.0710	0.0704	0.0806	0.0730	0.0689	0.0552	0.0556	0.0527	0.0601	0.0643	0.0632	0.0682	0.0629	0.0630
HCRF EnMAP rot (672 nm)	0.0719	0.0830	0.0790	0.0747	0.0723	0.0825	0.0744	0.0833	0.0793	0.0934	0.0841	0.0778	0.0618	0.0609	0.0578	0.0670	0.0735	0.0697	0.0780	0.0699	0.0699
HCRF EnMAP NIR (864 nm)	0.2746	0.2782	0.2727	0.2674	0.2338	0.2557	0.2439	0.2565	0.2589	0.2918	0.2643	0.2515	0.2199	0.2374	0.2339	0.2534	0.2639	0.2726	0.2875	0.2621	0.2550
ANIF EnMAP rot (672 nm)	1.3866	1.6006	1.5241	1.4418	1.3936	1.5911	1.4346	1.6061	1.5298	1.8023	1.6224	1.5009	1.1912	1.1740	1.1148	1.2917	1.4174	1.3448	1.5046	1.3490	1.3474
ANIF EnMAP NIR (864 nm)	1.4540	1.4734	1.4443	1.4163	1.2382	1.3539	1.2914	1.3583	1.3711	1.5454	1.3995	1.3317	1.1644	1.2569	1.2386	1.3418	1.3975	1.4435	1.5225	1.3880	1.3501
Rel. Blue Absorption Depth	0.4356	0.4117	0.3966	0.4220	0.3866	0.3905	0.3969	0.3902	0.4204	0.4152	0.4070	0.3814	0.3701	0.4064	0.4032	0.3821	0.3910	0.4341	0.4065	0.4223	0.4219
Rel. Red Absorption Depth	1.0726	0.9106	0.9308	0.9922	0.8526	0.8304	0.8770	0.8237	0.8959	0.8565	0.8643	0.8809	0.9878	1.0939	1.1236	1.0332	0.9794	1.1037	1.0284	1.0417	1.0206
NDVI (EnMAP)	0.5850	0.5405	0.5507	0.5631	0.5279	0.5121	0.5326	0.5098	0.5310	0.5149	0.5171	0.5274	0.5614	0.5918	0.6037	0.5819	0.5644	0.5926	0.5732	0.5787	0.5699
Nadir Norm. NDVI (AVHRR)	1.0348	0.9679	0.9822	0.9931	0.9354	0.9064	0.9450	0.9102	0.9454	0.9178	0.9226	0.9351	0.9888	1.0467	1.0630	1.0236	0.9963	1.0443	1.0200	1.0219	1.0104
Nadir Norm. NDVI (MODIS)	1.0374	0.9694	0.9825	0.9954	0.9364	0.9080	0.9464	0.9100	0.9462	0.9185	0.9227	0.9366	0.9905	1.0493	1.0655	1.0262	0.9994	1.0476	1.0215	1.0242	1.0130
Nadir Norm. NDVI (EnMAP)	1.0278	0.9497	0.9676	0.9893	0.9274	0.8997	0.9357	0.8957	0.9330	0.9047	0.9085	0.9266	0.9864	1.0398	1.0607	1.0224	0.9916	1.0412	1.0070	1.0168	1.0012

(cont.)

FBG1_06 (SZA = 68°; SAA = 278°)	Viewing Geometry (Viewing Zenith Angle | Viewing Azimuth Angle)																							
	20|135	20|157.5	20|170	30|180	30|190	30|202.5	30|225	30|270	30|315	30|337.5	30|350	30|0	30|10	30|122.5	30|45	30|90	30|135	30|157.5	30|170			
HCRF EnMAP blue (479 nm)	0.0485	0.0481	0.0427	0.0497	0.0540	0.0530	0.0491	0.0438	0.0383	0.0370	0.0360	0.0390	0.0387	0.0402	0.0364	0.0415	0.0529	0.0590	0.0520					
HCRF EnMAP green (549 nm)	0.0780	0.0808	0.0695	0.0811	0.0895	0.0843	0.0771	0.0678	0.0622	0.0564	0.0578	0.0629	0.0649	0.0644	0.0638	0.0687	0.0867	0.0946	0.0860					
HCRF EnMAP rot (672 nm)	0.0881	0.0866	0.0786	0.0962	0.1026	0.1002	0.0885	0.0776	0.0684	0.0668	0.0625	0.0690	0.0698	0.0733	0.0684	0.0747	0.1020	0.1146	0.0993					
HCRF EnMAP NIR (864 nm)	0.2769	0.3052	0.2752	0.2922	0.3179	0.2903	0.2654	0.2603	0.2675	0.2317	0.2490	0.2668	0.2749	0.2622	0.2850	0.2747	0.3184	0.3357	0.3133					
ANIF EnMAP rot (672 nm)	1.6996	1.6700	1.5161	1.8546	1.9787	1.9331	1.7064	1.4960	1.3187	1.2889	1.2049	1.3308	1.3471	1.4138	1.3187	1.4414	1.9665	2.2102	1.9149					
ANIF EnMAP NIR (864 nm)	1.4663	1.6162	1.4575	1.5473	1.6836	1.5371	1.4054	1.3784	1.4166	1.2272	1.3184	1.4127	1.4558	1.3887	1.5091	1.4545	1.6861	1.7779	1.6593					
Rel. Blue Absorption Depth	0.4196	0.4467	0.4161	0.4233	0.4321	0.4078	0.3869	0.3803	0.4142	0.3640	0.3894	0.3989	0.4402	0.4011	0.4815	0.4451	0.4395	0.4167	0.4408					
Rel. Red Absorption Depth	0.8412	0.9986	0.9824	0.8239	0.8607	0.7904	0.8152	0.9138	0.1084	0.9172	1.0943	1.0687	1.1015	0.9808	1.2087	1.0366	0.8447	0.7841	0.8673					
NDVI (EnMAP)	0.5172	0.5580	0.5557	0.5048	0.5121	0.4867	0.5000	0.5408	0.5929	0.5524	0.5988	0.5890	0.5948	0.5631	0.6130	0.5722	0.5149	0.4911	0.5188					
Nadir Norm. NDVI (AVHRR)	0.9127	0.9856	0.9829	0.9133	0.9172	0.8695	0.8934	0.9537	1.0411	0.9862	1.0521	1.0419	1.0451	0.9990	1.0849	1.0088	0.9142	0.8842	0.9281					
Nadir Norm. NDVI (MODIS)	0.9155	0.9885	0.9831	0.9114	0.9177	0.8693	0.8955	0.9556	1.0447	0.9867	1.0543	1.0452	1.0486	1.0006	1.0871	1.0136	0.9143	0.8831	0.9269					
Nadir Norm. NDVI (EnMAP)	0.9086	0.9804	0.9763	0.8869	0.8997	0.8551	0.8784	0.9502	1.0416	0.9704	1.0521	1.0349	1.0451	0.9893	1.0770	1.0054	0.9046	0.8628	0.9115					

V *Main Spectral Characteristics*

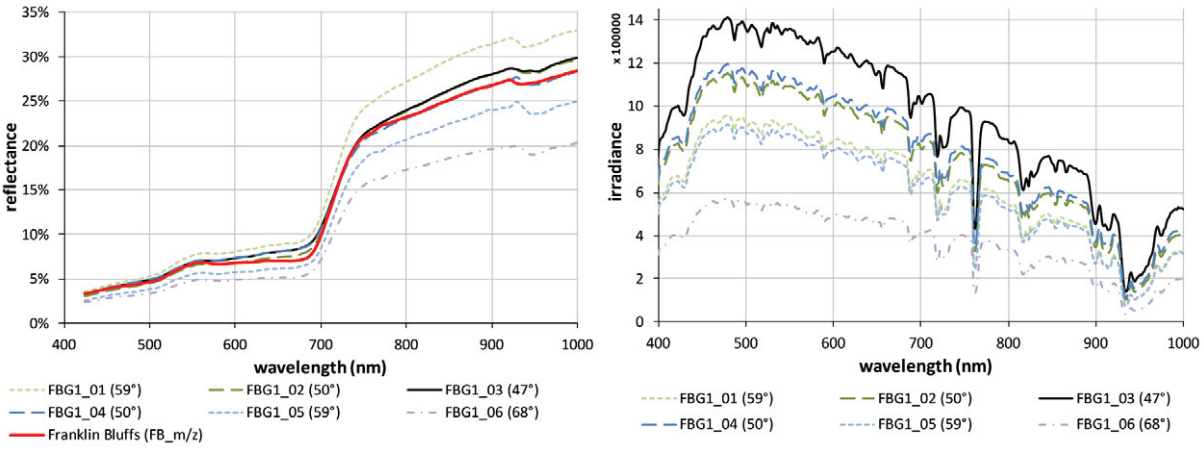

Figure C.1-6: Nadir reflectances and irradiance profiles of the FBG1 site at different sun zenith angles. Left: Comparison of the nadir reflectance signatures with the average zonal vegetation (MNT). Right: Comparison of the total irradiance profiles.

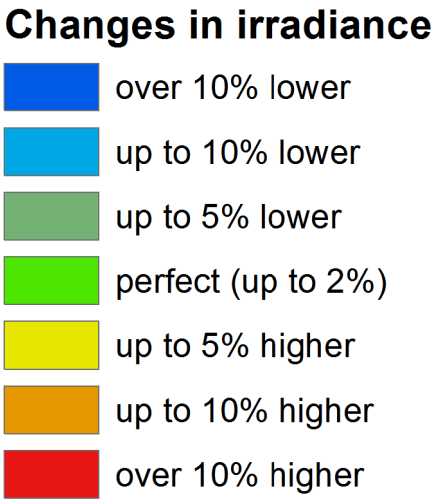

Figure C.1-7: Legend of the outlier indicator graphics shown in Figure C.1-9, C.1-10, and C.1-13

VI *HCRF Visualization*

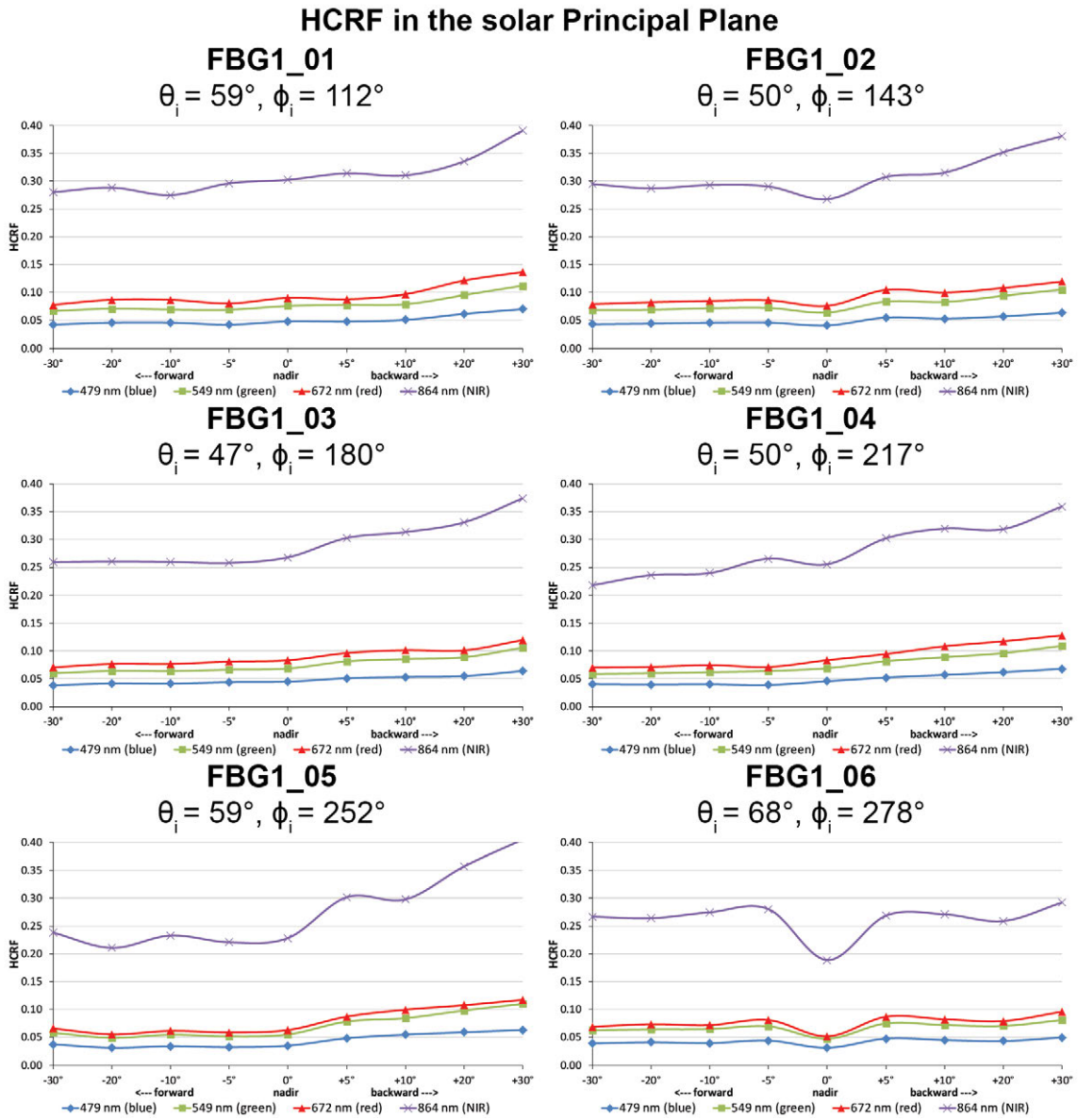

Figure C.1-8: Comparison of the HCRF values at 479 nm (blue), 549 nm (green), 672 nm (red), and 864 nm (NIR) in the solar principal plane of the FBG1 site at different sun zenith angles.

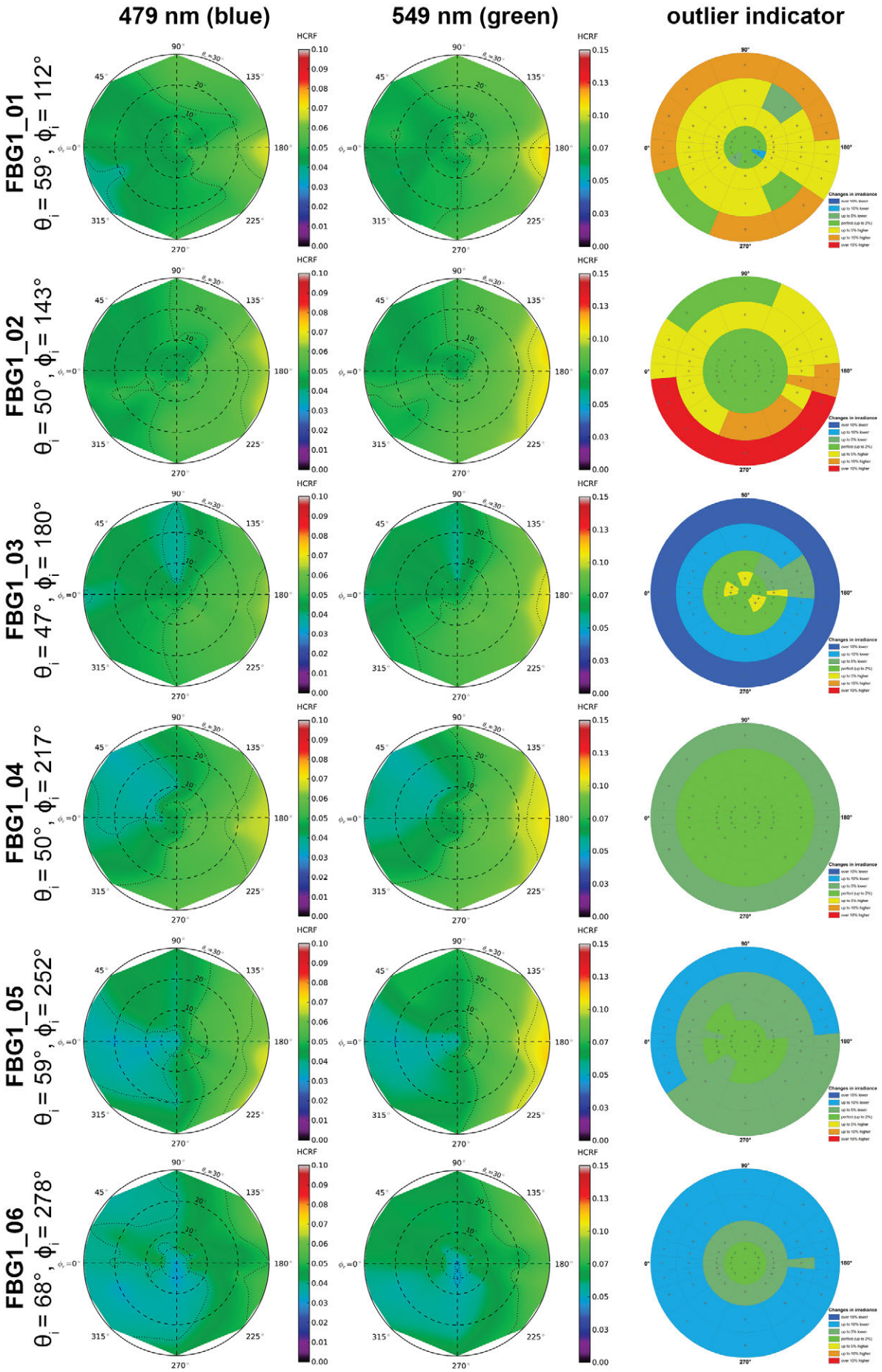

Figure C.1-9: HCRF visualization at 479 nm and 549 nm of the FBG1 site.

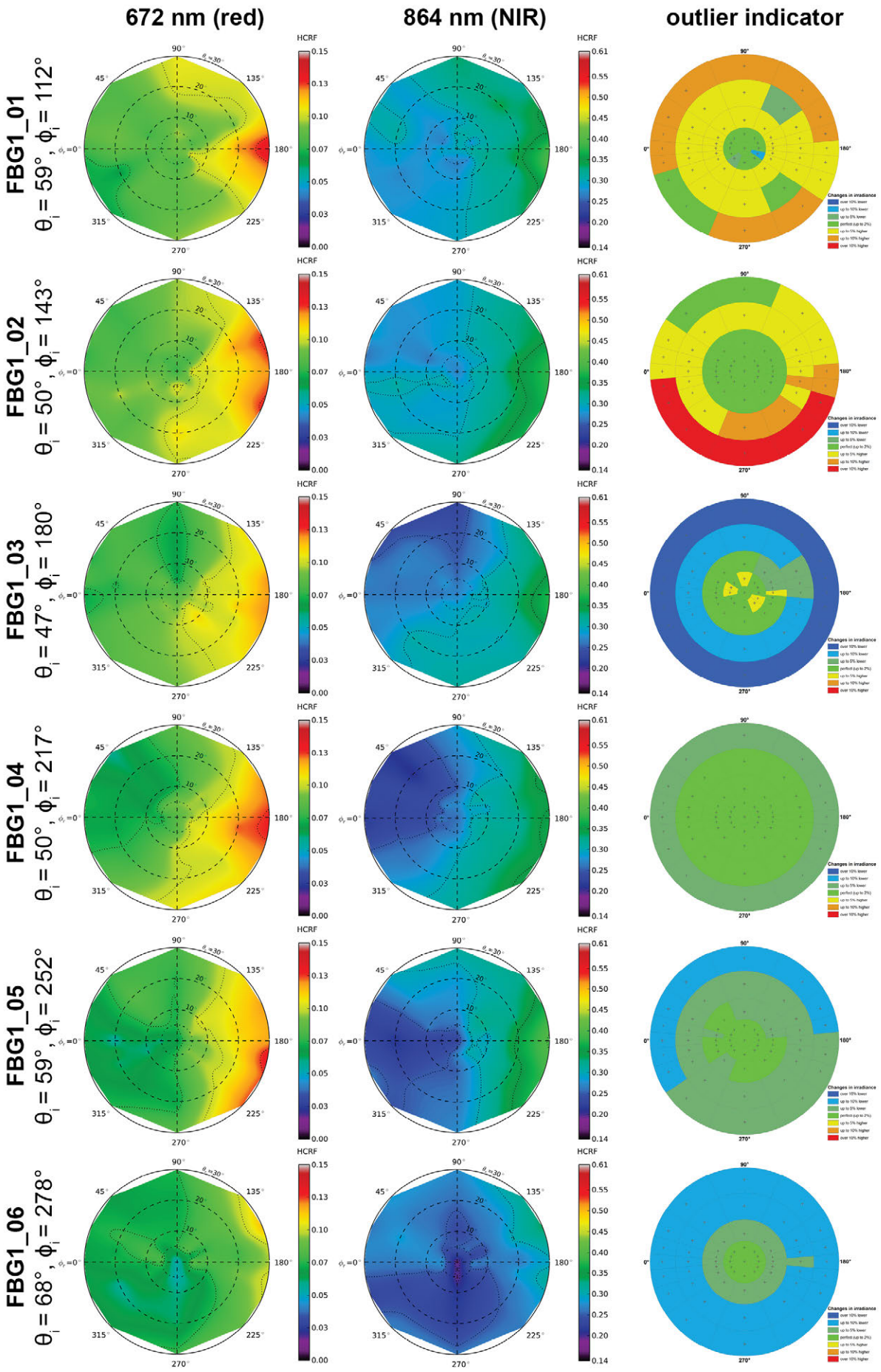

Figure C.1-10: HCRF visualization at 672 nm and 864 nm of the FBG1 site.

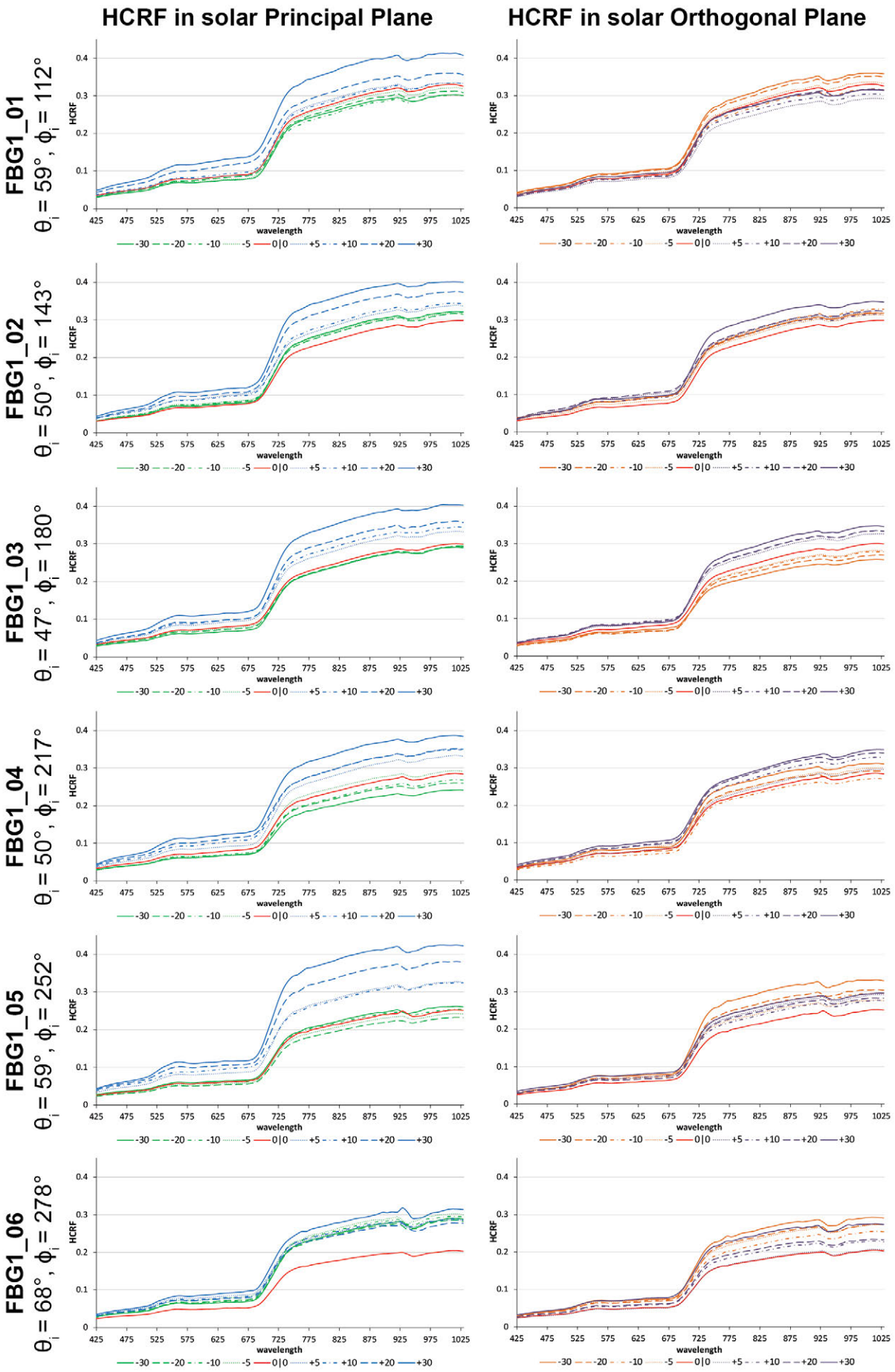

Figure C.1-11: HCRF visualization in principal & orthogonal plane of the FBG1 site.

VII *ANIF Visualization*

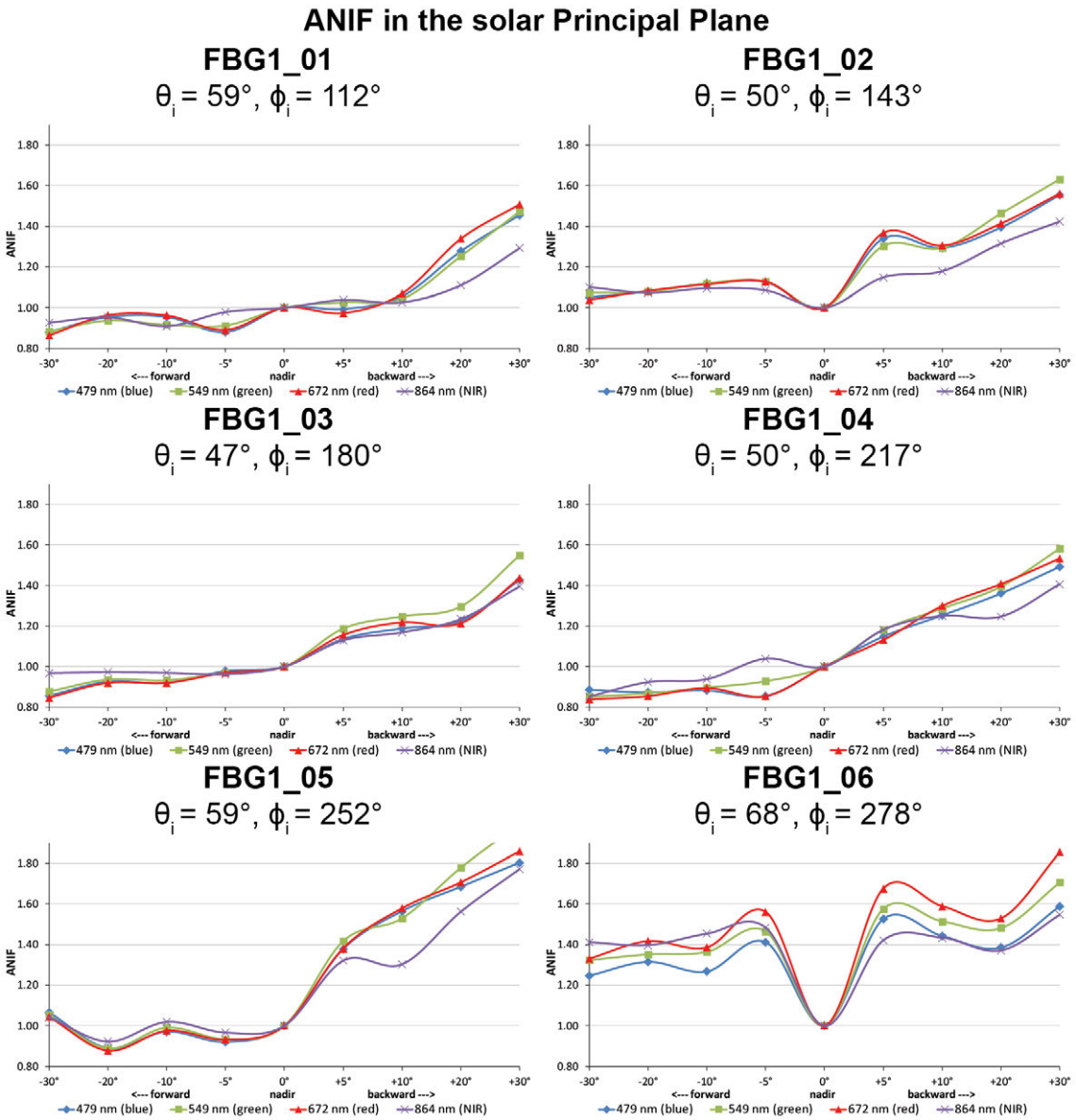

Figure C.1-12: Comparison of the ANIF values at 479 nm (blue), 549 nm (green), 672 nm (red), and 864 nm (NIR) in the solar principal plane of the FBG1 site at different sun zenith angles.

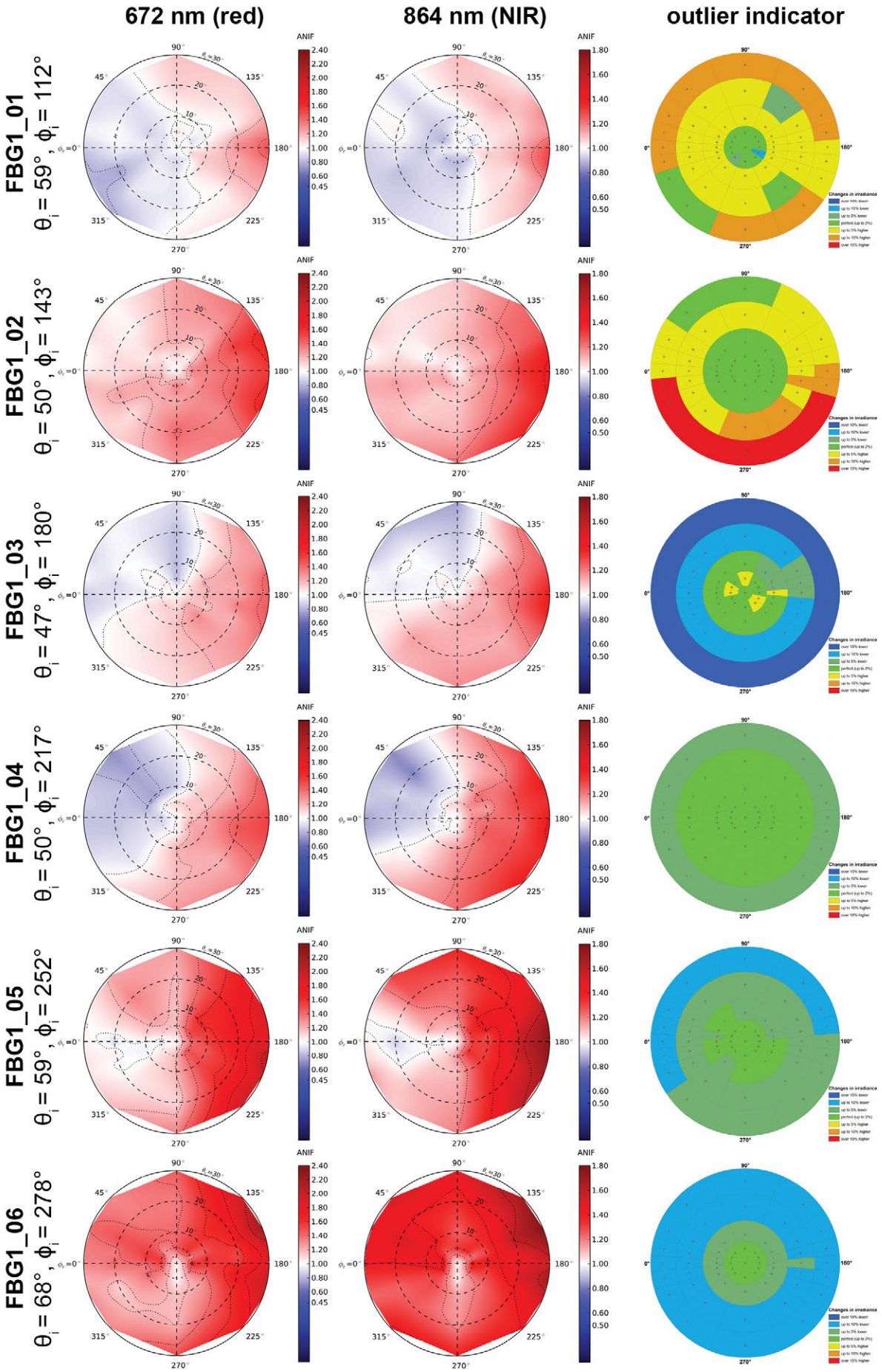

Figure C.1-13: ANIF visualization at 672 nm and 864 nm of the FBG1 site.

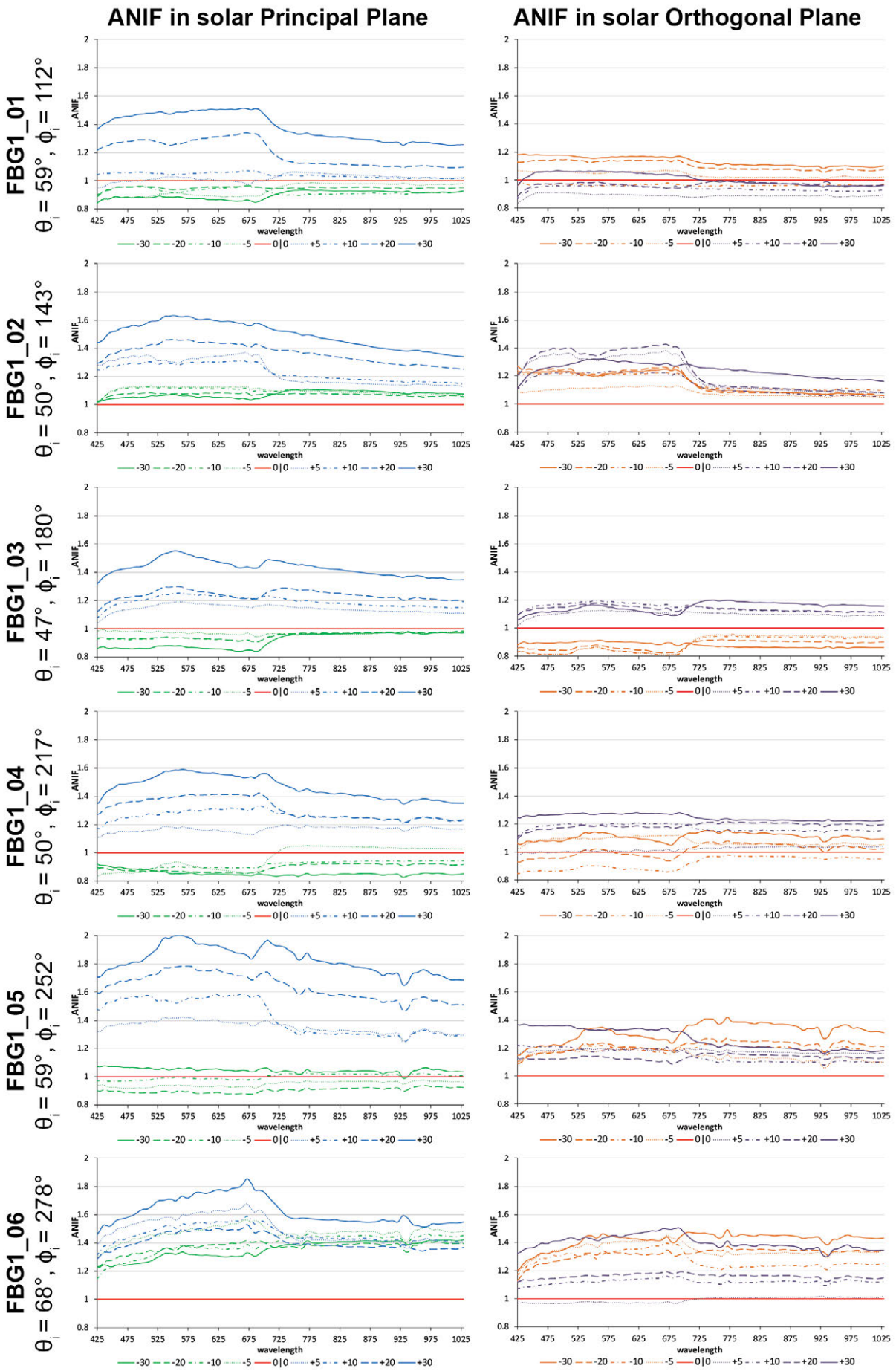

Figure C.1-14: ANIF visualization in principal & orthogonal plane of the FBG1 site.

VIII *ANIX Visualization*

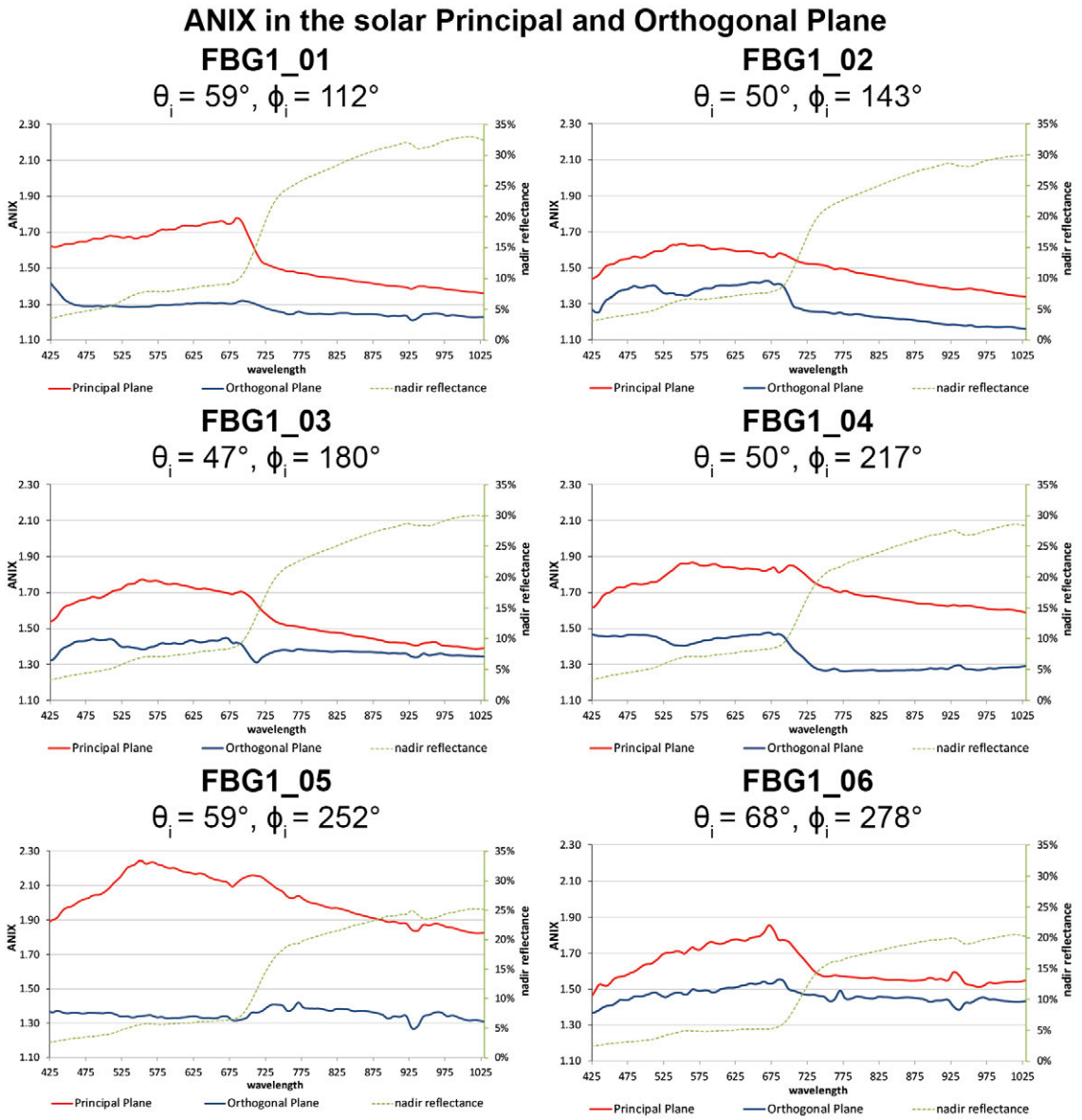

FigureC.1-15: Comparison of the ANIX in the solar principal and orthogonal plane with the nadir reflectance of the FBG1 site at different sun zenith angles.

IX *NDVI and Relative Absorption Depth Visualization*

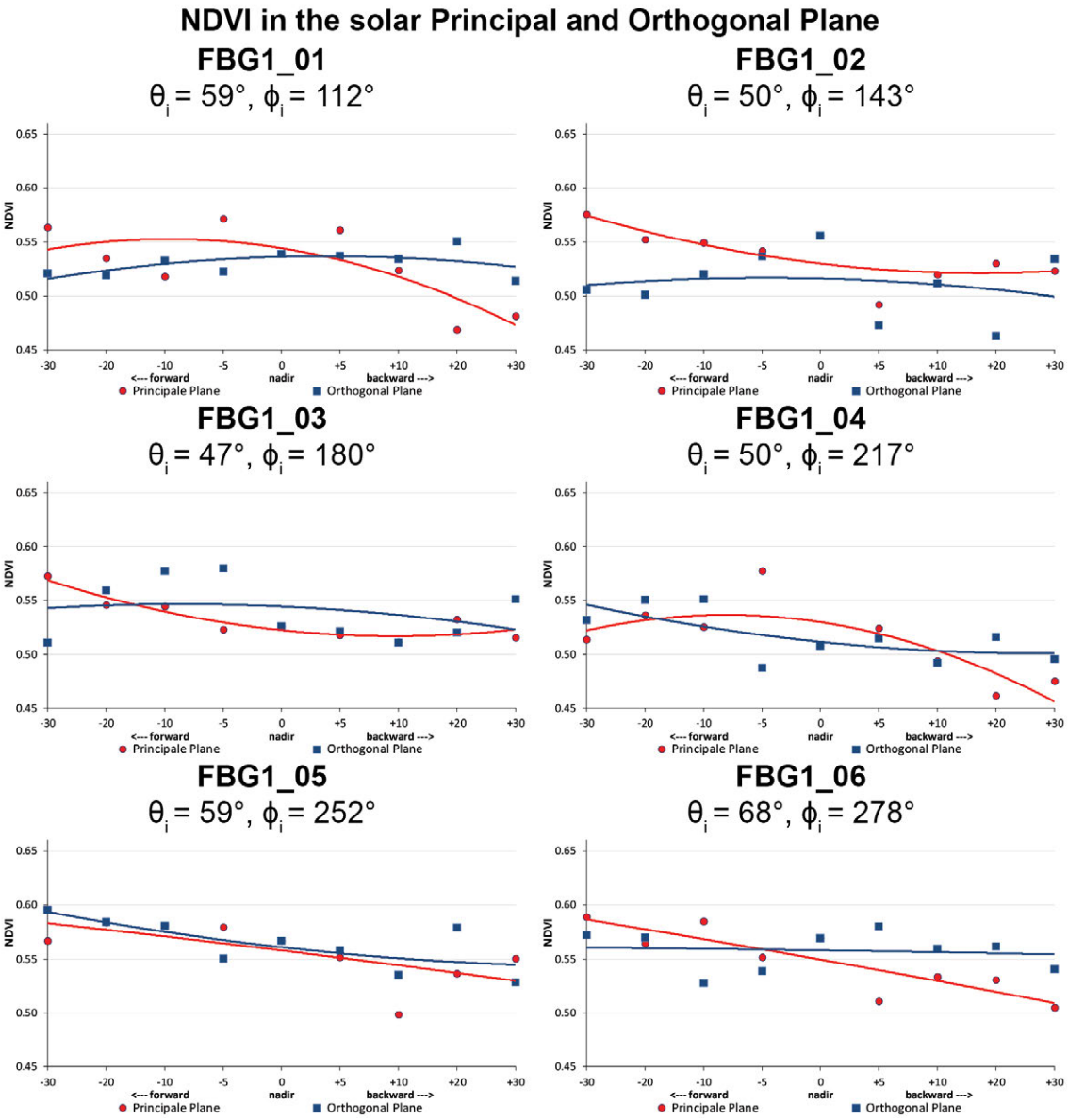

Figure C.1-16: Comparison of the NDVI in the solar principal and orthogonal plane of the FBG1 site at different sun zenith angles.

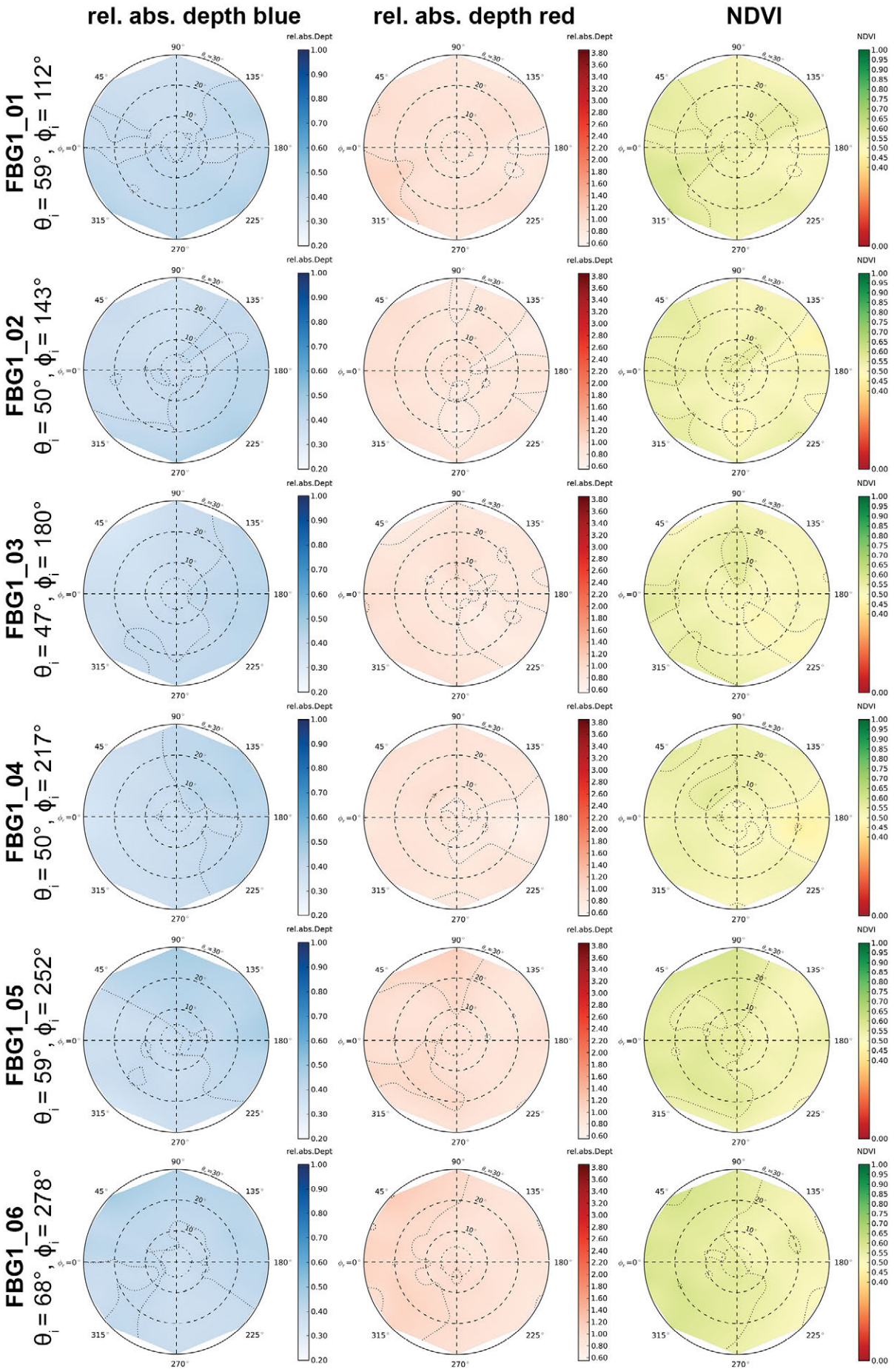

Figure C.1-17: Visualization of relative absorption depth & NDVI of the FBG1 site.

X *NDVI Comparison of Different Sensors*

Table C.1-8: Center wavelengths and band widths of the broadband and narrowband NDVIs, based on the spectral response curves of the AVHRR, MODIS and EnMAP sensors.

NDVI	Sensor	Sensor band	Center wavelength (nm)	band width (nm)
$NDVI_{AVHRR}$ [broadband]	AVHRR/3	red: band 1 NIR: band 2	630 865	100 275
$NDVI_{MODIS}$ [broadband]	MODIS	red: band 1 NIR: band 2	645 859	50 35
$NDVI_{EnMAP}$ [narrowband]	EnMAP	red: band 47 NIR: band 73	672 864	6.5 8

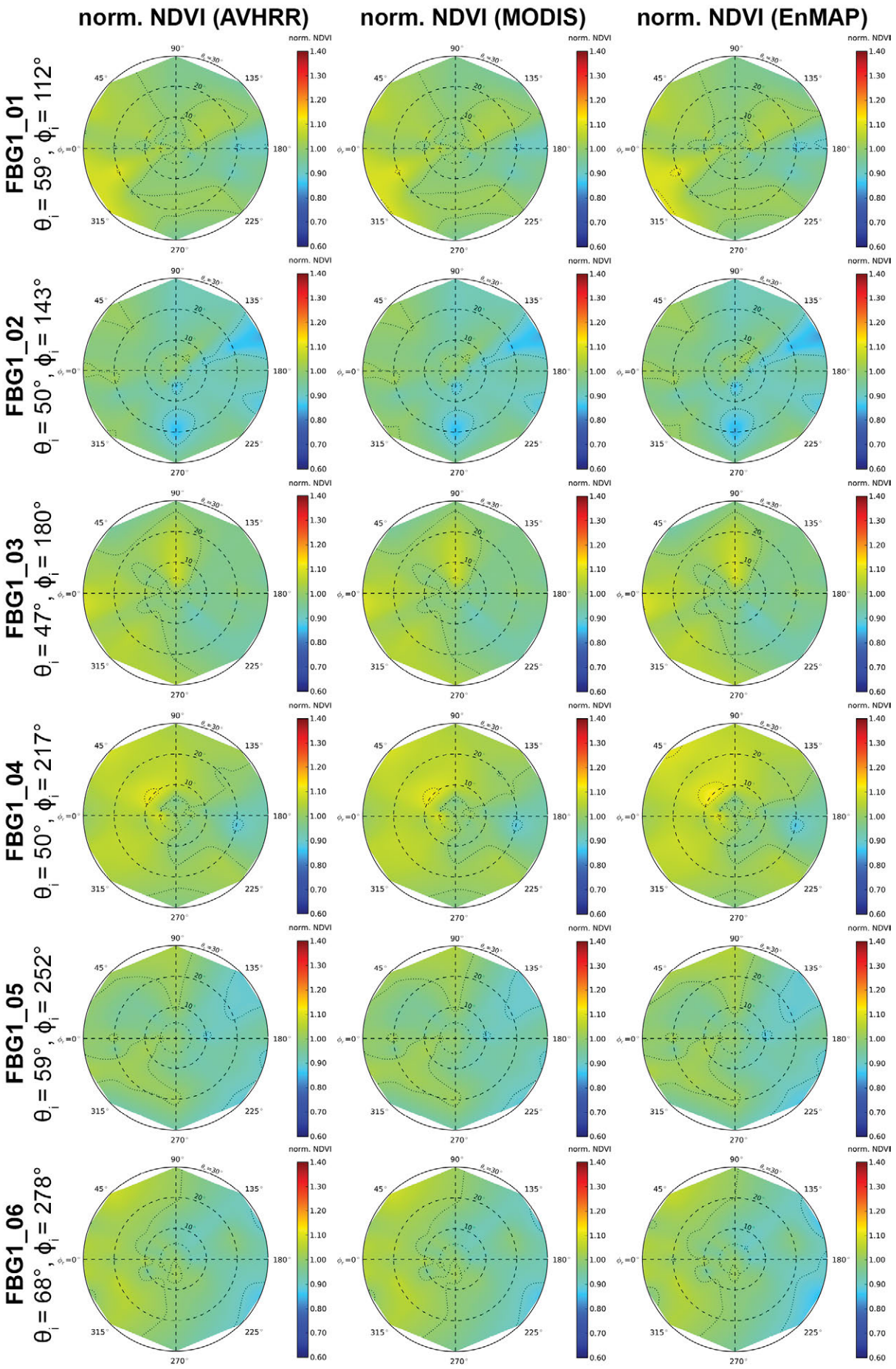

Figure C.1-18: Comparison of AVHRR, MODIS & EnMAP NDVI of the FBG1 site.

C.2 Study Site FBG2 (prostrate dwarf shrub community)

I *Location*

Name	Location	Latitude	Longitude	Altitude
FBG2	Franklin Bluffs, Arctic North Slope, Alaska, United States of America	69.67443°	-148.720725°	122 m

At an average elevation of 90 m, Franklin Bluffs is located in Subzone D about 1 km west of the Dalton Highway across from the pipeline access road APL/AMS 130 near green mile marker 375. This access road provides parking at the site. Three 10 x 10 m grids, designated dry, mesic, and wet, have been established at this location in 2002. The goniometer measurements have been carried out next to the moist / zonal site (FB_m/z). [*Barreda et al.*, 2006]

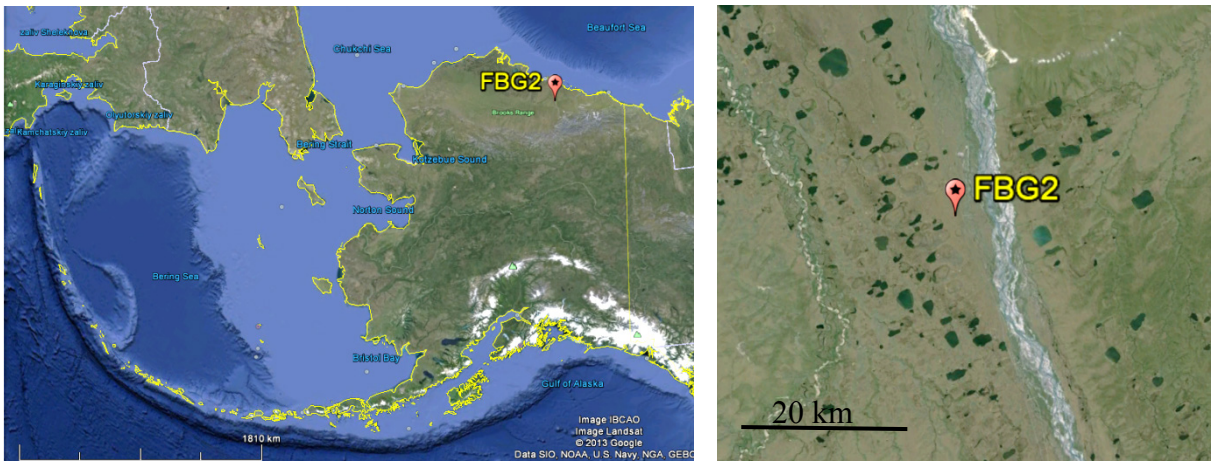

Figure C.2-1: Location of study site FBG2 in Alaska, USA. *Source:* Google Earth, 2013

Figure C.2-2: Aerial photo of a 10 x 10 m zonal grid at the Franklin Bluffs study location near the FBG2 site. *Source:* [*Barreda et al.*, 2006]

II *Main Vegetation Description*

The vegetation at the mesic Franklin Bluffs study location corresponds to the zonal vegetation in subzone D. The zonal plant community of bioclimate subzone D in northern Alaska is *Dryado integrifoliae-Caricetum bigelowii* [*Walker et al.*, 2005], also called moist non-acidic tundra (MNT), or 'nontussock sedge, dwarf-shrub, moss tundra' [*Walker et al.*, 2005]. It occurs on circumneutral to basic soils in association with silty loess that is blown from the major rivers in the eastern part of the Arctic Coastal Plain. The average soil pH of this plant community at Franklin Bluffs is 7.9; the average volumetric soil moisture of the top mineral horizon is 45 %, and average depth of thaw by late summer is 40 cm [*Kade et al.*, 2005]. The dominant plants in MNT are sedges (*Carex bigelowii, Eriophorum angustifolium* ssp. *triste, C. membranacea, C. scirpoidea, E. vaginatum*), prostrate and hemi-prostrate evergreen dwarf shrubs (*Dryas integrifolia, Cassiope tetragona*), prostrate dwarf deciduous shrubs (*Salix arctica, S. reticulata, Arctous rubra*), scattered erect dwarf deciduous shrubs (*Salix lanata, S. glauca*), several forbs (*Papaver macounii, Pedicularis lanata, Saussurea angustifolia, Senecio atropurpureus, Pedicularis capitata, Polygonum viviparum, Cardamine hyperborea, Astragalus umbellatus*), mosses *(Tomentypnum nitens, Hylocomium splendens, Aulacomnium turgidum, Rhytidium rugosum, Hypnum bambergeri, Distichium capillaceum, Ditrichum flexicaule*), and lichens (*Thamnolia subuliformis*, *Cetraria* spp.).

An important component of the MNT is the abundant nonsorted circles, also called frost boils, which are small patterned ground features caused by soil frost heave [*Walker et al.*, 2008; *Washburn*, 1980]. These features cover large parts of most MNT surfaces. The 10 x 10 m zonal grid at Franklin Bluffs has about 30 % cover of nonsorted circles. These features have drier plant communities than the mesic zonal plant communities between the circles, with high cover of lichens and bare soil.

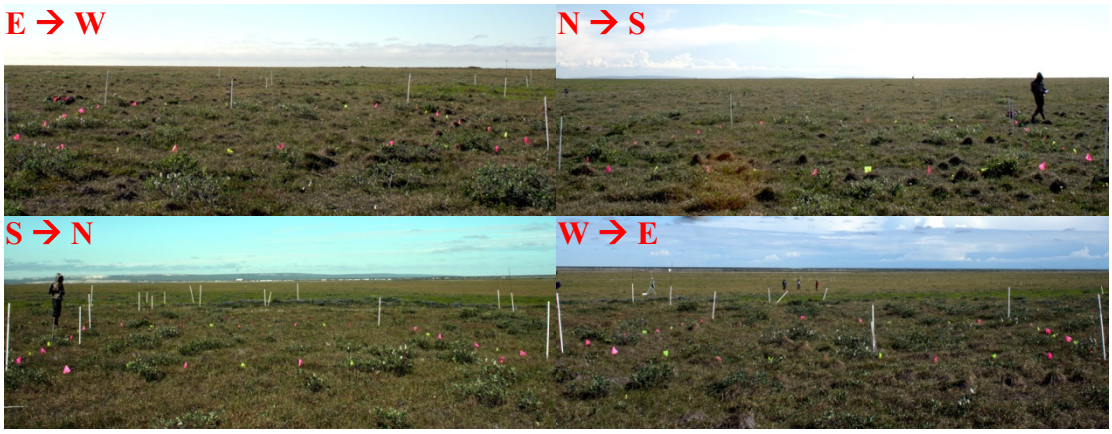

Figure C.2-3: Overview images of MNT tundra at the mesic Franklin Bluffs study location near the FBG2 site. *Source:* [*Buchhorn and Schwieder*, 2012]

III *Vegetation Description of the FBG2 Site*

The focus of the measurements at this goniometer site has been prostrate dwarf deciduous shrubs (Salix). The 1 x 1 m plot is homogeneously covered mainly with *Salix*, but with forbs, mosses and lichens in the understory.

Figure C.2-4: Overview images of the FBG2 vegetation from cardinal directions.

Figure C.2-5: Nadir image of the FBG2 vegetation (prostrate dwarf shrub).

IV *Overview of the Spectro-Goniometer Measurements*

Table C.2-1: Overview of the spectro-goniometer measurements at the FBG2 study site.

Name	Day	Starting Time	Duration	SAA	SZA	Sky
FBG2_01	2012-07-09	09:39:42	18 min	107°	60°	cirrostratus
FBG2_02	2012-07-09	12:04:07	19 min	146°	50°	cirrostratus
FBG2_03	2012-07-09	13:48:12	25 min	180°	47°	cirrostratus

Table C.2-2: Spectro-directional data of the FBG2_01 spectro-goniometer measurement.

FBG2_01 (SZA = 60°; SAA = 107°)	Viewing Geometry (Viewing Zenith Angle | Viewing Azimuth Angle)																						
	0|0	5|180	5|202.5	5|225	5|270	5|315	5|337.5	5|0	5|22.5	5|45	5|90	5|135	5|157.5	10|180	10|190	10|202.5	10|225	10|270	10|315	10|337.5	10|350
HCRF EnMAP blue (479 nm)	0.0445	0.0490	0.0474	0.0433	0.0453	0.0519	0.0459	0.0542	0.0532	0.0469	0.0483	0.0475	0.0531	0.0522	0.0499	0.0542	0.0489	0.0530	0.0492	0.0441	0.0474
HCRF EnMAP green (549 nm)	0.0722	0.0780	0.0749	0.0663	0.0766	0.0772	0.0717	0.0849	0.0860	0.0802	0.0717	0.0756	0.0782	0.0856	0.0852	0.0882	0.0753	0.0856	0.0737	0.0696	0.0711
HCRF EnMAP rot (672 nm)	0.0594	0.0646	0.0634	0.0598	0.0622	0.0749	0.0680	0.0770	0.0726	0.0652	0.0707	0.0637	0.0750	0.0718	0.0644	0.0687	0.0649	0.0735	0.0731	0.0624	0.0667
HCRF EnMAP NIR (864 nm)	0.3581	0.3699	0.3562	0.3140	0.4021	0.3198	0.3370	0.3983	0.4340	0.4338	0.3185	0.3838	0.3646	0.4414	0.4463	0.4216	0.3435	0.3969	0.3194	0.3388	0.3278
ANIF EnMAP rot (672 nm)	1.0000	1.0883	1.0678	1.0065	1.0474	1.2601	1.1447	1.2956	1.2228	1.0968	1.1903	1.0731	1.2624	1.2092	1.0841	1.1568	1.0926	1.2377	1.2311	1.0511	1.1231
ANIF EnMAP NIR (864 nm)	1.0000	1.0331	0.9948	0.8770	1.1230	0.8932	0.9411	1.1123	1.2121	1.2114	0.8896	1.0719	1.0183	1.2327	1.2465	1.1775	0.9594	1.1084	0.8920	0.9463	0.9155
Rel. Blue Absorption Depth	0.3863	0.3676	0.3746	0.3422	0.4208	0.3186	0.3567	0.3578	0.3784	0.4279	0.3120	0.3609	0.2964	0.3937	0.4298	0.3935	0.3382	0.3909	0.3255	0.3566	0.3161
Rel. Red Absorption Depth	1.9398	1.8290	1.7530	1.5960	2.0927	1.2274	1.5040	1.5984	1.9462	2.1948	1.3546	1.9277	1.5035	2.0175	2.3211	1.9735	1.6031	1.6780	1.2698	1.6775	1.4913
NDVI (EnMAP)	0.7154	0.7025	0.6977	0.6801	0.7320	0.6207	0.6642	0.6761	0.7133	0.7388	0.6367	0.7151	0.6588	0.7201	0.7478	0.7197	0.6822	0.6874	0.6274	0.6888	0.6618
Nadir Norm. NDVI (AVHRR)	1.0000	0.9809	0.9743	0.9541	1.0268	0.8750	0.9326	0.9470	0.9991	1.0375	0.9085	1.0027	0.9279	1.0085	1.0426	1.0012	0.9492	0.9645	0.8891	0.9702	0.9338
Nadir Norm. NDVI (MODIS)	1.0000	0.9818	0.9756	0.9551	1.0266	0.8753	0.9344	0.9491	1.0008	1.0377	0.9072	1.0027	0.9282	1.0089	1.0441	1.0041	0.9518	0.9657	0.8894	0.9715	0.9356
Nadir Norm. NDVI (EnMAP)	1.0000	0.9819	0.9752	0.9506	1.0232	0.8676	0.9284	0.9451	0.9970	1.0327	0.8900	0.9996	0.9209	1.0065	1.0453	1.0060	0.9535	0.9608	0.8769	0.9628	0.9250

(cont.)

FBG2_01 (SZA = 60°; SAA = 107°)	Viewing Geometry (Viewing Zenith Angle | Viewing Azimuth Angle)																						
	10|0	10|10	10|22.5	10|45	10|90	10|135	10|157.5	10|170	20|180	20|190	20|202.5	20|225	20|270	20|315	20|337.5	20|350	20|0	20|10	20|22.5	20|45	20|90
HCRF EnMAP blue (479 nm)	0.0537	0.0517	0.0496	0.0579	0.0479	0.0519	0.0515	0.0522	0.0592	0.0534	0.0536	0.0502	0.0521	0.0544	0.0480	0.0395	0.0421	0.0459	0.0472	0.0444	0.0483
HCRF EnMAP green (549 nm)	0.0824	0.0808	0.0800	0.0964	0.0749	0.0800	0.0764	0.0814	0.0956	0.0886	0.0887	0.0806	0.0838	0.0808	0.0789	0.0656	0.0688	0.0759	0.0761	0.0718	0.0760
HCRF EnMAP rot (672 nm)	0.0764	0.0720	0.0702	0.0820	0.0685	0.0716	0.0712	0.0716	0.0810	0.0702	0.0728	0.0676	0.0709	0.0793	0.0669	0.0559	0.0596	0.0664	0.0687	0.0623	0.0689
HCRF EnMAP NIR (864 nm)	0.3705	0.3874	0.4018	0.4804	0.3526	0.3728	0.3534	0.3958	0.4469	0.4513	0.4428	0.4062	0.4024	0.3513	0.4168	0.3591	0.3674	0.3847	0.3823	0.3703	0.3730
ANIF EnMAP rot (672 nm)	1.2863	1.2119	1.1822	1.3797	1.1525	1.2053	1.1989	1.2055	1.3636	1.1810	1.2261	1.1384	1.1940	1.3352	1.1264	0.9411	1.0034	1.1181	1.1565	1.0489	1.1600
ANIF EnMAP NIR (864 nm)	1.0348	1.0818	1.1222	1.3417	0.9848	1.0412	0.9871	1.1053	1.2482	1.2605	1.2366	1.1343	1.1237	0.9811	1.1642	1.0030	1.0262	1.0743	1.0677	1.0341	1.0417
Rel. Blue Absorption Depth	0.3412	0.3475	0.3754	0.4128	0.3474	0.3387	0.3018	0.3448	0.3840	0.3995	0.3959	0.3688	0.3735	0.3188	0.3871	0.3941	0.3810	0.3983	0.3819	0.3757	0.3541
Rel. Red Absorption Depth	1.4890	1.6881	1.8284	1.9178	1.6076	1.6041	1.5043	1.7458	1.7783	2.1173	2.0016	1.9109	1.7972	1.3289	2.0240	2.0757	1.9889	1.8703	1.7828	1.8999	1.7270
NDVI (EnMAP)	0.6581	0.6865	0.7024	0.7085	0.6748	0.6778	0.6646	0.6936	0.6931	0.7309	0.7175	0.7145	0.7003	0.6316	0.7233	0.7306	0.7208	0.7055	0.6953	0.7119	0.6881
Nadir Norm. NDVI (AVHRR)	0.9250	0.9650	0.9911	0.9980	0.9536	0.9500	0.9344	0.9689	0.9709	1.0209	1.0017	1.0010	0.9827	0.8989	1.0186	1.0338	1.0215	0.9992	0.9866	1.0061	0.9795
Nadir Norm. NDVI (MODIS)	0.9272	0.9665	0.9923	0.9993	0.9541	0.9507	0.9352	0.9701	0.9726	1.0225	1.0035	1.0018	0.9830	0.8997	1.0199	1.0336	1.0217	0.9997	0.9875	1.0070	0.9806
Nadir Norm. NDVI (EnMAP)	0.9198	0.9597	0.9819	0.9904	0.9433	0.9474	0.9289	0.9695	0.9688	1.0217	1.0029	0.9988	0.9789	0.8829	1.0111	1.0213	1.0076	0.9862	0.9720	0.9951	0.9618

(cont.)

FBG2_01 (SZA = 60°; SAA = 107°)	Viewing Geometry (Viewing Zenith Angle | Viewing Azimuth Angle)																						
	20|135	20|157.5	20|170	30|180	30|190	30|202.5	30|225	30|270	30|315	30|337.5	30|350	30|0	30|10	30|22.5	30|45	30|90	30|135	30|157.5	30|170		
HCRF EnMAP blue (479 nm)	0.0581	0.0616	0.0635	0.0861	0.0840	0.0717	0.0536	0.0482	0.0477	0.0439	0.0462	0.0425	0.0449	0.0443	0.0419	0.0507	0.0683	0.0745	0.0830				
HCRF EnMAP green (549 nm)	0.0915	0.0969	0.1000	0.1341	0.1328	0.1169	0.0882	0.0804	0.0743	0.0769	0.0771	0.0744	0.0719	0.0682	0.0665	0.0769	0.1105	0.1226	0.1323				
HCRF EnMAP rot (672 nm)	0.0781	0.0803	0.0900	0.1127	0.1079	0.0921	0.0726	0.0636	0.0674	0.0594	0.0643	0.0625	0.0652	0.0635	0.0596	0.0726	0.0907	0.0974	0.1069				
HCRF EnMAP NIR (864 nm)	0.4364	0.4251	0.4521	0.5424	0.5276	0.5231	0.4315	0.4191	0.3626	0.4291	0.4073	0.4002	0.3530	0.3329	0.3258	0.3385	0.5139	0.5535	0.5553				
ANIF EnMAP rot (672 nm)	1.3143	1.3520	1.5148	1.8964	1.8171	1.5498	1.2222	1.0709	1.1351	1.0000	1.0829	1.0524	1.0970	1.0691	1.0040	1.2219	1.5270	1.6393	1.7989				
ANIF EnMAP NIR (864 nm)	1.2189	1.1871	1.2625	1.5148	1.4735	1.4609	1.2050	1.1706	1.0126	1.1983	1.1375	1.1177	0.9858	0.9298	0.9098	0.9454	1.4352	1.5459	1.5510				
Rel. Blue Absorption Depth	0.3629	0.3633	0.3687	0.3597	0.3710	0.3909	0.3944	0.4056	0.3500	0.4422	0.4039	0.4467	0.3639	0.3366	0.3557	0.3272	0.3910	0.4062	0.3776				
Rel. Red Absorption Depth	1.7642	1.6579	1.5656	1.5001	1.5439	1.8685	1.9617	2.1701	1.6601	2.4346	2.0707	2.1018	1.7061	1.6288	1.6871	1.4150	1.8434	1.8489	1.6399				
NDVI (EnMAP)	0.6985	0.6822	0.6680	0.6560	0.6603	0.7007	0.7119	0.7364	0.6864	0.7568	0.7272	0.7298	0.6883	0.6796	0.6905	0.6469	0.6999	0.7008	0.6772				
Nadir Norm. NDVI (AVHRR)	0.9695	0.9472	0.9422	0.8993	0.9063	0.9670	0.9957	1.0328	0.9697	1.0638	1.0260	1.0324	0.9759	0.9677	0.9789	0.9134	0.9784	0.9658	0.9283				
Nadir Norm. NDVI (MODIS)	0.9726	0.9517	0.9440	0.9051	0.9130	0.9714	0.9978	1.0340	0.9706	1.0654	1.0273	1.0333	0.9774	0.9689	0.9797	0.9165	0.9825	0.9711	0.9339				
Nadir Norm. NDVI (EnMAP)	0.9736	0.9535	0.9337	0.9170	0.9230	0.9794	0.9951	1.0294	0.9594	1.0578	1.0165	1.0201	0.9621	0.9500	0.9652	0.9042	0.9784	0.9796	0.9467				

Table C.2-3: Spectro-directional data of the FBG2_02 spectro-goniometer measurement.

FBG2_02 (SZA = 50°; SAA = 146°)	Viewing Geometry (Viewing Zenith Angle | Viewing Azimuth Angle)																							
	0|0	5|180	5|202.5	5|225	5|270	5|315	5|337.5	5|0	5|22.5	5|45	5|90	5|135	5|157.5	10|180	10|202.5	10|225	10|270	10|315	10|337.5	10|350
HCRF EnMAP blue (479 nm)	0.0417	0.0500	0.0389	0.0437	0.0431	0.0440	0.0371	0.0437	0.0414	0.0445	0.0371	0.0363	0.0399	0.0513	0.0436	0.0471	0.0422	0.0438	0.0381	0.0384
HCRF EnMAP green (549 nm)	0.0655	0.0788	0.0622	0.0705	0.0639	0.0659	0.0587	0.0688	0.0668	0.0689	0.0610	0.0545	0.0650	0.0819	0.0697	0.0754	0.0635	0.0627	0.0612	0.0613
HCRF EnMAP rot (672 nm)	0.0554	0.0632	0.0520	0.0572	0.0632	0.0633	0.0493	0.0595	0.0556	0.0573	0.0481	0.0494	0.0515	0.0652	0.0620	0.0583	0.0607	0.0628	0.0506	0.0504
HCRF EnMAP NIR (864 nm)	0.3197	0.3438	0.3017	0.3462	0.2650	0.2859	0.2815	0.3407	0.3321	0.3273	0.3102	0.2562	0.3276	0.3601	0.3320	0.3228	0.3373	0.2661	0.2594	0.3147	0.3211
ANIF EnMAP rot (672 nm)	1.0000	1.1408	0.9379	1.0319	1.1400	1.1413	0.8899	1.0740	1.0029	1.0332	0.8670	0.8904	0.9298	1.1769	1.1187	1.0525	1.1134	1.0952	1.1321	0.9123	0.9088
ANIF EnMAP NIR (864 nm)	1.0000	1.0754	0.9436	1.0830	0.8288	0.8943	0.8805	1.0657	1.0386	1.0237	0.9701	0.8014	1.0246	1.1262	1.0384	1.0096	1.0551	0.8323	0.8114	0.9844	1.0045
Rel. Blue Absorption Depth	0.3551	0.3701	0.3639	0.3747	0.3135	0.3224	0.3599	0.3508	0.3808	0.3437	0.3867	0.3140	0.3800	0.3768	0.3778	0.3652	0.3786	0.3261	0.2806	0.3741	0.3576
Rel. Red Absorption Depth	1.8552	1.7118	1.8439	1.9628	1.2223	1.3496	1.7848	1.8267	1.9373	1.8249	2.1164	1.5825	2.0630	1.7545	1.6840	1.7659	1.7375	1.2769	1.1956	1.9851	2.0754
NDVI (EnMAP)	0.7045	0.6893	0.7060	0.7164	0.6149	0.6376	0.7018	0.7025	0.7132	0.7021	0.7317	0.6769	0.7281	0.6932	0.6852	0.6938	0.6906	0.6285	0.6104	0.7231	0.7288
Nadir Norm. NDVI (AVHRR)	1.0000	0.9619	0.9987	1.0169	0.8875	0.9114	0.9909	0.9981	1.0069	0.9924	1.0282	0.9632	1.0240	0.9693	0.9675	0.9804	0.9748	0.9014	0.8760	1.0221	1.0234
Nadir Norm. NDVI (MODIS)	1.0000	0.9645	0.9981	1.0167	0.8851	0.9098	0.9923	0.9979	1.0075	0.9926	1.0292	0.9623	1.0233	0.9714	0.9688	0.9817	0.9757	0.8986	0.8750	1.0224	1.0246
Nadir Norm. NDVI (EnMAP)	1.0000	0.9785	1.0021	1.0170	0.8728	0.9051	0.9962	0.9972	1.0123	0.9967	1.0386	0.9609	1.0335	0.9840	0.9727	0.9849	0.9804	0.8921	0.8665	1.0265	1.0346

(cont.)

FBG2_02 (SZA = 50°; SAA = 146°)	Viewing Geometry (Viewing Zenith Angle | Viewing Azimuth Angle)																							
	10|0	10|10	10|22.5	10|45	10|90	10|135	10|157.5	10|170	20|180	20|190	20|202.5	20|225	20|270	20|315	20|337.5	20|350	20|0	20|10	20|22.5	20|45	20|90
HCRF EnMAP blue (479 nm)	0.0434	0.0385	0.0431	0.0357	0.0378	0.0382	0.0404	0.0507	0.0433	0.0441	0.0470	0.0455	0.0439	0.0336	0.0368	0.0379	0.0418	0.0388	0.0388	0.0331	0.0351
HCRF EnMAP green (549 nm)	0.0667	0.0619	0.0674	0.0574	0.0610	0.0574	0.0658	0.0828	0.0707	0.0742	0.0768	0.0708	0.0660	0.0562	0.0577	0.0600	0.0636	0.0588	0.0592	0.0503	0.0553
HCRF EnMAP rot (672 nm)	0.0598	0.0506	0.0550	0.0447	0.0497	0.0508	0.0522	0.0635	0.0594	0.0602	0.0605	0.0592	0.0611	0.0462	0.0495	0.0503	0.0571	0.0527	0.0512	0.0439	0.0490
HCRF EnMAP NIR (864 nm)	0.3172	0.3251	0.3240	0.2790	0.2996	0.2612	0.3338	0.3718	0.3306	0.3511	0.3503	0.3139	0.2853	0.3007	0.2878	0.3089	0.3045	0.2801	0.2755	0.2483	0.2805
ANIF EnMAP rot (672 nm)	1.0794	0.9125	0.9920	0.8067	0.8973	0.9156	0.9416	1.1456	1.0708	1.0864	1.0918	1.0676	1.1025	0.8342	0.8929	0.9067	1.0294	0.9500	0.9235	0.7928	0.8832
ANIF EnMAP NIR (864 nm)	0.9920	1.0168	1.0134	0.8726	0.9370	0.8170	1.0441	1.1631	1.0340	1.0982	1.0956	0.9819	0.8924	0.9405	0.9003	0.9660	0.9524	0.8762	0.8616	0.7768	0.8773
Rel. Blue Absorption Depth	0.3315	0.3669	0.3526	0.3737	0.3722	0.3102	0.3781	0.4009	0.3850	0.4141	0.3943	0.3475	0.3226	0.4018	0.3490	0.3512	0.3222	0.3156	0.3250	0.3177	0.3570
Rel. Red Absorption Depth	1.6499	2.0691	1.9030	2.0058	1.9333	1.5717	2.0820	1.8974	1.7745	1.8717	1.8388	1.6653	1.3805	2.0988	1.8585	2.0048	1.8731	1.6507	1.6807	1.7627	1.7978
NDVI (EnMAP)	0.6826	0.7307	0.7098	0.7237	0.7152	0.6746	0.7295	0.7083	0.6955	0.7072	0.7053	0.6828	0.6472	0.7334	0.7066	0.7201	0.6844	0.6835	0.6865	0.6993	0.7028
Nadir Norm. NDVI (AVHRR)	0.9694	1.0368	1.0024	1.0191	1.0083	0.9506	1.0252	0.9883	0.9778	0.9967	0.9897	0.9621	0.9248	1.0389	0.9985	1.0194	0.9697	0.9736	0.9747	0.9950	1.0024
Nadir Norm. NDVI (MODIS)	0.9701	1.0374	1.0039	1.0197	1.0087	0.9513	1.0244	0.9907	0.9772	0.9969	0.9919	0.9619	0.9230	1.0387	1.0003	1.0199	0.9698	0.9743	0.9754	0.9950	1.0010
Nadir Norm. NDVI (EnMAP)	0.9689	1.0372	1.0076	1.0273	1.0152	0.9576	1.0356	1.0054	0.9873	1.0038	1.0013	0.9692	0.9186	1.0411	1.0030	1.0221	0.9715	0.9703	0.9746	0.9927	0.9976

(cont.)

FBG2_02 (SZA = 50°; SAA = 146°)	Viewing Geometry (Viewing Zenith Angle | Viewing Azimuth Angle)																							
	20|135	20|157.5	20|170	30|180	30|190	30|202.5	30|225	30|270	30|315	30|337.5	30|350	30|0	30|10	30|22.5	30|45	30|90	30|135	30|157.5	30|170			
HCRF EnMAP blue (479 nm)	0.0436	0.0451	0.0419	0.0635	0.0679	0.0625	0.0470	0.0379	0.0354	0.0367	0.0310	0.0287	0.0302	0.0332	0.0328	0.0423	0.0491	0.0535	0.0624					
HCRF EnMAP green (549 nm)	0.0662	0.0711	0.0665	0.0998	0.1052	0.0992	0.0733	0.0588	0.0571	0.0538	0.0482	0.0455	0.0456	0.0509	0.0511	0.0671	0.0750	0.0863	0.0960					
HCRF EnMAP rot (672 nm)	0.0578	0.0594	0.0547	0.0814	0.0885	0.0790	0.0586	0.0504	0.0489	0.0515	0.0438	0.0393	0.0421	0.0462	0.0449	0.0551	0.0647	0.0703	0.0813					
HCRF EnMAP NIR (864 nm)	0.2766	0.3261	0.3124	0.3849	0.4021	0.3919	0.3041	0.2841	0.2886	0.2497	0.2408	0.2368	0.2175	0.2327	0.2496	0.3376	0.3366	0.3930	0.3851					
ANIF EnMAP rot (672 nm)	1.0428	1.0719	0.9862	1.4685	1.5958	1.4258	1.0574	0.9098	0.8814	0.9283	0.7907	0.7093	0.7601	0.8334	0.8099	0.9940	1.1675	1.2674	1.4666					
ANIF EnMAP NIR (864 nm)	0.8651	1.0198	0.9773	1.2039	1.2577	1.2259	0.9510	0.8887	0.9026	0.7812	0.7531	0.7405	0.6803	0.7280	0.7807	1.0559	1.0528	1.2293	1.2044					
Rel. Blue Absorption Depth	0.3198	0.3533	0.3548	0.3629	0.3540	0.3780	0.3490	0.3459	0.3780	0.2933	0.3442	0.3505	0.3153	0.3320	0.3388	0.3591	0.3259	0.3675	0.3386					
Rel. Red Absorption Depth	1.4534	1.7320	1.8176	1.4585	1.3648	1.5355	1.5722	1.7465	1.8963	1.4636	1.6961	1.8788	1.5788	1.5118	1.7130	1.9858	1.6546	1.7976	1.4722					
NDVI (EnMAP)	0.6542	0.6917	0.7021	0.6508	0.6393	0.6644	0.6767	0.6985	0.7104	0.6583	0.6920	0.7152	0.6754	0.6687	0.6951	0.7193	0.6775	0.6967	0.6513					
Nadir Norm. NDVI (AVHRR)	0.9234	0.9710	0.9821	0.9064	0.8885	0.9206	0.9393	0.9893	1.0123	0.9470	0.9901	1.0203	0.9640	0.9536	0.9934	1.0119	0.9541	0.9774	0.9116					
Nadir Norm. NDVI (MODIS)	0.9249	0.9718	0.9827	0.9115	0.8928	0.9254	0.9442	0.9898	1.0138	0.9470	0.9901	1.0194	0.9637	0.9553	0.9940	1.0139	0.9550	0.9790	0.9146					
Nadir Norm. NDVI (EnMAP)	0.9287	0.9819	0.9967	0.9239	0.9076	0.9431	0.9607	0.9915	1.0084	0.9345	0.9823	1.0152	0.9588	0.9493	0.9867	1.0211	0.9617	0.9890	0.9246					

Table C.2-4: Spectro-directional data of the FBG2_03 spectro-goniometer measurement

FBG2_03 (SZA = 47°; SAA = 180°)	Viewing Geometry (Viewing Zenith Angle | Viewing Azimuth Angle)																							
	0|0	5|180	5|202.5	5|225	5|270	5|315	5|337.5	5|0	5|22.5	5|45	5|90	5|135	5|157.5	10|180	10|190	10|202.5	10|225	10|270	10|315	10|337.5	10|350
HCRF EnMAP blue (479 nm)	0.0461	0.0493	0.0493	0.0433	0.0443	0.0472	0.0422	0.0438	0.0440	0.0458	0.0442	0.0478	0.0486	0.0501	0.0529	0.0549	0.0424	0.0429	0.0471	0.0393	0.0425
HCRF EnMAP green (549 nm)	0.0723	0.0749	0.0745	0.0644	0.0665	0.0743	0.0670	0.0681	0.0678	0.0717	0.0681	0.0740	0.0736	0.0755	0.0824	0.0825	0.0657	0.0648	0.0708	0.0628	0.0667
HCRF EnMAP rot (672 nm)	0.0620	0.0696	0.0672	0.0606	0.0627	0.0645	0.0571	0.0582	0.0617	0.0634	0.0606	0.0621	0.0679	0.0703	0.0737	0.0764	0.0603	0.0608	0.0643	0.0518	0.0557
HCRF EnMAP NIR (864 nm)	0.3600	0.3214	0.3241	0.2729	0.2892	0.3699	0.3342	0.3419	0.3152	0.3425	0.3159	0.3430	0.3208	0.3200	0.3624	0.3472	0.2975	0.2838	0.3356	0.3218	0.3379
ANIF EnMAP rot (672 nm)	1.0000	1.1222	1.0842	0.9769	1.0112	1.0404	0.9213	0.9381	0.9959	1.0233	0.9771	1.0021	1.0958	1.1347	1.1879	1.2323	0.9720	0.9806	1.0367	0.8351	0.8992
ANIF EnMAP NIR (864 nm)	1.0000	0.8927	0.9003	0.7579	0.8032	1.0274	0.9282	0.9498	0.8755	0.9513	0.8774	0.9528	0.8911	0.8887	1.0065	0.9645	0.8264	0.7882	0.9321	0.8938	0.9386
Rel. Blue Absorption Depth	0.3531	0.3368	0.3278	0.3144	0.3203	0.3528	0.3589	0.3441	0.3378	0.3534	0.3308	0.3426	0.3232	0.3241	0.3541	0.3249	0.3492	0.3190	0.3140	0.3640	0.3517
Rel. Red Absorption Depth	1.8593	1.3916	1.4657	1.3226	1.3625	1.8396	1.8819	1.8768	1.5665	1.7002	1.6028	1.7392	1.4351	1.3746	1.5195	1.3721	1.5117	1.4023	1.6246	1.9914	1.9525
NDVI (EnMAP)	0.7062	0.6441	0.6565	0.6367	0.6436	0.7030	0.7080	0.7092	0.6724	0.6874	0.6781	0.6933	0.6505	0.6395	0.6622	0.6393	0.6631	0.6471	0.6785	0.7228	0.7168
Nadir Norm. NDVI (AVHRR)	1.0000	0.9164	0.9334	0.9064	0.9141	0.9970	1.0045	1.0035	0.9575	0.9775	0.9644	0.9789	0.9255	0.9128	0.9464	0.9126	0.9504	0.9232	0.9631	1.0243	1.0174
Nadir Norm. NDVI (MODIS)	1.0000	0.9146	0.9322	0.9055	0.9140	0.9972	1.0052	1.0039	0.9564	0.9779	0.9636	0.9801	0.9242	0.9108	0.9442	0.9123	0.9496	0.9217	0.9642	1.0255	1.0175
Nadir Norm. NDVI (EnMAP)	1.0000	0.9120	0.9296	0.9016	0.9114	0.9955	1.0026	1.0044	0.9521	0.9734	0.9603	0.9818	0.9211	0.9056	0.9377	0.9053	0.9390	0.9164	0.9608	1.0236	1.0150

(cont.)

FBG2_03 (SZA = 47°; SAA = 180°)	Viewing Geometry (Viewing Zenith Angle | Viewing Azimuth Angle)																							
	10|0	10|10	10|22.5	10|45	10|90	10|135	10|157.5	10|170	20|180	20|190	20|202.5	20|225	20|270	20|315	20|337.5	20|350	20|0	20|10	20|22.5	20|45	20|90	20|135
HCRF EnMAP blue (479 nm)	0.0428	0.0410	0.0384	0.0394	0.0465	0.0499	0.0481	0.0477	0.0516	0.0530	0.0560	0.0490	0.0440	0.0437	0.0386	0.0412	0.0375	0.0377	0.0391	0.0378	0.0427	0.0579
HCRF EnMAP green (549 nm)	0.0659	0.0642	0.0598	0.0640	0.0711	0.0794	0.0734	0.0735	0.0777	0.0783	0.0872	0.0748	0.0695	0.0688	0.0601	0.0620	0.0573	0.0581	0.0606	0.0584	0.0640	0.0887
HCRF EnMAP rot (672 nm)	0.0566	0.0563	0.0529	0.0549	0.0644	0.0651	0.0659	0.0672	0.0701	0.0735	0.0753	0.0672	0.0595	0.0601	0.0523	0.0564	0.0499	0.0516	0.0536	0.0514	0.0602	0.0758
HCRF EnMAP NIR (864 nm)	0.3225	0.3230	0.3014	0.3207	0.3254	0.3806	0.3240	0.3177	0.3290	0.3150	0.3832	0.3253	0.3343	0.3495	0.2960	0.2885	0.2836	0.2861	0.3069	0.2937	0.2872	0.3796
ANIF EnMAP rot (672 nm)	0.9136	0.9080	0.8535	0.8854	1.0387	1.0506	1.0631	1.0834	1.1299	1.1854	1.2142	1.0838	0.9600	0.9700	0.8441	0.9089	0.8053	0.8315	0.8643	0.8296	0.9705	1.2222
ANIF EnMAP NIR (864 nm)	0.8959	0.8973	0.8372	0.8908	0.9037	1.0572	0.8998	0.8826	0.9138	0.8749	1.0643	0.9036	0.9286	0.9708	0.8223	0.8013	0.7878	0.7948	0.8525	0.8158	0.7977	1.0545
Rel. Blue Absorption Depth	0.3361	0.3454	0.3474	0.3851	0.3333	0.3643	0.3296	0.3390	0.3193	0.3103	0.3566	0.3306	0.3523	0.3515	0.3403	0.3153	0.3242	0.3250	0.3355	0.3305	0.3157	0.3373
Rel. Red Absorption Depth	1.7927	1.8028	1.7664	1.8399	1.5404	1.8800	1.5098	1.4380	1.4252	1.2566	1.5715	1.4601	1.7843	1.8419	1.7576	1.5421	1.7430	1.7174	1.7914	1.7877	1.4290	1.5493
NDVI (EnMAP)	0.7012	0.7032	0.7013	0.7077	0.6695	0.7077	0.6619	0.6510	0.6489	0.6216	0.6716	0.6576	0.6977	0.7064	0.6995	0.6732	0.7006	0.6947	0.7027	0.7020	0.6536	0.6672
Nadir Norm. NDVI (AVHRR)	0.9961	0.9977	1.0008	1.0067	0.9510	0.9990	0.9431	0.9277	0.9174	0.8798	0.9483	0.9310	0.9918	1.0026	0.9946	0.9601	0.9983	0.9872	0.9995	1.0002	0.9310	0.9955
Nadir Norm. NDVI (MODIS)	0.9955	0.9971	0.9997	1.0062	0.9497	0.9993	0.9419	0.9261	0.9175	0.8805	0.9494	0.9313	0.9935	1.0034	0.9957	0.9616	0.9990	0.9882	0.9994	0.9988	0.9305	0.9545
Nadir Norm. NDVI (EnMAP)	0.9930	0.9958	0.9931	1.0022	0.9481	1.0022	0.9373	0.9218	0.9189	0.8803	0.9510	0.9312	0.9881	1.0003	0.9906	0.9533	0.9922	0.9837	0.9951	0.9940	0.9255	0.9373

(cont.)

FBG2_03 (SZA = 47°; SAA = 180°)	Viewing Geometry (Viewing Zenith Angle | Viewing Azimuth Angle)																							
	20|135	20|157.5	20|170	30|180	30|190	30|202.5	30|225	30|270	30|315	30|337.5	30|350	30|0	30|10	30|22.5	30|45	30|90	30|135	30|157.5	30|170			
HCRF EnMAP blue (479 nm)	0.0579	0.0512	0.0549	0.0657	0.0651	0.0621	0.0541	0.0402	0.0367	0.0365	0.0358	0.0340	0.0322	0.0340	0.0447	0.0417	0.0541	0.0586	0.0578					
HCRF EnMAP green (549 nm)	0.0887	0.0804	0.0857	0.1005	0.0967	0.0955	0.0861	0.0651	0.0570	0.0551	0.0540	0.0535	0.0507	0.0524	0.0709	0.0657	0.0837	0.0875	0.0869					
HCRF EnMAP rot (672 nm)	0.0758	0.0650	0.0730	0.0875	0.0877	0.0846	0.0738	0.0542	0.0507	0.0503	0.0494	0.0469	0.0433	0.0458	0.0571	0.0573	0.0725	0.0779	0.0786					
HCRF EnMAP NIR (864 nm)	0.3796	0.3676	0.3758	0.3762	0.3538	0.3786	0.3801	0.3426	0.2799	0.2550	0.2549	0.2737	0.2698	0.2703	0.3637	0.3379	0.3603	0.3510	0.3385					
ANIF EnMAP rot (672 nm)	1.2222	1.0486	1.1775	1.4113	1.4153	1.3649	1.1907	0.8740	0.8185	0.8105	0.7964	0.7559	0.6979	0.7390	0.9217	0.9240	1.1691	1.2559	1.2684					
ANIF EnMAP NIR (864 nm)	1.0545	1.0211	1.0438	1.0451	0.9828	1.0516	1.0559	0.9515	0.7775	0.7083	0.7081	0.7602	0.7495	0.7507	1.0104	0.9386	1.0007	0.9751	0.9403					
Rel. Blue Absorption Depth	0.3373	0.3546	0.3479	0.3465	0.3208	0.3536	0.3670	0.3789	0.3457	0.3163	0.3148	0.3496	0.3419	0.3249	0.3557	0.3513	0.3459	0.3085	0.3264					
Rel. Red Absorption Depth	1.5493	1.7696	1.5943	1.2613	1.1640	1.3205	1.6007	1.9992	1.7132	1.5245	1.5249	1.7912	1.9593	1.8429	2.0462	1.8956	1.5331	1.3449	1.2521					
NDVI (EnMAP)	0.6672	0.6995	0.6746	0.6226	0.6026	0.6346	0.6747	0.7269	0.6931	0.6708	0.6755	0.7076	0.7236	0.7101	0.7285	0.7101	0.6650	0.6369	0.6230					
Nadir Norm. NDVI (AVHRR)	0.9374	0.9800	0.9503	0.8714	0.8466	0.8975	0.9531	1.0306	0.9933	0.9555	0.9631	1.0112	1.0290	1.0123	1.0280	1.0145	0.9335	0.8940	0.8736					
Nadir Norm. NDVI (MODIS)	0.9390	0.9820	0.9510	0.8740	0.8478	0.8979	0.9532	1.0315	0.9930	0.9565	0.9652	1.0122	1.0296	1.0119	1.0299	1.0133	0.9365	0.8967	0.8750					
Nadir Norm. NDVI (EnMAP)	0.9448	0.9905	0.9554	0.8817	0.8533	0.8987	0.9555	1.0293	0.9815	0.9498	0.9565	1.0020	1.0247	1.0055	1.0316	1.0056	0.9417	0.9019	0.8822					

V *Main Spectral Characteristics*

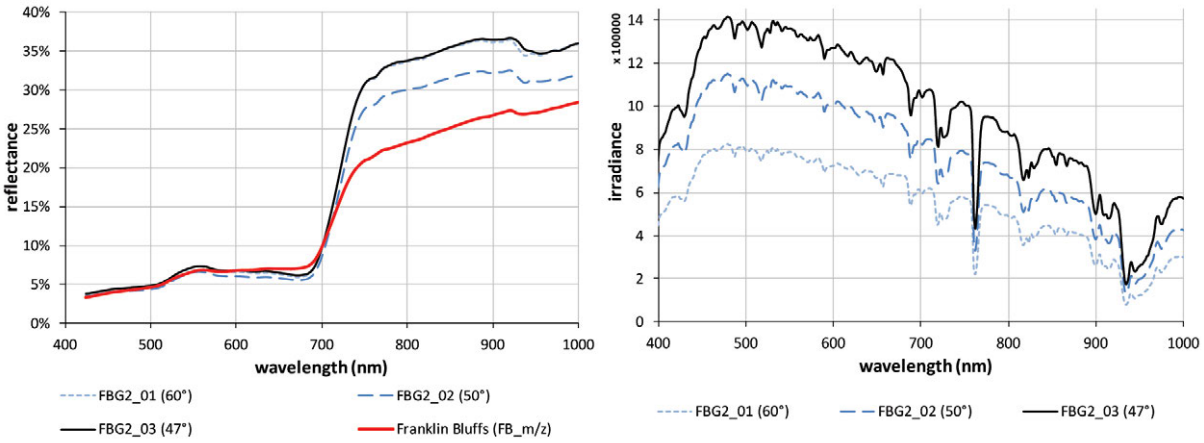

Figure C.2-6: Nadir reflectances and irradiance profiles of the FBG2 site at different sun zenith angles. Left: Comparison of the nadir reflectance signatures with the average zonal vegetation (MNT). Right: Comparison of the total irradiance profiles.

VI *HCRF Visualization*

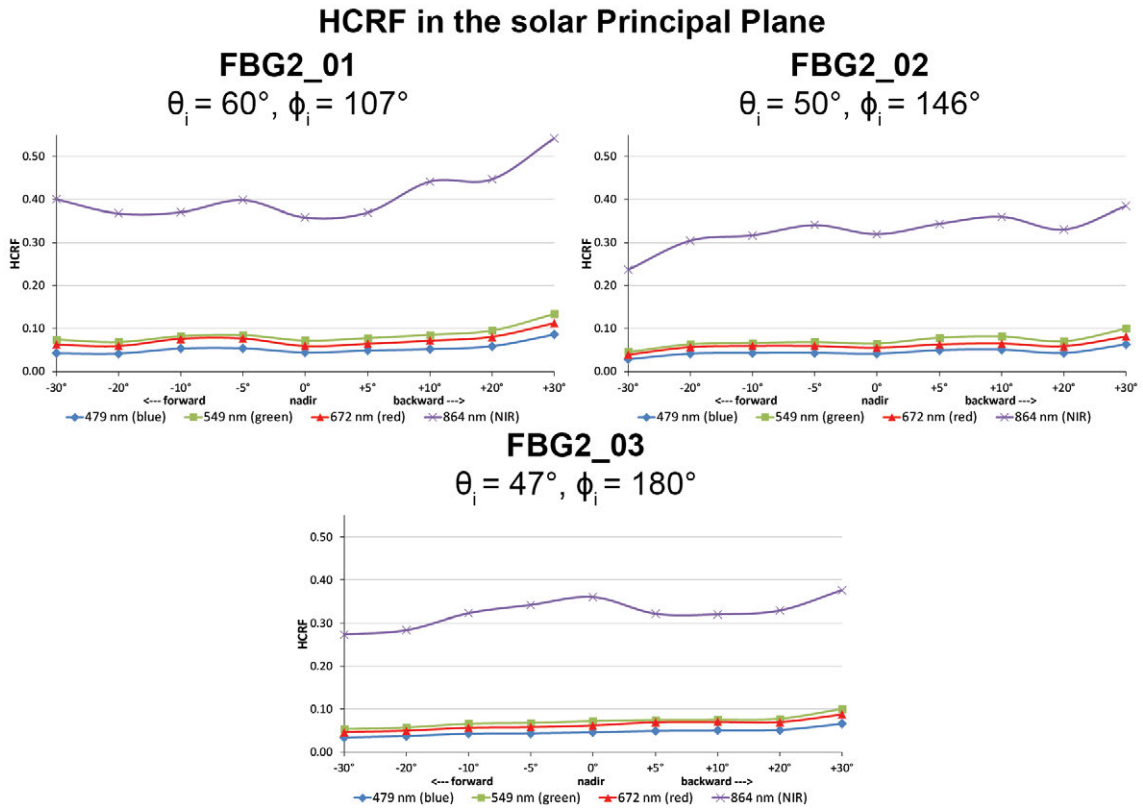

Figure C.2-7: Comparison of the HCRF values at 479 nm (blue), 549 nm (green), 672 nm (red), and 864 nm (NIR) in the solar principal plane of the FBG2 site at different sun zenith angles.

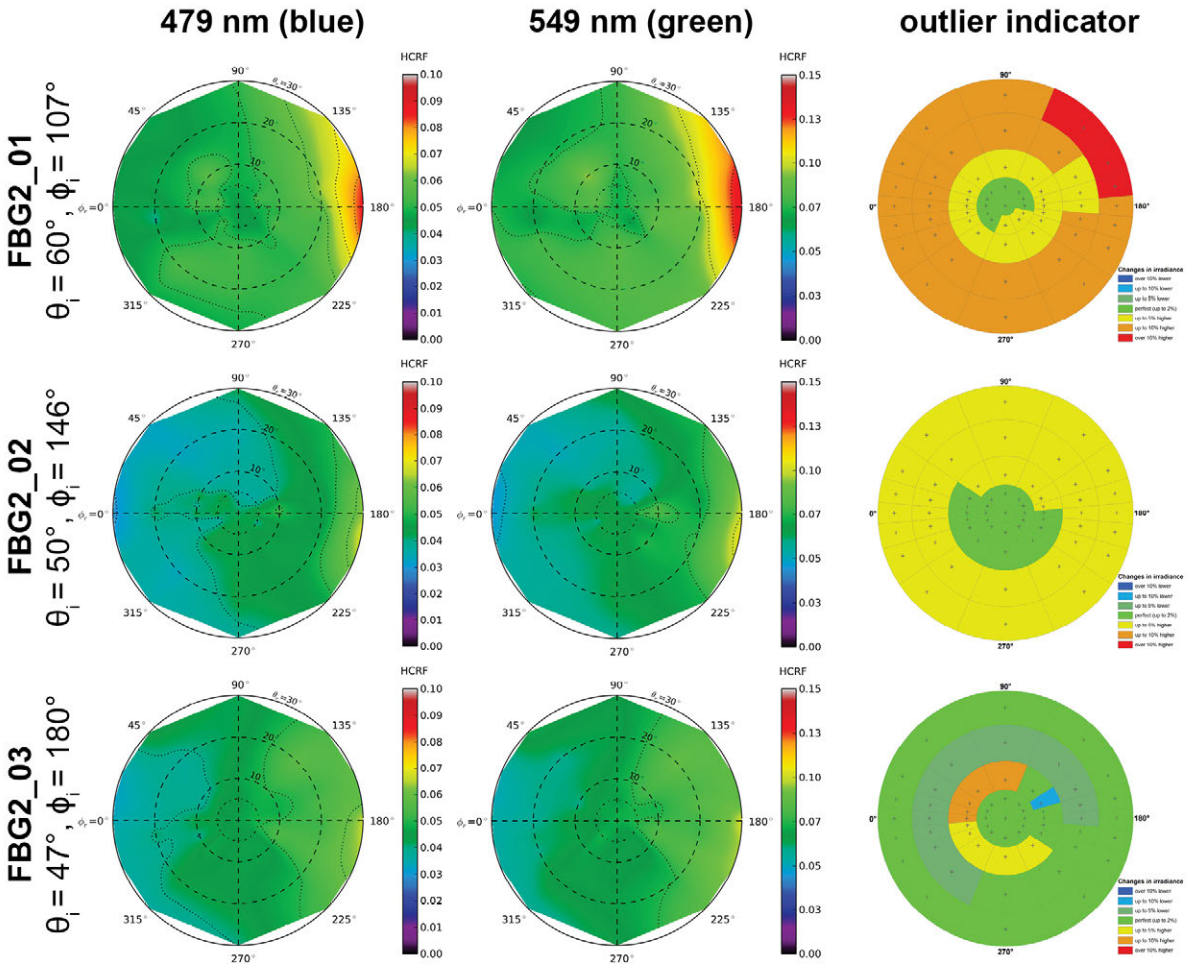

Figure C.2-8: HCRF visualization at 479 nm and 549 nm of the FBG2 site.

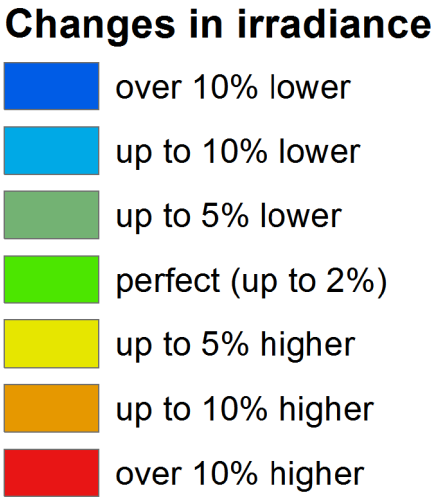

Figure C.2-9: Legend of the outlier indicator graphics shown in Figure C.2-8, C.2-10, and C.2-13

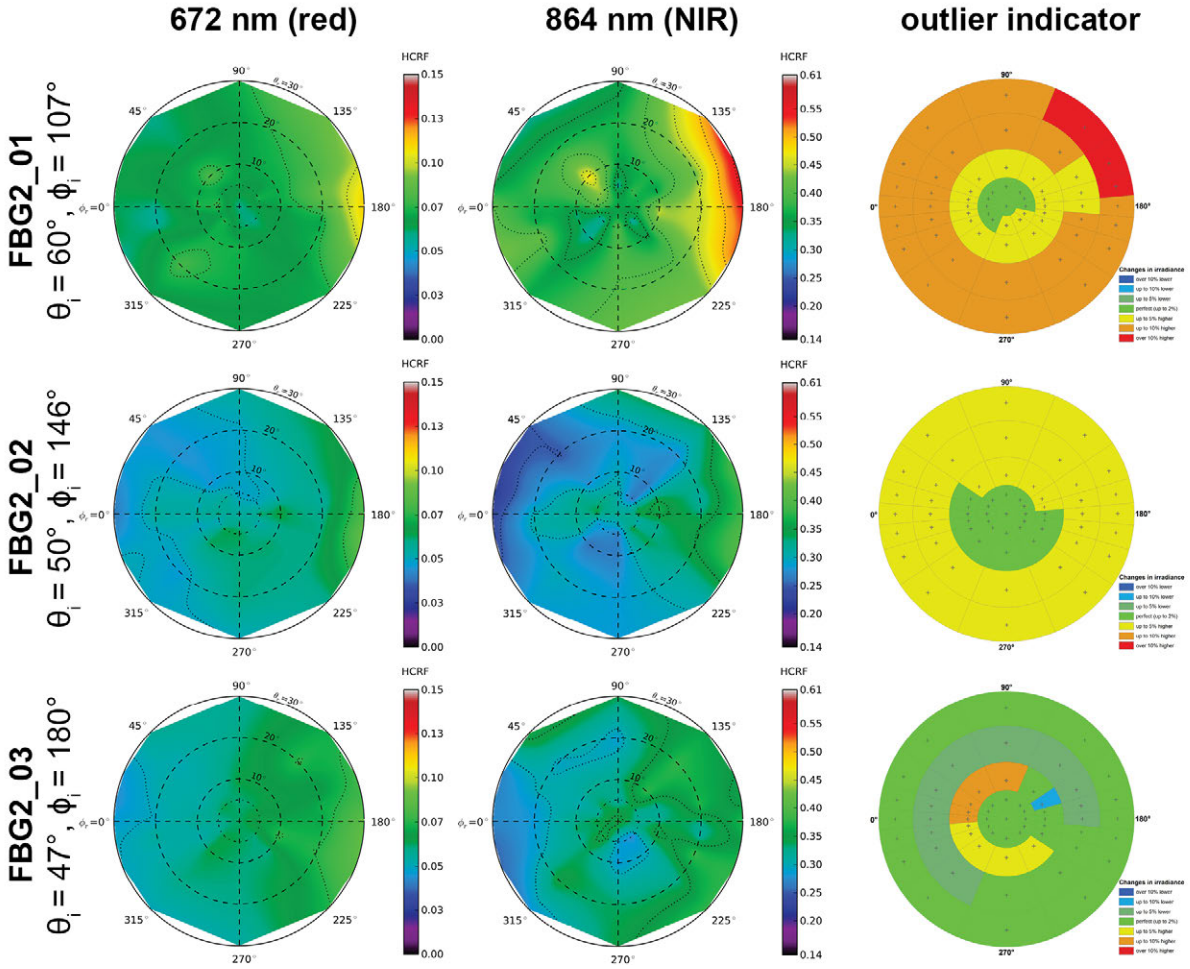

Figure C.2-10: HCRF visualization at 672 nm and 864 nm of the FBG2 site.

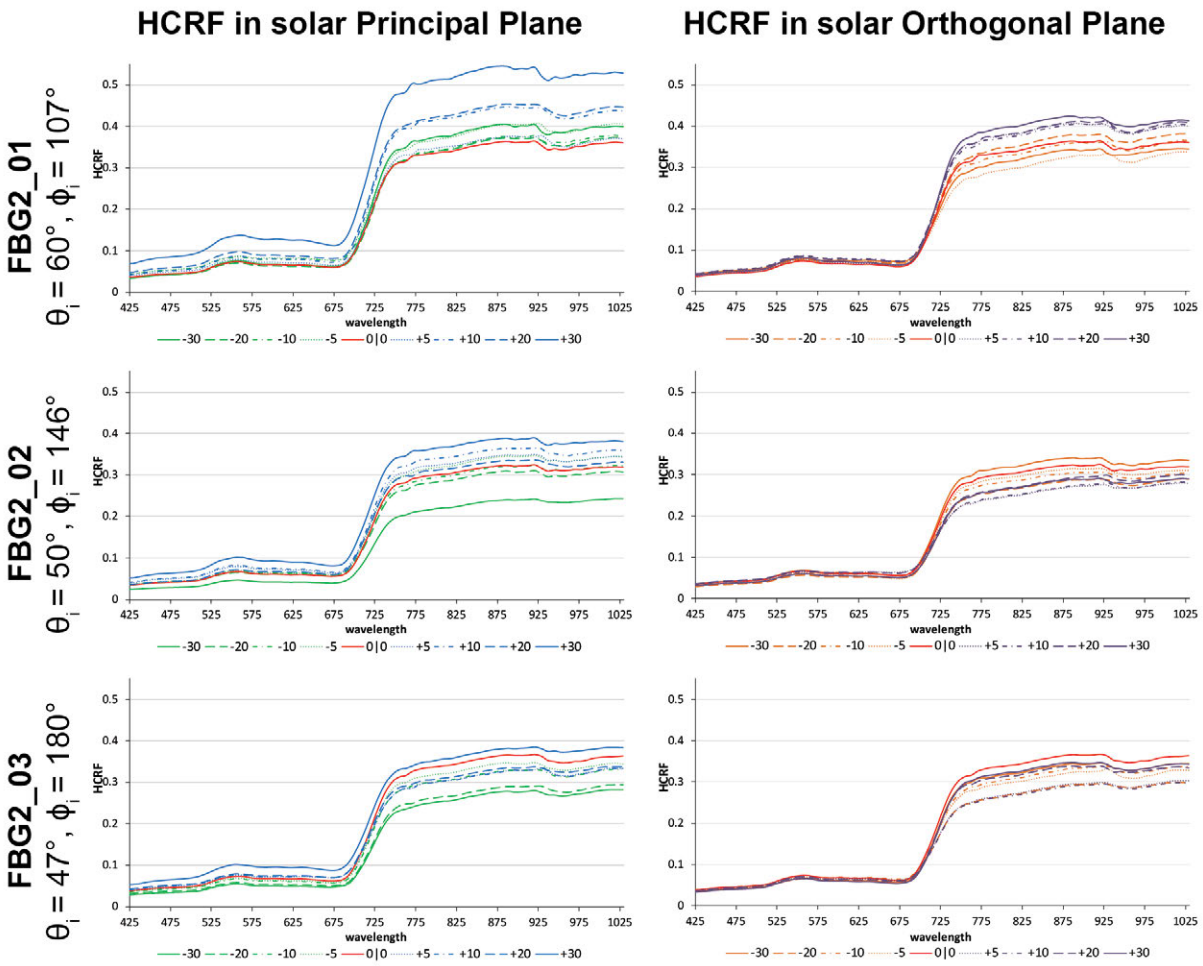

Figure C.2-11: HCRF visualization in principal & orthogonal plane of the FBG2 site.

VII *ANIF Visualization*

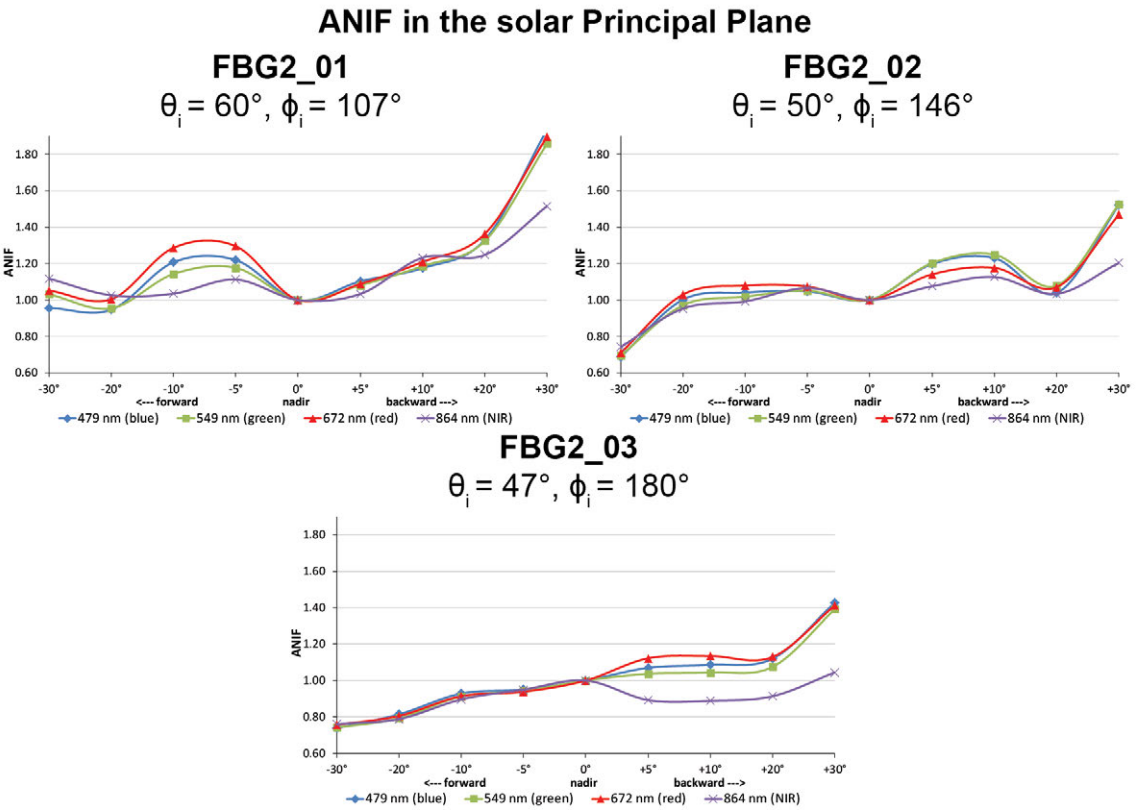

Figure C.2-12: Comparison of the ANIF values at 479 nm (blue), 549 nm (green), 672 nm (red), and 864 nm (NIR) in the solar principal plane of the FBG2 site at different sun zenith angles.

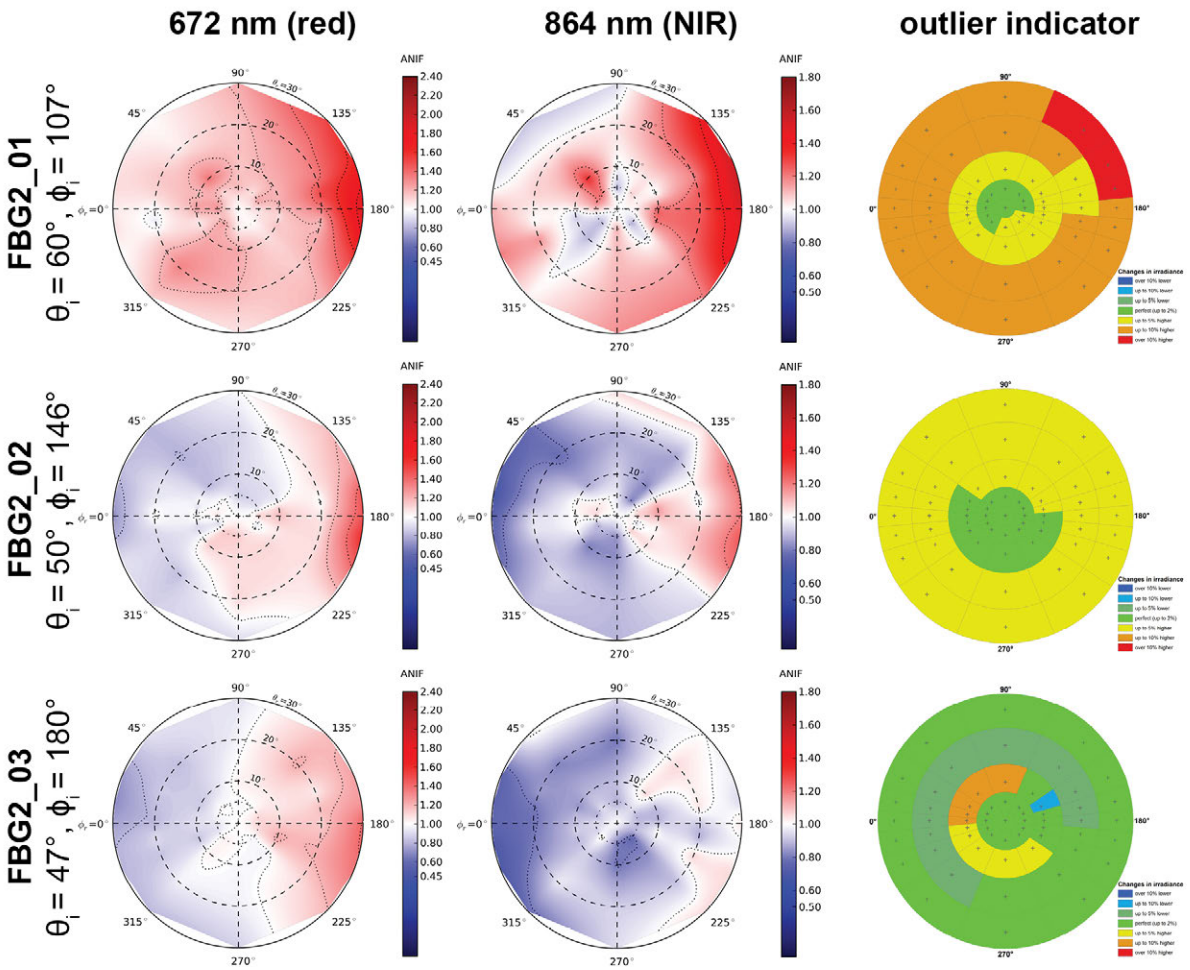

Figure C.2-13: ANIF visualization at 672 nm and 864 nm of the FBG2 site.

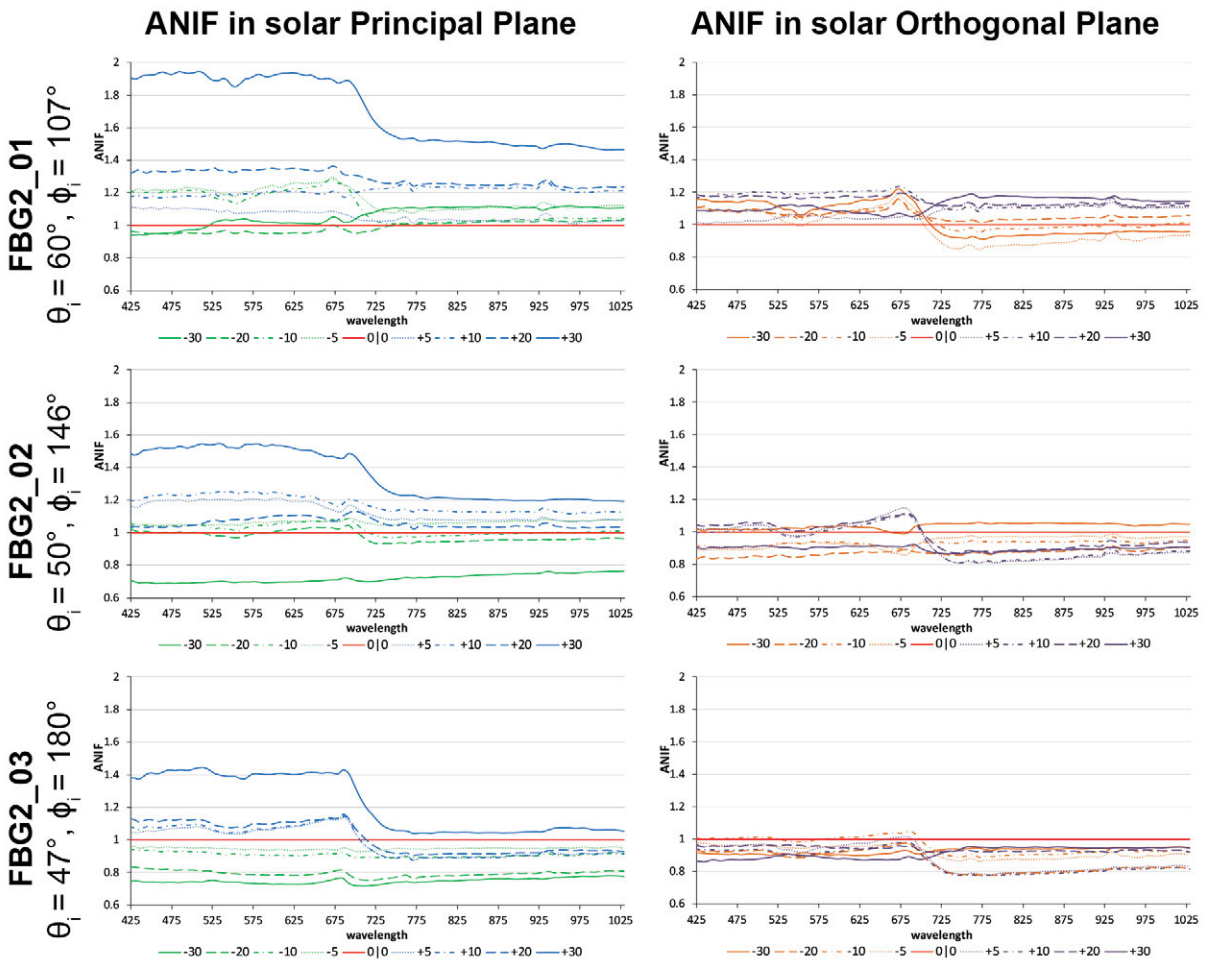

Figure C.2-14: ANIF visualization in principal & orthogonal plane of the FBG2 site.

VIII *ANIX Visualization*

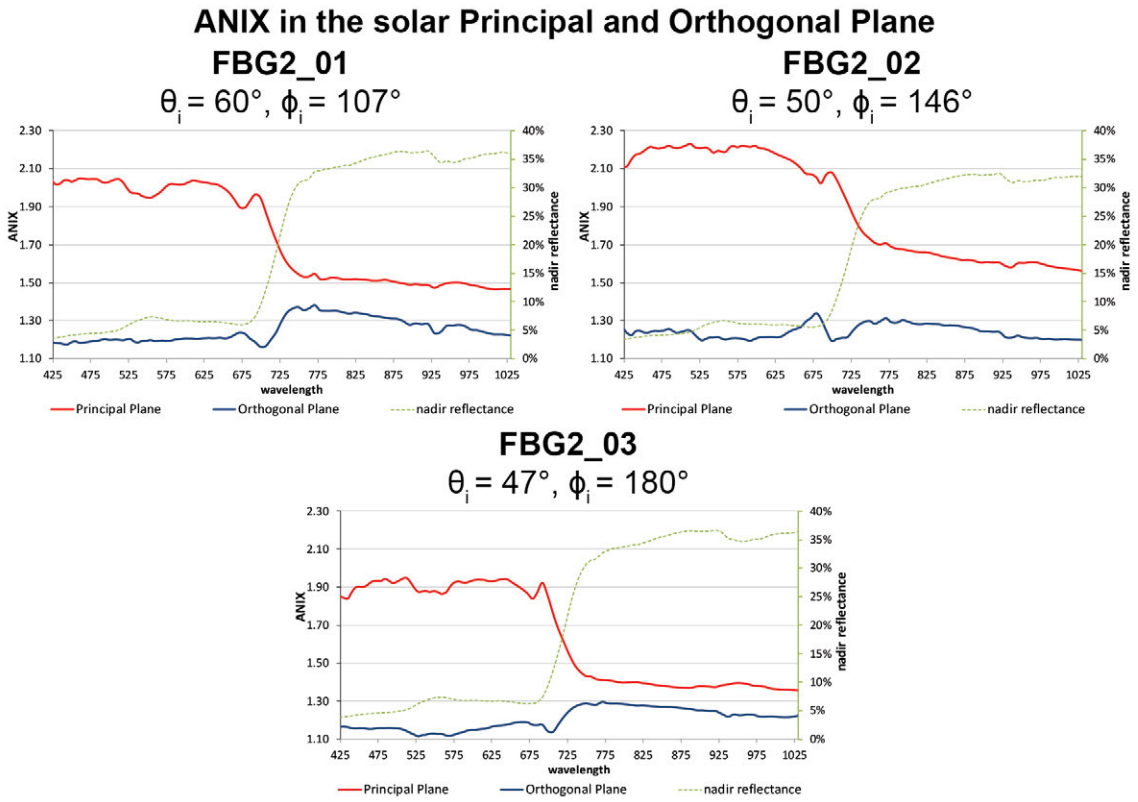

Figure C.2-15: Comparison of the ANIX in the solar principal and orthogonal plane with the nadir reflectance of the FBG2 site at different sun zenith angles.

IX *NDVI and Relative Absorption Depth Visualization*

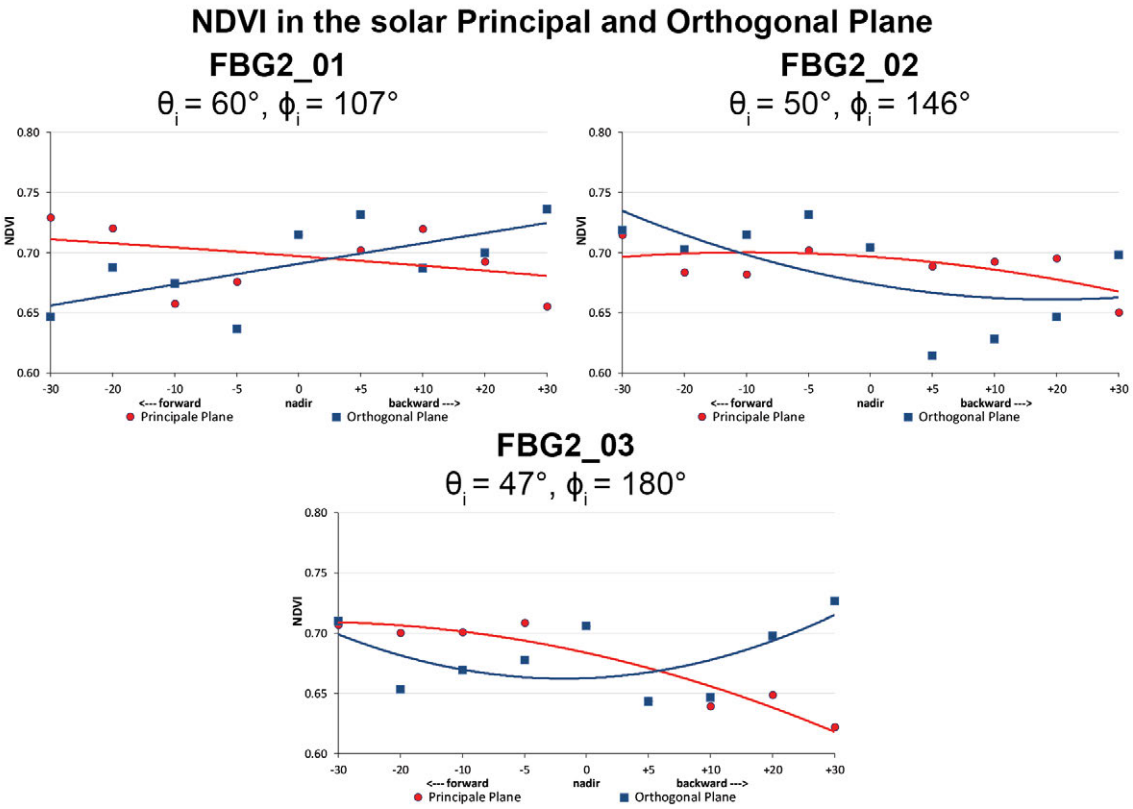

Figure C.2-16: Comparison of the NDVI in the solar principal and orthogonal plane of the FBG2 site at different sun zenith angles.

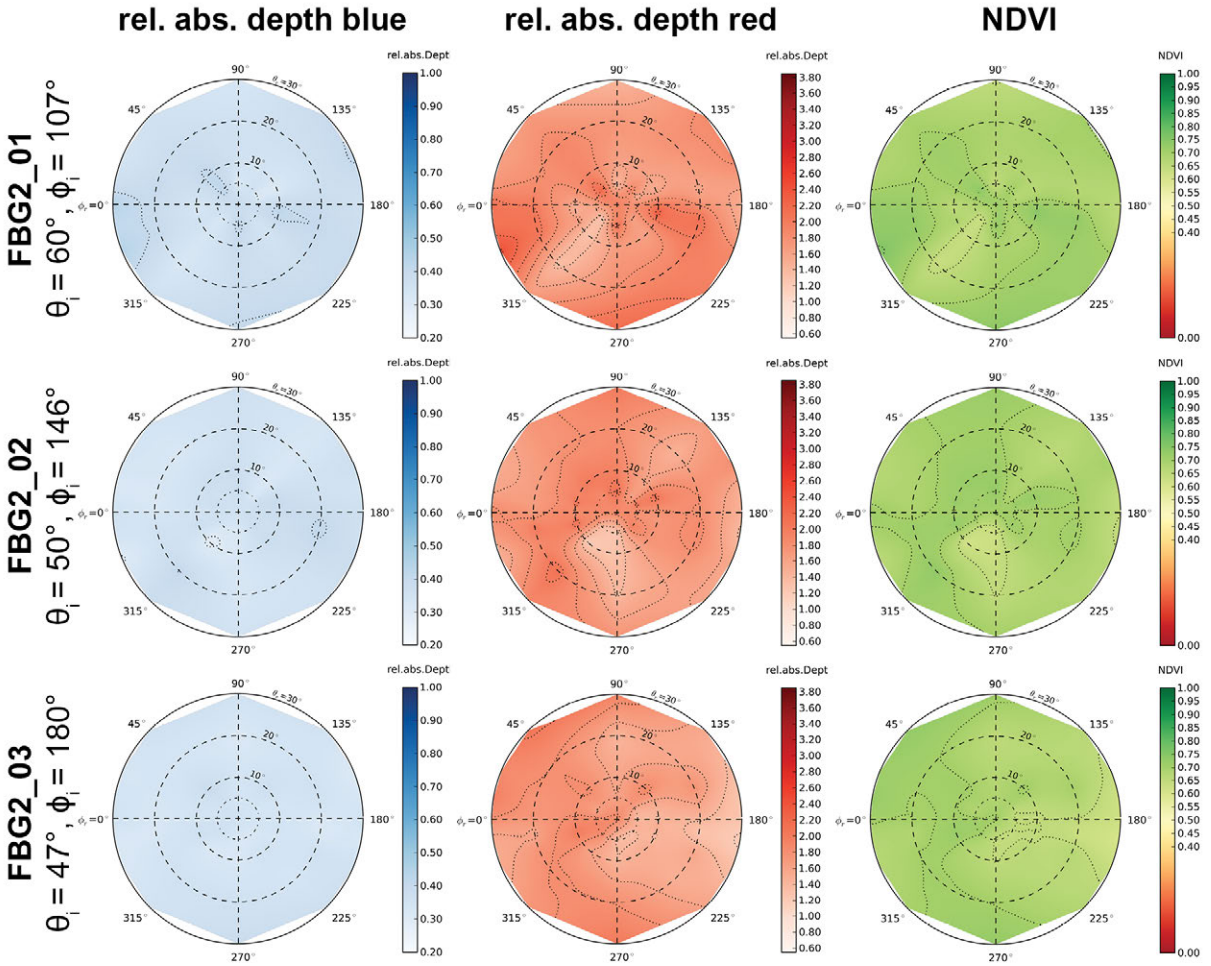

Figure C.2-17: Visualization of relative absorption depth & NDVI of the FBG2 site.

X *NDVI Comparison of Different Sensors*

Table C.2-5: Center wavelengths and band widths of the broadband and narrowband NDVIs, based on the spectral response curves of the AVHRR, MODIS and EnMAP sensors.

NDVI	Sensor	Sensor band	Center wavelength (nm)	band width (nm)
$NDVI_{AVHRR}$ [broadband]	AVHRR/3	red: band 1 NIR: band 2	630 865	100 275
$NDVI_{MODIS}$ [broadband]	MODIS	red: band 1 NIR: band 2	645 859	50 35
$NDVI_{EnMAP}$ [narrowband]	EnMAP	red: band 47 NIR: band 73	672 864	6.5 8

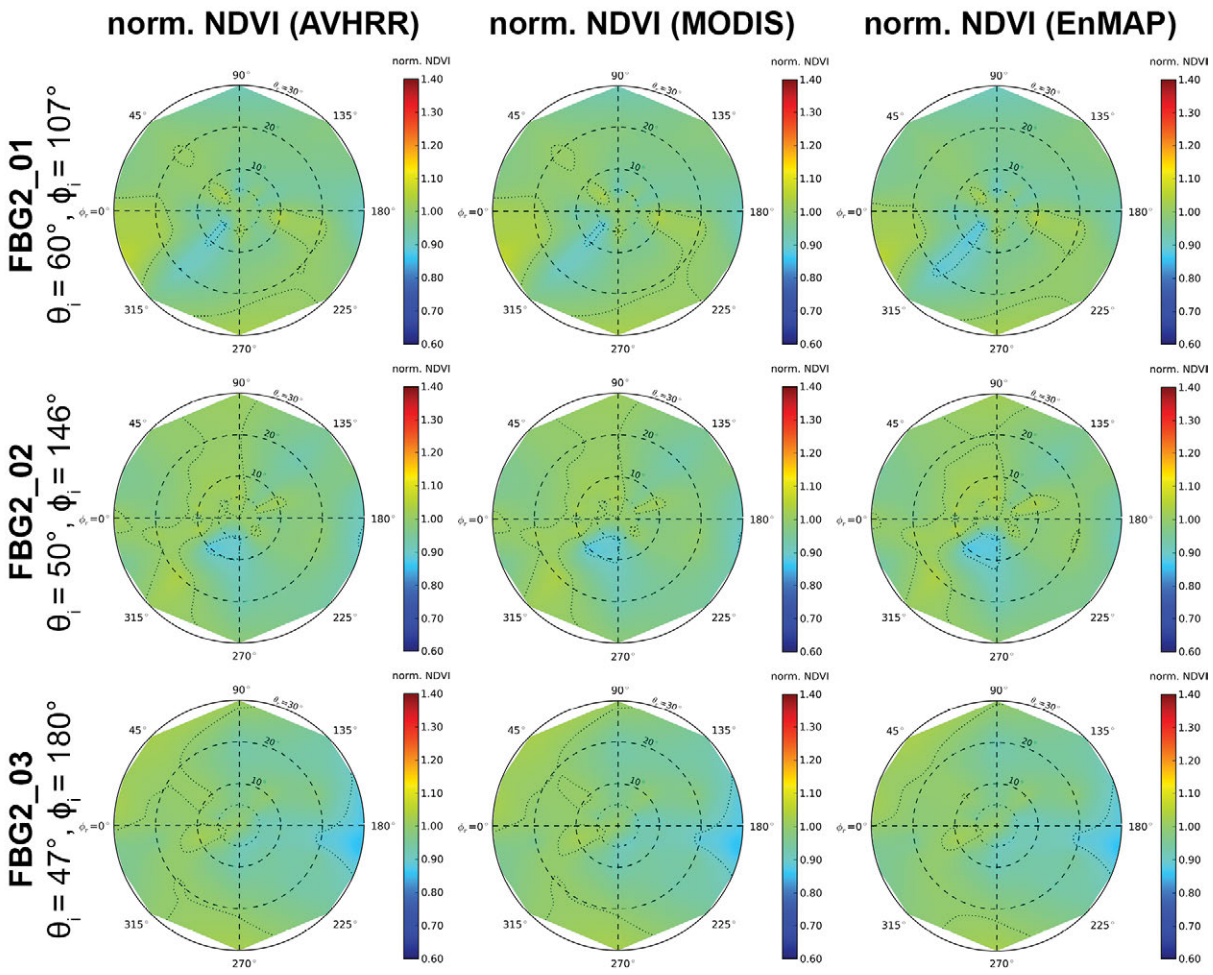

Figure C.2-18: Comparison of AVHRR, MODIS & EnMAP NDVI of the FBG2 site.

C.3 Study Site FBG3 (frost boil community)

I *Location*

Name	Location	Latitude	Longitude	Altitude
FBG3	Franklin Bluffs, Arctic North Slope, Alaska, United States of America	69.67445°	-148.720875°	123 m

At an average elevation of 90 m, Franklin Bluffs is located in Subzone D about 1 km west of the Dalton Highway across from the pipeline access road APL/AMS 130 near green mile marker 375. This access road provides parking at the site. Three 10 x 10 m grids, designated dry, mesic, and wet, have been established at this location in 2002. The goniometer measurements have been carried out next to the moist / zonal site (FB_m/z). [*Barreda et al.*, 2006]

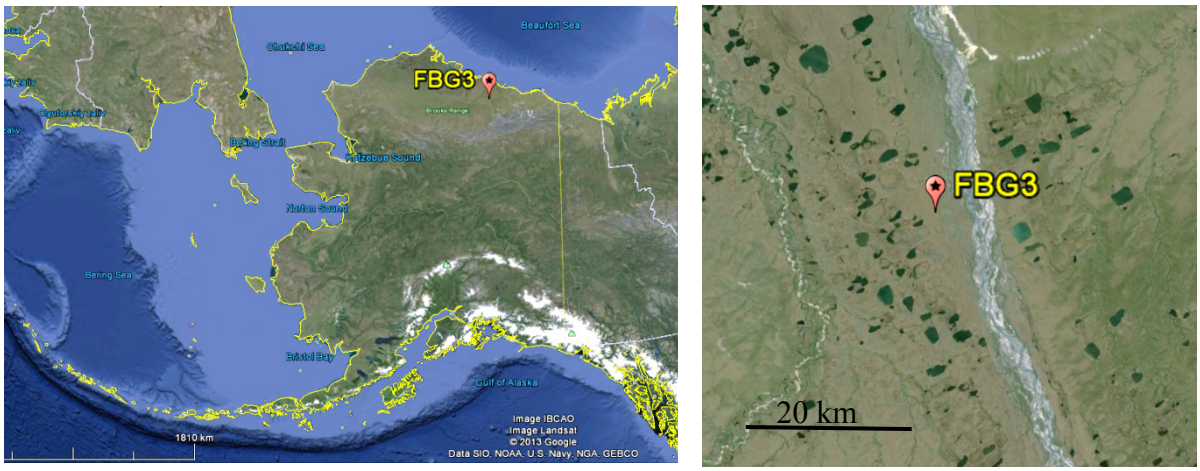

Figure C.3-1: Location of study site FBG3 in Alaska, USA. *Source:* Google Earth, 2013

Figure C.3-2: Aerial photo of a 10 x 10 m zonal grid at the Franklin Bluffs study location near the FBG3 site. *Source:* [*Barreda et al.*, 2006]

II *Main Vegetation Description*

The vegetation at the mesic Franklin Bluffs study location corresponds to the zonal vegetation in subzone D. The zonal plant community of bioclimate subzone D in northern Alaska is *Dryado integrifoliae-Caricetum bigelowii* [*Walker et al.*, 2005], also called moist non-acidic tundra (MNT), or 'nontussock sedge, dwarf-shrub, moss tundra' [*Walker et al.*, 2005]. It occurs on circumneutral to basic soils in association with silty loess that is blown from the major rivers in the eastern part of the Arctic Coastal Plain. The average soil pH of this plant community at Franklin Bluffs is 7.9; the average volumetric soil moisture of the top mineral horizon is 45 %, and average depth of thaw by late summer is 40 cm [*Kade et al.*, 2005]. The dominant plants in MNT are sedges (*Carex bigelowii, Eriophorum angustifolium* ssp. *triste, C. membranacea, C. scirpoidea, E. vaginatum*), prostrate and hemi-prostrate evergreen dwarf shrubs (*Dryas integrifolia, Cassiope tetragona*), prostrate dwarf deciduous shrubs (*Salix arctica, S. reticulata, Arctous rubra*), scattered erect dwarf deciduous shrubs (*Salix lanata, S. glauca*), several forbs (*Papaver macounii, Pedicularis lanata, Saussurea angustifolia, Senecio atropurpureus, Pedicularis capitata, Polygonum viviparum, Cardamine hyperborea, Astragalus umbellatus*), mosses *(Tomentypnum nitens, Hylocomium splendens, Aulacomnium turgidum, Rhytidium rugosum, Hypnum bambergeri, Distichium capillaceum, Ditrichum flexicaule*), and lichens (*Thamnolia subuliformis*, *Cetraria* spp.).

An important component of the MNT is the abundant nonsorted circles, also called frost boils, which are small patterned ground features caused by soil frost heave [*Walker et al.*, 2008; *Washburn*, 1980]. These features cover large parts of most MNT surfaces. The 10 x 10 m zonal grid at Franklin Bluffs has about 30 % cover of nonsorted circles. These features have drier plant communities than the mesic zonal plant communities between the circles, with high cover of lichens and bare soil.

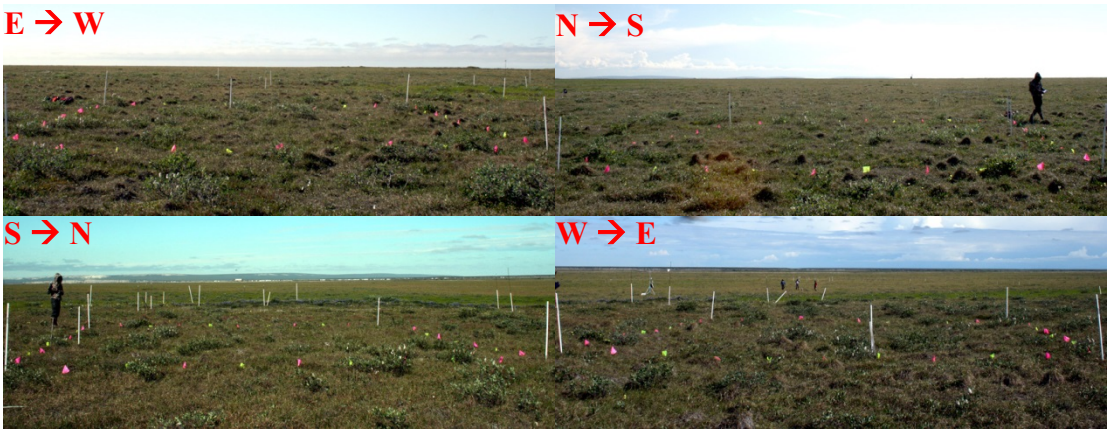

Figure C.3-3: Overview images of MNT tundra at the mesic Franklin Bluffs study location near the FBG3 site. *Source:* [*Buchhorn and Schwieder*, 2012]

III *Vegetation Description of the FBG3 Site*

The focus of the measurements at this goniometer site has been a frost boil community (*Junco biglumis-Dryadetum integrifoliae pedicularetosum*). The 1 x 1 m plot is homogeneously covered by the nonsorted circles community.

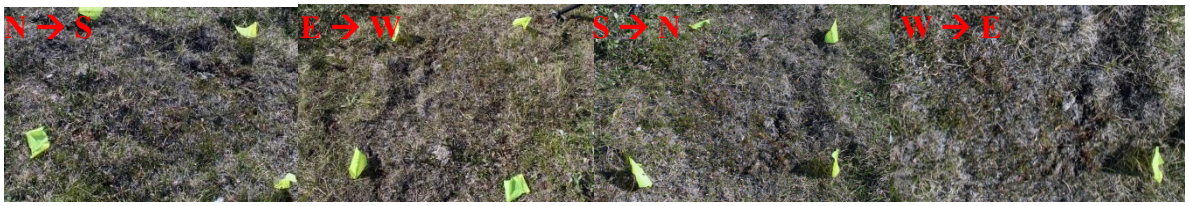

FigureC.3-4: Overview images of the FBG3 vegetation from cardinal directions.

Figure C.3-5: Nadir image of the FBG3 vegetation (frost boil).

IV *Overview of the Spectro-Goniometer Measurements*

Table C.3-1: Overview of the spectro-goniometer measurements at the FBG3 study site.

Name	Day	Starting Time	Duration	SAA	SZA	Sky
FBG3_01	2012-07-13	13:56:00	18 min	181°	48°	cirrostratus

Table C.3-2: Spectro-directional data of the FBG3_01 spectro-goniometer measurement.

FBG3_01 (SZA = 48°; SAA = 181°)	Viewing Geometry (Viewing Zenith Angle | Viewing Azimuth Angle)																							
	0|0	5|180	5|202.5	5|225	5|270	5|315	5|337.5	5|0	5|22.5	5|45	5|90	5|135	5|157.5	10|180	10|190	10|202.5	10|225	10|270	10|315	10|337.5	10|350
HCRF EnMAP blue (479 nm)	0.0435	0.0481	0.0472	0.0456	0.0427	0.0462	0.0424	0.0425	0.0466	0.0419	0.0460	0.0486	0.0460	0.0500	0.0483	0.0511	0.0460	0.0426	0.0465	0.0409	0.0414
HCRF EnMAP green (549 nm)	0.0610	0.0660	0.0620	0.0616	0.0595	0.0644	0.0593	0.0597	0.0647	0.0590	0.0631	0.0665	0.0629	0.0684	0.0671	0.0680	0.0630	0.0601	0.0632	0.0574	0.0576
HCRF EnMAP rot (672 nm)	0.0680	0.0755	0.0738	0.0708	0.0695	0.0723	0.0661	0.0669	0.0744	0.0672	0.0729	0.0751	0.0709	0.0774	0.0769	0.0799	0.0711	0.0678	0.0723	0.0645	0.0650
HCRF EnMAP NIR (864 nm)	0.2261	0.2161	0.1883	0.2034	0.2220	0.2342	0.2108	0.2207	0.2364	0.2121	0.2102	0.2122	0.2009	0.2208	0.2289	0.2081	0.2084	0.2233	0.2277	0.2132	0.2166
ANIF EnMAP rot (672 nm)	1.0000	1.1110	1.0853	1.0424	1.0232	1.0636	0.9722	0.9848	1.0950	0.9881	1.0732	1.1056	1.0426	1.1395	1.1320	1.1751	1.0463	0.9972	1.0633	0.9489	0.9568
ANIF EnMAP NIR (864 nm)	1.0000	0.9558	0.8329	0.8998	0.9819	1.0359	0.9324	0.9763	1.0457	0.9380	0.9298	0.9387	0.8886	0.9767	1.0125	0.9203	0.9220	0.9875	1.0070	0.9432	0.9580
Rel. Blue Absorption Depth	0.2630	0.2464	0.2157	0.2396	0.2616	0.2718	0.2670	0.2764	0.2700	0.2757	0.2527	0.2553	0.2481	0.2446	0.2583	0.2232	0.2451	0.2695	0.2453	0.2776	0.2726
Rel. Red Absorption Depth	0.8867	0.6904	0.5696	0.6989	0.8168	0.8473	0.8207	0.8812	0.8340	0.8256	0.7151	0.6742	0.6868	0.6871	0.7352	0.5918	0.7229	0.8505	0.8136	0.8795	0.8789
NDVI (EnMAP)	0.5377	0.4821	0.4371	0.4834	0.5229	0.5283	0.5227	0.5346	0.5212	0.5190	0.4848	0.4770	0.4785	0.4807	0.4969	0.4453	0.4913	0.5342	0.5181	0.5356	0.5382
Nadir Norm. NDVI (AVHRR)	1.0000	0.9036	0.8326	0.9073	0.9760	0.9814	0.9718	0.9923	0.9745	0.9661	0.9115	0.9911	0.8885	0.8974	0.9308	0.8419	0.9188	0.9938	0.9694	0.9922	1.0058
Nadir Norm. NDVI (MODIS)	1.0000	0.9048	0.8308	0.9072	0.9738	0.9824	0.9732	0.9941	0.9762	0.9668	0.9126	0.8939	0.8915	0.8990	0.9314	0.8410	0.9195	0.9942	0.9690	0.9926	1.0074
Nadir Norm. NDVI (EnMAP)	1.0000	0.8966	0.8128	0.8989	0.9724	0.9824	0.9721	0.9942	0.9692	0.9651	0.9015	0.8871	0.8899	0.8939	0.9240	0.8280	0.9136	0.9935	0.9636	0.9960	1.0008

(cont.)

FBG3_01 (SZA = 48°; SAA = 181°)	Viewing Geometry (Viewing Zenith Angle | Viewing Azimuth Angle)																							
	10|0	10|10	10|22.5	10|45	10|90	10|135	10|157.5	10|170	20|180	20|190	20|202.5	20|225	20|270	20|315	20|337.5	20|350	20|0	20|10	20|22.5	20|45	20|90
HCRF EnMAP blue (479 nm)	0.0404	0.0419	0.0456	0.0417	0.0489	0.0490	0.0515	0.0487	0.0583	0.0576	0.0591	0.0517	0.0417	0.0437	0.0406	0.0408	0.0377	0.0378	0.0377	0.0398	0.0434
HCRF EnMAP green (549 nm)	0.0567	0.0592	0.0633	0.0583	0.0661	0.0679	0.0701	0.0669	0.0798	0.0801	0.0795	0.0710	0.0601	0.0607	0.0559	0.0561	0.0519	0.0534	0.0533	0.0554	0.0620
HCRF EnMAP rot (672 nm)	0.0644	0.0665	0.0729	0.0666	0.0775	0.0754	0.0807	0.0770	0.0902	0.0888	0.0913	0.0825	0.0675	0.0677	0.0637	0.0645	0.0589	0.0587	0.0600	0.0629	0.0678
HCRF EnMAP NIR (864 nm)	0.2149	0.2294	0.2356	0.2093	0.2129	0.2254	0.2221	0.2211	0.2476	0.2566	0.2418	0.2323	0.2336	0.2276	0.2045	0.2056	0.1956	0.2098	0.2193	0.2033	0.2176
ANIF EnMAP rot (672 nm)	0.9477	0.9789	1.0725	0.9799	1.1404	1.1094	1.1871	1.1329	1.3277	1.3060	1.3438	1.2135	0.9929	0.9961	0.9372	0.9496	0.8668	0.8637	0.8823	0.9253	0.9978
ANIF EnMAP NIR (864 nm)	0.9507	1.0146	1.0422	0.9259	0.9416	0.9971	0.9826	0.9779	1.0950	1.1350	1.0696	1.0277	1.0334	1.0069	0.9048	0.9095	0.8651	0.9279	0.9700	0.8991	0.9625
Rel. Blue Absorption Depth	0.2715	0.2853	0.2682	0.2696	0.2408	0.2632	0.2468	0.2480	0.2440	0.2538	0.2327	0.2555	0.2877	0.2572	0.2696	0.2652	0.2634	0.2716	0.2681	0.2703	0.2777
Rel. Red Absorption Depth	0.8922	0.9381	0.8524	0.8125	0.6523	0.7354	0.6603	0.7039	0.6511	0.7059	0.6168	0.6787	0.9157	0.8999	0.8453	0.8322	0.8755	0.9711	0.9990	0.8515	0.8307
NDVI (EnMAP)	0.5388	0.5503	0.5275	0.5173	0.4662	0.4987	0.4671	0.4833	0.4657	0.4860	0.4517	0.4760	0.5518	0.5415	0.5251	0.5222	0.5370	0.5627	0.5705	0.5274	0.5248
Nadir Norm. NDVI (AVHRR)	1.0076	1.0228	0.9840	0.9661	0.8831	0.9252	0.8709	0.9020	0.8713	0.9019	0.8494	0.8949	1.0229	1.0070	0.9825	0.9812	1.0042	1.0430	1.0607	0.9803	0.9742
Nadir Norm. NDVI (MODIS)	1.0075	1.0238	0.9855	0.9674	0.8833	0.9287	0.8733	0.9035	0.8725	0.9037	0.8499	0.8947	1.0239	1.0093	0.9835	0.9820	1.0061	1.0463	1.0630	0.9818	0.9779
Nadir Norm. NDVI (EnMAP)	1.0021	1.0235	0.9809	0.9620	0.8669	0.9274	0.8687	0.8989	0.8661	0.9037	0.8401	0.8853	1.0261	1.0071	0.9765	0.9712	0.9987	1.0465	1.0611	0.9809	0.9760

(cont.)

FBG3_01 (SZA = 48°; SAA = 181°)	Viewing Geometry (Viewing Zenith Angle | Viewing Azimuth Angle)																							
	20|135	20|157.5	20|170	30|180	30|190	30|202.5	30|225	30|270	30|315	30|337.5	30|350	30|0	30|10	30|22.5	30|45	30|90	30|135	30|157.5	30|170			
HCRF EnMAP blue (479 nm)	0.0537	0.0598	0.0602	0.0702	0.0662	0.0666	0.0558	0.0393	0.0397	0.0399	0.0377	0.0378	0.0355	0.0368	0.0408	0.0446	0.0600	0.0674	0.0676					
HCRF EnMAP green (549 nm)	0.0758	0.0827	0.0843	0.0977	0.0915	0.0902	0.0778	0.0588	0.0557	0.0562	0.0522	0.0520	0.0490	0.0512	0.0568	0.0639	0.0866	0.0946	0.0966					
HCRF EnMAP rot (672 nm)	0.0838	0.0947	0.0960	0.1092	0.1020	0.1031	0.0877	0.0631	0.0637	0.0631	0.0592	0.0594	0.0554	0.0581	0.0648	0.0676	0.0954	0.1062	0.1054					
HCRF EnMAP NIR (864 nm)	0.2570	0.2588	0.2708	0.2998	0.2756	0.2632	0.2513	0.2475	0.2169	0.2190	0.1995	0.1948	0.1857	0.2030	0.2091	0.2252	0.2807	0.2940	0.3014					
ANIF EnMAP rot (672 nm)	1.2332	1.3933	1.4125	1.6062	1.5005	1.5169	1.2907	0.9285	0.9377	0.9289	0.8713	0.8735	0.8146	0.8543	0.9536	0.9943	1.4041	1.5620	1.5509					
ANIF EnMAP NIR (864 nm)	1.1368	1.1448	1.1979	1.3261	1.2191	1.1643	1.1114	1.0950	0.9595	0.9688	0.8825	0.8615	0.8215	0.8979	0.9247	0.9963	1.2415	1.3004	1.3330					
Rel. Blue Absorption Depth	0.2774	0.2666	0.2689	0.2603	0.2521	0.2375	0.2584	0.3157	0.2737	0.2815	0.2585	0.2535	0.2581	0.2614	0.2720	0.2763	0.3037	0.2743	0.2827					
Rel. Red Absorption Depth	0.7732	0.6630	0.7002	0.6666	0.6431	0.5797	0.7007	1.0856	0.9123	0.9438	0.8977	0.8557	0.8767	0.9321	0.8601	0.8800	0.7420	0.6740	0.7042					
NDVI (EnMAP)	0.5081	0.4643	0.4766	0.4662	0.4598	0.4371	0.4824	0.5937	0.5458	0.5525	0.5422	0.5328	0.5407	0.5552	0.5267	0.5384	0.4925	0.4694	0.4817					
Nadir Norm. NDVI (AVHRR)	0.9418	0.8689	0.8842	0.8659	0.8553	0.8172	0.8964	1.0866	1.0156	1.0263	1.0139	1.0016	1.0106	1.0327	0.9823	0.9940	0.9101	0.8756	0.8900					
Nadir Norm. NDVI (MODIS)	0.9461	0.8715	0.8855	0.8664	0.8564	0.8190	0.8983	1.0899	1.0185	1.0294	1.0153	1.0023	1.0135	1.0345	0.9846	0.9996	0.9151	0.8780	0.8937					
Nadir Norm. NDVI (EnMAP)	0.9450	0.8634	0.8863	0.8669	0.8551	0.8129	0.8972	1.1042	1.0151	1.0274	1.0084	0.9908	1.0056	1.0324	0.9795	1.0013	0.9160	0.8729	0.8959					

V *Main Spectral Characteristics*

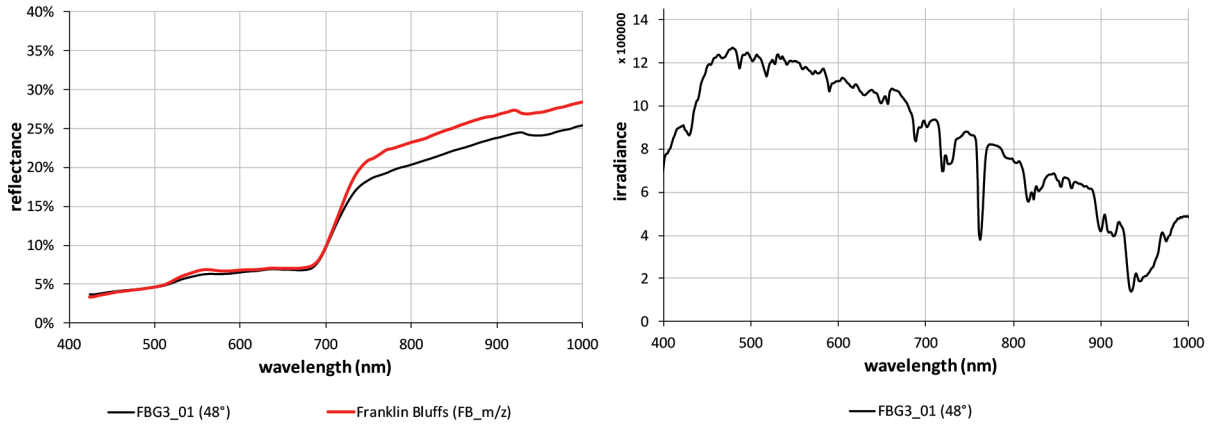

Figure C.3-6: Nadir reflectances and irradiance profiles of the FBG3 site. Left: Comparison of the nadir reflectance signatures with the average zonal vegetation (MNT). Right: Comparison of the total irradiance profiles.

VI *HCRF Visualization*

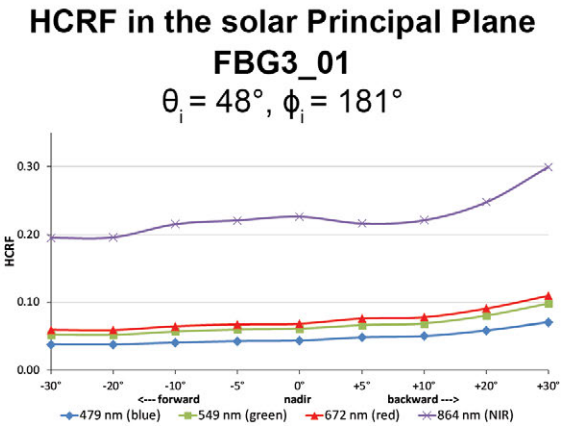

Figure C.3-7: Comparison of the HCRF values at 479 nm (blue), 549 nm (green), 672 nm (red), and 864 nm (NIR) in the solar principal plane of the FBG3 site.

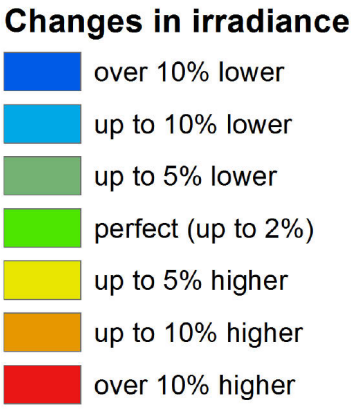

Figure C.3-8: Legend of the outlier indicator graphics shown in Figure C.3-9, C.3-10, and C.3-13

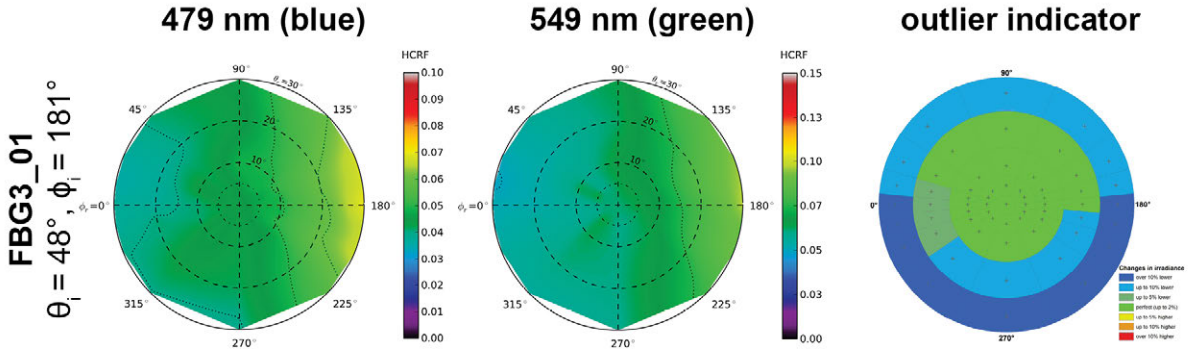

Figure C.3-9: HCRF visualization at 479 nm and 549 nm of the FBG3 site.

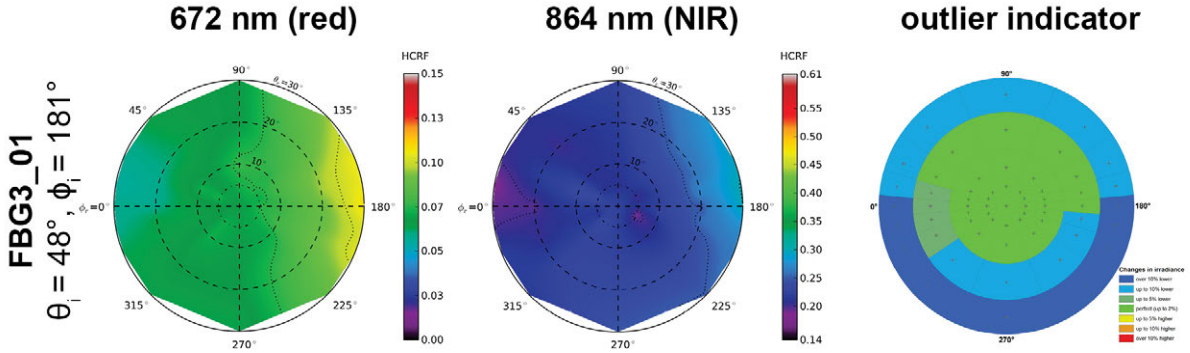

Figure C.3-10: HCRF visualization at 672 nm and 864 nm of the FBG3 site.

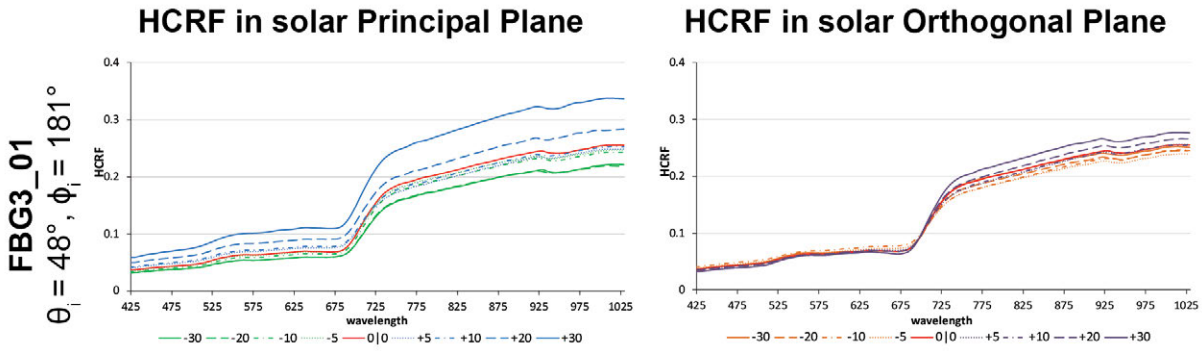

Figure C.3-11: HCRF visualization in principal & orthogonal plane of the FBG3 site.

VII *ANIF Visualization*

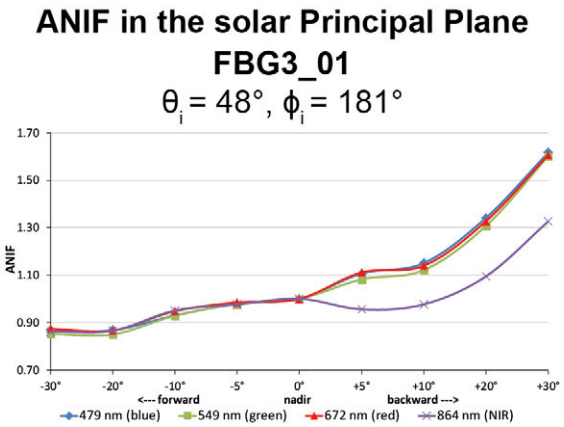

Figure C.3-12: Comparison of the ANIF values at 479 nm (blue), 549 nm (green), 672 nm (red), and 864 nm (NIR) in the solar principal plane of the FBG3 site.

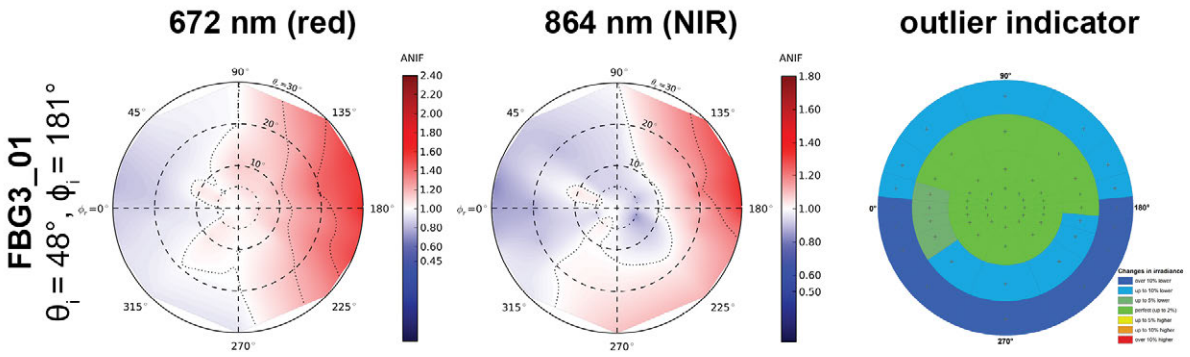

Figure C.3-13: ANIF visualization at 672 nm and 864 nm of the FBG3 site.

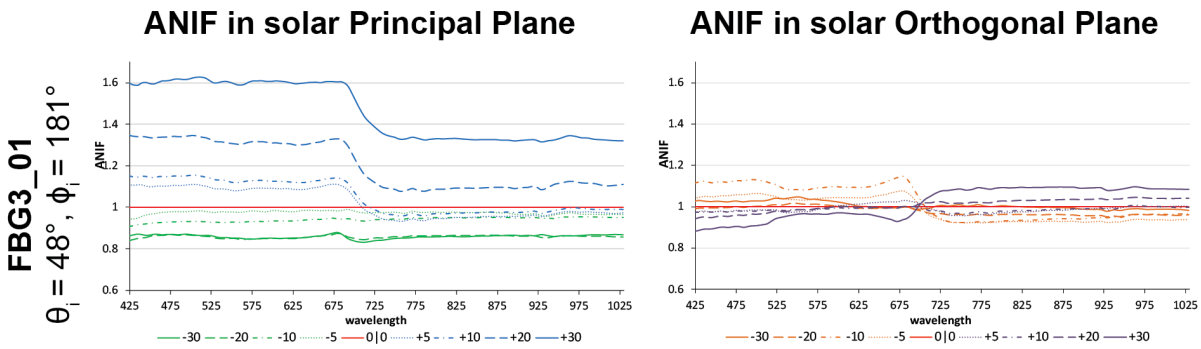

Figure C.3-14: ANIF visualization in principal & orthogonal plane of the FBG3 site.

VIII *ANIX Visualization*

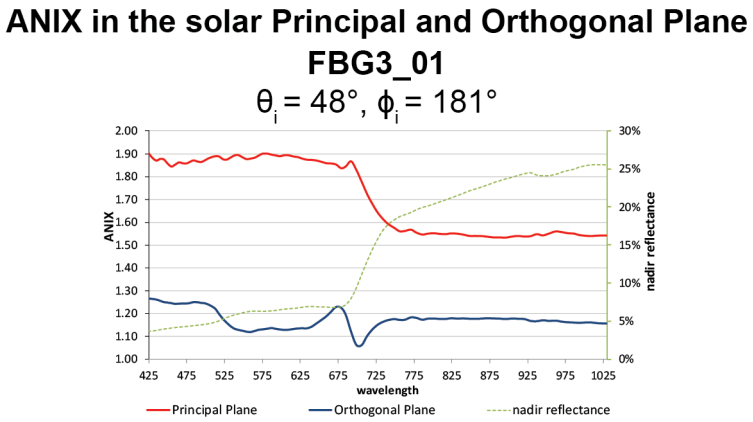

Figure C.3-15: Comparison of the ANIX in the solar principal and orthogonal plane with the nadir reflectance of the FBG3 site.

IX *NDVI and Relative Absorption Depth Visualization*

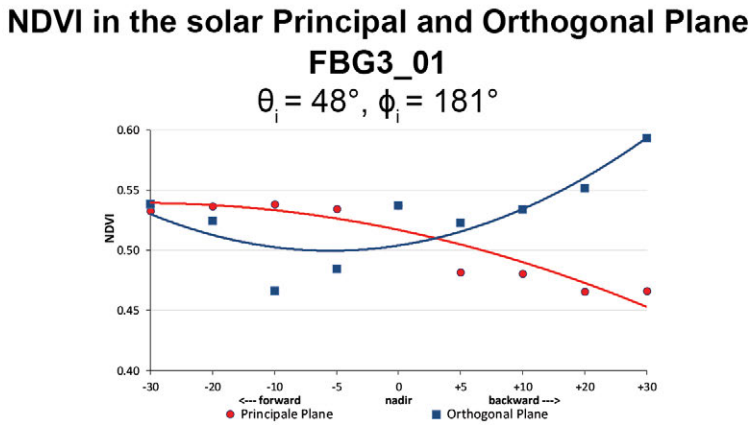

Figure C.3-16: Comparison of the NDVI in the solar principal and orthogonal plane of the FBG3 site.

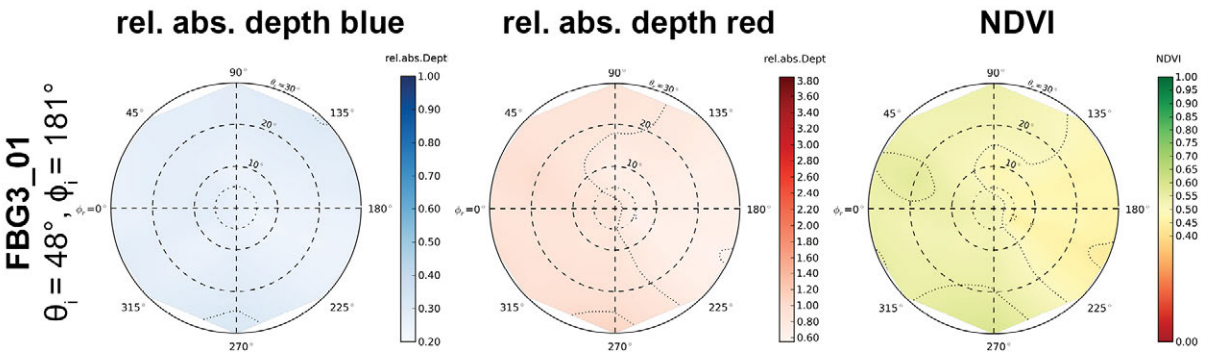

Figure C.3-17: Visualization of relative absorption depth & NDVI of the FBG3 site.

X *NDVI Comparison of Different Sensors*

Table C.3-3: Center wavelengths and band widths of the broadband and narrowband NDVIs, based on the spectral response curves of the AVHRR, MODIS and EnMAP sensors.

NDVI	Sensor	Sensor band	Center wavelength (nm)	band width (nm)
$NDVI_{AVHRR}$ [broadband]	AVHRR/3	red: band 1 NIR: band 2	630 865	100 275
$NDVI_{MODIS}$ [broadband]	MODIS	red: band 1 NIR: band 2	645 859	50 35
$NDVI_{EnMAP}$ [narrowband]	EnMAP	red: band 47 NIR: band 73	672 864	6.5 8

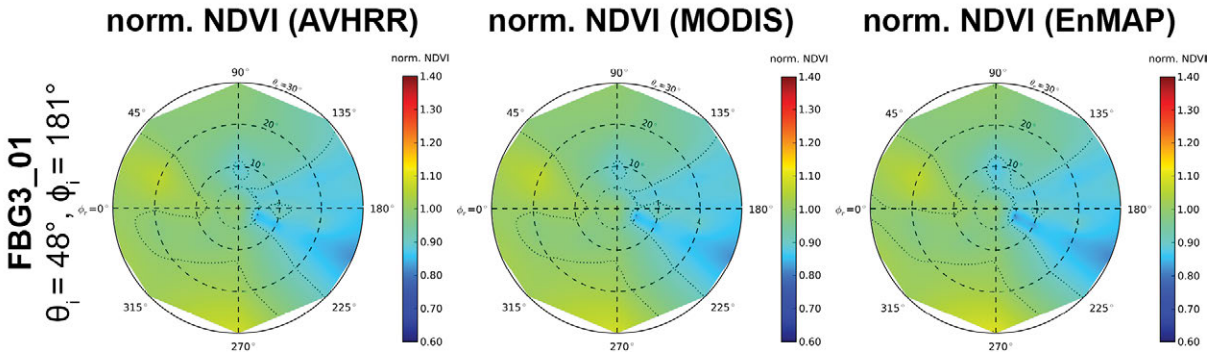

Figure C.3-18: Comparison of AVHRR, MODIS & EnMAP NDVI of the FBG3 site.

C.4 Study site FBG4 (horsetail community)

I *Location*

Name	Location	Latitude	Longitude	Altitude
FBG4	Franklin Bluffs, Arctic North Slope, Alaska, United States of America	69.6744°	-148.72022°	125 m

At an average elevation of 90 m, Franklin Bluffs is located in Subzone D about 1 km west of the Dalton Highway across from the pipeline access road APL/AMS 130 near green mile marker 375. This access road provides parking at the site. Three 10 x 10 m grids, designated dry, mesic, and wet, have been established at this location in 2002. The goniometer measurements have been carried out next to the moist / zonal site (FB_m/z). [*Barreda et al.*, 2006]

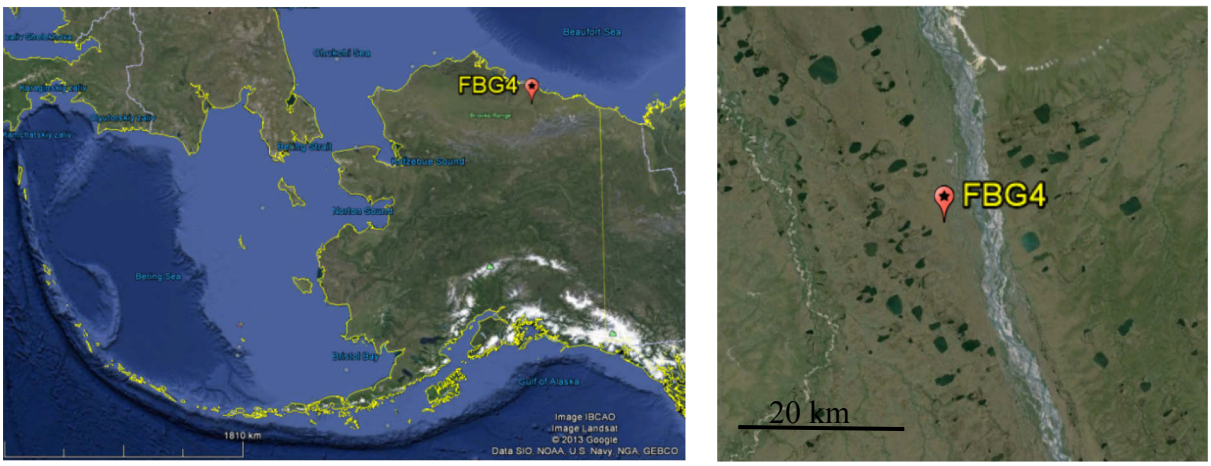

Figure C.4-1: Location of study site FBG4 in Alaska, USA. *Source:* Google Earth, 2013

Figure C.4-2: Aerial photo of a 10 x 10 m zonal grid at the Franklin Bluffs study location near the FBG4 site. *Source:* [*Barreda et al.*, 2006]

II *Main Vegetation Description*

The vegetation at the mesic Franklin Bluffs study location corresponds to the zonal vegetation in subzone D. The zonal plant community of bioclimate subzone D in northern Alaska is *Dryado integrifoliae-Caricetum bigelowii* [*Walker et al.*, 2005], also called moist non-acidic tundra (MNT), or 'nontussock sedge, dwarf-shrub, moss tundra' [*Walker et al.*, 2005]. It occurs on circumneutral to basic soils in association with silty loess that is blown from the major rivers in the eastern part of the Arctic Coastal Plain. The average soil pH of this plant community at Franklin Bluffs is 7.9; the average volumetric soil moisture of the top mineral horizon is 45 %, and average depth of thaw by late summer is 40 cm [*Kade et al.*, 2005]. The dominant plants in MNT are sedges (*Carex bigelowii, Eriophorum angustifolium* ssp. *triste, C. membranacea, C. scirpoidea, E. vaginatum*), prostrate and hemi-prostrate evergreen dwarf shrubs (*Dryas integrifolia, Cassiope tetragona*), prostrate dwarf deciduous shrubs (*Salix arctica, S. reticulata, Arctous rubra*), scattered erect dwarf deciduous shrubs (*Salix lanata, S. glauca*), several forbs (*Papaver macounii, Pedicularis lanata, Saussurea angustifolia, Senecio atropurpureus, Pedicularis capitata, Polygonum viviparum, Cardamine hyperborea, Astragalus umbellatus*), mosses *(Tomentypnum nitens, Hylocomium splendens, Aulacomnium turgidum, Rhytidium rugosum, Hypnum bambergeri, Distichium capillaceum, Ditrichum flexicaule*), and lichens (*Thamnolia subuliformis*, *Cetraria* spp.).

An important component of the MNT is the abundant nonsorted circles, also called frost boils, which are small patterned ground features caused by soil frost heave [*Walker et al.*, 2008; *Washburn*, 1980]. These features cover large parts of most MNT surfaces. The 10 x 10 m zonal grid at Franklin Bluffs has about 30 % cover of nonsorted circles. These features have drier plant communities than the mesic zonal plant communities between the circles, with high cover of lichens and bare soil.

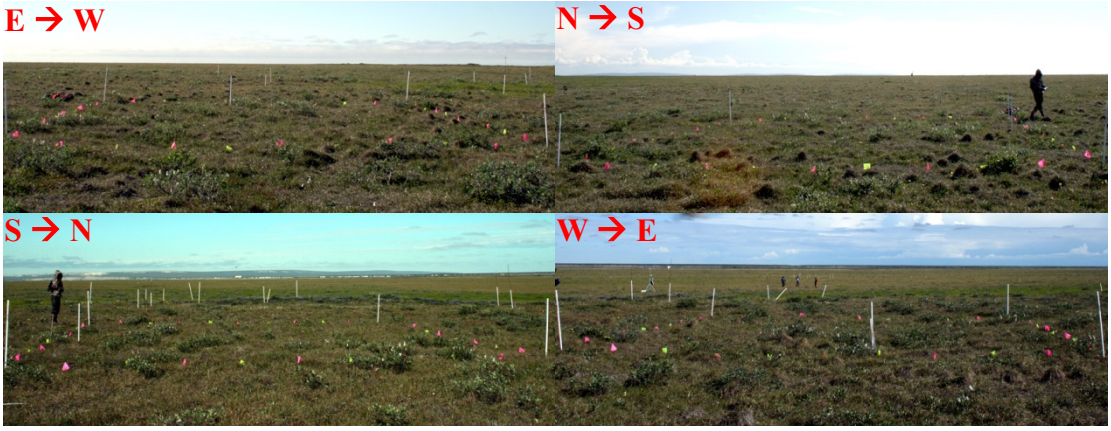

Figure C.4-3: Overview images of MNT tundra at the mesic Franklin Bluffs study location near the FBG4 site. *Source:* [*Buchhorn and Schwieder*, 2012]

III *Vegetation Description of the FBG4 Site*

The focus of the measurements at this goniometer site has been a horsetail patch. The 1 x 1 m plot is homogeneously covered with horsetail, but with forbs, mosses and lichens in the understory.

Figure C.4-4: Overview images of the FBG4 vegetation from cardinal directions.

Figure C.4-5: Nadir image of the FBG4 vegetation (horsetail).

IV *Overview of the Spectro-Goniometer Measurements*

Table C.4-1: Overview of the spectro-goniometer measurements at the FBG4 study site.

Name	Day	Starting Time	Duration	SAA	SZA	Sky
FBG4_01	2012-07-15	14:03:38	17 min	183°	48°	clear
FBG4_02	2012-07-15	15:32:07	17 min	211°	50°	clear
FBG4_03	2012-07-15	18:11:59	17 min	254°	60°	clear

Table C.4-2: Spectro-directional data of the FBG4_01 spectro-goniometer measurement.

FBG4_01 (SZA = 48°; SAA = 183°)	Viewing Geometry (Viewing Zenith Angle | Viewing Azimuth Angle)																								
	0|0	5|180	5|202.5	5|225	5|270	5|315	5|337.5	5|0	5|22.5	5|45	5|90	5|135	5|157.5	10|180	10|190	10|202.5	10|225	10|270	10|315	10|337.5	10|350
HCRF EnMAP blue (479 nm)	0.0176	0.0199	0.0201	0.0176	0.0169	0.0188	0.0193	0.0161	0.0154	0.0150	0.0173	0.0202	0.0220	0.0210	0.0209	0.0200	0.0186	0.0165	0.0192	0.0182	0.0152
HCRF EnMAP green (549 nm)	0.0473	0.0496	0.0482	0.0462	0.0423	0.0505	0.0507	0.0445	0.0388	0.0437	0.0513	0.0536	0.0534	0.0538	0.0522	0.0472	0.0501	0.0419	0.0519	0.0500	0.0462
HCRF EnMAP rot (672 nm)	0.0267	0.0325	0.0326	0.0281	0.0271	0.0281	0.0292	0.0264	0.0252	0.0221	0.0244	0.0300	0.0352	0.0336	0.0329	0.0332	0.0293	0.0257	0.0285	0.0270	0.0226
HCRF EnMAP NIR (864 nm)	0.3358	0.3104	0.3192	0.3178	0.2958	0.3276	0.3386	0.3151	0.2746	0.2882	0.3263	0.3456	0.3306	0.3389	0.3351	0.3076	0.3251	0.2914	0.3391	0.3484	0.3468
ANIF EnMAP rot (672 nm)	1.0000	1.2176	1.2209	1.0497	1.0136	1.0503	1.0930	0.9874	0.9424	0.8279	0.9118	1.1223	1.3151	1.2588	1.2323	1.2428	1.0968	0.9615	1.0660	1.0107	0.8457
ANIF EnMAP NIR (864 nm)	1.0000	0.9243	0.9505	0.9464	0.8809	0.9756	1.0082	0.9382	0.8176	0.8583	0.9717	1.0292	0.9846	1.0092	0.9978	0.9159	0.9681	0.8678	1.0098	1.0373	1.0327
Rel. Blue Absorption Depth	0.8798	0.7923	0.7398	0.8431	0.7803	0.8661	0.8401	0.9030	0.7897	0.9690	1.0047	0.8667	0.7643	0.8253	0.7938	0.7243	0.8779	0.8011	0.8753	0.8869	1.0159
Rel. Red Absorption Depth	4.1562	3.0210	3.1577	3.7265	3.5180	3.8164	3.8331	3.9070	3.4796	4.2559	4.4464	3.6920	3.0300	3.2401	3.2882	2.9695	3.6419	3.6586	3.8908	4.3395	5.2116
NDVI (EnMAP)	0.8525	0.8102	0.8145	0.8378	0.8322	0.8421	0.8411	0.8454	0.8319	0.8574	0.8610	0.8403	0.8078	0.8194	0.8210	0.8050	0.8346	0.8379	0.8450	0.8561	0.8776
Nadir Norm. NDVI (AVHRR)	1.0000	0.9484	0.9584	0.9843	0.9795	0.9813	0.9826	0.9932	0.9793	0.9925	0.9944	0.9757	0.9464	0.9578	0.9624	0.9481	0.9748	0.9833	0.9836	1.0020	1.0285
Nadir Norm. NDVI (MODIS)	1.0000	0.9492	0.9575	0.9836	0.9787	0.9821	0.9825	0.9926	0.9779	0.9947	0.9974	0.9769	0.9475	0.9587	0.9627	0.9473	0.9756	0.9829	0.9844	1.0016	1.0278
Nadir Norm. NDVI (EnMAP)	1.0000	0.9503	0.9553	0.9827	0.9761	0.9878	0.9866	0.9916	0.9758	1.0057	1.0099	0.9856	0.9475	0.9611	0.9630	0.9443	0.9789	0.9828	0.9911	1.0041	1.0294

(cont.)

FBG4_01 (SZA = 48°; SAA = 183°)	Viewing Geometry (Viewing Zenith Angle | Viewing Azimuth Angle)																								
	10|0	10|10	10|22.5	10|45	10|90	10|135	10|157.5	10|170	20|180	20|190	20|202.5	20|225	20|270	20|315	20|337.5	20|350	20|0	20|10	20|22.5	20|45	20|90	20|135	20|157.5	20|170
HCRF EnMAP blue (479 nm)	0.0162	0.0158	0.0150	0.0154	0.0169	0.0206	0.0234	0.0242	0.0249	0.0266	0.0216	0.0218	0.0157	0.0143	0.0146	0.0158	0.0144	0.0149	0.0150	0.0154	0.0168	0.0215	0.0237	0.0244
HCRF EnMAP green (549 nm)	0.0452	0.0446	0.0404	0.0472	0.0522	0.0546	0.0596	0.0588	0.0646	0.0700	0.0540	0.0584	0.0463	0.0468	0.0547	0.0550	0.0513	0.0539	0.0537	0.0556	0.0587	0.0604	0.0600	0.0616
HCRF EnMAP rot (672 nm)	0.0259	0.0251	0.0241	0.0226	0.0228	0.0306	0.0372	0.0405	0.0373	0.0390	0.0340	0.0346	0.0237	0.0212	0.0198	0.0230	0.0208	0.0217	0.0226	0.0224	0.0225	0.0309	0.0347	0.0359
HCRF EnMAP NIR (864 nm)	0.3153	0.3053	0.2799	0.3115	0.3270	0.3466	0.3551	0.3411	0.3618	0.3858	0.3171	0.3551	0.3102	0.3228	0.3823	0.3678	0.3587	0.3649	0.3610	0.3638	0.3768	0.3632	0.3440	0.3551
ANIF EnMAP rot (672 nm)	0.9691	0.9407	0.8997	0.8446	0.8529	1.1431	1.3925	1.5133	1.3972	1.4571	1.2711	1.2934	0.8854	0.7943	0.7410	0.8610	0.7775	0.8112	0.8466	0.8382	0.8408	1.1551	1.2996	1.3432
ANIF EnMAP NIR (864 nm)	0.9388	0.9093	0.8334	0.9276	0.9738	1.0321	1.0575	1.0158	1.0775	1.1487	0.9442	1.0573	0.9238	0.9612	1.1383	1.0951	1.0681	1.0866	1.0749	1.0832	1.1220	1.0814	1.0243	1.0573
Rel. Blue Absorption Depth	0.9117	0.9297	0.8711	1.0411	1.0586	0.8656	0.8237	0.7655	0.8482	0.8651	0.7971	0.8759	0.9859	1.1163	1.3112	1.1983	1.2368	1.2641	1.2430	1.2757	1.2339	0.9359	0.8149	0.8097
Rel. Red Absorption Depth	4.0154	3.9939	3.7399	4.5968	4.7607	3.6416	3.0730	2.6813	3.0946	3.2052	2.9680	3.3529	4.3411	5.0765	6.6453	5.4644	5.8946	5.7641	5.3711	5.5024	5.6758	3.8178	3.1318	3.1843
NDVI (EnMAP)	0.8481	0.8478	0.8417	0.8648	0.8696	0.8380	0.8102	0.7880	0.8129	0.8166	0.8064	0.8225	0.8582	0.8766	0.9015	0.8822	0.8905	0.8878	0.8820	0.8840	0.8874	0.8433	0.8165	0.8163
Nadir Norm. NDVI (AVHRR)	0.9945	0.9894	0.9857	1.0009	1.0007	0.9734	0.9443	0.9206	0.9380	0.9390	0.9377	0.9566	0.9980	1.0173	1.0417	1.0185	1.0310	1.0254	1.0191	1.0184	1.0170	0.9721	0.9417	0.9453
Nadir Norm. NDVI (MODIS)	0.9943	0.9901	0.9854	1.0032	1.0044	0.9747	0.9466	0.9225	0.9414	0.9429	0.9384	0.9575	0.9991	1.0186	1.0438	1.0211	1.0329	1.0280	1.0217	1.0219	1.0211	0.9750	0.9444	0.9477
Nadir Norm. NDVI (EnMAP)	0.9948	0.9945	0.9873	1.0144	1.0201	0.9829	0.9504	0.9243	0.9535	0.9578	0.9459	0.9648	1.0067	1.0282	1.0574	1.0348	1.0445	1.0414	1.0346	1.0369	1.0409	0.9891	0.9578	0.9575

(cont.)

FBG4_01 (SZA = 48°; SAA = 183°)	Viewing Geometry (Viewing Zenith Angle | Viewing Azimuth Angle)																								
	30|0	30|10	30|22.5	30|45	30|90	30|135	30|157.5	30|170	30|180	30|190	30|202.5	30|225	30|270	30|315	30|337.5	30|350	40|0	40|10	40|22.5	40|45	40|90	40|135	40|157.5	40|170
HCRF EnMAP blue (479 nm)	0.0138	0.0144	0.0164	0.0158	0.0174	0.0234	0.0314	0.0319	0.0332	0.0319	0.0297	0.0189	0.0156	0.0144	0.0141	0.0136	0.0144	0.0149	0.0150	0.0154	0.0168	0.0215	0.0237	0.0244
HCRF EnMAP green (549 nm)	0.0548	0.0577	0.0668	0.0634	0.0626	0.0710	0.0842	0.0798	0.0853	0.0892	0.0810	0.0570	0.0554	0.0540	0.0587	0.0537	0.0577	0.0610	0.0611	0.0625	0.0645	0.0604	0.0600	0.0616
HCRF EnMAP rot (672 nm)	0.0200	0.0204	0.0238	0.0221	0.0232	0.0320	0.0454	0.0480	0.0500	0.0441	0.0439	0.0278	0.0217	0.0209	0.0194	0.0185	0.0200	0.0224	0.0227	0.0232	0.0247	0.0309	0.0347	0.0359
HCRF EnMAP NIR (864 nm)	0.3654	0.3680	0.3969	0.3896	0.3685	0.3878	0.4350	0.4217	0.4148	0.4597	0.4148	0.3580	0.3710	0.3612	0.3913	0.3654	0.3610	0.3680	0.3969	0.3896	0.3685	0.3878	0.4350	0.4217
ANIF EnMAP rot (672 nm)	0.7493	0.7625	0.8918	0.8280	0.8696	1.1956	1.6999	1.7953	1.6509	1.6414	1.6509	1.6414	1.0407	0.8134	0.7827	0.7242	0.6911	0.7625	0.8918	0.8280	0.8696	1.1956	1.6999	1.7953
ANIF EnMAP NIR (864 nm)	1.0751	1.0957	1.1820	1.1602	1.0973	1.1548	1.2955	1.2557	1.2351	1.3688	1.2838	1.0659	1.1048	1.0757	1.1651	1.0880	1.0751	1.0957	1.1820	1.1602	1.0973	1.1548	1.2955	1.2557
Rel. Blue Absorption Depth	1.3919	1.4142	1.4441	1.4305	1.2780	1.0425	0.8878	0.8031	0.9117	0.9417	0.8372	1.0224	1.2381	1.3100	1.4775	1.3843	1.3919	1.4142	1.4441	1.4305	1.2780	1.0425	0.8878	0.8031
Rel. Red Absorption Depth	6.1510	6.1877	5.7690	6.0442	5.3145	3.9069	3.0246	2.7858	3.4125	3.0554	4.2727	4.2891	5.8572	6.9720	6.8169	6.9720	5.8572	5.8617	4.2891	3.0554	3.4125	2.7227	1.8715	1.6509
NDVI (EnMAP)	0.8949	0.8950	0.8867	0.8925	0.8813	0.8477	0.8109	0.7956	0.8248	0.8087	0.7921	0.8558	0.8893	0.8905	0.9057	0.9037	0.8949	0.8950	0.8867	0.8925	0.8813	0.8477	0.8109	0.7956
Nadir Norm. NDVI (AVHRR)	1.0282	1.0247	1.0093	1.0184	1.0020	0.9621	0.9255	0.9155	0.9383	0.9235	0.9075	0.9879	1.0264	1.0251	1.0374	1.0391	1.0282	1.0247	1.0093	1.0184	1.0020	0.9621	0.9255	0.9155
Nadir Norm. NDVI (MODIS)	1.0321	1.0293	1.0155	1.0239	1.0085	0.9682	0.9313	0.9195	0.9446	0.9290	0.9126	0.9907	1.0294	1.0282	1.0414	1.0425	1.0321	1.0293	1.0155	1.0239	1.0085	0.9682	0.9313	0.9195
Nadir Norm. NDVI (EnMAP)	1.0497	1.0498	1.0401	1.0469	1.0338	0.9944	0.9511	0.9333	0.9675	0.9485	0.9291	1.0038	1.0431	1.0445	1.0624	1.0601	1.0497	1.0498	1.0401	1.0469	1.0338	0.9944	0.9511	0.9333

Table C.4-3: Spectro-directional data of the FBG4_02 spectro-goniometer measurement.

FBG4_02 (SZA = 50°; SAA = 211°)	Viewing Geometry (Viewing Zenith Angle | Viewing Azimuth Angle)																							
	0|0	5|180	5|202.5	5|225	5|270	5|315	5|337.5	5|0	5|22.5	5|45	5|90	5|135	5|157.5	10|180	10|202.5	10|225	10|270	10|315	10|337.5	10|350
HCRF EnMAP blue (479 nm)	0.0140	0.0170	0.0161	0.0162	0.0192	0.0129	0.0113	0.0137	0.0137	0.0128	0.0136	0.0176	0.0185	0.0167	0.0166	0.0178	0.0186	0.0119	0.0106	0.0117
HCRF EnMAP green (549 nm)	0.0392	0.0433	0.0435	0.0424	0.0485	0.0394	0.0320	0.0343	0.0401	0.0408	0.0428	0.0447	0.0471	0.0394	0.0443	0.0475	0.0499	0.0380	0.0322	0.0327
HCRF EnMAP rot (672 nm)	0.0209	0.0273	0.0244	0.0241	0.0296	0.0181	0.0170	0.0206	0.0194	0.0175	0.0184	0.0274	0.0285	0.0263	0.0247	0.0265	0.0287	0.0164	0.0154	0.0179
HCRF EnMAP NIR (864 nm)	0.2868	0.2761	0.3014	0.2868	0.3067	0.3048	0.2438	0.2468	0.2703	0.2889	0.3070	0.2947	0.3059	0.2560	0.3042	0.3057	0.3030	0.3183	0.3025	0.2402	0.2426
ANIF EnMAP rot (672 nm)	1.0000	1.3069	1.1666	1.1541	1.4188	0.8671	0.8163	0.9847	0.9271	0.8367	0.8789	1.3141	1.3650	1.2587	1.1153	1.1847	1.2692	1.3732	0.7864	0.7359	0.8549
ANIF EnMAP NIR (864 nm)	1.0000	0.9627	1.0506	0.9998	1.0691	1.0628	0.8499	0.8603	0.9422	1.0073	1.0704	1.0274	1.0666	0.8925	1.0604	1.0659	1.0565	1.1098	1.0545	0.8375	0.8459
Rel. Blue Absorption Depth	0.9174	0.8152	0.8734	0.8412	0.7969	1.0234	0.9231	0.7693	0.9792	1.0912	1.0777	0.8093	0.8133	0.7239	0.9182	0.8591	0.8645	0.8674	1.0796	1.0118	0.9123
Rel. Red Absorption Depth	4.5877	3.2571	4.1114	3.9007	3.3630	5.7109	4.7012	3.9612	4.7114	5.5922	5.6963	3.4871	3.4724	3.0772	4.3145	4.1054	3.7700	3.6547	6.3038	5.1865	4.4921
NDVI (EnMAP)	0.8643	0.8201	0.8504	0.8450	0.8238	0.8879	0.8693	0.8462	0.8663	0.8860	0.8872	0.8296	0.8295	0.8138	0.8578	0.8503	0.8392	0.8347	0.8970	0.8797	0.8629
Nadir Norm. NDVI (AVHRR)	1.0000	0.9465	0.9837	0.9757	0.9513	1.0276	1.0076	0.9807	0.9942	1.0181	1.0187	0.9594	0.9598	0.9421	0.9887	0.9831	0.9638	0.9626	1.0372	1.0130	0.9967
Nadir Norm. NDVI (MODIS)	1.0000	0.9470	0.9832	0.9758	0.9516	1.0266	1.0067	0.9795	0.9955	1.0193	1.0192	0.9592	0.9600	0.9412	0.9893	0.9832	0.9653	0.9634	1.0363	1.0130	0.9959
Nadir Norm. NDVI (EnMAP)	1.0000	0.9489	0.9840	0.9777	0.9532	1.0273	1.0058	0.9790	1.0024	1.0251	1.0265	0.9599	0.9598	0.9416	0.9924	0.9838	0.9709	0.9658	1.0379	1.0179	0.9984

(cont.)

FBG4_02 (SZA = 50°; SAA = 211°)	Viewing Geometry (Viewing Zenith Angle | Viewing Azimuth Angle)																							
	10|0	10|10	10|22.5	10|45	10|90	10|135	10|157.5	10|170	20|180	20|190	20|202.5	20|225	20|270	20|315	20|337.5	20|350	20|0	20|10	20|22.5	20|45	20|90
HCRF EnMAP blue (479 nm)	0.0119	0.0121	0.0128	0.0132	0.0141	0.0193	0.0168	0.0171	0.0226	0.0185	0.0179	0.0178	0.0155	0.0114	0.0115	0.0129	0.0118	0.0123	0.0122	0.0146	0.0144
HCRF EnMAP green (549 nm)	0.0337	0.0352	0.0405	0.0411	0.0475	0.0520	0.0441	0.0411	0.0600	0.0490	0.0468	0.0476	0.0525	0.0436	0.0437	0.0487	0.0485	0.0483	0.0473	0.0512	0.0456
HCRF EnMAP rot (672 nm)	0.0175	0.0179	0.0173	0.0183	0.0185	0.0300	0.0254	0.0274	0.0331	0.0278	0.0258	0.0253	0.0222	0.0152	0.0159	0.0183	0.0161	0.0174	0.0167	0.0195	0.0195
HCRF EnMAP NIR (864 nm)	0.2405	0.2500	0.2830	0.2886	0.3271	0.3249	0.3020	0.2687	0.3193	0.3033	0.3043	0.2995	0.3459	0.3210	0.2899	0.3161	0.3152	0.3140	0.3125	0.3269	0.3124
ANIF EnMAP rot (672 nm)	0.8401	0.8583	0.8296	0.8775	0.8837	1.4379	1.2170	1.3122	1.5837	1.3302	1.2378	1.2122	1.0608	0.7292	0.7627	0.8771	0.7714	0.8334	0.7984	0.9321	0.9360
ANIF EnMAP NIR (864 nm)	0.8383	0.8716	0.9866	1.0061	1.1405	1.1328	1.0528	0.9368	1.1132	1.0574	1.0608	1.0443	1.2059	1.1190	1.0108	1.1021	1.0991	1.0946	1.0896	1.1397	1.0891
Rel. Blue Absorption Depth	0.9213	0.9750	1.0784	1.0513	1.1737	0.8895	0.8452	0.7522	0.8729	0.8624	0.8360	0.8619	1.1718	1.3419	1.3302	1.3324	1.4581	1.3895	1.3710	1.2256	1.0839
Rel. Red Absorption Depth	4.5272	4.6948	5.5263	5.3519	6.0744	3.5477	3.8726	3.1326	3.0690	3.5195	3.8799	3.9533	5.2555	7.3079	6.1976	5.9356	6.7763	6.1939	6.4155	5.7942	5.4400
NDVI (EnMAP)	0.8640	0.8662	0.8846	0.8806	0.8932	0.8308	0.8448	0.8149	0.8123	0.8322	0.8434	0.8442	0.8796	0.9094	0.8959	0.8905	0.9028	0.8950	0.8987	0.8876	0.8822
Nadir Norm. NDVI (AVHRR)	0.9937	0.9964	1.0145	1.0126	1.0204	0.9543	0.9769	0.9449	0.9198	0.9543	0.9708	0.9687	1.0029	1.0403	1.0176	1.0107	1.0205	1.0138	1.0185	1.0097	1.0104
Nadir Norm. NDVI (MODIS)	0.9937	0.9966	1.0159	1.0138	1.0223	0.9559	0.9767	0.9447	0.9239	0.9556	0.9718	0.9702	1.0055	1.0416	1.0208	1.0142	1.0245	1.0178	1.0225	1.0133	1.0122
Nadir Norm. NDVI (EnMAP)	0.9997	1.0022	1.0235	1.0189	1.0335	0.9613	0.9774	0.9429	0.9399	0.9629	0.9759	0.9767	1.0178	1.0522	1.0365	1.0303	1.0445	1.0355	1.0398	1.0270	1.0208

(cont.)

FBG4_02 (SZA = 50°; SAA = 211°)	Viewing Geometry (Viewing Zenith Angle | Viewing Azimuth Angle)																							
	20|135	20|157.5	20|170	30|180	30|190	30|202.5	30|225	30|270	30|315	30|337.5	30|350	30|0	30|10	30|122.5	30|45	30|90	30|135	30|157.5	30|170			
HCRF EnMAP blue (479 nm)	0.0224	0.0216	0.0216	0.0270	0.0247	0.0204	0.0215	0.0159	0.0123	0.0128	0.0136	0.0132	0.0152	0.0134	0.0141	0.0154	0.0219	0.0250	0.0289					
HCRF EnMAP green (549 nm)	0.0600	0.0593	0.0581	0.0716	0.0712	0.0587	0.0682	0.0528	0.0541	0.0554	0.0589	0.0617	0.0632	0.0586	0.0641	0.0554	0.0585	0.0714	0.0800					
HCRF EnMAP rot (672 nm)	0.0335	0.0303	0.0313	0.0396	0.0343	0.0289	0.0290	0.0229	0.0164	0.0178	0.0190	0.0179	0.0199	0.0183	0.0184	0.0208	0.0326	0.0354	0.0410					
HCRF EnMAP NIR (864 nm)	0.3682	0.3470	0.3143	0.3677	0.3626	0.3488	0.3856	0.3307	0.3668	0.3492	0.3647	0.3753	0.3837	0.3710	0.3920	0.3423	0.3385	0.3932	0.4006					
ANIF EnMAP rot (672 nm)	1.6052	1.4530	1.4989	1.8944	1.6449	1.3864	1.3899	1.0957	0.7873	0.8522	0.9106	0.8590	0.9514	0.8755	0.8824	0.9942	1.5606	1.6962	1.9615					
ANIF EnMAP NIR (864 nm)	1.2836	1.2099	1.0956	1.2819	1.2641	1.2160	1.3445	1.1530	1.2786	1.2174	1.2714	1.3084	1.3378	1.2934	1.3667	1.1935	1.1802	1.3710	1.3967					
Rel. Blue Absorption Depth	0.8731	0.9093	0.8906	0.8733	0.9785	0.9682	1.1016	1.1455	1.5547	1.5370	1.5359	1.6639	1.4935	1.5608	1.6403	1.2758	0.8758	0.9638	0.9381					
Rel. Red Absorption Depth	3.6852	3.7371	3.1861	2.9649	3.4241	4.0177	4.4669	4.9159	7.8351	6.8036	6.7221	7.2900	6.7298	7.0741	7.4278	5.5853	3.3865	3.6633	3.1575					
NDVI (EnMAP)	0.8331	0.8392	0.8189	0.8057	0.8269	0.8467	0.8600	0.8706	0.9142	0.9030	0.9009	0.9088	0.9015	0.9061	0.9102	0.8857	0.8244	0.8348	0.8145					
Nadir Norm. NDVI (AVHRR)	0.9593	0.9553	0.9262	0.9121	0.9255	0.9630	0.9680	0.9903	1.0365	1.0185	1.0143	1.0181	1.0130	1.0200	1.0208	0.9993	0.9413	0.9455	0.9149					
Nadir Norm. NDVI (MODIS)	0.9602	0.9580	0.9302	0.9167	0.9321	0.9667	0.9738	0.9937	1.0401	1.0236	1.0198	1.0247	1.0189	1.0252	1.0272	1.0043	0.9440	0.9498	0.9206					
Nadir Norm. NDVI (EnMAP)	0.9639	0.9710	0.9474	0.9323	0.9568	0.9797	0.9951	1.0073	1.0578	1.0448	1.0423	1.0515	1.0431	1.0484	1.0531	1.0247	0.9538	0.9658	0.9424					

Table C.4-4: Spectro-directional data of the FBG4_03 spectro-goniometer measurement.

FBG4_03 (SZA = 60°; SAA = 254°)	Viewing Geometry (Viewing Zenith Angle | Viewing Azimuth Angle)																							
	0|0	5|180	5|202.5	5|225	5|270	5|315	5|337.5	5|0	5|22.5	5|45	5|90	5|135	5|157.5	10|180	10|190	10|202.5	10|225	10|270	10|315	10|337.5	10|350
HCRF EnMAP blue (479 nm)	0.0090	0.0115	0.0100	0.0101	0.0090	0.0098	0.0106	0.0108	0.0104	0.0102	0.0097	0.0095	0.0097	0.0128	0.0119	0.0100	0.0109	0.0094	0.0096	0.0108	0.0118
HCRF EnMAP green (549 nm)	0.0302	0.0352	0.0270	0.0306	0.0309	0.0286	0.0352	0.0337	0.0400	0.0347	0.0297	0.0290	0.0303	0.0399	0.0362	0.0291	0.0347	0.0321	0.0326	0.0420	0.0412
HCRF EnMAP rot (672 nm)	0.0109	0.0148	0.0126	0.0129	0.0108	0.0137	0.0140	0.0145	0.0127	0.0127	0.0125	0.0124	0.0124	0.0164	0.0153	0.0124	0.0138	0.0115	0.0132	0.0139	0.0154
HCRF EnMAP NIR (864 nm)	0.2351	0.2448	0.2014	0.2171	0.2342	0.2252	0.2506	0.2456	0.2948	0.2631	0.2312	0.2172	0.2231	0.2675	0.2406	0.2103	0.2393	0.2528	0.2501	0.2912	0.2876
ANIF EnMAP rot (672 nm)	1.0000	1.3607	1.1613	1.1879	0.9876	1.2554	1.2855	1.3313	1.1623	1.1628	1.1509	1.1372	1.1382	1.5045	1.4026	1.1425	1.2690	1.0556	1.2085	1.2793	1.4119
ANIF EnMAP NIR (864 nm)	1.0000	1.0413	0.8567	0.9232	0.9961	0.9577	1.0660	1.0446	1.2537	1.1190	0.9836	0.9239	0.9490	1.1376	1.0235	0.8945	1.0179	1.0753	1.0639	1.2387	1.2231
Rel. Blue Absorption Depth	1.1390	1.0313	0.8585	1.0148	1.1741	0.9562	1.1394	1.0510	1.3681	1.1703	1.0310	1.0271	1.0522	1.0560	1.0246	0.9562	1.0877	1.1621	1.1643	1.3670	1.2134
Rel. Red Absorption Depth	7.3934	5.5694	5.2584	5.6791	7.4252	5.4771	6.0834	5.6895	8.0557	7.0986	6.2882	6.0216	6.0887	5.5795	5.2867	5.5980	5.8945	7.4873	6.3099	7.2448	6.3306
NDVI (EnMAP)	0.9114	0.8858	0.8818	0.8875	0.9122	0.8855	0.8942	0.8885	0.9176	0.9081	0.8971	0.8921	0.8947	0.8845	0.8806	0.8883	0.8908	0.9130	0.9000	0.9087	0.8985
Nadir Norm. NDVI (AVHRR)	1.0000	0.9698	0.9722	0.9723	0.9965	0.9771	0.9772	0.9739	1.0011	0.9933	0.9893	0.9795	0.9822	0.9651	0.9593	0.9744	0.9736	1.0024	0.9867	0.9869	0.9784
Nadir Norm. NDVI (MODIS)	1.0000	0.9713	0.9718	0.9731	0.9974	0.9759	0.9788	0.9745	1.0022	0.9936	0.9887	0.9797	0.9823	0.9674	0.9621	0.9750	0.9748	1.0021	0.9868	0.9896	0.9805
Nadir Norm. NDVI (EnMAP)	1.0000	0.9719	0.9675	0.9737	1.0008	0.9715	0.9811	0.9748	1.0068	0.9964	0.9843	0.9788	0.9816	0.9705	0.9662	0.9746	0.9773	1.0017	0.9875	0.9970	0.9858

(cont.)

FBG4_03 (SZA = 60°; SAA = 254°)	Viewing Geometry (Viewing Zenith Angle | Viewing Azimuth Angle)																							
	10|0	10|10	10|22.5	10|45	10|90	10|135	10|157.5	10|170	20|180	20|190	20|202.5	20|225	20|270	20|315	20|337.5	20|350	20|0	20|10	20|22.5	20|45	20|90
HCRF EnMAP blue (479 nm)	0.0108	0.0111	0.0101	0.0107	0.0101	0.0085	0.0105	0.0102	0.0144	0.0140	0.0134	0.0129	0.0121	0.0100	0.0112	0.0116	0.0120	0.0116	0.0109	0.0102	0.0101
HCRF EnMAP green (549 nm)	0.0391	0.0408	0.0406	0.0412	0.0324	0.0230	0.0319	0.0327	0.0453	0.0458	0.0465	0.0470	0.0499	0.0440	0.0490	0.0541	0.0560	0.0534	0.0484	0.0413	0.0321
HCRF EnMAP rot (672 nm)	0.0140	0.0144	0.0125	0.0131	0.0132	0.0109	0.0135	0.0124	0.0181	0.0173	0.0163	0.0156	0.0144	0.0126	0.0142	0.0146	0.0148	0.0144	0.0136	0.0124	0.0127
HCRF EnMAP NIR (864 nm)	0.2857	0.2974	0.3066	0.2975	0.2448	0.1849	0.2242	0.2346	0.2690	0.2708	0.2805	0.2954	0.3348	0.2949	0.3172	0.3483	0.3571	0.3453	0.3226	0.2993	0.2335
ANIF EnMAP rot (672 nm)	1.2850	1.3191	1.1450	1.1993	1.2130	1.0033	1.2363	1.1403	1.6617	1.5893	1.4993	1.4340	1.3257	1.1551	1.3077	1.3401	1.3611	1.3237	1.2528	1.1365	1.1668
ANIF EnMAP NIR (864 nm)	1.2153	1.2648	1.3041	1.2652	1.0412	0.7864	0.9538	0.9978	1.1442	1.1516	1.1931	1.2563	1.4240	1.2541	1.3490	1.4812	1.5187	1.4689	1.3722	1.2730	0.9934
Rel. Blue Absorption Depth	1.2516	1.2880	1.4265	1.3629	1.0856	0.8644	1.0214	1.0963	1.0822	1.1364	1.2220	1.2904	1.4718	1.5786	1.5627	1.6594	1.6710	1.6563	1.5809	1.4324	1.0764
Rel. Red Absorption Depth	6.9751	7.0867	8.4952	7.8407	6.3085	5.5853	5.6208	6.3974	5.0075	5.2697	5.8153	6.4665	8.1010	8.0264	7.7071	8.3080	8.4794	8.3872	8.2298	8.3915	6.1839
NDVI (EnMAP)	0.9066	0.9078	0.9218	0.9159	0.8976	0.8884	0.8867	0.8994	0.8739	0.8798	0.8900	0.8995	0.9173	0.9181	0.9140	0.9195	0.9203	0.9198	0.9188	0.9206	0.8968
Nadir Norm. NDVI (AVHRR)	0.9891	0.9909	1.0071	0.9955	0.9859	0.9809	0.9700	0.9827	0.9409	0.9468	0.9571	0.9695	0.9924	0.9894	0.9828	0.9877	0.9875	0.9889	0.9904	1.0010	0.9811
Nadir Norm. NDVI (MODIS)	0.9905	0.9922	1.0079	0.9973	0.9861	0.9795	0.9711	0.9839	0.9457	0.9521	0.9623	0.9742	0.9957	0.9936	0.9874	0.9924	0.9924	0.9933	0.9942	1.0031	0.9819
Nadir Norm. NDVI (EnMAP)	0.9947	0.9960	1.0114	1.0048	0.9848	0.9747	0.9728	0.9868	0.9588	0.9653	0.9764	0.9869	1.0064	1.0074	1.0028	1.0089	1.0097	1.0092	1.0081	1.0100	0.9839

(cont.)

FBG4_03 (SZA = 60°; SAA = 254°)	Viewing Geometry (Viewing Zenith Angle | Viewing Azimuth Angle)																							
	20|135	20|157.5	20|170	30|180	30|190	30|202.5	30|225	30|270	30|315	30|337.5	30|350	30|0	30|10	30|22.5	30|45	30|90	30|135	30|157.5	30|170			
HCRF EnMAP blue (479 nm)	0.0112	0.0117	0.0145	0.0188	0.0203	0.0186	0.0158	0.0133	0.0132	0.0124	0.0134	0.0136	0.0134	0.0122	0.0112	0.0118	0.0141	0.0164	0.0197					
HCRF EnMAP green (549 nm)	0.0343	0.0358	0.0449	0.0594	0.0697	0.0682	0.0584	0.0581	0.0693	0.0618	0.0638	0.0672	0.0683	0.0576	0.0472	0.0447	0.0475	0.0543	0.0610					
HCRF EnMAP rot (672 nm)	0.0142	0.0146	0.0179	0.0234	0.0251	0.0220	0.0196	0.0159	0.0166	0.0155	0.0167	0.0174	0.0173	0.0154	0.0139	0.0151	0.0169	0.0199	0.0253					
HCRF EnMAP NIR (864 nm)	0.2277	0.2453	0.2798	0.3260	0.3644	0.3780	0.3456	0.3832	0.4130	0.3806	0.3839	0.4057	0.4076	0.3643	0.3160	0.2892	0.2915	0.3068	0.3299					
ANIF EnMAP rot (672 nm)	1.2995	1.3363	1.6392	2.1502	2.3047	2.0172	1.8023	1.4623	1.5205	1.4220	1.5347	1.5996	1.5861	1.4173	1.2796	1.3829	1.5527	1.8301	2.3194					
ANIF EnMAP NIR (864 nm)	0.9686	1.0435	1.1900	1.3868	1.5497	1.6077	1.4702	1.6300	1.7565	1.6186	1.6329	1.7254	1.7337	1.5497	1.3439	1.2303	1.2399	1.3049	1.4031					
Rel. Blue Absorption Depth	1.0300	1.0395	1.0683	1.0990	1.2220	1.3203	1.3065	1.5655	1.8747	1.7765	1.6967	1.7641	1.8235	1.6906	1.4980	1.3386	1.1855	1.1608	1.0783					
Rel. Red Absorption Depth	5.3376	5.6334	5.3551	4.6266	4.8951	5.8343	6.0441	8.4845	8.8032	8.6157	8.0243	8.2253	8.3129	8.2093	7.7965	6.5367	5.8031	5.1818	4.3250					
NDVI (EnMAP)	0.8830	0.8880	0.8800	0.8660	0.8711	0.8901	0.8925	0.9202	0.9229	0.9218	0.9165	0.9176	0.9187	0.9187	0.9155	0.9010	0.8903	0.8780	0.8577					
Nadir Norm. NDVI (AVHRR)	0.9592	0.9679	0.9516	0.9272	0.9242	0.9456	0.9599	0.9934	0.9810	0.9840	0.9765	0.9784	0.9764	0.9833	0.9865	0.9709	0.9584	0.9381	0.9172					
Nadir Norm. NDVI (MODIS)	0.9614	0.9697	0.9557	0.9338	0.9322	0.9534	0.9656	0.9976	0.9884	0.9899	0.9827	0.9846	0.9830	0.9886	0.9903	0.9752	0.9630	0.9446	0.9240					
Nadir Norm. NDVI (EnMAP)	0.9687	0.9743	0.9655	0.9501	0.9557	0.9766	0.9792	1.0096	1.0125	1.0113	1.0056	1.0068	1.0079	1.0080	1.0045	0.9885	0.9768	0.9633	0.9411					

V *Main Spectral Characteristics*

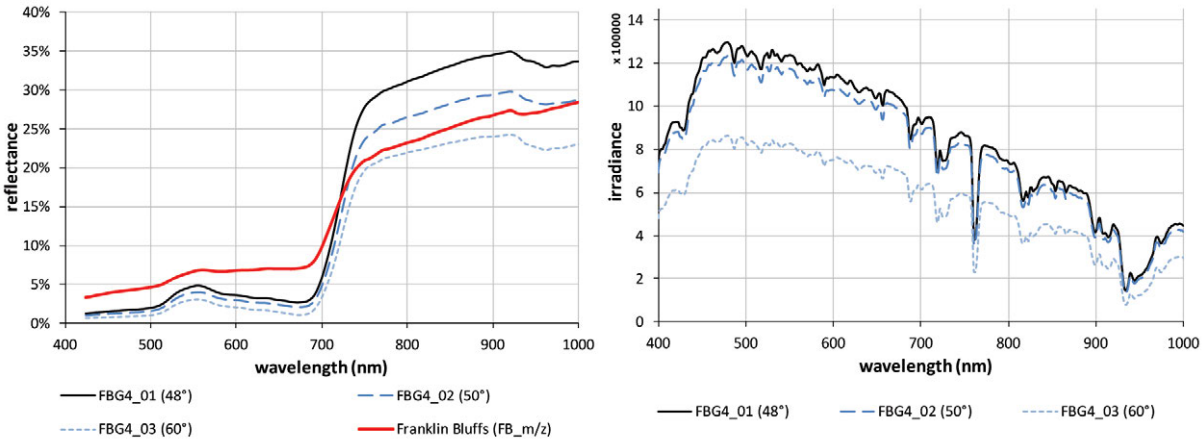

Figure C.4-6: Nadir reflectances and irradiance profiles of the FBG4 site at different sun zenith angles. Left: Comparison of the nadir reflectance signatures with the average zonal vegetation (MNT). Right: Comparison of the total irradiance profiles.

VI *HCRF Visualization*

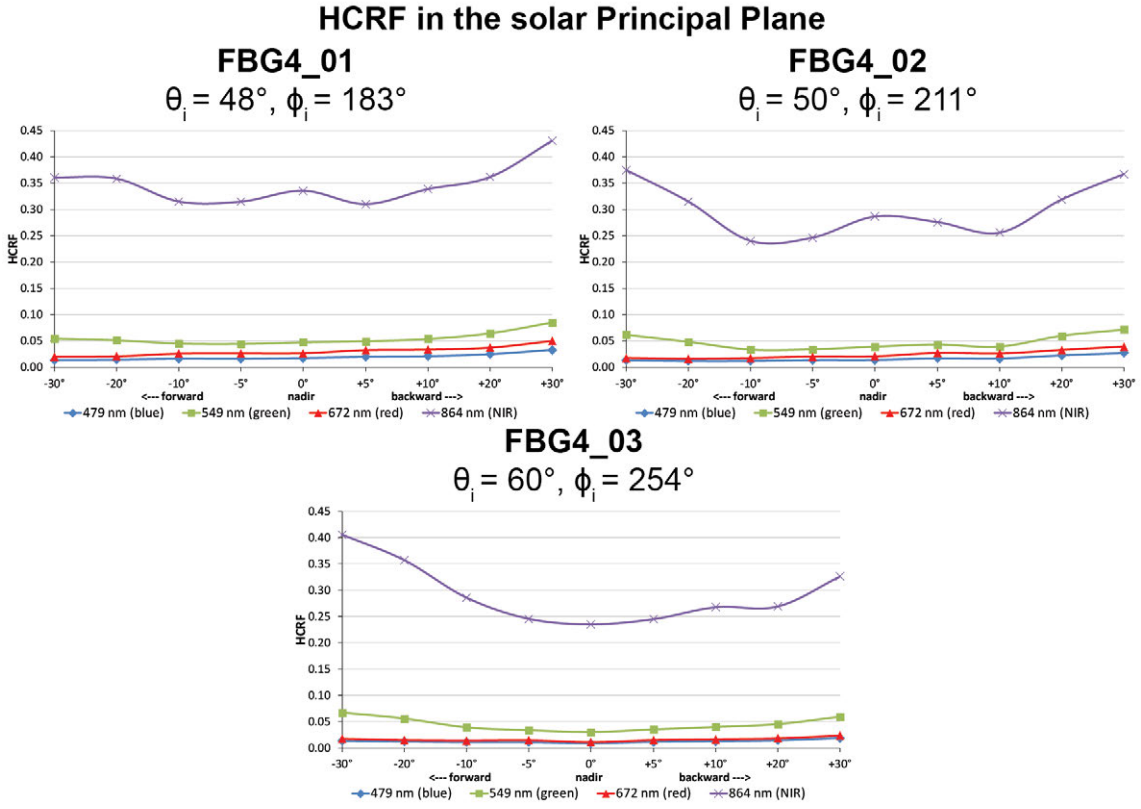

Figure C.4-7: Comparison of the HCRF values at 479 nm (blue), 549 nm (green), 672 nm (red), and 864 nm (NIR) in the solar principal plane of the FBG4 site at different sun zenith angles.

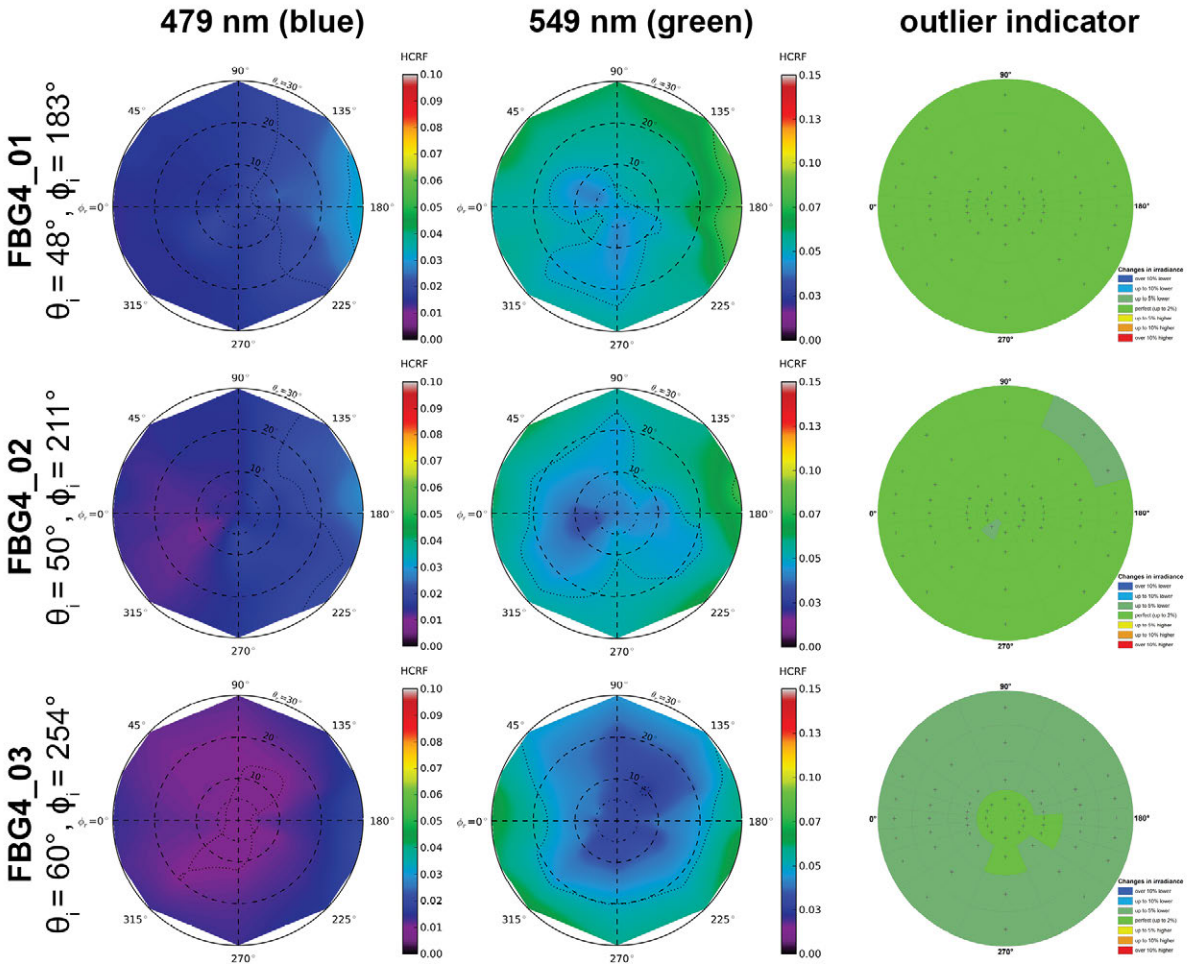

Figure C.4-8: HCRF visualization at 479 nm and 549 nm of the FBG4 site.

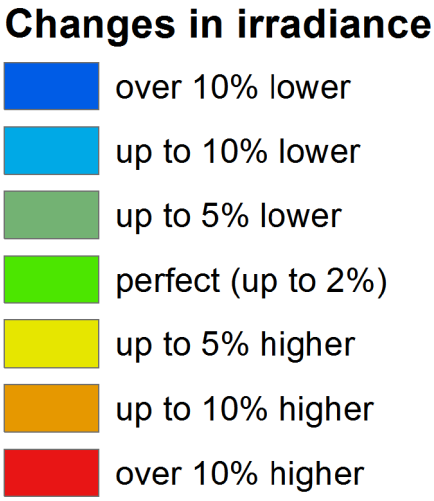

Figure C.4-9: Legend of the outlier indicator graphics shown in Figure C.4-8, C.4-10, and C.4-13

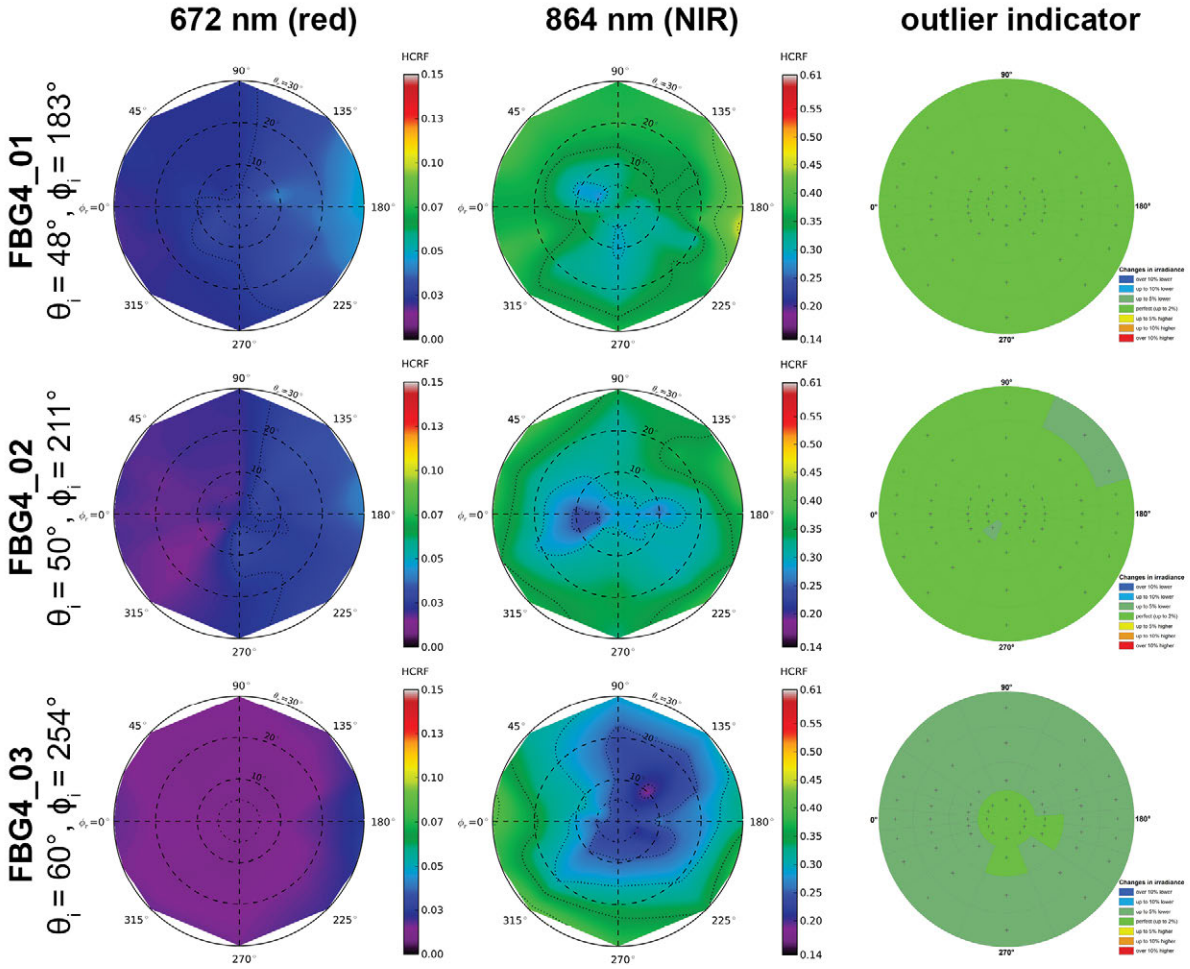

Figure C.4-10: HCRF visualization at 672 nm and 864 nm of the FBG4 site.

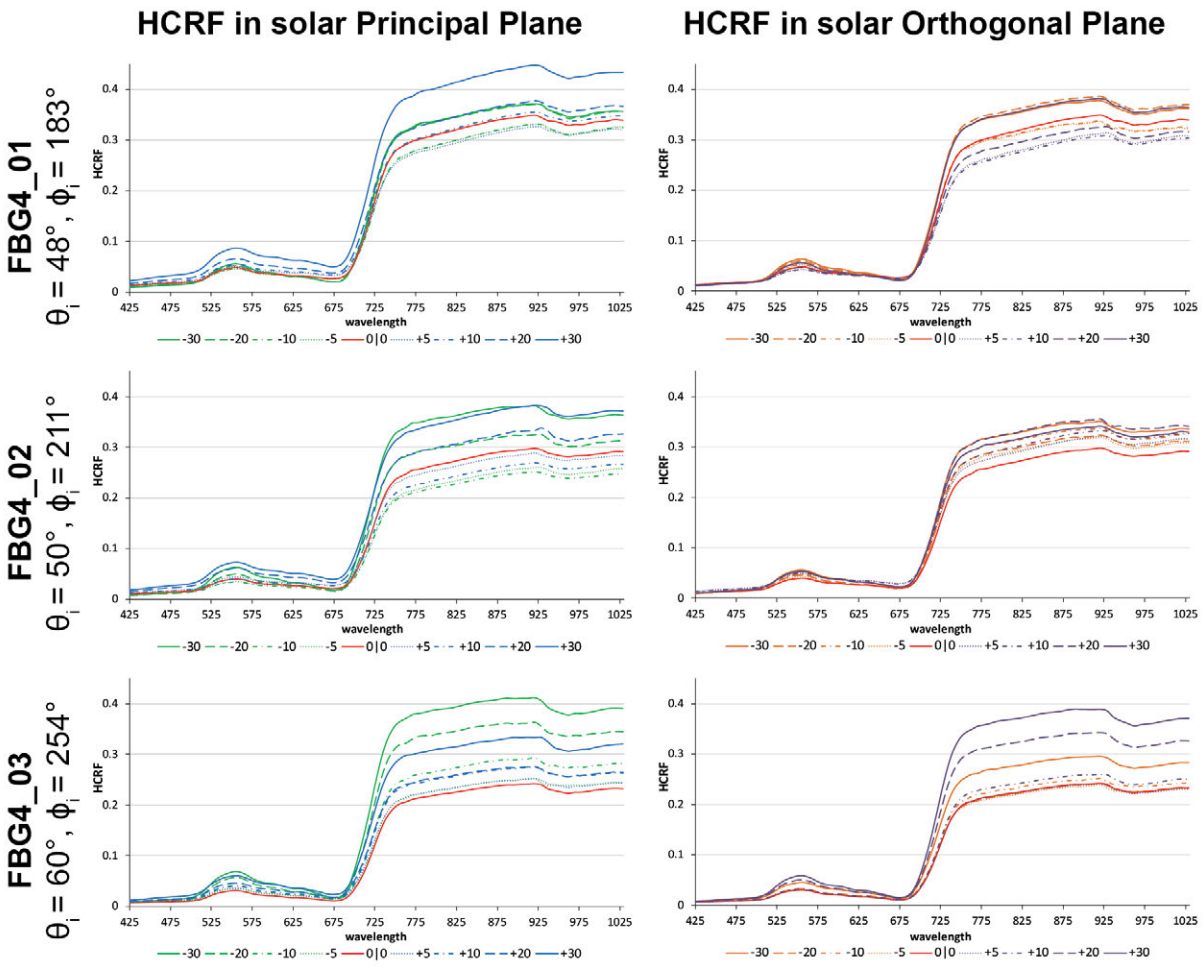

Figure C.4-11: HCRF visualization in principal & orthogonal plane of the FBG4 site.

VII *ANIF Visualization*

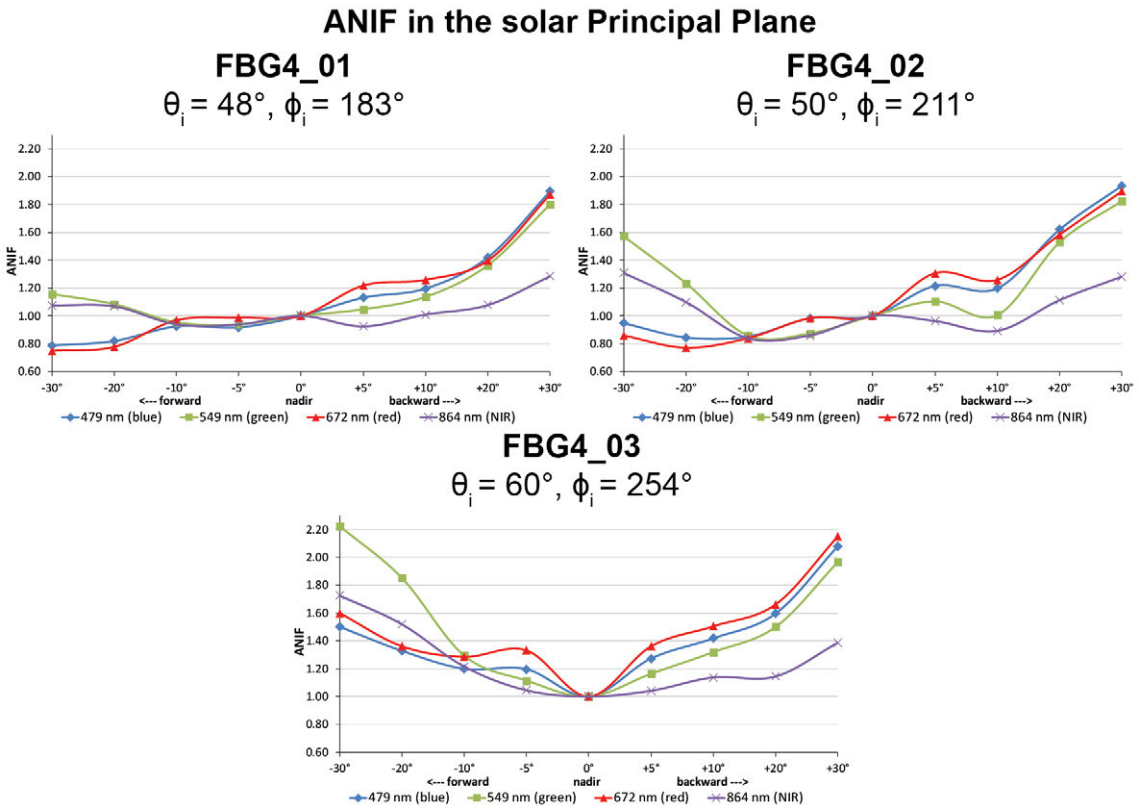

Figure C.4-12: Comparison of the ANIF values at 479 nm (blue), 549 nm (green), 672 nm (red), and 864 nm (NIR) in the solar principal plane of the FBG4 site at different sun zenith angles.

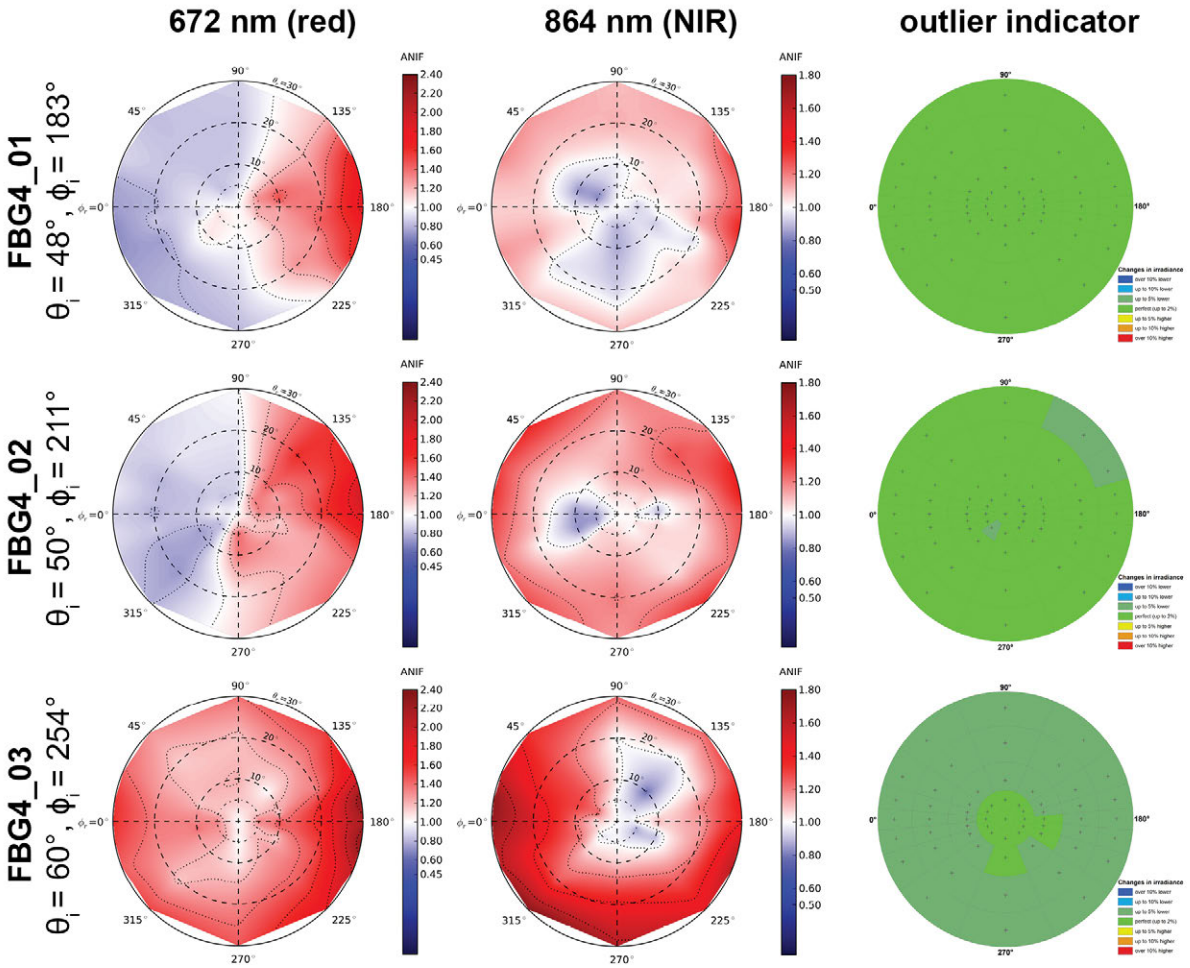

Figure C.4-13: ANIF visualization at 672 nm and 864 nm of the FBG4 site.

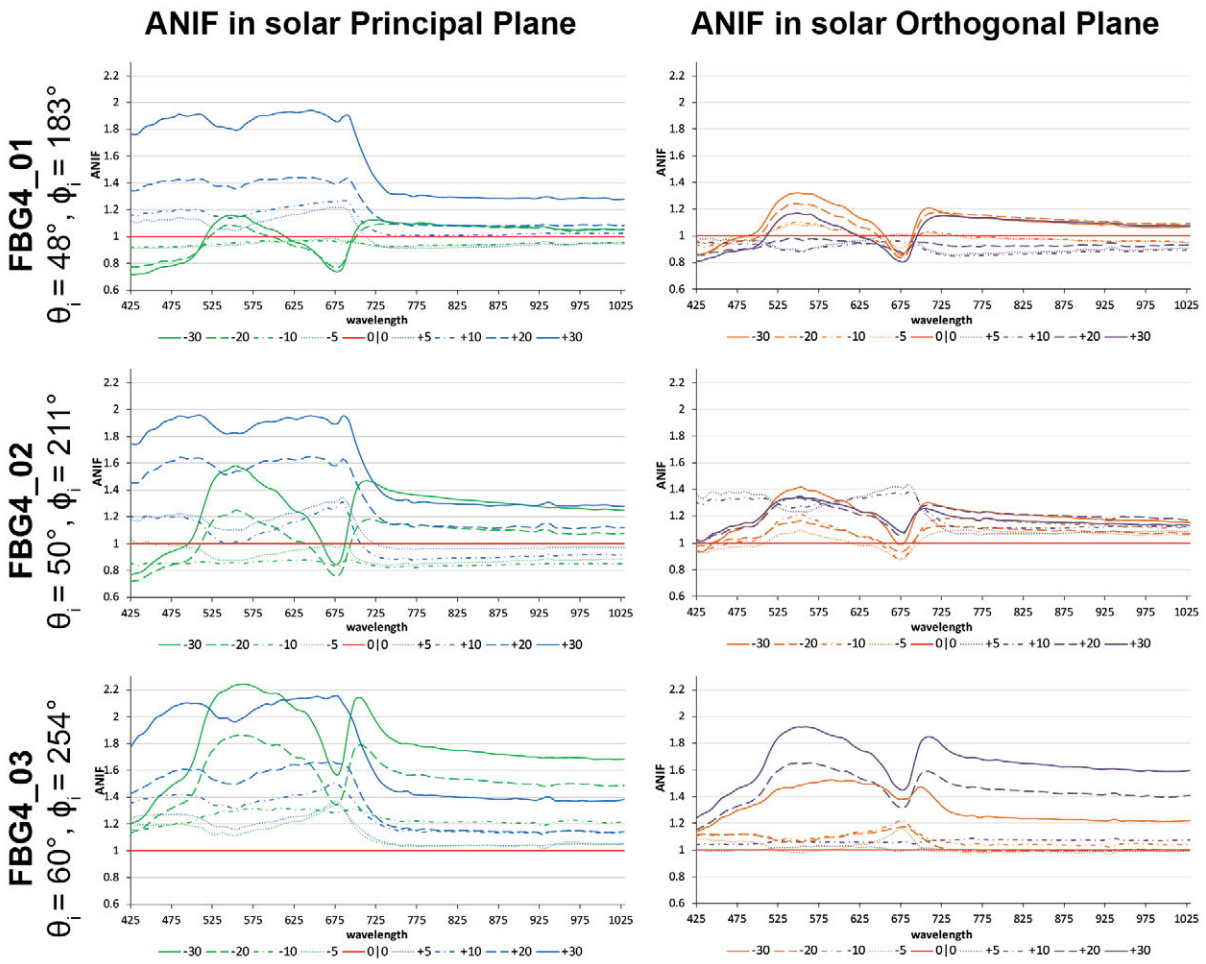

Figure C.4-14: ANIF visualization in principal & orthogonal plane of the FBG4 site.

VIII *ANIX Visualization*

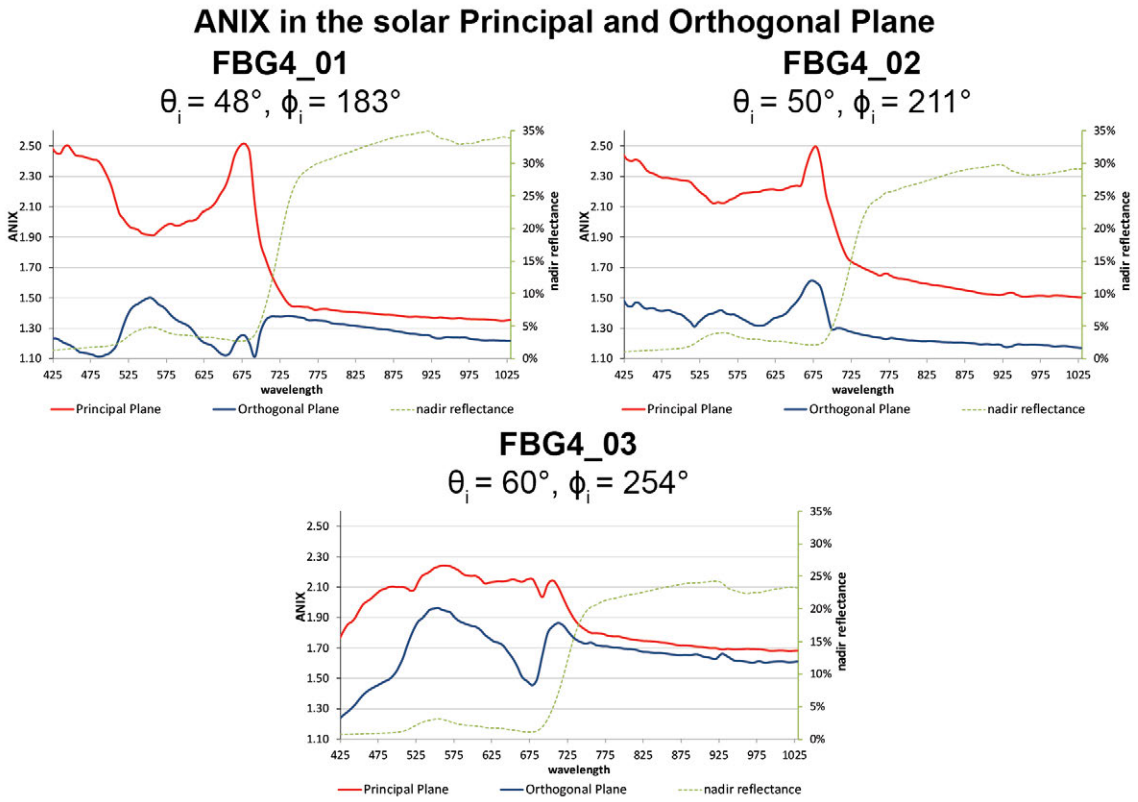

Figure C.4-15: Comparison of the ANIX in the solar principal and orthogonal plane with the nadir reflectance of the FBG4 site at different sun zenith angles.

IX *NDVI and Relative Absorption Depth Visualization*

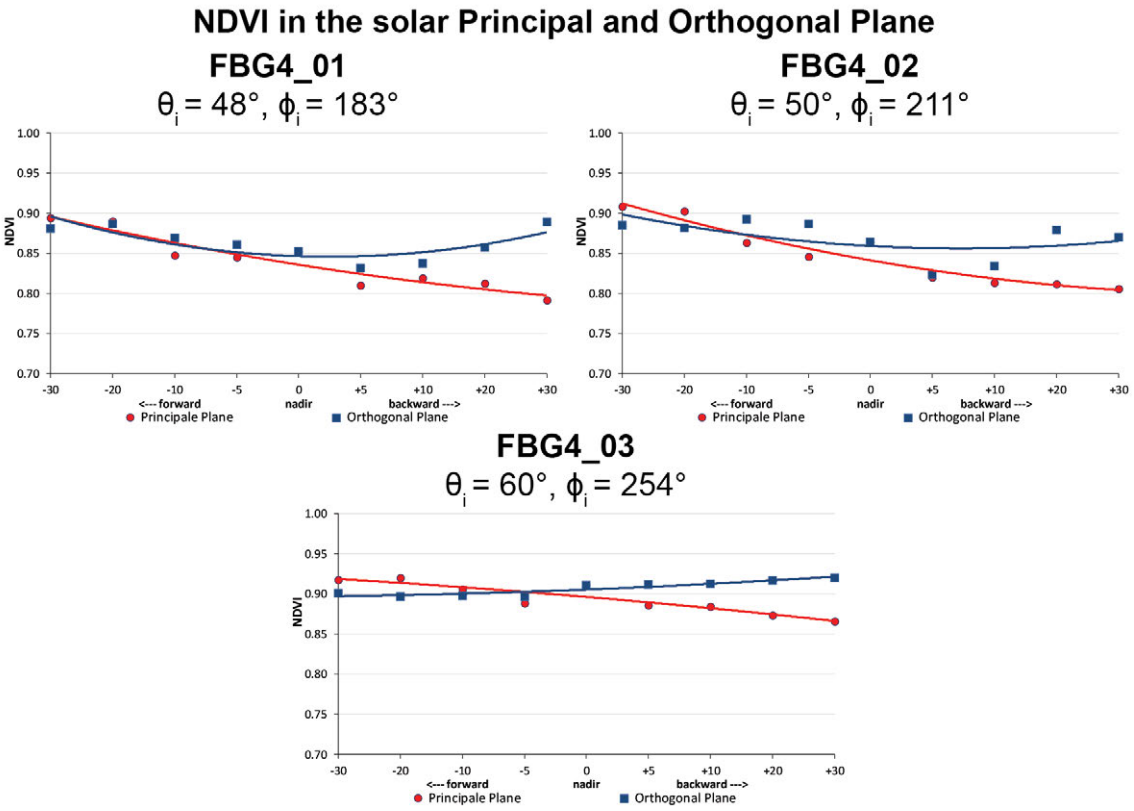

Figure C.4-16: Comparison of the NDVI in the solar principal and orthogonal plane of the FBG4 site at different sun zenith angles.

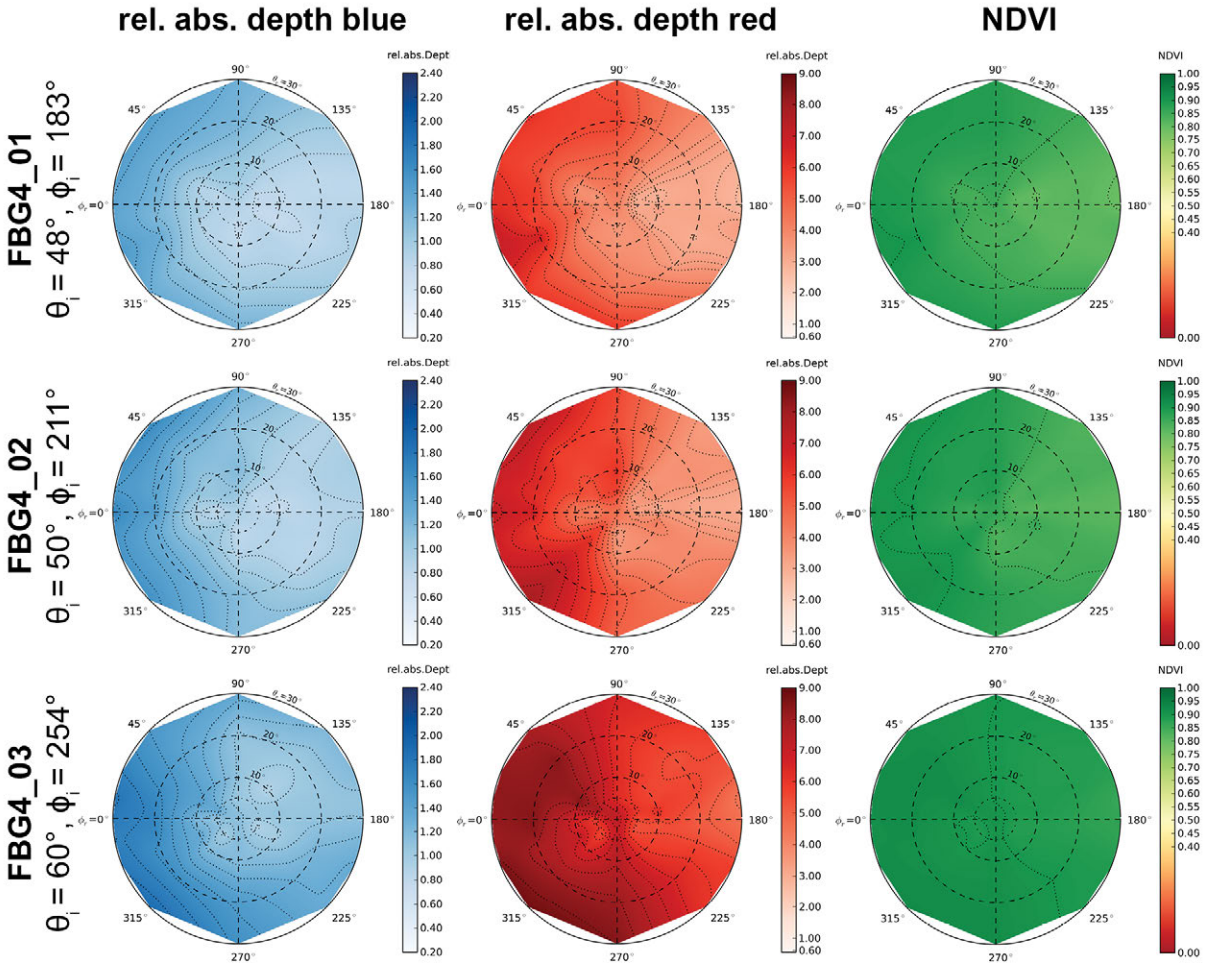

Figure C.4-17: Visualization of relative absorption depth & NDVI of the FBG4 site.

X *NDVI Comparison of Different Sensors*

Table C.4-5: Center wavelengths and band widths of the broadband and narrowband NDVIs, based on the spectral response curves of the AVHRR, MODIS and EnMAP sensors.

NDVI	Sensor	Sensor band	Center wavelength (nm)	band width (nm)
$NDVI_{AVHRR}$ [broadband]	AVHRR/3	red: band 1 NIR: band 2	630 865	100 275
$NDVI_{MODIS}$ [broadband]	MODIS	red: band 1 NIR: band 2	645 859	50 35
$NDVI_{EnMAP}$ [narrowband]	EnMAP	red: band 47 NIR: band 73	672 864	6.5 8

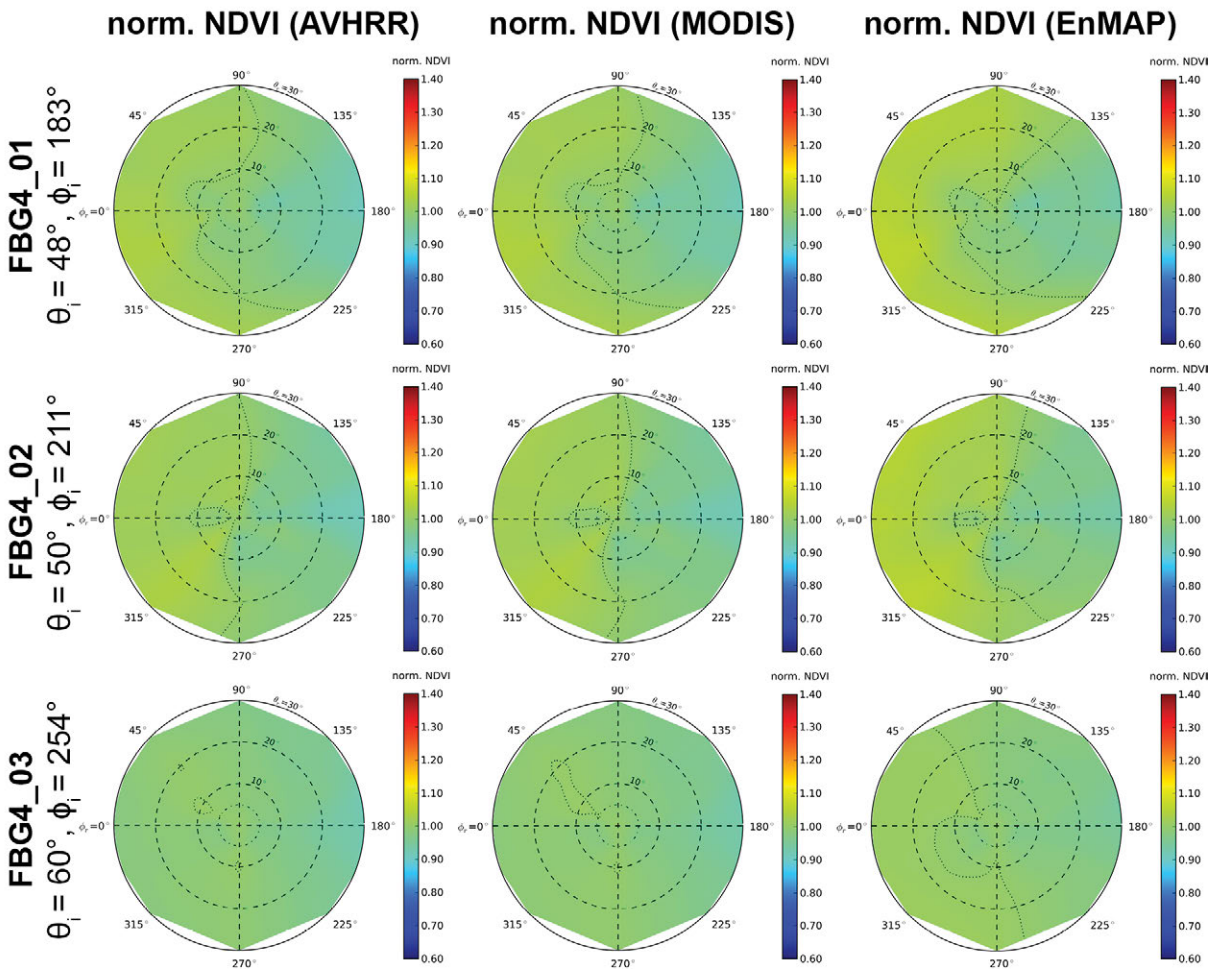

Figure C.4-18: Comparison of AVHRR, MODIS & EnMAP NDVI of the FBG4 site.

C.5 Study site HVG1 (tussock sedge, dwarf shrub, moss tundra)

I *Location*

Name	Location	Latitude	Longitude	Altitude
HVG1	Happy Valley, Arctic North Slope, Alaska, United States of America	69.146897°	-148.85183°	325 m

Happy Valley is located just west of the Dalton Highway in the foothills of the Arctic Slope approximately 82 km (52 mi) north of Toolik Lake, Alaska at an elevation of about 320 m. Within the five subzones of the circumpolar Arctic, Happy Valley is found in subzone E. Green mile marker 334 is positioned just before the turn-off to the site. Three 10 x 10 m grids, designated at the hill crest, midslope and at the footslope have been established at this location in 2002. The goniometer measurements have been carried out next to the midslope / zonal site (HV_ms/z). [*Barreda et al.*, 2006]

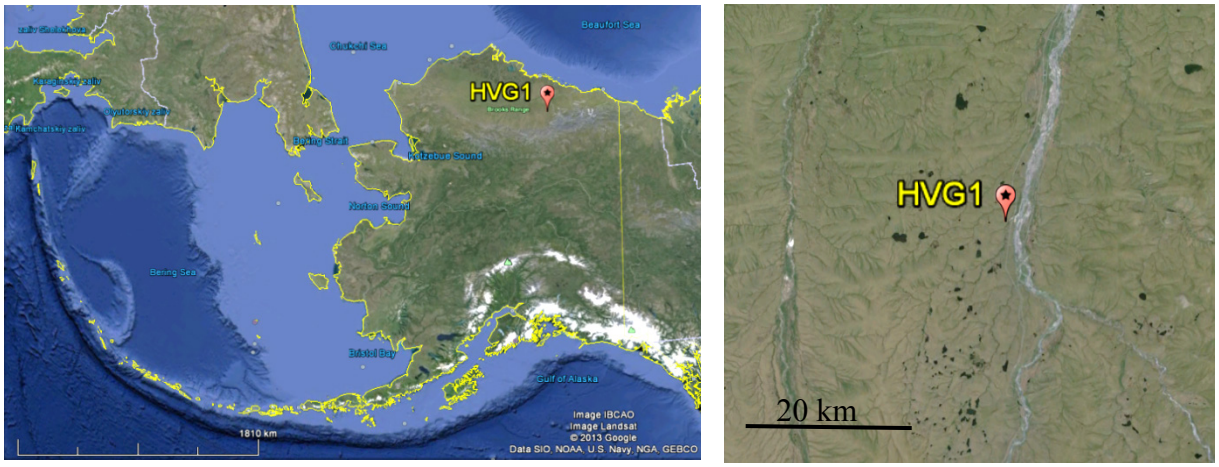

Figure C.5-1: Location of study site HVG1 in Alaska, USA. *Source:* Google Earth, 2013

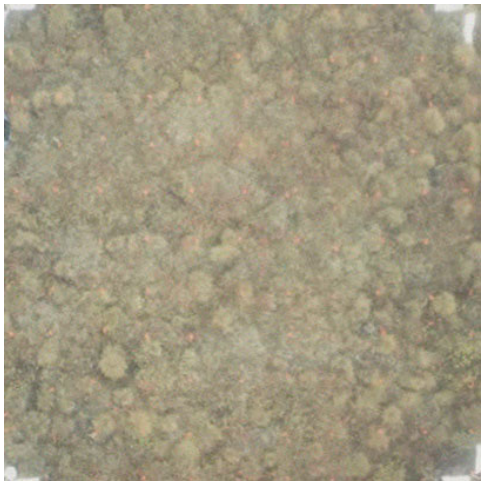

Figure C.5-2: Aerial photo of a 10x10 m zonal grid at the Happy Valley study location near the HVG1 site. *Source:* [*Barreda et al.*, 2006]

II *Main Vegetation Description*

The vegetation at the mesic Happy Valley study location corresponds to the zonal vegetation in subzone E. The zonal plant community of bioclimate subzone E in northern Alaska is *Sphagno- Eriophoretum vaginati* [*Walker et al.*, 1994], also called moist acidic tundra (MAT), 'acidic tussock tundra' or 'tussock-sedge, dwarf-shrub, moss tundra' [*Walker et al.*, 2005]. It occurs widely across the foothills of northern Alaska on old upland surfaces not glaciated during the Last Glacial Maximum. At Happy Valley the average soil pH of this plant community is 5.3; the average volumetric soil moisture of the top mineral horizon is 44 %, and average depth of thaw by late summer is 34 cm [*Kade et al.*, 2005]. The vegetation is composed of a mixture of tussock sedges (*Eriophorum vaginatum*), deciduous dwarf shrubs (e.g., *Betula nana, Salix planifolia* ssp. *pulchra*), evergreen dwarf shrubs (e.g., *Ledum palustre* ssp. *decumbens, Vaccinium vitis-idaea, Cassiope tetragona, Empetrum nigrum*), a few forbs (*Polygonum bistorta* var. *plumosum, Petasites frigidus*), mosses (*Hylocomium splendens, Sphagnum* spp., *Aulacomnium* spp., *Dicranum* spp.) and lichens (*Cladina* spp., *Dactylina arctica*, *Cetraria* spp.).

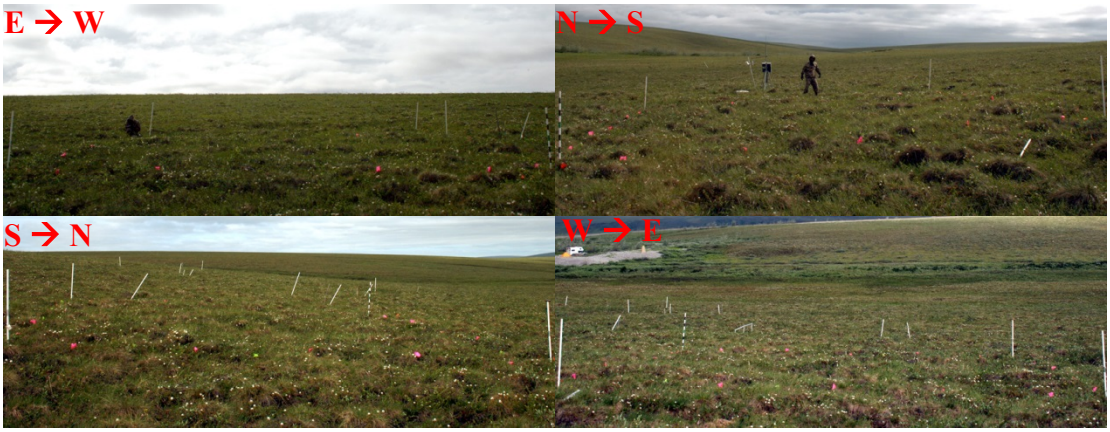

Figure C.5-3: Overview images of MNT tundra at the mesic Happy Valley study location near the HVG1 site. *Source:* [*Buchhorn and Schwieder*, 2012]

III *Vegetation Description of the HVG1 Site*

The focus of the measurements at this goniometer site has been tussock sedge – dwarf shrub – moss tundra. The 1 x 1 m plot is homogeneously covered with this tussock structure, but with forbs, mosses and lichens in the understory. Moreover, this plot correspond with the zonal plant community of Alaskan bioclimate subzone E (MAT vegetation).

Figure C.5-4: Overview images of the HVG1 vegetation from cardinal directions.

Figure C.5-5: Quasi-nadir image of the HVG1 vegetation (tussock sedge).

IV *Overview of the Spectro-Goniometer Measurements*

Table C.5-1: Overview of the spectro-goniometer measurements at the HVG1 study site.

Name	Day	Starting Time	Duration	SAA	SZA	Sky
HVG1_01	2012-06-30	10:17:57	24 min	118°	56°	cirrostratus
HVG1_02	2012-06-30	11:35:48	21 min	139°	50°	clear
HVG1_03	2012-06-30	13:47:45	20 min	179°	46°	clear

Table C.5-2: Spectro-directional data of the HVG1_01 spectro-goniometer measurement.

HVG1_01 (SZA = 56°; SAA = 118°)	Viewing Geometry (Viewing Zenith Angle | Viewing Azimuth Angle)																							
	0|0	5|180	5|202.5	5|225	5|270	5|315	5|337.5	5|0	5|22.5	5|45	5|90	5|135	5|157.5	10|180	10|202.5	10|225	10|270	10|315	10|337.5	10|350
HCRF EnMAP blue (479 nm)	0.0364	0.0362	0.0351	0.0337	0.0468	0.0461	0.0510	0.0365	0.0416	0.0448	0.0398	0.0401	0.0380	0.0360	0.0352	0.0343	0.0430	0.0577	0.0555	0.0393
HCRF EnMAP green (549 nm)	0.0695	0.0714	0.0613	0.0621	0.0827	0.0689	0.0792	0.0578	0.0638	0.0736	0.0711	0.0812	0.0731	0.0734	0.0689	0.0681	0.0803	0.0831	0.0865	0.0620
HCRF EnMAP rot (672 nm)	0.0667	0.0615	0.0577	0.0562	0.0748	0.0756	0.0880	0.0613	0.0722	0.0781	0.0759	0.0739	0.0671	0.0636	0.0607	0.0589	0.0702	0.0924	0.0893	0.0624
HCRF EnMAP NIR (864 nm)	0.3139	0.3101	0.2435	0.2842	0.3690	0.2617	0.2883	0.2237	0.2359	0.2731	0.3098	0.3731	0.3117	0.3243	0.3260	0.2991	0.3290	0.3676	0.2756	0.3004	0.2314
ANIF EnMAP rot (672 nm)	1.0000	0.9225	0.8656	0.8437	1.1226	1.1344	1.3201	0.9196	1.0831	1.1710	1.1391	1.1091	1.0071	0.9545	0.9553	0.9108	0.8838	1.0534	1.3860	1.3397	0.9364
ANIF EnMAP NIR (864 nm)	1.0000	0.9877	0.7756	0.9052	1.1755	0.8335	0.9183	0.7126	0.7513	0.8700	0.9869	1.1884	0.9929	1.0329	1.0384	0.9527	1.0481	1.1710	0.8780	0.9568	0.7371
Rel. Blue Absorption Depth	0.5068	0.5391	0.4513	0.5074	0.4965	0.3607	0.3714	0.3720	0.3498	0.4014	0.4595	0.5597	0.5234	0.5683	0.5587	0.5306	0.5597	0.5264	0.3419	0.3749	0.3736
Rel. Red Absorption Depth	1.4401	1.5558	1.2292	1.5189	1.4475	0.8878	0.8475	0.9621	0.8665	0.9516	1.1934	1.5799	1.4140	1.5782	1.5877	1.4982	1.7314	1.5643	0.7270	0.8899	1.0080
NDVI (EnMAP)	0.6497	0.6690	0.6168	0.6695	0.6628	0.5516	0.5322	0.5698	0.5312	0.5554	0.6063	0.6692	0.6455	0.6719	0.6731	0.6624	0.6962	0.6792	0.4978	0.5416	0.5750
Nadir Norm. NDVI (AVHRR)	1.0000	1.0183	0.9397	1.0220	0.9996	0.8529	0.8263	0.8719	0.8264	0.8575	0.9441	1.0237	0.9854	1.0219	1.0165	1.0030	1.0599	1.0252	0.7669	0.8324	0.8837
Nadir Norm. NDVI (MODIS)	1.0000	1.0228	0.9429	1.0224	1.0002	0.8499	0.8234	0.8696	0.8229	0.8549	0.9431	1.0255	0.9864	1.0236	1.0192	1.0048	1.0618	1.0257	0.7646	0.8318	0.8830
Nadir Norm. NDVI (EnMAP)	1.0000	1.0297	0.9494	1.0306	1.0202	0.8490	0.8192	0.8770	0.8176	0.8549	0.9332	1.0301	0.9937	1.0342	1.0361	1.0197	1.0717	1.0454	0.7663	0.8336	0.8852

(cont.)

HVG1_01 (SZA = 56°; SAA = 118°)	Viewing Geometry (Viewing Zenith Angle | Viewing Azimuth Angle)																							
	10|0	10|10	10|22.5	10|45	10|90	10|135	10|157.5	10|170	20|180	20|190	20|202.5	20|225	20|270	20|315	20|337.5	20|350	20|0	20|10	20|22.5	20|45	20|90
HCRF EnMAP blue (479 nm)	0.0362	0.0375	0.0405	0.0441	0.0418	0.0403	0.0415	0.0383	0.0461	0.0436	0.0412	0.0453	0.0382	0.0510	0.0380	0.0396	0.0351	0.0378	0.0415	0.0430	0.0384
HCRF EnMAP green (549 nm)	0.0561	0.0587	0.0633	0.0709	0.0706	0.0772	0.0787	0.0758	0.0882	0.0844	0.0814	0.0922	0.0802	0.0809	0.0605	0.0582	0.0528	0.0577	0.0648	0.0707	0.0646
HCRF EnMAP rot (672 nm)	0.0582	0.0624	0.0710	0.0766	0.0767	0.0722	0.0724	0.0677	0.0855	0.0782	0.0742	0.0802	0.0679	0.0866	0.0613	0.0639	0.0561	0.0625	0.0706	0.0746	0.0703
HCRF EnMAP NIR (864 nm)	0.2121	0.2238	0.2432	0.2688	0.2817	0.3413	0.3200	0.3249	0.3460	0.3375	0.3482	0.4091	0.3774	0.3022	0.2302	0.2109	0.2039	0.2220	0.2520	0.2751	0.2610
ANIF EnMAP rot (672 nm)	0.8731	0.9365	1.0651	1.1494	1.1504	1.0822	1.0854	1.0155	1.2819	1.1730	1.1135	1.2025	1.0183	1.2995	0.9188	0.9581	0.8409	0.9375	1.0590	1.1196	1.0546
ANIF EnMAP NIR (864 nm)	0.6756	0.7128	0.7748	0.8563	0.8974	1.0870	1.0193	1.0349	1.1020	1.0751	1.1091	1.3032	1.2020	0.9625	0.7333	0.6719	0.6494	0.7071	0.8027	0.8764	0.8315
Rel. Blue Absorption Depth	0.3541	0.3531	0.3684	0.3846	0.4180	0.5158	0.5176	0.5505	0.5101	0.5341	0.5490	0.5840	0.5998	0.3932	0.3849	0.3213	0.3346	0.3487	0.3650	0.3952	0.4089
Rel. Red Absorption Depth	0.9821	0.9727	0.9385	0.9685	1.0518	1.4516	1.3300	1.4701	1.1871	1.2999	1.4223	1.5838	1.6988	0.9287	1.0059	0.8844	0.9708	0.9631	0.9829	1.0533	1.0734
NDVI (EnMAP)	0.5693	0.5637	0.5481	0.5564	0.5720	0.6510	0.6312	0.6551	0.6038	0.6237	0.6485	0.6723	0.6950	0.5543	0.5797	0.5351	0.5686	0.5606	0.5623	0.5732	0.5756
Nadir Norm. NDVI (AVHRR)	0.8741	0.8688	0.8481	0.8606	0.8960	0.9980	0.9631	1.0008	0.9163	0.9443	0.9888	1.0170	1.0528	0.8503	0.8898	0.8362	0.8773	0.8657	0.8653	0.8840	0.8955
Nadir Norm. NDVI (MODIS)	0.8731	0.8670	0.8447	0.8591	0.8942	0.9993	0.9648	1.0025	0.9176	0.9469	0.9898	1.0194	1.0534	0.8478	0.8886	0.8338	0.8750	0.8642	0.8636	0.8842	0.8941
Nadir Norm. NDVI (EnMAP)	0.8763	0.8677	0.8436	0.8564	0.8805	1.0020	0.9715	1.0084	0.9294	0.9601	0.9982	1.0349	1.0698	0.8532	0.8923	0.8237	0.8753	0.8629	0.8655	0.8823	0.8860

(cont.)

HVG1_01 (SZA = 56°; SAA = 118°)	Viewing Geometry (Viewing Zenith Angle | Viewing Azimuth Angle)																							
	20|135	20|157.5	20|170	30|180	30|190	30|202.5	30|225	30|270	30|315	30|337.5	30|350	30|0	30|10	30|122.5	30|45	30|90	30|135	30|157.5	30|170
HCRF EnMAP blue (479 nm)	0.0330	0.0404	0.0434	0.0574	0.0519	0.0436	0.0420	0.0365	0.0473	0.0425	0.0318	0.0337	0.0381	0.0430	0.0455	0.0402	0.0450	0.0521	0.0547					
HCRF EnMAP green (549 nm)	0.0663	0.0809	0.0882	0.1184	0.0998	0.0882	0.0919	0.0663	0.0778	0.0629	0.0492	0.0503	0.0557	0.0628	0.0675	0.0663	0.0858	0.1039	0.1109					
HCRF EnMAP rot (672 nm)	0.0591	0.0739	0.0796	0.1099	0.0977	0.0782	0.0759	0.0632	0.0787	0.0679	0.0525	0.0552	0.0610	0.0686	0.0753	0.0732	0.0825	0.1007	0.1062					
HCRF EnMAP NIR (864 nm)	0.3018	0.3415	0.3636	0.4776	0.3804	0.3554	0.4209	0.3094	0.2937	0.2161	0.2024	0.2004	0.2086	0.2244	0.2408	0.2640	0.3487	0.4224	0.4382					
ANIF EnMAP rot (672 nm)	0.8865	1.1083	1.1931	1.6488	1.4648	1.1725	1.1381	0.9478	1.1806	1.0183	0.7880	0.8285	0.9150	1.0286	1.1287	1.0984	1.2369	1.5099	1.5922					
ANIF EnMAP NIR (864 nm)	0.9613	1.0879	1.1581	1.5214	1.2116	1.1321	1.3408	0.9857	0.9356	0.6885	0.6446	0.6384	0.6644	0.7149	0.7671	0.8410	1.1109	1.3453	1.3959					
Rel. Blue Absorption Depth	0.5443	0.5481	0.5650	0.5794	0.5281	0.5706	0.6428	0.4878	0.4109	0.3152	0.3452	0.3307	0.3143	0.3197	0.3237	0.3919	0.5076	0.5551	0.5640					
Rel. Red Absorption Depth	1.5658	1.4174	1.3929	1.3217	1.1557	1.3519	1.7272	1.4412	1.0374	0.8145	1.0576	0.9973	0.8900	0.8642	0.8483	1.0315	1.2624	1.2769	1.2431					
NDVI (EnMAP)	0.6724	0.6442	0.6410	0.6258	0.5914	0.6394	0.6945	0.6608	0.5773	0.5220	0.5878	0.5679	0.5474	0.5319	0.5238	0.5657	0.6175	0.6150	0.6100					
Nadir Norm. NDVI (AVHRR)	1.0225	0.9835	0.9720	0.9528	0.9030	0.9705	1.0480	1.0083	0.8815	0.8069	0.9113	0.8840	0.8429	0.8212	0.8115	0.8810	0.9452	0.9426	0.9351					
Nadir Norm. NDVI (MODIS)	1.0248	0.9856	0.9744	0.9541	0.9050	0.9727	1.0493	1.0077	0.8820	0.8059	0.9100	0.8818	0.8418	0.8215	0.8101	0.8793	0.9463	0.9427	0.9363					
Nadir Norm. NDVI (EnMAP)	1.0351	0.9917	0.9866	0.9633	0.9103	0.9842	1.0691	1.0172	0.8886	0.8034	0.9048	0.8741	0.8426	0.8187	0.8063	0.8708	0.9505	0.9467	0.9390					

Table C.5-3: Spectro-directional data of the HVG1_02 spectro-goniometer measurement.

HVG1_02 (SZA = 50°; SAA = 139°)	Viewing Geometry (Viewing Zenith Angle | Viewing Azimuth Angle)																							
	0|0	5|180	5|202.5	5|225	5|270	5|315	5|337.5	5|0	5|22.5	5|45	5|90	5|135	5|157.5	10|180	10|190	10|202.5	10|225	10|270	10|315	10|337.5	10|350
HCRF EnMAP blue (479 nm)	0.0514	0.0379	0.0481	0.0619	0.0551	0.0680	0.0410	0.0423	0.0437	0.0485	0.0472	0.0432	0.0385	0.0351	0.0355	0.0365	0.0568	0.0621	0.0617	0.0387	0.0373
HCRF EnMAP green (549 nm)	0.0921	0.0644	0.0786	0.0939	0.0903	0.0974	0.0649	0.0682	0.0731	0.0822	0.0877	0.0796	0.0771	0.0701	0.0680	0.0667	0.0933	0.0992	0.0953	0.0587	0.0585
HCRF EnMAP rot (672 nm)	0.0932	0.0608	0.0731	0.0910	0.0844	0.1057	0.0651	0.0731	0.0782	0.0891	0.0845	0.0764	0.0647	0.0595	0.0571	0.0598	0.0890	0.0964	0.0985	0.0624	0.0621
HCRF EnMAP NIR (864 nm)	0.3461	0.2313	0.2785	0.3146	0.3374	0.2876	0.2328	0.2493	0.2664	0.2968	0.3444	0.3078	0.3095	0.2781	0.2661	0.2729	0.3485	0.3583	0.3057	0.2005	0.2158
ANIF EnMAP rot (672 nm)	1.0000	0.6521	0.7847	0.9762	0.9061	1.1337	0.6984	0.7844	0.8389	0.9557	0.9068	0.8200	0.6937	0.6388	0.6126	0.6414	0.9550	1.0340	1.0569	0.6692	0.6669
ANIF EnMAP NIR (864 nm)	1.0000	0.6684	0.8047	0.9089	0.9749	0.8310	0.6727	0.7203	0.7698	0.8574	0.9951	0.8894	0.8943	0.8034	0.7687	0.7885	1.0070	1.0351	0.8833	0.5792	0.6234
Rel. Blue Absorption Depth	0.4663	0.4245	0.4329	0.3964	0.4272	0.3242	0.3717	0.3873	0.4080	0.4174	0.4861	0.4873	0.5397	0.5324	0.5044	0.4874	0.4393	0.4232	0.3651	0.3365	0.3538
Rel. Red Absorption Depth	1.0909	1.1144	1.1291	0.9719	1.1444	0.6776	0.9638	0.9542	0.9589	0.9497	1.2316	1.2263	1.4969	1.4435	1.4453	1.3807	1.1172	1.0374	0.8124	0.8396	0.9596
NDVI (EnMAP)	0.5757	0.5839	0.5841	0.5513	0.5997	0.4627	0.5631	0.5466	0.5463	0.5383	0.6060	0.6022	0.6544	0.6473	0.6466	0.6406	0.5932	0.5761	0.5127	0.5254	0.5527
Nadir Norm. NDVI (AVHRR)	1.0000	1.0083	1.0100	0.9405	1.0351	0.8055	0.9661	0.9504	0.9547	0.9470	1.0471	1.0487	1.1117	1.1061	1.1056	1.1035	1.0096	0.9880	0.8844	0.9116	0.9589
Nadir Norm. NDVI (MODIS)	1.0000	1.0109	1.0152	0.9430	1.0345	0.8045	0.9639	0.9466	0.9513	0.9436	1.0478	1.0499	1.1154	1.1085	1.1097	1.1064	1.0120	0.9871	0.8837	0.9086	0.9556
Nadir Norm. NDVI (EnMAP)	1.0000	1.0142	1.0145	0.9577	1.0416	0.8037	0.9780	0.9493	0.9488	0.9350	1.0525	1.0460	1.1367	1.1243	1.1232	1.1127	1.0303	1.0006	0.8905	0.9126	0.9601

(cont.)

HVG1_02 (SZA = 50°; SAA = 139°)	Viewing Geometry (Viewing Zenith Angle | Viewing Azimuth Angle)																							
	10|0	10|10	10|22.5	10|45	10|90	10|135	10|157.5	10|170	20|180	20|190	20|202.5	20|225	20|270	20|315	20|337.5	20|350	20|0	20|10	20|22.5	20|45	20|90
HCRF EnMAP blue (479 nm)	0.0409	0.0399	0.0406	0.0474	0.0485	0.0470	0.0413	0.0396	0.0488	0.0478	0.0612	0.0594	0.0525	0.0452	0.0368	0.0386	0.0418	0.0409	0.0374	0.0362	0.0356
HCRF EnMAP green (549 nm)	0.0652	0.0666	0.0679	0.0771	0.0864	0.0858	0.0833	0.0796	0.0892	0.0935	0.1030	0.1055	0.0861	0.0693	0.0546	0.0588	0.0645	0.0658	0.0633	0.0591	0.0664
HCRF EnMAP rot (672 nm)	0.0714	0.0698	0.0704	0.0842	0.0839	0.0838	0.0721	0.0678	0.0826	0.0794	0.1000	0.1019	0.0892	0.0693	0.0579	0.0631	0.0692	0.0695	0.0635	0.0630	0.0640
HCRF EnMAP NIR (864 nm)	0.2427	0.2519	0.2514	0.2720	0.3313	0.3240	0.3371	0.3221	0.3222	0.3515	0.3503	0.4141	0.3296	0.2315	0.1953	0.2109	0.2333	0.2433	0.2369	0.2188	0.2833
ANIF EnMAP rot (672 nm)	0.7659	0.7490	0.7552	0.9035	0.9008	0.8996	0.7736	0.7273	0.8867	0.8518	1.0726	1.0931	0.9573	0.7432	0.6211	0.6774	0.7422	0.7458	0.6811	0.6763	0.6869
ANIF EnMAP NIR (864 nm)	0.7012	0.7278	0.7263	0.7860	0.9572	0.9361	0.9738	0.9305	0.9309	1.0155	1.0120	1.1964	0.9524	0.6689	0.5642	0.6093	0.6741	0.7028	0.6843	0.6320	0.8184
Rel. Blue Absorption Depth	0.3780	0.4056	0.4080	0.3862	0.4591	0.4855	0.5618	0.5517	0.4937	0.5475	0.4529	0.5005	0.4202	0.3573	0.3276	0.3498	0.3539	0.3800	0.4088	0.3841	0.4825
Rel. Red Absorption Depth	0.9527	1.0164	1.0235	0.9099	1.1762	1.1684	1.4777	1.4912	1.1739	1.3745	1.0179	1.2022	1.0207	0.8785	0.8998	0.9077	0.9269	0.9866	1.0750	0.9840	1.3609
NDVI (EnMAP)	0.5455	0.5660	0.5625	0.5273	0.5957	0.5889	0.6476	0.6523	0.5918	0.6315	0.5560	0.6051	0.5740	0.5394	0.5427	0.5392	0.5427	0.5556	0.5773	0.5527	0.6313
Nadir Norm. NDVI (AVHRR)	0.9545	0.9822	0.9786	0.9303	1.0321	1.0254	1.1085	1.1109	1.0169	1.0818	0.9610	1.0335	0.9954	0.9286	0.9455	0.9390	0.9461	0.9660	1.0010	0.9681	1.0972
Nadir Norm. NDVI (MODIS)	0.9500	0.9787	0.9766	0.9268	1.0333	1.0261	1.1108	1.1138	1.0205	1.0862	0.9636	1.0322	0.9933	0.9270	0.9425	0.9356	0.9428	0.9636	1.0014	0.9651	1.0978
Nadir Norm. NDVI (EnMAP)	0.9475	0.9831	0.9771	0.9158	1.0347	1.0228	1.1248	1.1329	1.0278	1.0969	0.9657	1.0511	0.9970	0.9369	0.9426	0.9366	0.9427	0.9650	1.0027	0.9599	1.0966

(cont.)

HVG1_02 (SZA = 50°; SAA = 139°)	Viewing Geometry (Viewing Zenith Angle | Viewing Azimuth Angle)																							
	20|135	20|157.5	20|170	30|180	30|190	30|202.5	30|225	30|270	30|315	30|337.5	30|350	30|0	30|10	30|22.5	30|45	30|90	30|135	30|157.5	30|170			
HCRF EnMAP blue (479 nm)	0.0413	0.0495	0.0514	0.0638	0.0491	0.0517	0.0683	0.0529	0.0408	0.0324	0.0363	0.0396	0.0354	0.0394	0.0364	0.0386	0.0534	0.0585	0.0615					
HCRF EnMAP green (549 nm)	0.0816	0.0940	0.0958	0.1281	0.1032	0.1099	0.1239	0.0828	0.0615	0.0477	0.0559	0.0606	0.0541	0.0603	0.0545	0.0695	0.1036	0.1179	0.1185					
HCRF EnMAP rot (672 nm)	0.0739	0.0891	0.0891	0.1177	0.0924	0.0910	0.1173	0.0913	0.0646	0.0508	0.0576	0.0623	0.0590	0.0673	0.0628	0.0685	0.0973	0.1086	0.1172					
HCRF EnMAP NIR (864 nm)	0.3246	0.3410	0.3407	0.4631	0.4051	0.4442	0.4714	0.3201	0.2116	0.1816	0.2134	0.2227	0.1987	0.2093	0.1889	0.2796	0.3898	0.4341	0.4180					
ANIF EnMAP rot (672 nm)	0.7930	0.9564	0.9557	1.2631	0.9919	0.9761	1.2588	0.9792	0.6929	0.5450	0.6185	0.6688	0.6327	0.7221	0.6742	0.7350	1.0436	1.1656	1.2574					
ANIF EnMAP NIR (864 nm)	0.9378	0.9851	0.9843	1.3379	1.1704	1.2832	1.3619	0.9249	0.6115	0.5248	0.6166	0.6434	0.5741	0.6047	0.5459	0.8078	1.1263	1.2543	1.2077					
Rel. Blue Absorption Depth	0.5345	0.5150	0.5069	0.5660	0.6003	0.6187	0.5158	0.3820	0.3299	0.3214	0.3566	0.3400	0.3324	0.3364	0.3181	0.4585	0.5284	0.5626	0.5300					
Rel. Red Absorption Depth	1.3670	1.1432	1.1456	1.1822	1.3527	1.5233	1.1859	0.9938	0.8679	0.9788	1.0396	1.0015	0.9031	0.8546	0.8205	1.2425	1.2305	1.2129	1.0594					
NDVI (EnMAP)	0.6291	0.5855	0.5855	0.5946	0.6284	0.6600	0.6014	0.5563	0.5325	0.5630	0.5747	0.5626	0.5424	0.5134	0.5008	0.6065	0.6007	0.5997	0.5621					
Nadir Norm. NDVI (AVHRR)	1.0800	1.0052	1.0059	1.0141	1.0824	1.1242	1.0259	0.9721	0.9321	0.9833	0.9852	0.9694	0.9489	0.9067	0.8908	1.0514	1.0365	1.0276	0.9700					
Nadir Norm. NDVI (MODIS)	1.0830	1.0062	1.0090	1.0165	1.0837	1.1276	1.0278	0.9673	0.9309	0.9820	0.9839	0.9693	0.9462	0.9030	0.8863	1.0513	1.0382	1.0294	0.9708					
Nadir Norm. NDVI (EnMAP)	1.0927	1.0170	1.0170	1.0328	1.0915	1.1464	1.0447	0.9663	0.9249	0.9778	0.9982	0.9772	0.9421	0.8918	0.8699	1.0534	1.0433	1.0417	0.9763					

Table C.5-4: Spectro-directional data of the HVG1_03 spectro-goniometer measurement.

HVG1_03 (SZA = 46°; SAA = 179°)	Viewing Geometry (Viewing Zenith Angle | Viewing Azimuth Angle)																								
	0|0	5|180	5|202.5	5|225	5|270	5|315	5|337.5	5|0	5|22.5	5|45	5|90	5|135	5|157.5	10|180	10|202.5	10|225	10|270	10|315	10|337.5	10|350
HCRF EnMAP blue (479 nm)	0.0334	0.0282	0.0277	0.0299	0.0469	0.0274	0.0261	0.0278	0.0338	0.0276	0.0281	0.0287	0.0282	0.0209	0.0210	0.0264	0.0517	0.0281	0.0244	0.0256
HCRF EnMAP green (549 nm)	0.0650	0.0441	0.0408	0.0466	0.0641	0.0435	0.0433	0.0492	0.0593	0.0546	0.0526	0.0535	0.0449	0.0372	0.0376	0.0361	0.0719	0.0448	0.0413	0.0437
HCRF EnMAP rot (672 nm)	0.0638	0.0414	0.0393	0.0422	0.0687	0.0426	0.0429	0.0483	0.0630	0.0472	0.0494	0.0446	0.0411	0.0349	0.0336	0.0308	0.0756	0.0444	0.0408	0.0442
HCRF EnMAP NIR (864 nm)	0.2781	0.1600	0.1407	0.1624	0.1764	0.1572	0.1634	0.2024	0.2426	0.2526	0.2341	0.2158	0.1698	0.1490	0.1568	0.1621	0.2009	0.1626	0.1618	0.1773
ANIF EnMAP rot (672 nm)	1.0000	0.6495	0.6165	0.6611	1.0775	0.6680	0.6729	0.7570	0.9874	0.7397	0.7750	0.6988	0.6443	0.5470	0.5268	0.4828	0.6109	1.1857	0.6965	0.6394	0.6938
ANIF EnMAP NIR (864 nm)	1.0000	0.5754	0.5058	0.5838	0.6342	0.5651	0.5875	0.7278	0.8724	0.9081	0.8418	0.7761	0.6107	0.5358	0.5638	0.5829	0.6876	0.7223	0.5846	0.5819	0.6377
Rel. Blue Absorption Depth	0.5277	0.3876	0.3504	0.3930	0.3192	0.3772	0.4039	0.4553	0.4542	0.5456	0.4915	0.5026	0.4010	0.4544	0.4633	0.4875	0.4718	0.3192	0.3848	0.4179	0.4263
Rel. Red Absorption Depth	1.3011	1.1320	0.9902	1.1029	0.6149	1.0159	1.0640	1.2220	1.1400	1.6703	1.4535	1.4768	1.2106	1.2651	1.3831	1.5861	1.4425	0.6424	1.0031	1.1229	1.1418
NDVI (EnMAP)	0.6270	0.5888	0.5632	0.5878	0.4393	0.5735	0.5840	0.6149	0.5879	0.6853	0.6514	0.6578	0.6104	0.6207	0.6471	0.6808	0.6616	0.4531	0.5709	0.5975	0.6007
Nadir Norm. NDVI (AVHRR)	1.0000	0.9276	0.8789	0.9170	0.6997	0.9075	0.9303	0.9762	0.9462	1.0793	1.0308	1.0216	0.9606	0.9812	1.0107	1.0565	1.0353	0.7177	0.9060	0.9512	0.9605
Nadir Norm. NDVI (MODIS)	1.0000	0.9351	0.8849	0.9204	0.7004	0.9089	0.9308	0.9773	0.9444	1.0818	1.0334	1.0303	0.9699	0.9845	1.0149	1.0596	1.0373	0.7182	0.9061	0.9529	0.9611
Nadir Norm. NDVI (EnMAP)	1.0000	0.9391	0.8983	0.9375	0.7007	0.9148	0.9315	0.9807	0.9377	1.0930	1.0390	1.0491	0.9736	0.9899	1.0321	1.0858	1.0552	0.7227	0.9106	0.9530	0.9581

(cont.)

HVG1_03 (SZA = 46°; SAA = 179°)	Viewing Geometry (Viewing Zenith Angle | Viewing Azimuth Angle)																								
	10|0	10|10	10|22.5	10|45	10|90	10|135	10|157.5	10|170	20|180	20|190	20|202.5	20|225	20|270	20|315	20|337.5	20|350	20|0	20|10	20|22.5	20|45	20|90
HCRF EnMAP blue (479 nm)	0.0285	0.0327	0.0322	0.0246	0.0295	0.0239	0.0266	0.0253	0.0451	0.0413	0.0304	0.0329	0.0321	0.0232	0.0203	0.0207	0.0220	0.0239	0.0267	0.0242	0.0246
HCRF EnMAP green (549 nm)	0.0513	0.0566	0.0590	0.0460	0.0549	0.0474	0.0460	0.0403	0.0731	0.0682	0.0606	0.0627	0.0504	0.0365	0.0347	0.0352	0.0371	0.0394	0.0438	0.0424	0.0477
HCRF EnMAP rot (672 nm)	0.0497	0.0583	0.0596	0.0414	0.0516	0.0380	0.0388	0.0375	0.0720	0.0674	0.0530	0.0563	0.0495	0.0360	0.0332	0.0351	0.0375	0.0419	0.0472	0.0428	0.0413
HCRF EnMAP NIR (864 nm)	0.2220	0.2339	0.2552	0.2156	0.2336	0.2025	0.1826	0.1491	0.2493	0.2405	0.2589	0.2701	0.1742	0.1446	0.1449	0.1509	0.1661	0.1725	0.1864	0.1925	0.2159
ANIF EnMAP rot (672 nm)	0.7795	0.9144	0.9345	0.6497	0.8086	0.5959	0.6078	0.5888	1.1292	1.0572	0.8305	0.8832	0.7766	0.5646	0.5208	0.5509	0.5882	0.6564	0.7396	0.6708	0.6472
ANIF EnMAP NIR (864 nm)	0.7984	0.8410	0.9176	0.7753	0.8399	0.7282	0.6565	0.5362	0.8964	0.8647	0.9311	0.9712	0.6264	0.5199	0.5212	0.5427	0.5974	0.6202	0.6702	0.6923	0.7762
Rel. Blue Absorption Depth	0.4689	0.4369	0.4856	0.4957	0.4872	0.5432	0.4501	0.3899	0.4404	0.4395	0.5541	0.5216	0.3773	0.3622	0.4057	0.4064	0.4031	0.3909	0.3858	0.4326	0.5113
Rel. Red Absorption Depth	1.3177	1.1670	1.2947	1.5972	1.3689	1.6483	1.4280	1.1520	0.9860	1.0084	1.4570	1.4122	0.9262	1.1080	1.2472	1.2468	1.2811	1.1834	1.1457	1.3579	1.6137
NDVI (EnMAP)	0.6342	0.6009	0.6214	0.6777	0.6384	0.6840	0.6498	0.5978	0.5518	0.5621	0.6604	0.6550	0.5573	0.6013	0.6272	0.6224	0.6317	0.6094	0.5961	0.6365	0.6790
Nadir Norm. NDVI (AVHRR)	1.0052	0.9602	0.9927	1.0708	1.0057	1.0578	1.0177	0.9434	0.8708	0.8889	1.0285	1.0240	0.8727	0.9465	0.9908	0.9926	1.0050	0.9755	0.9600	1.0169	1.0603
Nadir Norm. NDVI (MODIS)	1.0058	0.9591	0.9926	1.0725	1.0094	1.0656	1.0259	0.9504	0.8757	0.8918	1.0302	1.0240	0.8724	0.9473	0.9927	0.9927	1.0048	0.9753	0.9595	1.0175	1.0654
Nadir Norm. NDVI (EnMAP)	1.0116	0.9584	0.9911	1.0808	1.0182	1.0910	1.0364	0.9534	0.8802	0.8965	1.0533	1.0446	0.8889	0.9591	1.0004	0.9927	1.0075	0.9720	0.9508	1.0151	1.0830

(cont.)

HVG1_03 (SZA = 46°; SAA = 179°)	Viewing Geometry (Viewing Zenith Angle | Viewing Azimuth Angle)																								
	20|135	20|157.5	20|170	30|180	30|190	30|202.5	30|225	30|270	30|315	30|337.5	30|350	30|0	30|10	30|122.5	30|45	30|90	30|135	30|157.5	30|170					
HCRF EnMAP blue (479 nm)	0.0455	0.0524	0.0493	0.0408	0.0499	0.0529	0.0423	0.0420	0.0318	0.0257	0.0228	0.0207	0.0203	0.0245	0.0250	0.0321	0.0408	0.0370	0.0408						
HCRF EnMAP green (549 nm)	0.0747	0.0852	0.0772	0.0907	0.0906	0.0940	0.0694	0.0624	0.0448	0.0392	0.0372	0.0330	0.0325	0.0405	0.0419	0.0625	0.0867	0.0835	0.0861						
HCRF EnMAP rot (672 nm)	0.0700	0.0766	0.0737	0.0728	0.0830	0.0858	0.0737	0.0676	0.0477	0.0389	0.0361	0.0337	0.0333	0.0422	0.0433	0.0579	0.0760	0.0666	0.0753						
HCRF EnMAP NIR (864 nm)	0.2521	0.2835	0.2464	0.3792	0.3397	0.3507	0.2861	0.1953	0.1565	0.1528	0.1560	0.1382	0.1417	0.1758	0.1863	0.2758	0.3551	0.3540	0.3563						
ANIF EnMAP rot (672 nm)	1.0984	1.2019	1.1559	1.1412	1.3013	1.3455	1.1551	1.0595	0.7482	0.6093	0.5664	0.5292	0.5226	0.6616	0.6788	0.9087	1.1917	1.0445	1.1814						
ANIF EnMAP NIR (864 nm)	0.9065	1.0193	0.8860	1.3633	1.2215	1.2611	1.0286	0.7023	0.5627	0.5494	0.5608	0.4968	0.5095	0.6321	0.6700	0.9919	1.2770	1.2729	1.2812						
Rel. Blue Absorption Depth	0.4409	0.4410	0.4141	0.6673	0.5155	0.5075	0.4187	0.3327	0.3139	0.3455	0.3817	0.3617	0.3570	0.3890	0.3965	0.5294	0.6142	0.6699	0.6185						
Rel. Red Absorption Depth	1.0443	1.0689	0.9284	1.6331	1.2049	1.1673	1.1229	0.7558	0.8503	1.0777	1.2349	1.1481	1.1881	1.2072	1.2679	1.4656	1.4356	1.6548	1.4627						
NDVI (EnMAP)	0.5652	0.5744	0.5395	0.6780	0.6074	0.6069	0.5905	0.4860	0.5327	0.5945	0.6239	0.6074	0.6193	0.6129	0.6230	0.6528	0.6475	0.6833	0.6510						
Nadir Norm. NDVI (AVHRR)	0.8888	0.8951	0.8441	1.0541	0.9414	0.9400	0.9400	0.7858	0.8428	0.9330	0.9796	0.9667	0.9838	0.9815	0.9985	1.0297	1.0059	1.0586	1.0186						
Nadir Norm. NDVI (MODIS)	0.8972	0.9038	0.8514	1.0582	0.9456	0.9450	0.9356	0.7850	0.8445	0.9352	0.9829	0.9678	0.9841	0.9817	0.9983	1.0334	1.0105	1.0622	1.0206						
Nadir Norm. NDVI (EnMAP)	0.9014	0.9161	0.8605	1.0813	0.9688	0.9680	0.9418	0.7752	0.8496	0.9483	0.9951	0.9688	0.9877	0.9776	0.9937	1.0413	1.0327	1.0899	1.0383						

V *Main Spectral Characteristics*

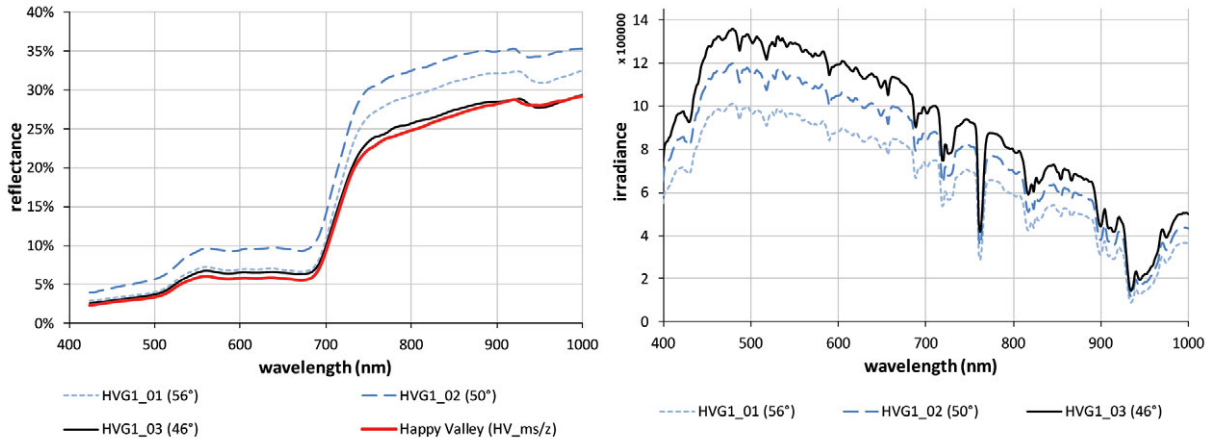

Figure C.5-6: Nadir reflectances and irradiance profiles of the HVG1 site at different sun zenith angles. Left: Comparison of the nadir reflectance signatures with the average zonal vegetation (MAT). Right: Comparison of the total irradiance profiles.

VI *HCRF Visualization*

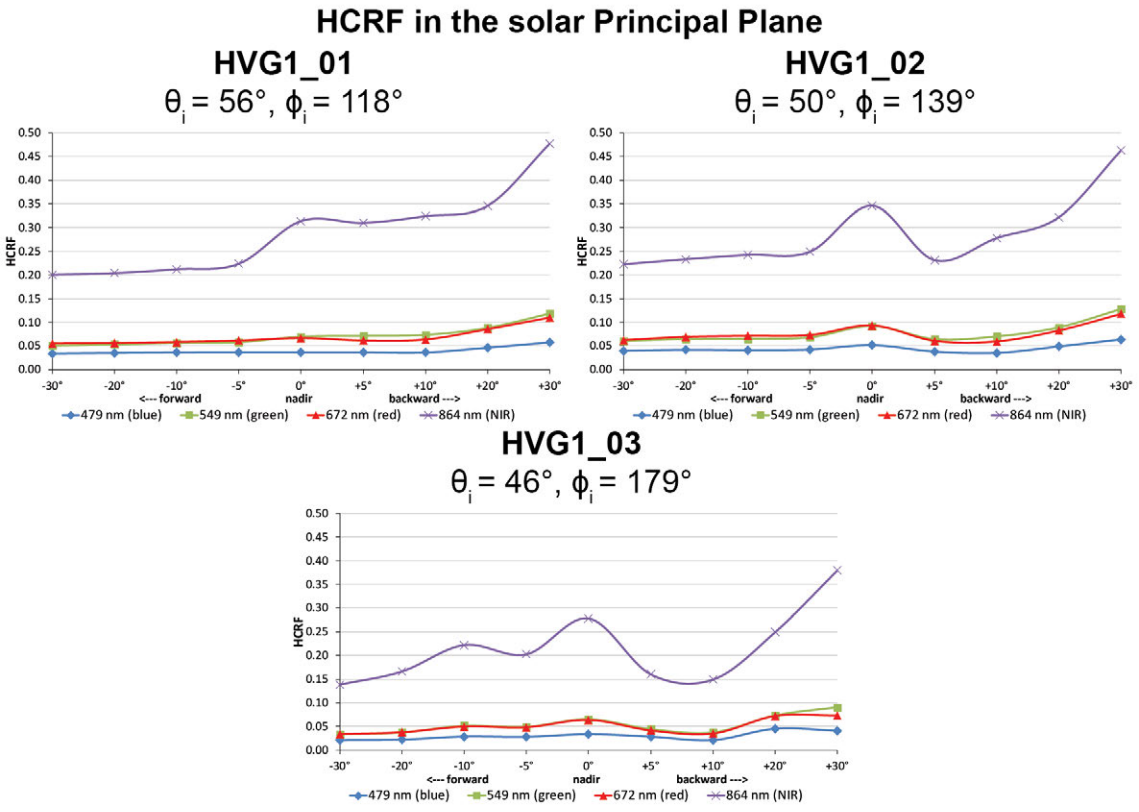

Figure C.5-7: Comparison of the HCRF values at 479 nm (blue), 549 nm (green), 672 nm (red), and 864 nm (NIR) in the solar principal plane of the HVG1 site at different sun zenith angles.

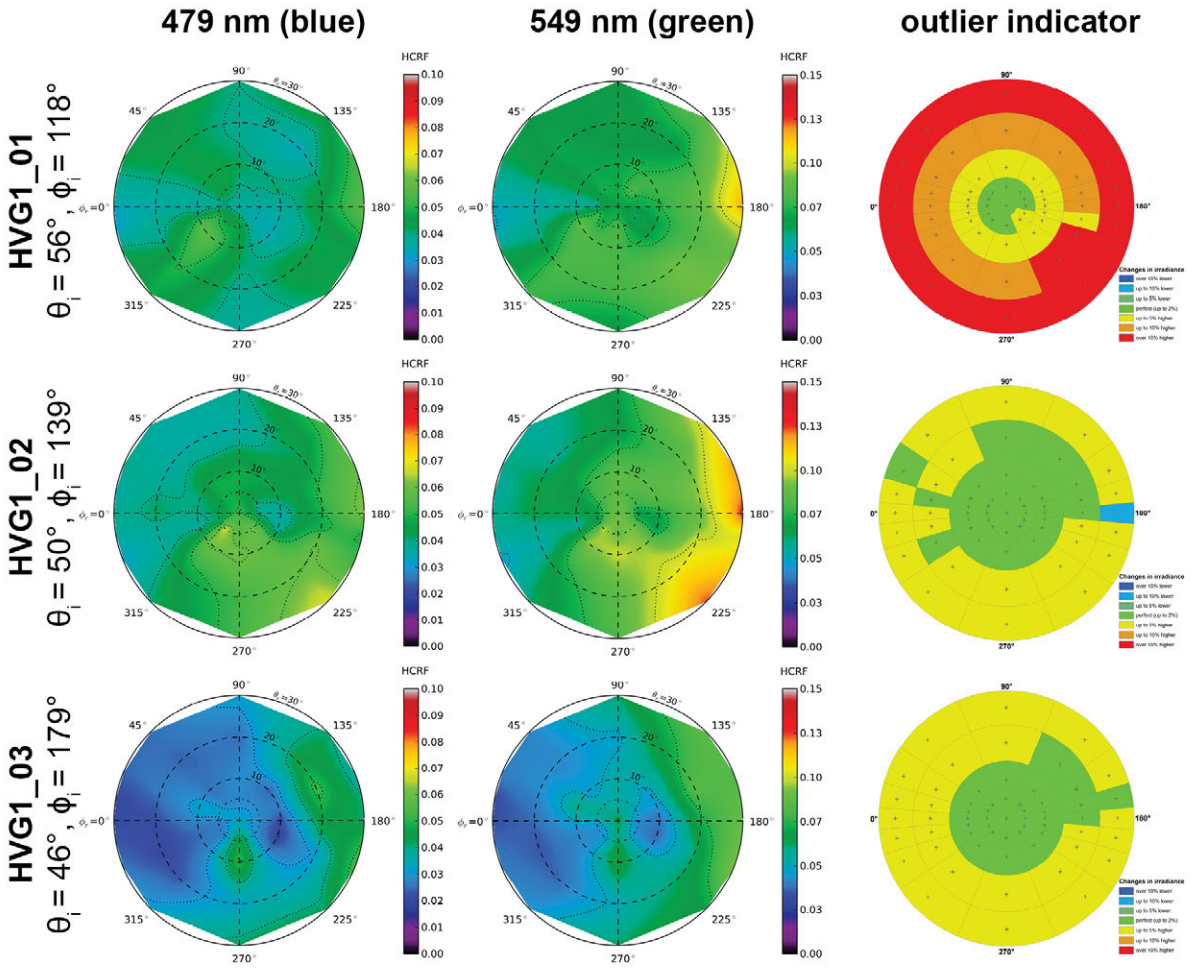

Figure C.5-8: HCRF visualization at 479 nm and 549 nm of the HVG1 site.

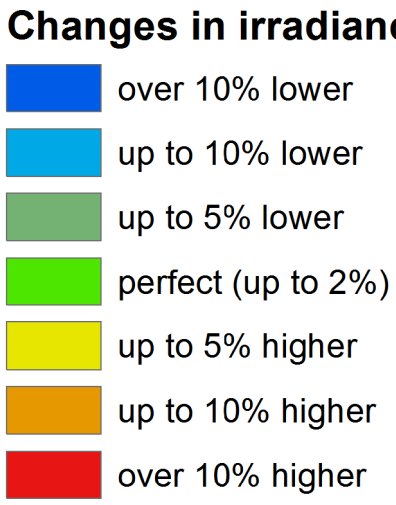

Figure C.5-9: Legend of the outlier indicator graphics shown in Figure C.5-8, C.5-10, and C.5-13

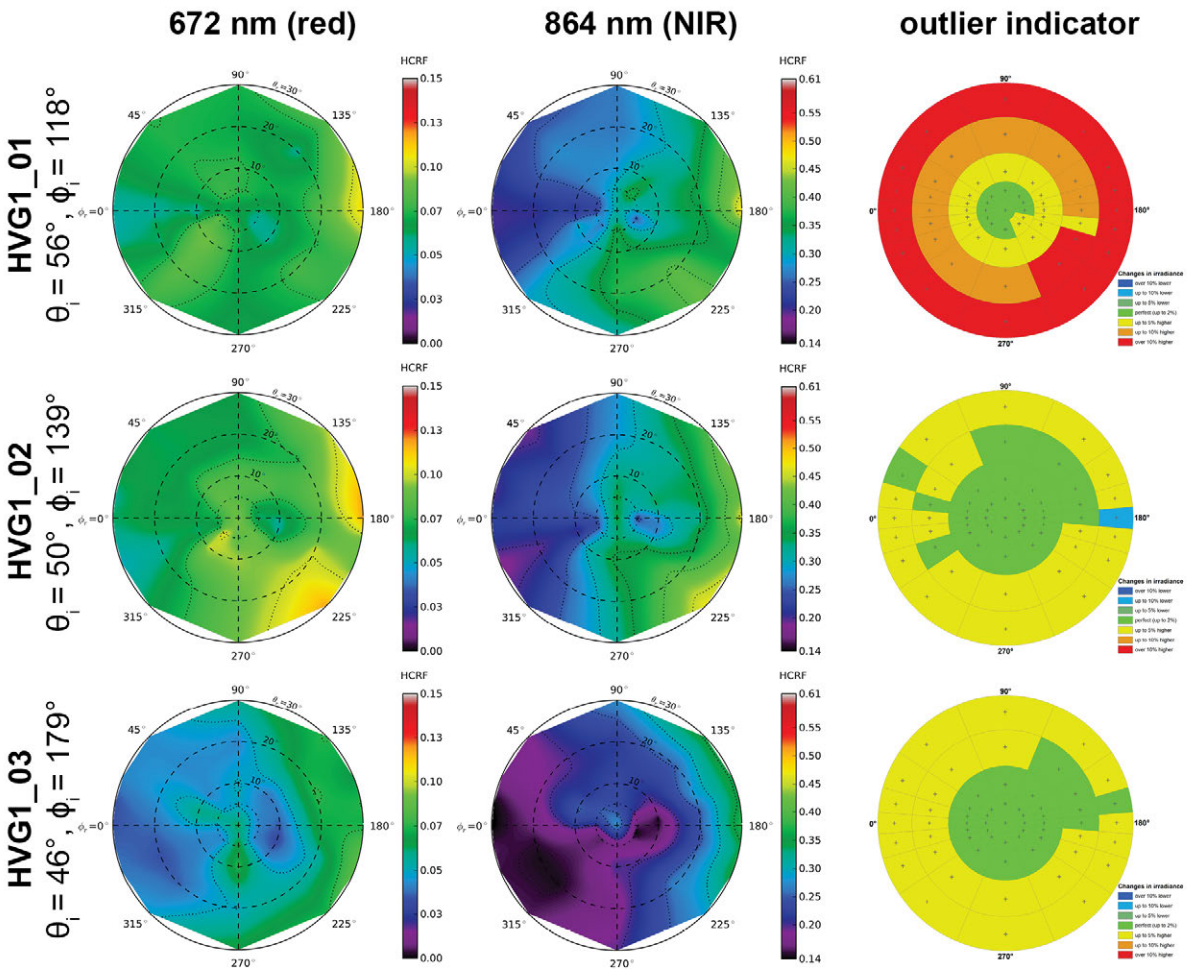

Figure C.5-10: HCRF visualization at 672 nm and 864 nm of the HVG1 site.

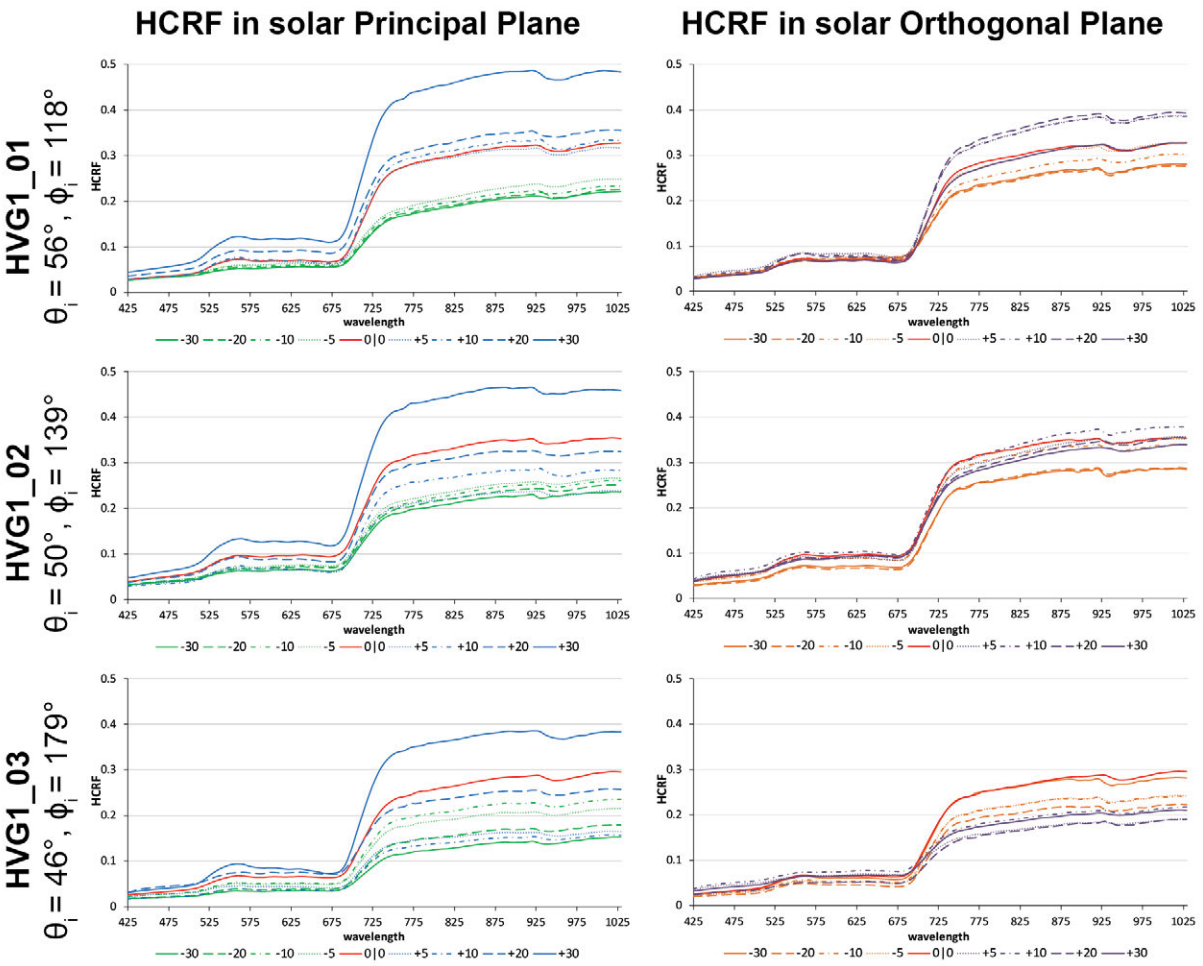

Figure C.5-11: HCRF visualization in principal & orthogonal plane of the HVG1 site.

VII *ANIF Visualization*

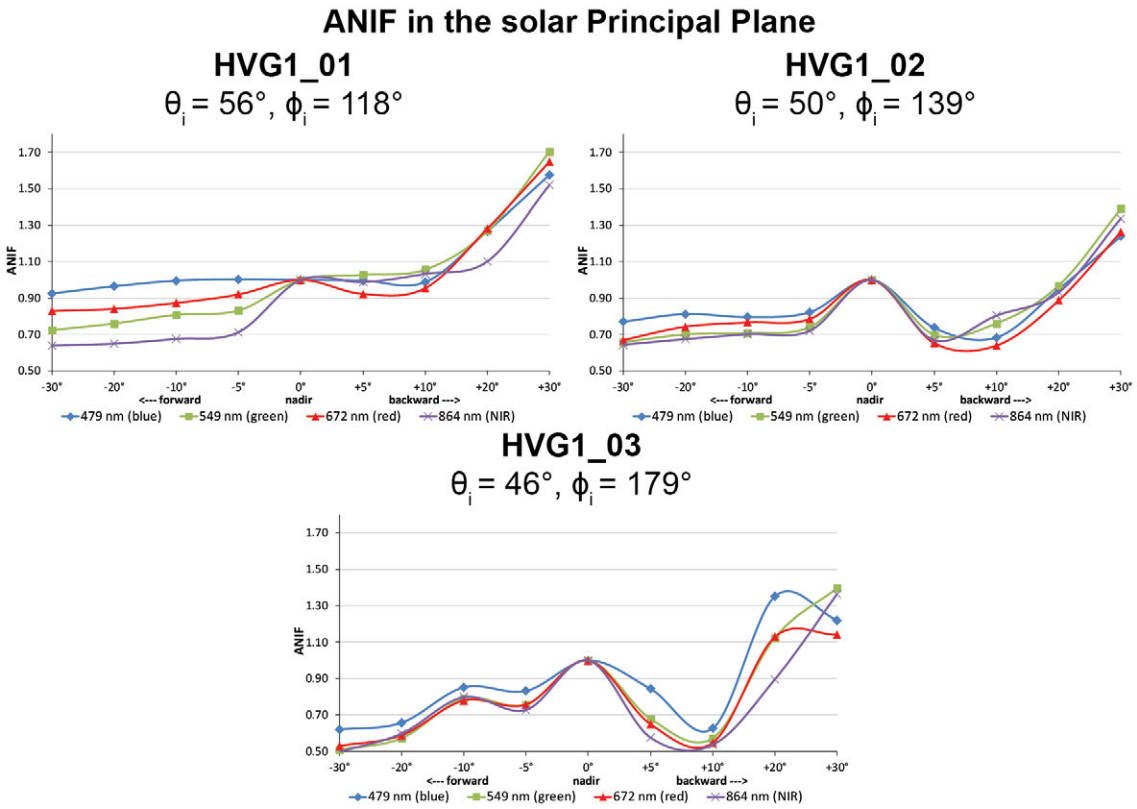

Figure C.5-12: Comparison of the ANIF values at 479 nm (blue), 549 nm (green), 672 nm (red), and 864 nm (NIR) in the solar principal plane of the HVG1 site at different sun zenith angles.

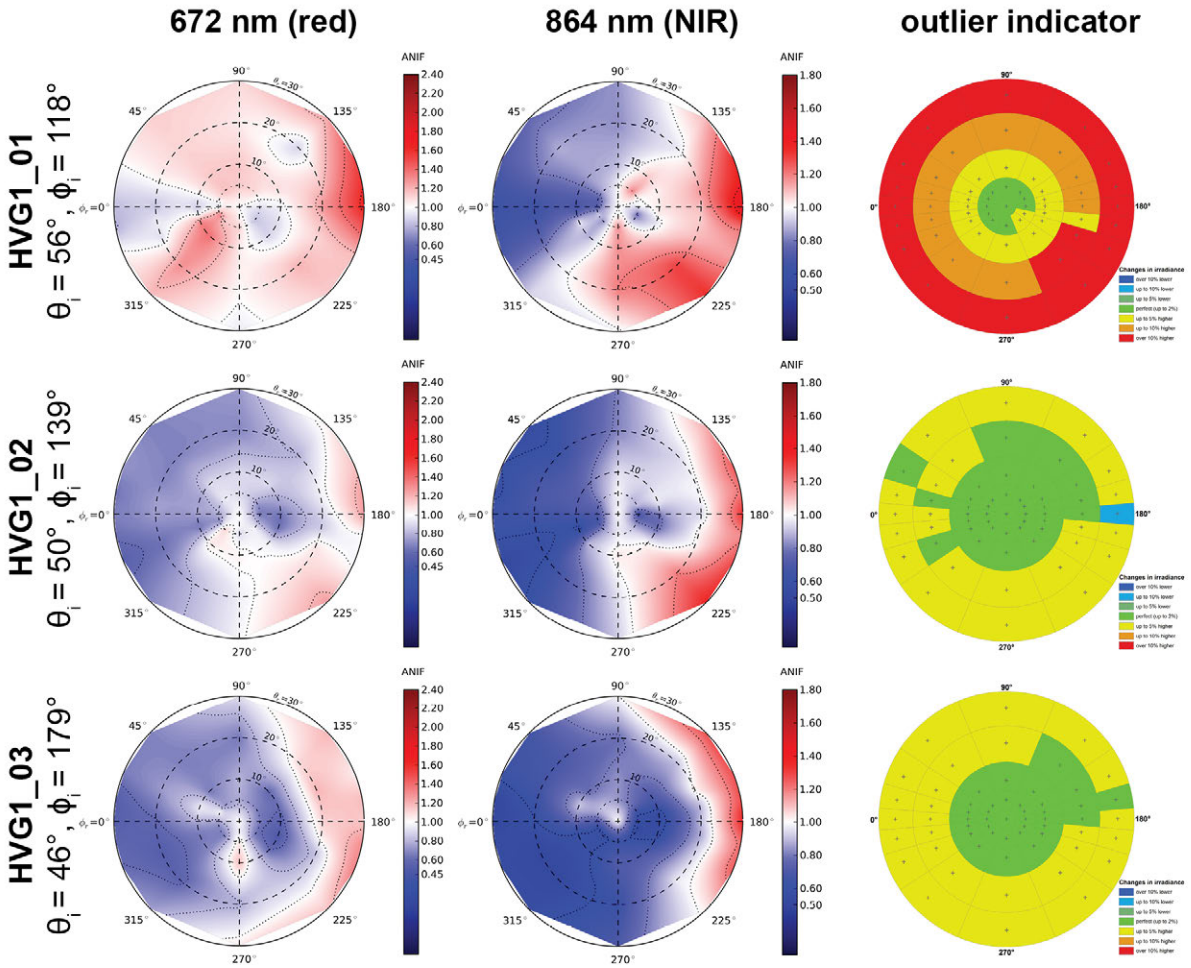

Figure C.5-13: ANIF visualization at 672 nm and 864 nm of the HVG1 site.

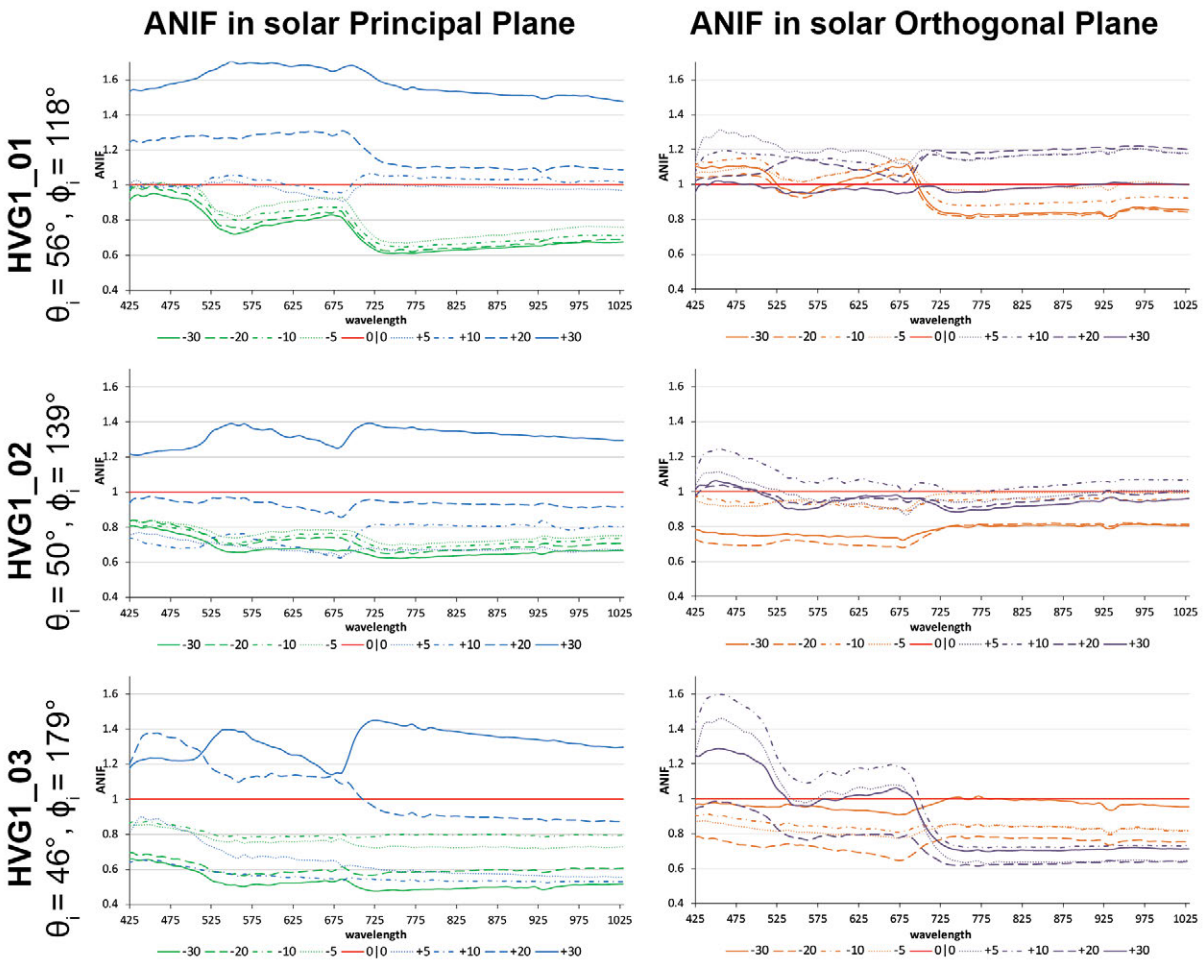

Figure C.5-14: ANIF visualization in principal & orthogonal plane of the HVG1 site.

VIII *ANIX Visualization*

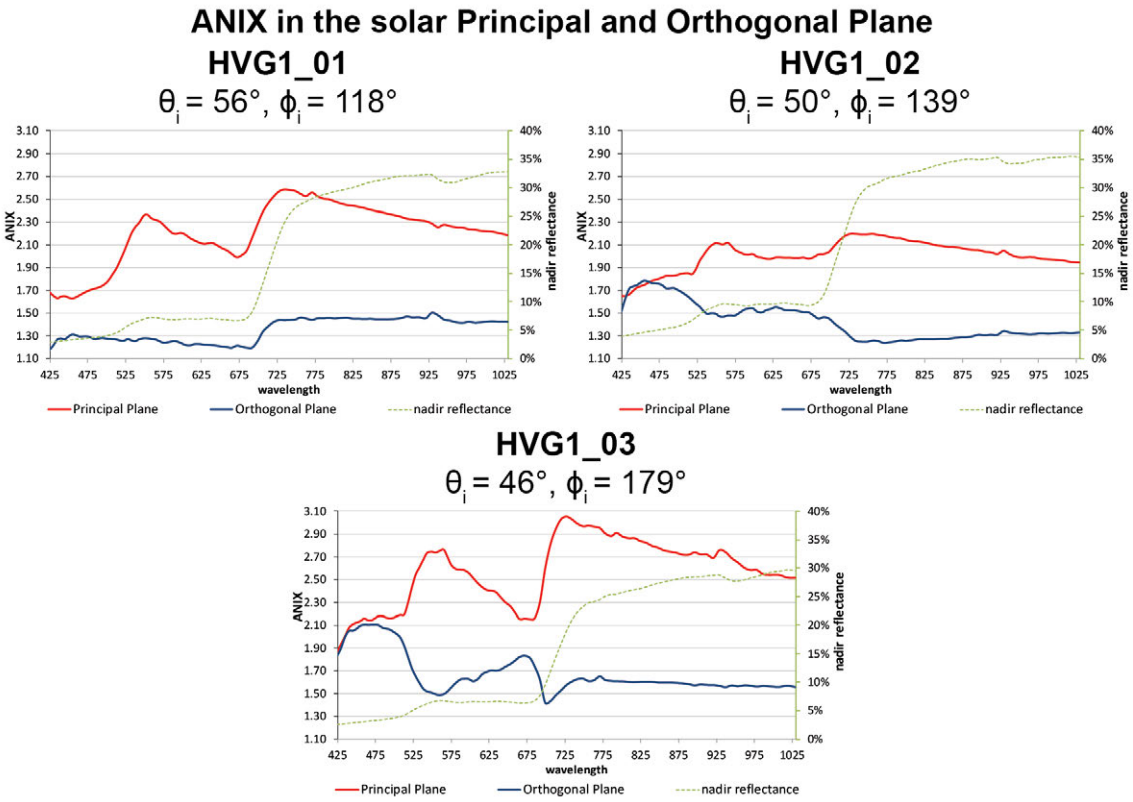

Figure C.5-15: Comparison of the ANIX in the solar principal and orthogonal plane with the nadir reflectance of the HVG1 site at different sun zenith angles.

IX *NDVI and Relative Absorption Depth Visualization*

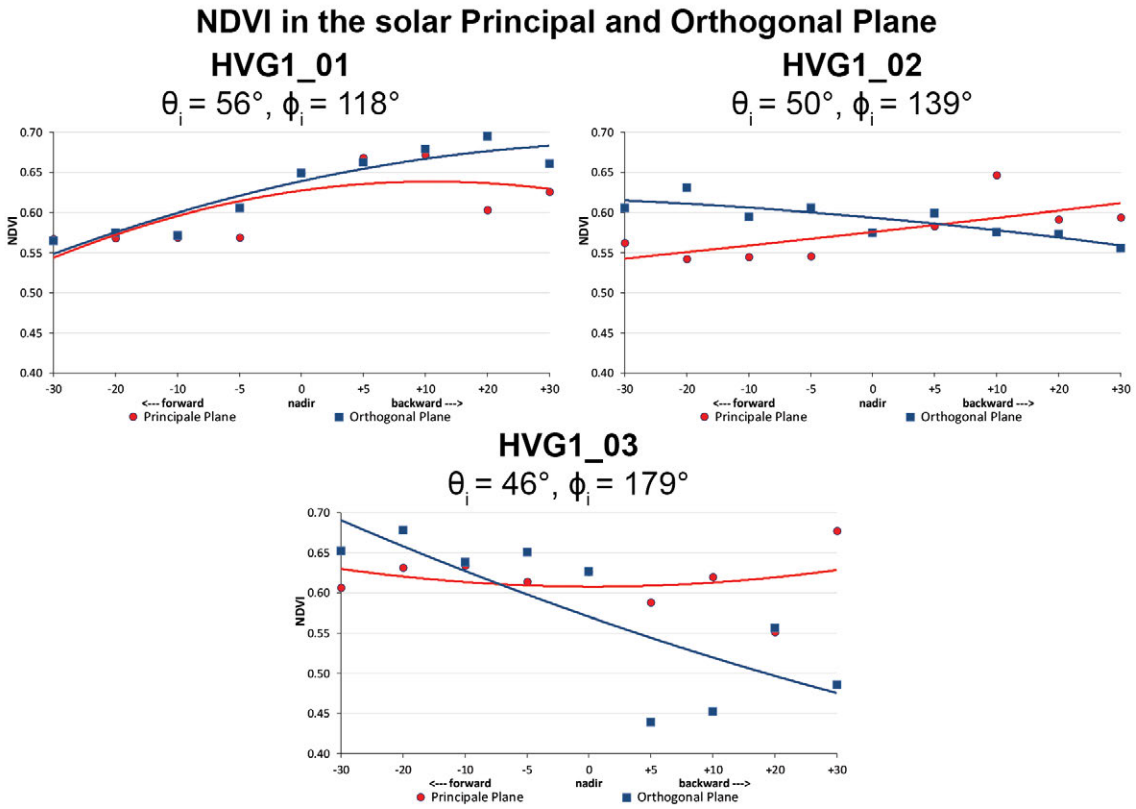

Figure C.5-16: Comparison of the NDVI in the solar principal and orthogonal plane of the HVG1 site at different sun zenith angles.

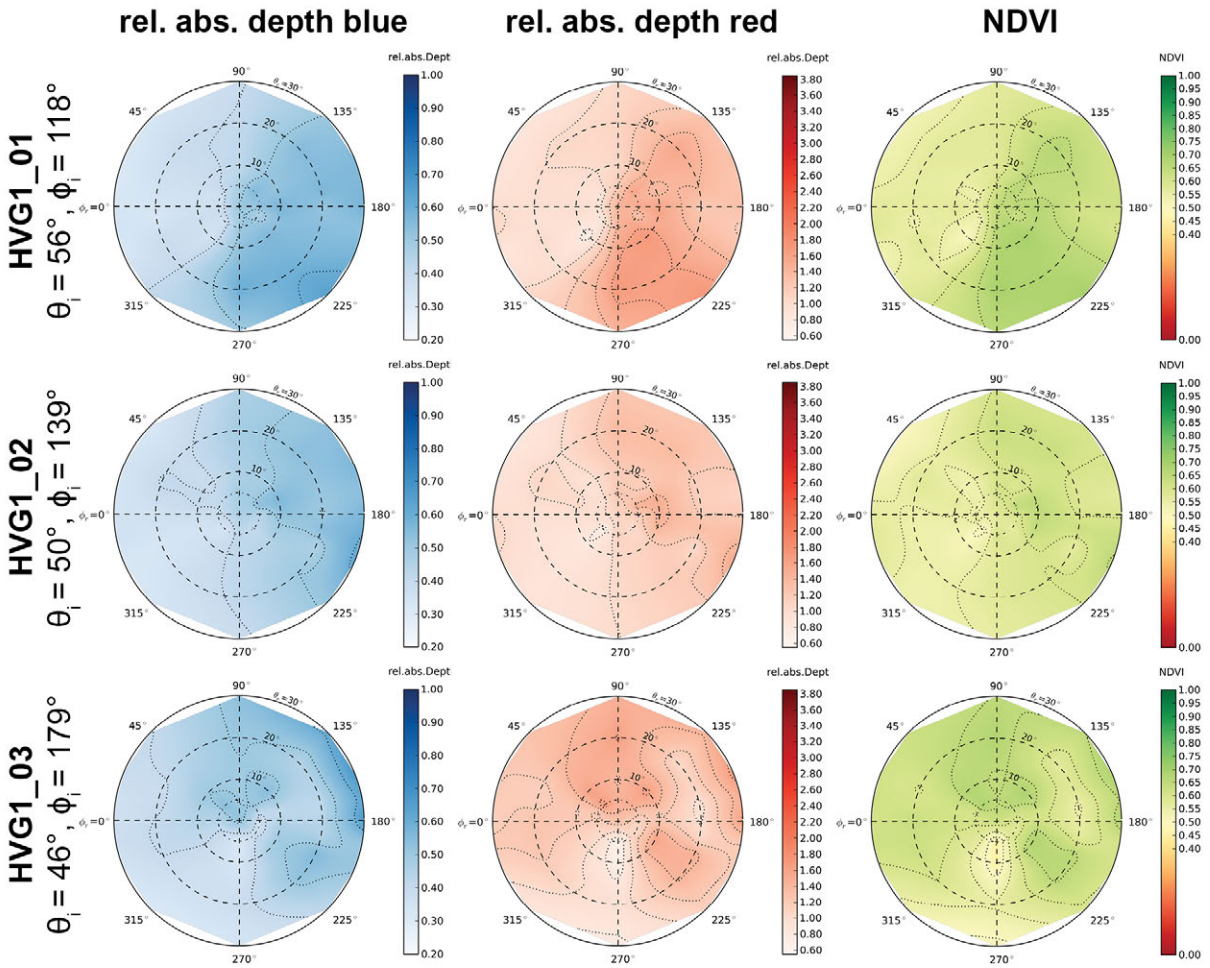

Figure C.5-17: Visualization of relative absorption depth & NDVI of the HVG1 site.

X *NDVI Comparison of Different Sensors*

Table C.5-5: Center wavelengths and band widths of the broadband and narrowband NDVIs, based on the spectral response curves of the AVHRR, MODIS and EnMAP sensors.

NDVI	Sensor	Sensor band	Center wavelength (nm)	band width (nm)
$NDVI_{AVHRR}$ [broadband]	AVHRR/3	red: band 1 NIR: band 2	630 865	100 275
$NDVI_{MODIS}$ [broadband]	MODIS	red: band 1 NIR: band 2	645 859	50 35
$NDVI_{EnMAP}$ [narrowband]	EnMAP	red: band 47 NIR: band 73	672 864	6.5 8

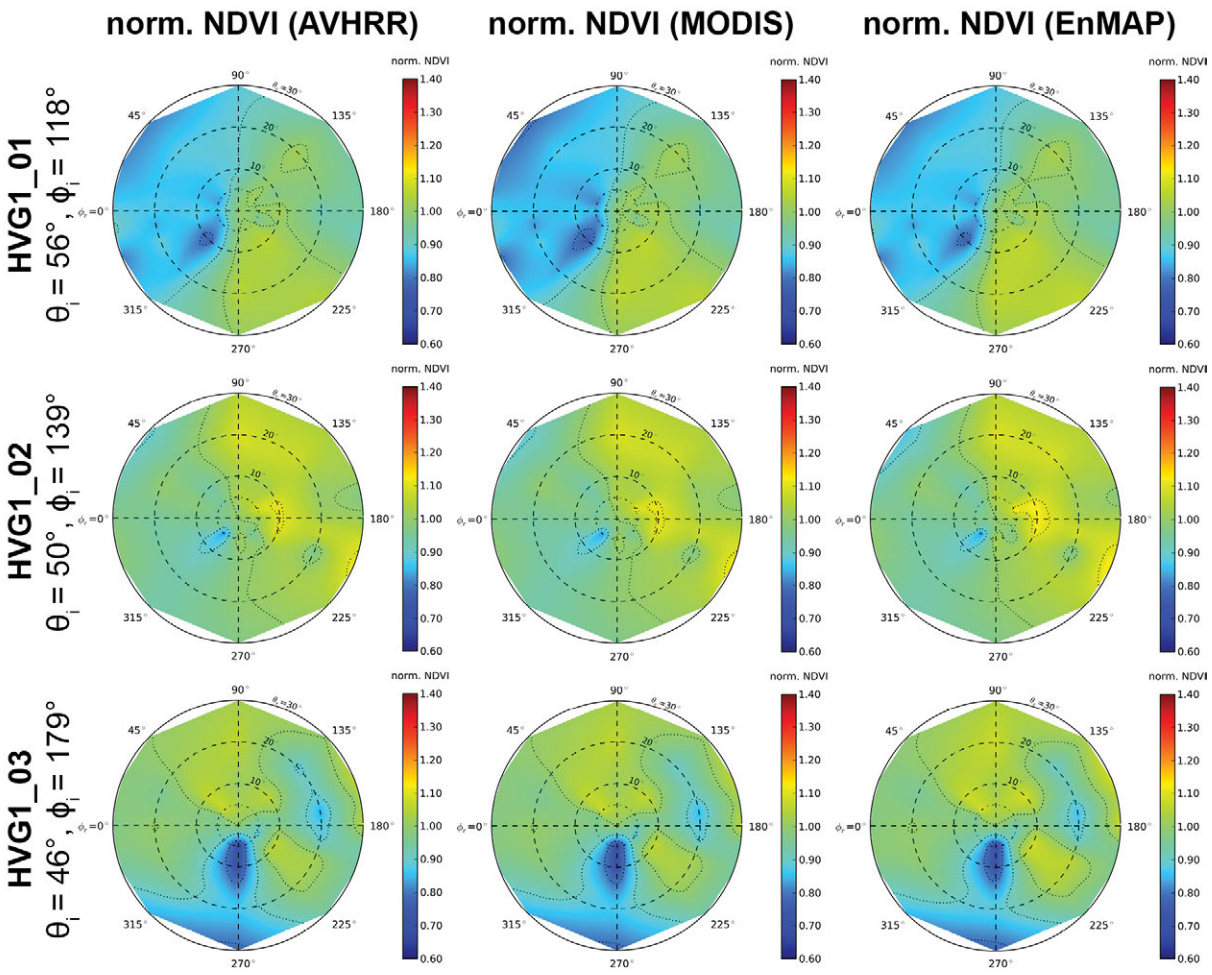

Figure C.5-18: Comparison of AVHRR, MODIS & EnMAP NDVI of the HVG1 site.

C.6 Study site HVG2 (erect dwarf shrub community)

I *Location*

Name	Location	Latitude	Longitude	Altitude
HVG2	Happy Valley, Arctic North Slope, Alaska, United States of America	69.146928°	-148.852042°	325 m

Happy Valley is located just west of the Dalton Highway in the foothills of the Arctic Slope approximately 82 km (52 mi) north of Toolik Lake, Alaska at an elevation of about 320 m. Within the five subzones of the circumpolar Arctic, Happy Valley is found in subzone E. Green mile marker 334 is positioned just before the turn-off to the site. Three 10 x 10 m grids, designated at the hill crest, midslope and at the footslope have been established at this location in 2002. The goniometer measurements have been carried out next to the midslope / zonal site (HV_ms/z). [*Barreda et al.*, 2006]

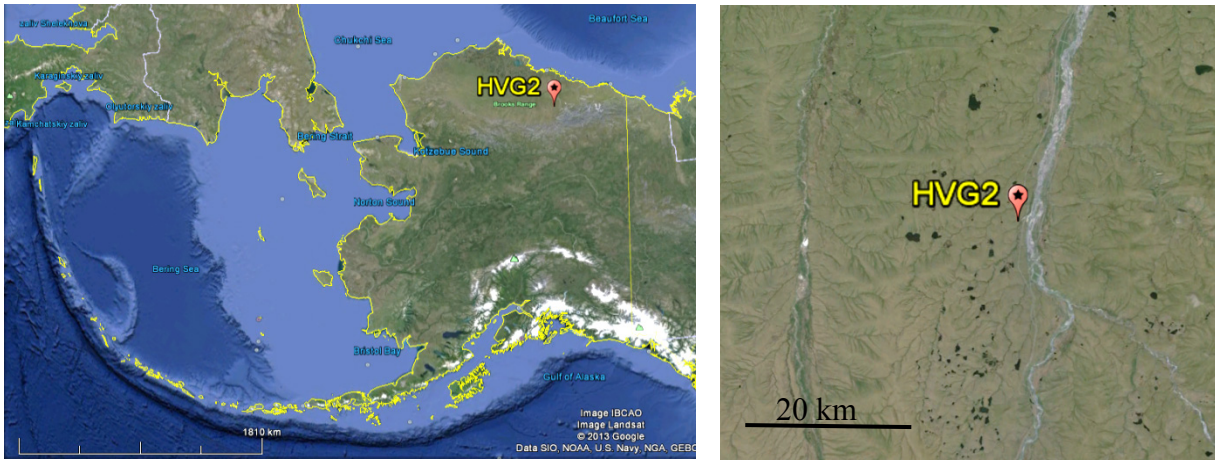

Figure C.6-1: Location of study site HVG2 in Alaska, USA. *Source:* Google Earth, 2013

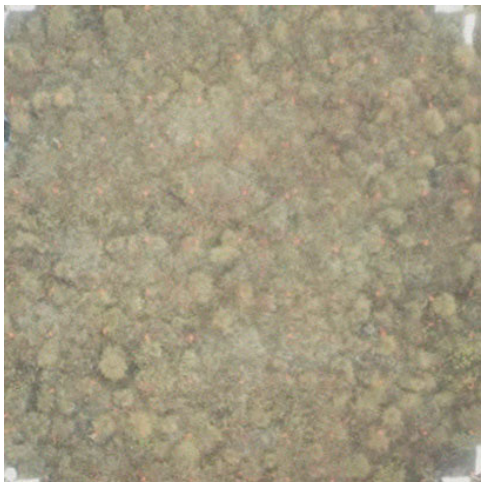

Figure C.6-2: Aerial photo of a 10 x 10 m zonal grid at the Happy Valley study location near the HVG2 site. *Source:* [*Barreda et al.*, 2006]

II *Main Vegetation Description*

The vegetation at the mesic Happy Valley study location corresponds to the zonal vegetation in subzone E. The zonal plant community of bioclimate subzone E in northern Alaska is *Sphagno- Eriophoretum vaginati* [*Walker et al.*, 1994], also called moist acidic tundra (MAT), 'acidic tussock tundra' or 'tussock-sedge, dwarf-shrub, moss tundra' [*Walker et al.*, 2005]. It occurs widely across the foothills of northern Alaska on old upland surfaces not glaciated during the Last Glacial Maximum. At Happy Valley the average soil pH of this plant community is 5.3; the average volumetric soil moisture of the top mineral horizon is 44 %, and average depth of thaw by late summer is 34 cm [*Kade et al.*, 2005]. The vegetation is composed of a mixture of tussock sedges (*Eriophorum vaginatum*), deciduous dwarf shrubs (e.g., *Betula nana, Salix planifolia* ssp. *pulchra*), evergreen dwarf shrubs (e.g., *Ledum palustre* ssp. *decumbens, Vaccinium vitis-idaea, Cassiope tetragona, Empetrum nigrum*), a few forbs (*Polygonum bistorta* var. *plumosum, Petasites frigidus*), mosses (*Hylocomium splendens, Sphagnum* spp., *Aulacomnium* spp., *Dicranum* spp.) and lichens (*Cladina* spp., *Dactylina arctica*, *Cetraria* spp.).

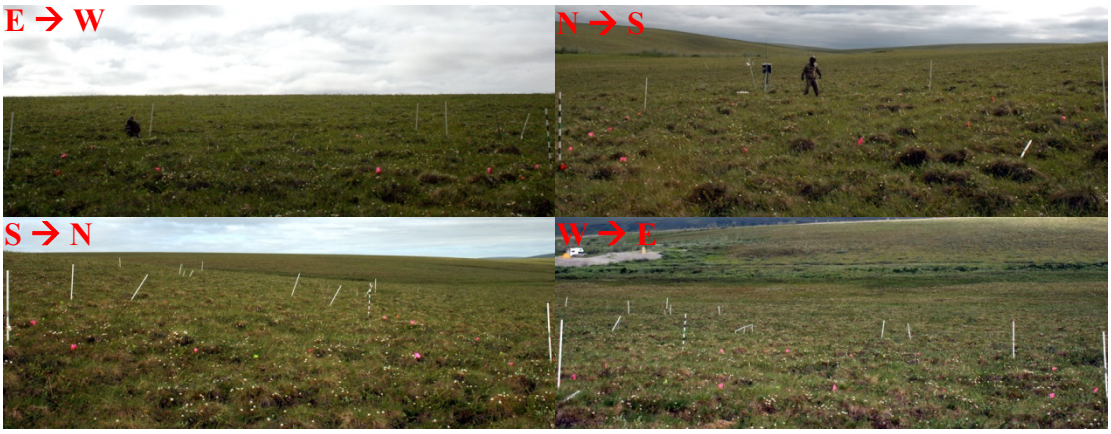

Figure C.6-3: Overview images of MNT tundra at the mesic Happy Valley study location near the HVG2 site. *Source:* [*Buchhorn and Schwieder*, 2012]

III *Vegetation Description of the HVG2 Site*

The focus of the measurements at this goniometer site has been an erect dwarf shrub community between tussock sedges. The 1x1 m plot is homogeneously covered with this dwarf shrub, but with forbs, mosses and lichens in the understory and tussock sedges nearby.

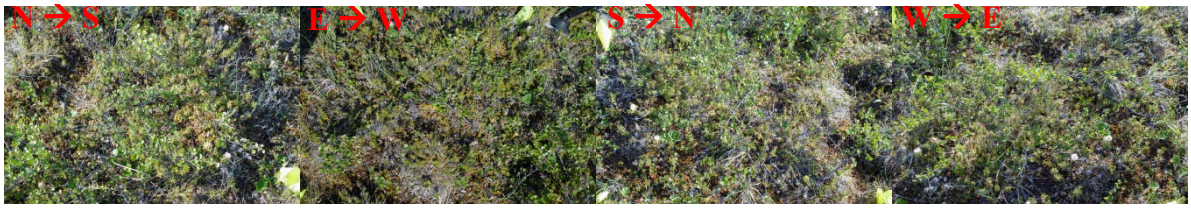

Figure C.6-4: Overview images of the HVG2 vegetation from cardinal directions.

Figure C.6-5: Quasi-nadir image of the HVG2 vegetation (dwarf shrub).

IV *Overview of the Spectro-Goniometer Measurements*

Table C.6-1: Overview of the spectro-goniometer measurements at the HVG2 study site.

Name	Day	Starting Time	Duration	SAA	SZA	Sky
HVG2_01	2012-07-02	9:27:32	20 min	104°	60°	cirrostratus
HVG2_02	2012-07-02	11:32:41	17 min	137°	50°	cirrostratus
HVG2_03	2012-07-02	13:52:06	67 min	189°	46°	cirrostratus
HVG2_04	2012-07-02	15:52:37	18 min	217°	50°	cirrostratus

Table C.6-2: Spectro-directional data of the HVG2_01 spectro-goniometer measurement.

HVG2_01 (SZA = 60°; SAA = 104°)	Viewing Geometry (Viewing Zenith Angle | Viewing Azimuth Angle)																							
	0|0	5|180	5|202.5	5|225	5|270	5|315	5|337.5	5|0	5|22.5	5|45	5|90	5|135	5|157.5	10|180	10|190	10|202.5	10|225	10|270	10|315	10|337.5	10|350
HCRF EnMAP blue (479 nm)	0.0355	0.0327	0.0298	0.0360	0.0353	0.0404	0.0364	0.0377	0.0363	0.0355	0.0326	0.0337	0.0312	0.0371	0.0355	0.0390	0.0393	0.0344	0.0382	0.0371	0.0398
HCRF EnMAP green (549 nm)	0.0900	0.0779	0.0702	0.0759	0.0721	0.0828	0.0849	0.0804	0.0770	0.0761	0.0703	0.0797	0.0677	0.0877	0.0866	0.0993	0.0997	0.0923	0.0794	0.0825	0.0863
HCRF EnMAP rot (672 nm)	0.0516	0.0499	0.0472	0.0556	0.0558	0.0695	0.0583	0.0585	0.0578	0.0575	0.0542	0.0499	0.0518	0.0537	0.0513	0.0587	0.0577	0.0508	0.0623	0.0602	0.0631
HCRF EnMAP NIR (864 nm)	0.5252	0.4665	0.4075	0.4120	0.3784	0.4404	0.4764	0.4427	0.4194	0.4105	0.4031	0.4388	0.4005	0.4828	0.4932	0.5334	0.5499	0.5371	0.4254	0.4448	0.4694
ANIF EnMAP rot (672 nm)	1.0000	0.9667	0.9139	1.0774	1.0813	1.3457	1.1293	1.1325	1.1185	1.1142	1.0497	0.9660	1.0026	1.0390	0.9834	1.1359	1.1177	0.9832	1.2070	1.1664	1.2221
ANIF EnMAP NIR (864 nm)	1.0000	0.8882	0.7758	0.7845	0.7205	0.8385	0.9071	0.8429	0.7986	0.7815	0.7676	0.8355	0.7625	0.9191	0.9390	1.0156	1.0470	1.0225	0.8100	0.8468	0.8936
Rel. Blue Absorption Depth	0.8042	0.7282	0.7172	0.6042	0.5839	0.5787	0.7032	0.6132	0.6031	0.6171	0.6198	0.7296	0.6321	0.7249	0.7561	0.8109	0.8108	0.8653	0.5943	0.6521	0.6233
Rel. Red Absorption Depth	3.4336	3.0745	2.7771	2.3216	2.0702	1.9645	2.6656	2.4368	2.2822	2.2766	2.3741	2.8790	2.5042	2.9990	3.2200	3.0207	3.2042	3.5900	2.1279	2.3594	2.3935
NDVI (EnMAP)	0.8209	0.8067	0.7924	0.7620	0.7428	0.7274	0.7819	0.7666	0.7579	0.7541	0.7629	0.7958	0.7710	0.7999	0.8115	0.8018	0.8100	0.8272	0.7444	0.7614	0.7629
Nadir Norm. NDVI (AVHRR)	1.0000	0.9830	0.9640	0.9350	0.9086	0.8915	0.9474	0.9413	0.9303	0.9276	0.9377	0.9732	0.9487	0.9693	0.9898	0.9712	0.9789	1.0000	0.9164	0.9261	0.9365
Nadir Norm. NDVI (MODIS)	1.0000	0.9819	0.9635	0.9340	0.9067	0.8890	0.9469	0.9395	0.9287	0.9254	0.9365	0.9737	0.9464	0.9709	0.9911	0.9731	0.9805	1.0011	0.9129	0.9239	0.9346
Nadir Norm. NDVI (EnMAP)	1.0000	0.9826	0.9652	0.9283	0.9048	0.8860	0.9524	0.9338	0.9232	0.9186	0.9293	0.9694	0.9392	0.9744	0.9885	0.9767	0.9867	1.0077	0.9068	0.9275	0.9293

(cont.)

HVG2_01 (SZA = 60°; SAA = 104°)	Viewing Geometry (Viewing Zenith Angle | Viewing Azimuth Angle)																							
	10|0	10|10	10|22.5	10|45	10|90	10|135	10|157.5	10|170	20|180	20|190	20|202.5	20|225	20|270	20|315	20|337.5	20|350	20|0	20|10	20|22.5	20|45	20|90
HCRF EnMAP blue (479 nm)	0.0374	0.0374	0.0385	0.0385	0.0351	0.0415	0.0416	0.0357	0.0391	0.0414	0.0434	0.0421	0.0368	0.0399	0.0427	0.0406	0.0377	0.0391	0.0409	0.0418	0.0344
HCRF EnMAP green (549 nm)	0.0828	0.0832	0.0798	0.0835	0.0757	0.0958	0.0893	0.0835	0.0958	0.0994	0.1054	0.1029	0.0952	0.0822	0.0877	0.0864	0.0822	0.0826	0.0841	0.0828	0.0748
HCRF EnMAP rot (672 nm)	0.0594	0.0623	0.0642	0.0627	0.0610	0.0652	0.0639	0.0542	0.0583	0.0616	0.0665	0.0629	0.0559	0.0638	0.0684	0.0644	0.0643	0.0665	0.0694	0.0669	0.0566
HCRF EnMAP NIR (864 nm)	0.4504	0.4552	0.4178	0.4498	0.3998	0.5094	0.4586	0.4549	0.5042	0.5303	0.5568	0.5500	0.5358	0.4397	0.4649	0.4824	0.4559	0.4407	0.4492	0.4270	0.4148
ANIF EnMAP rot (672 nm)	1.1508	1.2067	1.2421	1.2145	1.1818	1.2629	1.2379	1.0486	1.1290	1.1927	1.2868	1.2173	1.0814	1.2352	1.3243	1.2476	1.2441	1.2872	1.3440	1.2951	1.0956
ANIF EnMAP NIR (864 nm)	0.8575	0.8667	0.7955	0.8564	0.7612	0.9699	0.8732	0.8661	0.9600	1.0097	1.0601	1.0472	1.0200	0.8372	0.8851	0.9184	0.8679	0.8390	0.8552	0.8130	0.7897
Rel. Blue Absorption Depth	0.6481	0.6552	0.5895	0.6302	0.6144	0.7007	0.6225	0.7173	0.7683	0.7507	0.7721	0.7699	0.8241	0.5824	0.5747	0.6088	0.6343	0.6097	0.5863	0.5464	0.6301
Rel. Red Absorption Depth	2.4509	2.3364	2.0209	2.2838	2.0337	2.5353	2.2913	2.7412	2.8577	2.8519	2.7495	2.8887	3.2247	2.2009	2.1810	2.4494	2.2392	2.0804	2.0318	1.9921	2.3014
NDVI (EnMAP)	0.7668	0.7592	0.7338	0.7552	0.7351	0.7730	0.7553	0.7872	0.7927	0.7919	0.7867	0.7948	0.8112	0.7466	0.7435	0.7643	0.7529	0.7378	0.7323	0.7292	0.7599
Nadir Norm. NDVI (AVHRR)	0.9364	0.9306	0.9052	0.9151	0.9094	0.9456	0.9250	0.9575	0.9553	0.9590	0.9521	0.9652	0.9809	0.9161	0.9091	0.9386	0.9208	0.9068	0.9046	0.8961	0.9369
Nadir Norm. NDVI (MODIS)	0.9350	0.9286	0.9025	0.9138	0.9067	0.9456	0.9248	0.9589	0.9582	0.9609	0.9532	0.9664	0.9814	0.9144	0.9076	0.9369	0.9177	0.9035	0.9018	0.8942	0.9354
Nadir Norm. NDVI (EnMAP)	0.9341	0.9247	0.8939	0.9200	0.8954	0.9416	0.9200	0.9589	0.9656	0.9646	0.9583	0.9682	0.9881	0.9094	0.9057	0.9310	0.9171	0.8988	0.8920	0.8882	0.9257

(cont.)

HVG2_01 (SZA = 60°; SAA = 104°)	Viewing Geometry (Viewing Zenith Angle | Viewing Azimuth Angle)																							
	20|135	20|157.5	20|170	30|180	30|190	30|202.5	30|225	30|270	30|315	30|337.5	30|350	30|0	30|10	30|22.5	30|45	30|90	30|135	30|157.5	30|170			
HCRF EnMAP blue (479 nm)	0.0424	0.0423	0.0399	0.0464	0.0464	0.0512	0.0440	0.0396	0.0370	0.0412	0.0398	0.0334	0.0324	0.0422	0.0387	0.0359	0.0505	0.0482	0.0446					
HCRF EnMAP green (549 nm)	0.0974	0.0940	0.0951	0.1071	0.1052	0.1231	0.1097	0.1008	0.0794	0.0806	0.0786	0.0778	0.0724	0.0867	0.0751	0.0785	0.1092	0.1109	0.1018					
HCRF EnMAP rot (672 nm)	0.0650	0.0638	0.0624	0.0700	0.0703	0.0758	0.0666	0.0586	0.0597	0.0671	0.0657	0.0559	0.0528	0.0694	0.0643	0.0612	0.0746	0.0722	0.0694					
HCRF EnMAP NIR (864 nm)	0.5118	0.4736	0.4979	0.5351	0.5165	0.6146	0.5754	0.5629	0.4435	0.4064	0.4139	0.4482	0.4248	0.4528	0.3987	0.4322	0.5322	0.5327	0.5039					
ANIF EnMAP rot (672 nm)	1.2583	1.2351	1.2084	1.3553	1.3619	1.4682	1.2900	1.1351	1.1551	1.2996	1.2724	1.0825	1.0221	1.3447	1.2451	1.1842	1.4452	1.3987	1.3439					
ANIF EnMAP NIR (864 nm)	0.9744	0.9016	0.9479	1.0187	0.9834	1.1701	1.0956	1.0716	0.8444	0.7738	0.7880	0.8534	0.8088	0.8621	0.7592	0.8229	1.0133	1.0142	0.9594					
Rel. Blue Absorption Depth	0.7012	0.6575	0.7369	0.7138	0.6974	0.7623	0.7912	0.7980	0.6227	0.5285	0.5397	0.7061	0.6581	0.5810	0.5302	0.6512	0.6454	0.7021	0.6973					
Rel. Red Absorption Depth	2.5763	2.3801	2.6224	2.4929	2.3537	2.6879	2.8548	3.2084	2.3521	1.8892	1.9766	2.6164	2.6082	2.0464	1.9160	2.2406	2.3098	2.3431	2.3390					
NDVI (EnMAP)	0.7747	0.7626	0.7772	0.7686	0.7603	0.7803	0.7925	0.8113	0.7629	0.7165	0.7260	0.7782	0.7789	0.7340	0.7222	0.7521	0.7540	0.7612	0.7579					
Nadir Norm. NDVI (AVHRR)	0.9437	0.9267	0.9429	0.9332	0.9214	0.9404	0.9597	0.9833	0.9289	0.8780	0.8919	0.9463	0.9526	0.9007	0.8969	0.9230	0.9155	0.9192	0.9165					
Nadir Norm. NDVI (MODIS)	0.9445	0.9282	0.9449	0.9358	0.9236	0.9433	0.9613	0.9837	0.9270	0.8755	0.8897	0.9452	0.9509	0.8983	0.8939	0.9218	0.9172	0.9217	0.9188					
Nadir Norm. NDVI (EnMAP)	0.9436	0.9289	0.9467	0.9363	0.9261	0.9505	0.9653	0.9883	0.9293	0.8728	0.8843	0.9479	0.9488	0.8941	0.8798	0.9161	0.9185	0.9272	0.9232					

Table C.6-3: Spectro-directional data of the HVG2_02 spectro-goniometer measurement.

HVG2_02 (SZA = 50°; SAA = 137°)	Viewing Geometry (Viewing Zenith Angle | Viewing Azimuth Angle)																							
	0|0	5|180	5|202.5	5|225	5|270	5|315	5|337.5	5|0	5|22.5	5|45	5|90	5|135	5|157.5	10|180	10|202.5	10|225	10|270	10|315	10|337.5	10|350
HCRF EnMAP blue (479 nm)	0.0274	0.0290	0.0287	0.0278	0.0306	0.0312	0.0290	0.0270	0.0296	0.0255	0.0263	0.0263	0.0279	0.0283	0.0325	0.0289	0.0341	0.0309	0.0317	0.0293
HCRF EnMAP green (549 nm)	0.0625	0.0724	0.0621	0.0651	0.0711	0.0694	0.0625	0.0596	0.0632	0.0657	0.0609	0.0657	0.0733	0.0710	0.0757	0.0721	0.0715	0.0695	0.0655	0.0590
HCRF EnMAP rot (672 nm)	0.0456	0.0442	0.0441	0.0457	0.0502	0.0493	0.0433	0.0450	0.0455	0.0375	0.0397	0.0408	0.0415	0.0444	0.0482	0.0435	0.0553	0.0493	0.0511	0.0483
HCRF EnMAP NIR (864 nm)	0.3398	0.3852	0.3267	0.3485	0.3804	0.3700	0.3315	0.3269	0.3202	0.3752	0.3468	0.3700	0.4161	0.3929	0.3983	0.3982	0.3593	0.3723	0.3331	0.3084
ANIF EnMAP rot (672 nm)	1.0000	0.9686	0.9664	1.0009	1.1012	1.0794	0.9489	0.9865	0.9962	0.8216	0.8694	0.8951	0.9089	0.9731	0.9542	0.9542	1.0552	0.9613	1.2111	1.0803	1.1202	1.0593
ANIF EnMAP NIR (864 nm)	1.0000	1.1337	0.9616	1.0256	1.1194	1.0889	0.9755	0.9622	0.9424	1.1041	1.0206	1.0890	1.2247	1.1563	1.1719	1.1721	1.0889	1.0574	1.0958	0.9804	0.9804	0.9077
Rel. Blue Absorption Depth	0.6754	0.8002	0.6272	0.7100	0.6978	0.6615	0.6147	0.6433	0.6095	0.8144	0.6972	0.7981	0.8462	0.8086	0.7853	0.7106	0.7185	0.5964	0.6691	0.5755	0.5755	0.5493
Rel. Red Absorption Depth	2.3546	2.8555	2.3571	2.4478	2.4488	2.3921	2.4158	2.2710	2.1863	3.3081	2.8789	2.9798	3.3260	2.9333	3.0090	2.7161	2.7319	2.0445	2.4210	2.0300	1.9588	1.9588
NDVI (EnMAP)	0.7632	0.7941	0.7622	0.7683	0.7666	0.7651	0.7689	0.7580	0.7514	0.8183	0.7947	0.8012	0.8187	0.7969	0.8029	0.7843	0.7880	0.7334	0.7662	0.7339	0.7290	0.7290
Nadir Norm. NDVI (AVHRR)	1.0000	1.0298	0.9996	1.0032	1.0045	1.0059	1.0076	0.9985	0.9841	1.0644	1.0452	1.0467	1.0698	1.0433	1.0481	1.0207	1.0334	0.9663	0.9998	0.9679	0.9644	0.9644
Nadir Norm. NDVI (MODIS)	1.0000	1.0330	1.0009	1.0035	1.0036	1.0047	1.0072	0.9980	0.9849	1.0671	1.0458	1.0485	1.0725	1.0454	1.0503	1.0233	1.0350	0.9661	0.9999	0.9675	0.9637	0.9637
Nadir Norm. NDVI (EnMAP)	1.0000	1.0405	0.9986	1.0066	1.0045	1.0024	1.0075	0.9931	0.9845	1.0722	1.0412	1.0498	1.0728	1.0442	1.0519	1.0276	1.0325	0.9609	1.0039	0.9616	0.9552	0.9552

(cont.)

HVG2_02 (SZA = 50°; SAA = 137°)	Viewing Geometry (Viewing Zenith Angle | Viewing Azimuth Angle)																							
	10|0	10|10	10|22.5	10|45	10|90	10|135	10|157.5	10|170	20|180	20|190	20|202.5	20|225	20|270	20|315	20|337.5	20|350	20|0	20|10	20|22.5	20|45	20|90
HCRF EnMAP blue (479 nm)	0.0292	0.0284	0.0299	0.0259	0.0246	0.0269	0.0266	0.0274	0.0339	0.0333	0.0329	0.0356	0.0335	0.0298	0.0269	0.0271	0.0327	0.0281	0.0265	0.0260	0.0260	0.0286
HCRF EnMAP green (549 nm)	0.0592	0.0632	0.0697	0.0599	0.0600	0.0649	0.0686	0.0686	0.0860	0.0805	0.0718	0.0714	0.0751	0.0642	0.0578	0.0593	0.0692	0.0617	0.0634	0.0559	0.0559	0.0754
HCRF EnMAP rot (672 nm)	0.0485	0.0483	0.0474	0.0444	0.0370	0.0403	0.0393	0.0420	0.0519	0.0511	0.0513	0.0581	0.0552	0.0495	0.0408	0.0430	0.0503	0.0431	0.0420	0.0415	0.0405	0.0405
HCRF EnMAP NIR (864 nm)	0.3059	0.3462	0.3779	0.3332	0.3485	0.3453	0.3977	0.3763	0.4335	0.4069	0.3543	0.3507	0.3914	0.3516	0.3201	0.3227	0.3582	0.3348	0.3568	0.3312	0.4347	0.4347
ANIF EnMAP rot (672 nm)	1.0637	1.0584	1.0395	0.9725	0.8114	0.8836	0.8608	0.9205	1.1369	1.1204	1.1250	1.2724	1.2098	1.0855	0.8935	0.9433	1.1015	0.9456	0.9207	0.9096	0.8881	0.8881
ANIF EnMAP NIR (864 nm)	0.9002	1.0190	1.1121	0.9806	1.0256	1.0163	1.1706	1.1075	1.2758	1.1974	1.0428	1.0320	1.1518	1.0348	0.9421	0.9498	1.0541	0.9853	1.0499	0.9748	1.2793	1.2793
Rel. Blue Absorption Depth	0.5593	0.6493	0.6953	0.6940	0.7507	0.7464	0.8199	0.7964	0.8170	0.7592	0.6422	0.5706	0.6685	0.6224	0.6095	0.6347	0.5991	0.6312	0.7219	0.6213	0.8533	0.8533
Rel. Red Absorption Depth	1.9191	2.2583	2.5455	2.3797	3.0886	2.7551	3.3756	2.9181	2.7272	2.5748	2.1686	1.8332	2.2504	2.2352	2.4911	2.3727	2.2511	2.4433	2.7309	2.5503	3.5955	3.5955
NDVI (EnMAP)	0.7261	0.7552	0.7770	0.7650	0.8079	0.7909	0.8203	0.7992	0.7862	0.7767	0.7469	0.7159	0.7528	0.7531	0.7741	0.7646	0.7539	0.7717	0.7893	0.7773	0.8294	0.8294
Nadir Norm. NDVI (AVHRR)	0.9571	0.9888	1.0136	1.0099	1.0594	1.0309	1.0693	1.0402	1.0141	1.0061	0.9728	0.9402	0.9889	0.9921	1.0185	1.0062	0.9888	1.0087	1.0325	1.0256	1.0810	1.0810
Nadir Norm. NDVI (MODIS)	0.9553	0.9890	1.0142	1.0092	1.0613	1.0339	1.0719	1.0422	1.0188	1.0094	0.9742	0.9397	0.9888	0.9903	1.0192	1.0075	0.9913	1.0101	1.0347	1.0259	1.0838	1.0838
Nadir Norm. NDVI (EnMAP)	0.9514	0.9895	1.0180	1.0023	1.0586	1.0363	1.0747	1.0471	1.0302	1.0177	0.9786	0.9380	0.9863	0.9867	1.0142	1.0019	0.9878	1.0111	1.0342	1.0184	1.0868	1.0868

(cont.)

HVG2_02 (SZA = 50°; SAA = 137°)	Viewing Geometry (Viewing Zenith Angle | Viewing Azimuth Angle)																							
	20|135	20|157.5	20|170	30|180	30|190	30|202.5	30|225	30|270	30|315	30|337.5	30|350	30|0	30|10	30|122.5	30|45	30|90	30|135	30|157.5	30|170
HCRF EnMAP blue (479 nm)	0.0295	0.0311	0.0313	0.0389	0.0374	0.0377	0.0373	0.0362	0.0259	0.0263	0.0250	0.0254	0.0274	0.0246	0.0213	0.0269	0.0291	0.0337	0.0360	0.0360
HCRF EnMAP green (549 nm)	0.0679	0.0800	0.0807	0.1013	0.0902	0.0862	0.0828	0.0780	0.0628	0.0582	0.0559	0.0577	0.0604	0.0523	0.0458	0.0679	0.0682	0.0836	0.0930	0.0930
HCRF EnMAP rot (672 nm)	0.0455	0.0456	0.0463	0.0563	0.0555	0.0585	0.0587	0.0605	0.0398	0.0408	0.0393	0.0394	0.0418	0.0389	0.0331	0.0401	0.0479	0.0514	0.0524	0.0524
HCRF EnMAP NIR (864 nm)	0.3711	0.4207	0.4197	0.4924	0.4362	0.4123	0.3889	0.3895	0.3628	0.3174	0.3216	0.3239	0.3338	0.3066	0.2777	0.3858	0.3559	0.4292	0.4646	0.4646
ANIF EnMAP rot (672 nm)	0.9979	0.9996	1.0155	1.2346	1.2160	1.2827	1.2863	1.3254	0.8717	0.8942	0.8604	0.8637	0.9157	0.8523	0.7247	0.8782	1.0506	1.1267	1.1493	1.1493
ANIF EnMAP NIR (864 nm)	1.0921	1.2382	1.2353	1.4492	1.2837	1.2135	1.1445	1.1464	1.0678	0.9340	0.9465	0.9533	0.9825	0.9024	0.8174	1.1355	1.0476	1.2632	1.3673	1.3673
Rel. Blue Absorption Depth	0.6904	0.8286	0.8255	0.8419	0.7620	0.7051	0.6658	0.6289	0.7544	0.6384	0.6485	0.6719	0.6384	0.6022	0.6104	0.8146	0.7218	0.7914	0.8359	0.8359
Rel. Red Absorption Depth	2.6326	3.0366	2.9742	2.8868	2.5580	2.2599	2.1053	2.0466	3.0281	2.4695	2.6486	2.6487	2.5554	2.5127	2.6631	3.2804	2.4016	2.7588	2.9229	2.9229
NDVI (EnMAP)	0.7814	0.8044	0.8012	0.7947	0.7743	0.7514	0.7377	0.7312	0.8024	0.7722	0.7824	0.7831	0.7775	0.7749	0.7872	0.8118	0.7626	0.7861	0.7971	0.7971
Nadir Norm. NDVI (AVHRR)	1.0228	1.0411	1.0338	1.0234	1.0009	0.9769	0.9588	0.9626	1.0473	1.0145	1.0290	1.0249	1.0239	1.0256	1.0396	1.0640	1.0001	1.0237	1.0305	1.0305
Nadir Norm. NDVI (MODIS)	1.0250	1.0450	1.0388	1.0290	1.0054	0.9791	0.9611	0.9625	1.0481	1.0149	1.0298	1.0262	1.0244	1.0255	1.0396	1.0663	1.0025	1.0274	1.0352	1.0352
Nadir Norm. NDVI (EnMAP)	1.0238	1.0539	1.0497	1.0412	1.0145	0.9845	0.9666	0.9581	1.0513	1.0117	1.0251	1.0260	1.0187	1.0153	1.0314	1.0637	0.9992	1.0299	1.0444	1.0444

Table C.6-4: Spectro-directional data of the HVG2_03 spectro-goniometer measurement.

HVG2_03 (SZA = 46°; SAA = 189°)	Viewing Geometry (Viewing Zenith Angle | Viewing Azimuth Angle)																							
	0|0	5|180	5|202.5	5|225	5|270	5|315	5|337.5	5|0	5|22.5	5|45	5|90	5|135	5|157.5	10|180	10|190	10|202.5	10|225	10|270	10|315	10|337.5	10|350
HCRF EnMAP blue (479 nm)	0.0244	0.0227	0.0220	0.0268	0.0274	0.0267	0.0255	0.0269	0.0209	0.0191	0.0199	0.0256	0.0247	0.0241	0.0262	0.0282	0.0323	0.0301	0.0225	0.0220	0.0201
HCRF EnMAP green (549 nm)	0.0654	0.0627	0.0553	0.0572	0.0670	0.0583	0.0518	0.0610	0.0481	0.0428	0.0493	0.0628	0.0620	0.0558	0.0578	0.0604	0.0725	0.0683	0.0521	0.0494	0.0508
HCRF EnMAP rot (672 nm)	0.0363	0.0329	0.0336	0.0433	0.0431	0.0429	0.0431	0.0429	0.0338	0.0298	0.0274	0.0377	0.0388	0.0391	0.0435	0.0451	0.0526	0.0469	0.0367	0.0324	0.0329
HCRF EnMAP NIR (864 nm)	0.3671	0.3650	0.3112	0.2979	0.3470	0.3025	0.2703	0.3199	0.2602	0.2453	0.2846	0.3456	0.3368	0.2994	0.2980	0.2964	0.3548	0.3431	0.2821	0.2724	0.3013
ANIF EnMAP rot (672 nm)	1.0000	0.9059	0.9269	1.1924	1.1890	1.1823	1.1892	1.1825	0.9313	0.8202	0.7555	1.0381	1.0685	1.0779	1.1988	1.2446	1.4499	1.2924	1.0112	0.8935	0.9059
ANIF EnMAP NIR (864 nm)	1.0000	0.9944	0.8479	0.8115	0.9453	0.8240	0.7362	0.8715	0.7089	0.6682	0.7753	0.9415	0.9176	0.8156	0.8118	0.8075	0.9665	0.9346	0.7686	0.7420	0.8208
Rel. Blue Absorption Depth	0.8581	0.9138	0.7994	0.6182	0.7580	0.6398	0.5645	0.6661	0.6837	0.6448	0.7706	0.7723	0.7983	0.7000	0.6560	0.6201	0.6629	0.6801	0.6996	0.6603	0.7851
Rel. Red Absorption Depth	3.3661	3.7645	3.0430	2.1682	2.5840	2.2384	1.8926	2.3925	2.4148	2.6130	3.3675	3.0228	2.8664	2.4422	2.1635	2.0674	2.1448	2.3714	2.4531	2.7027	3.0371
NDVI (EnMAP)	0.8202	0.8348	0.8050	0.7465	0.7789	0.7517	0.7247	0.7636	0.7702	0.7837	0.8243	0.8035	0.7936	0.7690	0.7453	0.7357	0.7418	0.7596	0.7699	0.7873	0.8033
Nadir Norm. NDVI (AVHRR)	1.0000	1.0292	0.9928	0.9240	0.9530	0.9294	0.9027	0.9426	0.9444	0.9757	1.0124	0.9858	0.9748	0.9468	0.9186	0.9040	0.9065	0.9319	0.9487	0.9675	0.9923
Nadir Norm. NDVI (MODIS)	1.0000	1.0268	0.9902	0.9208	0.9520	0.9261	0.8982	0.9389	0.9420	0.9725	1.0118	0.9847	0.9736	0.9444	0.9158	0.9021	0.9042	0.9299	0.9462	0.9653	0.9893
Nadir Norm. NDVI (EnMAP)	1.0000	1.0179	0.9816	0.9101	0.9497	0.9165	0.8837	0.9310	0.9391	0.9555	1.0051	0.9797	0.9677	0.9376	0.9088	0.8970	0.9045	0.9261	0.9387	0.9600	0.9795

(cont.)

HVG2_03 (SZA = 46°; SAA = 189°)	Viewing Geometry (Viewing Zenith Angle | Viewing Azimuth Angle)																							
	10|0	10|10	10|22.5	10|45	10|90	10|135	10|157.5	10|170	20|180	20|190	20|202.5	20|225	20|270	20|315	20|337.5	20|350	20|0	20|10	20|22.5	20|45	20|90
HCRF EnMAP blue (479 nm)	0.0217	0.0209	0.0228	0.0206	0.0212	0.0266	0.0249	0.0249	0.0322	0.0314	0.0329	0.0330	0.0266	0.0204	0.0190	0.0188	0.0192	0.0208	0.0193	0.0174	0.0208
HCRF EnMAP green (549 nm)	0.0545	0.0501	0.0604	0.0472	0.0521	0.0691	0.0587	0.0616	0.0667	0.0691	0.0753	0.0775	0.0578	0.0461	0.0439	0.0421	0.0433	0.0500	0.0484	0.0423	0.0551
HCRF EnMAP rot (672 nm)	0.0327	0.0319	0.0342	0.0308	0.0307	0.0400	0.0353	0.0372	0.0524	0.0479	0.0515	0.0523	0.0413	0.0303	0.0292	0.0285	0.0302	0.0308	0.0283	0.0254	0.0303
HCRF EnMAP NIR (864 nm)	0.3117	0.3011	0.3530	0.2802	0.2937	0.3744	0.3181	0.3318	0.3214	0.3295	0.3497	0.3908	0.2985	0.2650	0.2691	0.2643	0.2668	0.2990	0.3046	0.2665	0.3226
ANIF EnMAP rot (672 nm)	0.9015	0.8806	0.9425	0.8481	0.8477	1.1040	0.9738	1.0261	1.4450	1.3219	1.4190	1.4425	1.1375	0.8362	0.8047	0.7863	0.8328	0.8480	0.7803	0.6996	0.8365
ANIF EnMAP NIR (864 nm)	0.8492	0.8201	0.9615	0.7632	0.8001	1.0200	0.8664	0.9037	0.8755	0.8977	0.9527	1.0647	0.8131	0.7220	0.7332	0.7200	0.7268	0.8145	0.8297	0.7258	0.8787
Rel. Blue Absorption Depth	0.7762	0.7291	0.8482	0.6881	0.7571	0.8428	0.7159	0.7661	0.6024	0.6562	0.6864	0.7166	0.6216	0.6580	0.6765	0.6556	0.6541	0.7263	0.7738	0.7490	0.8571
Rel. Red Absorption Depth	3.0984	3.0756	3.4550	3.0136	3.0970	3.0942	2.9226	2.9282	1.9073	2.1771	2.1572	2.4219	2.2667	2.8195	2.9320	2.9493	2.7847	3.1865	3.6085	3.4723	3.5754
NDVI (EnMAP)	0.8101	0.8082	0.8234	0.8021	0.8105	0.8068	0.8001	0.7983	0.7196	0.7460	0.7434	0.7639	0.7571	0.7946	0.8043	0.8052	0.7966	0.8134	0.8300	0.8261	0.8280
Nadir Norm. NDVI (AVHRR)	0.9966	1.0018	1.0086	0.9941	0.9946	0.9864	0.9765	0.9802	0.8853	0.9150	0.9046	0.9317	0.9341	0.9785	0.9954	1.0004	0.9880	1.0012	1.0223	1.0241	1.0163
Nadir Norm. NDVI (MODIS)	0.9948	0.9988	1.0076	0.9910	0.9938	0.9862	0.9757	0.9793	0.8826	0.9128	0.9043	0.9296	0.9308	0.9753	0.9923	0.9968	0.9850	0.9995	1.0198	1.0210	1.0149
Nadir Norm. NDVI (EnMAP)	0.9878	0.9854	1.0040	0.9780	0.9882	0.9837	0.9755	0.9733	0.8774	0.9095	0.9064	0.9314	0.9231	0.9689	0.9807	0.9818	0.9713	0.9918	1.0120	1.0072	1.0096

(cont.)

HVG2_03 (SZA = 46°; SAA = 189°)	Viewing Geometry (Viewing Zenith Angle | Viewing Azimuth Angle)																							
	20|135	20|157.5	20|170	30|180	30|190	30|202.5	30|225	30|270	30|315	30|337.5	30|350	30|0	30|10	30|122.5	30|45	30|90	30|135	30|157.5	30|170
HCRF EnMAP blue (479 nm)	0.0249	0.0265	0.0286	0.0354	0.0358	0.0422	0.0370	0.0252	0.0188	0.0190	0.0190	0.0200	0.0197	0.0192	0.0189	0.0229	0.0246	0.0333	0.0377
HCRF EnMAP green (549 nm)	0.0622	0.0630	0.0639	0.0829	0.0829	0.0924	0.0859	0.0579	0.0438	0.0428	0.0426	0.0451	0.0463	0.0475	0.0451	0.0600	0.0610	0.0743	0.0831
HCRF EnMAP rot (672 nm)	0.0360	0.0406	0.0459	0.0552	0.0542	0.0694	0.0618	0.0375	0.0280	0.0291	0.0307	0.0303	0.0281	0.0282	0.0280	0.0337	0.0356	0.0530	0.0595
HCRF EnMAP NIR (864 nm)	0.3351	0.3157	0.3116	0.3876	0.4035	0.4258	0.4284	0.3136	0.2698	0.2690	0.2733	0.2848	0.2935	0.3065	0.2854	0.3389	0.3220	0.3502	0.3750
ANIF EnMAP rot (672 nm)	0.9914	1.1187	1.2665	1.5227	1.4953	1.9129	1.7050	1.0325	0.7720	0.8032	0.8451	0.8351	0.7753	0.7773	0.7729	0.9296	0.9816	1.4611	1.6396
ANIF EnMAP NIR (864 nm)	0.9128	0.8601	0.8488	1.0558	1.0992	1.1600	1.1671	0.8542	0.7349	0.7328	0.7445	0.7759	0.7996	0.8350	0.7775	0.9232	0.8771	0.9541	1.0215
Rel. Blue Absorption Depth	0.7868	0.7286	0.6704	0.7240	0.7100	0.6464	0.7071	0.6931	0.6920	0.6544	0.6553	0.6504	0.6948	0.7775	0.7299	0.8346	0.7816	0.6736	0.6731
Rel. Red Absorption Depth	3.0692	2.5027	2.1545	2.2222	2.4129	1.9304	2.1975	2.6634	3.1024	2.9639	2.8377	3.0293	3.4554	3.6369	3.3634	3.3452	2.9443	2.0933	1.9698
NDVI (EnMAP)	0.8062	0.7722	0.7430	0.7505	0.7630	0.7198	0.7477	0.7866	0.8119	0.8046	0.7983	0.8077	0.8251	0.8315	0.8211	0.8190	0.8009	0.7371	0.7262
Nadir Norm. NDVI (AVHRR)	0.9810	0.9419	0.9044	0.9161	0.9316	0.8819	0.9170	0.9680	1.0021	0.9950	0.9921	0.9971	1.0149	1.0281	1.0168	0.9960	0.9740	0.9008	0.8842
Nadir Norm. NDVI (MODIS)	0.9806	0.9418	0.9044	0.9156	0.9318	0.8801	0.9144	0.9657	1.0004	0.9923	0.9883	0.9953	1.0133	1.0250	1.0135	0.9957	0.9742	0.8997	0.8827
Nadir Norm. NDVI (EnMAP)	0.9829	0.9416	0.9060	0.9151	0.9303	0.8776	0.9117	0.9591	0.9900	0.9810	0.9734	0.9849	1.0061	1.0139	1.0012	0.9986	0.9765	0.8988	0.8855

Table C.6-5: Spectro-directional data of the HVG2_04 spectro-goniometer measurement.

HVG2_04 (SZA = 50°; SAA = 217°)	Viewing Geometry (Viewing Zenith Angle | Viewing Azimuth Angle)																								
	0|0	5|180	5|202.5	5|225	5|270	5|315	5|337.5	5|0	5|22.5	5|45	5|90	5|135	5|157.5	10|180	10|202.5	10|225	10|270	10|315	10|337.5	10|350
HCRF EnMAP blue (479 nm)	0.0193	0.0195	0.0205	0.0213	0.0196	0.0174	0.0154	0.0188	0.0166	0.0181	0.0184	0.0190	0.0209	0.0235	0.0230	0.0225	0.0198	0.0189	0.0166	0.0184
HCRF EnMAP green (549 nm)	0.0417	0.0434	0.0523	0.0520	0.0407	0.0425	0.0396	0.0481	0.0404	0.0423	0.0468	0.0469	0.0456	0.0530	0.0594	0.0536	0.0409	0.0457	0.0434	0.0448
HCRF EnMAP rot (672 nm)	0.0272	0.0296	0.0314	0.0307	0.0316	0.0294	0.0221	0.0269	0.0232	0.0273	0.0271	0.0263	0.0336	0.0368	0.0349	0.0331	0.0304	0.0297	0.0251	0.0257
HCRF EnMAP NIR (864 nm)	0.2199	0.2242	0.2803	0.2697	0.2156	0.2445	0.2414	0.2807	0.2441	0.2351	0.2666	0.2591	0.2278	0.2553	0.2850	0.2722	0.2126	0.2531	0.2640	0.2642
ANIF EnMAP rot (672 nm)	1.0000	1.0864	1.1540	1.1282	1.1610	1.0793	0.8119	0.9898	0.8520	1.0029	0.9953	0.9648	1.2338	1.3515	1.4501	1.2817	1.2161	1.1152	1.0916	0.9239	0.9451
ANIF EnMAP NIR (864 nm)	1.0000	1.0193	1.2745	1.2262	0.9802	1.1118	1.0975	1.2763	1.1097	1.0687	1.2120	1.1781	1.0359	1.1607	1.2958	1.4147	1.2375	0.9665	1.1505	1.2002	1.2014
Rel. Blue Absorption Depth	0.6063	0.6414	0.7944	0.7496	0.5750	0.7344	0.8006	0.7949	0.7394	0.6901	0.7994	0.7633	0.6292	0.6558	0.6832	0.8063	0.7326	0.5679	0.7252	0.8037	0.7392
Rel. Red Absorption Depth	2.5782	2.3864	2.9570	2.8733	2.1043	2.7139	3.6069	3.4572	3.4978	2.7847	3.2604	3.2426	2.1257	2.2030	2.3211	3.0100	2.6827	2.1581	2.7616	3.4446	3.3875
NDVI (EnMAP)	0.7798	0.7669	0.7985	0.7956	0.7443	0.7855	0.8323	0.8249	0.8264	0.7919	0.8155	0.8160	0.7431	0.7481	0.7567	0.7984	0.7831	0.7501	0.7899	0.8260	0.8226
Nadir Norm. NDVI (AVHRR)	1.0000	0.9843	1.0176	1.0090	0.9655	1.0122	1.0659	1.0537	1.0631	1.0163	1.0415	1.0416	0.9556	0.9559	0.9583	1.0080	0.9937	0.9640	1.0096	1.0530	1.0521
Nadir Norm. NDVI (MODIS)	1.0000	0.9837	1.0181	1.0104	0.9639	1.0117	1.0658	1.0544	1.0624	1.0166	1.0421	1.0418	0.9550	0.9566	0.9593	1.0097	0.9938	0.9633	1.0101	1.0535	1.0529
Nadir Norm. NDVI (EnMAP)	1.0000	0.9836	1.0240	1.0203	0.9546	1.0074	1.0673	1.0578	1.0599	1.0156	1.0458	1.0464	0.9530	0.9594	0.9705	1.0239	1.0044	0.9620	1.0130	1.0594	1.0549

(cont.)

HVG2_04 (SZA = 50°; SAA = 217°)	Viewing Geometry (Viewing Zenith Angle | Viewing Azimuth Angle)																								
	10|0	10|10	10|22.5	10|45	10|90	10|135	10|157.5	10|170	20|180	20|190	20|202.5	20|225	20|270	20|315	20|337.5	20|350	20|0	20|10	20|22.5	20|45	20|90
HCRF EnMAP blue (479 nm)	0.0171	0.0163	0.0171	0.0190	0.0191	0.0188	0.0219	0.0219	0.0253	0.0276	0.0238	0.0260	0.0207	0.0173	0.0149	0.0182	0.0163	0.0162	0.0166	0.0170	0.0198
HCRF EnMAP green (549 nm)	0.0432	0.0416	0.0430	0.0450	0.0499	0.0441	0.0453	0.0451	0.0589	0.0605	0.0585	0.0627	0.0450	0.0385	0.0350	0.0442	0.0408	0.0415	0.0406	0.0399	0.0536
HCRF EnMAP rot (672 nm)	0.0244	0.0229	0.0241	0.0305	0.0269	0.0267	0.0349	0.0340	0.0396	0.0445	0.0367	0.0394	0.0309	0.0268	0.0223	0.0253	0.0238	0.0238	0.0241	0.0266	0.0289
HCRF EnMAP NIR (864 nm)	0.2661	0.2585	0.2566	0.2610	0.2825	0.2384	0.2231	0.2178	0.2810	0.2799	0.2995	0.3145	0.2337	0.2206	0.2217	0.2714	0.2625	0.2647	0.2513	0.2360	0.3014
ANIF EnMAP rot (672 nm)	0.8947	0.8412	0.8846	1.1193	0.9886	0.9799	1.2821	1.2505	1.4543	1.6360	1.3484	1.4462	1.1339	0.9855	0.8195	0.9313	0.8734	0.8739	0.8853	0.9762	1.0633
ANIF EnMAP NIR (864 nm)	1.2098	1.1752	1.1667	1.1868	1.2844	1.0840	1.0144	0.9901	1.2775	1.2727	1.3616	1.4298	1.0623	1.0028	1.0079	1.2340	1.1933	1.2036	1.1426	1.0730	1.3705
Rel. Blue Absorption Depth	0.7842	0.7970	0.7772	0.7054	0.8449	0.7045	0.5812	0.5722	0.6972	0.6484	0.7548	0.7515	0.6189	0.6312	0.6825	0.7310	0.7737	0.8037	0.7511	0.7003	0.8868
Rel. Red Absorption Depth	3.6334	3.7776	3.5524	2.8269	3.4955	2.9053	2.0052	1.9502	2.2620	1.9756	2.6516	2.6035	2.4132	2.6297	3.1726	3.5518	3.7072	3.7395	3.4699	2.9106	3.4801
NDVI (EnMAP)	0.8323	0.8373	0.8284	0.7910	0.8261	0.7988	0.7295	0.7297	0.7530	0.7255	0.7816	0.7775	0.7666	0.7831	0.8172	0.8292	0.8339	0.8351	0.8250	0.7976	0.8248
Nadir Norm. NDVI (AVHRR)	1.0663	1.0754	1.0647	1.0209	1.0510	1.0158	0.9410	0.9369	0.9541	0.9222	0.9884	0.9847	0.9820	1.0054	1.0470	1.0599	1.0719	1.0765	1.0650	1.0273	1.0473
Nadir Norm. NDVI (MODIS)	1.0664	1.0747	1.0651	1.0205	1.0526	1.0173	0.9404	0.9362	0.9561	0.9223	0.9891	0.9847	0.9821	1.0048	1.0466	1.0607	1.0704	1.0745	1.0637	1.0270	1.0490
Nadir Norm. NDVI (EnMAP)	1.0674	1.0737	1.0625	1.0144	1.0594	1.0244	0.9355	0.9358	0.9657	0.9304	1.0024	0.9971	0.9832	1.0043	1.0480	1.0634	1.0694	1.0710	1.0580	1.0229	1.0578

(cont.)

HVG2_04 (SZA = 50°; SAA = 217°)	Viewing Geometry (Viewing Zenith Angle | Viewing Azimuth Angle)																								
	20|135	20|157.5	20|170	30|180	30|190	30|202.5	30|225	30|270	30|315	30|337.5	30|350	30|0	30|10	30|122.5	30|45	30|90	30|135	30|157.5	30|170				
HCRF EnMAP blue (479 nm)	0.0211	0.0268	0.0253	0.0364	0.0339	0.0323	0.0292	0.0210	0.0173	0.0176	0.0191	0.0190	0.0182	0.0166	0.0158	0.0200	0.0231	0.0306	0.0300						
HCRF EnMAP green (549 nm)	0.0515	0.0563	0.0593	0.0819	0.0732	0.0719	0.0643	0.0491	0.0381	0.0401	0.0455	0.0460	0.0465	0.0378	0.0368	0.0531	0.0539	0.0671	0.0721						
HCRF EnMAP rot (672 nm)	0.0317	0.0434	0.0381	0.0597	0.0548	0.0538	0.0461	0.0287	0.0260	0.0264	0.0264	0.0272	0.0258	0.0238	0.0227	0.0280	0.0342	0.0503	0.0451						
HCRF EnMAP NIR (864 nm)	0.2686	0.2666	0.2848	0.3666	0.3254	0.3386	0.3114	0.2655	0.2296	0.2502	0.2812	0.2889	0.2918	0.2369	0.2206	0.3019	0.2720	0.3109	0.3444						
ANIF EnMAP rot (672 nm)	1.1640	1.5963	1.4016	2.1930	2.0120	1.9754	1.6945	1.0559	0.9547	0.9682	0.9696	1.0000	0.9469	0.8727	0.8330	1.0303	1.2571	1.8473	1.6574						
ANIF EnMAP NIR (864 nm)	1.2213	1.2122	1.2950	1.6669	1.4794	1.5396	1.4160	1.2073	1.0441	1.1375	1.2785	1.3136	1.3269	1.0773	1.0031	1.3727	1.2366	1.4135	1.5659						
Rel. Blue Absorption Depth	0.7527	0.6019	0.7135	0.6735	0.6368	0.6546	0.6520	0.6969	0.6294	0.6587	0.7091	0.7443	0.8058	0.6730	0.6913	0.8516	0.7132	0.6605	0.7373						
Rel. Red Absorption Depth	2.7104	1.9154	2.3720	1.9283	1.8454	1.9616	2.1738	3.0116	2.8018	3.0441	3.5354	3.5743	3.8279	3.2589	3.1676	3.6231	2.5512	1.9317	2.4705						
NDVI (EnMAP)	0.7890	0.7197	0.7638	0.7200	0.7119	0.7259	0.7420	0.8047	0.7967	0.8094	0.8284	0.8278	0.8377	0.8178	0.8136	0.8300	0.7765	0.7216	0.7684						
Nadir Norm. NDVI (AVHRR)	1.0033	0.9261	0.9671	0.9107	0.9006	0.9218	0.9467	1.0251	1.0202	1.0358	1.0574	1.0650	1.0726	1.0550	1.0417	1.0540	0.9865	0.9232	0.9689						
Nadir Norm. NDVI (MODIS)	1.0049	0.9258	0.9685	0.9112	0.9000	0.9214	0.9457	1.0264	1.0192	1.0355	1.0581	1.0642	1.0724	1.0537	1.0419	1.0552	0.9883	0.9230	0.9718						
Nadir Norm. NDVI (EnMAP)	1.0119	0.9230	0.9795	0.9233	0.9130	0.9310	0.9516	1.0320	1.0217	1.0380	1.0624	1.0616	1.0743	1.0487	1.0434	1.0645	0.9959	0.9254	0.9854						

V *Main Spectral Characteristics*

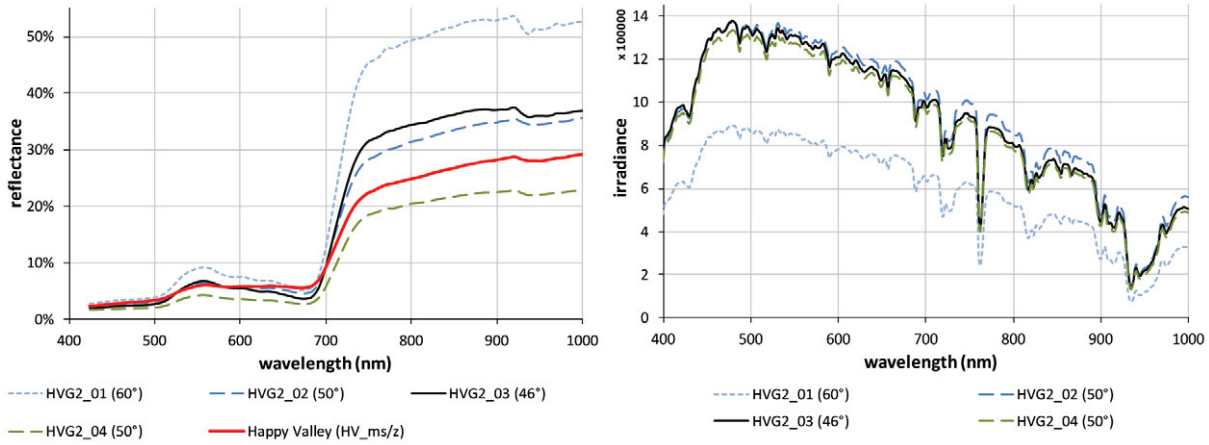

Figure C.6-6: Nadir reflectances and irradiance profiles of the HVG2 site at different sun zenith angles. Left: Comparison of the nadir reflectance signatures with the average zonal vegetation (MAT). Right: Comparison of the total irradiance profiles.

VI *HCRF Visualization*

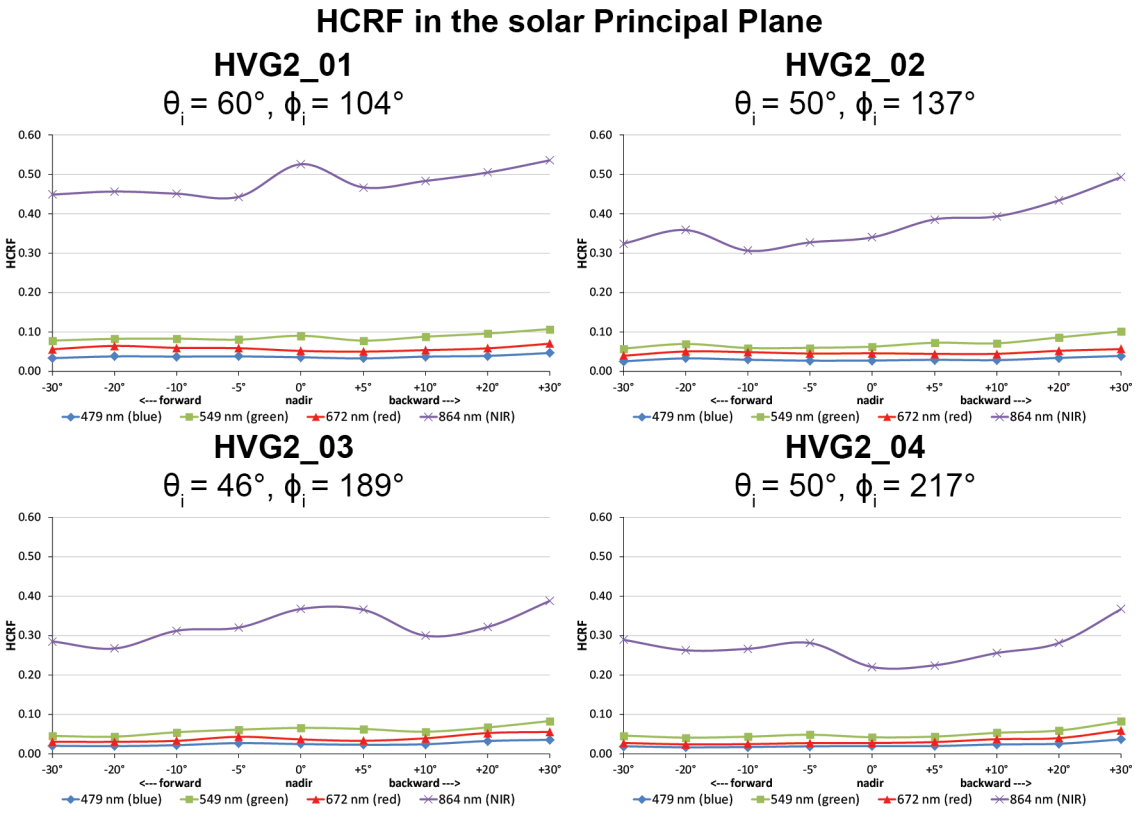

Figure C.6-7: Comparison of the HCRF values at 479 nm (blue), 549 nm (green), 672 nm (red), and 864 nm (NIR) in the solar principal plane of the HVG2 site at different sun zenith angles.

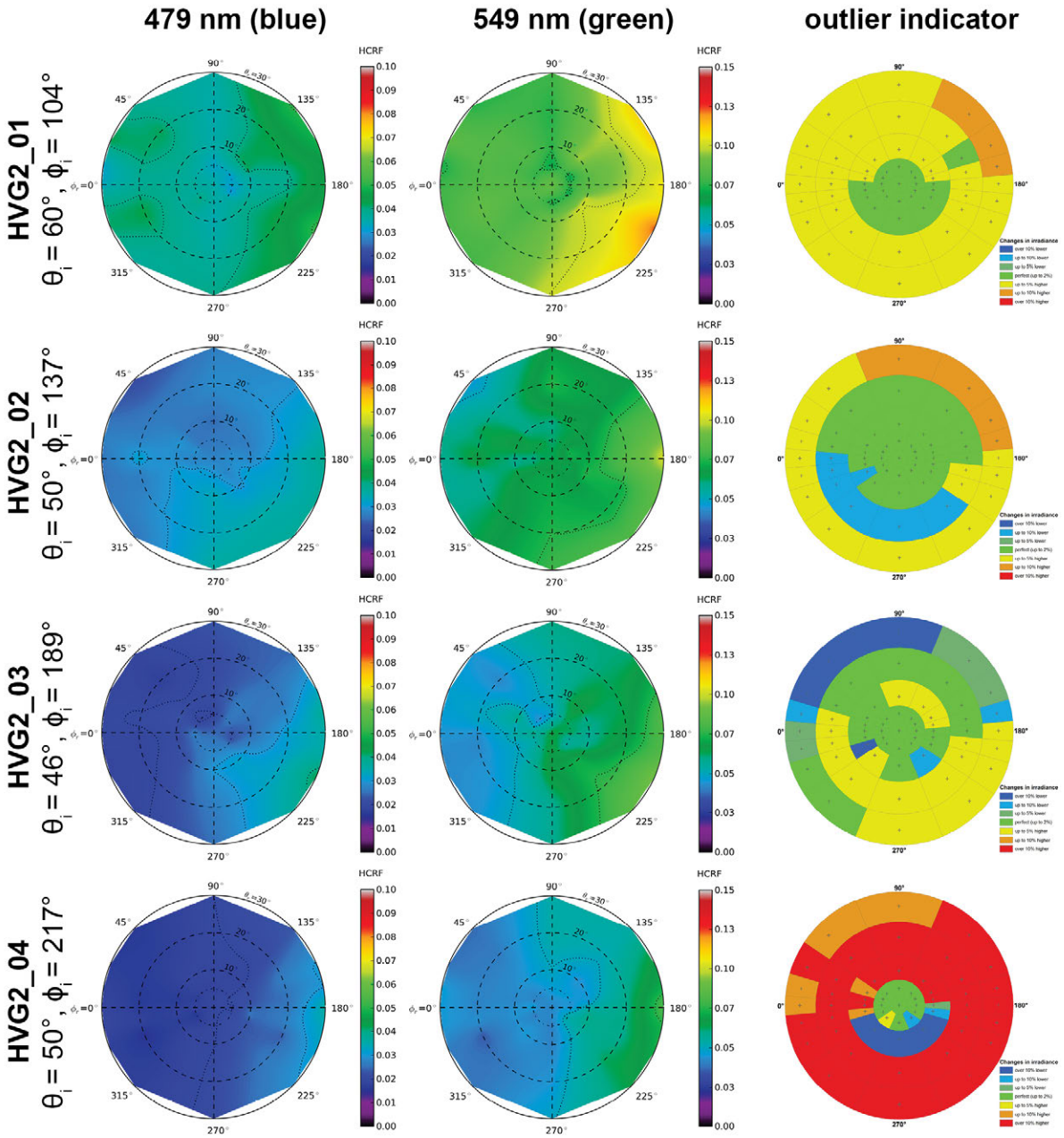

Figure C.6-8: HCRF visualization at 479 nm and 549 nm of the HVG2 site.

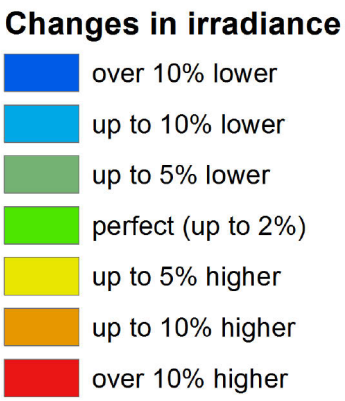

Figure C.6-9: Legend of the outlier indicator graphics shown in Figure C.6-8, C.6-10, and C.6-13

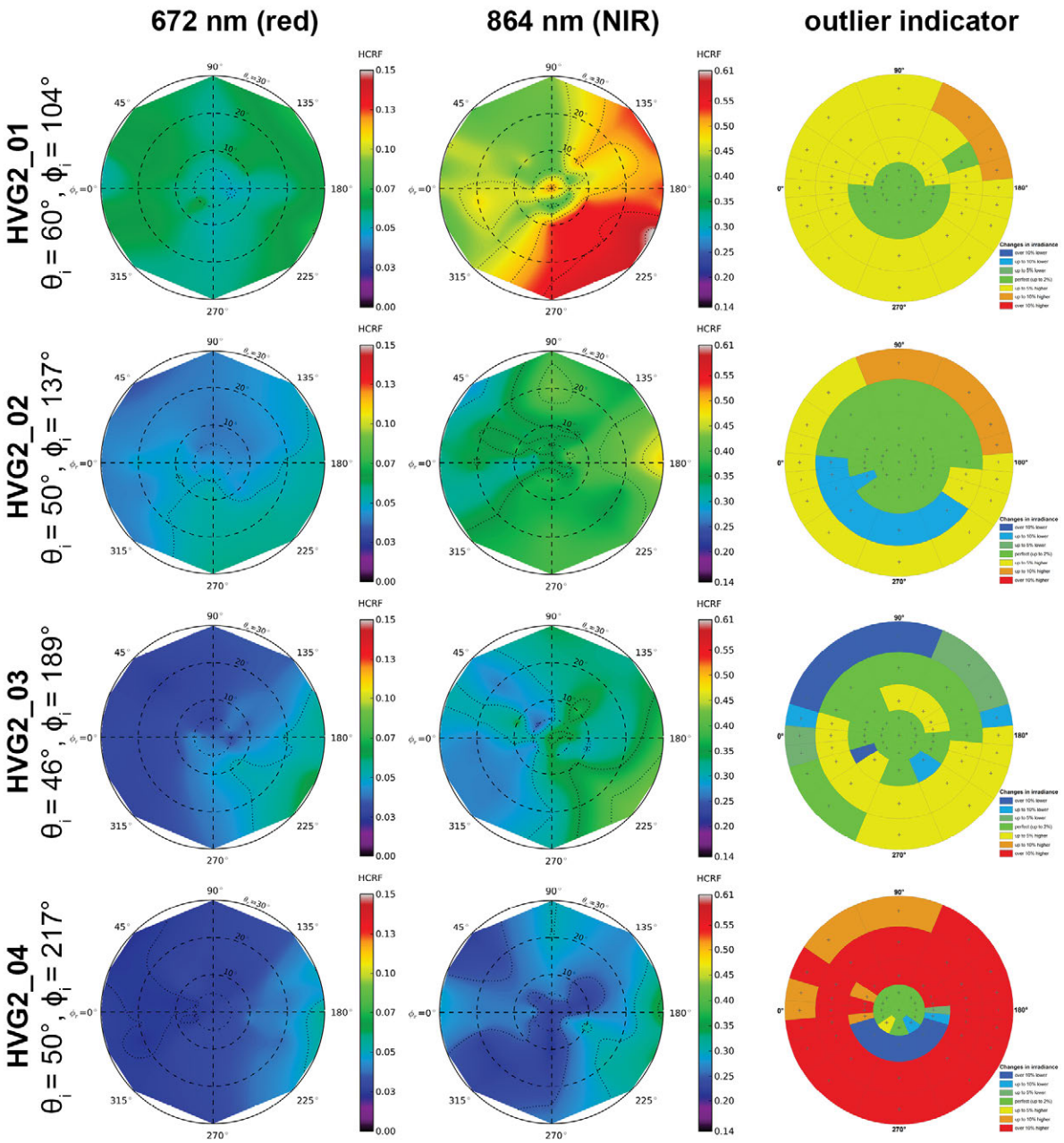

Figure C.6-10: HCRF visualization at 672 nm and 864 nm of the HVG2 site.

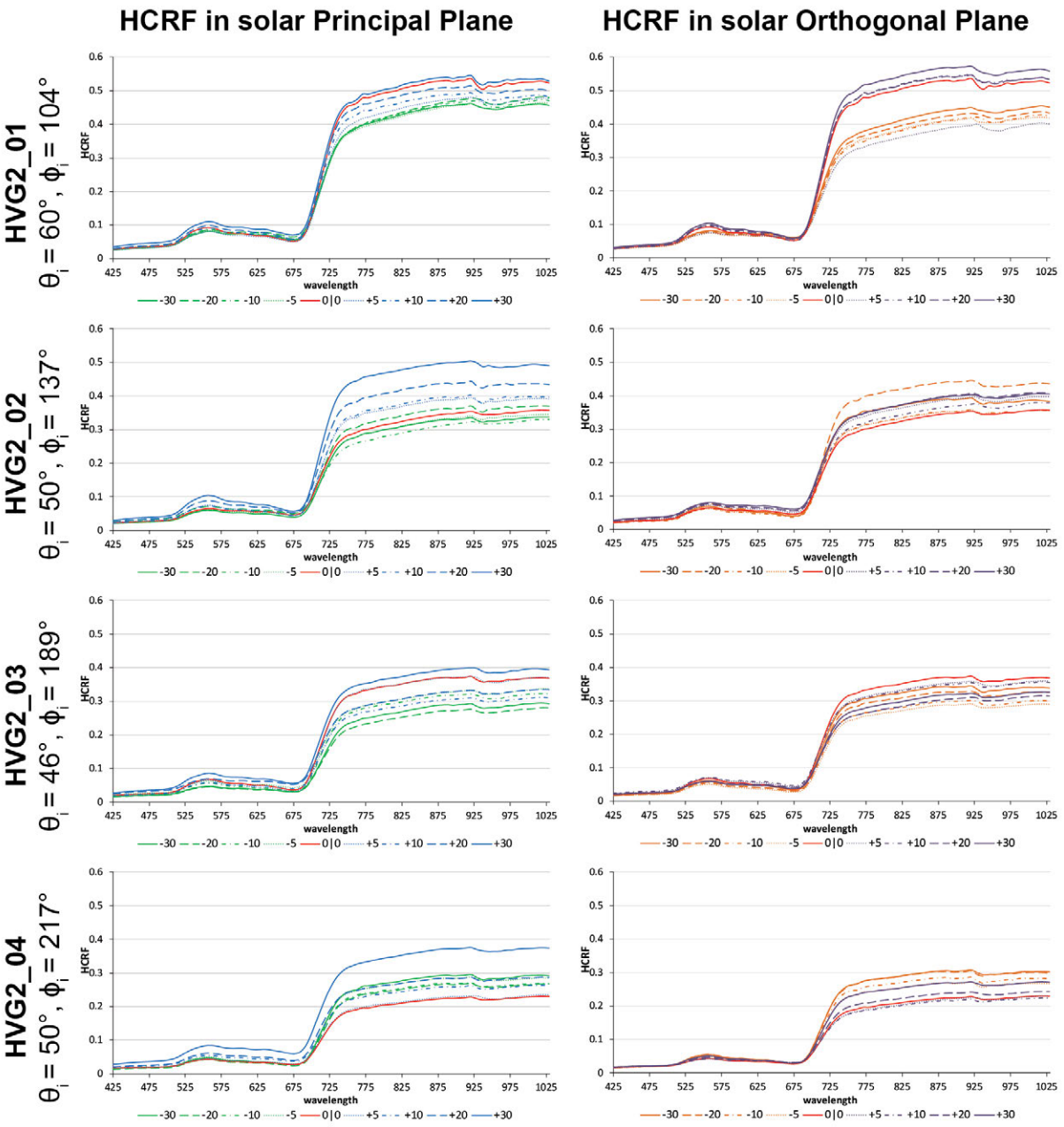

Figure C.6-11: HCRF visualization in principal & orthogonal plane of the HVG2 site.

VII *ANIF Visualization*

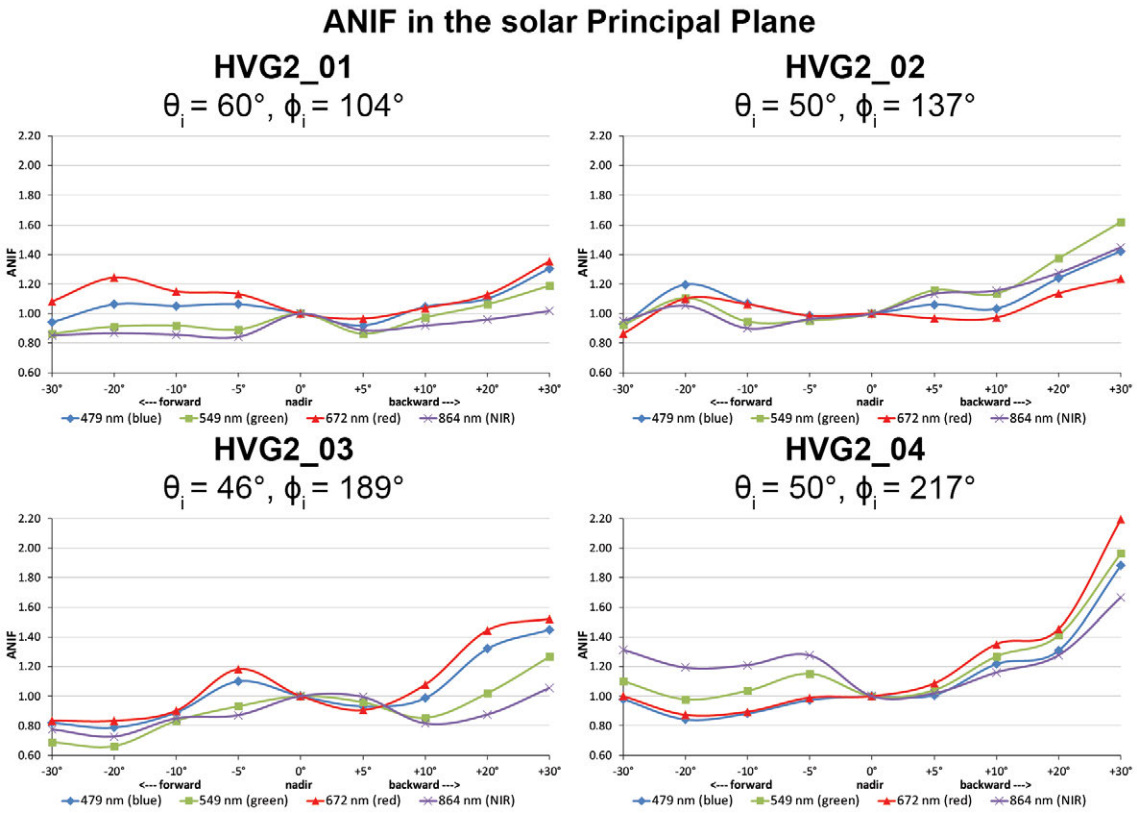

Figure C.6-12: Comparison of the ANIF values at 479 nm (blue), 549 nm (green), 672 nm (red), and 864 nm (NIR) in the solar principal plane of the HVG2 site at different sun zenith angles.

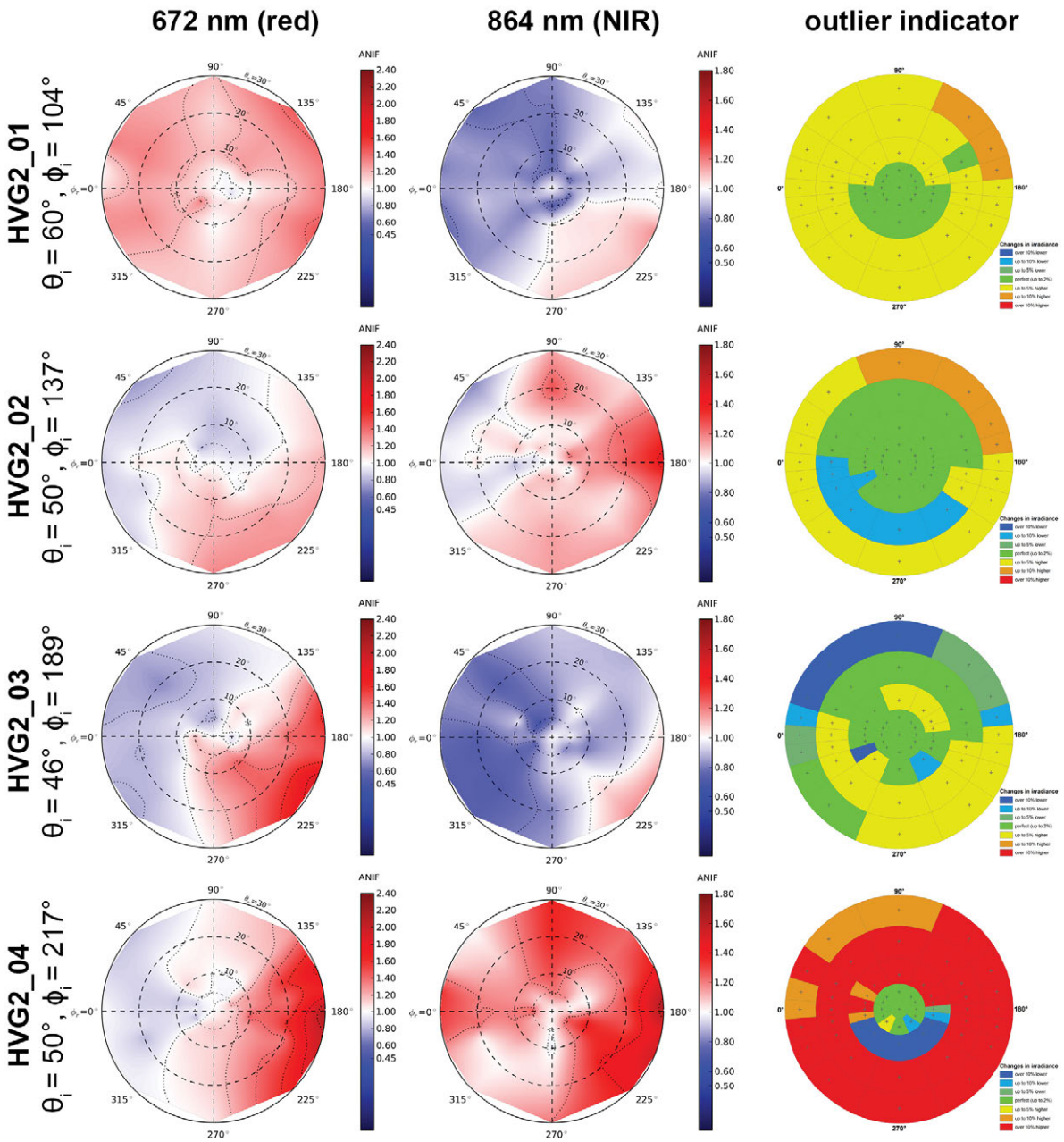

Figure C.6-13: ANIF visualization at 672 nm and 864 nm of the HVG2 site.

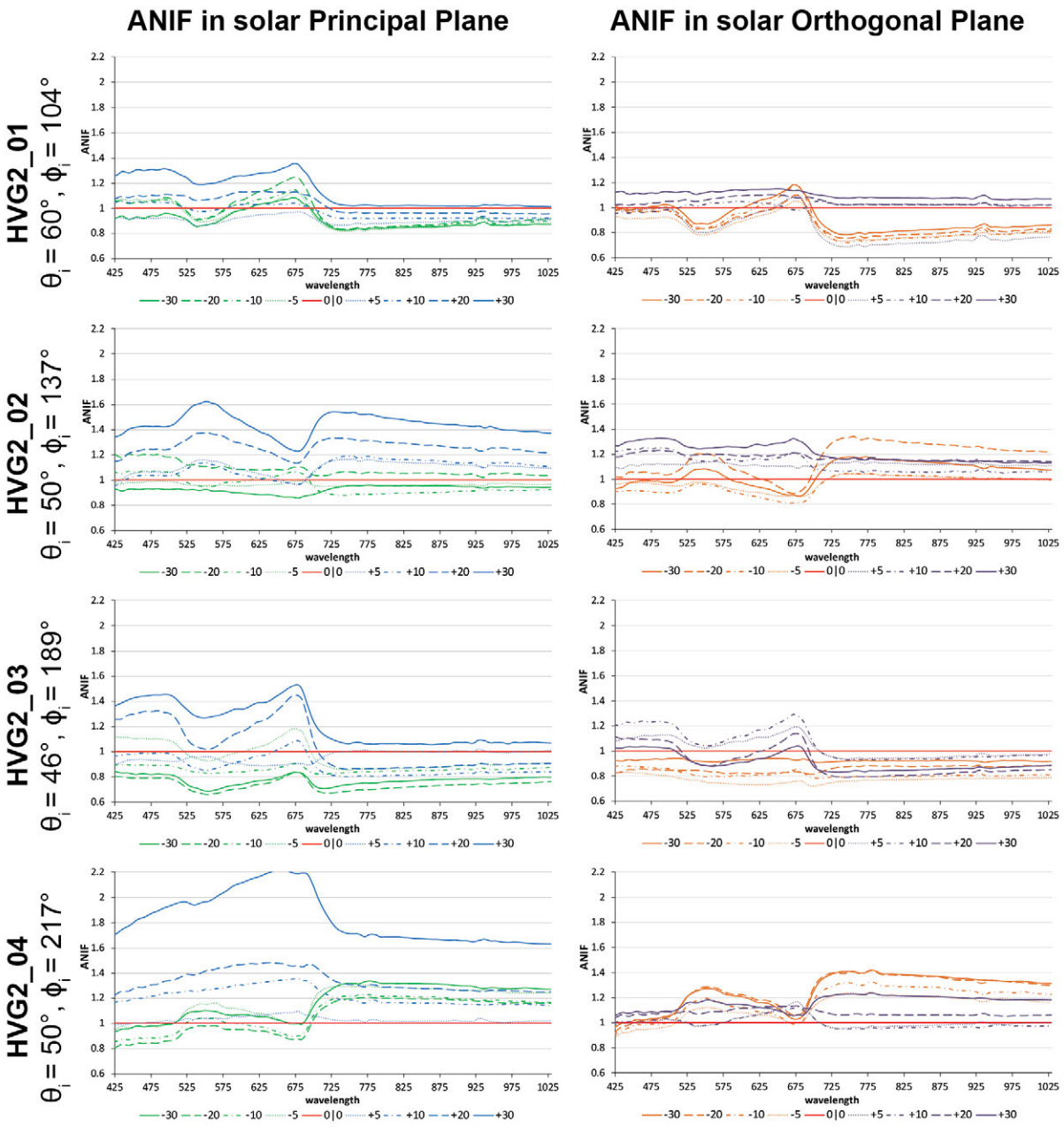

Figure C.6-14: ANIF visualization in principal & orthogonal plane of the HVG2 site.

VIII *ANIX Visualization*

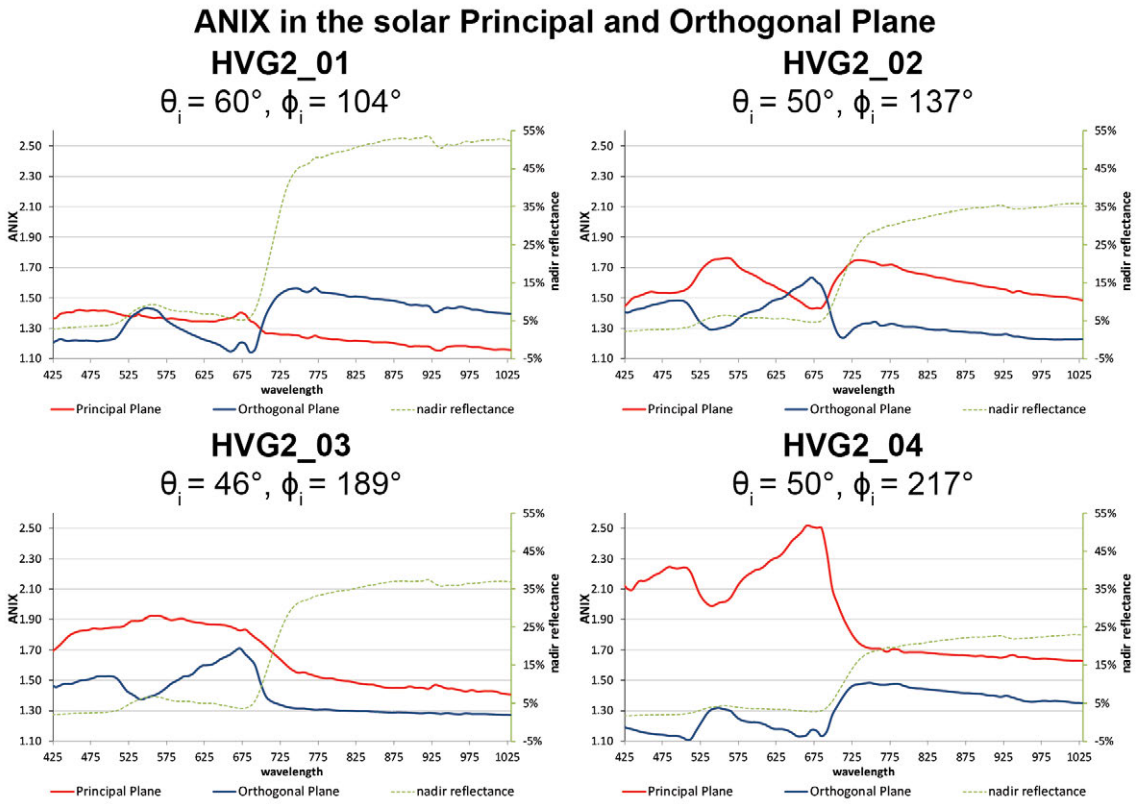

Figure C.6-15: Comparison of the ANIX in the solar principal and orthogonal plane with the nadir reflectance of the HVG2 site at different sun zenith angles.

IX *NDVI and Relative Absorption Depth Visualization*

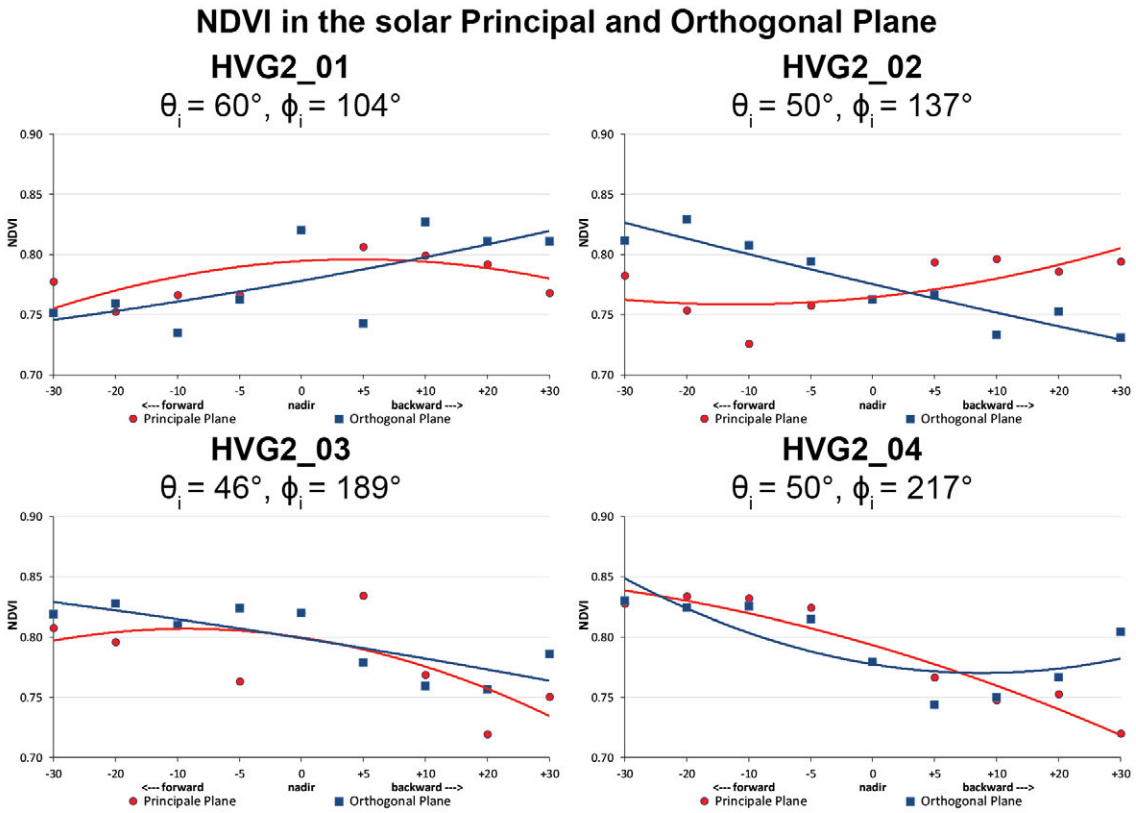

Figure C.6-16: Comparison of the NDVI in the solar principal and orthogonal plane of the HVG2 site at different sun zenith angles.

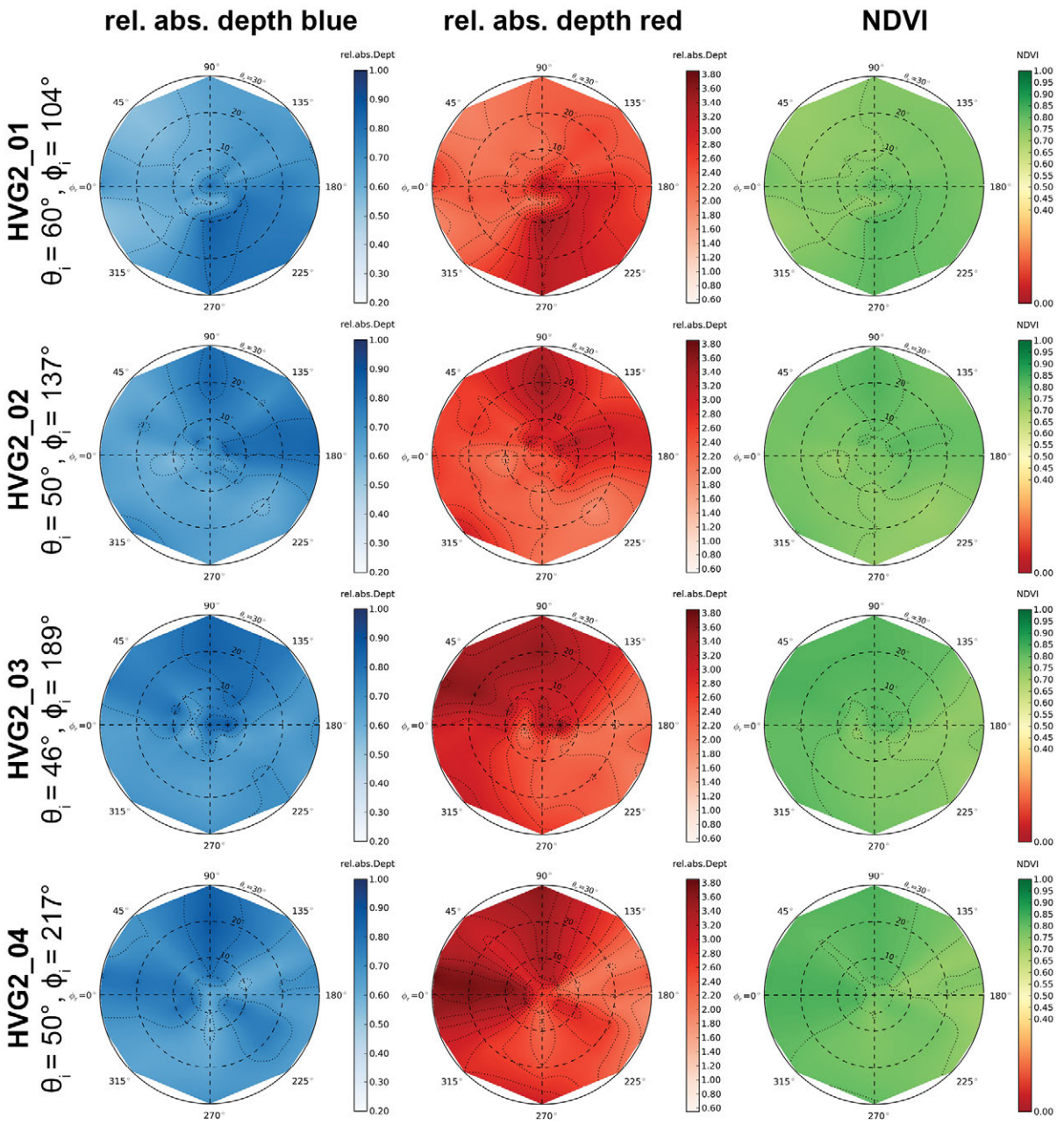

Figure C.6-17: Visualization of relative absorption depth & NDVI of the HVG2 site.

X *NDVI Comparison of Different Sensors*

Table C.6-6: Center wavelengths & band widths of broadband and narrowband NDVIs, based on the spectral response curves of the AVHRR, MODIS and EnMAP sensors.

NDVI	Sensor	Sensor band	Center wavelength (nm)	band width (nm)
$NDVI_{AVHRR}$ [broadband]	AVHRR/3	red: band 1 NIR: band 2	630 865	100 275
$NDVI_{MODIS}$ [broadband]	MODIS	red: band 1 NIR: band 2	645 859	50 35
$NDVI_{EnMAP}$ [narrowband]	EnMAP	red: band 47 NIR: band 73	672 864	6.5 8

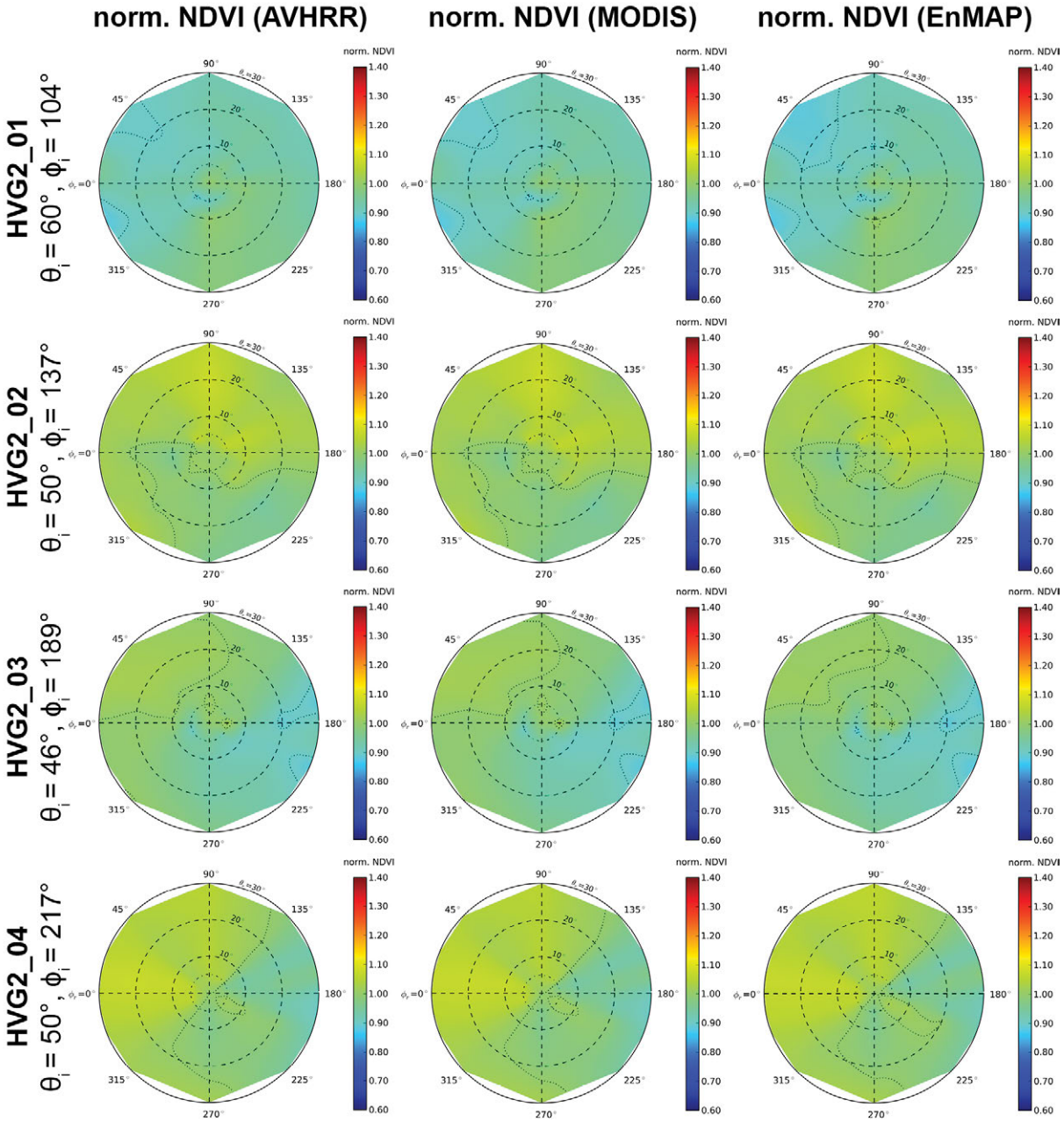

Figure C.6-18: Comparison of AVHRR, MODIS & EnMAP NDVI of the HVG2 site.

C.7 Study site VDG1 (sedge, dwarf shrub, moss tundra)

I *Location*

Name	Location	Latitude	Longitude	Altitude
VDG1	Vaskiny Dachi, Yamal Peninsula, West Siberia, Russian Federation	70.275783°	68.89125°	45 m

Vaskiny Dachi is located southeast of the main Bovanenkova gas field in the central part of the Yamal Peninsula. Vaskiny Dachi is the name of a field camp established by Dr. Marina Leibman. The research sites are located in the watersheds of the Se-Yakha and Mordy-Ykha rivers. The Vaskiny Dachi-1 study site is on a gentle Terrace-IV hill-top, which is on a Kazantsevskaya coastal-marine plain (Terrace IV) at 40-45 m elevation and built of interbedding of clayey and sandy deposits with a considerable amount of organic matter dispersed in the section. [*Walker et al.*, 2009]

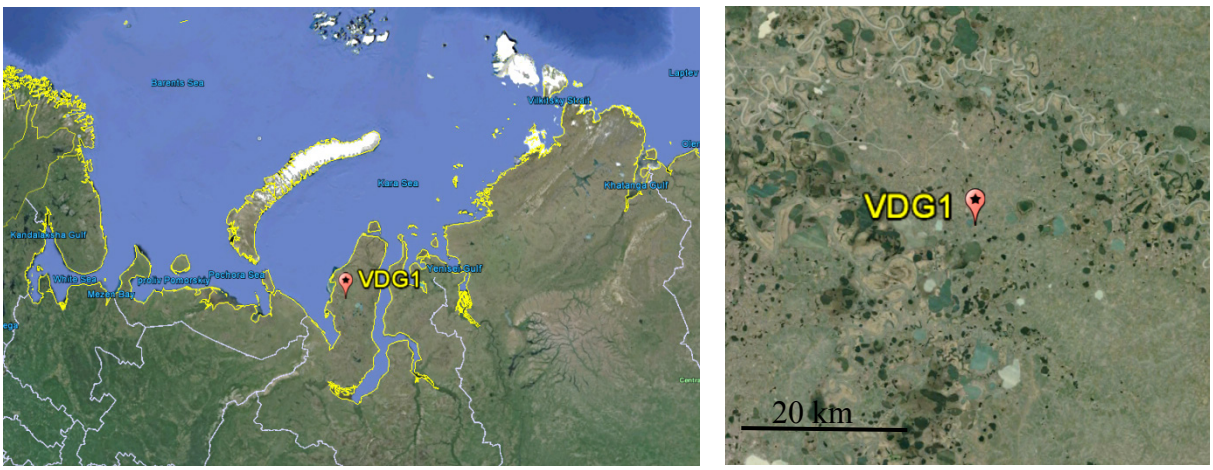

Figure C.7-1: Location of study site VDG1 in Yamal, Russia. *Source:* Google Earth, 2013

Figure C.7-2: Satellite image of the 100 x 100 m zonal grid at the Vaskiny Dachi study location where the VDG1 site is located. *Source:* Google Earth, 2013

II *Main Vegetation Description*

The soils are clay and the vegetation is heavily grazed sedge - dwarf shrub - moss tundra dominated by *Carex bigelowii*, *Vaccinium vitis-idaea*, *Salix glauca*, *Hylocomium splendens*, and *Aulacomnium turgidum*. The surfaces sometimes have windblown sands, but are mainly tussocky, hummocky or frost-boil tundra and peatland in the lower areas. [*Walker et al.*, 2009]

Figure C.7-3: Overview images of the grazed tundra at the mesic Vaskiny Dachi study location near the VDG1 site. *Source:* [*Heim et al.*, 2012]

III *Vegetation Description of the VDG1 Site*

The focus of the measurements at this goniometer site has been sedge – dwarf shrub - moss tundra. The 1x1 m plot is homogeneously covered with dwarf-shrub-moss tundra.

Figure C.7-4: Overview images of the VDG1 vegetation. Left: Photo in the visible wavelength range. Middle: Photo in the NIR wavelength range. Right: Vegetation height measurement with help of the card box approach. *Source:* [*Heim et al.*, 2012]

Figure C.7-5: Quasi-nadir image of the VDG1 vegetation (dwarf-shrub-moss tundra).

IV *Overview of the Spectro-Goniometer Measurements*

Table C.7-1: Overview of the spectro-goniometer measurements at the VDG1 study site.

Name	Day	Starting Time	Duration	SAA	SZA	Sky
VDG1_02	2011-08-12	13:20:18	40 min	180°	55°	cirrostratus

Table C.7-2: Spectro-directional data of the VDG1_02 spectro-goniometer measurement.

VDG1_02 (SZA = 55°; SAA = 180°)	Viewing Geometry (Viewing Zenith Angle | Viewing Azimuth Angle)																							
	0|0	5|180	5|202.5	5|225	5|270	5|315	5|337.5	5|0	5|22.5	5|45	5|90	5|135	5|157.5	10|180	10|190	10|202.5	10|225	10|270	10|315	10|337.5	10|350
HCRF EnMAP blue (479 nm)	0.0210	0.0197	0.0189	0.0187	0.0160	0.0187	0.0261	0.0245	0.0251	0.0210	0.0187	0.0193	0.0154	0.0181	0.0208	0.0206	0.0176	0.0178	0.0201	0.0217	0.0237
HCRF EnMAP green (549 nm)	0.0445	0.0404	0.0387	0.0381	0.0326	0.0390	0.0540	0.0518	0.0499	0.0406	0.0349	0.0372	0.0338	0.0349	0.0440	0.0422	0.0385	0.0370	0.0401	0.0500	0.0512
HCRF EnMAP rot (672 nm)	0.0355	0.0343	0.0348	0.0339	0.0281	0.0327	0.0426	0.0418	0.0425	0.0361	0.0333	0.0344	0.0273	0.0304	0.0365	0.0353	0.0312	0.0311	0.0363	0.0363	0.0391
HCRF EnMAP NIR (864 nm)	0.2440	0.1907	0.1759	0.1815	0.1602	0.2023	0.2683	0.2710	0.2468	0.2091	0.1747	0.1816	0.1784	0.1635	0.2093	0.1980	0.1812	0.1785	0.1952	0.2766	0.2696
ANIF EnMAP rot (672 nm)	1.0000	0.9668	0.9803	0.9573	0.7937	0.9233	1.2001	1.1786	1.1988	1.0172	0.9382	0.9704	0.7686	0.8563	1.0289	0.9942	0.8791	0.8762	1.0250	1.0247	1.1029
ANIF EnMAP NIR (864 nm)	1.0000	0.7812	0.7209	0.7435	0.6563	0.8288	1.0995	1.1103	1.0112	0.8569	0.7160	0.7442	0.7312	0.6698	0.8577	0.8112	0.7425	0.7314	0.8000	1.1333	1.1048
Rel. Blue Absorption Depth	0.6062	0.5805	0.5784	0.5746	0.5785	0.5976	0.5921	0.6129	0.5546	0.5313	0.4924	0.5210	0.6329	0.5236	0.6152	0.5806	0.6444	0.6010	0.5464	0.6989	0.6347
Rel. Red Absorption Depth	2.1227	1.6601	1.4566	1.5355	1.6645	1.8361	1.9401	1.9637	1.7491	1.7322	1.5144	1.5551	1.9897	1.5476	1.7085	1.6652	1.7020	1.7126	1.5668	2.4282	2.1430
NDVI (EnMAP)	0.7463	0.6952	0.6701	0.6848	0.7011	0.7214	0.7262	0.7327	0.7061	0.7058	0.6801	0.6815	0.7350	0.6867	0.7032	0.6977	0.7065	0.7035	0.6861	0.7678	0.7467
Nadir Norm. NDVI (AVHRR)	1.0000	0.9345	0.9030	0.9237	0.9309	0.9621	0.9686	0.9761	0.9427	0.9525	0.9230	0.9223	0.9827	0.9227	0.9413	0.9310	0.9390	0.9377	0.9258	1.0202	0.9994
Nadir Norm. NDVI (MODIS)	1.0000	0.9381	0.9032	0.9226	0.9328	0.9627	0.9704	0.9772	0.9430	0.9517	0.9182	0.9190	0.9831	0.9269	0.9452	0.9348	0.9416	0.9385	0.9235	1.0229	1.0020
Nadir Norm. NDVI (EnMAP)	1.0000	0.9315	0.8979	0.9177	0.9395	0.9666	0.9731	0.9819	0.9462	0.9458	0.9114	0.9131	0.9849	0.9202	0.9422	0.9349	0.9466	0.9427	0.9194	1.0288	1.0005

(cont.)

VDG1_02 (SZA = 55°; SAA = 180°)	Viewing Geometry (Viewing Zenith Angle | Viewing Azimuth Angle)																							
	10|0	10|10	10|22.5	10|45	10|90	10|135	10|157.5	10|170	20|180	20|190	20|202.5	20|225	20|270	20|315	20|337.5	20|350	20|0	20|10	20|22.5	20|45	20|90
HCRF EnMAP blue (479 nm)	0.0235	0.0246	0.0251	0.0199	0.0213	0.0197	0.0155	0.0174	0.0198	0.0204	0.0213	0.0220	0.0171	0.0178	0.0183	0.0175	0.0172	0.0178	0.0180	0.0198	0.0199
HCRF EnMAP green (549 nm)	0.0506	0.0518	0.0509	0.0410	0.0393	0.0397	0.0329	0.0355	0.0450	0.0445	0.0468	0.0466	0.0357	0.0375	0.0391	0.0364	0.0347	0.0384	0.0387	0.0414	0.0405
HCRF EnMAP rot (672 nm)	0.0377	0.0398	0.0404	0.0349	0.0366	0.0337	0.0272	0.0304	0.0347	0.0366	0.0396	0.0399	0.0293	0.0322	0.0307	0.0304	0.0300	0.0295	0.0291	0.0311	0.0326
HCRF EnMAP NIR (864 nm)	0.2650	0.2677	0.2593	0.2219	0.1976	0.1943	0.1654	0.1671	0.2206	0.2105	0.2212	0.2194	0.1763	0.1878	0.2103	0.1956	0.1923	0.2185	0.2132	0.2203	0.2092
ANIF EnMAP rot (672 nm)	1.0629	1.1231	1.1387	0.9856	1.0314	0.9515	0.7660	0.8560	0.9780	1.0321	1.1160	1.1249	0.8256	0.9095	0.8654	0.8562	0.8457	0.8329	0.8210	0.8769	0.9181
ANIF EnMAP NIR (864 nm)	1.0858	1.0970	1.0625	0.9093	0.8096	0.7962	0.6778	0.6848	0.9039	0.8625	0.9066	0.8990	0.7225	0.7695	0.8619	0.8014	0.7882	0.8952	0.8737	0.9027	0.8574
Rel. Blue Absorption Depth	0.6331	0.6027	0.5676	0.5904	0.4807	0.5644	0.6092	0.5693	0.6760	0.6358	0.6521	0.6202	0.5924	0.6097	0.6232	0.5831	0.5595	0.6182	0.6206	0.5934	0.5749
Rel. Red Absorption Depth	2.1891	2.0666	1.9586	1.9222	1.5878	1.7464	1.7881	1.6069	1.8983	1.6880	1.6634	1.6184	1.7955	1.7370	2.1066	1.9591	1.9214	2.2993	2.2444	2.1769	1.9478
NDVI (EnMAP)	0.7510	0.7410	0.7305	0.7279	0.6876	0.7041	0.7179	0.6926	0.7283	0.7038	0.6966	0.6923	0.7153	0.7069	0.7454	0.7313	0.7303	0.7618	0.7597	0.7526	0.7307
Nadir Norm. NDVI (AVHRR)	1.0014	0.9924	0.9791	0.9776	0.9299	0.9471	0.9640	0.9320	0.9654	0.9387	0.9359	0.9266	0.9541	0.9492	1.0005	0.9845	0.9895	1.0206	1.0145	1.0085	0.9769
Nadir Norm. NDVI (MODIS)	1.0033	0.9941	0.9797	0.9769	0.9281	0.9498	0.9653	0.9331	0.9682	0.9409	0.9374	0.9287	0.9555	0.9490	1.0007	0.9827	0.9875	1.0206	1.0174	1.0110	0.9796
Nadir Norm. NDVI (EnMAP)	1.0083	0.9929	0.9789	0.9753	0.9214	0.9435	0.9620	0.9281	0.9759	0.9431	0.9334	0.9277	0.9584	0.9472	0.9988	0.9799	0.9785	1.0208	1.0180	1.0085	0.9792

(cont.)

VDG1_02 (SZA = 55°; SAA = 180°)	Viewing Geometry (Viewing Zenith Angle | Viewing Azimuth Angle)																							
	20|135	20|157.5	20|170	30|180	30|190	30|202.5	30|225	30|270	30|315	30|337.5	30|350	30|0	30|10	30|22.5	30|45	30|90	30|135	30|157.5	30|170			
HCRF EnMAP blue (479 nm)	0.0189	0.0201	0.0210	0.0266	0.0251	0.0256	0.0235	0.0215	0.0205	0.0163	0.0172	0.0172	0.0226	0.0227	0.0169	0.0189	0.0193	0.0248	0.0258					
HCRF EnMAP green (549 nm)	0.0395	0.0444	0.0446	0.0566	0.0552	0.0544	0.0523	0.0440	0.0423	0.0331	0.0335	0.0367	0.0451	0.0450	0.0337	0.0352	0.0418	0.0535	0.0578					
HCRF EnMAP rot (672 nm)	0.0337	0.0349	0.0379	0.0482	0.0449	0.0456	0.0420	0.0386	0.0345	0.0277	0.0296	0.0289	0.0380	0.0364	0.0274	0.0316	0.0343	0.0423	0.0438					
HCRF EnMAP NIR (864 nm)	0.1845	0.2051	0.2048	0.2530	0.2509	0.2457	0.2541	0.2169	0.2110	0.1933	0.1773	0.2068	0.2372	0.2378	0.1889	0.1758	0.1968	0.2402	0.2607					
ANIF EnMAP rot (672 nm)	0.9514	0.9840	1.0681	1.3599	1.2674	1.2865	1.1847	1.0878	0.9740	0.7817	0.8343	0.8138	1.0707	1.0263	0.7719	0.8918	0.9684	1.1934	1.2344					
ANIF EnMAP NIR (864 nm)	0.7559	0.8405	0.8392	1.0369	1.0281	1.0067	1.0411	0.8887	0.8646	0.7922	0.7267	0.8473	0.9719	0.9744	0.7740	0.7203	0.8066	0.9842	1.0682					
Rel. Blue Absorption Depth	0.5961	0.6517	0.6106	0.6200	0.6506	0.6230	0.6678	0.5804	0.5858	0.5687	0.5236	0.6118	0.5600	0.5397	0.5479	0.4882	0.6406	0.6322	0.6706					
Rel. Red Absorption Depth	1.5956	1.7546	1.5834	1.5565	1.6834	1.6066	1.8338	1.6887	1.8523	2.1754	1.7802	2.2069	1.8682	2.0009	2.0895	1.6192	1.6822	1.6986	1.8246					
NDVI (EnMAP)	0.6908	0.7092	0.6879	0.6799	0.6962	0.6868	0.7162	0.6980	0.7187	0.7492	0.7141	0.7551	0.7240	0.7346	0.7469	0.6951	0.7029	0.7004	0.7125					
Nadir Norm. NDVI (AVHRR)	0.9308	0.9448	0.9145	0.9088	0.9302	0.9149	0.9494	0.9374	0.9634	1.0152	0.9642	1.0160	0.9762	0.9872	1.0076	0.9400	0.9434	0.9327	0.9442					
Nadir Norm. NDVI (MODIS)	0.9307	0.9490	0.9181	0.9109	0.9335	0.9185	0.9538	0.9383	0.9671	1.0128	0.9632	1.0155	0.9761	0.9890	1.0077	0.9417	0.9471	0.9367	0.9480					
Nadir Norm. NDVI (EnMAP)	0.9257	0.9504	0.9217	0.9111	0.9329	0.9203	0.9597	0.9354	0.9630	1.0039	0.9569	1.0118	0.9702	0.9843	1.0008	0.9314	0.9419	0.9386	0.9547					

V *Main Spectral Characteristics*

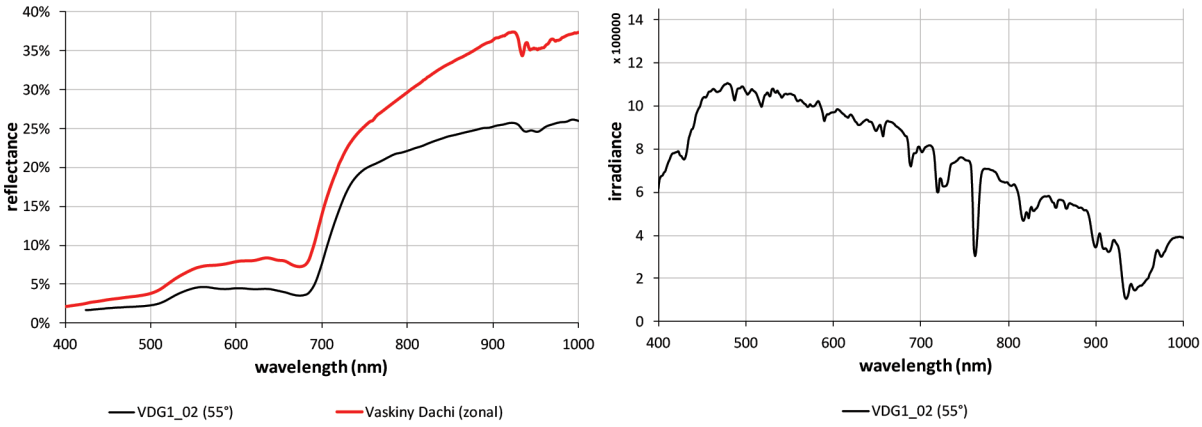

Figure C.7-6: Nadir reflectances and irradiance profiles of the VDG1 site. Left: Comparison of the nadir reflectance signatures with the average zonal vegetation. Right: Comparison of the total irradiance profiles.

VI *HCRF Visualization*

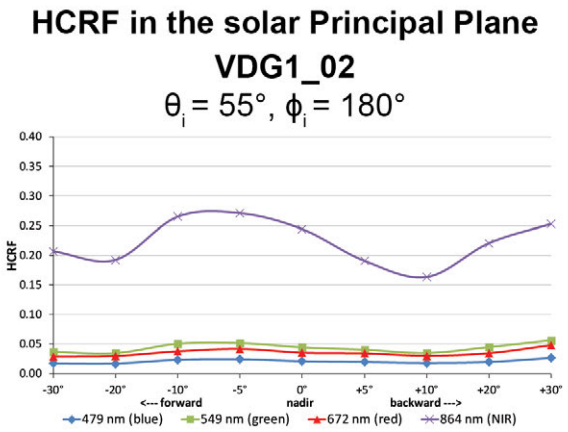

Figure C.7-7: Comparison of the HCRF values at 479 nm (blue), 549 nm (green), 672 nm (red), and 864 nm (NIR) in the solar principal plane of the VDG1 site.

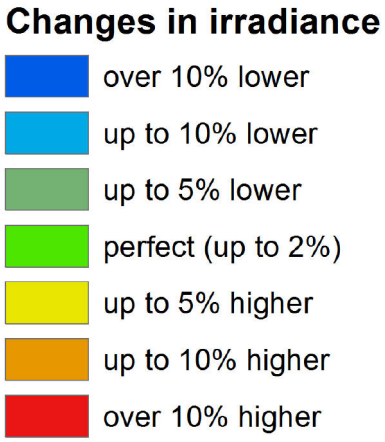

Figure C.7-8: Legend of the outlier indicator graphics shown in Figure C.7-9, C.7-10, and C.7-13

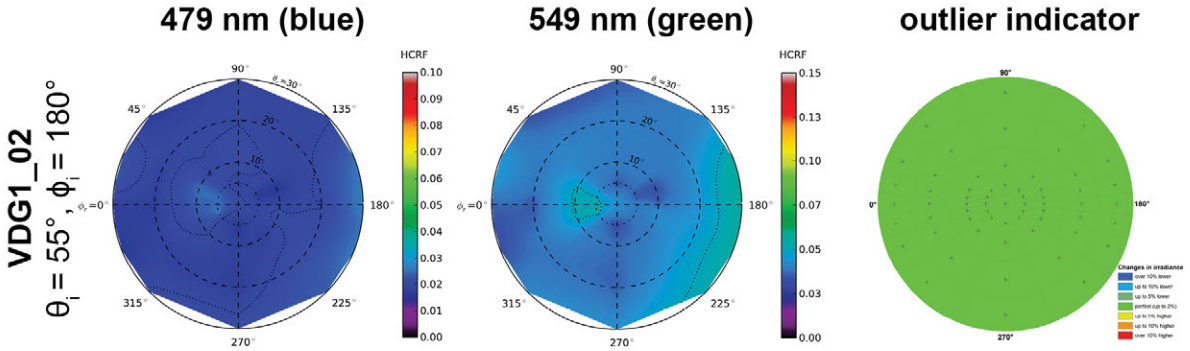

Figure C.7-9: HCRF visualization at 479 nm and 549 nm of the VDG1 site.

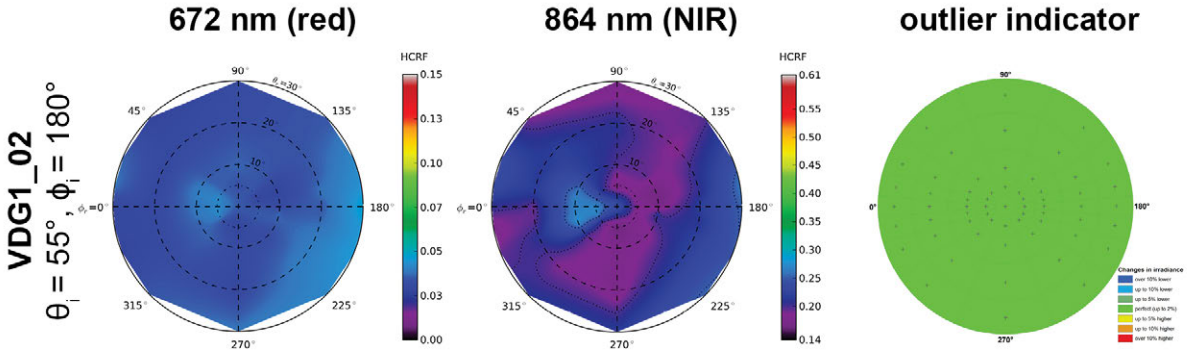

Figure C.7-10: HCRF visualization at 672 nm and 864 nm of the VDG1 site.

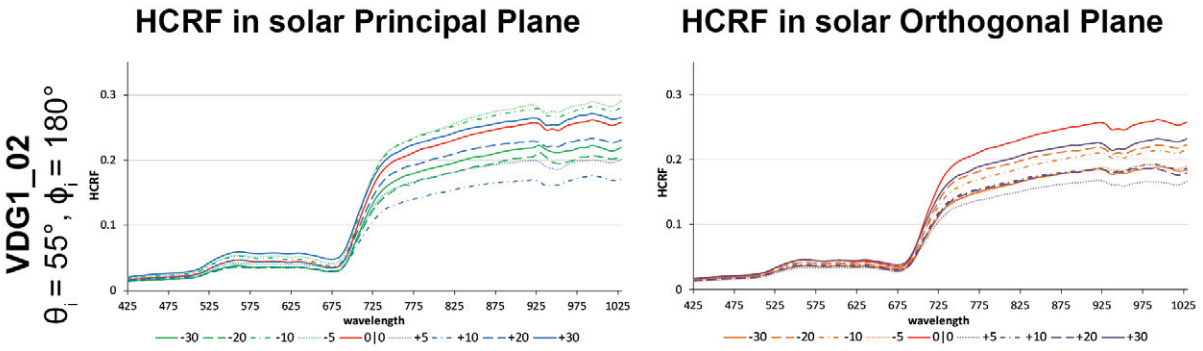

Figure C.7-11: HCRF visualization in principal & orthogonal plane of the VDG1 site.

VII *ANIF Visualization*

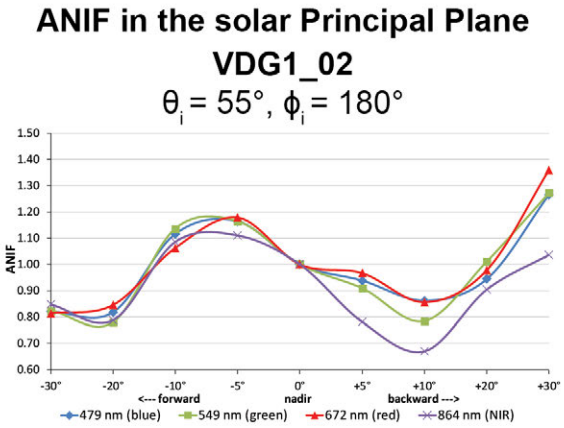

Figure C.7-12: Comparison of the ANIF values at 479 nm (blue), 549 nm (green), 672 nm (red), and 864 nm (NIR) in the solar principal plane of the VDG1 site.

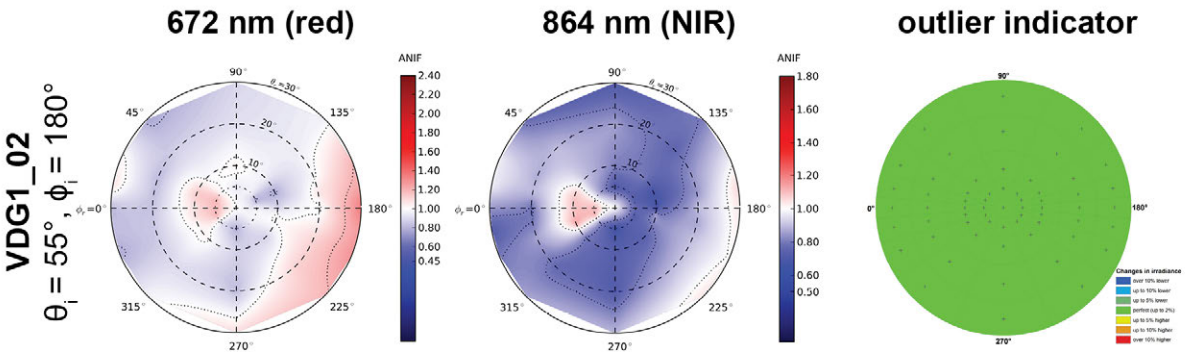

Figure C.7-13: ANIF visualization at 672 nm and 864 nm of the VDG1 site.

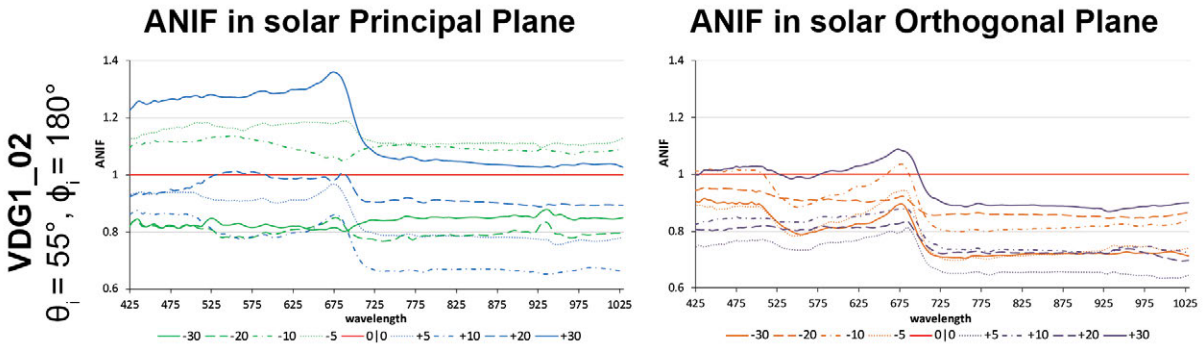

Figure C.7-14: ANIF visualization in principal & orthogonal plane of the VDG1 site.

VIII *ANIX Visualization*

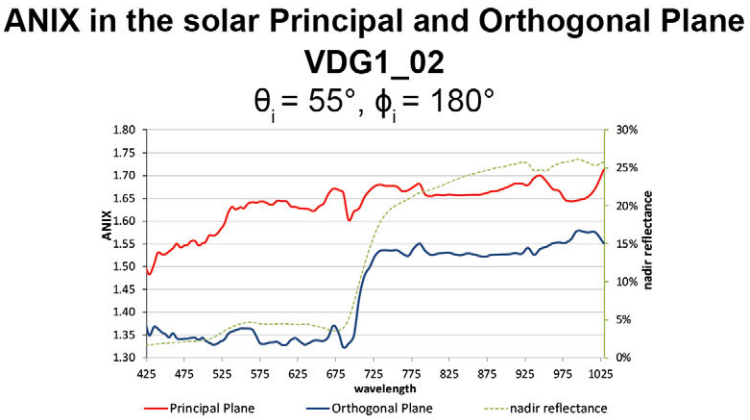

Figure C.7-15: Comparison of the ANIX in the solar principal and orthogonal plane with the nadir reflectance of the VDG1 site.

IX *NDVI and Relative Absorption Depth Visualization*

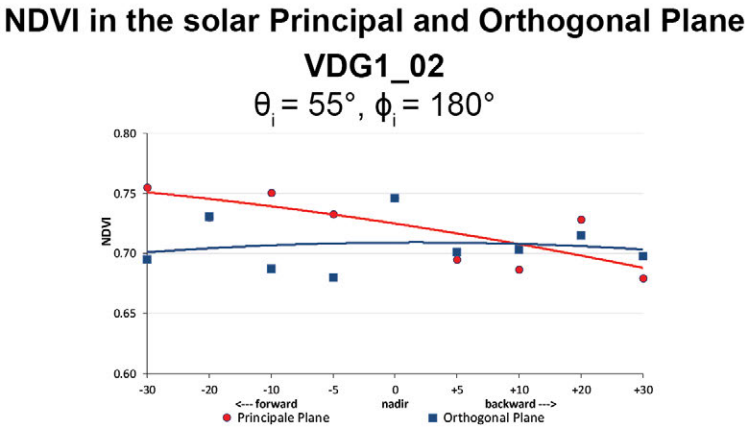

Figure C.7-16: Comparison of the NDVI in the solar principal and orthogonal plane of the VDG1 site.

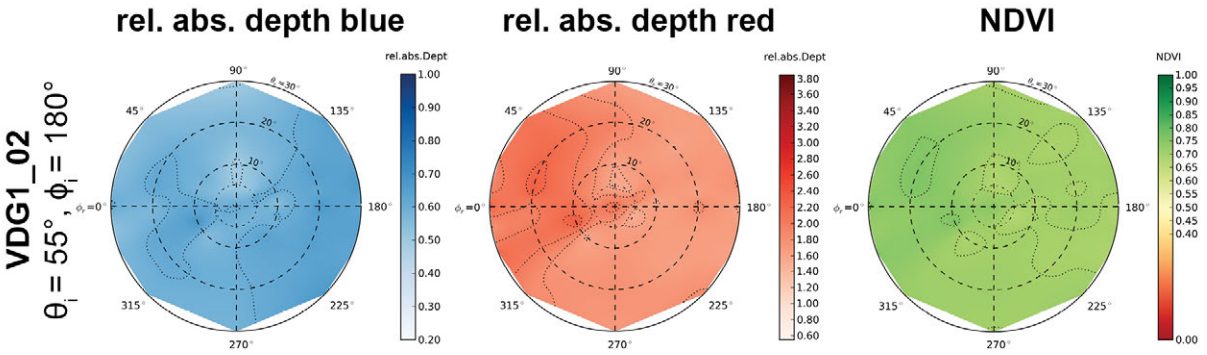

Figure C.7-17: Visualization of relative absorption depth & NDVI of the VDG1 site.

X *NDVI Comparison of Different Sensors*

Table C.7-3: Center wavelengths and band widths of the broadband and narrowband NDVIs, based on the spectral response curves of the AVHRR, MODIS and EnMAP sensors.

NDVI	Sensor	Sensor band	Center wavelength (nm)	band width (nm)
$NDVI_{AVHRR}$ [broadband]	AVHRR/3	red: band 1 NIR: band 2	630 865	100 275
$NDVI_{MODIS}$ [broadband]	MODIS	red: band 1 NIR: band 2	645 859	50 35
$NDVI_{EnMAP}$ [narrowband]	EnMAP	red: band 47 NIR: band 73	672 864	6.5 8

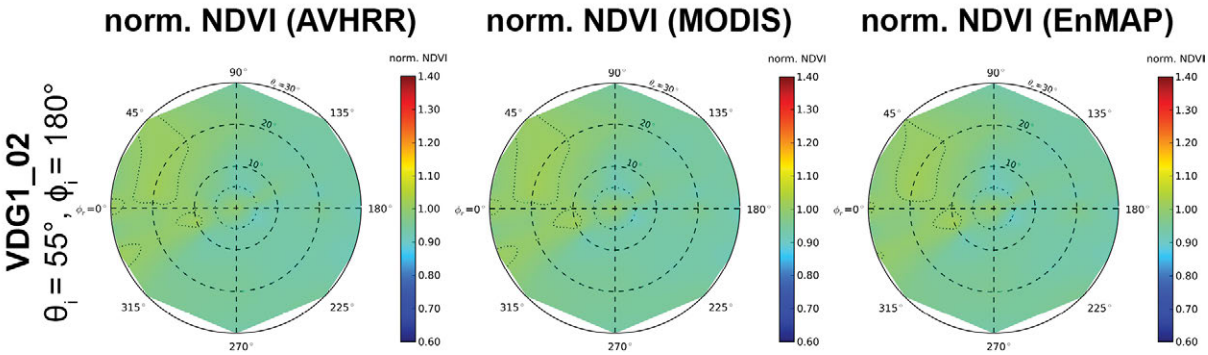

Figure C.7-18: Comparison of AVHRR, MODIS & EnMAP NDVI of the VDG1 site.

C.8 Study site VDG2 (grazed sedge, dwarf shrub, moss tundra)

I *Location*

Name	Location	Latitude	Longitude	Altitude
VDG2	Vaskiny Dachi, Yamal Peninsula, West Siberia, Russian Federation	70.275667°	68.890767°	45 m

Vaskiny Dachi is located southeast of the main Bovanenkova gas field in the central part of the Yamal Peninsula. Vaskiny Dachi is the name of a field camp established by Dr. Marina Leibman. The research sites are located in the watersheds of the Se-Yakha and Mordy-Ykha rivers. The Vaskiny Dachi-1 study site is on a gentle Terrace-IV hill-top, which is on a Kazantsevskaya coastal-marine plain (Terrace IV) at 40-45 m elevation and built of interbedding of clayey and sandy deposits with a considerable amount of organic matter dispersed in the section. [*Walker et al.*, 2009]

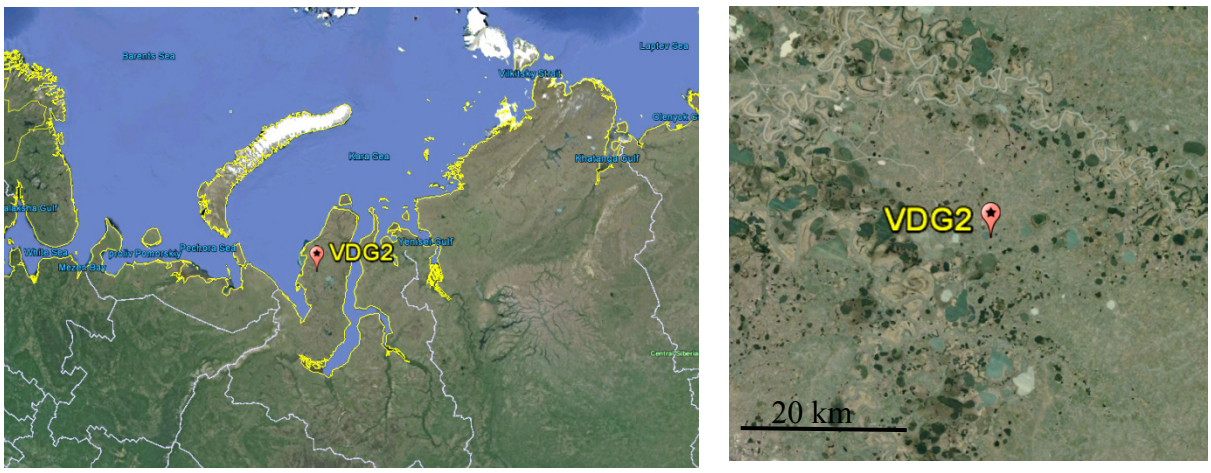

Figure C.8-1: Location of study site VDG2 in Yamal, Russia. *Source:* Google Earth, 2013

Figure C.8-2: Satellite image of the 100 x 100 m zonal grid at the Vaskiny Dachi study location where the VDG2 site is located. *Source:* Google Earth, 2013

II *Main Vegetation Description*

The soils are clay and the vegetation is heavily grazed sedge – dwarf shrub - moss tundra dominated by *Carex bigelowii*, *Vaccinium vitis-idaea*, *Salix glauca*, *Hylocomium splendens*, and *Aulacomnium turgidum*. The surfaces sometimes have windblown sands, but are mainly tussocky, hummocky or frost-boil tundra and peatland in the lower areas. [*Walker et al.*, 2009]

Figure C.8-3: Overview images of the grazed tundra at the mesic Vaskiny Dachi study location near the VDG2 site. *Source:* [*Heim et al.*, 2012]

III *Vegetation Description of the VDG2 Site*

The focus of the measurements at this goniometer site has been grazed sedge – dwarf shrub - moss tundra. The 1 x 1 m plot was homogeneously grazed by reindeer.

Figure C.8-4: Overview images of the VDG2 vegetation from cardinal directions.

Figure C.8-5: Quasi-nadir image of the VDG2 vegetation (grazed tundra).

IV *Overview of the Spectro-Goniometer Measurements*

Table C.8-1: Overview of the spectro-goniometer measurements at the VDG2 study site.

Name	Day	Starting Time	Duration	SAA	SZA	Sky
VDG2_01	2011-08-29	10:04:03	39 min	124°	69°	cirrostratus
VDG2_02	2011-08-29	11:15:22	38 min	143°	64°	cirrostratus
VDG2_03	2011-08-29	12:31:47	42 min	164°	61°	cirrostratus

Table C.8-2: Spectro-directional data of the VDG2_01 spectro-goniometer measurement.

VDG2_01 (SZA = 69°; SAA = 124°)	Viewing Geometry (Viewing Zenith Angle | Viewing Azimuth Angle)																							
	0|0	5|180	5|202.5	5|225	5|270	5|315	5|337.5	5|0	5|22.5	5|45	5|90	5|135	5|157.5	10|180	10|202.5	10|225	10|270	10|315	10|337.5	10|350
HCRF EnMAP blue (479 nm)	0.0228	0.0230	0.0217	0.0213	0.0200	0.0198	0.0246	0.0272	0.0223	0.0223	0.0209	0.0211	0.0200	0.0267	0.0240	0.0209	0.0176	0.0201	0.0178	0.0195	0.0267
HCRF EnMAP green (549 nm)	0.0381	0.0393	0.0362	0.0405	0.0343	0.0341	0.0426	0.0458	0.0390	0.0387	0.0384	0.0351	0.0330	0.0450	0.0415	0.0361	0.0302	0.0342	0.0289	0.0343	0.0433
HCRF EnMAP rot (672 nm)	0.0572	0.0575	0.0583	0.0577	0.0499	0.0483	0.0626	0.0690	0.0600	0.0584	0.0587	0.0524	0.0514	0.0687	0.0622	0.0569	0.0480	0.0536	0.0439	0.0529	0.0654
HCRF EnMAP NIR (864 nm)	0.2265	0.2186	0.2154	0.2155	0.1943	0.1842	0.2420	0.2555	0.2217	0.2171	0.2355	0.1957	0.2047	0.2582	0.2269	0.2209	0.2046	0.1949	0.1676	0.2042	0.2414
ANIF EnMAP rot (672 nm)	1.0000	1.0051	1.0197	1.0094	0.8730	0.8447	1.0943	1.2064	1.0489	1.0217	1.0266	0.9162	0.8986	1.2025	1.0878	0.9950	0.8404	0.9375	0.7684	0.9261	1.1438
ANIF EnMAP NIR (864 nm)	1.0000	0.9652	0.9512	0.9517	0.8581	0.8134	1.0686	1.1283	0.9788	0.9587	1.0398	0.8640	0.9040	1.1403	1.0021	0.9756	0.9034	0.8604	0.7400	0.9017	1.0662
Rel. Blue Absorption Depth	0.4046	0.4046	0.3911	0.5215	0.4173	0.4236	0.4324	0.4069	0.4336	0.4214	0.4743	0.3804	0.3895	0.4017	0.4283	0.4161	0.4134	0.4190	0.3579	0.4250	0.3832
Rel. Red Absorption Depth	0.9838	0.9649	0.9386	0.9319	0.9670	0.9432	0.9710	0.9158	0.9198	0.9318	1.0423	0.9193	1.0310	0.9685	0.9294	1.0225	1.1326	0.9070	0.9655	0.9639	0.9363
NDVI (EnMAP)	0.5969	0.5837	0.5741	0.5776	0.5913	0.5846	0.5892	0.5749	0.5742	0.5760	0.6010	0.5777	0.5988	0.5795	0.5698	0.5905	0.6197	0.5686	0.5847	0.5882	0.5738
Nadir Norm. NDVI (AVHRR)	1.0000	0.9743	0.9842	0.9789	0.9928	0.9841	0.9857	0.9666	0.9748	0.9675	1.0110	0.9702	1.0086	0.9684	0.9604	0.9916	1.0365	0.9678	0.9914	0.9922	0.9714
Nadir Norm. NDVI (MODIS)	1.0000	0.9717	0.9750	0.9743	0.9835	0.9784	0.9844	0.9646	0.9726	0.9672	1.0084	0.9679	1.0012	0.9698	0.9580	0.9873	1.0327	0.9634	0.9874	0.9904	0.9679
Nadir Norm. NDVI (EnMAP)	1.0000	0.9779	0.9618	0.9677	0.9906	0.9794	0.9871	0.9632	0.9619	0.9650	1.0069	0.9678	1.0032	0.9709	0.9546	0.9893	1.0381	0.9525	0.9795	0.9855	0.9613

(cont.)

VDG2_01 (SZA = 69°; SAA = 124°)	Viewing Geometry (Viewing Zenith Angle | Viewing Azimuth Angle)																							
	10|0	10|10	10|22.5	10|45	10|90	10|135	10|157.5	10|170	20|180	20|190	20|202.5	20|225	20|270	20|315	20|337.5	20|350	20|0	20|10	20|22.5	20|45	20|90
HCRF EnMAP blue (479 nm)	0.0254	0.0212	0.0210	0.0206	0.0226	0.0192	0.0245	0.0262	0.0277	0.0253	0.0221	0.0208	0.0214	0.0200	0.0234	0.0243	0.0205	0.0222	0.0228	0.0246	0.0226
HCRF EnMAP green (549 nm)	0.0420	0.0366	0.0361	0.0335	0.0378	0.0314	0.0393	0.0425	0.0470	0.0444	0.0371	0.0361	0.0371	0.0322	0.0387	0.0422	0.0350	0.0390	0.0388	0.0406	0.0377
HCRF EnMAP rot (672 nm)	0.0615	0.0550	0.0543	0.0527	0.0567	0.0497	0.0587	0.0655	0.0691	0.0669	0.0606	0.0548	0.0571	0.0499	0.0581	0.0617	0.0544	0.0592	0.0594	0.0627	0.0557
HCRF EnMAP NIR (864 nm)	0.2393	0.2061	0.1955	0.2033	0.2387	0.1905	0.2252	0.2532	0.2572	0.2463	0.2367	0.2248	0.2082	0.1859	0.2218	0.2412	0.2102	0.2169	0.2139	0.2344	0.2303
ANIF EnMAP rot (672 nm)	1.0760	0.9614	0.9504	0.9216	0.9915	0.8688	1.0267	1.1462	1.2090	1.1707	1.0607	0.9590	0.9996	0.8731	1.0166	1.0794	0.9516	1.0362	1.0390	1.0961	0.9736
ANIF EnMAP NIR (864 nm)	1.0565	0.9100	0.8632	0.8978	1.0541	0.8410	0.9942	1.1182	1.1357	1.0875	1.0452	0.9928	0.9195	0.8211	0.9796	1.0650	0.9281	0.9576	0.9445	1.0350	1.0171
Rel. Blue Absorption Depth	0.3774	0.4225	0.4202	0.3808	0.4028	0.3779	0.3490	0.3671	0.4160	0.4321	0.3886	0.4287	0.4325	0.3605	0.3948	0.4218	0.4115	0.4415	0.4287	0.3864	0.4070
Rel. Red Absorption Depth	0.9793	0.9298	0.8934	0.9883	1.1233	0.9720	0.9793	1.0215	0.9561	0.9452	1.0412	1.1009	0.9097	0.9444	0.9596	0.9754	0.9586	0.9189	0.8785	0.9463	1.0913
NDVI (EnMAP)	0.5910	0.5789	0.5651	0.5884	0.6163	0.5863	0.5865	0.5889	0.5764	0.5727	0.5922	0.6079	0.5694	0.5768	0.5848	0.5926	0.5888	0.5709	0.5653	0.5781	0.6108
Nadir Norm. NDVI (AVHRR)	0.9854	0.9737	0.9568	0.9935	1.0207	0.9961	0.9833	0.9940	0.9636	0.9595	1.0092	1.0171	0.9640	0.9807	0.9814	0.9935	0.9947	0.9653	0.9612	0.9858	1.0147
Nadir Norm. NDVI (MODIS)	0.9831	0.9710	0.9568	0.9924	1.0177	0.9901	0.9786	0.9865	0.9598	0.9553	1.0027	1.0127	0.9637	0.9762	0.9776	0.9920	0.9918	0.9642	0.9610	0.9776	1.0109
Nadir Norm. NDVI (EnMAP)	0.9901	0.9699	0.9467	0.9858	1.0324	0.9823	0.9825	0.9866	0.9656	0.9594	0.9920	1.0185	0.9538	0.9663	0.9798	0.9927	0.9864	0.9565	0.9471	0.9685	1.0233

(cont.)

VDG2_01 (SZA = 69°; SAA = 124°)	Viewing Geometry (Viewing Zenith Angle | Viewing Azimuth Angle)																							
	20|135	20|157.5	20|170	30|180	30|190	30|202.5	30|225	30|270	30|315	30|337.5	30|350	30|0	30|10	30|122.5	30|45	30|90	30|135	30|157.5	30|170			
HCRF EnMAP blue (479 nm)	0.0241	0.0283	0.0300	0.0288	0.0284	0.0282	0.0266	0.0228	0.0226	0.0253	0.0253	0.0258	0.0209	0.0243	0.0267	0.0225	0.0292	0.0338	0.0307					
HCRF EnMAP green (549 nm)	0.0388	0.0460	0.0497	0.0477	0.0486	0.0495	0.0464	0.0389	0.0378	0.0439	0.0421	0.0430	0.0379	0.0427	0.0437	0.0391	0.0473	0.0563	0.0521					
HCRF EnMAP rot (672 nm)	0.0597	0.0694	0.0739	0.0763	0.0762	0.0719	0.0711	0.0574	0.0558	0.0625	0.0614	0.0638	0.0525	0.0603	0.0621	0.0555	0.0710	0.0815	0.0787					
HCRF EnMAP NIR (864 nm)	0.2295	0.2571	0.2691	0.2747	0.2672	0.2588	0.2419	0.2045	0.2060	0.2367	0.2316	0.2376	0.2151	0.2408	0.2315	0.2143	0.2420	0.2836	0.2856					
ANIF EnMAP rot (672 nm)	1.0448	1.2148	1.2932	1.3348	1.3323	1.2572	1.2436	1.0034	0.9758	1.0926	1.0747	1.1167	0.9189	1.0549	1.0860	0.9703	1.2424	1.4250	1.3766					
ANIF EnMAP NIR (864 nm)	1.0132	1.1352	1.1882	1.2128	1.1797	1.1430	1.0680	0.9028	0.9094	1.0451	1.0225	1.0490	0.9497	1.0633	1.0220	0.9465	1.0685	1.2525	1.2609					
Rel. Blue Absorption Depth	0.3666	0.3693	0.3824	0.3901	0.4133	0.4324	0.4219	0.4113	0.3937	0.4352	0.3976	0.3959	0.4654	0.4416	0.3847	0.4361	0.3586	0.3906	0.4099					
Rel. Red Absorption Depth	0.9896	0.9686	0.9500	0.9688	0.9173	0.9332	0.8548	0.8889	0.9269	0.9455	0.9431	0.9433	1.0346	1.0350	0.9665	0.9829	0.8527	0.9237	0.9737					
NDVI (EnMAP)	0.5869	0.5747	0.5690	0.5652	0.5563	0.5654	0.5457	0.5618	0.5738	0.5824	0.5806	0.5764	0.6074	0.5995	0.5770	0.5888	0.5462	0.5538	0.5679					
Nadir Norm. NDVI (AVHRR)	0.9819	0.9628	0.9571	0.9591	0.9431	0.9506	0.9276	0.9517	0.9688	0.9728	0.9712	0.9686	0.9982	0.9895	0.9637	0.9822	0.9256	0.9278	0.9525					
Nadir Norm. NDVI (MODIS)	0.9798	0.9602	0.9525	0.9505	0.9377	0.9461	0.9234	0.9500	0.9661	0.9750	0.9720	0.9674	1.0006	0.9898	0.9626	0.9854	0.9235	0.9269	0.9465					
Nadir Norm. NDVI (EnMAP)	0.9833	0.9628	0.9532	0.9468	0.9321	0.9472	0.9142	0.9413	0.9612	0.9757	0.9727	0.9657	1.0176	1.0043	0.9667	0.9865	0.9150	0.9277	0.9514					

Table C.8-3: Spectro-directional data of the VDG2_02 spectro-goniometer measurement.

VDG2_02 (SZA = 64°; SAA = 143°)	Viewing Geometry (Viewing Zenith Angle | Viewing Azimuth Angle)																							
	0|0	5|180	5|202.5	5|225	5|270	5|315	5|337.5	5|0	5|22.5	5|45	5|90	5|135	5|157.5	10|180	10|190	10|202.5	10|225	10|270	10|315	10|337.5	10|350
HCRF EnMAP blue (479 nm)	0.0217	0.0256	0.0221	0.0215	0.0233	0.0224	0.0273	0.0254	0.0227	0.0258	0.0221	0.0253	0.0261	0.0249	0.0251	0.0225	0.0226	0.0244	0.0231	0.0257	0.0269
HCRF EnMAP green (549 nm)	0.0368	0.0435	0.0366	0.0351	0.0402	0.0370	0.0457	0.0422	0.0374	0.0417	0.0383	0.0431	0.0442	0.0432	0.0415	0.0360	0.0376	0.0393	0.0395	0.0415	0.0438
HCRF EnMAP rot (672 nm)	0.0583	0.0658	0.0595	0.0563	0.0602	0.0578	0.0663	0.0647	0.0572	0.0629	0.0569	0.0640	0.0666	0.0642	0.0639	0.0570	0.0609	0.0611	0.0604	0.0605	0.0648
HCRF EnMAP NIR (864 nm)	0.2209	0.2471	0.2378	0.2203	0.2126	0.2168	0.2543	0.2414	0.2285	0.2450	0.2244	0.2561	0.2652	0.2465	0.2642	0.2417	0.2306	0.2132	0.2303	0.2290	0.2356
ANIF EnMAP rot (672 nm)	1.0000	1.1277	1.0203	0.9652	1.0318	0.9905	1.1363	1.1097	0.9807	1.0783	0.9752	1.0969	1.1419	1.0998	1.0945	0.9774	1.0437	1.0465	1.0357	1.0364	1.1105
ANIF EnMAP NIR (864 nm)	1.0000	1.1186	1.0765	0.9974	0.9625	0.9812	1.1513	1.0926	1.0342	1.1091	1.0159	1.1591	1.2006	1.1157	1.1958	1.0941	1.0438	0.9650	1.0424	1.0365	1.0665
Rel. Blue Absorption Depth	0.4057	0.4054	0.3787	0.3689	0.4295	0.3765	0.3952	0.3954	0.3843	0.3651	0.4146	0.3947	0.3957	0.4226	0.3757	0.3449	0.3812	0.3655	0.4004	0.3542	0.3761
Rel. Red Absorption Depth	0.9373	0.9255	1.0286	1.0310	0.8512	0.9528	0.9490	0.9153	1.0109	0.9846	0.9683	1.0341	1.0350	0.9846	1.0870	1.1454	0.9836	0.8652	0.9667	0.9598	0.9104
NDVI (EnMAP)	0.5822	0.5795	0.5996	0.5929	0.5587	0.5790	0.5865	0.5770	0.5994	0.5914	0.5955	0.6001	0.5985	0.5869	0.6107	0.6182	0.5822	0.5547	0.5843	0.5822	0.5686
Nadir Norm. NDVI (AVHRR)	1.0000	0.9896	1.0284	1.0160	0.9583	0.9944	0.9896	0.9857	1.0215	1.0075	1.0106	1.0131	1.0198	0.9969	1.0291	1.0486	1.0016	0.9525	0.9928	0.9816	0.9698
Nadir Norm. NDVI (MODIS)	1.0000	0.9901	1.0229	1.0100	0.9609	0.9902	0.9910	0.9863	1.0192	1.0057	1.0142	1.0141	1.0193	0.9965	1.0249	1.0407	0.9967	0.9559	0.9964	0.9832	0.9729
Nadir Norm. NDVI (EnMAP)	1.0000	0.9954	1.0300	1.0185	0.9597	0.9946	1.0074	0.9911	1.0297	1.0159	1.0229	1.0308	1.0280	1.0081	1.0490	1.0619	1.0001	0.9529	1.0037	1.0001	0.9768

(cont.)

VDG2_02 (SZA = 64°; SAA = 143°)	Viewing Geometry (Viewing Zenith Angle | Viewing Azimuth Angle)																							
	10|0	10|10	10|22.5	10|45	10|90	10|135	10|157.5	10|170	20|180	20|190	20|202.5	20|225	20|270	20|315	20|337.5	20|350	20|0	20|10	20|22.5	20|45	20|90	20|135
HCRF EnMAP blue (479 nm)	0.0243	0.0237	0.0248	0.0218	0.0235	0.0275	0.0280	0.0271	0.0276	0.0287	0.0302	0.0212	0.0225	0.0254	0.0274	0.0256	0.0241	0.0284	0.0240	0.0243	0.0232	0.0305
HCRF EnMAP green (549 nm)	0.0415	0.0404	0.0416	0.0388	0.0389	0.0470	0.0455	0.0437	0.0452	0.0447	0.0469	0.0343	0.0376	0.0437	0.0442	0.0427	0.0415	0.0472	0.0414	0.0423	0.0394	0.0489
HCRF EnMAP rot (672 nm)	0.0601	0.0581	0.0587	0.0566	0.0585	0.0687	0.0708	0.0669	0.0708	0.0700	0.0710	0.0558	0.0565	0.0637	0.0670	0.0654	0.0638	0.0699	0.0613	0.0599	0.0560	0.0718
HCRF EnMAP NIR (864 nm)	0.2447	0.2318	0.2265	0.2289	0.2316	0.2676	0.2705	0.2469	0.2745	0.2666	0.2589	0.2046	0.2056	0.2486	0.2604	0.2601	0.2617	0.2671	0.2387	0.2382	0.2090	0.2612
ANIF EnMAP rot (672 nm)	1.0307	0.9960	1.0056	0.9700	1.0021	1.1773	1.2136	1.1470	1.2137	1.1995	1.2165	0.9566	0.9678	1.0920	1.1478	1.1211	1.0937	1.1977	1.0501	1.0275	0.9595	1.2302
ANIF EnMAP NIR (864 nm)	1.1077	1.0493	1.0253	1.0361	1.0482	1.2112	1.2247	1.1179	1.2427	1.2069	1.1720	0.9261	0.9305	1.1252	1.1789	1.1773	1.1849	1.2090	1.0805	1.0784	0.9461	1.1822
Rel. Blue Absorption Depth	0.4179	0.4069	0.4145	0.4519	0.3767	0.4159	0.3804	0.3640	0.3656	0.3324	0.3324	0.3692	0.3912	0.4169	0.3638	0.3962	0.4126	0.4008	0.4131	0.4318	0.4095	0.3586
Rel. Red Absorption Depth	1.0354	1.0073	0.9644	1.0299	1.0274	0.9919	1.0074	0.9581	1.0023	0.9788	0.9477	0.9048	0.8859	0.9628	0.9772	0.9836	1.0402	0.9528	0.9705	1.0133	0.9180	0.9226
NDVI (EnMAP)	0.6055	0.5991	0.5885	0.6035	0.5968	0.5915	0.5852	0.5736	0.5899	0.5842	0.5697	0.5714	0.5690	0.5920	0.5909	0.5981	0.6080	0.5853	0.5915	0.5979	0.5775	0.5689
Nadir Norm. NDVI (AVHRR)	1.0138	1.0106	0.9917	1.0199	1.0053	1.0011	0.9961	0.9729	1.0068	0.9975	0.9703	0.9854	0.9745	1.0030	1.0071	1.0199	1.0347	0.9928	1.0013	1.0060	0.9746	0.9666
Nadir Norm. NDVI (MODIS)	1.0178	1.0143	0.9930	1.0242	1.0066	1.0042	0.9960	0.9694	1.0030	0.9922	0.9648	0.9808	0.9735	1.0050	1.0055	1.0195	1.0339	0.9948	1.0067	1.0116	0.9789	0.9685
Nadir Norm. NDVI (EnMAP)	1.0400	1.0291	1.0110	1.0367	1.0252	1.0160	1.0052	0.9853	1.0133	1.0035	0.9786	0.9814	0.9774	1.0169	1.0150	1.0274	1.0444	1.0053	1.0160	1.0271	0.9920	0.9771

(cont.)

VDG2_02 (SZA = 64°; SAA = 143°)	Viewing Geometry (Viewing Zenith Angle | Viewing Azimuth Angle)																							
	20|135	20|157.5	20|170	30|180	30|190	30|202.5	30|225	30|270	30|315	30|337.5	30|350	30|0	30|10	30|22.5	30|45	30|90	30|135	30|157.5	30|170			
HCRF EnMAP blue (479 nm)	0.0305	0.0306	0.0261	0.0344	0.0301	0.0293	0.0301	0.0267	0.0298	0.0262	0.0263	0.0262	0.0252	0.0249	0.0265	0.0282	0.0345	0.0299	0.0342					
HCRF EnMAP green (549 nm)	0.0489	0.0535	0.0448	0.0564	0.0526	0.0481	0.0519	0.0418	0.0469	0.0435	0.0458	0.0442	0.0414	0.0413	0.0445	0.0458	0.0553	0.0499	0.0564					
HCRF EnMAP rot (672 nm)	0.0718	0.0747	0.0659	0.0865	0.0753	0.0732	0.0725	0.0633	0.0692	0.0638	0.0650	0.0625	0.0589	0.0576	0.0647	0.0679	0.0832	0.0763	0.0859					
HCRF EnMAP NIR (864 nm)	0.2612	0.2790	0.2465	0.2987	0.2642	0.2532	0.2576	0.2292	0.2618	0.2468	0.2575	0.2465	0.2390	0.2370	0.2356	0.2514	0.2735	0.2600	0.3029					
ANIF EnMAP rot (672 nm)	1.2302	1.2796	1.1290	1.4829	1.2911	1.2544	1.2420	1.0848	1.1863	1.0932	1.1138	1.0704	1.0092	0.9866	1.1085	1.1635	1.4255	1.3080	1.4726					
ANIF EnMAP NIR (864 nm)	1.1822	1.2629	1.1159	1.3522	1.1961	1.1461	1.1663	1.0375	1.1851	1.1171	1.1654	1.1157	1.0817	1.0727	1.0864	1.1382	1.2383	1.1772	1.3713					
Rel. Blue Absorption Depth	0.3586	0.4239	0.4047	0.3709	0.4153	0.3833	0.4256	0.3444	0.3511	0.3933	0.4229	0.4021	0.3883	0.3966	0.3923	0.3801	0.3674	0.3974	0.3768					
Rel. Red Absorption Depth	0.9226	0.9376	0.9600	0.8746	0.8610	0.8427	0.8407	0.9053	0.9615	0.9638	0.9869	1.0058	1.0309	1.0640	0.9060	0.9729	0.8118	0.8579	0.9109					
NDVI (EnMAP)	0.5689	0.5778	0.5783	0.5509	0.5563	0.5515	0.5610	0.5672	0.5818	0.5893	0.5969	0.5957	0.6046	0.6092	0.5692	0.5749	0.5337	0.5463	0.5581					
Nadir Norm. NDVI (AVHRR)	0.9666	0.9657	0.9763	0.9454	0.9523	0.9496	0.9482	0.9707	0.9866	0.9970	1.0048	0.9969	1.0110	1.0199	0.9702	0.9720	0.9166	0.9304	0.9546					
Nadir Norm. NDVI (MODIS)	0.9685	0.9682	0.9749	0.9430	0.9490	0.9470	0.9542	0.9710	0.9884	1.0054	1.0058	1.0052	1.0148	1.0208	0.9723	0.9725	0.9163	0.9314	0.9536					
Nadir Norm. NDVI (EnMAP)	0.9771	0.9925	0.9933	0.9462	0.9556	0.9474	0.9637	0.9743	0.9995	1.0122	1.0254	1.0232	1.0386	1.0464	0.9778	0.9875	0.9168	0.9383	0.9587					

Table C.8-4: Spectro-directional data of the VDG2_03 spectro-goniometer measurement.

VDG2_03 (SZA = 61°; SAA = 164°)	Viewing Geometry (Viewing Zenith Angle | Viewing Azimuth Angle)																							
	0|0	5|180	5|202.5	5|225	5|270	5|315	5|337.5	5|0	5|22.5	5|45	5|90	5|135	5|157.5	10|180	10|202.5	10|225	10|270	10|315	10|337.5	10|350
HCRF EnMAP blue (479 nm)	0.0277	0.0316	0.0298	0.0313	0.0303	0.0315	0.0309	0.0303	0.0299	0.0266	0.0282	0.0301	0.0316	0.0315	0.0334	0.0319	0.0341	0.0319	0.0302	0.0362	0.0290
HCRF EnMAP green (549 nm)	0.0486	0.0522	0.0469	0.0532	0.0478	0.0526	0.0509	0.0493	0.0490	0.0435	0.0478	0.0501	0.0529	0.0502	0.0548	0.0520	0.0558	0.0501	0.0496	0.0592	0.0485
HCRF EnMAP rot (672 nm)	0.0679	0.0773	0.0742	0.0798	0.0737	0.0771	0.0782	0.0730	0.0749	0.0670	0.0717	0.0733	0.0769	0.0796	0.0810	0.0825	0.0848	0.0763	0.0795	0.0869	0.0725
HCRF EnMAP NIR (864 nm)	0.2479	0.2716	0.2737	0.2669	0.2546	0.2756	0.2658	0.2588	0.2764	0.2514	0.2623	0.2580	0.2647	0.2889	0.2859	0.2815	0.2810	0.2645	0.2762	0.2935	0.2532
ANIF EnMAP rot (672 nm)	1.0000	1.1389	1.0935	1.1764	1.0856	1.1352	1.1519	1.0749	1.1038	0.9877	1.0563	1.0792	1.1322	1.1731	1.1938	1.2154	1.2495	1.1247	1.1706	1.2796	1.0682
ANIF EnMAP NIR (864 nm)	1.0000	1.0958	1.1043	1.0766	1.0271	1.1120	1.0723	1.0440	1.1152	1.0141	1.0583	1.0407	1.0679	1.1656	1.1536	1.1356	1.1337	1.0671	1.1141	1.1839	1.0216
Rel. Blue Absorption Depth	0.4274	0.4028	0.3520	0.4210	0.3576	0.3999	0.3962	0.3625	0.3795	0.3775	0.4173	0.3939	0.3987	0.3673	0.3897	0.3762	0.3933	0.3595	0.3865	0.3892	0.3969
Rel. Red Absorption Depth	0.9520	0.9175	0.9862	0.8617	0.8710	0.8974	0.8455	0.8917	0.9732	0.9778	0.9445	0.8692	0.8678	0.9536	0.9144	0.8890	0.8388	0.8767	0.8875	0.8333	0.8707
NDVI (EnMAP)	0.5701	0.5569	0.5734	0.5394	0.5511	0.5630	0.5454	0.5601	0.5735	0.5789	0.5707	0.5577	0.5500	0.5679	0.5584	0.5467	0.5363	0.5521	0.5531	0.5433	0.5548
Nadir Norm. NDVI (AVHRR)	1.0000	0.9945	1.0300	0.9692	0.9857	0.9925	0.9806	1.0051	1.0262	1.0368	1.0150	0.9963	0.9782	1.0251	0.9937	0.9909	0.9684	0.9880	1.0003	0.9740	0.9928
Nadir Norm. NDVI (MODIS)	1.0000	0.9913	1.0189	0.9656	0.9807	0.9945	0.9800	1.0039	1.0230	1.0308	1.0138	0.9971	0.9798	1.0165	0.9900	0.9853	0.9648	0.9840	0.9982	0.9749	0.9936
Nadir Norm. NDVI (EnMAP)	1.0000	0.9769	1.0058	0.9462	0.9667	0.9877	0.9567	0.9826	1.0061	1.0155	1.0011	0.9783	0.9648	0.9962	0.9795	0.9590	0.9408	0.9684	0.9703	0.9530	0.9732

(cont.)

VDG2_03 (SZA = 61°; SAA = 164°)	Viewing Geometry (Viewing Zenith Angle | Viewing Azimuth Angle)																							
	10|0	10|10	10|22.5	10|45	10|90	10|135	10|157.5	10|170	20|180	20|190	20|202.5	20|225	20|270	20|315	20|337.5	20|350	20|0	20|10	20|22.5	20|45	20|90
HCRF EnMAP blue (479 nm)	0.0286	0.0312	0.0297	0.0286	0.0317	0.0341	0.0379	0.0319	0.0384	0.0367	0.0369	0.0373	0.0305	0.0319	0.0324	0.0298	0.0300	0.0282	0.0280	0.0297	0.0340
HCRF EnMAP green (549 nm)	0.0492	0.0509	0.0490	0.0478	0.0509	0.0587	0.0612	0.0533	0.0614	0.0597	0.0599	0.0643	0.0496	0.0521	0.0527	0.0470	0.0451	0.0447	0.0463	0.0482	0.0546
HCRF EnMAP rot (672 nm)	0.0726	0.0728	0.0732	0.0739	0.0787	0.0827	0.0907	0.0822	0.0924	0.0989	0.0931	0.0928	0.0768	0.0780	0.0797	0.0712	0.0703	0.0676	0.0703	0.0754	0.0858
HCRF EnMAP NIR (864 nm)	0.2677	0.2716	0.2789	0.2747	0.2765	0.2920	0.3282	0.2900	0.3078	0.3314	0.3102	0.3008	0.2645	0.2897	0.2881	0.2683	0.2686	0.2629	0.2669	0.2590	0.2971
ANIF EnMAP rot (672 nm)	1.0697	1.0726	1.0789	1.0892	1.1599	1.2187	1.3360	1.2108	1.3606	1.4563	1.3715	1.3669	1.1308	1.1489	1.1747	1.0496	1.0351	0.9956	1.0357	1.1108	1.2637
ANIF EnMAP NIR (864 nm)	1.0801	1.0959	1.1251	1.1083	1.1155	1.1780	1.3239	1.1698	1.2419	1.3371	1.2514	1.2137	1.0672	1.1688	1.1623	1.0823	1.0837	1.0605	1.0766	1.0450	1.1987
Rel. Blue Absorption Depth	0.4207	0.3777	0.3739	0.3997	0.3645	0.4190	0.3738	0.4061	0.3725	0.3758	0.3845	0.4334	0.3756	0.3797	0.3850	0.3571	0.3301	0.3671	0.4004	0.3675	0.3607
Rel. Red Absorption Depth	0.9415	0.9621	0.9696	0.9580	0.8972	0.9008	0.9719	0.9167	0.8384	0.8768	0.8508	0.8186	0.8521	0.9339	0.9178	0.9735	0.9912	1.0178	0.9797	0.8656	0.9069
NDVI (EnMAP)	0.5733	0.5773	0.5840	0.5759	0.5567	0.5585	0.5670	0.5583	0.5384	0.5405	0.5383	0.5286	0.5502	0.5758	0.5664	0.5803	0.5853	0.5910	0.5830	0.5491	0.5520
Nadir Norm. NDVI (AVHRR)	1.0216	1.0218	1.0435	1.0349	0.9993	0.9870	1.0104	1.0108	0.9659	0.9881	0.9726	0.9392	0.9883	1.0279	1.0145	1.0326	1.0468	1.0481	1.0396	0.9985	0.9915
Nadir Norm. NDVI (MODIS)	1.0206	1.0203	1.0424	1.0285	0.9961	0.9855	1.0049	1.0058	0.9628	0.9790	0.9712	0.9378	0.9861	1.0315	1.0127	1.0317	1.0439	1.0468	1.0380	0.9930	0.9864
Nadir Norm. NDVI (EnMAP)	1.0057	1.0127	1.0245	1.0102	0.9766	0.9797	0.9946	0.9794	0.9445	0.9482	0.9443	0.9272	0.9652	1.0101	0.9937	1.0180	1.0268	1.0367	1.0227	0.9632	0.9683

(cont.)

VDG2_03 (SZA = 61°; SAA = 164°)	Viewing Geometry (Viewing Zenith Angle | Viewing Azimuth Angle)																							
	20|135	20|157.5	20|170	30|180	30|190	30|202.5	30|225	30|270	30|315	30|337.5	30|350	30|0	30|10	30|122.5	30|45	30|90	30|135	30|157.5	30|170			
HCRF EnMAP blue (479 nm)	0.0341	0.0385	0.0353	0.0393	0.0410	0.0388	0.0381	0.0309	0.0331	0.0321	0.0328	0.0283	0.0285	0.0314	0.0312	0.0365	0.0413	0.0412	0.0410					
HCRF EnMAP green (549 nm)	0.0507	0.0642	0.0572	0.0649	0.0666	0.0670	0.0610	0.0510	0.0551	0.0510	0.0510	0.0447	0.0455	0.0517	0.0484	0.0603	0.0656	0.0694	0.0673					
HCRF EnMAP rot (672 nm)	0.0810	0.0920	0.0857	0.1032	0.1051	0.0995	0.0951	0.0762	0.0773	0.0741	0.0772	0.0682	0.0687	0.0788	0.0731	0.0902	0.1035	0.1068	0.1048					
HCRF EnMAP NIR (864 nm)	0.2808	0.3205	0.2895	0.3233	0.3544	0.3292	0.2940	0.2681	0.2796	0.2698	0.2797	0.2579	0.2550	0.2778	0.2718	0.2999	0.3480	0.3462	0.3346					
ANIF EnMAP rot (672 nm)	1.1927	1.3560	1.2627	1.5210	1.5478	1.4663	1.4012	1.1223	1.1386	1.0922	1.1371	1.0046	1.0127	1.1603	1.0775	1.3286	1.5245	1.5734	1.5433					
ANIF EnMAP NIR (864 nm)	1.1329	1.2932	1.1678	1.3042	1.4296	1.3282	1.1860	1.0817	1.1279	1.0885	1.1285	1.0406	1.0287	1.1208	1.0967	1.2099	1.4039	1.3969	1.3499					
Rel. Blue Absorption Depth	0.3125	0.3912	0.3679	0.3986	0.3858	0.4369	0.3790	0.3987	0.4007	0.3622	0.3360	0.3489	0.3563	0.3902	0.3272	0.3944	0.3550	0.3935	0.3856					
Rel. Red Absorption Depth	0.9101	0.8860	0.8555	0.8068	0.8667	0.8385	0.7764	0.8837	0.9321	0.9376	0.9264	0.9787	0.9561	0.9005	0.9771	0.8486	0.8879	0.8363	0.8070					
NDVI (EnMAP)	0.5525	0.5538	0.5431	0.5159	0.5426	0.5358	0.5111	0.5575	0.5669	0.5689	0.5675	0.5818	0.5753	0.5583	0.5760	0.5376	0.5416	0.5285	0.5232					
Nadir Norm. NDVI (AVHRR)	0.9970	0.9912	0.9762	0.9372	0.9808	0.9641	0.9419	0.9984	1.0035	1.0047	1.0111	1.0343	1.0237	1.0081	1.0226	0.9653	0.9792	0.9532	0.9468					
Nadir Norm. NDVI (MODIS)	0.9889	0.9899	0.9716	0.9316	0.9761	0.9631	0.9398	0.9962	1.0077	1.0058	1.0122	1.0336	1.0235	1.0053	1.0247	0.9661	0.9741	0.9489	0.9393					
Nadir Norm. NDVI (EnMAP)	0.9691	0.9715	0.9527	0.9050	0.9519	0.9398	0.8966	0.9780	0.9944	0.9980	0.9955	1.0206	1.0092	0.9793	1.0104	0.9431	0.9501	0.9272	0.9177					

V *Main Spectral Characteristics*

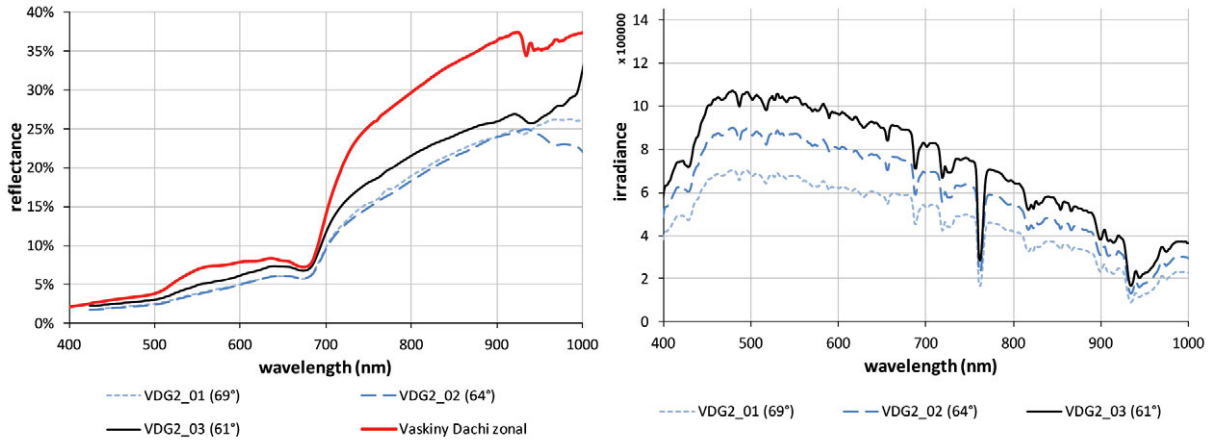

Figure C.8-6: Nadir reflectances and irradiance profiles of the VDG2 site at different sun zenith angles. Left: Comparison of the nadir reflectance signatures with the average zonal vegetation. Right: Comparison of the total irradiance profiles.

VI *HCRF Visualization*

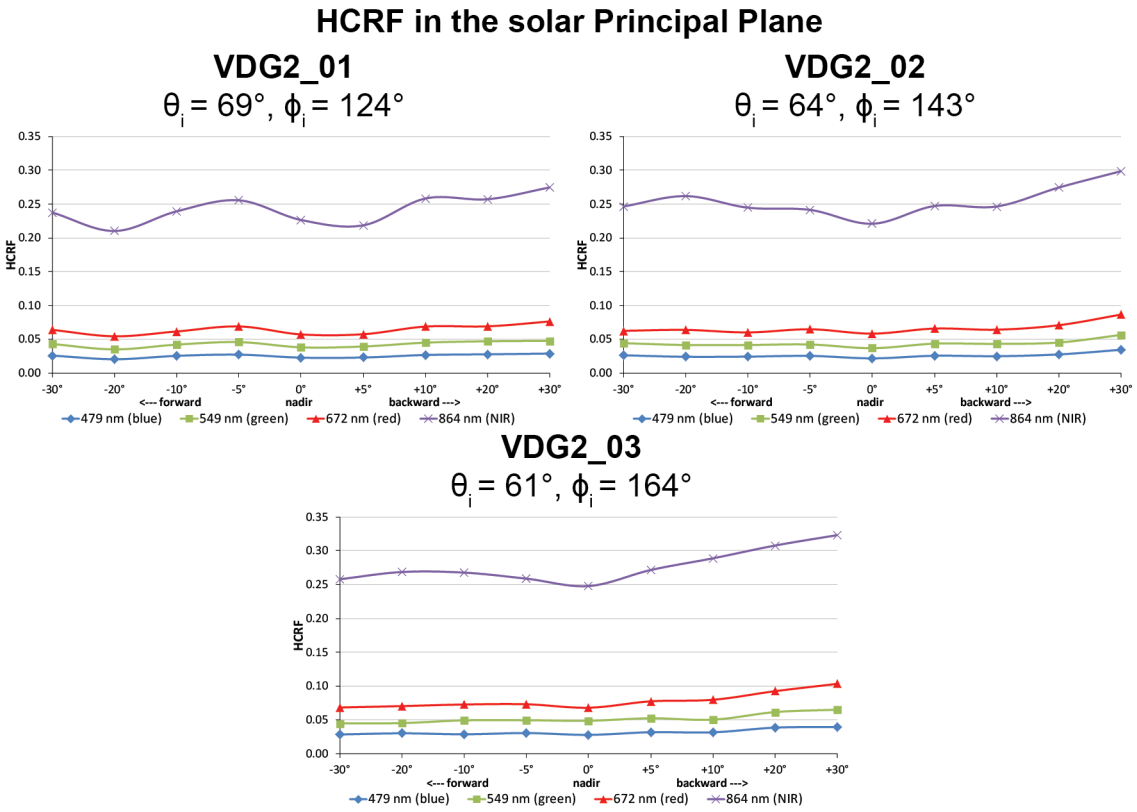

Figure C.8-7: Comparison of the HCRF values at 479 nm (blue), 549 nm (green), 672 nm (red), and 864 nm (NIR) in the solar principal plane of the VDG2 site at different sun zenith angles.

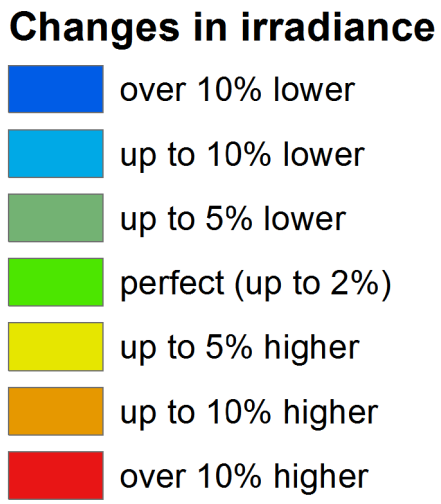

Figure C.8-8: Legend of the outlier indicator graphics shown in Figure C.8-9, C.8-10, and C.8-13

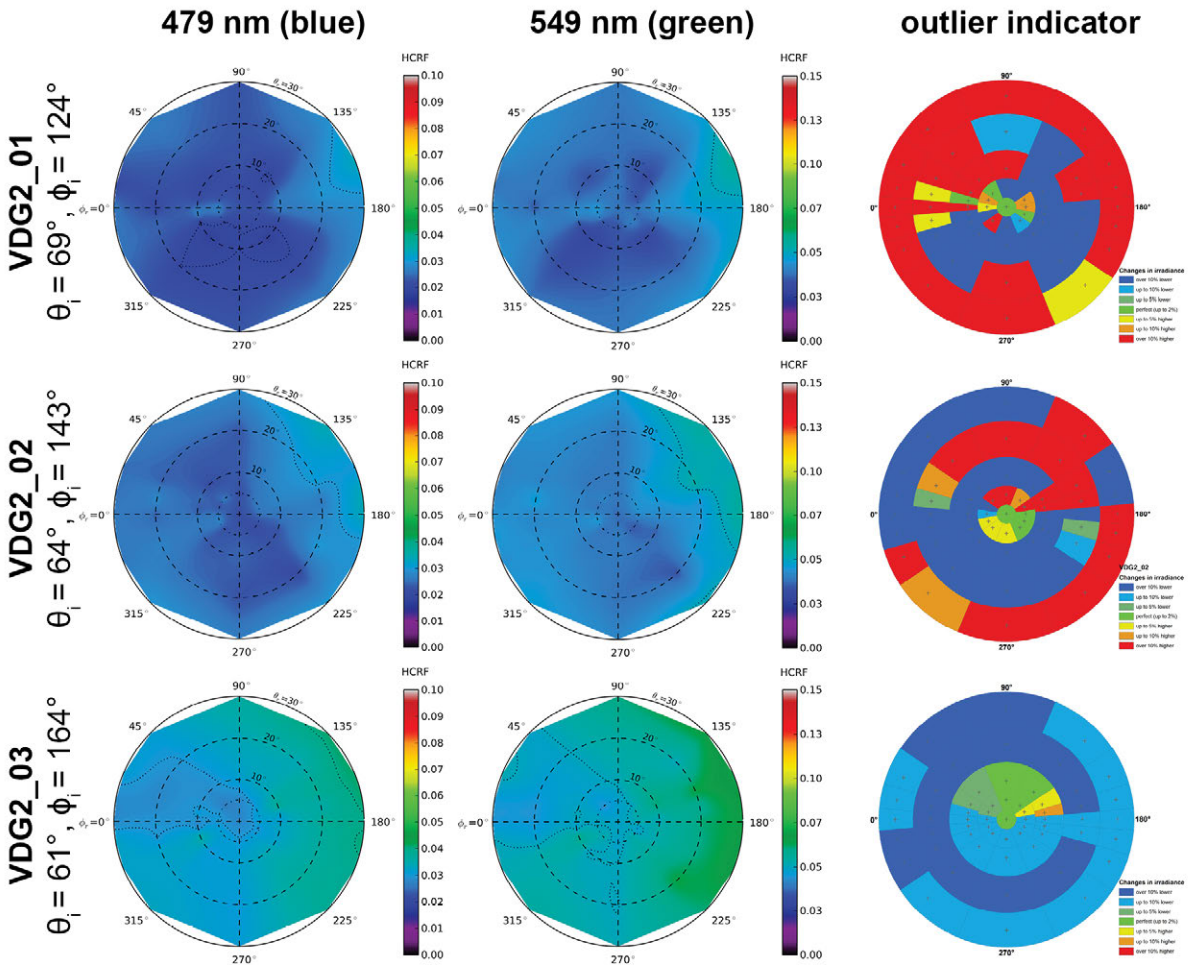

Figure C.8-9: HCRF visualization at 479 nm and 549 nm of the VDG2 site.

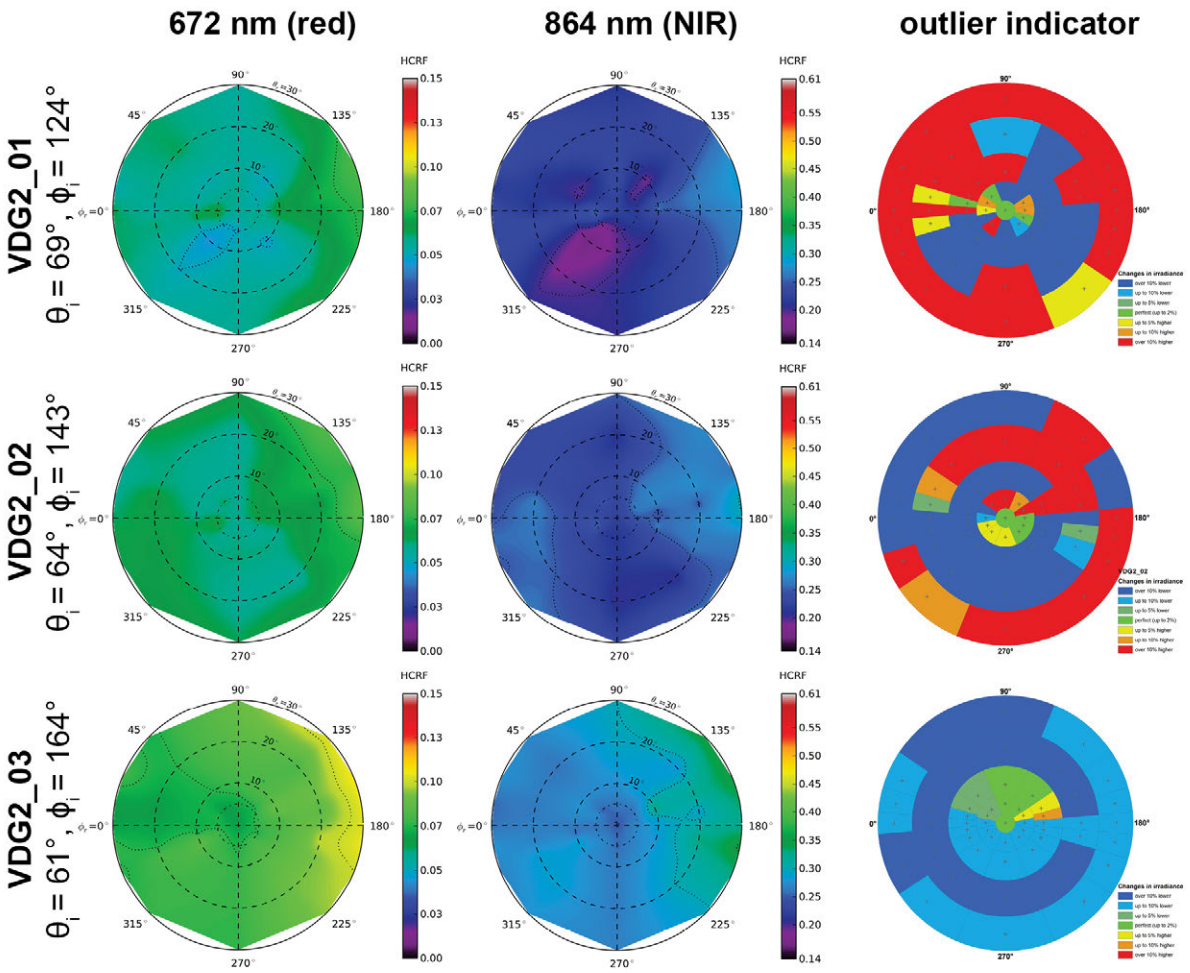

Figure C.8-10: HCRF visualization at 672 nm and 864 nm of the VDG2 site.

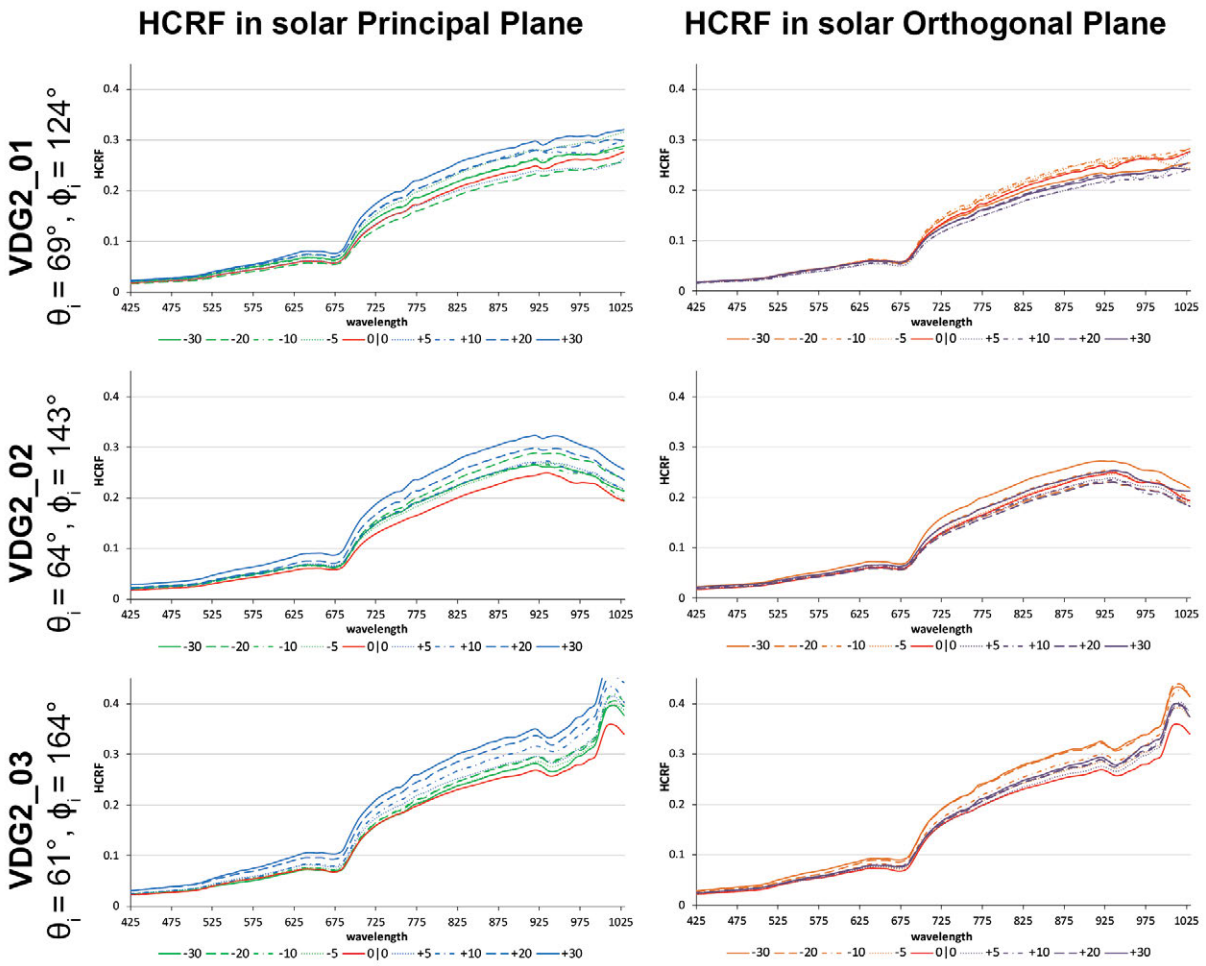

Figure C.8-11: HCRF visualization in principal & orthogonal plane of the VDG2 site.

VII *ANIF Visualization*

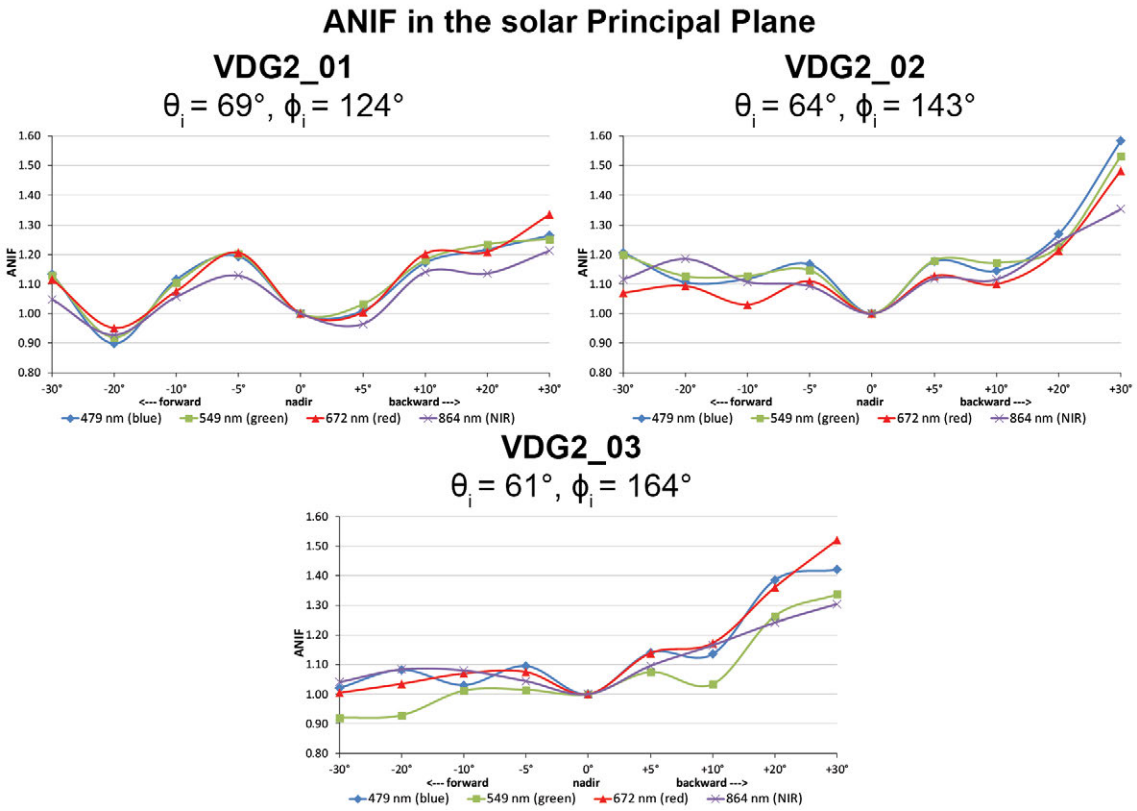

Figure C.8-12: Comparison of the ANIF values at 479 nm (blue), 549 nm (green), 672 nm (red), and 864 nm (NIR) in the solar principal plane of the VDG2 site at different sun zenith angles.

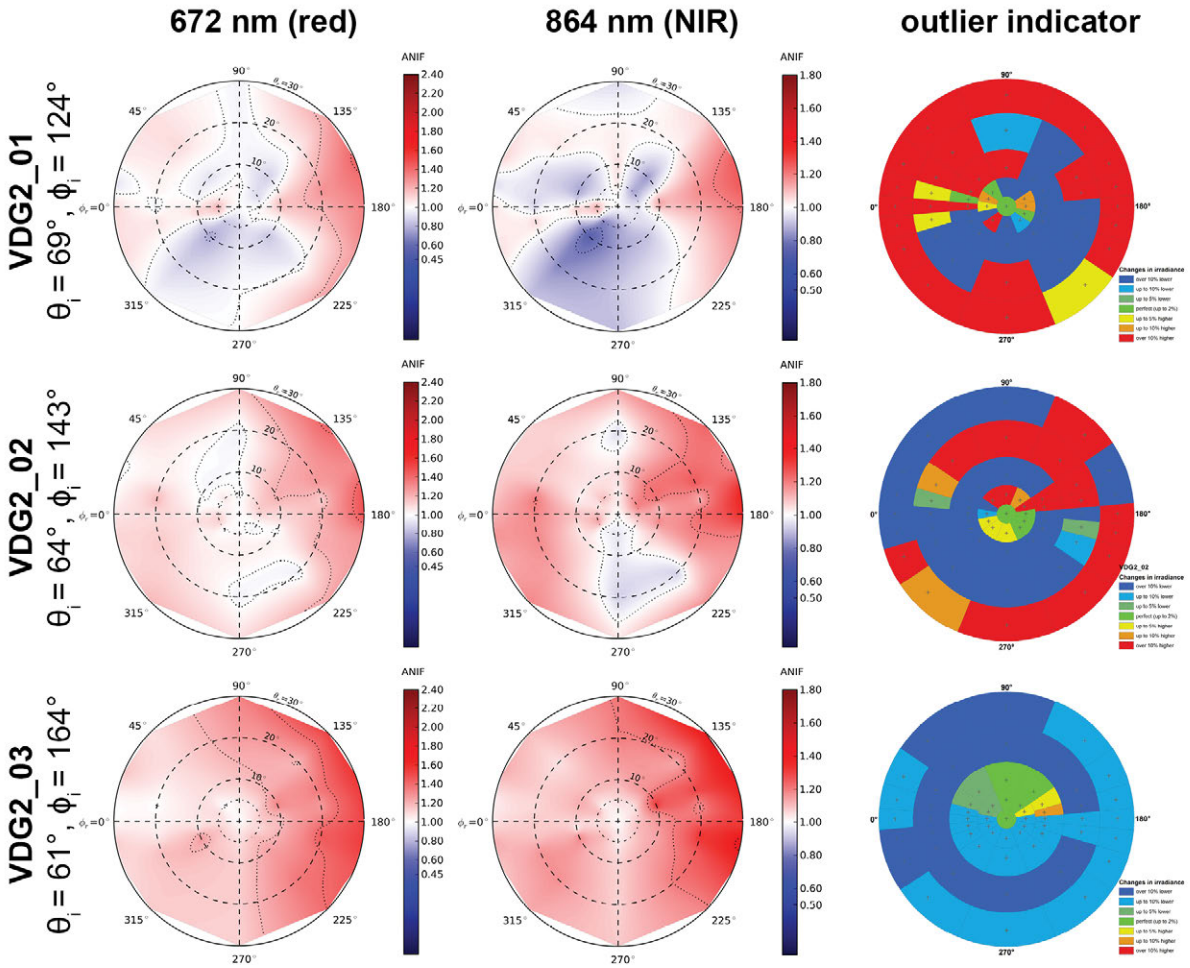

Figure C.8-13: ANIF visualization at 672 nm and 864 nm of the VDG2 site.

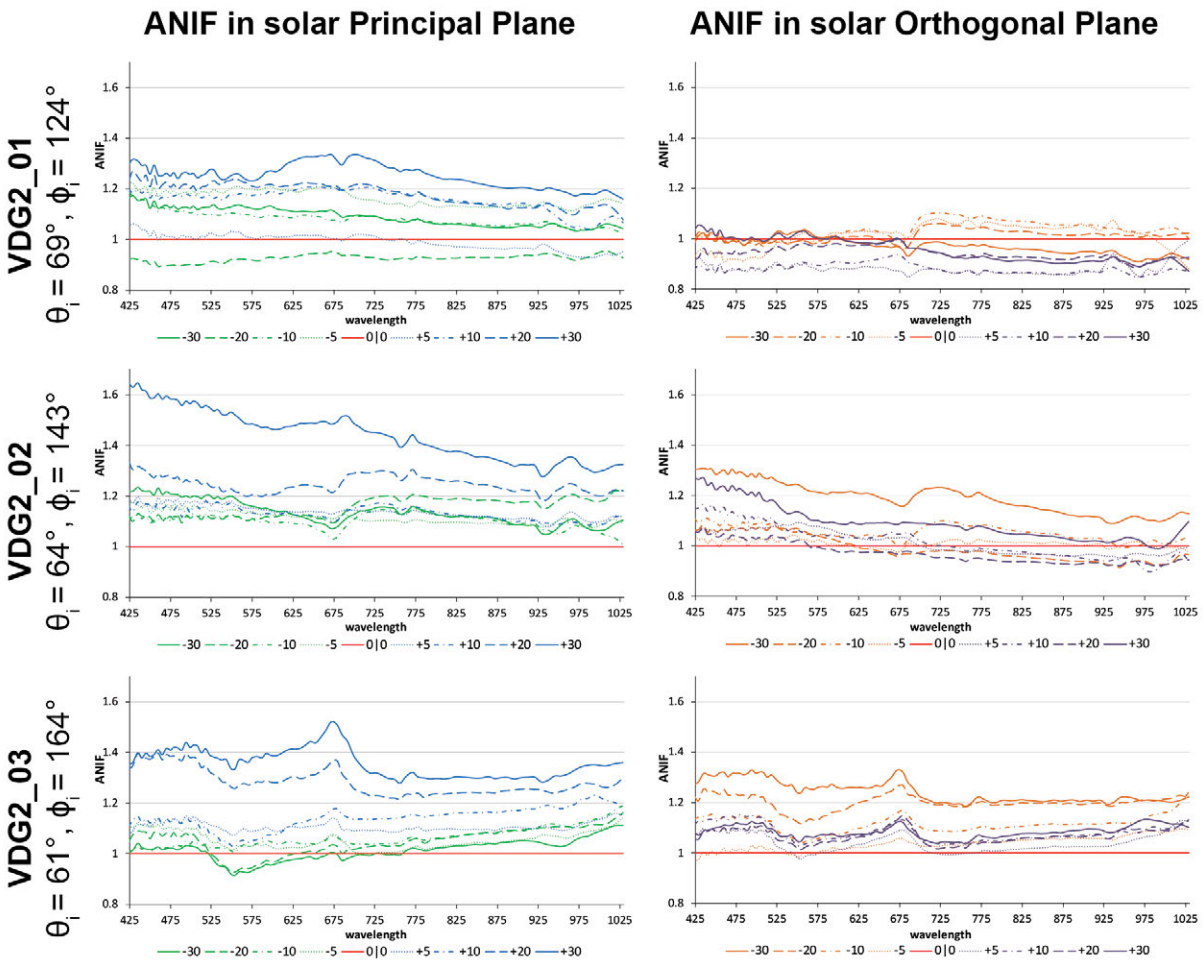

Figure C.8-14: ANIF visualization in principal & orthogonal plane of the VDG2 site.

VIII *ANIX Visualization*

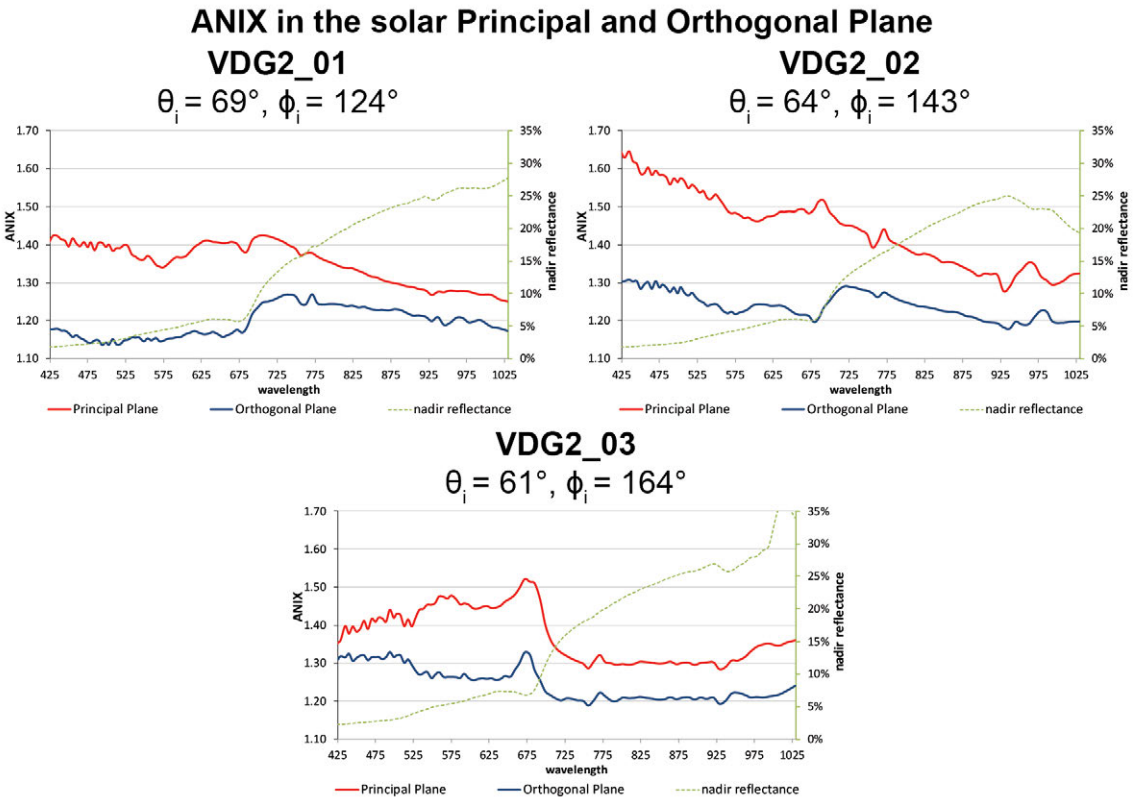

Figure C.8-15: Comparison of the ANIX in the solar principal and orthogonal plane with the nadir reflectance of the VDG2 site at different sun zenith angles.

IX *NDVI and Relative Absorption Depth Visualization*

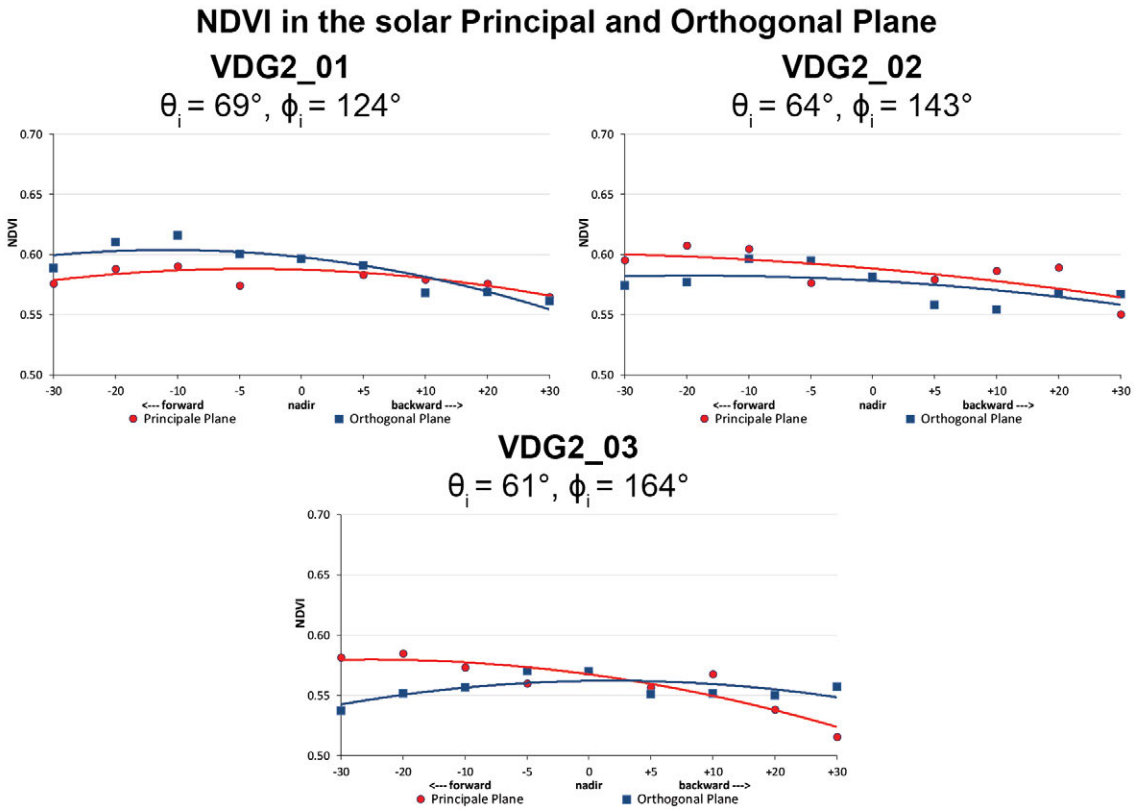

Figure C.8-16: Comparison of the NDVI in the solar principal and orthogonal plane of the VDG2 site at different sun zenith angles.

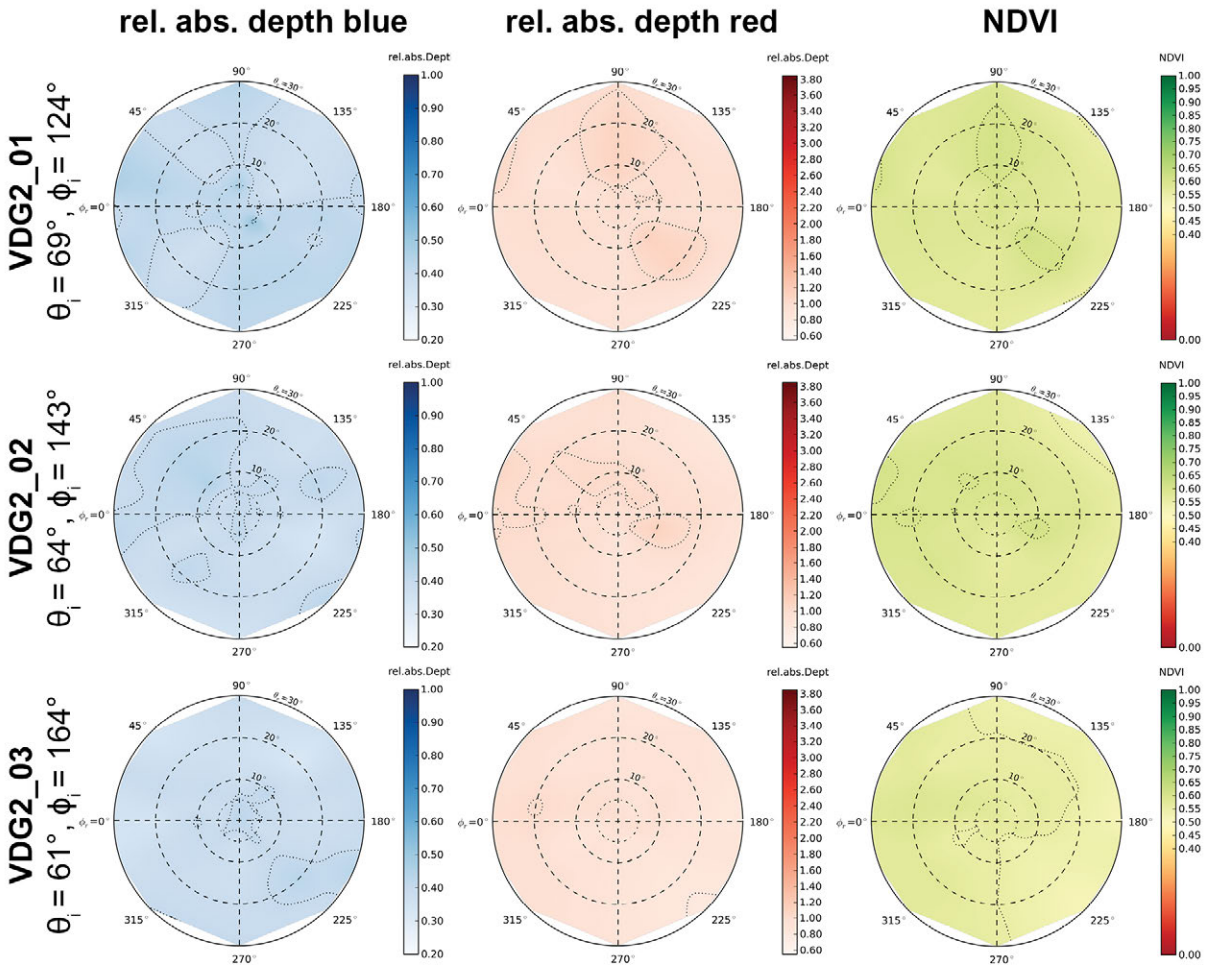

Figure C.8-17: Visualization of relative absorption depth & NDVI of the VDG2 site.

X *NDVI Comparison of Different Sensors*

Table C.8-5: Center wavelengths and band widths of the broadband and narrowband NDVIs, based on the spectral response curves of the AVHRR, MODIS and EnMAP sensors.

NDVI	Sensor	Sensor band	Center wavelength (nm)	band width (nm)
$NDVI_{AVHRR}$ [broadband]	AVHRR/3	red: band 1 NIR: band 2	630 865	100 275
$NDVI_{MODIS}$ [broadband]	MODIS	red: band 1 NIR: band 2	645 859	50 35
$NDVI_{EnMAP}$ [narrowband]	EnMAP	red: band 47 NIR: band 73	672 864	6.5 8

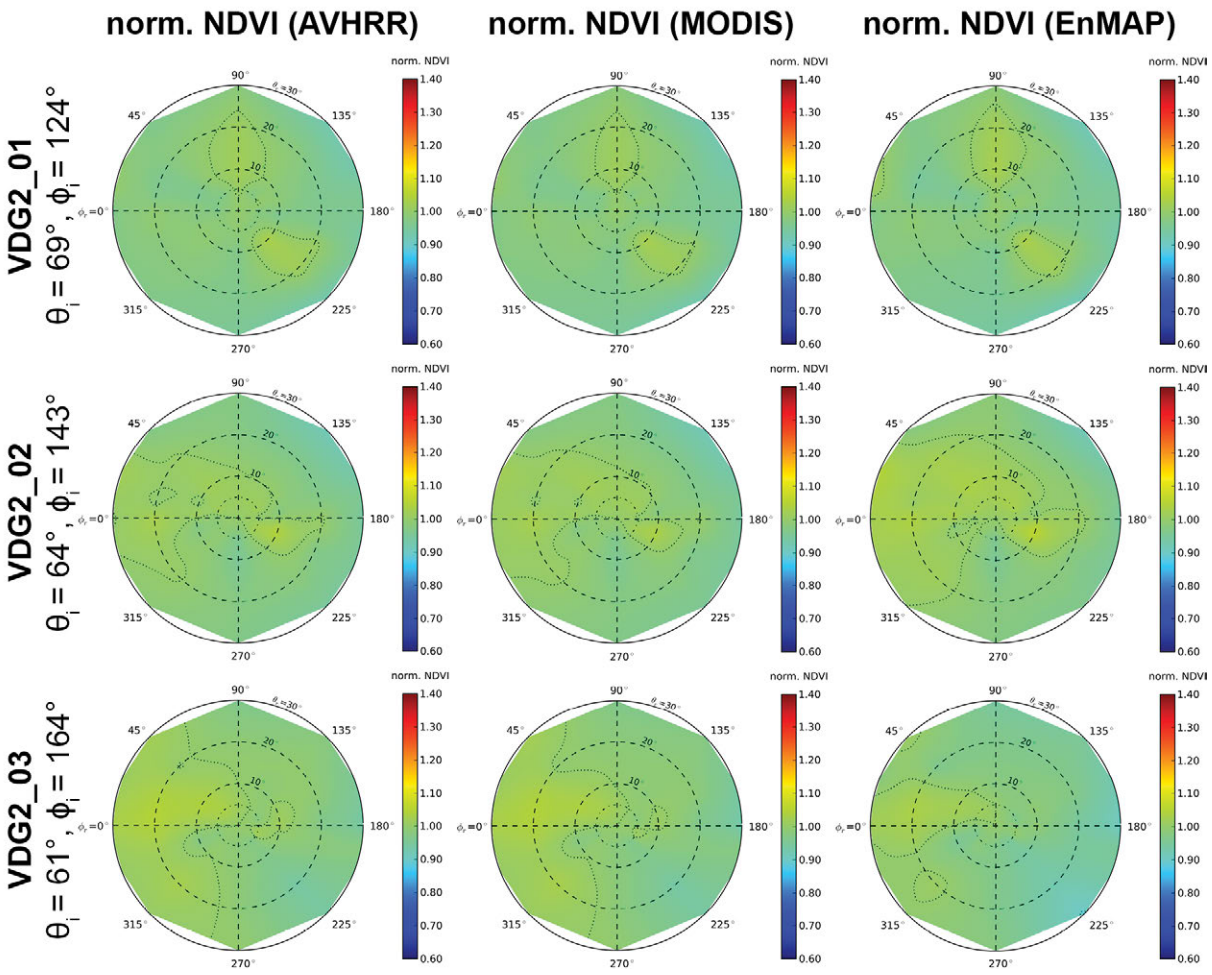

Figure C.8-18: Comparison of AVHRR, MODIS & EnMAP NDVI of the VDG2 site.

References of the Appendix

Anderson, K., H. Croft, E. J. Milton, and N. J. Kuhn (2012), A simple spectro-goniometer for collection of multiple view angle reflectance factors, *Remote Sensing Letters, 3*(2), 131–140.

Apel, O., C. Goerling, U. Leinhos, K. R. Mann, B. Schaefer, G. J. Exarhos, A. H. Guenther, M. R. Kozlowski, K. L. Lewis, and M. J. Soileau (2001), CHARISMA: a new way for angular-resolved scattering measurements, in *Laser-Induced Damage in Optical Materials: 2000, SPIE Proceedings*, pp. 569–578, SPIE.

Asmail, C. C., C. L. Cromer, J. Proctor, J. J. Hsia, and R. P. Breault (1994), Instrumentation at the National Institue of Standards and Technology for bidirectional reflectance distribution function (BRDF) measurements, in *SPIE's 1994 International Symposium on Optics, Imaging, and Instrumentation, SPIE Proceedings*, pp. 52–61, SPIE.

Baribeau, R., É. Côté, and W. S. Neil (2008), NRC robot-based gonioreflectometer for spectral BRDF measurement, *Conference on Colour in Graphics, Imaging, and Vision, 2008*(1), 457–460, http://www.ingentaconnect.com/content/ist/cgiv/2008/00002008/00000001/art00098.

Barreda, J. E., J. Knudson, D. A. Walker, M. K. Raynolds, A. Kade, and C. Munger (2006), *Biocomplexity of Patterned Ground Data Report Dalton Highway, 2001-2005*, Fairbanks.

Bausch, W., D. Lund, and M. Blue (1989), Robotic data acquisition of directional reflectance factors, *Remote Sensing of Environment, 30*(2), 159–168.

Biliouris, D., K. Vom Berge, S. Fleck, K. Nackaerts, P. Dutre, B. Muys, Y. Willems, and P. Coppin (2003), CLabSpeG: a compact laboratory spectro-goniometer system enabling rapid and complete BRDF assessments of forest elements, in *IGARSS 2003. 2003 IEEE International Geoscience and Remote Sensing Symposium*, pp. 4422–4424.

Bourgeois, C. S., A. Ohmura, K. Schroff, H.-J. Frei, and P. Calanca (2006), IAC ETH Goniospectrometer: A Tool for Hyperspectral HDRF Measurements, *J. Atmos. Oceanic Technol, 23*(4), 573–584.

Bruegge, C. J., M. C. Helmlinger, J. E. Conel, B. J. Gaitley, and W. A. Abdou (2000), PARABOLA III: A sphere-scanning radiometer for field determination of surface anisotropic reflectance functions, *Remote Sensing Reviews, 19*(1), 75–94.

Buchhorn, M., and R. Petereit (2011), *Transportables Goniospektrometer mit konstantem Observationszentrum, G01N 21/55 (2011.01)*(DE102011117713.A1), 22pp.

Buchhorn, M., and M. Schwieder (2012), Expedition "EyeSight-NAAT-Alaska" 2012, in *Expeditions to permafrost 2012 : "Alaskan North Slope/Itkillik", "Thermokarst in Central Yakutia", "EyeSight-NAAT-Alaska", Berichte zur Polar- und Meeresforschung = Reports on polar and marine research*, pp. 41–65, Alfred-Wegener-Inst. für Polar- und Meeresforschung. Bremerhaven.

Coburn, C. A., and D. R. Peddle (2006), A low-cost field and laboratory goniometer system for estimating hyperspectral bidirectional reflectance, *Canadian Journal of Remote Sensing, 32*(3), 244–253, http://article.pubs.nrc-cnrc.gc.ca/RPAS/RPViewDoc?_handler_=HandleInitialGet&calyLang=eng&journal=cjrs&volume=32&articleFile=m06-021.pdf.

Combes, D., L. Bousquet, S. Jacquemoud, H. Sinoquet, C. Varlet-Grancher, and I. Moya (2007), A new spectrogoniophotometer to measure leaf spectral and directional optical properties, *Remote Sensing of Environment, 109*(1), 107–117.

Czapla-Myers, J. S., K. J. Thome, S. F. Biggar, M. R. Descour, and S. S. Shen (2002), Optical sensor package for multiangle measurements of surface reflectance, in *International Symposium on Optical Science and Technology, SPIE Proceedings*, pp. 326–333, SPIE.

Dangel, S., M. Kneubuhler, R. Kohler, M. Schaepman, J. Schopfer, G. Schaepman-Strub, and K. Itten (2003), Combined field and laboratory goniometer system - FIGOS and LAGOS, in *IGARSS 2003. 2003 IEEE International Geoscience and Remote Sensing Symposium*, pp. 4428–4430.

Deering, D. W., and P. Leone (1986), A sphere-scanning radiometer for rapid directional measurements of sky and ground radiance, *Remote Sensing of Environment, 19*(1), 1–24.

Demircan, A., R. Schuster, M. Radke, M. Schönermark, and H. Röser (2000), Use of a wide angle CCD line camera for BRDF measurements, *Infrared Physics & Technology, 41*(1), 11–19.

Feingersh, T., W. Dorigo, R. Richter, and E. Ben-Dor (2005), A new model-driven correction factor for BRDF effects in HRS data, in *Proceedings of 4th EARSeL Workshop on Imaging Spectroscopy*, edited by B. Zagajewski, M. Sobczak, and M. Wrzesien, pp. 501–511.

Fiorentin, P., and A. Scroccaro (2008), Analysis of the Performance of a Goniometer for Studying Surface Reflection, *IEEE Trans. Instrum. Meas, 57*(11), 2522–2527.

Gibbs, D. P., C. L. Betty, A. K. Fung, A. J. Blanchard, J. R. Irons, and W. L. Balsam (1993), Automated measurement of polarized bidirectional reflectance, *Remote Sensing of Environment, 43*(1), 97–114.

Hahlweg, C., H. Rothe, A. Duparré, R. Geyl, and L. Wang (2005), Design of a full-hemispherical spectro-radiometer with high dynamic range for characterization of surface properties using multispectral BRDF data from VIS to NIR, in *Optical Systems Design 2005, SPIE Proceedings*, pp. 596519–596519-13, SPIE.

Hakala, T., J. Suomalainen, and J. I. Peltoniemi (2010), Acquisition of Bidirectional Reflectance Factor Dataset Using a Micro Unmanned Aerial Vehicle and a Consumer Camera, *Remote Sensing, 2*(3), 819–832.

Heim, B., M. Buchhorn, and H.-W. Hubberten (2012), *YAMAL2011 Expedition from 11th July to 9th September, 2011 - Part: AWI Data Report*, Fairbanks, Alaska.

Johnson, J. R., W. M. Grundy, and M. K. Shepard (2004), Visible/near-infrared spectrogoniometric observations and modeling of dust-coated rocks, *Icarus, 171*(2), 546–556.

Kade, A., D. A. Walker, and M. K. Raynolds (2005), Plant communities and soils in cryoturbated tundra along a bioclimate gradient in the Low Arctic, Alaska, *Phytocoenologia, 35*(4), 761–820.

Koechler, C., B. Hosgood, G. Andreoli, G. Schmuck, J. Verdebout, A. Pegoraro, J. Hill, W. Mehl, D. Roberts, and M. Smith (1994), The European optical goniometric facility: technical description and first experiments on spectral unmixing, in *IGARSS '94 - 1994 IEEE International Geoscience and Remote Sensing Symposium*, edited by IEEE, pp. 2375–2377.

Landis, B., and J. S. Aber (2007), Low-cost field goniometer for multiangular reflectance measurements, *Emporia State Research Studies, 44*(1), 1–6, http://www.emporia.edu/esrs/vol44/landis.pdf.

Leroux, C., J.-L. Deuzé, P. Goloub, C. Sergent, and M. Fily (1998), Ground measurements of the polarized bidirectional reflectance of snow in the near-infrared spectral domain: Comparisons with model results, *J. Geophys. Res., 103*(D16), 19721.

Li, Z.-L., R. Zhang, X. Sun, H. Su, X. Tang, Z. Zhu, and J. A. Sobrino (2004), Experimental system for the study of the directional thermal emission of natural surfaces, *International Journal of Remote Sensing, 25*(1), 195–204.

Mazzinghi, P., M. Calzolai, L. Masotti, and I. Ambrosini (1995), A new narrow angle spectrogoniometer for the measurement of bidirectional reflectance, in *1995 International Geoscience and Remote Sensing Symposium, IGARSS '95. Quantitative Remote Sensing for Science and Applications*, pp. 2075–2077, IEEE.

Painter, T. H., B. Paden, and J. Dozier (2003), Automated spectro-goniometer: A spherical robot for the field measurement of the directional reflectance of snow, *Review of Scientific Instruments, 74*(12), 5179–5188.

Pegrum, H., N. Fox, M. Chapman, and E. Milton (2006), Design and Testing a New Instrument to Measure the Angular Reflectance of Terrestrial Surfaces, in *International Geoscience and Remote Sensing Symposium, 2006. IGARSS 2006 Proceedings*, pp. 1119–1122, IEEE. [Piscataway, NJ].

Peltoniemi, J., S. Kaasalainen, J. NARANEN, L. Matikainen, and J. PIIRONEN (2005), Measurement of directional and spectral signatures of light reflectance by snow, *IEEE Trans. Geosci. Remote Sensing, 43*(10), 2294–2304.

Roosjen, P., J. Clevers, H. Bartholomeus, M. Schaepman, G. Schaepman-Strub, H. Jalink, R. van der Schoor, and A. de Jong (2012), A Laboratory Goniometer System for Measuring Reflectance and Emittance Anisotropy, *Sensors, 12*(12), 17358–17371.

Sandmeier, S., W. Sandmeier, K. I. Itten, M. E. Schaepman, and T. W. Kellenberger (1995), Swiss field-goniometer system (FIGOS), in *International Geoscience and Remote Sensing Symposium (IGARSS)*, pp. 2078–2080.

Schaepman-Strub, G. (2004), Spectrodirectional Reflectance Analysis and Definition for the Estimation of Vegetation Variables, *Dissertation*, Universität Zürich, Zürich.

Schneider, T., S. Zimmermann, and I. Manakos (2004), Field Goniometer System for Accompanying Directional Measurements, in *Proceedings of the Second CHRIS/Proba Workshop. 28 - 30 April 2004, ESA/ESRIN, Frascati, Italy, ESA SP*, vol. 578, edited by H. Lacoste-Francis, ESA Publications Div. Noordwijk, The Netherlands.

Schopfer, J., S. Dangel, M. Kneubühler, and K. I. Itten (2008), The Improved Dual-view Field Goniometer System FIGOS, *Sensors, 8*(8), 5120–5140.

Schopfer, J. T. (2008), Spectrodirectional Ground-Based Remote Sensing Using Dual-View Goniometry. Field BRF Retrieval and Assessment of the Diffuse Irradiance Distribution in Spectrodirectional Field Measurements, *Dissertation*, Universität Zürich, Zürich.

Serrot, G., M. Bodilis, X. Briottet, and H. Cosnefroy (1998), Presentation of a new BRDF measurement device, in *Proceedings of SPIE*, pp. 34–40, SPIE.

Snyder, W. C., and Z. Wan (1996), Surface temperature correction for active infrared reflectance measurements of natural materials, *Appl. Opt., 35*(13), 2216.

Stockton, P. H., D. W. Deering, and N. K. Minnifield (1994), PARABOLA II: a field sphere-scanning radiometer for radiance measurements of sky and ground, in *SPIE's 1994 International Symposium on Optics, Imaging, and Instrumentation, SPIE Proceedings*, pp. 115–122, SPIE.

Suomalainen, J., T. Hakala, J. Peltoniemi, and E. Puttonen (2009), Polarised Multiangular Reflectance Measurements Using the Finnish Geodetic Institute Field Goniospectrometer, *Sensors, 9*(5), 3891–3907.

Susaki, J., K. Hara, K. Kajiwara, and Y. Honda (2004), Robust estimation of BRDF model parameters, *Remote Sensing of Environment, 89*(1), 63–71.

Timmermans, J., A. Ambro Gieske, C. van der Tol, W. Verhoef, and Z. Su (2009), Automated Directional Measurement System for the Acquisition of Thermal Radiative Measurements of Vegetative Canopies, *Sensors, 9*(3), 1409–1422.

Turner, M., and J. Brown (2000), The Sandmeier Field Goniometer: A Measurement Tool for Bi-Directional Reflectance, in *34th Aerospace Mechanisms Symposium*, edited by NASA Ames Research Center, pp. 167–174.

Walker, D. A., H. E. Epstein, M. O. Leibman, N. G. Moskalenko, J. P. Kuss, G. V. Matyshak, E. Kaarlejärvi, and E. M. Barbour (2009), *Data Report of the 2007 and 2008 Yamal Expeditions: Nadym, Laborovaya, Vaskiny Dachi, and Kharasavey*, AGC Data Report, Fairbanks, Alaska, USA.

Walker, D. A., H. E. Epstein, V. E. Romanovsky, C. L. Ping, G. J. Michaelson, R. P. Daanen, Y. Shur, R. A. Peterson, W. B. Krantz, M. K. Raynolds et al. (2008), Arctic patterned-ground ecosystems: A synthesis of field studies and models along a North American Arctic Transect, *J. Geophys. Res, 113*(G3).

Walker, D. A., M. K. Raynolds, F. J. A. Daniëls, E. Einarsson, A. Elvebakk, W. A. Gould, A. E. Katenin, S. S. Kholod, C. J. Markon, E. S. Melnikov et al. (2005), The Circumpolar Arctic vegetation map, *Journal of Vegetation Science, 16*(3), 267–282, http://dx.doi.org/10.1111/j.1654-1103.2005.tb02365.x.

Walker, M. D., D. A. Walker, and N. A. Auerbach (1994), Plant Communities of a Tussock Tundra Landscape in the Brooks Range Foothills, Alaska, *Journal of Vegetation Science, 5*(6), 843–866, http://www.jstor.org/stable/3236198.

Walter-Shea, E. A., C. J. Hays, M. A. Mesarch, and R. D. Jackson (1993), An improved goniometer system for calibrating field reference-reflectance panels, *Remote Sensing of Environment, 43*(2), 131–138, http://dx.doi.org/10.1016/0034-4257(93)90002-F.

Washburn, A. L. (1980), *Geocryology. A survey of periglacial processes and environments,* 406pp., Wiley, New York.

Yan, G., H. Ren, R. Hu, K. Yan, and W. Zhang (2012), A portable Multi-Angle Observation System, in *IGARSS 2012 - 2012 IEEE International Geoscience and Remote Sensing Symposium*, pp. 6916–6919.

STATUTORY DECLARATION / EIDESSTATTLICHE ERKLÄRUNG

I declare that I have developed and written the enclosed doctoral thesis entitled

Ground-Based Hyperspectral and Spectro-Directional Reflectance Characterization of Arctic Tundra Vegetation Communities – *Field Spectroscopy and Field Spectro-Goniometry of Siberian and Alaskan Tundra in Preparation of the EnMAP Satellite Mission* –

entirely by myself, that I have not used other than the declared sources / resources, and that I have explicitly marked all material which has been quoted either literally or by content from the used sources.

The dissertation has been edited by me at the Alfred Wegener Institute, Helmholtz Centre for Polar and Marine Research (AWI) in Potsdam, written in English and will be submitted for the first time and only at the University of Potsdam.

Ich versichere eidesstattlich, dass die vorliegende Doktorarbeit mit dem Titel

Ground-Based Hyperspectral and Spectro-Directional Reflectance Characterization of Arctic Tundra Vegetation Communities – *Field Spectroscopy and Field Spectro-Goniometry of Siberian and Alaskan Tundra in Preparation of the EnMAP Satellite Mission* –

von mir selbstständig verfasst wurde, andere als die angegebenen Quellen/Hilfsmittel nicht benutzt wurden, und ich die den benutzten Quellen wörtlich und inhaltlich entnommenen Stellen als solche kenntlich gemacht habe.

Die Dissertation wurde von mir am Alfred-Wegener-Institut, Helmholtz-Zentrum für Polar- und Meeresforschung (AWI) in Potsdam bearbeitet, in englischer Sprache verfasst und wird erstmalig und nur an der Universität Potsdam eingereicht.

Die dem Verfahren zugrunde liegende Promotionsordnung ist mir bekannt.

_____

Marcel Buchhorn

Potsdam, November 13, 2013